Rational design of bimetallic nanoparticles based catalysts : application for apgrading biomass

Miquel Cardona-Farreny

Université Fédérale
Toulouse Midi-Pyrénées

THÈSE

En vue de l'obtention du
DOCTORAT DE L'UNIVERSITÉ DE TOULOUSE
Délivré par l'Université Toulouse 3 - Paul Sabatier

Présentée et soutenue par

Miquel CARDONA FARRENY

Le 25 janvier 2023

Conception rationnelle de catalyseurs à base de nanoparticules bimétalliques: application à la valorisation de la biomasse.

Ecole doctorale : **SDM - SCIENCES DE LA MATIERE - Toulouse**

Spécialité : **Chimie Organométallique et de Coordination**

Unité de recherche :
LCC - Laboratoire de Chimie de Coordination

Thèse dirigée par
M. Rosa AXET MARTI et Karine PHILIPPOT

Jury

Mme Karine VIGIER DE OLIVEIRA, Rapporteure
Mme Audrey DENICOURT, Rapporteure
M. Albert POATER TEIXIDOR, Examinateur
Mme Rosa AXET MARTI, Directrice de thèse
Mme Karine PHILIPPOT, Co-directrice de thèse
Mme Katerina SOULANTIKA, Présidente

Acknowledgements

First of all, I would like to thank Dr. Katerina Soulantika, Dr. Karine Vigier de Oliveira, Dr. Audrey Denicourt and Dr. Albert Poater Teixidor for accepting to be the members of the jury of my PhD thesis.

I must continue thanking my two supervisors who guided me during this research, who put me under pressure when I was needing it and who tried to cheer me up when I needed it the most. Dr. M. Rosa Axet, moltíssimes gràcies per tot el que has fet per mi durant aquests anys, sempre seràs la meva mare científica, mai no ho oblidaré! Dr. Karine Philippot, un grand merci pour l'accueil dans l'équipe et le soutien reçu pendant ces années, parfois dans les moments les plus nécessaires.

I should continue thanking Alain Moreau, Vincent Collière, Yannick Coppel, Jerome Esvan and Pierre Lecante and all the other technical services for the help with the characterization techniques.

I would like to thank also Dr. Romuald Poteau, Dr. Iker del Rosal and Dr. Chiara Dinoi for accepting me in their team to learn how to use VASP and for all the discussions concerning DFT studies.

I would like to thank the NanoX program for giving me the opportunity to do a 3-month internship at LIKAT in Rostock (Germany). Vielen Dank an Dr. Matthias Beller und Dr. Helfried Neumann für die Aufnahme in Ihr Team und für die vielen Gespräche. Thanks to all the team for sharing moments and experience. Special thanks to Dr. Kangkang Sun, Dr. Yaxin Wang and Zhusong Cao for all the laughs, discussions and Chinese learning: Xie xie! Gràcies al Juanjo per les xerrades i menjars compartits.

I would also like to thank all the members of the team "Engineering of metal nanoparticles" for the support, discussions and helping with different tasks: Quyen, Núria, François, Lorraine, Laurent, Emmanuel, Laura, Lassané, Catherine, Tatiana… it has really been a pleasure! Gracias especialmente a Núria y a Lola por soportarme y reir juntos durante tantas y tantas horas!

Finally, moltes gràcies a la meva familia per ser sempre un recolzament moral fins i tot estant en un altre país. Un grand merci aussi à tous les frères et sœurs dans le scoutisme pour tout ce qu'on a vécu ensemble ces dernières années, spécialement dans le Chœur Scout Tolosa. Je ne peux pas, bien évidemment, finir sans remercier Cassandre : merci, merci et encore merci pour tout ce que tu as fait pour moi cette dernière année, je te serai toujours très reconnaissant ! ☺

Table of contents

Abstract

An accumulation of social, economic, and energetic crises occurring for decades drives the society to a critical situation. The dependency on fossil fuels for energy and chemicals production is noticeable and needs to be rapidly reduced by replacing those sources with renewable ones. Lignocellulosic biomass appears as a good alternative to the production of sustainable chemicals and fuels. This renewable feedstock is composed of cellulose, hemicelluloses and lignin, and can be vastly found in waste streams, wood, energy crops and agricultural residues. Liquid fuels may be produced from second generation feedstocks of biomass, which are chemically identical to the ones from petroleum, and which can be used in the same combustion engines as those present nowadays. The replacement of fossil by biomass feedstocks for the production of chemicals is of great interest for environmental purposes. This promising feedstock can produce several platform molecules, such as furfural and 5-hydroxymethylfurfural, from which a vast range of value-added compounds can be obtained.

For a better performance of these transformations, selective and effective bimetallic nanocatalysts have been developed in this work, containing earth-abundant metals, thinking about their potential incorporation in industrial processes for energy transition. For this purpose, a series of Ru bimetallic materials containing either Ni or Cu as second metal were synthesised. Several stabilisers for the nanoparticles were used such as polyvinylpyrrolidone, diphenyl-2-pyridylphosphine and hexadecylamine. The synthesis of ultra-small (< 2 nm) RuCu and RuNi bimetallic nanomaterials, as well as their monometallic counterparts, was successful, by controlling the metal ratio between metals.

RuNi/PVP nanoparticles showed synergetic effects between metals in both efficient and selective catalytic hydrogenations of furfural and 5-hydroxymethylfurfural. DFT calculations were performed to help us understand the experimental results, by modelling Ru, Ni and RuNi nanoparticles and adsorbing the different species on their surface. The results from theoretical calculations are in the line of the activity and selectivity observed in experimental catalytic experiments. RuCu/PVP nanoparticles, used as catalysts in the same hydrogenation reaction, were less performant than the corresponding monometallic counterparts, as well as the RuNi/PVP nanoparticles.

RuNi/PVP and RuNi/PPh_2Py nanoparticles were used as catalysts on the selective hydrogenation of quinoline, observing a dependence of the activity on the temperature and the Ru content. By using 1-propanol as solvent, N-alkylation of the substrate occurred, noticeably from 125 ºC.

Deuterium-labelled molecules, being a stable and safe hydrogen isotope, have received great interest in different scientific domains, especially in pharmaceutical industry for the design of new drugs. Ru/PVP nanoparticles were tested for deuteration reactions of 4-methoxyaniline, 4-trifluoromethylbenzaldehyde, methyl-2,3-O-Isopropylidene-β-D-ribofuranoside and adenosine. Deuterations were not successful in the two first substrates nor in the third, where, nevertheless, deprotection and epimerisation reactions were observed. In the case of adenosine, the deuteration took place in a selective manner.

This work offers the synthesis of new bimetallic nanomaterials with tunable properties. Some of the developed catalysts were tested in the hydrogenation of platform molecules, such as furfural and 5-hydroxymethylfurfural, and the monometallic Ru/PVP nanoparticles were used as catalysts in deuteration reactions.

Résumé

L'accumulation de crises sociales, économiques et énergétiques depuis des décennies conduit la société à une situation critique. La dépendance aux combustibles fossiles pour la production d'énergie et de produits chimiques doit être rapidement réduite en remplaçant les sources fossiles par des sources renouvelables. La biomasse lignocellulosique apparaît comme une bonne alternative pour la production de produits chimiques et de carburants durables. Cette matière première renouvelable, composée de cellulose, d'hémicelluloses et de lignine, se trouve en grande partie dans les déchets, le bois, les cultures énergétiques et les résidus agricoles. Les matières premières de deuxième génération issues de la biomasse permettent la production de carburants liquides chimiquement identiques à ceux issus du pétrole et utilisables dans les moteurs à combustion d'aujourd'hui. Utiliser la biomasse pour la production de produits chimiques est donc une voie prometteuse et d'un grand intérêt pour l'environnement. Plusieurs molécules plateformes, telles que le furfural et le 5-hydroxyméthylfurfural, sont accessibles à partir de la biomasse, pouvant conduire à une vaste gamme de composés à valeur ajoutée.

Pour réaliser ces transformations de façon performante, des nanocatalyseurs bimétalliques à base de métaux abondants ont été développés, en pensant à leur incorporation potentielle dans des processus industriels pour la transition énergétique. Une série de matériaux bimétalliques associant le Ru au Ni ou au Cu comme second métal a été synthétisée avec succès et entièrement caractérisée. Différents stabilisants ont été utilisés, tels que la polyvinylpyr-rolidone, la diphényl-2-pyridylphosphine et l'hexadécylamine, conduisant à des nanomatériaux bimétalliques RuNi et RuCu bien contrôlés et de très petite taille (< 2 nm), avec différents ratios en métaux. Des homologues monométalliques ont aussi été préparés à des fins de comparaison.

Les nanoparticules RuNi/PVP ont montré des effets synergiques entre les métaux dans l'hydrogénation catalytique efficace et sélective du furfural et du 5-hydroxyméthylfurfural. Des calculs DFT par modélisation des nanoparticules de Ru, Ni et RuNi avec adsorption de diverses espèces à leur surface ont permis de mieux comprendre les résultats expérimentaux. Les résultats obtenus confirment l'activité et la sélectivité observées en catalyse. Lorsqu'utilisées comme catalyseurs dans la même réaction d'hydrogénation, les nanoparticules de RuCu/PVP sont moins performantes que les homologues monométalliques correspondants et que les nanoparticules RuNi/PVP.

Les nanoparticules RuNi/PVP et RuNi/PPh_2Py ont également catalysé l'hydrogénation sélective de la quinoléine, en observant une dépendance de l'activité par rapport à la température et la teneur en Ru. En utilisant le 1-propanol comme solvant, la N-alkylation du substrat s'est produite de façon notable à partir de 125 ºC.

Le deutérium étant un isotope stable et sûr de l'hydrogène, les molécules marquées au deutérium suscitent un grand intérêt, notamment dans l'industrie médicinale et pharmaceutique pour la conception de nouveaux médicaments. Les nanoparticules Ru/PVP ont été testées pour la deutération d'une série de substrats modèles (4-méthoxyaniline, 4-trifluorométhylbenzaldéhyde, méthyl-2,3-O-Isopropylidène-β-D-ribofuranoside et adénosine). Malgré l'absence de deutération, des réactions intéressantes de déprotection et d'épimérisation ont été observées pour les trois premiers substrats. Avec l'adénosine, la deutération a eu lieu de manière sélective.

Ce travail décrit la synthèse de nouveaux nanomatériaux bimétalliques présentant des propriétés modulables et prometteuses pour la catalyse. L'hydrogénation de molécules dérivées de la biomasse, telles que le furfural et le 5-hydroxyméthylfurfural, a été menée avec succès. Des nanoparticules monométalliques de Ru/PVP ont également permis de catalyser des réactions de deutération.

List of abbreviations

1,2-PeD: 1,2-pentanediol

1-PrOH: 1-propanol

1-THQ: 1,2,3,4-tetrahydroquinoline

1-THPQ: 1,2,3,4-tetrahydro-n-propyl-quinoline

4-MeOAn: 4-methoxyaniline

5-THQ: 5,6,7,8-tetrahydroquinoline

ABF: annular bright field

AdCOOH: 1-adamantanecarboxylic acid

ADNS: adenosine

ATR-IR: attenuated total reflection infrared

Bα: body-centred cubic

Ca.: circa

CCD: charge coupled device

$CDCl_3$: deuterated chloroform

CEMES : Centre d'Élaboration de Matériaux et d'Etudes Structurales

$CHCl_3$: chloroform

CID : charge injection device

CIRIMAT: Centre Inter-universitaire de Recherche et d'Ingénierie des Matériaux

CO: carbon monoxide

CTAB: cetyltrimethylammonium bromide

D_2O : deuterated water

DDA: dodecylamine

DFT : density functional theory

DHPQ: decahydro-1-propyl-quinoline

DHQ: decahydroquinoline

DMF: 2,5-dimethylfuran

EDX: energy dispersive X-ray

Eq.: equivalents

Et_2O: diethyl ether

EXAFS: extended X-ray absorption fine structure

Fα: face-centred cubic

FF: furfural

FID: flame ionisation detector

FP: Fisher Porter

GC : gas chromatography

GC-MS: gas chromatography – mass spectroscopy

H_2: hydrogen

HAADF: high angle annular dark field

HAT: hydrogen atom transfer

Hcp: hexagonal close-packed

HDA: hexadecylamine

HF: furfuryl alcohol

HIE: Hydrogen Isotope Exchange

HMF: 2,5-hydroxymethylfurfural

HMTHF: tetrahydrofurfuryl alcohol

HRTEM: high resolution transmission electron microscopy

ICP-OES: inductively coupled plasma - optical emission spectroscopy

LCC: Laboratoire de Chimie de Coordination

LiAlH4 : lithium aluminium hydride

LIKAT : Leibniz Institute for Catalysis

m/z: mass-to-charge

MEBRIBOF: methyl β-D-ribofuranoside

MEF: 2-methylfuran

MOIBRIBOF: methyl 2,3-O-isopropylidene-β-D-ribofuranoside

Ms: magnetic saturation

MS: mass spectrometry

N.D.: non-determined

NMR: nuclear magnetic resonance

NP: nanoparticle

PDF: pair distribution function

PPh_2Py: diphenylphosphinopyridine

PVP: polyvinylpyrrolidone

QN: quinoline

RDF: radial distribution function

RT: room temperature

RuNiP/PPh_2Py: RuNi/PPh_2Py synthesised from $[Ni(\eta^4\text{- } C_8H_{12})(PPh_2Py)_2]$

RuPNi/PPh_2Py: RuNi/PPh_2Py synthesised from $[Ru(\eta^4\text{-}C_8H_{12})(PPh_2Py)_2]$

SF: Schlenk flask

SQUID: superconducting quantum interface device

SS: solid state

STEM: scanning transmission electron microscopy

TEM: transmission electron microscopy

TFMBAL: 4-(trifluoromethyl)benzaldehyde

TFMAPO: 4-(trifluoromethyl)acetophenone

THF: tetrahydrofuran

TGA: thermogravimetric analysis

TOF: turnover frequency

UHV: ultra-high vacuum

WAXS: wide angle X-ray scattering

XPS: X-ray photoelectron spectroscopy

General Introduction

In 2021, the 77 % of the world energy consumption was coming from fossil fuels and this dependency is even higher for chemicals production. For this reason, we need renewable alternatives like lignocellulosic biomass which has risen as an interesting feedstock for both, energy and chemicals production. In order to use the same production chain of petroleum-sourced fuels and to avoid its corrosion, the reduction of the oxygenated platform molecules from lignocellulosic biomass is needed.

Furfural, a lignocellulosic biomass platform molecule, can be converted through different type of reactions such as oxidation, decarbonylation or hydrogenations. It contains different moieties that can be reduced, producing a variety of products such as furfuryl alcohol, a chemical used in the resin industry; 2-methylfuran, a potential biofuel; and 1,2-pentanediol, which can be used as a solvent. In order to obtain pure products, we need selective catalysts for furfural reduction.

Nanocatalysts appear to be important as, by tuning their properties, their selectivity and catalytic performances can be modified. The nanocatalysts' parameters that can be tune are the size, the shape, the nature of the stabiliser, the composition or the chemical order. In our team, we have developed an organometallic approach for the synthesis of metal nanoparticles by modifying these parameters for their applications in catalysis. This organometallic approach consists on the decomposition of the metallic precursors in a solvent under H_2 pressure, with the presence of a stabiliser such as ligands, polymers, ionic liquids or supports, followed by the nucleation of "naked" metal atoms and the growth of metal nanoparticles. Apart from modifying the nature of the stabiliser, we can also play on the metallic composition by using one or more metals, and their chemical order, which can be, for example, an alloy or a core-shell.

The nanocatalysts' properties depend on the chemical order, which can be different depending on the decomposition of the metallic precursors and the metals miscibility. In our work, we have synthesised bimetallic NPs and applied them in catalytic reductions. For the application of these nanoparticles in the industry, they need to be performing and cheap catalysts. Earth abundant metals, such as Ni or Cu, need drastic conditions for reductive reactions. In order to decrease these harsh conditions, combining them with a noble-metal could be an option. Ru is one of the most abundant noble-metals and very efficient in hydrogenation reactions. Ni and Cu are known to be immiscible with Ru but this miscibility between metals can be modified when changing the reaction conditions. For this reason, in our work we played with the reaction conditions of the organometallic approach to design RuNi and RuCu bimetallic NPs for the selective hydrogenation of furfural.

In the case of bimetallic catalysts, the presence of two metals may improve the performance of the two separated metals. This improvement it is caused by a synergy between the two metals. Synergetic effects between Ru and the earth abundant metals used in this work, Ni and Cu, have already been reported in literature for different catalytic reductions.

The first chapter of this work is dedicated to a global context of the research and it is mainly focused on the use of RuNi catalysts for hydrogenation reactions. The different references reported in literature for RuNi systems are summarised in a table with some of the most important details of each.

The second chapter is mainly focused on the synthesis and characterisation of RuNi NPs using polyvinylpyrrolidone (PVP), diphenylpyridylphosphine (PPH_2Py) and adamantanecarboxylic acid (AdCOOH). The synthesis and characterisation of RuCu NPs stabilised by PVP and of monometallic Cu NPs stabilised by hexadecylamine (HDA) are also described in this chapter.

In Chapter 3, the use of RuNi/PVP NPs and RuCu/PVP NPs as catalysts for furfural hydrogenation is discussed. Moreover, the use of RuNi/PVP NPs and RuNi/PPh_2Py NPs as catalysts for quinoline hydrogenation is also treated in this chapter.

In the fourth chapter, Density Functional Theory (DFT) calculations, performed in Prof. Dr. Romuald Poteau's research group at Laboratoire de Physique et Chimie des Nano-Objets (LPCNO) in Toulouse, are reported to rationalise some of the catalytic results from Chapter 3. Different models have been built for monometallic Ru, monometallic Ni and bimetallic RuNi NPs in order to better understand the selectivity, the solvent and the metallic effect.

Chapter 5 describes the application of monometallic Ru/PVP NPs as catalysts for the deuteration of several organic molecules, which has been performed during a three months internship in Prof. Dr. Matthias Beller's research group at Leibniz-Institut für Katalyse in Rostock (Germany).

Finally, the sixth chapter is dedicated to the experimental techniques that have been used during the synthesis, characterisation and application in catalysis of the different NPs synthesised. It is followed, to summarise the most important results, by the general conclusions and the perspectives of this work.

CHAPTER 1: Introduction

Summary

1.1 Global context

The pandemic COVID-19, discovered in Wuhan on December 2019, has rapidly spread all over the world,[1,2] creating health and social crises and evidencing that the global society was not ready to face this kind of situation. It has been described as one of the biggest world-wide crises after World War II, with a big impact even in rich and industrialised nations.[3] Apart from social and health domains, the environmental and economic ones were also affected.[4] Even if the pollution from industries and transports decreased with the lock-down,[5] social and economical issues increased around the globe,[6] and as a post effect, the issue of medical waste treatment and single-use plastics removal appeared as a new problem.[5]

The current world situation is a clear example of what is called cascading disasters.[7] Hazards are not the real cause of disasters but only the trigger, the real cause being vulnerability.[8] In 2018, the year before the pandemic appears, consequences of financial crises of the past decades were still a matter of actuality.[9] If it was not enough, in 2022, the war between Russia and Ukraine worsen the situation, with a new global humanitarian, economic and energetic crisis appeared.[10]

Moreover, climate change, which is another cause for health issues, is present since decades, for example, global warming which is increasing the global temperature without stop. In the 2020 *Lancet* Countdown report, 43 indicators concerning the climate change were published.[11] The World Meteorological Organisation, a specialised agency of the United Nations, stated in 2018 six important indicators to evaluate the state of the climate: temperature, greenhouse gases and ozone, the oceans, the cryosphere, drivers of interannual variability and extreme events.[12] The report from 2015 was already proposing a list of ten recommendations to face climate change around the world, regarding health wellness, which consisted on investing more in climate change research, protecting respiratory and cardiovascular health and promoting healthy lifestyles, increase taxes to fossil fuels, support low-carbon energy transitions and invest on renewable energy sources while facing global environment changes.

In 2015, the participants on the 21st Conference of the Parties (COP21) agreed on limiting the increase of the global average temperature at 1.5 ºC in comparison to the preindustrial levels.[13,14] In order to success on this agreement, the recommendations were: to suppress the power generation from fossil fuels by a complete decarbonisation and reversing the trend started with industrial revolution, to install a sustainable global food and agricultural systems, to study the structure and function of spatial infrastructures and cities and the

transports between them, to preserve the planetary boundaries, to reverse deforestation and to change the use of the land and the methods to deliver health care.[15,16]

Concerning the first of these recommendations, research on the energy consumption and the renewable sources of energy is continuously needed. As it may be observed in Figure 1, fossil fuels represented in 2021 the 77 % of the world energy consumption.[17]

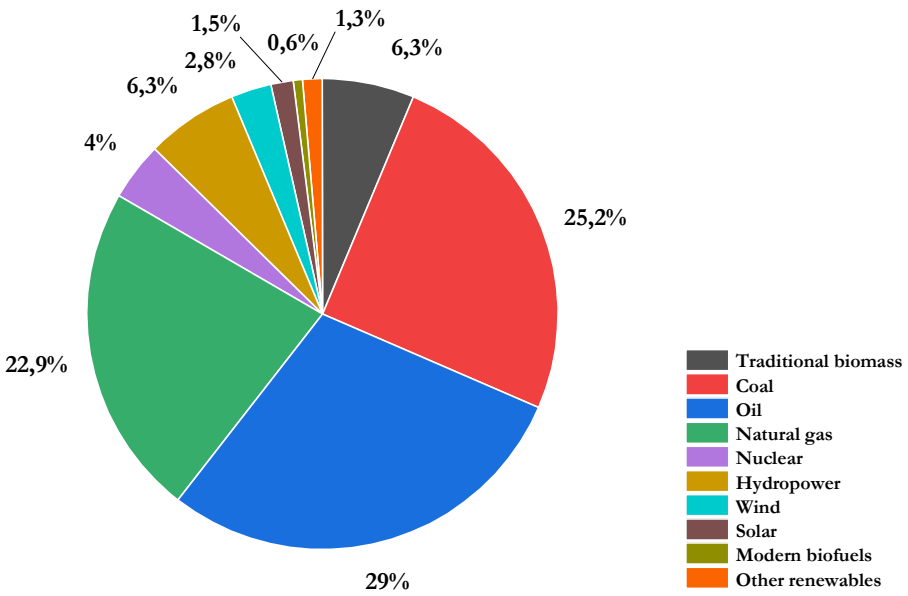

Figure 1: World primary energy consumption by source in 2021.

Together with the evolution of new technologies, the energy demand has not stopped increasing and the prevision until 2050 and 2100 goes on the same direction.[18,19] The main concern is that we are currently dependant on fossil fuels which are finite resources.[20] Furthermore, another important problem is the CO_2 emissions associated to their use.[19] The prevision of carbon emissions rate in 2050 is to double the ones from 2001 and, as a direct consequence, the CO_2 accumulation at the atmosphere will continue to increase, as earth and oceans will not be able to store it all.[21,22]

Several climate models have predicted the consequences of an atmosphere containing 550 ppm of CO_2 or more, being some of the results, changes in the hydrological cycle or rises of the sea level.[23] In 2021, the global averaged CO_2 concentration at the atmosphere reached 414.71 ppm and the preliminary data obtained in 2022 already reached 417.2 ppm, showing an increase of *circa* 3 ppm per year.[24] If this tendency is maintained, the CO_2 levels will be reaching over 500 ppm in 2050.

After observing this context full of crises, now is the time to implement medium and long term objectives to reactivate the economy in a more sustainable way, to take profit of the

critical situation to start or transform current businesses to entrepreneurial sustainable businesses models.[25] Chemical leasing is an innovative business model concerned by circular economy which can rapidly integrate green and sustainable chemistry in international policy regimes and industries to advance towards a greener and more sustainable world with prosperity for either people and planet.[26]

1.2 The 12 green chemistry principles

In today's world, almost every type of industry use chemicals in their daily routines, as chemical products are, together with food, beverage, machinery and equipment industries, one of the most manufactured products around the world.[27] Over the years, many theories and concepts have been developed in the direction of removing hazardous chemicals.[26] One of them, Sustainable Chemistry, consists on the chemistry which uses resources, including also energy, that the rate of natural replacement is faster than its consumption and where the waste treatment is also faster than its formation.[28] In 1987, the World Commission on Environment and Development stated about sustainable development that it should allow to fulfil the needs and aspirations of the present without compromising the ones that may come in the future.[29]

Another concept, and the one which this section is about, is Green Chemistry which is based on 12 principles (Figure 2) that protect and benefit the people, the planet and the economy, when they are applied on chemical products and processes.[30] The final goal of Green Chemistry is the reduction of any chemical which has negative consequences on humans and environment.[31]

Figure 2: The 12 principles of green chemistry.[32]

The first of these twelve principles is prevention, as it is always better to prevent the formation of waste (any product without any value or the loss of energy) than to worry about how to treat it.[33] This waste may appeared with different forms and its impact depends on how it is released, its toxicity, its nature or its quantity.[34] E-Factor, also known as Environmental Impact Factor and which was described in 1992, consists on a relation between the weight of waste and the weight of product formed.[35] This factor has been applied in several industrial processes to evaluate their efficiency, being of these examples the production of ethylene oxide.[36,37] However, in some cases, wastes cannot be eliminated and so research is performed to try to give value at these wastes in other processes.[38,39] Moreover, especially in synthetic and biopharma sectors, another concept called process mass intensity, which consists on the relation of the weights of all the used materials and the active drug produced.[40]

The second principle is the atom economy, as synthetic methods are supposed to integrate all the atoms used to the final product.[33] Atom economy, or atom efficiency, was stated in 1990 as taking the maximum profit of the raw materials by including as many atoms from the reagents as possible to the final product.[41] It is a theoretical concept that can be calculated by dividing the molecular weight of the product by the sum of all the molecular weights of the reactants. Atom economy is applied to different kind of reactions such as Diels-Alder,[41] A^3-couplings[42] and Grignard reactions[43].

The third principle is the less hazardous chemical synthesis, as synthetic methods should be producing little or no toxic substances for humans and the environment.[33] Chemists need efficient and cleaner synthetic tools and, for this reason, new reactions such as enzymatic,[44] metathesis,[45] cascade or tandem[46,47] and C-H activation reactions[48–50] have been developed, being alkene metathesis a cleaner option for Wittig reactions, for instance.[51]

The fourth principle is the designing of safer chemicals, which is in line with the third principle, as effective, safer, non-toxic chemicals are needed for cleaner reactions.[33] Over the years, a plethora of chemicals have been designed but, without thinking about their hazard, which is not suitable for sustainability. More recently, studies on toxicology have improved the design of safer chemicals, allowing the creation of correlations, models and equations to relate different aspects of the chemicals.[52–55]

The fifth principle concerns the use of safer solvents and auxiliaries, as when is possible is better to not use them and when it is not feasible their suppression, they should be safe chemicals.[33] Solvents normally represent between 50 and 80% of mass waste,[56,57] and are in some cases toxic, flammable, corrosive, and pollutant, becoming thus an important field of research for green chemistry.[58–60] In order to eliminate or reduce the use of these conventional solvents, research has been performed for greener methods such as using water,[61–65] as apart of being a safe solvent, can help on the separation of organic products by hydrophobic effect;[66,67] supercritical fluids,[64,68–70] [64,68–70]for instance supercritical CO_2 can be eliminated easily by degassing the system;[71,72] ionic liquids[73–78] as solvents, or even solventless systems.[64,79–82] Reactions solvent free are very appealing, as solvent represent the majority of the waste to treat, as aforementioned.[56,57]

The sixth principle is the design for energy efficiency, as chemical reactions at room temperature (RT) and ambient pressure should be preferred to reduce the environmental and economical impact of energy.[33] The increase of energy consumption and the concern about fossil fuels have motivated the research on more efficient processes and renewable energies.[83,84] Alternative energy sources are identified as solar power,[85–89] biofuels production,[90–95] hydrogen fuel cells,[96–101] and wind,[102–104] hydro,[105–107] and geothermal energies.[108–111]

The seventh principle is the use of renewable feedstocks, as, from an economical and technical point of view, it is much more practical than non-renewable ones.[33] The majority of materials and energy are actually coming from fossil fuels and that is why the use of biomass (wood, agricultural residues, crops, food,...), as the most available renewable feedstock on Earth, for their production has become crucial.[112–115] Some of the most known renewable feedstocks are cellulose, lignin, glycerol, starch, oil or chitin.[116–120] Lignin, in the past,

was considered as a waste of paper industry, and nowadays is a raw material to synthesise vanillin or DMSO.[121–123] Similarly, chitin is a by-product of the seafood industry, which via deacetylation can be transformed to chitosan, a chemical with several applications.[124–127]

The eighth principle is to reduce derivatives, as the increase of derivatisation, such as the addition of protecting groups, increases the reagents and thus the waste.[33] Covalent[128,129] and non-covalent derivatisations are possible, being the latest less energy demanding, simpler, often occurring under solventless or aqueous media, and with reduced toxicity and environmental impact.[130–133]

The ninth principle is catalysis, as catalytic reagents are better than stoichiometric ones, being as selective as possible.[33] The use of catalytic amounts results to a decrease of stoichiometric amounts of reagents and thus, a reduction of the generated wastes.[134–137] The application of catalysts in the chemical industry is vast, by reducing in all cases the amount of stoichiometric reagents, the energy required and hence, the waste.[138–141] Moreover, biocatalysis has appeared to be an interesting tool due to natural or modified enzymes, which might obtain higher selectivities in catalytic reactions.[142,143]

The tenth principle is the design for biodegradation, as chemicals should be conceived to degradate into innocuous products safe for the environment when their function is accomplished.[33] The persistence and not degradation of several materials and chemicals have been observed during the history of industrialisation,[144–146] being two of the examples acrylamides or propylene oxides.[147] In order to face bioaccumulation of wastes, especially the toxic ones, biodegradable molecules were designed to replace the chemicals, such as plastics, used in the past.[53,148,149]

The eleventh principle is the real-time analysis for pollution prevention, as it is needed to analyse and determine hazardous substances before their formation to be able to prevent.[33] The main goal of green analytical chemistry is to be able to analyse chemicals without generating waste or any impact to the environment and, for this reason, several improvement in analytical techniques have been performed.[150–153] A new concept called process analytical chemistry, consisting on the ability to control a reaction to prevent undesired results to happen at the exact moment which is about to occur, has been defined.[154,155]

The twelfth principle is the inherently safer chemistry for accident prevention, as, in order to reduce chemical accidents, the substances used and their form in a chemical process should be chosen to minimise them.[33] The first and most important step to prevent chemical accidents is to identify and evaluate the different hazards present.[156] A further step for the chemical accidents prevention is the chemical substitution of the hazardous chemicals

for a safer design of the process. For example, in the production of polycarbonates where the toxic phosgene gas can be replaced by CO_2 reacting with ethylene oxide, although new hazards appeared associated to ethylene oxide.[157]

Having seen the general context, the application of these twelve green chemistry principles is of high importance at any industry related to chemicals, as was performed in the crop protection industry.[158]

1.3 Renewable feedstocks

Different kind of renewable sources of energy, such as solar or wind power, to substitute fossil fuels has been developed.[159] However, in the production of chemicals, this replacement of fossil fuels is mainly restricted to biomass.[113]

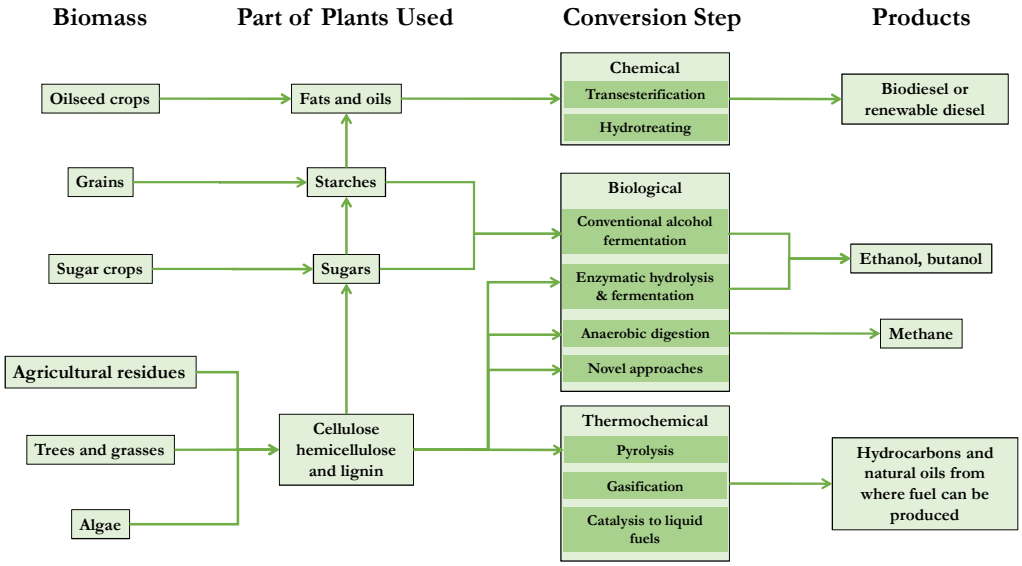

Figure 3: Flow-chart for the obtention of several products from biomass of different origins.[160]

Different biomass renewable feedstocks are shown in Figure 3 with their pathways to obtain chemical products produced mainly from fossil fuels. One of these feedstocks, lignocellulosic biomass, constituted by cellulose, hemicelluloses and lignin, has risen as an interesting alternative to fossil fuels for either energy and chemicals production.[161,162]

From the three components of lignocellulosic biomass, several platform molecules such as furfural (FF) and 2,5-hydroxymethylfurfural (HMF), can be obtained and, at their turn, to be transformed to other chemicals by, for example, hydrogenation, oxidation, acetalisation or decarbonylation reactions.[163–168] All these transformations need to be efficient in order to

integrate them in the industry for the energy transition; in particular, catalysis may be key to reach this objective, that is the reason why performing and efficient catalysts are needed to be designed.[169]

1.4 RuNi catalysed hydrogenations

Molecules coming from biomass processed by cracking and hydrotreating steps resemble the ones from fossil fuels, allowing thus the use of the same production machinery, as they reduce the oxygen atoms in the molecules.[170] A plethora of catalysts have been explored to find the most performant ones for such transformations. In particular, nanoalloys used as catalysts in oil refineries, petrochemical manufacturing, fine chemical synthesis, hydrogen evolution or oxygen reduction reactions, are predicted to be efficient with biomass-sourced molecules.[171–175]

Nanoalloys, containing two or more metals, have shown to be interesting materials with vast applications[176,177] and with catalytic activity that can be higher than their respective monometallic counterparts. Their catalytic activities depend on the different properties of the nanoparticles (NPs), such as the difference of electronic properties between metals, structure (Figure 4), size or shape.[178–181]

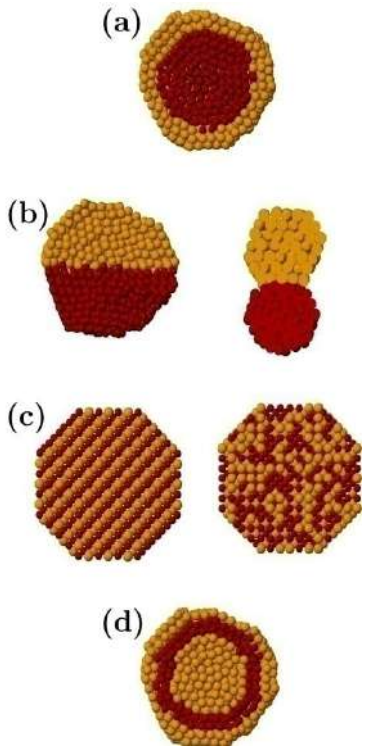

Figure 4: Schematic representation of some possible mixing patterns: core−shell (a), sub-cluster segregated (b), mixed (c), three shell (d). The pictures show cross sections of the clusters.[176]

Bimetallic catalysts have been used for upgrading lignocellulosic biomass into different value-added chemicals, using reactions such as reforming, oxidation, hydrogenolysis, hydrodeoxygenation or hydrogenations.[182,183] For instance, in reforming reactions, the presence of Re and Sn in Ni based catalysts, has had a positive effect for the formation of hydrogen (H_2).[184,185] In oxidation reactions of glucose to gluconic acid and of furan-derived compounds, such as furfuryl alcohol (HF), to their corresponding carboxylic acids, synergetic effects have been observed for PtPd and NiPd catalysts, respectively, displaying higher activities than their monometallic counterparts.[186,187] In hydrogenolysis reactions, glycerol was converted to 1,2-propanediol on a RuCu bimetallic catalyst at 230 ºC and 80 bar of H_2, while it was converted to 1,3-propanediol on a PtCu bimetallic catalyst at 210 ºC and 1 bar of H_2.[188,189] In hydrodeoxygenation reactions, vanillin was converted to methylcyclohexanol on a CoNi bimetallic catalyst at 200 ºC and 10 bar of H_2, while several oxygenated biomass molecules, such as HMF obtained also better activities and selectivities with the bimetallic $Co_5Zn_1O_x$ catalysts than with their monometallic counterparts.[190,191] In hydrogenation reactions, levulinic acid was converted to γ-valerolactone on a RuSn bimetallic catalyst at 180ºC and 35 bar of H_2, while several oxygenated biomass aldehydes, such as FF, where converted to their corresponding alcohols on a bimetallic PtNi catalyst at 100 ºC and 10 bar of H_2, showing better performances than with their monometallic counterparts.[192,193] Furthermore, synergetic effects have been also observed with bimetallic RuNi catalysts for the upgrading of biomass using hydrogenolysis reactions.[194–200]

RuNi based catalysts have been used as efficient catalysts for several hydrogenation reactions, including substrates like, CO,[201] CO_2,[202] N_2,[203] alkenes,[204] nitro- compounds,[205] aldehydes,[206]; and also being efficient as catalysts for C-O cleavage reactions.[200] Specifically, being highly performant for the hydrogenolysis of lignin.[195] In many occasions, a synergism between both metals have been found,[196,202,207] at a specific Ru/Ni ratio or structure.[208] The combination of Ni with Ru provides to the later metal different electronic properties as it has been shown by XPS,[209–211] even if the material is composed of independent monometallic NPs of Ru and Ni in close vicinity.[194,195] It has been also proposed that Ru is able to reduce Ni^{2+} through hydrogen spillover.[196,212] Thus, aside of the electronic effects, the hydride mobility could imply enhanced catalytic reactivity for RuNi NPs based catalysts. Several structures have been described for RuNi based catalysts, homogenous alloyed structure,[197,213] core-shell, with both Ru[198] or Ni[202] on the core, and others.[198]

Table 1 summarizes recent examples on the application of RuNi catalysts for hydrogenation reactions.

Table 1: RuNi based catalysts for hydrogenation reactions.

Catalyst	Synthetic methodology	Characterisation	Catalytic reaction conditions	Comments	Ref.
$[Et_4N]_2[Ru_3Ni_3C(CO)_{13}]$	1) Dissolve the precursors in 30 mL of acetone + SiO_2 under N_2. 2) Stir 30 min + evacuate at RT. 3) Calcinate in O_2 flow (1 bar, 40 $mL \cdot min^{-1}$) at 423 K for 2 h. 4) Reduce in H_2 flow (1 bar, 40 $mL \cdot min^{-1}$) at the programmed T from 293 to 573 K for 2 h and at 573 K for 2 h. 5) Reduce in H_2 flow at 573 K for 1 h before the introduction of syngas.	GC, FT-IR, GCMS	1 g of catalyst (Ru 1 wt. %), 5 bar of $CO/H_2 = 0.5$, 246 °C	CO hydrogenation (16 % selectivity to oxygenates with the bimetallic compared to almost 0 % for the monometallic)	[233]
RuNi/BEA	1) Dissolve Ni(NO3)2·6H2O in DI H_2O, Al2O3 and $RuCl_3$. 2) Heat at 65 °C for 5 h. 3) Dry in oven at 100 °C over-night. 4) Calcinate at 600 °C for 6 h under air. 5) Reduce before use at 400 °C for 5 h with a 60 mL min^{-1} flow of 5 % H_2/N_2.	BET and N_2 ad-sorption, TPR, NH_3-TPD, XRD, TEM, GC	500 mg catalyst, 50-60 mL MeOH, 120 °C, 75 bar CO/H_2 = 0.5	CO hydrogenation (>4 $mmol \cdot g_{cat}^{-1} \cdot L_{MeOH}^{-1}$ dimeth-oxymethane yield for bimetallic Ru-Ni, more than twice than monometallic Ru)	[201]

Catalyst	Synthetic methodology	Characterisation	Catalytic reaction conditions	Comments	Ref.
$RuNi/BMI.NTf_2$	1) Reduce $[Ni(COD)_2]$ and $[Ru(2\text{-methylallyl})_2(COD)]$ in presence of $BMI.NTf_2$ ionic liquid with 8 bar H_2 at 120 ºC for 17 h. 2) Evaporate the black colloidal solution.	STEM, PXRD, XPS, RBS, EXAFS	20 mg catalyst, 0.5 mL IL, 8.5 bar or 16 bar of CO_2:H_2 (1:4 or 1:6), 150 ºC	CO_2 hydrogenation (76 % selectivity to C_2-C_4 hydrocarbons with Ru_3Ni_2 higher than monometallics)	202
$[(Cp)NiRu_3H_3(CO)_9]$	1) Chemically decomposate by KOH in THF at RT. 2) Centrifugate and wash with H_2O, EtOH and Et_2O. 3) Dry in vacuum. 4) Support on Al_2O_3.	X-ray, EA, TEM, EDX, IR	360-450 ºC, 100 mL·min^{-1} of an N_2-H_2 (3:1) mixture, 2% of metal	Ammonia synthesis (productivity of NH_3 is lower for bimetallic than monometallic Ru at all temperatures)	203
$[(Cp)NiRu_3H_3(CO)_9]$	1) Wet with the hydrocarbon solution. 2) Add the silanised chromosorb. 3) Dry under N_2 at RT. 4) Heat at 230 ºC for 7 h with 25 mL·min^{-1} H_2. 5) Extract with $CHCl_3$.	GC, GCMS	80, 150, 230 ºC, H_2 (or N_2)	Diene, cyclodiene and benzene hydrogenation and hydrogenolysis (100 % selectivity to pentane and cyclohexane with bimetallics)	204

Catalyst	Synthetic methodology	Characterisation	Catalytic reaction conditions	Comments	Ref.
RuNi/No, RuNi/PVP, RuNi/CTAB	1) Mix 0.72 g $NiCl_2 \cdot 6H_2O$ with 35 mL anhydrous EtOH and stir for 10 min. 2) Adjust pH with 5 mL of NaOH, add PVP or CTAB and stir for 10 min. 3) Add 5mL of hydrazine hydrate (85 %) and leave at RT for 18 h. 4) Filtrate the black turbid solution, wash with absolute EtOH and deionised H_2O and dry at 60 °C under vacuum for 6 h. 5) Galvanic replacement of 0.1 g of Ni crystals in aqueous $RuCl_3$ (9.64×10^{-3} M) solution US treatment at RT for 2 h. 6) Filtrate, wash with anhydrous EtOH and deionised H_2O until no Cl^{-1} ions detected and dry at 60 °C under vacuum for 6 h.	XPS, SEM, XRD, SEM-EDS elemental mapping, HRTEM, HS-LEIS, GC	0.05 g catalyst, 10 mL benzene, purge with N_2 and H_2, 50 bar H_2, 100 °C	Benzene hydrogenation (100 % yield to cyclohexane obtained with bimetallic NPs compared to <0.1 % for monometallic Ni)	[237]
RuCoNi/EDA	1) Mix 0.65 g $NiCl_2 \cdot 6H_2O$ and 0.65 g $CoCl_2 \cdot H_2O$ in 30 mL of DI H_2O (or EtOH), 5 mL of anhydrous EtOH and stir at RT for 10 min. 2) Add 5 mL of EDA, 5 mL of an aqueous solution of 1.813 g NaOH and stir for 10 min. 3) Add 5 mL of hydrazine hydrate (85 %), stir for 10 min and leave for 1 h at 120, 150 or 180 °C.	EDS, ICP-MS, XRD, SEM, XPS, HS-LEIS, GC, GC-MS	10 mL benzene, 53 bar H_2, 100 °C, 0.05 g of catalyst	Benzene hydrogenation (100 % yield to cyclohexane obtained with trimetallic NPs synthesised in ethanol)	[224]

Catalyst	Synthetic methodology	Characterisation	Catalytic reaction conditions	Comments	Ref.
Ru-Ni/C	1) Mix $NiCl_2 \cdot 6H_2O$ with a mixture of 12.5 mL of anhydrous EtOH and 82.5 mL of DI H_2O and stir for 10 min. 2) Inject 12.5 mL of a NaOH aqueous solution and stir for 10 min. 3) Add 25 mL of hydrazine hydrate (85 %), 1.25 g of black carbon and leave at RT for 18 h. 4) Filtrate the black turbid solution, wash with absolute EtOH and DI H_2O and dry at 60 ºC under vacuum for 6h. 5) Galvanic replacement of 0.3 g of Ni crystals in 200 mL aqueous solution of $RuCl_3$ (9.64×10^{-3} M) US treatment at RT for 6 h. 6) Filtrate, wash with anhydrous EtOH and DI H_2O until no Cl^{-1} ions detected and dry at 60 ºC under vacuum for 6 h. 7) Calcinate in N_2 at 380 ºC for 3 h.	ICP-MS, XRD, TEM, HRTEM, XAS, XANES, EXAFS, GC, GCMS	0.05 g catalyst, 10 mL benzene, purge with N_2 and H_2, 53 bar H_2, 60 ºC	Benzene hydrogenation (85 % yield to cyclohexane reached with bimetallic NPs compared to the 8 % of monometallics)	[238]

Catalyst	Synthetic methodology	Characterisation	Catalytic reaction conditions	Comments	Ref.
Ru-Ni/C	1) Mix $NiCl_2 \cdot 6H_2O$ with a mixture of 12.5 mL of anhydrous EtOH and 82.5 mL of DI H_2O and stir at RT for 10 min. 2) Inject dropwise 12.5 mL of a 0.3 g PVP aqueous solution and stir for 10 min. 3) Add 1.25 g of black carbon, after 10 min, 25 mL of hydrazine hydrate (85 %), 12.5 mL of a 1.813 g NaOH aqueous solution and leave at RT for 12 h. 4) Filtrate the black turbid solution, wash with absolute EtOH and DI H_2O and dry at 60 ºC under vacuum for 6 h. 5) Galvanic replacement of 0.3 g of Ni crystals in 200 mL aqueous solution of RuCl3 (9.64x10-3 M) US treatment at RT for 6 h. 6) Filtrate, wash with anhydrous EtOH and DI H_2O until no Cl^{-1} ions detected and dry at 60 ºC under vacuum for 6 h. 7) Calcinate in N_2 at 380 ºC for 3 h.	H_2-TPD, XPS, XRD, SEM, SEM-EDS, TEM, HRTEM, GC, GC-MS	10 mL benzene, 50 mg catalyst, purge with N_2 and H_2, 2.8-48.3 bar of H_2, at 20-60 ºC.	Benzene hydrogenation (100 % yield to cyclohexane obtained with bimetallic NPs compared to <64 % with monometallics)	[239]

Catalyst	Synthetic methodology	Characterisation	Catalytic reaction conditions	Comments	Ref.
RuNi/C-PVP	1) Mix PVP in a 12.5 mL of anhydrous EtOH and 82.5 mL aqueous solution of $NiCl_2 \cdot 6H_2O$ and stir at RT for 10 min. 2) Inject 12.5 mL of a 1.813 g NaOH aqueous solution and stir for 10 min. 3) Add 25 mL of hydrazine hydrate (85 %), after 10 minutes, 1.25 g of black carbon and stir at RT for 18 h. 4) Filtrate the black turbid solution, wash with absolute EtOH and DI H_2O and dry at 60 ºC under vacuum for 6 h. 5) Add Ni crystals in an aqueous solution of $RuCl_3$ and stir at RT for 12 h. 6) Filtrate, wash with anhydrous EtOH and DI H_2O until no Cl^{-1} ions detected and dry at 60 ºC under vacuum for 6 h. 7) Anneal in N_2 at different T for 3h.	ICP-MS, XPS, TEM, HRTEM, HAADF-STEM, STEM-EDS, HS-LEIS, GC, GC-MS	10 mL benzene, 50 mg catalyst, purge with N_2 and H_2, 60 ºC, 53 bar of H_2	Benzene hydrogenation (100 % yield to cyclohexane with RuNi/C-PVP calcinated at 380 ºC compared to <10 % with monometallics)	[227]

Catalyst	Synthetic methodology	Characterisation	Catalytic reaction conditions	Comments	Ref.
Ru/Ni-EDA, Ru/Ni-PVP, Ru/Ni-CTAB	1) Mix 0.72 g $NiCl_2 \cdot 6H_2O$ in 30 mL DI H_2O and 5 mL anhydrous EtOH and stir for 10 min. 2) Add 5 mL of surfactant (EDA, PVP or CTAB), 5 mL of an aqueous solution of NaOH, and stir for 10 min. 3) Add 5 mL of hydrazine hydrate (85 %), stir for 10 minutes and leave 1 h at 120, 150 or 180 °C. 4) Filtrate the black turbid solution, wash with absolute EtOH and DI H_2O and dry at 60 °C under vacuum for 6 h. 5) Add Ni crystals in an aqueous solution of $RuCl_3$ (9.64×10^{-3} M) and US at RT for 2 h. 6) Filtrate, wash with anhydrous EtOH and DI H_2O until no Cl^{-1} ions detected and dry at 60 °C under vacuum for 6 h.	ICP-MS, XRD, SEM-EDS, XPS, HS-LEIS, TEM, HRTEM, GC, GC-MS	10 mL benzene, 100 °C, 53 bar H_2, 0.05 g of catalyst	Benzene hydrogenation (100 % yield to cyclohexane with Ru/Ni-EDA synthesised at 150 °C compared to <0.1 % with monometallic Ni)	[218]

Catalyst	Synthetic methodology	Characterisation	Catalytic reaction conditions	Comments	Ref.
RuNi/C	1) Mix $NiCl_2 \cdot 6H_2O$ with a mixture of 12.5 mL of anhydrous EtOH and 82.5 mL of DI H_2O and stir for 10 min at RT. 2) Inject dropwise 12.5 mL of a 0.3 g PVP aqueous solution and stir 10 min. 3) Add 1.25 g of black carbon, after 10 min, 25 mL of hydrazine hydrate (85 %) and 12.5 mL of a 1.813 g NaOH aqueous solution and leave at RT 12 h. 4) Filtrate the black turbid solution, wash with absolute EtOH and DI H_2O and dry at 60 °C under vacuum for 6 h. 5) Add Ni crystals in an aqueous solution of $RuCl_3$ and stir at RT, 12 h. 6) Filtrate, wash with anhydrous EtOH and DI H_2O until no Cl^{-1} ions detected and dry at 60 °C under vacuum for 6 h. 7) Calcinate in N_2 at different T, 3 h.	ICP-MS, XRD, XPS, TEM, HRTEM, HAADF-STEM, STEM-EDS, HS-LEIS, GC, GC-MS	10 mL benzene, 50 mg catalyst, purge with N_2 and H_2, 53 bar of H_2, 60 °C	Benzene hydrogenation (74.2 % yield to cyclohexane with Ru-Ni/C calcinated at 30 °C compared to lower yields at higher calcination temperatures)	[222]

Catalyst	Synthetic methodology	Characterisation	Catalytic reaction conditions	Comments	Ref.
RuNi/C-PVP	1) Mix $NiCl_2 \cdot 6H_2O$ in 12.5 mL of anhydrous EtOH and 82.5 mL of aqueous solution of PVP and stir at RT for 10 min. 2) Inject 12.5 mL of a 1.813 g NaOH aqueous solution and stir for 10 min. 3) Add 25 mL of hydrazine hydrate (85 %), after 10 minutes, 1.25 g of black carbon and stir at RT for 18 h. 4) Filtrate the black turbid solution, wash with absolute EtOH and DI H_2O and dry at 60 °C under vacuum for 6 h. 5) Add Ni crystals in an aqueous solution of $RuCl_3$ and stir at RT for 12 h. 6) Filtrate, wash with anhydrous EtOH and DI H_2O until no Cl^{-1} ions detected and dry at 60 °C under vacuum for 6 h. 7) Calcinate in N_2 at 380 °C for 3 h. 8)	ICP-MS, XRD, XPS, TEM, HRTEM, HAADF-STEM, GC, GC-MS	10 mL benzene, 50 mg catalyst, purge with N_2 and H_2, 60 °C, 53 bar of H_2	Benzene hydrogenation (100 % yield to cyclohexane with $Ru_{0.56}Ni_{0.44}/C$ and $Ru_{0.34}Ni_{0.66}/C$ compared to lower yields with other bimetallic ratios)	[209]

Catalyst	Synthetic methodology	Characterisation	Catalytic reaction conditions	Comments	Ref.
Ru-Ni/C and Ru-Ni/NiO/C	1) Mix $NiCl_2 \cdot 6H_2O$ with a mixture of 12.5 mL of anhydrous EtOH and 82.5 mL of DI H_2O and stir at RT for 10 min. 2) Inject dropwise 12.5 mL of a 0.3 g of PVP aqueous solution and stir for 10 min. 3) Add 1.25 g of black carbon, after 10 min, 25 mL of hydrazine hydrate (85 %) and 12.5 mL of a 1.813 g NaOH aqueous solution and leave at RT for 12 h. 4) Filtrate the black turbid solution wash with absolute EtOH and DI H_2O and dry at 60 °C under vacuum for 6 h. 5) Add Ni crystals in an aqueous solution of $RuCl_3$ and stir at RT for 12 h.	TGA, XRD, XPS, TEM, HRTEM, HAADF-STEM, GC, GC-MS	10 mL benzene, 50 mg catalyst, purge with N_2 and H_2, 53 bar of H_2, 60 °C.	Benzene hydrogenation (100 % yield to cyclohexane with Ru-Ni/NiO/C compared to 9.4 % with Ru/C)	[240]

Catalyst	Synthetic methodology	Characterisation	Catalytic reaction conditions	Comments	Ref.
$Ru/Ni/Ni(OH)_2/C$	1) Mix 0.9 g $NiCl_2 \cdot 6H_2O$ with a mixture of 12.5 mL of anhydrous EtOH and 82.5 mL of DI H_2O and stir at RT for 10 min. 2) Add 12.5 mL of a 1.813 g NaOH aqueous solution and stir for 10 min. 3) Add 25 mL of hydrazine hydrate (85 %), 1.25 g of black carbon and stir at RT for 18 h. 4) Filtrate the black turbid solution, wash with absolute EtOH and DI H_2O and dry at 60 °C in a vacuum oven for 6 h. 5) Add Ni crystals in an aqueous solution of $RuCl_3$ (9.64×10^{-3} M) and stir at RT for 6 h. 6) Filtrate, wash with anhydrous EtOH and DI H_2O and dry at 60 °C in a vacuum oven for 6 h.	ICP-MS, XRD, XPS, TEM, HRTEM, HAADF-STEM, EDS, HS-LEIS, HE-XRD, XAS, XANES, EXAFS, GC, GC-MS	0.05 g catalyst, 30 mL naphthalene, purge with N_2 and H_2, 48 bar H_2, 15 – 100 °C	Naphthalene hydrogenation (100 % yield to decalin obtained with bimetallic catalysts compared to 0 % with the monometallic)	[223]
Ru/Ni/Ni O/C	1) $Ni(OH)_2/C$ synthesised at RT via hydrazine hydrate reduction on black carbon. 2) Ni/NiO/C produced by calcination in N_2 at 380 °C. 3) Galvanic replacement at RT for 6h forming the Ru/Ni/NiO/C.	TG, XRD, XPS, TEM, HRTEM, HAADF-STEM, TPR, HS-LEIS, XANES, EXAFS, ICP-MS, GC, GC-MS	30 mL cyclohexane naphthalene solution (3.02 % weight naphthalene), 45 bar H_2, 25 °C to 100 °C and 0.05 g to 0.3 g of catalyst	Naphthalene hydrogenation (100 % yield to decalin obtained with bimetallic catalysts compared to 0 % with monometallic Ni and 31 % with Ru)	[234]

Catalyst	Synthetic methodology	Characterisation	Catalytic reaction conditions	Comments	Ref.
RuO_2/NiO/Al-SBA	1) Dissolve 4 g of Pluronic (P123) in 30 mL of DI H_2O and stir for 4 h. 2) Add 70 g of HCl (0.28 M) and stir for 2 h. 3) Add 9 g of tetraethylorthosilicate and aluminiumisopropoxide and stir at 40 °C for 24 h. 4) Dry in an oven at 100 °C for 48 h. 5) Filtrate, wash with DI H_2O and dry at 100 °C overnight. 6) Calcinate at 540 °C for 6 h. 7) Reduce before catalysis at 500 °C with 50 $mL \cdot min^{-1}$ flow of H_2.	XRD, BET, H_2-TPR, NH_3-TPD, XPS, HRTEM, GC	0.3 g of catalyst, 300-450 °C, atmospheric pressure, anisole flow 1 $mL \cdot h^{-1}$	Anisole hydrodeoxygenation (60 % selectivity to benzene obtained with $Ru_{0.4}Ni_{7.0}$ compared to 40 % with monometallics)	226
$NiRu/Al_2O_3$	1) Dissolve $Ni(NO_3)_2 \cdot 6H_2O$, $RuCl_3 \cdot H_2O$ and urea (urea:M = 2:1) in 5 mL of DI H_2O. 2) Add 5 g of γ-Al_2O_3 and leave it for 1 h. 3) Age at 130 °C for 24 h. 4) Wash with DI H_2O until pH = 7 and dry at 70 °C for 12 h. 5) Treat under H_2 flow at 450 °C for 4 h.	XRD, SEM, ICP, EA, HRTEM, HAADF-STEM, STEM-EDX, TEM, XPS, H_2-TPR, H_2-TPD, GC	PyGas (10 wt.% Styrene, 35 wt.% toluene and 55 wt.% n-heptane) 1.1 g catalyst precursor (20-40 mesh) diluted with 3.3 g of SiC, 60 °C, 20 bar H_2	Gasoline hydrogenation (100 % selectivity to ethylbenzene reached with all catalysts and $Ni_4Ru_{0.05}$ reached 100 % conversion compared to monometallics)	235

Catalyst	Synthetic methodology	Characterisation	Catalytic reaction conditions	Comments	Ref.
$RuNi/Al_2O_3$	1) Dissolve $Ni(NO_3)_2 \cdot 6H_2O$ in 2 mL of DI H_2O with US at 25 °C for 1 h. 2) Add 1.9 g of Al_2O_3 and US at 40 °C for 4 h. 3) Wash with DI H_2O and slowly add 20 mL of NaOH (pH = 12) with 0.4 g $NaBH_4$. 4) Filtrate by suction, wash with DI H_2O and dry at 80 °C under N_2. 5) Dissolve $RuCl_3$ in 2 mL of DI H_2O and add the Ni/Al_2O_3 obtained at step 4 to the $RuCl_3$ solution under US for 4 h. 6) Add 20 mL of NaOH (pH = 12) with 0.4 g $NaBH_4$. 7) Filtrate, wash with DI H_2O and dry at 80 °C under N_2.	GC-MS, BET, ICP-OES, H_2-TPD, XRD, XPS, TEM, HRTEM, DFT	150 °C to 180 °C, 40 bar of H_2, 3 g of N-propylcarbazole, 40 mL of cyclohexane and 0.3 g of catalyst	N-propylcarbazole hydrogenation (1.083 min^{-1} TOF value obtained with $Ru_{2.5}Ni_{2.5}$ compared to lower activities with other bimetallics and monometallics)	[236]
$RuNi/TiO_2$	1) Dissolve 51.4 mg $RuCl_3$ and 55.2 mg $NiCl_2$ in DI H_2O and US. 2) Add dropwise the solution into TiO_2 aqueous slurry (1 g TiO_2 in 10 mL H_2O) and stir 12 h. 3) Freeze-dry and reduce in H_2/Ar (2/5) at 200 °C for 2 h and 400 °C for 4 h.	XRD, HRTEM, XPS, H_2-TPR, TEM, GC-MS, NMR	2.5 g N-ethylcarbazole, 125 mg catalyst, 150 °C, 70 bar H_2	N-ethylcarbazole hydrogenation (90 % selectivity to fully hydrogenated product obtained on anatase and P25 compared to lower selectivity with rutile)	[242]

Catalyst	Synthetic methodology	Characterisation	Catalytic reaction conditions	Comments	Ref.
$NiRu/Al_2O_3$	1) Dissolve $RuCl_3 \cdot H_2O$ and $Ni(NO_3)_2 \cdot 6H_2O$ in DI H_2O and stir for 12 h. 2) Add the solutions dropwise on γ-Al_2O_3 and stir overnight. 3) Dry 5 h at 110 ºC, heated in air at 550 ºC for 4 h and after at 400 ºC for 4 h in 10 % H_2/He.	GC-MS, GC-FID, XRD, XPS, FE-TEM	300 ºC, 350 ºC or 400 ºC, 200 bar or 250 bar H_2, catalyst:quinoline molar ratio (1:1), formic acid: quinoline molar ratio (6:1)	Quinoline hydrogenation (95 % conversion of quinoline obtained with $Ni_{80}Ru_{20}$ bimetallic catalyst with a 16 % yield to 2-hexene at 400 ºC)	[243]
RuNi/meso_SC	1) Dissolve 2 g of 2,2-bithiophene and 1 g of $Co(NO_3)_2 \cdot 6H_2O$ in 120 mL of THF. 2) Add 2 g of SiO_2, stir 4 h and dry by rotary evaporator and pyrolysis at 800 ºC under N_2 for 2 h. 3) Etch with 2 M NaOH solution for 3 days at RT, followed by 0.5M H_2SO_4 at 90 ºC for 8 h. 4) Impregnate with $RuCl_3$ and $Ni(NO_3)_2 \cdot 6H_2O$ solutions over 50 mg of meso_SC obtained at step 3, in 50 mL of DI H_2O and stir overnight. 5) US for 1 h followed by rotary evaporator. 6) Reduce at 600 ºC under 5 % H_2/Ar for 2 h.	ICP-OES, XRD, HAADF-STEM, EDS, H_2-TPR, XPS, GC	1 mmol of quinoline, 1 mL EtOH, purge with H_2, 10 bar H_2, 100 ºC, n(Ru)/n(substrate) = 5‰	Quinoline hydrogenation (100 % selectivity to 1,2,3,4-tetrahydroquinoline with 43 % quinoline conversion, lower conversion compared to monometallic Ru)	[244]

Catalyst	Synthetic methodology	Characterisation	Catalytic reaction conditions	Comments	Ref.
RuNi/C	1) Dissolve $NiCl_2 \cdot 6H_2O$ in 82.5 mL of DI H_2O and 12.5 mL anhydrous EtOH and stir at RT for 10 min. 2) Add 20 mL of a 1.813 g NaOH aqueous solution and stir for 10 min. 3) Add 1.25 g of black carbon, stir for 10 min and leave at RT for 18.5 h. 4) Filtrate, wash with DI H_2O and absolute EtOH and dry in vacuum oven at 60 ºC for 6 h. 5) Add 1 g $RuCl_3 \cdot xH_2O$ in 250 mL DI H_2O and stir for 6 h. 6) Filtrate, wash and dry in vacuum oven at 60 ºC for 6 h.	XRD, HAADF-STEM,STEM-EDX, HS-LEIS, SEM, GC, GC-MS	10 mL EtOH quinoline solution (0.69 %), 0.05 g catalyst, 50 bar H_2, 100 ºC	Quinoline hydrogenation (59 % selectivity to 1,2,3,4-tetrahydroquinoline obtained with RuNi compared to lower selectivity and conversion with both monometallic Ru and Ni)	232
$RuNi/Al_2O_3$	1) Dissolve $1.44x10^{-5}$ mol of $RuCl_3 \cdot nH_2O$ and $1.73x10^{-4}$ mol PVP in 30 mL ethylene glycol and stir. 2) Heat 0.009325 moles of $NiCl_2 \cdot 6H_2O$ with 2-3 drops of diluted HCl at 60 ºC for 2 min. 3) Mix both solutions and MW for 24 min, 300 W (~200 ºC). 4) Transfer the solution on the Al_2O_3. 5) Treat with MeOH, wash with acetone and dry for 12-16 h at 220 ºC under vacuum. 6) Calcinate at 300 ºC for 10-12 h and reduce before catalysis 1 h under H_2 flow.	UV, XRD, HRTEM, GC-MS	0.3 g catalyst, 30 mL butanol, 3 g of DB18C6 (substrate), 90 bar of H_2, 120 ºC.	Dibenzo-18-Crown-6 Ether hydrogenation (reduction of only one benzene ring with RuNi catalyst compared to the reduction of the two benzene rings with RuPd and monometallic Ru catalysts)	216

Catalyst	Synthetic methodology	Characterisation	Catalytic reaction conditions	Comments	Ref.
NiRu-HT	1) Prepare a solution with 5 mmol $Ni(NO_3)_2 \cdot 6H_2O$ and 1 mmol of $RuCl_3 \cdot 3H_2O$ and a solution of 6 mmol of $(NH_4)_2CO_3$ and 30 mmol of NH_4OH in 40 mL of DI H_2O. 2) Add dropwise the second solution on the first one, stir at 65 ºC during 2 h and age during 18 h. 3) Filtrate, wash with DI H_2O and dry overnight.	XRD, FT-IR, XPS, ICP-AES, TPR, BET, SEM, GC	0.1 g of catalyst, 10 mmol substrate, 20 mmol hydrazine, 20 mL isorpopanol, 35 ºC or 80 ºC	Nitrobenzene hydrogenation (100 % selectivity to aniline obtained with bimetallic RuNi compared to 80 % to azoxybenzene with monometallic Ni)	216
NiRu/MgAl	1) Dissolve 34.72 mmol of $Mg(NO_3)_2$ and 17.48 mmol of $Al(NO_3)_2$ in 96 mL of H_2O. 2) Dissolve 25.79 mmol Na_2CO_3 and 125.89 mmol of NaOH in 85.6 mL of H_2O. 3) Add solution 2 to the 1, stir at 60 ºC for 1 h and age at 60 ºC during 18 h. 4) Filtrate, wash with DI H_2O and dry at 70 ºC overnight. 5) Calcinate at 400 ºC for 4 h. 6) Dissolve 0.75 mmol of $Ni(NO_3)_2 \cdot 6H_2O$ and 0.25 mmol of $RuCl_3 \cdot 3H_2O$ in 4.45 mL of H_2O. 7) Add the solution dropwise on the support with continuous agitation, age 3 h at RT and dry at 70 ºC overnight. 8) Calcinate at 400 ºC for 4 h.	FR-IR, XRD, Thermal decomposition, UV-Vis, N_2 adsorption-desorption, BET, SEM, TEM, ICP-AES, XPS, TPR, GC, GC-MS	2.5 mmol of nitrobenzene, 1 mL of isopropyl alcohol, 0.05 g of catalyst, 80 ºC, N_2 atmosphere, 5 mmol of hydrazine hydrate	Nitrobenzene hydrogenation (93 % conversion with a 81 % selectivity to aniline with Ni_2Ru_1 and without using any solvent compared to lower conversions when using solvents)	205

Catalyst	Synthetic methodology	Characterisation	Catalytic reaction conditions	Comments	Ref.
$RuNi/Al_2O_3$	1) Dissolve 3.36 g of urea, 9.33 g of $Al_2(SO_4)_3 \cdot 18H_2O$ and 0.32 g of sodium tartrate in 140 mL of DI H_2O, and heat to 170 ºC for 3 h. 2) Wash with DI H_2O, dry and calcinate at 500 ºC for 4 h. 3) Dissolve 0.2 g of the resulting Al_2O_3 with 5.8 g of $Ni(NO_3)_2 \cdot 6H_2O$ and 9.6 g of NH_4NO_3 in 200 mL of DI H_2O, adjust the pH to 6.5 with $NH_3 \cdot H_2O$ (1 M) and age at 90 ºC for 48 h. 4) Reduce at 500ºC with a flow of 35 $mL \cdot min^{-1}$ of H_2/N_2 (10/90) for 4 h. 5) Disperse 0.2 g of the resulting Ni/Al_2O_3 in 30 mL of DI H_2O, add slowly a $RuCl_3$ solution and stir for 1 h under N_2.	XRD, ICP-AES, SEM, BET, TEM, EDS, XAFS, H_2-TPD, GC-MS, GC	1 mmol of substrate, 8 mL EtOH, 0.02 g of catalyst, purge with H_2, 10 bar of H_2, 50 ºC	Nitrostyrene hydrogenation (100 % selectivity to 4-aminostyrene obtained with low Ru loading RuNi catalysts while 98 % to 4-aminoethylbenzene is obtained at high Ru loading)	[217]
$RuNi/SiO_2$	1) Dissolve $RuCl_3 \cdot xH_2O$, $Ni(NO_3)_2 \cdot 6H_2O$ and SiO_2 and stir at RT for 8 h. 2) Dry at 120 ºC overnight. 3) Calcinate in air at 550 ºC for 4 h. 4) Before catalysis, press into small disks.	XRD, TEM, HRTEM, SAED, H_2-TPD, N_2-physisorption (BET), H_2-TPR, XPS, GC	1 g catalyst, 10 - 70 bar of H_2, 10 wt.% substrate aqueous solution, 80 ºC	3-hydroxypropanal hydrogenation (100 % conversion and selectivity to 1,3-propanediol obtained with bimetallic catalyst compared to lower values with monometallics)	[206]

Catalyst	Synthetic methodology	Characterisation	Catalytic reaction conditions	Comments	Ref.
$RuNi/Al_2O_3$	1) Wet impregnation with aqueous solution of $Ru(NO)(NO_3)_3$ and $Ni(NO_3)2{\cdot}6H_2O$ on γ-Al_2O_3. 2) Dry at 100 °C for 12 h and then calcinate at 250 °C for 4 h in static air.	Static H_2 chemisorption, pulse CO chemisorption, TPR, BET, XRD, GC, HPLC with UV-Vis and RID detectors	3.3 g of catalyst, 100 °C, 54.1 bar H_2, 4.8 wt. % furfural	Furfural hydrogenation (15 % furfural conversion obtained with Ru_1Ni_3 compared to 2 % with monometallic Ru)	246
$Ru\text{-}NiO/TiO_2$	1) Immerse TiO_2 in an aqueous solution of $NiCl_2$ and stir. 2) Dry at 60 °C under vacuum and calcinate at 500 °C for 10 h in air. 3) Re-impregnate the resulting monometallic in an aqueous solution of $RuCl_3$ (5 wt. %) and keep in an oven at 60 °C for 12 h. 4) Reduce at 200 °C with continuous flow of H_2 (5 %)/Ar for 3 h.	XRD, TEM, SEM, ICP-OES, XPS, BET, TPR, TGA, HPLC	20 g of lactose, 180 mL H_2O, 1 g catalyst, purge with H_2, 120 °C, 55 bar of H_2	Lactose hydrogenation (97 % conversion with 99.4 % selectivity to lactitol with $Ru_5(NiO)_5$ compared to other bimetallics with lower Ru loading)	215

Catalyst	Synthetic methodology	Characterisation	Catalytic reaction conditions	Comments	Ref.
RuNi/C and RuNi/CNT	1) Impregnate active C or CNT with aqueous solution of Ni. 2) Dry at 110 ºC overnight. 3) Heat treatment under N_2 for 3 h and reduce under H_2 flow for 3 h at 500 ºC. 4) Impregnate the Ni/AC or Ni/CNT with an aqueous $RuCl_3$ solution. 5) Dry at 110 ºC overnight. 6) Heat treatment under N_2 for 3 h and reduce under H_2 flow for 3 h at 250 ºC.	TPR, BET, TEM, HAADF-STEM, XEDS, pH, HPLC, TOC	750 mg cellulose, 300 mg catalyst, 300 mL H_2O, 205 ºC, 50 bar H_2	Cellulose hydrolytic hydrogenation (86 % selectivity to sorbitol with RuNi/AC and 71 % with RuNi/CNT compared to lower values for monometallics using ball-milling)	[220]
NiRu/CNF	1) Decompose biogas (CDB) on Ni:Co/Al_2O_3 catalyst at 650 ºC for 4 h with a mixture CH_4:CO_2 (v:v = 1:1). 2) Dissolve the material in HCl (37 %) at 60 ºC under US 4 h and oxidise in HNO_3 (65 wt. %) at reflux at 130 ºC 1 h. 3) Recover CNF from the acid solutions at step 2 and 3 by vacuum filtration and rinse with DI H_2O and oven dry at 70 ºC overnight. 4) Impregnate with 4.05 mL aqueous solution containing both $Ni(NO_3)_2{\cdot}6H_2O$ and $RuCl_2{\cdot}H_2O$ and reduce catalyst under N_2 flow for 3h.	H_2-TPR, XRD, TEM, HRTEM, ICP-OES, XPS, EDS, pH, HPLC, GC	150 mL of 0.25 wt. % of cellobiose aqueous solution, purge with N_2 and H_2, 40 bar of H_2, 180 ºC-200 ºC. Catalyst recovered after catalysis by vacuum filtration	Cellobiose hydrolytic hydrogenation (100 % conversion with 84.5 % selectivity to polyols (47 % cellobitol and 37.5 % sorbitol) after 3 h with bimetallic NiRu, reaching similar values to monometallic Ru)	[247]

Catalyst	Synthetic methodology	Characterisation	Catalytic reaction conditions	Comments	Ref.
Ru:Ni/MCM-48	1) Dissolve 2 g of n-hexadecyltrimethylammoonium bromide template in 42 mL of DI H_2O and stir for 15 min. 2) Add dropwise 4 mL of tetraethyl orthosilicate and stir for 18 h in a H_2O bath at 30 °C. 3) Filtrate, wash with DI H_2O and dry at 60 °C overnight. 4) Calcinate at 550 °C overnight. 5) Deposit a solution of the metal with the highest metal loading ($RuCl_3$ or $Ni(NO_3)_2 \cdot 6H_2O$) on MCM-48. 6) Mix and heat at 105 °C, evaporate the solvent and dry at 105 °C overnight. 7) Deposit the second metal solution, mix and heat at 105 °C, evaporate the solvent and dry at 105 °C overnight. 8) Reduce under H_2 at 250 °C for 1 h.	SAXS, XRD, BET, NH_3-TPD, H_2-TPR,TEM, EDS, STEM, AA, HPLC	Purge with N_2 and H_2, 120 – 140 °C, 25 bar of H_2, 5 mL of D-glucose, ratio C:Ru = 142	D-glucose hydrogenation (100 % selectivity to sorbitol obtained with bimetallic RuNi catalysts compared to 93-95 % selectivity for monometallic Ni)	[221]
NiRu/ZrO_2 and Ni-Ru/Al_2O_3	1) Dissolve $RuCl_3 \cdot xH_2O$ in DI H_2O and add dropwise on the support. 2) Dry in air at 100 °C for 12 h. 3) Impregnate the dried monometallic Ru catalyst with $Ni(NO_3)_2 \cdot 6H_2O$. 4) Dry at 100 °C for 12 h and calcinate at 450 °C in air for 4 h. 5) Reduce before catalysis at 350 °C under H_2 flow in N_2 for 6 h.	NH_3-TPD, N_2-sorption (BET), ICP-OES, XRD, XPS, TEM, GC	0.05 mL of levulinic acid, 0.3 mL formic acid, 0.1 g catalyst, 300 W microwaves at 150 °C	Levulinic acid hydrogenation (100 % selectivity to γ-valerolactone with the highest conversion (70 %) on the Al_2O_3 support)	[225]

Catalyst	Synthetic methodology	Characterisation	Catalytic reaction conditions	Comments	Ref.
RuNi/MMT	1) Dissolve $RuCl_3 \cdot xH_2O$ and $Ni(NO_3)_2 \cdot 6H_2O$ in 40 mL of H_2O under stirring with the slow addition of MMT-K10 support and stir for 2 h at RT under N_2 atmosphere. 2) Precipitate with a 10 M mixture of NaOH and K_2CO_3 (1:1) until pH = 7-8. 3) Reduce with sodium borohydride and stir for 30 min. 4) Filtrate and wash with DI H_2O. 5) Dry in air at 110 °C for 8-10 h.	XRD, HRTEM, SEM, XPS, NH_3-TPD, FT-IR, H_2-TPR, GC, GC-MS	4 g levulinic acid, 95 mL H_2O, 0.25 g catalyst, purge with N_2 and H_2, 17.2 bar, 220 °C	Levulinic acid hydrogenation (100 % selectivity to γ-valerolactone and 91 % conversion with 0.25 g of $Ru_{0.5}Ni_5$/MMT)	[248]
NiRu/TiO_2	1) Co-impregnate the TiO_2, synthesised by sol-gel method, with an aqueous solution of $Ni(NO_3)_2 \cdot 6H_2O$ and $Ru(NO)(NO_3)_3$. 2) Dry at 120 °C for 12 h and calcinate at 500 °C in static air. 3) Reduce before catalysis under H_2 flow at 500 °C for calcinated catalysts (350 °C for uncalcinated) for 2 h.	XRD, H_2-chemisorption, GC, HRTEM, TPR, XPS, NH_3-TPD, HPLC, TGA	0.15 g of catalyst, 30 bar of H_2, 320 °C	Phenol hydrodeoxygenation (149 μmol/g of catalyst s reaction rate for uncalcinated catalyst compared to 17.8 μmol/g of catalyst s for calcinated)	[228]

Catalyst	Synthetic methodology	Characterisation	Catalytic reaction conditions	Comments	Ref.
$NiRu/Al_2O_3$	1) Dissolve $RuCl_3$ and $Ni(NO_3)_2{\cdot}6H_2O$ in DI H_2O and stir 6 h. 2) Add Al_2O_3 and stir for 12 h. 3) Dry in vacuum dryer and calcinate in air at 550 °C for 4 h. 4) Reduce at 400 °C under H_2 flow.	GC, GC-MS, BET, XRD, H_2-TPR, SEM, EDS, TEM, DFT	450 °C, 0.32 M of phenol, 10 wt. % of catalyst in report to phenol, 3 bar of He, SCW (~250 bar)	Phenol hydrogenation (70 % phenol conversion to cyclohexanol obtained with the $Ru_{0.4}Ni_{0.6}$ compared to monometallics)	219
$NiRu/Al_2O_3$, TiO_2 and ZrO_2	1) Impregnate the support with aqueous solution of $Ni(NO_3)_2{\cdot}6H_2O$ and $Ru(NO)(NO_3)_3$. 2) Dry at 120 °C for 12 h. 3) Calcinate at 500 °C under air and reduce under 60 mL min^{-1} H_2 flow.	TPR, TCD, chemisorption, XPS, HRTEM, NH_3-TPD	320 °C, 54 bar of H_2, 100 mL phenol + dodecane, purge with N_2	Phenol hydrodeoxygenation (52 % selectivity to cyclohexanol obtained with the $RuNi/ZrO_2$ compared to 41 % and 10 % for monometallic Ni and Ru)	196

Catalyst	Synthetic methodology	Characterisation	Catalytic reaction conditions	Comments	Ref.
RuNi/HZSM-5	1) Dissolve 2.4778 g in a mixture of 122.016 g of TPAOH and 70.488 g DI H2O and stir for 2 h at RT. 2) Add dropwise 126.762 g TEOS and stir for 4 h. 3) Crystallisation for 72 h at 170 °C. 4) Washed at RT to neutrality and centrifugate to remove supernatant. 5) Dry at 110 °C overnight and calcined under air at 550 °C for 6 h. 6) Wet impregnation with solutions of $Ni(NO_3)_2 \cdot 6H_2O$ and $RuCl_3 \cdot 3H_2O$.	XRD, HR-TEM, STEM-HAADF, TEM-EELS, XAFS, XPS, H_2-TPR, H_2-TPD, IR, DFT	1.0 g guaiacol, 0.03 g of catalyst, 100 mL H_2O, 240 °C, 2 bar H_2	Guaiacol hydrodeoxygenation (90 % selectivity and 120 mmol·g·h^{-1} hydrogenolysis rate with bimetallic RuNi compared to 30 mmol·g·h^{-1} hydrogenolysis rate for monometallic Ru)	194
RuNi/HY	7) Impregnate the HY with the metallic solutions and stir at RT for 24 h. 8) Evaporate excess of H_2O and dry at 120 °C. 9) Calcinate at 550 °C for 4 h. 10) Reduce before catalysis at 250 °C for 2 h under 20 bar H_2.	XRD, STEM, N_2 physisorption, NH_3-TPD	30 mL H_2O, 100 mg catalyst, 100 mg guaiacol, 40 bar H_2, 250 °C	Guaiacol hydrodeoxygenation (91 % conversion with 40.5 % yield to hydrocarbons (cyclohexane, dimmers, ring-open products with bimetallics compared to lower values for Ru)	230

Catalyst	Synthetic methodology	Characterisation	Catalytic reaction conditions	Comments	Ref.
RuNi/SiO2-ZrO2	1) Dissolve 3.0 g $ZrOCl_2 \cdot 8H_2O$ and 14.4 g $Na_2SiO_3 \cdot 9H_2O$ in 200 mL DI H_2O. 2) Add dropwise NH_4OH until pH = 9-10. 3) Age at 60 ºC for 6 h under vigorous stirring, filtrate, dry and calcinate at 500 ºC for 5 h. 4) Wet impregnation with $RuCl_3$ and $Ni(NO_3)_2 \cdot 6H_2O$. 5) Dry and calcinate at 500 ºC for 6 h and reduce under H_2 at 550 ºC for 6 h.	XRD, TEM, XPS, H_2-TPF, GC-MS, GC-TCD, GC-FID	0.05 g catalyst, 0.1 g guaiacol, 20 mL octane, 10 bar H_2, 260 ºC	Guaiacol hydrodeoxygenation (100 % selectivity to hydrocarbons (74.5 % benzene and 25.5 % benzene dimer) with RuNi compared to lower values with monometallics)	[249]
RuNi/C	1) Dissolve 1,10-phenanthroline monohydrate in 25 mL of EtOH, mix with 25 mL of aqueous solution of H_2SO_4 (5 g 98%) and, after 4 h of stirring, remove EtOH and H_2O by distillation. 2) Mix 2.5 g with 5 g of activated carbon in 80 mL of DI H_2O and 50 mL of EtOH at RT for 12 h. 3) Evaporate solvent and calcinate at 900 ºC for 6 h under N_2. 4) Dissolve 0.15 g $NiCl_2 \cdot 6H_2O$ and 0.02 g of $RuCl_3 \cdot 3H_2O$ in 5 mL of H_2O, add 0.75 g of the N-doped C support and stir for 5h at RT. 5) Remove H_2O by rotary evaporator, dry at 110 ºC overnight, and reduce at 200 ºC for 5h under H_2 flow.	BET, XRD, HRTEM, EDS, XPS, H_2-TPR, ICP-MS, H_2-TPD, GC, GC-MS	6 mmol of substrate, 0.1 g catalyst, 35 mL H_2O, 230 ºC, 10 bar H_2	Lignin hydrogenolisis (68 % to 87 % selectivity towards compounds with non-hydrogenated phenyl ring with bimetallic RuNi, being $Ru_{1.5}Ni_{10}$ the most performant)	[195]

Catalyst	Synthetic methodology	Characterisation	Catalytic reaction conditions	Comments	Ref.
$NiRu/Al_2O_3$	1) Dissolve 9.2 g of $Ni(NO_3)_2 \cdot 6H_2O$, 2075 g $Al(NO_3)_3 \cdot 9H_2O$ and 0.68 g $RuCl_3 \cdot xH_2O$ in 100 mL of DI H_2O. 2) Add slowly 100 mL of a 12.96 g NaOH aqueous solution into 100 mL of Na_2CO_3 at 60 ºC and stir for 20 h, keeping pH = 9.5-10. 3) Filter, wash with DI H_2O until pH = 7 and dry at 80 ºC overnight. 4) Calcinate at 460 ºC for 6 h. 5) Reduce under H_2 at 450-550 ºC for 6 h. 6) Passivate with O_2/N_2 at RT.	N_2-sorption, HRTEM, XRD, XPS	0.025 g catalyst, 0.5 mmol of substrate, 10 mL isopropanol, purge with N_2, 100-150 ºC	Lignin hydrogenolysis (100 % conversion of benzyl phenyl ether with 54.72 % selectivity to toluene and 45.28 % to cyclohexanol with $Ni_{40}Ru_5$ compared to lower values for other lignin model compounds)	[229]
RuNi/SBA-15	1) Dissolve $RuCl_3 \cdot xH_2O$ and $NiCl_2$ in acetone with 0.1 M of HCl. 2) Introduce the solution on the SBA-15 for impregnation. 3) Dry at 50 ºC overnight. 4) Calcinate at 500 ºC for 3 h.	N_2-adsorption and desorption (BET), XRD, SEM, EDS, HRTEM, TPR, H_2-TPD, NH_3-TPD, ICP-ES, GC with FID, GC-MS, GPC, 2D-HSQC NMR	0.5 g lignin, 20 mL EtOH, 0.025 g catalyst, 30 bar H_2, 350 ºC	Lignin depolimerization (77.5 % yield of lignin depolimerization to monomeric phenols with $Ru_{0.6}Ni_{0.4}$ compared to other tested metal ratios)	[250]

Catalyst	Synthetic methodology	Characterisation	Catalytic reaction conditions	Comments	Ref.
NiRu/C	1) Add $Ni(NO_3)_2 \cdot 6H_2O$ aqueous solution to 5 g of active carbon. 2) After 24 h, dry at 110 ºC for 24 h. 3) Calcinate under Ar for 3 h at 450 ºC. 4) Add the Ni/C on an aqueous solution of $RuCl_3$. 5) Dry for 24 at 110 ºC and calcinate under Ar (70 mL/min) for 3 h at 300 ºC.	Physisorption, TEM, EDS, EDX, XRD, XPS, LA-ICP-MS, GC-MS	0.1 g - 0.2 g lignin, 20 mL EtOH, 0.05 - 0.2 g catalyst, purge with H_2, 2 - 40 bar H_2, 120 – 280 ºC	Lignin and its model compounds catalytic hydrogenolysis (CH) (100 % conversion with 96.8 % yield to toluene and 90.3 % to phenol with $Ni_{10}Ru_1$ compared to other catalysts)	207
RuNi/Al-HY	1) Dry HY in an oven at 105 ºC for 10 h. 2) Impregnate with an $Al(NO_3)_3 \cdot 9H_2O$ aqueous solution, stir, US for 20 min and leave it static for 24 h. 3) Dry at 105 ºC for 10 h and calcinate at 550 ºC for 5 h. 4) Dissolve $RuCl_3 \cdot xH_2O$ and $Ni(NO_3)_2 \cdot 6H_2O$ in H_2O and add 2 g of Al-HY, stir, US for 20 min and leave it static for 24 h. 5) Dry at 105 ºC for 10 h and reduce at 550 ºC (for monometallic Ru 400 ºC) for 3 h under H_2 and finally passivate under N_2.	GC, GC-MS, BET, XRD, SEM, XPS, TEM, NH_3-TPD	0.3 g organosolv lignin (eucalyptus), 0.15 g catalyst, 35 mL EtOH, purge with N_2, 10 bar of H_2, 280 ºC	Lignin hydrogenation (91.7 % conversion with 20.2 yield to phenolic monomers obtained with $Ru_{2.5}Ni_{10}$ compared to monometallics and other bimetallic ratios)	214

Catalyst	Synthetic methodology	Characterisation	Catalytic reaction conditions	Comments	Ref.
RuNi/CTAB NCs	1) Dissolve 7.8 mg of $RuCl_3 \cdot 3H_2O$ and 40.4 mg of $NiCl_2 \cdot 6H_2O$ and 100 mg CTAB in 3 mL of H_2O, sonicate 15 min and stir in an ice bath for 30 min. 2) Add dropwise 1.5 mL of an aqueous solution with 30 mg of $NaBH_4$ with vigorous stirring. 3) Stir in an ice bath for 20 min adding H_2O until reaching a 10 mL solution.	TEM, HAADF, STEM-EDS, XRD, XPS	5 mol % RuNi catalyst, H_2O, 95 °C under 1 atm of H_2	Lignin hydrogenolysis (100 % conversion with >90 % yield to non-hydrogenated monomers such as toluene and phenol with the $Ru_{15}Ni_{85}$ compared to lower values with other metallic ratios)	[200]

Small molecules, such as, N_2, CO and CO_2 have been successfully reduced in the presence of RuNi based catalysts, in some cases displaying better performances than the corresponding monometallic counterparts.[201–203] CO hydrogenation on bimetallic $[Et_4N]_2[Ru_3Ni_3C(CO)_{13}]$ at 246 ºC using 5 bar of a mixture CO/H_2 = 0.5, increases the selectivity towards oxygenates such as methanol, methanal, ethanol and propanol, compared to the monometallic Ru catalyst, as the generation of hydrocarbons decreases, obtaining in both cases a low CO conversion.[215] More recently, dimethoxymethane has been produced on RuNi/β-zeolite (BEA) bimetallic catalysts by CO hydrogenation, obtaining its better yield after 48 h at 120 ºC using 75 bar of the mixture CO/H_2 = 0.5 in methanol, yield higher than the observed with the corresponding monometallic counterparts.[201]

CO_2 hydrogenation using RuNi/BMI.NTf_2 NPs at 150 ºC with 8.5 bar of a mixture CO_2/H_2 = 0.25, displays synergetic effects between metals. Several Ru/Ni ratios were used, and concerning the activity, Ru_3Ni_2 NPs was the most selective towards low weight hydrocarbons (C_2-C_4).[202]

Ammonia synthesis was performed on $NiRu_3$ catalysts (2 wt. % metal) at temperatures from 375 ºC to 450 ºC using a mixture N_2/H_2 = 3. In this case, the productivity was lower than the monometallic Ru catalyst, which was attributed to a strong absorption of the hydrides to the metallic surface because of the presence of Ni.[203]

Aliphatic and aromatic alkene hydrogenations have been achieved as well with this class of bimetallic catalysts. RuNi based materials have been used for the hydrogenation of pentadienes,[204] cyclohexene,[204] benzene,[216] naphthalene,[217] mixtures of hydrocarbons modelling gasoline,[218] phenol,[219] and carbazol derivatives.[214]

Hydrogenation of linear dienes, such as 1,3-pentandiene and 1,4-pentandiene to pentane, occurs on the bimetallic cluster $[(Cp)NiRu_3H_3(CO)_9]$ at 80 ºC under H_2 pressure with a 100 % selectivity, observing an increase of hydrogenolysis when increasing the temperature.[204]

Using the same catalysts and reaction conditions, cyclohexene, 1,3-cylochexadiene and 1,4-cyclohexadiene were converted to cyclohexane with a 100 % selectivity, as similarly observed with the monometallic Ru catalyst. Toluene was also hydrogenated, in this case, synergetic effects between metals were observed in terms of selectivity, as the highest amount of methylcyclohexane was obtained with the bimetallic catalyst, having as a minor product cyclohexane.[204]

Benzene hydrogenation was also possible using Ru/Ni catalysts with different stabilisers, PVP and CTAB, at 100 ºC under 50 bar of H_2. In all cases, the presence of Ru increased the yield to cyclohexane compared to the monometallic Ni catalyst.[220] Benzene hydrogenation on bimetallic Ru-Ni/C at 60 ºC under 53 bar of H_2, shows synergetic effects between metals and a higher activity of bimetallic Ru-Ni-NiO interfaces than the RuO_2-NiO ones.[221] Benzene hydrogenation studied at lower temperatures(20-60 ºC) and pressures (3-48 bar) with the same catalyst, allowed observing synergetic effects between metals on the activity, as TOFs and yields towards cyclohexane were higher.[222] Benzene hydrogenation on bimetallic Ru-Ni/NiO/C at 60 ºC and 53 bar of H_2 is the most active and selective to cyclohexane of the tested bimetallic and monometallic NPs, which the authors explained by the high dispersion of Ru atoms on the structure of Ni/NiO NPs.[223] RuNi/C were also tested for benzene hydrogenation at 60 ºC under 53 bar of H_2, observing that lower calcination temperatures for the preparation of the catalysts, enhance the activity of the catalyst towards cyclohexane and also observing synergetic effects between Ru (activating H_2), $Ni(OH)_2$ (activating benzene) and Ni acting as a bridge for hydrogen transfer.[224] Synergetic effects between Ru, NiO and Ni are also observed on the activities with the benzene hydrogenation on bimetallic RuNi/C-PVP catalysts at 60 ºC under 53 bar of H_2, observing a high selectivity towards cyclohexane.[216] Synergetic effects were further observed between the Ru, Ni and NiO species, and being the most active composition the $Ru_{0.56}Ni_{0.44}$.[209] Benzene hydrogenation is also evaluated on bimetallic Ru/Ni catalysts, obtained through galvanic replacement using EDA, PVP or CTAB as stabilisers, at 100 ºC using 53 bar of H_2, synergetic effects were observed as bimetallic catalysts yielded to cyclohexane, in higher yields than monometallic Ni, and being Ru/Ni-EDA more active than its PVP and CTAB homologues, attributed to a better dispersion of Ru atoms.[225] Benzene hydrogenation was also tested on trimetallic Ru/CoNi catalysts at 100 ºC under 53 bar of H_2, showing a high selectivity of the catalysts synthesised in ethanol and a synergy between the three metals.[226]

Ru/Ni/$Ni(OH)_2$/C was able to reduce naphthalene, using as reaction conditions 48 bar of H_2 at different temperatures, being 100 ºC the one with highest activity. At this temperature, the bimetallic system displayed higher activity than the monometallic catalyst, observing a synergetic effect between the Ru, Ni and $Ni(OH)_2$ species. The selectivity towards decalin, the fully hydrogenated product, was high, reaching a value of >99 %.[227] The same reaction was tested on Ru/Ni/NiO/C bimetallic catalyst also at different temperatures and using several amounts of catalyst, observing a synergy effect between metals and a 100 % of selectivity towards decalin in this case at a low temperature, 25 ºC.[217] Anisole hydrogenation on bimetallic RuO_2/NiO/Al-SBA catalyst at temperatures ranging from 300 to 450 ºC and a 50 $mL \cdot min^{-1}$ flow of H_2 shows a good selectivity towards benzene for the catalyst with a

weight Ru of 0.4 % although, it was observed that the increase of weight Ru percentage to 1 % increased the activity, being the most active catalyst.[228]

A mixture of 10 wt. % styrene, 35 wt. % toluene and 55 wt. % n-heptane, as a model for gasoline, was successfully hydrogenated on bimetallic $NiRu/Al_2O_3$ catalysts at 60 ºC with 20 bar of H_2. Several compositions were tested being $Ni_4Ru_{0.05}$ the most active and selective towards ethylbenzene; the observed synergetic effects between metals were attributed to an increase of exposure of the Ni atoms compared to monometallic Ni.[218] Hydrogenation of phenolic compounds, like phenol, by supercritical water gasification on $NiRu/Al_2O_3$ bi-metallic catalysts at 450 ºC occurs. The incorporation of Ru on the catalyst leads to an increase of the activity and the selectivity towards cyclohexanol.[219,229]

The aromatic rings of N-ethylcarbazole and N-propylcarbazole were successfully hydrogenated using $RuNi/TiO_2$[230]and $RuNi/Al_2O_3$,[214] respectively. For the former, temperatures as high as 150 ºC and pressures of 70 bar of H_2 were needed, yet, $RuNi/TiO_2$ performed better than the corresponding Ru catalyst. Support effects were observed, and the crystal structure of TiO_2 modified the outcome of the reaction.[230] N-propylcarbazole hydrogenation using $RuNi/Al_2O_3$ as catalyst was also performed at high temperature, 150 ºC, under lower pressure, 40 bar of H_2. Several Ru/Ni ratios were tested, and the $Ru_{2.5}Ni_{2.5}$ catalyst displayed the best activity and selectivity towards the perhydro-N-propylcarbazole of the series. The synergetic effects observed were attributed to a favoured hydrogen spillover, in comparison to the monometallic counterparts.[214]

Alumina was also used as support for a bimetallic $NiRu/Al_2O_3$ active for the quinoline hydrogenation.[231] Elevated temperatures and pressures, 300 to 400 ºC, H_2 pressures from 200 bar to 250 bar, were applied, which lead to the hydrodenitrogenation of the quinoline to produce 2-hexene. At lower temperatures and pressures, 100 ºC and 50 bar of H_2, quinoline hydrogenation was achieved using RuNi/C. The activity observed with the bimetallic system was enhanced compared to the monometallic counterparts; selectivity towards the partially hydrogenated product, 1,2,3,4-tetrahydroquinoline (1-THQ), was high.[232] On the other hand, RuNi/meso_SC catalyst was less performant than others Ru-M (M = Ga, In, Ge, Sn, Ni) bimetallic catalysts tested for the hydrogenation of quinoline at 80 ºC under 10 bar of H_2. In this work, Ru-Sn displayed the best performances of all tested catalysts.[233] Interestingly, $RuNi/Al_2O_3$ selectively hydrogenated only one of the two benzene rings present on the dibenzo-18-crown-6 ether compound, using relatively drastic conditions, 120 ºC under 90 bar of H_2 and microwaves. This behaviour was in contrast with a RuPd catalyst also tested which hydrogenates both rings.[234]

Oxygen containing functional groups such as aldehydes,[206]and nitro- compounds,[205] are also hydrogenated by using RuNi based catalysts. Nitrobenzene hydrogenation was performed on bimetallic NiRu-HT at 80 ºC and hydrazine as reducing agent (1 mL). Aniline was obtained in higher yields and selectivity compared to the monometallic Ni catalyst.[235] Nitrobenzene was also hydrogenated on NiRu/MgAl bimetallic catalysts at 80 ºC using hydrazine hydrate as reducing agent, observing a full conversion of nitrobenzene with an 81 % of selectivity towards aniline without the use of solvent, in this case a synergy between metals was also observed in terms of activity.[205] Furthermore, a bimetallic RuNi/Al_2O_3 was able to reduce selectively the nitro group of nitrostyrene, giving 4-aminostyrene as the major product. This achievement was performed at 50 °C under 10 bar of H_2 pressure; 4-aminostyrene was the main product obtained with Ni rich bimetallic catalysts and 4-aminoethylbenzene produced for Ru-rich catalysts.[236] Concerning aldehydes, hydroxypropanal reduction to produce 1,3-propanediol was described over RuNi/SiO_2 bimetallic catalyst at 80 ºC under 20 bar of H_2.[206] RuNi bimetallic catalyst performed better than others, which was attributed to the effect of the introduction of Ru on the structure of the catalysts, decreasing the size of Ni particles and increasing the porosity.[206] Furfural hydrogenation was studied on RuNi/Al_2O_3 bimetallic catalysts, using a temperature of 100 ºC and a pressure of 54 bar of H_2, in water. Synergetic effects between metals were observed on activity, with almost complete selectivity to HF.[237]

Highly oxygenated compounds, such as cellulose and sugars,[238,239] have also been successfully transformed over RuNi catalysts. Hydrodeoxygenations, reaction which allows the elimination of oxygen from a given compound with hydrogen, of several substrates[196,240] have been achieved. These are promising results in order to apply this kind of bimetallic catalysts for the upgrading of highly oxygenated molecules from biomass.

Lactose hydrogenation occurs on RuNiO/TiO_2 bimetallic catalyst at 120 ºC under 55 bar of H_2. Of all the catalysts compositions used, $Ru_5(NiO)_5/TiO_2$ catalyst was the most active and selective to lactitol (99.4 %), displaying also better performance than its monometallic counterparts in terms of activity and selectivity.[241]

Cellulose[229] and cellobiose[242] were hydrogenated on RuNi bimetallic systems, RuNi/AC and RuNi/CNT, and NiRu/CNF, respectively, using harsh conditions. High selectivities towards sorbitol (>70 %), were reached in the former catalytic system; while for the later polyols cellobitol and sorbitol were obtained with high selectivity, up to 84.5 %. In both cases, bimetallic systems were compared to the corresponding monometallic catalysts, performing better than them.

Glucose hydrogenation occurs on Ru:Ni/MCM-48 bimetallic catalysts at 120 ºC using 25 bar of H_2, evidencing synergetic effects between metals as the catalysts with Ru/Ni ratios higher than 0.45 improve the activity of the monometallic homologues, apart of observing complete selectivity towards sorbitol.[238]

RuNi/montmorillonate (MMT) bimetallic catalysts hydrogenated levulinic acid γ-valerolactone, reaching 100 % selectivity in the case of the catalyst being composed by 0.5 wt. % Ru and 5 wt. % Ni. The authors attributed to an electron transfer between metals.[243] NiRu/ZrO_2 and NiRu/Al_2O_3 were also used as catalysts for this reaction, in this case using formic acid as hydrogen donor, and not H_2. The support played a role in the outcome of the reaction, and NiRu/Al_2O_3 was the most active and obtaining also a 100 % selectivity towards γ-valerolactone.[244]

Support effects were observed in the hydrodeoxygenation of phenol – at harsh reaction conditions, 320 ºC under 54 bar of H_2- using bimetallic RuNi. Al_2O_3, ZrO_2 and TiO_2 were used to support the metallic nanoparticles; Al_2O_3 based catalyst was the most active and selective to cyclohexane, while in TiO_2 the catalysis was less active and was selective towards cyclohexanol, which was attributed to decrease of active sites in Ru/TiO_2.[196] Hydrodeoxygenation of phenolic compounds, like guaiacol, and other lignin-oil compounds is observed on RuNi/SiO_2-ZrO_2 bimetallic catalysts at 260 ºC under 10 bar of H_2, showing a high selectivity towards the hydrocarbons and a good performance of the bimetallic catalysts, compared to the monometallic counterparts, ascribed to a better adsorption of guaiacol on the bimetallic surface.[245] RuNi/HY[240] and RuNi/HZSM-5[194] were also active for this reaction using harsh conditions as well. RuNi supported on HY was more selective for the production of hydrocarbons, providing cyclohexane as major product. Using RuNi/HZSM-5 leads to a high selectivity towards phenol, while the aromatic ring remained intact.

RuNi based catalysts are performant catalysts for the hydrogenolysis/depolymerisation of lignin and related model compounds. RuNi-AC/N,[195] NiRu/Al_2O_3,[246] RuNi/SBA-15,[247] NiRu/AC,[207] and RuNi/Al-HY [248] displayed good activities for the C-O cleavage, as well as high selectivities towards the not fully hydrogenated products, as aromatic rings were not transformed. In addition to that, several Ru/Ni ratios were tested in some of these works, pointing to a synergy between metals at a given composition. Lignin hydrogenolysis on RuNi-AC/N bimetallic catalyst was performed at 230 ºC under 10 bar of H_2; 1.5 %Ru-10 % Ni catalyst was the most active and selective towards aromatics and showing synergetic effects between metals.[195] Hydrogenolysis of several lignin model compounds was also studied on $Ni_{40}Ru_5/Al_2O_3$ bimetallic catalysts at 120 ºC in isopropanol, reaching 100 %

conversion in the case of benzyl phenyl ether hydrogenolysis, obtaining toluene and cyclohexanol as only products.[246] Lignin depolymerisation on RuNi/SBA-15 bimetallic catalyst was achieved at harsh reaction conditions, 350 ºC under 30 bar of H_2. $Ru_{0.6}Ni_{0.4}$ was the most active and selective catalyst to phenols, attributed to a strong bonding of the substrate on bimetallic surfaces was high.[247] Depolymerisation of lignin on NiRu/AC catalysts was carried out at different temperatures and H_2 pressures, observing in all cases the synergy between metals on the bimetallic as activities were higher than the observed while using monometallic catalysts.[207] Lignin depolymerisation is also observed on RuNi/Al-HY bimetallic catalyst at 280 ºC under 10 bar of H_2. Phenolic monomers such as hydrocarbyl guaiacol or hydrocarbyl phenols were selectively obtained while using a catalysts having a $Ru_{2.5}Ni_{10}$ composition.[248] Lignin hydrogenolysis on RuNi/CTAB nanocatalysts at 95 ºC under 1 atm of H_2 showed synergetic effects between Ru and Ni being $Ru_{15}Ni_{85}$ the most active and selective catalyst towards non-hydrogenated monomers.[200]

RuNi based catalysts for hydrogenation reactions are an interesting alternative to Ru based catalysts as they offer comparable or higher performances than the later, due to the presence of the second, earth-abundant, metal. In addition to that, they are usually more stable and active than Ni based catalysts. If these are not *per se* reasons to explore further this kind of bimetallic systems, the use of an earth-abundant metal on the composition of the catalysts, gives excellent perspectives in socio-economical terms, as its implementation fulfils some of the requirements to base a sustainable future. Particularly, the synergy observed between Ru and Ni in a plethora of works, in most cases attributed to charge transfer between metals, but also to H_2 spillover events, which is sometimes correlated to the composition of the catalysts, opens the door to explore more this type of catalysts, as the composition is usually easily tuned. A less explored issue is the modulation of the catalytic properties by changing the structure of the bimetallic systems. In this sense, many works do not provide full characterisation to better understand the nanostructure of these RuNi based catalysts. Even if all types of structures have been reported for RuNi nanoparticles, core-shell organization with Ni on the shell examples are very abundant on the literature. Finally, support and ligand effects have also been described to have an impact in the catalytic properties of these catalysts, thus, giving more opportunities to tune them. It is worth mentioning, that RuNi based catalysts are very efficient to cleave C-O bonds. This interesting property is of interest to transform biomass based molecules, as its high oxygen content must be lowered to be used as an alternative to the fossil fuel based technologies. Taking into consideration all these premises, the furfural hydrogenation/hydrogenolysis using Ru based catalysts alloyed with earth-abundant metals has been explored in this thesis. FF, a biomass derived compound, may be transformed under hydrogen and the presence of a catalyst, to a plethora of interesting compounds; thus highly selective processes are needed to avoid separa-

tion issues. In order to tune the catalysts prepared here, the ratio between metals have been analysed, as well as ligand effects in the synthesis, thus structure and other properties defined during the synthesis, and its catalytic performances impact. Chapter 2 is devoted to the synthesis and characterisation of bimetallic catalysts; followed by the Chapter 3 in which the catalytic applications of those systems are explored. In order to better understand the catalytic systems developed, theoretical calculations have been performed, which are detailed in Chapter 4. These four chapters are thus dedicated to the main objectives of this work, the upgrade of biomass derived compounds with earth-abundant metal based catalysts, from an experimental and theoretical point of view. Additionally, other directions have been explored, such as the application of RuNi compounds as catalysts for the hydrogenation of quinoline, Chapter 3, or the deuteration reactions of several molecules using Ru based catalysts, work which was developed during a 3-month internship at Matthias Beller group in Germany, Chapter 5. To close the manuscript the main conclusions and the perspectives of this work are reviewed.

1.5 References

(1) Zhou, P.; Yang, X.-L.; Wang, X.-G.; Hu, B.; Zhang, L.; Zhang, W.; Si, H.-R.; Zhu, Y.; Li, B.; Huang, C.-L.; Chen, H.-D.; Chen, J.; Luo, Y.; Guo, H.; Jiang, R.-D.; Liu, M.-Q.; Chen, Y.; Shen, X.-R.; Wang, X.; Zheng, X.-S.; Zhao, K.; Chen, Q.-J.; Deng, F.; Liu, L.-L.; Yan, B.; Zhan, F.-X.; Wang, Y.-Y.; Xiao, G.-F.; Shi, Z.-L. A Pneumonia Outbreak Associated with a New Coronavirus of Probable Bat Origin. *Nature* **2020**, *579* (7798), 270. https://doi.org/10.1038/s41586-020-2012-7

(2) Kabir, Md. T.; Uddin, Md. S.; Hossain, Md. F.; Abdulhakim, J. A.; Alam, Md. A.; Ashraf, G. M.; Bungau, S. G.; Bin-Jumah, M. N.; Abdel-Daim, M. M.; Aleya, L. NCOVID-19 Pandemic: From Molecular Pathogenesis to Potential Investigational Therapeutics. *Front. Cell Dev. Biol.* **2020**, *8*, 616. https://doi.org/10.3389/fcell.2020.00616

(3) Bittmann, F. How Trust Makes a Difference: The Impact of the First Wave of the COVID-19 Pandemic on Life Satisfaction in Germany. *Appl. Res. Qual. Life* **2022**, *17* (3), 1389. https://doi.org/10.1007/s11482-021-09956-0

(4) Mofijur, M.; Fattah, I. M. R.; Alam, M. A.; Islam, A. B. M. S.; Ong, H. C.; Rahman, S. M. A.; Najafi, G.; Ahmed, S. F.; Uddin, Md. A.; Mahlia, T. M. I. Impact of COVID-19 on the Social, Economic, Environmental and Energy Domains: Lessons Learnt from a Global Pandemic. *Sustain. Prod. Consum.* **2021**, *26*, 343. https://doi.org/10.1016/j.spc.2020.10.016

(5) Jiang, P.; Fu, X.; Fan, Y. V.; Klemeš, J. J.; Chen, P.; Ma, S.; Zhang, W. Spatial-Temporal Potential Exposure Risk Analytics and Urban Sustainability Impacts Related to COVID-19 Mitigation: A Perspective from Car Mobility Behaviour. *J. Clean. Prod.* **2021**, *279*, 123673. https://doi.org/10.1016/j.jclepro.2020.123673

(6) Leal Filho, W.; Brandli, L. L.; Lange Salvia, A.; Rayman-Bacchus, L.; Platje, J. COVID-19 and the UN Sustainable Development Goals: Threat to Solidarity or an Opportunity? *Sustainability* **2020**, *12* (13), 5343. https://doi.org/10.3390/su12135343

(7) Alexander, D.; Pescaroli, G. What Are Cascading Disasters? *UCL Open Environ.* **2019**, *1*. https://doi.org/10.14324/111.444/ucloe.000003

(8) Hewitt, K. Editor. Interpretations of Calamity from the Viewpoint of Human Ecology. London Unwin-Hyman; **1983**, 3. https://doi.org/10.4324/9780429329579

(9) Saraceno, F. The End of the Consensus? The Economic Crisis and the Crisis of Macroeconomics. *Rev. OFCE* **2018**, *157* (3), 319. https://doi.org/10.3917/reof.157.0319

(10) OECD. *OECD Economic Outlook, Interim Report March 2022: Economic and Social Impacts and Policy Implications of the War in Ukraine*; OECD Economic Outlook; OECD, **2022**. https://doi.org/10.1787/4181d61b-en
(11) Watts, N.; Amann, M.; Arnell, N.; Ayeb-Karlsson, S.; Beagley, J.; Belesova, K.; Boykoff, M.; Byass, P.; Cai, W.; Campbell-Lendrum, D.; Capstick, S.; Chambers, J.; Coleman, S.; Dalin, C.; Daly, M.; Dasandi, N.; Dasgupta, S.; Davies, M.; Di Napoli, C.; Dominguez-Salas, P.; Drummond, P.; Dubrow, R.; Ebi, K. L.; Eckelman, M.; Ekins, P.; Escobar, L. E.; Georgeson, L.; Golder, S.; Grace, D.; Graham, H.; Haggar, P.; Hamilton, I.; Hartinger, S.; Hess, J.; Hsu, S.-C.; Hughes, N.; Jankin Mikhaylov, S.; Jimenez, M. P.; Kelman, I.; Kennard, H.; Kiesewetter, G.; Kinney, P. L.; Kjellstrom, T.; Kniveton, D.; Lampard, P.; Lemke, B.; Liu, Y.; Liu, Z.; Lott, M.; Lowe, R.; Martinez-Urtaza, J.; Maslin, M.; McAllister, L.; McGushin, A.; McMichael, C.; Milner, J.; Moradi-Lakeh, M.; Morrissey, K.; Munzert, S.; Murray, K. A.; Neville, T.; Nilsson, M.; Sewe, M. O.; Oreszczyn, T.; Otto, M.; Owfi, F.; Pearman, O.; Pencheon, D.; Quinn, R.; Rabbaniha, M.; Robinson, E.; Rocklöv, J.; Romanello, M.; Semenza, J. C.; Sherman, J.; Shi, L.; Springmann, M.; Tabatabaei, M.; Taylor, J.; Triñanes, J.; Shumake-Guillemot, J.; Vu, B.; Wilkinson, P.; Winning, M.; Gong, P.; Montgomery, H.; Costello, A. The 2020 Report of The Lancet Countdown on Health and Climate Change: Responding to Converging Crises. *The Lancet* **2021**, *397* (10269), 129. https://doi.org/10.1016/S0140-6736(20)32290-X
(12) Taalas, P.; Guterres, A. *WMO Statement on the State of the Global Climate in 2018*; World Meteorological Organization (WMO): Genf, **2019**. https://library.wmo.int/doc_num.php?explnum_id=10211
(13) Alfieri, L.; Bisselink, B.; Dottori, F.; Naumann, G.; de Roo, A.; Salamon, P.; Wyser, K.; Feyen, L. Global Projections of River Flood Risk in a Warmer World: RIVER FLOOD RISK IN A WARMER WORLD. *Earths Future* **2017**, *5* (2), 171. https://doi.org/10.1002/2016EF000485
(14) Watts, N.; Amann, M.; Arnell, N.; Ayeb-Karlsson, S.; Belesova, K.; Berry, H.; Bouley, T.; Boykoff, M.; Byass, P.; Cai, W.; Campbell-Lendrum, D.; Chambers, J.; Daly, M.; Dasandi, N.; Davies, M.; Depoux, A.; Dominguez-Salas, P.; Drummond, P.; Ebi, K. L.; Ekins, P.; Montoya, L. F.; Fischer, H.; Georgeson, L.; Grace, D.; Graham, H.; Hamilton, I.; Hartinger, S.; Hess, J.; Kelman, I.; Kiesewetter, G.; Kjellstrom, T.; Kniveton, D.; Lemke, B.; Liang, L.; Lott, M.; Lowe, R.; Sewe, M. O.; Martinez-Urtaza, J.; Maslin, M.; McAllister, L.; Mikhaylov, S. J.; Milner, J.; Moradi-Lakeh, M.; Morrissey, K.; Murray, K.; Nilsson, M.; Neville, T.; Oreszczyn, T.; Owfi, F.; Pearman, O.; Pencheon, D.; Pye, S.; Rabbaniha, M.; Robinson, E.; Rocklöv, J.; Saxer, O.; Schütte, S.; Semenza, J. C.; Shumake-Guillemot, J.; Steinbach, R.; Tabatabaei, M.; Tomei, J.; Trinanes, J.; Wheeler, N.; Wilkinson, P.; Gong, P.; Montgomery, H.; Costello, A. The 2018 Report of the Lancet Countdown on Health and Climate Change: Shaping the Health of Nations for Centuries to Come. *The Lancet* **2018**, *392* (10163), 2479. https://doi.org/10.1016/S0140-6736(18)32594-7
(15) Rydin, Y.; Bleahu, A.; Davies, M.; Dávila, J. D.; Friel, S.; De Grandis, G.; Groce, N.; Hallal, P. C.; Hamilton, I.; Howden-Chapman, P.; Lai, K.-M.; Lim, C.; Martins, J.; Osrin, D.; Ridley, I.; Scott, I.; Taylor, M.; Wilkinson, P.; Wilson, J. Shaping Cities for Health: Complexity and the Planning of Urban Environments in the 21st Century. *The Lancet* **2012**, *379* (9831), 2079. https://doi.org/10.1016/S0140-6736(12)60435-8
(16) Whitmee, S.; Haines, A.; Beyrer, C.; Boltz, F.; Capon, A. G.; de Souza Dias, B. F.; Ezeh, A.; Frumkin, H.; Gong, P.; Head, P.; Horton, R.; Mace, G. M.; Marten, R.; Myers, S. S.; Nishtar, S.; Osofsky, S. A.; Pattanayak, S. K.; Pongsiri, M. J.; Romanelli, C.; Soucat, A.; Vega, J.; Yach, D. Safeguarding Human Health in the Anthropocene Epoch: Report of The Rockefeller Foundation–Lancet Commission on Planetary Health. *The Lancet* **2015**, *386* (10007), 1973. https://doi.org/10.1016/S0140-6736(15)60901-1
(17) Energy Production and Consumption - Our World in Data. https://ourworldindata.org/energy-production-consumption

(18) Hoffert, M. I.; Caldeira, K.; Jain, A. K.; Haites, E. F.; Harvey, L. D. D.; Potter, S. D.; Schlesinger, M. E.; Schneider, S. H.; Watts, R. G.; Wigley, T. M. L.; Wuebbles, D. J. Energy Implications of Future Stabilization of Atmospheric CO_2 Content. *Nature* **1998**, *395* (6705), 881. https://doi.org/10.1038/27638

(19) Lewis, N. S.; Nocera, D. G. Powering the Planet: Chemical Challenges in Solar Energy Utilization. *Proc. Natl. Acad. Sci.* **2006**, *103* (43), 15729. https://doi.org/10.1073/pnas.0603395103

(20) *World Energy Assessment: Energy and the Challenge of Sustainability*; Goldemberg, J., United Nations Development Programme, United Nations, World Energy Council, Eds.; United Nations Development Programme: New York, NY, **2000**. https://sustainabledevelopment.un.org/index.php?page=view&type=400&nr=2423&menu=35

(21) Maier-Reimer, E.; Hasselmann, K. Transport and Storage of C02 in the Ocean - an Inorganic Ocean-Circulation Carbon Cycle Model. *Clim. Dyn.* **1987**, *2*, 63. https://doi.org/10.1007/BF01054491

(22) Nakićenović, N., *Special Report on Emissions Scenarios: A Special Report of Working Group III of the Intergovernmental Panel on Climate Change*; Intergovernmental Panel on Climate Change, Eds.; Cambridge University Press: Cambridge ; New York, **2000**. https://www.ipcc.ch/site/assets/uploads/2018/03/sres-en.pdf

(23) Watson, R. T.; Albritton, D. L., *Climate Change 2001: Synthesis Report*; Intergovernmental Panel on Climate Change, Eds.; Cambridge University Press: Cambridge ; New York, **2001**. https://www.ipcc.ch/site/assets/uploads/2018/05/SYR_TAR_full_report.pdf

(24) Friedlingstein, P.; O'Sullivan, M.; Jones, M. W.; Andrew, R. M.; Gregor, L.; Hauck, J.; Le Quéré, C.; Luijkx, I. T.; Olsen, A.; Peters, G. P.; Peters, W.; Pongratz, J.; Schwingshackl, C.; Sitch, S.; Canadell, J. G.; Ciais, P.; Jackson, R. B.; Alin, S. R.; Alkama, R.; Arneth, A.; Arora, V. K.; Bates, N. R.; Becker, M.; Bellouin, N.; Bittig, H. C.; Bopp, L.; Chevallier, F.; Chini, L. P.; Cronin, M.; Evans, W.; Falk, S.; Feely, R. A.; Gasser, T.; Gehlen, M.; Gkritzalis, T.; Gloege, L.; Grassi, G.; Gruber, N.; Gürses, Ö.; Harris, I.; Hefner, M.; Houghton, R. A.; Hurtt, G. C.; Iida, Y.; Ilyina, T.; Jain, A. K.; Jersild, A.; Kadono, K.; Kato, E.; Kennedy, D.; Klein Goldewijk, K.; Knauer, J.; Korsbakken, J. I.; Landschützer, P.; Lefèvre, N.; Lindsay, K.; Liu, J.; Liu, Z.; Marland, G.; Mayot, N.; McGrath, M. J.; Metzl, N.; Monacci, N. M.; Munro, D. R.; Nakaoka, S.-I.; Niwa, Y.; O'Brien, K.; Ono, T.; Palmer, P. I.; Pan, N.; Pierrot, D.; Pocock, K.; Poulter, B.; Resplandy, L.; Robertson, E.; Rödenbeck, C.; Rodriguez, C.; Rosan, T. M.; Schwinger, J.; Séférian, R.; Shutler, J. D.; Skjelvan, I.; Steinhoff, T.; Sun, Q.; Sutton, A. J.; Sweeney, C.; Takao, S.; Tanhua, T.; Tans, P. P.; Tian, X.; Tian, H.; Tilbrook, B.; Tsujino, H.; Tubiello, F.; van der Werf, G. R.; Walker, A. P.; Wanninkhof, R.; Whitehead, C.; Willstrand Wranne, A.; Wright, R.; Yuan, W.; Yue, C.; Yue, X.; Zaehle, S.; Zeng, J.; Zheng, B. Global Carbon Budget 2022. *Earth Syst. Sci. Data* **2022**, *14* (11), 4811. https://doi.org/10.5194/essd-14-4811-2022

(25) Nicola, M.; Alsafi, Z.; Sohrabi, C.; Kerwan, A.; Al-Jabir, A.; Iosifidis, C.; Agha, M.; Agha, R. The Socio-Economic Implications of the Coronavirus Pandemic (COVID-19): A Review. *Int. J. Surg.* **2020**, *78*, 185. https://doi.org/10.1016/j.ijsu.2020.04.018

(26) Schwager, P.; Decker, N.; Kaltenegger, I. Exploring Green Chemistry, Sustainable Chemistry and Innovative Business Models Such as Chemical Leasing in the Context of International Policy Discussions. *Curr. Opin. Green Sustain. Chem.* **2016**, *1*, 18. https://doi.org/10.1016/j.cogsc.2016.07.005

(27) United Nations Industrial Development Organization. *Industrial Development Report 2016: The Role of Technology and Innovation in Inclusive and Sustainable Industrial Development*; Industrial Development Report; UN, **2015**. https://doi.org/10.18356/a1cf26ea-en

(28) Horváth, I. T. Introduction: Sustainable Chemistry. *Chem. Rev.* **2018**, *118* (2), 369. https://doi.org/10.1021/acs.chemrev.7b00721

(29) Report of the World Commission on Environment and Development: Our Common Future, Oxford University Press, **1987**. https://sustainabledevelopment.un.org/content/documents/5987our-common-future.pdf

(30) Wang, Z. Green Chemistry: Recent Advances in Developing Catalytic Processes in Environmentally-Benign Solvent Systems. **2008**. http://ccc.chem.pitt.edu/wipf/Frontiers/Zhiyong.pdf
(31) Cannon, A. S.; Warner, J. C. The Science of Green Chemistry and Its Role in Chemicals Policy and Educational Reform. *NEW Solut. J. Environ. Occup. Health Policy* **2011**, *21* (3), 499. https://doi.org/10.2190/NS.21.3.m
(32) 12 Principles of Green Chemistry - American Chemical Society. https://www.acs.org/greenchemistry/principles/12-principles-of-green-chemistry.html
(33) Anastas, P.; Eghbali, N. Green Chemistry: Principles and Practice. *Chem. Soc. Rev.* **2010**, *39* (1), 301. https://doi.org/10.1039/B918763B
(34) Sheldon, R. A. E Factors, Green Chemistry and Catalysis: An Odyssey. *Chem. Commun.* **2008**, *29*, 3352. https://doi.org/10.1039/b803584a
(35) Sheldon, R. A. The E Factor: Fifteen Years On. *Green Chem.* **2007**, *9* (12), 1273. https://doi.org/10.1039/b713736m
(36) McClellan, P. P. Manufacture and Uses of Ethylene Oxide and Ethylene Glycol. *Ind. Eng. Chem.* **1950**, *42* (12), 2402. https://doi.org/10.1021/ie50492a013
(37) Kilty, P. A.; Sachtler, W. M. H. The Mechanism of the Selective Oxidation of Ethylene to Ethylene Oxide. *Catal. Rev.* **1974**, *10* (1), 1. https://doi.org/10.1080/01614947408079624
(38) Khanal, S. K.; Rasmussen, M.; Shrestha, P.; Van Leeuwen, H. J.; Visvanathan, C.; Liu, H. Bioenergy and Biofuel Production from Wastes/Residues of Emerging Biofuel Industries. *Water Environ. Res.* **2008**, *80* (10), 1625. https://doi.org/10.2175/106143008X328752
(39) *Catalysis for Renewables: From Feedstock to Energy Production*; Centi, G.; Santen, R. A. van, Eds.; Wiley-VCH: Weinheim, **2007**. https://www.wiley.com/en-us/Catalysis+for+Renewables%3A+From+Feedstock+to+Energy+Production-p-9783527621125
(40) Jimenez-Gonzalez, C.; Ponder, C. S.; Broxterman, Q. B.; Manley, J. B. Using the Right Green Yardstick: Why Process Mass Intensity Is Used in the Pharmaceutical Industry To Drive More Sustainable Processes. *Org. Process Res. Dev.* **2011**, *15* (4), 912. https://doi.org/10.1021/op200097d
(41) Trost, B. The Atom Economy—A Search for Synthetic Efficiency. *Science* **1991**, *254* (5037), 1471. https://doi.org/10.1126/science.1962206
(42) Wei, C.; Li, Z.; Li, C.-J. The Development of A^3-Coupling (Aldehyde-Alkyne-Amine) and AA^3-Coupling (Asymmetric Aldehyde-Alkyne-Amine). *Synlett* **2004**, *9*, 1472. https://doi.org/10.1055/s-2004-829531
(43) Heijnen, D.; van Zuijlen, M.; Tosi, F.; Feringa, B. L. An Atom Efficient Synthesis of Tamoxifen. *Org. Biomol. Chem.* **2019**, *17* (9), 2315. https://doi.org/10.1039/C8OB02977F
(44) Cavell, K.; Golunski, S.; Miller, D. "Handbook of Green Chemistry - Green Catalysis". *Platin. Met. Rev.* **2010**, *54* (4), 233. https://doi.org/10.1595/147106710X527928
(45) Grubbs, R. H. Olefin Metathesis. *Tetrahedron* **2004**, *60* (34), 7117. https://doi.org/10.1016/j.tet.2004.05.124
(46) Padwa, A. Tandem Methodology for Heterocyclic Synthesis. *Pure Appl. Chem.* **2004**, *76* (11), 1933. http://dx.doi.org/10.1351/pac200476111933
(47) Nicolaou, K. C.; Edmonds, D. J.; Bulger, P. G. Cascade Reactions in Total Synthesis. *Angew. Chem. Int. Ed.* **2006**, *45* (43), 7134. https://doi.org/10.1002/anie.200601872
(48) Herrerías, C. I.; Yao, X.; Li, Z.; Li, C.-J. Reactions of C−H Bonds in Water. *Chem. Rev.* **2007**, *107* (6), 2546. https://doi.org/10.1021/cr050980b
(49) Murai, S.; Kakiuchi, F.; Sekine, S.; Tanaka, Y.; Kamatani, A.; Sonoda, M.; Chatani, N. Efficient Catalytic Addition of Aromatic Carbon-Hydrogen Bonds to Olefins. *Nature* **1993**, *366* (6455), 529. https://doi.org/10.1038/366529a0
(50) Stuart, D. R.; Fagnou, K. The Catalytic Cross-Coupling of Unactivated Arenes. *Science* **2007**, *316* (5828), 1172. https://doi.org/10.1126/science.1141956
(51) Smith, M. B.; March, J. *March's Advanced Organic Chemistry*; John Wiley & Sons, Inc.: Hoboken, NJ, USA, **2006**. https://doi.org/10.1002/0470084960

(52) Ariëns, E. J. Domestication of Chemistry by Design of Safer Chemicals: Structure-Activity Relationships. *Drug Metab. Rev.* **1984**, *15* (3), 425. https://doi.org/10.3109/03602538409029970
(53) *Designing Safer Chemicals: Green Chemistry for Pollution Prevention*; DeVito, S. C., Garrett, R. L., Eds.; ACS Symposium Series; American Chemical Society: Washington, DC, **1996**, 640. https://doi.org/10.1021/bk-1996-0640
(54) Dearden, J. C. In Silico Prediction of Drug Toxicity. **2003**, *17*, 119. https://doi.org/10.1023/a:1025361621494
(55) Voutchkova, A. M.; Ferris, L. A.; Zimmerman, J. B.; Anastas, P. T. Toward Molecular Design for Hazard Reduction—Fundamental Relationships between Chemical Properties and Toxicity. *Tetrahedron* **2010**, *66* (5), 1031. https://doi.org/10.1016/j.tet.2009.11.002
(56) Curzons, A. D.; Mortimer, D. N.; Constable, D. J. C.; Cunningham, V. L. So You Think Your Process Is Green, How Do You Know? - Using Principles of Sustainability to Determine What Is Green - a Corporate Perspective. *Green Chem.* **2001**, *3* (1), 1. https://doi.org/10.1039/b007871i
(57) Constable, D. J. C.; Curzons, A. D.; Cunningham, V. L. Metrics to 'Green' Chemistry-Which Are the Best? *Green Chem.* **2002**, *4* (6), 521. https://doi.org/10.1039/B206169B
(58) DeSimone, J. M. Practical Approaches to Green Solvents. *Science* **2002**, *297* (5582), 799. https://doi.org/10.1126/science.1069622
(59) Sheldon, R. A. Green Solvents for Sustainable Organic Synthesis: State of the Art. *Green Chem.* **2005**, *7* (5), 267. https://doi.org/10.1039/b418069k
(60) Li, C.-J.; Trost, B. M. Green Chemistry for Chemical Synthesis. *Proc. Natl. Acad. Sci.* **2008**, *105* (36), 13197. https://doi.org/10.1073/pnas.0804348105
(61) Li, C.-J. Organic Reactions in Aqueous Media with a Focus on Carbon−Carbon Bond Formations: A Decade Update. *Chem. Rev.* **2005**, *105* (8), 3095. https://doi.org/10.1021/cr030009u
(62) Li, C.-J.; Chen, L. Organic Chemistry in Water. *Chem. Soc. Rev.* **2006**, *35* (1), 68. https://doi.org/10.1039/B507207G
(63) Li, C.-J.; Chan, T.-H. *Comprehensive Organic Reactions in Aqueous Media*; John Wiley & Sons, Inc.: Hoboken, NJ, USA, **2007**. https://doi.org/10.1002/9780470131442
(64) Kerton, F. Chapter 3: Water, Alternative Solvents for Green Chemistry. In *Green Chemistry Series*; Royal Society of Chemistry: Cambridge, **2009**, *3*, 44. https://doi.org/10.1039/9781847559524-00044
(65) Castro-Puyana, M.; Marina, M. L.; Plaza, M. Water as Green Extraction Solvent: Principles and Reasons for Its Use. *Curr. Opin. Green Sustain. Chem.* **2017**, *5*, 31. https://doi.org/10.1016/j.cogsc.2017.03.009
(66) Breslow, R. Hydrophobic Effects on Simple Organic Reactions in Water. *Acc. Chem. Res.* **1991**, *24* (6), 159. https://doi.org/10.1021/ar00006a001
(67) Nagata, K.; Nakagawa, C.; Yokoyama, W.; Usui, H.; Mochizuki, R.; Kanemitsu, T.; Miyazaki, M.; Itoh, T. Synthesis and Catalytic Activities of 3-Decyl-β-Proline for Michael Reactions in Water without an Organic Solvent. *ACS Omega* **2021**, *6* (30), 19642. https://doi.org/10.1021/acsomega.1c02289
(68) *Supercritical Fluids*; Arai, Y., Sako, T., Takebayashi, Y., Eds.; Springer Berlin Heidelberg: Berlin, Heidelberg, **2002**. https://doi.org/10.1007/978-3-642-56238-9
(69) *Carbon Dioxide Recovery and Utilization*; Aresta, M., Ed.; Springer Netherlands: Dordrecht, **2003**. https://doi.org/10.1007/978-94-017-0245-4
(70) Poliakoff, M.; Licence, P. Supercritical Fluids: Green Solvents for Green Chemistry? *Philos. Trans. R. Soc. Math. Phys. Eng. Sci.* **2015**, *373* (2057), 20150018. https://doi.org/10.1098/rsta.2015.0018
(71) *Green Chemistry Using Liquid and Supercritical Carbon Dioxide*; DeSimone, J. M., Tumas, W., Eds.; Oxford University Press, **2004**. https://doi.org/10.1093/oso/9780195154832.001.0001
(72) Jessop, P. G.; Subramaniam, B. Gas-Expanded Liquids. *Chem. Rev.* **2007**, *107* (6), 2666. https://doi.org/10.1021/cr040199o

(73) Welton, T. Room-Temperature Ionic Liquids. Solvents for Synthesis and Catalysis. *Chem. Rev.* **1999**, *99* (8), 2071. https://doi.org/10.1021/cr980032t
(74) Earle, M. J.; Seddon, K. R. Ionic Liquids. Green Solvents for the Future. *Pure Appl. Chem.* **2000**, *72* (7), 1391. https://doi.org/10.1351/pac200072071391
(75) Rogers, R. D.; Seddon, K. R. Ionic Liquids--Solvents of the Future? *Science* **2003**, *302* (5646), 792. https://doi.org/10.1126/science.1090313
(76) Plechkova, N. V.; Seddon, K. R. Ionic Liquids:"Designer" Solvents for Green Chemistry. In *Methods and Reagents for Green Chemistry*; Tundo, P., Perosa, A., Zecchini, F., Eds.; John Wiley & Sons, Inc.: Hoboken, NJ, USA, **2007**, 103. https://doi.org/10.1002/9780470124086.ch5
(77) Shiflett, M. B.; Scurto, A. M. Ionic Liquids: Current State and Future Directions. *ACS Symp. Ser.* **2017**, *1250*, 1. https://doi.org/10.1021/bk-2017-1250.ch001
(78) Villa, R.; Alvarez, E.; Porcar, R.; Garcia-Verdugo, E.; Luis, S. V.; Lozano, P. Ionic Liquids as an Enabling Tool to Integrate Reaction and Separation Processes. *Green Chem.* **2019**, *21* (24), 6527. https://doi.org/10.1039/C9GC02553G
(79) Cave, G. W. V.; Raston, C. L.; Scott, J. L. Recent Advances in Solventless Organic Reactions: Towards Benign Synthesis with Remarkable Versatility. *Chem. Commun.* **2001**, *21*, 2159. https://doi.org/10.1039/b106677n
(80) Tanaka, K. Solvent-Free Organic Synthesis. WILEY-VCH Verlag GmbH & Co. KGaA, Weinheim. **2003**. https://www.wiley.com/en-ie/Solvent+free+Organic+Synthesis-p-9783527605361
(81) Avila-Ortiz, C. G.; Juaristi, E. Novel Methodologies for Chemical Activation in Organic Synthesis under Solvent-Free Reaction Conditions. *Molecules* **2020**, *25* (16), 3579. https://doi.org/10.3390/molecules25163579
(82) Sahoo, B. M.; Banik, B. K. Chapter 14: Solvent-Less Reactions: Green and Sustainable Approaches in Medicinal Chemistry. In *Green Approaches in Medicinal Chemistry for Sustainable Drug Design*; Elsevier, **2020**, 523. https://doi.org/10.1016/B978-0-12-817592-7.00014-9
(83) Handbook of Energy Efficiency and Renewable Energy. Goswami, Y.; Kreith, F., Eds., CRC Press, **2007**. https://doi.org/10.1201/9781420003482
(84) Laughton, M. A. *Renewable Energy Sources*; Published on behalf of the Watt Committee on Energy by Elsevier Applied Science ; Sole distributor in the USA and Canada, Elsevier Science Pub. Co.: London, New York, **2003**. https://www.academia.edu/33687951/_M_A_Laughton_Watt_Committee_on_Energy_Working_G_BookZZ_org_
(85) Crabtree, G. W.; Lewis, N. S. Solar Energy Conversion. *Phys. Today* **2007**, *60* (3), 37. https://doi.org/10.1063/1.2718755
(86) Foster, R.; Ghassemi, M.; Cota, A. *Solar Energy: Renewable Energy and the Environment*; CRC Press: Boca Raton, **2009**. https://doi.org/10.1201/9781420075670
(87) Alnaimat, F.; Rashid, Y. Thermal Energy Storage in Solar Power Plants: A Review of the Materials, Associated Limitations, and Proposed Solutions. *Energies* **2019**, *12* (21), 4164. https://doi.org/10.3390/en12214164
(88) Günes, S.; Neugebauer, H.; Sariciftci, N. S. Conjugated Polymer-Based Organic Solar Cells. *Chem. Rev.* **2007**, *107* (4), 1324. https://doi.org/10.1021/cr050149z
(89) Brédas, J.-L.; Norton, J. E.; Cornil, J.; Coropceanu, V. Molecular Understanding of Organic Solar Cells: The Challenges. *Acc. Chem. Res.* **2009**, *42* (11), 1691. https://doi.org/10.1021/ar900099h
(90) Huber, G. W.; Iborra, S.; Corma, A. Synthesis of Transportation Fuels from Biomass: Chemistry, Catalysts, and Engineering. *Chem. Rev.* **2006**, *106* (9), 4044. https://doi.org/10.1021/cr068360d
(91) Mousdale, D. M. *Biofuels: Biotechnology, Chemistry, and Sustainable Development*; CRC Press: Boca Raton, **2008**. https://doi.org/10.1201/9781420051254
(92) *Handbook of Plant-Based Biofuels*; Pandey, A., Ed.; CRC Press: Boca Raton, **2009**. https://doi.org/10.1201/9780789038746

(93) Soetaert, W.; Vandamme, E. J. Biofuels in Perspective. In *Biofuels*; Soetaert, W., Vandamme, E. J., Eds.; John Wiley & Sons, Ltd: Chichester, UK, **2009**, 1. https://doi.org/10.1002/9780470754108.ch1
(94) Najafi, G.; Ghobadian, B.; Yusaf, T. F. Algae as a Sustainable Energy Source for Biofuel Production in Iran: A Case Study. *Renew. Sustain. Energy Rev.* **2011**, *15* (8), 3870. https://doi.org/10.1016/j.rser.2011.07.010
(95) Ahmad, A. L.; Yasin, N. H. M.; Derek, C. J. C.; Lim, J. K. Microalgae as a Sustainable Energy Source for Biodiesel Production: A Review. *Renew. Sustain. Energy Rev.* **2011**, *15* (1), 584. https://doi.org/10.1016/j.rser.2010.09.018
(96) Hamnett, A. The Components of an Electrochemical Cell. In *Handbook of Fuel Cells*; Vielstich, W., Lamm, A., Gasteiger, H. A., Yokokawa, H., Eds.; John Wiley & Sons, Ltd: Chichester, UK, **2010**. https://doi.org/10.1002/9780470974001.f101001
(97) Sørensen, B. *Hydrogen and Fuel Cells: Emerging Technologies and Applications*, 2nd ed.; Sustainable world; Academic Press: Oxford ; Burlington, MA, **2012**. https://www.semanticscholar.org/paper/Hydrogen-and-Fuel-Cells%3A-Emerging-Technologies-and-S%C3%B8rensen/53a5f1087692ce9ab01cacd1734d3a8e5bc7e1d3
(98) Staffell, I.; Scamman, D.; Velazquez Abad, A.; Balcombe, P.; Dodds, P. E.; Ekins, P.; Shah, N.; Ward, K. R. The Role of Hydrogen and Fuel Cells in the Global Energy System. *Energy Environ. Sci.* **2019**, *12* (2), 463. https://doi.org/10.1039/C8EE01157E
(99) Felseghi, R.-A.; Carcadea, E.; Raboaca, M. S.; Trufin, C. N.; Filote, C. Hydrogen Fuel Cell Technology for the Sustainable Future of Stationary Applications. *Energies* **2019**, *12* (23), 4593. https://doi.org/10.3390/en12234593
(100) Tye, J. W.; Hall, M. B.; Darensbourg, M. Y. Better than Platinum? Fuel Cells Energized by Enzymes. *Proc. Natl. Acad. Sci.* **2005**, *102* (47), 16911. https://doi.org/10.1073/pnas.0508740102
(101) Gasteiger, H. A.; Marković, N. M. Just a Dream—or Future Reality? *Science* **2009**, *324* (5923), 48. https://doi.org/10.1126/science.1172083
(102) Ackermann, T. Wind Power in Power Systems. Ackermann, T., Ed., Academic Press Elsevier Ltd., Oxford, UK, **2005**. https://www.wiley.com/en-us/Wind+Power+in+Power+Systems%2C+2nd+Edition-p-9780470974162
(103) Apostolou, D.; Enevoldsen, P. The Past, Present and Potential of Hydrogen as a Multifunctional Storage Application for Wind Power. *Renew. Sustain. Energy Rev.* **2019**, *112*, 917. https://doi.org/10.1016/j.rser.2019.06.049
(104) Yousif, M.; Ai, Q.; Wattoo, W. A.; Jiang, Z.; Hao, R.; Gao, Y. Least Cost Combinations of Solar Power, Wind Power, and Energy Storage System for Powering Large-Scale Grid. *J. Power Sources* **2019**, *412*, 710. https://doi.org/10.1016/j.jpowsour.2018.11.084
(105) Yüksek, Ö.; Kaygusuz, K. Small Hydropower Plants as a New and Renewable Energy Source. *Energy Sources Part B Econ. Plan. Policy* **2006**, *1* (3), 279. https://doi.org/10.1080/15567240500397976
(106) Kömürcü, M. İ.; Akpinar, A. Hydropower Energy Versus Other Energy Sources in Turkey. *Energy Sources Part B Econ. Plan. Policy* **2010**, *5* (2), 185. https://doi.org/10.1080/15567240802532627
(107) Badescu, V.; Lazaroiu, G. C.; Barelli, L. Advances and Challenges, Part A: Thermal, Hydro and Nuclear Power. *Power Engineering*, Badescu, V.; Lazaroiu, G. C.; Barelli, L., Eds., **2018**. https://doi.org/10.1201/9781315202105
(108) Fridleifsson, I. B. Geothermal Energy for the Benefit of the People. *Renew. Sustain. Energy Rev.* **2001**, *5* (3), 299. https://doi.org/10.1016/S1364-0321(01)00002-8
(109) Orr, T. *Geothermal Energy*; Power up!; Orr, T. Ed., Cherry Lake Publishing, **2008**. https://www.getepic.com/book/11691055/power-up-geothermal-energy
(110) Tomaszewska, B.; Pająk, L.; Bundschuh, J.; Bujakowski, W. Low-Enthalpy Geothermal Energy as a Source of Energy and Integrated Freshwater Production in Inland Areas: Technological and Economic Feasibility. *Desalination* **2018**, *435*, 35. https://doi.org/10.1016/j.desal.2017.12.032
(111) Okati, V.; Ebrahimi-Moghadam, A.; Behzadmehr, A.; Farzaneh-Gord, M. Proposal and Assessment of a Novel Hybrid System for Water Desalination Using Solar and

Geothermal Energy Sources. *Desalination* **2019**, *467*, 229. https://doi.org/10.1016/j.desal.2019.06.011

(112) Bozell, J. J., Patel, M. K. *Feedstocks for the Future: Renewables for the Production of Chemicals and Materials*; Bozell, J. J., Patel, M. K., Eds.; ACS Symposium Series; American Chemical Society: Washington, DC, **2006**, *921*. https://doi.org/10.1021/bk-2006-0921

(113) Gallezot, P. Process Options for Converting Renewable Feedstocks to Bioproducts. *Green Chem.* **2007**, *9* (4), 295. https://doi.org/10.1039/b615413a

(114) Kamm, E. B.; Gruber, P. R.; Kamm, M. Biorefineries - Industrial Processes and Products. Status Quo and Future Directions. Kamm, E. B.; Gruber, P. R.; Kamm, M. Eds., Wiley-VCH, Weinheim, **2010**. https://dokumen.tips/documents/birgit-kamm-patrick-r-gruber-michael-kamm-biobookfiorg.html?page=558

(115) Graziani, M.; Fornasiero, P. Renewable Resources and Renewable Energy. Graziani, M.; Fornasiero, P. Eds., CRC Press, Boca Raton, **2012**. https://doi.org/10.1201/b16003

(116) Meier, M. A. R.; Metzger, J. O.; Schubert, U. S. Plant Oil Renewable Resources as Green Alternatives in Polymer Science. *Chem. Soc. Rev.* **2007**, *36* (11), 1788. https://doi.org/10.1039/b703294c

(117) Naceur Belgacem, M.; Gandini, A. *Monomers, Polymers and Composites from Renewable Resources*; Naceur Belgacem, M.; Gandini, A. Eds., Elsevier, **2008**. https://doi.org/10.1016/B978-0-08-045316-3.X0001-4

(118) Gandini, A. Polymers from Renewable Resources: A Challenge for the Future of Macromolecular Materials. *Macromolecules* **2008**, *41* (24), 9491. https://doi.org/10.1021/ma801735u

(119) Tokiwa, Y.; Calabia, B. P. Biological Production of Functional Chemicals from Renewable Resources. *Can. J. Chem.* **2008**, *86* (6), 548. https://doi.org/10.1139/v08-046

(120) Kühlborn, J.; Groß, J.; Opatz, T. Making Natural Products from Renewable Feedstocks: Back to the Roots? *Nat. Prod. Rep.* **2020**, *37* (3), 380. https://doi.org/10.1039/C9NP00040B

(121) Hu, T. Q. *Chemical Modification, Properties, and Usage of Lignin*; Hu, T. Q., Ed.; Springer US: Boston, MA, **2002**. https://doi.org/10.1007/978-1-4615-0643-0

(122) Gellerstedt, G. Softwood Kraft Lignin: Raw Material for the Future. *Ind. Crops Prod.* **2015**, *77*, 845. https://doi.org/10.1016/j.indcrop.2015.09.040

(123) Gadhave, R. V.; Srivastava, S.; Mahanwar, P. A.; Gadekar, P. T. Lignin: Renewable Raw Material for Adhesive. *Open J. Polym. Chem.* **2019**, *9* (2), 27. https://doi.org/10.4236/ojpchem.2019.92003

(124) Pillai, C. K. S.; Paul, W.; Sharma, C. P. Chitin and Chitosan Polymers: Chemistry, Solubility and Fiber Formation. *Prog. Polym. Sci.* **2009**, *34* (7), 641. https://doi.org/10.1016/j.progpolymsci.2009.04.001

(125) Andrade, S. M. B. de; Ladchumananandasivam, R.; Rocha, B. G. da; Belarmino, D. D.; Galvão, A. O. The Use of Exoskeletons of Shrimp (Litopenaeus vanammei) and Crab (Ucides cordatus) for the Extraction of Chitosan and Production of Nanomembrane. *Mater. Sci. Appl.* **2012**, *3* (7), 495. https://doi.org/10.4236/msa.2012.37070

(126) Thomas, S., Pius, A., Gopi, S. *Handbook of Chitin and Chitosan*; Thomas, S., Pius, A., Gopi, S., Eds.; Elsevier: Amsterdam, Netherlands ; Cambridge, MA, **2020**. https://www.elsevier.com/books/handbook-of-chitin-and-chitosan/thomas/978-0-12-817968-0

(127) Amiri, H.; Aghbashlo, M.; Sharma, M.; Gaffey, J.; Manning, L.; Moosavi Basri, S. M.; Kennedy, J. F.; Gupta, V. K.; Tabatabaei, M. Chitin and Chitosan Derived from Crustacean Waste Valorization Streams Can Support Food Systems and the UN Sustainable Development Goals. *Nat. Food* **2022**, *3* (10), 822. https://doi.org/10.1038/s43016-022-00591-y

(128) Frey, B. L.; Corn, R. M. Covalent Attachment and Derivatization of Poly(L-Lysine) Monolayers on Gold Surfaces As Characterized by Polarization−Modulation FT-IR Spectroscopy. *Anal. Chem.* **1996**, *68* (18), 3187. https://doi.org/10.1021/ac9605861

(129) Lin, S.; Ashrafi, B.; Laqua, K.; Su Kim, K.; Simard, B. Covalent Derivatization of Boron Nitride Nanotubes with Peroxides and Their Application in Polycarbonate Composites. *New J. Chem.* **2017**, *41* (15), 7571. https://doi.org/10.1039/C7NJ00193B
(130) Warner, J. C.; Stoler, E. Chapter 6: Innovation with Non-Covalent Derivatization. In *Green Techniques for Organic Synthesis and Medicinal Chemistry*; Zhang, W., Cue, B. W., Eds.; John Wiley & Sons, Ltd: Chichester, UK, **2018**, 117. https://doi.org/10.1002/9781119288152.ch6
(131) Cannon, A. S.; Warner, J. C. Noncovalent Derivatization: Green Chemistry Applications of Crystal Engineering. *Cryst. Growth Des.* **2002**, *2* (4), 255. https://doi.org/10.1021/cg0255218
(132) Trakhtenberg, S.; Warner, J. C. Green Chemistry Considerations in Entropic Control of Materials and Processes. *Chem. Rev.* **2007**, *107* (6), 2174. https://doi.org/10.1021/cr0509455
(133) Warner, J. C. Entropic Control in Green Chemistry and Materials Design. *Pure Appl. Chem.* **2006**, *78* (11), 2035. https://doi.org/10.1351/pac200678112035
(134) Sheldon, R. A. Atom Utilisation, E Factors and the Catalytic Solution. *Comptes Rendus Académie Sci. - Ser. IIC - Chem.* **2000**, *3* (7), 541. https://doi.org/10.1016/S1387-1609(00)01174-9
(135) Sheldon, R. A. Atom Efficiency and Catalysis in Organic Synthesis. *Pure Appl. Chem.* **2000**, *72* (7), 1233. https://doi.org/10.1351/pac200072071233
(136) Sheldon, R. A.; Arends, I.; Hanefeld, U. Green Chemistry and Catalysis, Wiley-VCH, Weinheim, **2007**. https://www.wiley.com/en-us/Green+Chemistry+and+Catalysis-p-9783527307159
(137) Rothenberg, G. *Catalysis: Concepts and Green Applications*; Rothenberg, G., Ed., Wiley-VCH: Weinheim, **2008**. https://www.wiley.com/en-sg/Catalysis:+Concepts+and+Green+Applications,+2nd+Edition-p-9783527343058
(138) Noyori, R.; Ohkuma, T.; Kitamura, M.; Takaya, H.; Sayo, N.; Kumobayashi, H.; Akutagawa, S. Asymmetric Hydrogenation of .Beta.-Keto Carboxylic Esters. A Practical, Purely Chemical Access to .Beta.-Hydroxy Esters in High Enantiomeric Purity. *J. Am. Chem. Soc.* **1987**, *109* (19), 5856. https://doi.org/10.1021/ja00253a051
(139) Anastas, P. T.; Kirchhoff, M. M.; Williamson, T. C. Catalysis as a Foundational Pillar of Green Chemistry. *Appl. Catal. Gen.* **2001**, *221* (1–2), 3. https://doi.org/10.1016/S0926-860X(01)00793-1
(140) Sheldon, R. A. Engineering a More Sustainable World through Catalysis and Green Chemistry. *J. R. Soc. Interface* **2016**, *13* (116), 20160087. https://doi.org/10.1098/rsif.2016.0087
(141) Mallesham, B. Chapter 1: The Role of Catalysis in Green Synthesis of Chemicals for Sustainable Future. Advanced Functional Solid Catalysts for Biomass Valorization. Mallesham, B.; Raikwar, D.; Shee, D. Eds., Elsevier, **2020**. http://doi.org/10.1016/B978-0-12-820236-4.00001-5
(142) Hobbs, H. R.; Thomas, N. R. Biocatalysis in Supercritical Fluids, in Fluorous Solvents, and under Solvent-Free Conditions. *Chem. Rev.* **2007**, *107* (6), 2786. https://doi.org/10.1021/cr0683820
(143) Bell, E. L.; Finnigan, W.; France, S. P.; Green, A. P.; Hayes, M. A.; Hepworth, L. J.; Lovelock, S. L.; Niikura, H.; Osuna, S.; Romero, E.; Ryan, K. S.; Turner, N. J.; Flitsch, S. L. Biocatalysis. *Nat. Rev. Methods Primer* **2021**, *1* (1), 46. https://doi.org/10.1038/s43586-021-00044-z
(144) DeVito, S. C. Present and Future Regulatory Trends of the United States Environmental Protection Agency. *Prog. Org. Coat.* **1999**, *35* (1–4), 55. https://doi.org/10.1016/S0300-9440(98)00055-1
(145) Rattner, B. A. History of Wildlife Toxicology. *Ecotoxicology* **2009**, *18* (7), 773. https://doi.org/10.1007/s10646-009-0354-x
(146) Wijbenga, A.; Hutzinger, O. Chemicals, Man and the Environment: A Historic Perspective of Pollution and Related Topics. *Naturwissenschaften* **1984**, *71* (5), 239. https://doi.org/10.1007/BF00441332

(147) Agteren, M. H.; Keuning, S.; Janssen, D. B. *Handbook on Biodegradation and Biological Treatment of Hazardous Organic Compounds*; Environment & Chemistry; Agteren, M. H.; Keuning, S.; Janssen, D. B., Eds., Springer Netherlands: Dordrecht, **1998**, 2. https://doi.org/10.1007/978-94-015-9062-4
(148) Boethling, R. S.; Sommer, E.; DiFiore, D. Designing Small Molecules for Biodegradability. *Chem. Rev.* **2007**, *107* (6), 2207. https://doi.org/10.1021/cr050952t
(149) Feghali, E.; Tauk, L.; Ortiz, P.; Vanbroekhoven, K.; Eevers, W. Catalytic Chemical Recycling of Biodegradable Polyesters. *Polym. Degrad. Stab.* **2020**, *179*, 109241. https://doi.org/10.1016/j.polymdegradstab.2020.109241
(150) Anastas, P. T. Green Chemistry and the Role of Analytical Methodology Development. *Crit. Rev. Anal. Chem.* **1999**, *29* (3), 167. https://doi.org/10.1080/10408349891199356
(151) Rocha, F. R. P.; Nóbrega, J. A.; Filho, O. F. Flow Analysis Strategies to Greener Analytical Chemistry. An Overview. *Green Chem.* **2001**, *3* (5), 216. https://doi.org/10.1039/b103187m
(152) Keith, L. H.; Gron, L. U.; Young, J. L. Green Analytical Methodologies. *Chem. Rev.* **2007**, *107* (6), 2695. https://doi.org/10.1021/cr068359e
(153) de la Guardia, M.; Garrigues, S. Chapter 1: Past, Present and Future of Green Analytical Chemistry. In *Green Chemistry Series*; Garrigues, S., de la Guardia, M., Eds.; Royal Society of Chemistry: Cambridge, **2020**, 1. https://doi.org/10.1039/9781788016148-00001
(154) Callis, J. B.; Illman, D. L.; Kowalski, B. R. Process Analytical Chemistry. **1987**, *59* (9), 14. https://doi.org/10.1021/ac00136a001
(155) McLennan, F., Kowalski, B. R. Process Analytical Chemistry; McLennan, F., Kowalski, B. R., Eds.; Springer Netherlands: Dordrecht, **1995**. https://doi.org/10.1007/978-94-011-0591-0
(156) *OECD Guiding Principles for Chemical Accident Prevention, Preparedness and Response: Guidance for Industry (Including Management and Labour), Public Authorities, Communities and Other Stakeholders*, 2nd ed.; Organisation for Economic Co-operation and Development, Inter-Organization Programme for the Sound Management of Chemicals, Eds.; OECD environment, health and safety publications. Series on chemical accidents; OECD: Paris, **2003**. https://www.oecd.org/env/ehs/chemical-accidents/Guiding-principles-chemical-accident.pdf
(157) Khan, E. A.; Syeda, S. R. Chemical Substitution in Processes for Inherently Safer Design: Pros and Cons. *Pure Appl. Chem.* **2022**, *94* (7), 889. https://doi.org/10.1515/pac-2021-1201
(158) Whiteker, G. T. Applications of the 12 Principles of Green Chemistry in the Crop Protection Industry. *Org. Process Res. Dev.* **2019**, *23* (10), 2109. https://doi.org/10.1021/acs.oprd.9b00305
(159) Owusu, P. A.; Asumadu-Sarkodie, S. A Review of Renewable Energy Sources, Sustainability Issues and Climate Change Mitigation. *Cogent Eng.* **2016**, *3* (1), 1167990. https://doi.org/10.1080/23311916.2016.1167990
(160) CDM Investment Newsletter Biofuels Transportation, Nr. 3/2007, **2007**. https://www.c2es.org/wp-content/uploads/2007/11/cdm-investment-newsletter-biofuels-transportation.pdf
(161) Nanda, S.; Azargohar, R.; Dalai, A. K.; Kozinski, J. A. An Assessment on the Sustainability of Lignocellulosic Biomass for Biorefining. *Renew. Sustain. Energy Rev.* **2015**, *50*, 925. https://doi.org/10.1016/j.rser.2015.05.058
(162) Putro, J. N.; Soetaredjo, F. E.; Lin, S.-Y.; Ju, Y.-H.; Ismadji, S. Pretreatment and Conversion of Lignocellulose Biomass into Valuable Chemicals. *RSC Adv.* **2016**, *6* (52), 46834. https://doi.org/10.1039/C6RA09851G
(163) Lange, J.-P.; van der Heide, E.; van Buijtenen, J.; Price, R. Furfural-A Promising Platform for Lignocellulosic Biofuels. *ChemSusChem* **2012**, *5* (1), 150. https://doi.org/10.1002/cssc.201100648
(164) Cai, C. M.; Zhang, T.; Kumar, R.; Wyman, C. E. Integrated Furfural Production as a Renewable Fuel and Chemical Platform from Lignocellulosic Biomass: Furfural Pro-

duction from Lignocellulosic Biomass. *J. Chem. Technol. Biotechnol.* **2014**, *89* (1), 2. https://doi.org/10.1002/jctb.4168

(165) Peleteiro, S.; Rivas, S.; Alonso, J. L.; Santos, V.; Parajó, J. C. Furfural Production Using Ionic Liquids: A Review. *Bioresour. Technol.* **2016**, *202*, 181. https://doi.org/10.1016/j.biortech.2015.12.017

(166) D. Mthembu, L.; Gupta, R.; Deenadayalu, N. Conversion of Cellulose into Value-Added Products. In *Cellulose Science and Derivatives*; Sand, A., Banga, S., Eds.; IntechOpen, **2021**. https://doi.org/10.5772/intechopen.100022

(167) Agirrezabal-Telleria, I.; Gandarias, I.; Arias, P. L. Heterogeneous Acid-Catalysts for the Production of Furan-Derived Compounds (Furfural and Hydroxymethylfurfural) from Renewable Carbohydrates: A Review. *Catal. Today* **2014**, *234*, 42. https://doi.org/10.1016/j.cattod.2013.11.027

(168) Yue, X.; Queneau, Y. 5-Hydroxymethylfurfural and Furfural Chemistry Toward Biobased Surfactants. *ChemSusChem* **2022**, *15* (13), e202102660. https://doi.org/10.1002/cssc.202102660

(169) Palkovits, R.; Delidovich, I. Efficient Utilization of Renewable Feedstocks: The Role of Catalysis and Process Design. *Philos. Trans. R. Soc. Math. Phys. Eng. Sci.* **2018**, *376* (2110), 20170064. https://doi.org/10.1098/rsta.2017.0064

(170) Huber, G. W.; Corma, A. Synergies between Bio- and Oil Refineries for the Production of Fuels from Biomass. *Angew. Chem. Int. Ed.* **2007**, *46* (38), 7184. https://doi.org/10.1002/anie.200604504

(171) Bing, Y.; Liu, H.; Zhang, L.; Ghosh, D.; Zhang, J. Nanostructured Pt-Alloy Electrocatalysts for PEM Fuel Cell Oxygen Reduction Reaction. *Chem. Soc. Rev.* **2010**, *39* (6), 2184. https://doi.org/10.1039/b912552c

(172) Gilroy, K. D.; Ruditskiy, A.; Peng, H.-C.; Qin, D.; Xia, Y. Bimetallic Nanocrystals: Syntheses, Properties, and Applications. *Chem. Rev.* **2016**, *116* (18), 10414. https://doi.org/10.1021/acs.chemrev.6b00211

(173) Fang, H.; Yang, J.; Wen, M.; Wu, Q. Nanoalloy Materials for Chemical Catalysis. *Adv. Mater.* **2018**, *30* (17), 1705698. https://doi.org/10.1002/adma.201705698

(174) Sun, J.; Xu, H.; Ma, H.; Zhan, X.; Zhu, J.; Cheng, D. Isoprene Selective Hydrogenation Using AgCu-Promoted Pd Nanoalloys. *Faraday Discuss.* **2023**, *242*, 418. https://doi.org/10.1039/D2FD00074A

(175) Wei, Q.; Wang, L.; Chen, X.; Wu, C.; Liang, J.; Wei, X.; Deng, K. MoNi Nano-Alloy Loaded on Carbon Nanotubes with High Activity and Stability for the Catalytic Hydrogenation of Petro Resin. *React. Kinet. Mech. Catal.* **2022**, *135* (5), 2503–2517. https://doi.org/10.1007/s11144-022-02250-6

(176) Ferrando, R.; Jellinek, J.; Johnston, R. L. Nanoalloys: From Theory to Applications of Alloy Clusters and Nanoparticles. *Chem. Rev.* **2008**, *108* (3), 845. https://doi.org/10.1021/cr040090g

(177) Jiang, H.; Liu, X.; Zhu, M.-N.; Xu, J.; An, L.; Sui, P.-F.; Luo, J.-L.; Cheng, G. J. Nanoalloy Libraries from Laser-Induced Thermionic Emission Reduction. *Sci. Adv.* **2022**, *8* (16), eabm6541. https://doi.org/10.1126/sciadv.abm6541

(178) Sankar, M.; Dimitratos, N.; Miedziak, P. J.; Wells, P. P.; Kiely, C. J.; Hutchings, G. J. Designing Bimetallic Catalysts for a Green and Sustainable Future. *Chem. Soc. Rev.* **2012**, *41* (24), 8099. https://doi.org/10.1039/c2cs35296f

(179) Luneau, M.; Lim, J. S.; Patel, D. A.; Sykes, E. C. H.; Friend, C. M.; Sautet, P. Guidelines to Achieving High Selectivity for the Hydrogenation of α,β-Unsaturated Aldehydes with Bimetallic and Dilute Alloy Catalysts: A Review. *Chem. Rev.* **2020**, *120* (23), 12834. https://doi.org/10.1021/acs.chemrev.0c00582

(180) Kang, X.; Li, Y.; Zhu, M.; Jin, R. Atomically Precise Alloy Nanoclusters: Syntheses, Structures, and Properties. *Chem. Soc. Rev.* **2020**, *49* (17), 6443. https://doi.org/10.1039/C9CS00633H

(181) Wang, B.; Ai, Y.; Yao, Y.; Jiang, M.; Yan, L.; Xu, S.; Sun, W. Electrochemical Synergy between FeNi Nanoalloy@tungsten Carbide on N-Doped Graphitized Carbon Layers as an Excellent Electrocatalyst for Oxygen Evolution Reaction. *Electrochimica Acta* **2022**, *415*, 140254. https://doi.org/10.1016/j.electacta.2022.140254

(182) Alonso, D. M.; Wettstein, S. G.; Dumesic, J. A. Bimetallic Catalysts for Upgrading of Biomass to Fuels and Chemicals. *Chem. Soc. Rev.* **2012**, *41* (24), 8075. https://doi.org/10.1039/c2cs35188a

(183) Piumetti, M., Bensaid, S. Chapter 5: Nanostructured Bimetallic Pd-based Catalysts for the Valorization of Lignocellulosic Biomasses. *Nanostructured Catalysts for Environmental Applications*; Piumetti, M., Bensaid, S., Eds., Springer International Publishing: Cham, **2021**,. 127. https://doi.org/10.1007/978-3-030-58934-9

(184) Huber, G. W.; Shabaker, J. W.; Dumesic, J. A. Raney Ni-Sn Catalyst for H $_2$ Production from Biomass-Derived Hydrocarbons. *Science* **2003**, *300* (5628), 2075. https://doi.org/10.1126/science.1085597

(185) Daorattanachai, P.; Laosiripojana, W.; Laobuthee, A.; Laosiripojana, N. Type of Contribution: Research Article Catalytic Activity of Sewage Sludge Char Supported Re-Ni Bimetallic Catalyst toward Cracking/Reforming of Biomass Tar. *Renew. Energy* **2018**, *121*, 644. https://doi.org/10.1016/j.renene.2018.01.096

(186) Jin, X.; Zhao, M.; Vora, M.; Shen, J.; Zeng, C.; Yan, W.; Thapa, P. S.; Subramaniam, B.; Chaudhari, R. V. Synergistic Effects of Bimetallic PtPd/TiO $_2$ Nanocatalysts in Oxidation of Glucose to Glucaric Acid: Structure Dependent Activity and Selectivity. *Ind. Eng. Chem. Res.* **2016**, *55* (11), 2932. https://doi.org/10.1021/acs.iecr.5b04841

(187) Gupta, K.; Rai, R. K.; Dwivedi, A. D.; Singh, S. K. Catalytic Aerial Oxidation of Biomass-Derived Furans to Furan Carboxylic Acids in Water over Bimetallic Nickel-Palladium Alloy Nanoparticles. *ChemCatChem* **2017**, *9* (14), 2760. https://doi.org/10.1002/cctc.201600942

(188) Jiang, T.; Zhou, Y.; Liang, S.; Liu, H.; Han, B. Hydrogenolysis of Glycerol Catalyzed by Ru-Cu Bimetallic Catalysts Supported on Clay with the Aid of Ionic Liquids. *Green Chem.* **2009**, *11* (7), 1000. https://doi.org/10.1039/b901425j

(189) Priya, S. S.; Bhanuchander, P.; Kumar, V. P.; Bhargava, S. K.; Chary, K. V. R. Activity and Selectivity of Platinum–Copper Bimetallic Catalysts Supported on Mordenite for Glycerol Hydrogenolysis to 1,3-Propanediol. *Ind. Eng. Chem. Res.* **2016**, *55* (16), 4461. https://doi.org/10.1021/acs.iecr.6b00161

(190) Liu, M.; Zhang, J.; Zheng, L.; Fan, G.; Yang, L.; Li, F. Significant Promotion of Surface Oxygen Vacancies on Bimetallic CoNi Nanocatalysts for Hydrodeoxygenation of Biomass-Derived Vanillin to Produce Methylcyclohexanol. *ACS Sustain. Chem. Eng.* **2020**, *8* (15), 6075. https://doi.org/10.1021/acssuschemeng.0c01015

(191) He, Z.-H.; Jiang, C.-S.; Wang, Z.-Y.; Wang, K.; Sun, Y.-C.; Yao, M.-Q.; Li, Z.-H.; Liu, Z.-T. Catalytic Hydrodeoxygenation of Biomass-Derived Oxygenates to Bio-Fuels over Co-Based Bimetallic Catalysts. *Sustain. Energy Fuels* **2020**, *4* (9), 4558. https://doi.org/10.1039/d0se00332h

(192) Wettstein, S. G.; Bond, J. Q.; Alonso, D. M.; Pham, H. N.; Datye, A. K.; Dumesic, J. A. RuSn Bimetallic Catalysts for Selective Hydrogenation of Levulinic Acid to γ-Valerolactone. *Appl. Catal. B Environ.* **2012**, *117–118*, 321. https://doi.org/10.1016/j.apcatb.2012.01.033

(193) Wu, J.; Liu, C.; Zhu, Y.; Song, X.; Wen, C.; Zhang, X.; Wang, C.; Ma, L. Understanding the Geometric and Electronic Factors of PtNi Bimetallic Surfaces for Efficient and Selective Catalytic Hydrogenation of Biomass-Derived Oxygenates. *J. Energy Chem.* **2021**, *60*, 16. https://doi.org/10.1016/j.jechem.2020.12.011

(194) Luo, Z.; Zheng, Z.; Li, L.; Cui, Y.-T.; Zhao, C. Bimetallic Ru–Ni Catalyzed Aqueous-Phase Guaiacol Hydrogenolysis at Low H $_2$ Pressures. *ACS Catal.* **2017**, *7* (12), 8304. https://doi.org/10.1021/acscatal.7b02317

(195) Hu, Y.; Jiang, G.; Xu, G.; Mu, X. Hydrogenolysis of Lignin Model Compounds into Aromatics with Bimetallic Ru-Ni Supported onto Nitrogen-Doped Activated Carbon Catalyst. *Mol. Catal.* **2018**, *445*, 316. https://doi.org/10.1016/j.mcat.2017.12.009

(196) Valdés-Martínez, O. U.; Suárez-Toriello, V. A.; Reyes, J. A. de los; Pawelec, B.; Fierro, J. L. G. Support Effect and Metals Interactions for NiRu/Al_2O_3, TiO_2 and ZrO_2 Catalysts in the Hydrodeoxygenation of Phenol. *Catal. Today* **2017**, *296*, 219. https://doi.org/10.1016/j.cattod.2017.04.007

(197) Yang, Y.; Gao, G.; Zhang, X.; Li, F. Facile Fabrication of Composition-Tuned Ru–Ni Bimetallics in Ordered Mesoporous Carbon for Levulinic Acid Hydrogenation. *ACS Catal.* **2014**, *4* (5), 1419. https://doi.org/10.1021/cs401030u

(198) Zhang, J.; Teo, J.; Chen, X.; Asakura, H.; Tanaka, T.; Teramura, K.; Yan, N. A Series of NiM (M = Ru, Rh, and Pd) Bimetallic Catalysts for Effective Lignin Hydrogenolysis in Water. *ACS Catal.* **2014**, *4* (5), 1574. https://doi.org/10.1021/cs401199f

(199) Mishra, D. K.; Lee, J.-M.; Chang, J.-S.; Hwang, J.-S. Liquid Phase Hydrogenation of D-Glucose to d-Sorbitol over the Catalyst (Ru/NiO–TiO_2) of Ruthenium on a NiO-Modified TiO_2 Support. *Catal. Today* **2012**, *185* (1), 104. https://doi.org/10.1016/j.cattod.2011.11.020

(200) Bulut, S.; Siankevich, S.; van Muyden, A. P.; Alexander, D. T. L.; Savoglidis, G.; Zhang, J.; Hatzimanikatis, V.; Yan, N.; Dyson, P. J. Efficient Cleavage of Aryl Ether C–O Linkages by Rh–Ni and Ru–Ni Nanoscale Catalysts Operating in Water. *Chem. Sci.* **2018**, *9* (25), 5530. https://doi.org/10.1039/C8SC00742J

(201) Ahmad, W.; Chan, F. L.; Chaffee, A. L.; Wang, H.; Hoadley, A.; Tanksale, A. Dimethoxymethane Production via Catalytic Hydrogenation of Carbon Monoxide in Methanol Media. *ACS Sustain. Chem. Eng.* **2020**, *8* (4), 2081. https://doi.org/10.1021/acssuschemeng.9b06913

(202) Qadir, M. I.; Bernardi, F.; Scholten, J. D.; Baptista, D. L.; Dupont, J. Synergistic CO2 Hydrogenation over Bimetallic Ru/Ni Nanoparticles in Ionic Liquids. *Appl. Catal. B Environ.* **2019**, *252*, 10. https://doi.org/10.1016/j.apcatb.2019.04.005

(203) Predieri, G.; Moggi, P. Characterization of an Ultrafine Ni-Ru Alloy Powder and of Alumina-Dispersed Bimetallic Particles Derived from the Molecular Cluster $(C_5H_5)NiRu_3H_3(CO)_9$. *J. Chem. Soc. Chem. Commun.* **1990**, 1736. https://doi.org/10.1039/C39900001736

(204) Castiglioni, M.; Giordano, R.; Sappa, E. $(\eta^5\text{-}C_5H_5)NiRu_3(\mu\text{-}H)_3(CO)_9$, $Ru_3(CO)_{12}$ and $(\eta^5\text{-}C_5H_5)_2Ni_2(CO)_2$ as heterogeneous catalyst precursors: hydrogenation, dehydrogenation and isomerization of linear and cyclic monoenes and dienes, and of aromatic hydrocarbons. *J. Mol. Catal.* **1987**, *42* (3), 307. https://doi.org/10.1016/0304-5102(87)85005-8

(205) Sreenavya, A.; Ahammed, S.; Ramachandran, A.; Ganesh, V.; Sakthivel, A. Nickel–Ruthenium Bimetallic Species on Hydrotalcite Support: A Potential Hydrogenation Catalyst. *Catal. Lett.* **2022**, *152* (3), 848. https://doi.org/10.1007/s10562-021-03673-x

(206) Li, L.-J.; Yi, W.-J.; Liu, T.-W.; Huang, C.; Chao, Z.-S. Hydrogenation of 3-Hydroxypropanal into 1,3-Propanediol over Bimetallic Ru–Ni Catalyst. *RSC Adv.* **2017**, *7* (51), 32027. https://doi.org/10.1039/C7RA01184A

(207) Zhu, C.; Cao, J.-P.; Zhao, X.-Y.; Xie, T.; Zhao, M.; Wei, X.-Y. Bimetallic Effects in the Catalytic Hydrogenolysis of Lignin and Its Model Compounds on Nickel-Ruthenium Catalysts. *Fuel Process. Technol.* **2019**, *194*, 106126. https://doi.org/10.1016/j.fuproc.2019.106126

(208) Polanski, J.; Lach, D.; Kapkowski, M.; Bartczak, P.; Siudyga, T.; Smolinski, A. Ru and Ni-Privileged Metal Combination for Environmental Nanocatalysis. *Catalysts* **2020**, *10* (9), 992. https://doi.org/10.3390/catal10090992

(209) Zhu, L.; Sun, H.; Fu, H.; Zheng, J.; Zhang, N.; Li, Y.; Chen, B. H. Effect of Ruthenium Nickel Bimetallic Composition on the Catalytic Performance for Benzene Hydrogenation to Cyclohexane. *Appl. Catal. Gen.* **2015**, *499*, 124. https://doi.org/10.1016/j.apcata.2015.04.016

(210) Zhang, P.-F.; Zhang, J.-Y.; Sheng, T.; Lu, Y.-Q.; Yin, Z.-W.; Li, Y.-Y.; Peng, X.-X.; Zhou, Y.; Li, J.-T.; Wu, Y.-J.; Lin, J.-X.; Xu, B.-B.; Qu, X.-M.; Huang, L.; Sun, S.-G. Synergetic Effect of Ru and NiO in the Electrocatalytic Decomposition of Li_2CO_3 to Enhance the Performance of a Li-CO_2 /O_2 Battery. *ACS Catal.* **2020**, *10* (2), 1640. https://doi.org/10.1021/acscatal.9b04138

(211) Li, M.; Wang, H.; Zhu, W.; Li, W.; Wang, C.; Lu, X. RuNi Nanoparticles Embedded in N-Doped Carbon Nanofibers as a Robust Bifunctional Catalyst for Efficient Overall Water Splitting. *Adv. Sci.* **2020**, *7* (2), 1901833. https://doi.org/10.1002/advs.201901833

(212) Tada, S.; Kikuchi, R.; Wada, K.; Osada, K.; Akiyama, K.; Satokawa, S.; Kawashima, Y. Long-Term Durability of Ni/TiO2 and Ru–Ni/TiO2 Catalysts for Selective CO Methanation. *J. Power Sources* **2014**, *264*, 59. https://doi.org/10.1016/j.jpowsour.2014.04.075

(213) Chen, G.; Desinan, S.; Rosei, R.; Rosei, F.; Ma, D. Synthesis of Ni-Ru Alloy Nanoparticles and Their High Catalytic Activity in Dehydrogenation of Ammonia Borane. *Chem. - Eur. J.* **2012**, *18* (25), 7925. https://doi.org/10.1002/chem.201200292

(214) Li, C.; Yang, M.; Liu, Z.; Zhang, Z.; Zhu, T.; Chen, X.; Dong, Y.; Cheng, H. Ru–Ni/Al_2O_3 Bimetallic Catalysts with High Catalytic Activity for *N* -Propylcarbazole Hydrogenation. *Catal. Sci. Technol.* **2020**, *10* (7), 2268. https://doi.org/10.1039/C9CY02528F

(215) Xiao, F.-S.; Fukuoka, A.; Ichikawa, M.; Henderson, W.; Shriver, D. F. Si02-Supported Bimetallic Ruthenium Cluster-Derived Catalysts for Selectivity and Activity Control in CO Hydrogenation toward C1-C5 Alcohols. *J. Mol. Catal.* **1992**, *74* (1–3), 379. https://doi.org/10.1016/0304-5102(92)80255-f

(216) Zhu, L.; Zheng, J.; Yu, C.; Zhang, N.; Shu, Q.; Zhou, H.; Li, Y.; Chen, B. H. Effect of the Thermal Treatment Temperature of RuNi Bimetallic Nanocatalysts on Their Catalytic Performance for Benzene Hydrogenation. *RSC Adv.* **2016**, *6* (16), 13110. https://doi.org/10.1039/C5RA24424B

(217) Deng, X.; Zhu, L.; Zhang, H.; Kroner, A.; Zheng, J.; Zhang, N.; He, J.; Chen, B. H. Ruthenium Stabilized on Transition Metal-on-Transition Metal Oxide Nanoparticles for Naphthalene Hydrogenation. *Int. J. Hydrog. Energy* **2018**, *43* (32), 15055. https://doi.org/10.1016/j.ijhydene.2018.05.170

(218) Yang, Z.; Han, J.; Fan, Q.; Jia, H.; Zhang, F. Catalytic Hydrogenation of a Pyrolysis Gasoline Model Feed over Supported NiRu Bimetallic Catalysts with Ru Content from 0.01 wt% to 0.1 wt%. *Appl. Catal. Gen.* **2018**, *568*, 183. https://doi.org/10.1016/j.apcata.2018.09.021

(219) Zhang, J.; Dasgupta, A.; Chen, Z.; Xu, D.; Savage, P. E.; Guo, Y. Supercritical Water Gasification of Phenol over Ni-Ru Bimetallic Catalysts. *Water Res.* **2019**, *152*, 12. https://doi.org/10.1016/j.watres.2018.12.030

(220) Zhu, L.; Cui, J.; Zhang, H.; Ruan, L.; Ma, N.; Zou, L.; Deng, T.; Chen, B. H.; Xiao, Q. Room-Temperature Morphology-Controlled Synthesis of Nickel and Catalytic Properties of Corresponding Ru/Ni Catalysts. *ChemCatChem* **2019**, *11* (13), 3109. https://doi.org/10.1002/cctc.201900565

(221) Zhu, L.; Zhang, H.; Ma, N.; Yu, C.; Ding, N.; Chen, J.-L.; Pao, C.-W.; Lee, J.-F.; Xiao, Q.; Hui Chen, B. Tuning the Interfaces in the Ruthenium-Nickel/Carbon Nanocatalysts for Enhancing Catalytic Hydrogenation Performance. *J. Catal.* **2019**, *377*, 299. https://doi.org/10.1016/j.jcat.2019.07.041

(222 Zhu, L.; Zheng, L.; Du, K.; Fu, H.; Li, Y.; You, G.; Chen, B. H. An Efficient and Stable Ru–Ni/C Nano-Bimetallic Catalyst with a Comparatively Low Ru Loading for Benzenehydrogenation under Mild Reaction Conditions. *RSC Adv* **2013**, *3* (3), 713. https://doi.org/10.1039/C2RA22181K

(223) Zhu, L.; Jiang, Y.; Zheng, J.; Zhang, N.; Yu, C.; Li, Y.; Pao, C.-W.; Chen, J.-L.; Jin, C.; Lee, J.-F.; Zhong, C.-J.; Chen, B. H. Ultrafine Nanoparticle-Supported Ru Nanoclusters with Ultrahigh Catalytic Activity. *Small* **2015**, *11* (34), 4385. https://doi.org/10.1002/smll.201500654

(224) Zhu, L.; Sun, H.; Zheng, J.; Yu, C.; Zhang, N.; Shu, Q.; Chen, B. H. Combining Ru, Ni and $Ni(OH)_2$ Active Sites for Improving Catalytic Performance in Benzene Hydrogenation. *Mater. Chem. Phys.* **2017**, *192*, 8. https://doi.org/10.1016/j.matchemphys.2017.01.047

(225) Zhu, L.; Zheng, T.; Zheng, J.; Yu, C.; Zhang, N.; Zhou, Q.; Chen, B. H. Shape Control of Nickel Crystals and Catalytic Hydrogenation Performance of Ruthenium-on-Ni Crystals. *CrystEngComm* **2018**, *20* (1), 113. https://doi.org/10.1039/c7ce01847a

(226) Zhu, L.; Zheng, T.; Zheng, J.; Yu, C.; Zhang, N.; Liao, Q.; Chen, B. H. Synthesis of Ru/CoNi Crystals with Different Morphologies for Catalytic Hydrogenation. *CrystEngComm* **2017**, *19* (25), 3430. https://doi.org/10.1039/c7ce00702g

(227) Zhu, L.; Shan, S.; Petkov, V.; Hu, W.; Kroner, A.; Zheng, J.; Yu, C.; Zhang, N.; Li, Y.; Luque, R.; Zhong, C.-J.; Ye, H.; Yang, Z.; Chen, B. H. Ruthenium–Nickel–Nickel Hydroxide Nanoparticles for Room Temperature Catalytic Hydrogenation. *J. Mater. Chem. A* **2017**, *5* (17), 7869. https://doi.org/10.1039/C7TA01437F

(228) Pichaikaran, S.; Arumugam, P. Vapour Phase Hydrodeoxygenation of Anisole over Ruthenium and Nickel Supported Mesoporous Aluminosilicate. *Green Chem.* **2016**, *18* (9), 2888. https://doi.org/10.1039/C5GC01854D

(229) Yang, M.; Zhang, J.; Guo, Y. Supercritical Water Gasification of Phenol over Ni-Ru Bimetallic Catalyst: Intermediates and Kinetics. *J. Supercrit. Fluids* **2020**, *160*, 104810. https://doi.org/10.1016/j.supflu.2020.104810

(230) Yu, H.; Yang, X.; Wu, Y.; Guo, Y.; Li, S.; Lin, W.; Li, X.; Zheng, J. Bimetallic Ru-Ni/TiO_2 Catalysts for Hydrogenation of N-Ethylcarbazole: Role of TiO_2 Crystal Structure. *J. Energy Chem.* **2020**, *40*, 188. https://doi.org/10.1016/j.jechem.2019.04.009

(231) Xie, D.; Liu, X.; Lv, H.; Guo, Y. Products, Pathways, and Kinetics for Catalytic Hydrodenitrogenation of Quinoline in Hydrothermal Condition. *J. Supercrit. Fluids* **2022**, *182*, 105509. https://doi.org/10.1016/j.supflu.2021.105509

(232) Zhang, H.; Pei, A.; Liao, J.; Ruan, L.; Yang, K.; Wang, J.; Zhu, L.; Chen, B. H. PtRuNi/C Novel Nanostructures of Platinum-Ruthenium Island-on-Ni/$Ni(OH)_2$ Nanoparticles for the Selective Hydrogenation of Quinoline. *J. Alloys Compd.* **2020**, *834*, 155203. https://doi.org/10.1016/j.jallcom.2020.155203

(233) Li, L.; Xu, S.; Shen, S.; Wang, L.; Zuo, M.; Chen, P.; Liang, H. A Sulfur-Fixing Strategy toward Carbon-Supported Ru-Based Bimetallic Nanocluster Catalysts. *ChemNanoMat* **2020**, *6* (6), 969. https://doi.org/10.1002/cnma.202000054

(234) Suryawanshi, Y. R.; Chakraborty, M.; Jauhari, S.; Mukhopadhyay, S.; Shenoy, Kalsanka. T. Hydrogenation of Dibenzo-18-Crown-6 Ether Using γ-Al2O3 Supported Ru-Pd and Ru-Ni Bimetallic Nanoalloy Catalysts. *Int. J. Chem. React. Eng.* **2019**, *17* (4), 20180049. https://doi.org/10.1515/ijcre-2018-0049

(235) Sreenavya, A.; Baskaran, T.; Ganesh, V.; Sharma, D.; Nagendra, K.; Sakthivel, A. Framework of Ruthenium-Containing Nickel Hydrotalcite-Type Material: Preparation, Characterisation, and Its Catalytic Application. *RSC Adv.* **2018**, *8* (44), 25248. https://doi.org/10.1039/C8RA03506G

(236) Liu, W.; Feng, H.; Yang, Y.; Niu, Y.; Wang, L.; Yin, P.; Hong, S.; Zhang, B.; Zhang, X.; Wei, M. Highly-Efficient RuNi Single-Atom Alloy Catalysts toward Chemoselective Hydrogenation of Nitroarenes. *Nat. Commun.* **2022**, *13* (1), 3188. https://doi.org/10.1038/s41467-022-30536-9

(237) Lee, J.; Kim, Y. T.; Huber, G. W. Aqueous-Phase Hydrogenation and Hydrodeoxygenation of Biomass-Derived Oxygenates with Bimetallic Catalysts. *Green Chem.* **2014**, *16* (2), 708. https://doi.org/10.1039/c3gc41071d

(238) Romero, A.; Nieto-Márquez, A.; Alonso, E. Bimetallic Ru:Ni/MCM-48 Catalysts for the Effective Hydrogenation of d -Glucose into Sorbitol. *Appl. Catal. Gen.* **2017**, *529*, 49. https://doi.org/10.1016/j.apcata.2016.10.018

(239) Ribeiro, L. S.; Delgado, J. J.; Órfão, J. J. M.; Pereira, M. F. R. Carbon Supported Ru-Ni Bimetallic Catalysts for the Enhanced One-Pot Conversion of Cellulose to Sorbitol. *Appl. Catal. B Environ.* **2017**, *217*, 265. https://doi.org/10.1016/j.apcatb.2017.04.078

(240) Wang, H.; Ruan, H.; Feng, M.; Qin, Y.; Job, H.; Luo, L.; Wang, C.; Engelhard, M. H.; Kuhn, E.; Chen, X.; Tucker, M. P.; Yang, B. One-Pot Process for Hydrodeoxygenation of Lignin to Alkanes Using Ru-Based Bimetallic and Bifunctional Catalysts Supported on Zeolite Y. *ChemSusChem* **2017**, *10* (8), 1846. https://doi.org/10.1002/cssc.201700160

(241) Mishra, D. K.; Dabbawala, A. A.; Truong, C. C.; Alhassan, S. M.; Jegal, J.; Hwang, J. S. Ru–NiO_x Nanohybrids on TiO_2 Support Prepared by Impregnation-Reduction Method for Efficient Hydrogenation of Lactose to Lactitol. *J. Ind. Eng. Chem.* **2018**, *68*, 325. https://doi.org/10.1016/j.jiec.2018.08.003

(242) Frecha, E.; Torres, D.; Pueyo, A.; Suelves, I.; Pinilla, J. L. Scanning Different Ni-Noble Metal (Pt, Pd, Ru) Bimetallic Nanoparticles Supported on Carbon Nanofibers

for One-Pot Cellobiose Conversion. *Appl. Catal. Gen.* **2019**, *585*, 117182. https://doi.org/10.1016/j.apcata.2019.117182

(243) Kasar, G. B.; Medhekar, R. S.; Bhosale, P. N.; Rode, C. V. Kinetics of Hydrogenation of Aqueous Levulinic Acid over Bimetallic Ru–Ni/MMT Catalyst. *Ind. Eng. Chem. Res.* **2019**, *58* (43), 19803. https://doi.org/10.1021/acs.iecr.9b03748

(244) Al-Naji, M.; Yepez, A.; Balu, A. M.; Romero, A. A.; Chen, Z.; Wilde, N.; Li, H.; Shih, K.; Gläser, R.; Luqueb, R. Insights into the Selective Hydrogenation of Levulinic Acid to γ-Valerolactone Using Supported Mono- and Bimetallic Catalysts. *J. Mol. Catal. Chem.* **2016**, *417*, 145. https://doi.org/10.1016/j.molcata.2016.03.015

(245) Li, R.; Qiu, J.; Chen, H.; Shu, R.; Chen, Y.; Liu, Y.; Liu, P.-F. Hydrodeoxygenation of Phenolic Compounds and Raw Lignin-Oil over Bimetallic RuNi Catalyst: An Experimental and Modeling Study Focusing on Adsorption Properties. *Fuel* **2020**, *281*, 118758. https://doi.org/10.1016/j.fuel.2020.118758

(246) Wang, H.-T.; Li, Z.-K.; Yan, H.-L.; Lei, Z.-P.; Yan, J.-C.; Ren, S.-B.; Wang, Z.-C.; Kang, S.-G.; Shui, H.-F. Catalytic Hydrogenolysis of Lignin and Model Compounds over Highly Dispersed Ni-Ru/Al_2O_3 without Additional H_2. *Fuel* **2022**, *326*, 125027. https://doi.org/10.1016/j.fuel.2022.125027

(247) Kim, J.-Y.; Park, S. Y.; Choi, I.-G.; Choi, J. W. Evaluation of Ru_xNi_{1-x}/SBA-15 Catalysts for Depolymerization Features of Lignin Macromolecule into Monomeric Phenols. *Chem. Eng. J.* **2018**, *336*, 640. https://doi.org/10.1016/j.cej.2017.11.118

(248) Wu, J.; Zhu, X.; Fu, Y.; Chang, J. Study on Selective Preparation of Phenolic Products from Lignin over Ru–Ni Bimetallic Catalysts Supported on Modified HY Zeolite. *Ind. Eng. Chem. Res.* **2022**, *61* (8), 3206. https://doi.org/10.1021/acs.iecr.1c04594

CHAPTER 2: Synthesis and characterisation of metallic nanoparticles

Summary

2.1 Introduction

In 2021, the 77 % of the world energy was supplied from fossil fuels,[1] and there is an urgent need to find renewable alternatives to them. Lignocellulosic biomass has appeared to be a promising alternative[2,3] but, for its application in the industry to go towards the energy transition, high performing and cheap catalysts need to be discovered.

In order to obtain competitive catalysts, earth abundant metals are targeted to be part of their composition, even if their usual drawback is that they need harsh reaction conditions, such as 200-400 bars of hydrogen (H_2), in the catalytic reduction of amides to primary amines.[4] On the other hand, noble metals such as Pt,[5] Ru,[6] Rh,[7] Re[8] and Ir[9] are active at more mild conditions. An interesting alternative is to produce bimetallic systems in which earth-abundant and noble metals are combined, to integrate the low-cost and the efficiency of both kind of metals. Bimetallic and trimetallic, or even more, catalysts are promising, as their performance may be improved, in comparison to their monometallic counterparts, by the so-called synergetic effects.[10–12]

With the aim to reduce platform molecules coming from lignocellulosic biomass we produced a series of bimetallic catalysts. Ru was chosen due to its effectiveness as catalysts for hydrogenation reactions,[13–16] and also because it is one of the less expensive noble metals. Ru was combined to the earth abundant metals Ni and Cu.[17–20]

The presence of both Ni and Ru in a material, conferees different electronic properties to the metals, as supported by X-ray photoelectron spectroscopy (XPS) analyses,[21–23] even when a catalyst is a mixture of monometallic Ru and Ni nanoparticles (NPs).[24,25] Ru has also been observed to be able to reduce, through hydrogen spillover, Ni^{2+}.[26,27] RuNi based catalysts have been described in different types of structures such as homogeneous alloys,[28,29] core-shells with Ru[30] or Ni[31] in the core, or NPs' surfaces rich on Ru or Ni;[30] and synergetic effects have been reported. The presence of both Cu and Ru in the same catalyst has shown as well synergetic effects for applications in catalysis.[32] RuCu based NPs have been described in different types of structures such as face-centred cubic (*fcc*) alloy NPs[33,34] By modifying the structure[35] or the metal ratio[29,30,32,34,36,37] of the bimetallic catalysts, their catalytic activity may be tuned.

The decomposition of organometallic complexes under H_2 pressure in the presence of stabilisers is a versatile tool for the synthesis of NPs.[38] Some NPs' properties can be modulated such as the size, the shape and the composition. The same synthetic methodology has been used for the formation of bimetallic NPs with interesting properties in catalysis.[39,40] In this

methodology, the nature of the metal precursors can influence the different characteristics of the NPs. Moreover, the ligands, apart from acting as stabilisers to prevent the growth and the coalescence of the NPS, may also play a role in the formation of the NPs by interacting with the metal precursors,[41,42] and later on in catalysis.[43]

In the case of bimetallic NPs, the stabiliser may affect the metal surface compositions. This is the case of RuPt NPs which, stabilised by polyvinylpyrrolidone (PVP), possess a core-shell structure[44] but, when stabilised by a stronger coordinating ligand such diphenylphosphino-butane (dppb), results to Ru cores with disordered metal layers around, of both Ru and Pt, as diphoshpines have an affinity for both metals.[45]

In the next sections, the synthesis and characterization of bimetallic RuNi and RuCu NPs is addressed. In the case of RuNi NPs several ligands have been used for their synthesis, PVP, a phosphine, and an organic acid, with the aim to study their effect on the NPs properties. The procedure has been extended to the synthesis of RuCu NPs. Finally, in view of the promising results of Cu/PVP NPs in catalysis (see Chapter 3), monometallic Cu NPs stabilized with amines have been also synthesised.

2.2 Synthesis of RuNi/PVP nanoparticles

The synthesis of the RuNi/PVP NPs series was performed by decomposing the [Ru(η^4-C_8H_{12})(η^6-C_8H_{10})] and [Ni(η^4-C_8H_{12})$_2$] complexes under 3 bar of H_2 pressure, in the presence of PVP and using tetrahydrofuran (THF) as solvent (Scheme 1). All the experimental details are given in Chapter 6. The reaction was carried out at room temperature (RT) and at 85 °C. Several Ru/Ni ratios were applied in order to produce RuNi NPs of different compositions, as detailed in Table 1. Monometallic Ru/PVP and Ni/PVP NPs were also synthesised, using the same procedure, for comparison purposes.

$$[Ru(\eta^4\text{-}C_8H_{12})(\eta^6\text{-}C_8H_{10})] + [Ni(\eta^4\text{-}C_8H_{12})_2] \xrightarrow[THF,\ T]{\text{3 bar } H_2,\ PVP} RuNi/PVP + C_8H_{16}$$

Scheme 1: Synthesis of RuNi/PVP NPs.

The decomposition of [Ni(η^4-C_8H_{12})$_2$] did not occur at RT, as the typical colour change from pale yellow to black was not observed after 16 h of reaction. From this result, it was concluded that this Ni precursor needs higher temperature to be decomposed. In contrast, the synthesis of all the bimetallic NPs synthesised from [Ru(η^4-C_8H_{12})(η^6-C_8H_{10})] and [Ni(η^4-C_8H_{12})$_2$] complexes, conducted at RT, displayed the expected characteristic colour change

(Figure 1), from yellow to black in some minutes. The colour change observed for the bimetallic reactions performed at RT pointed out that the presence of the Ru precursor, with a faster decomposition rate, triggered the decomposition of the Ni precursor, acting like a mediator for the formation of the bimetallic NPs. However, the high resolution transmission electron microscopy (HRTEM) images of these RuNi NPs synthesised at RT showed that the sample was not homogeneous both in terms of size and composition. Two populations of NPs of different sizes were observed, of *ca.* 1.3 nm and 5.0 nm. Then, Energy Dispersive X-ray (EDX) analyses performed on isolated NPs (Figure 2) evidenced that the larger NPs were composed of Ni while the smaller ones, of Ru. These results indicate that using RT did not allow the formation of bimetallic RuNi NPs but, instead, a mixture of monometallic Ru NPs and Ni NPs. Taking into consideration that the desired materials should be homogeneous and bimetallic, no further characterisation was performed in this series, and the procedure, discarded.

Figure 1: Colour change in a typical synthesis of RuNi/PVP NPs at RT; left, before the hydrogenation reaction, and right, after the reaction.

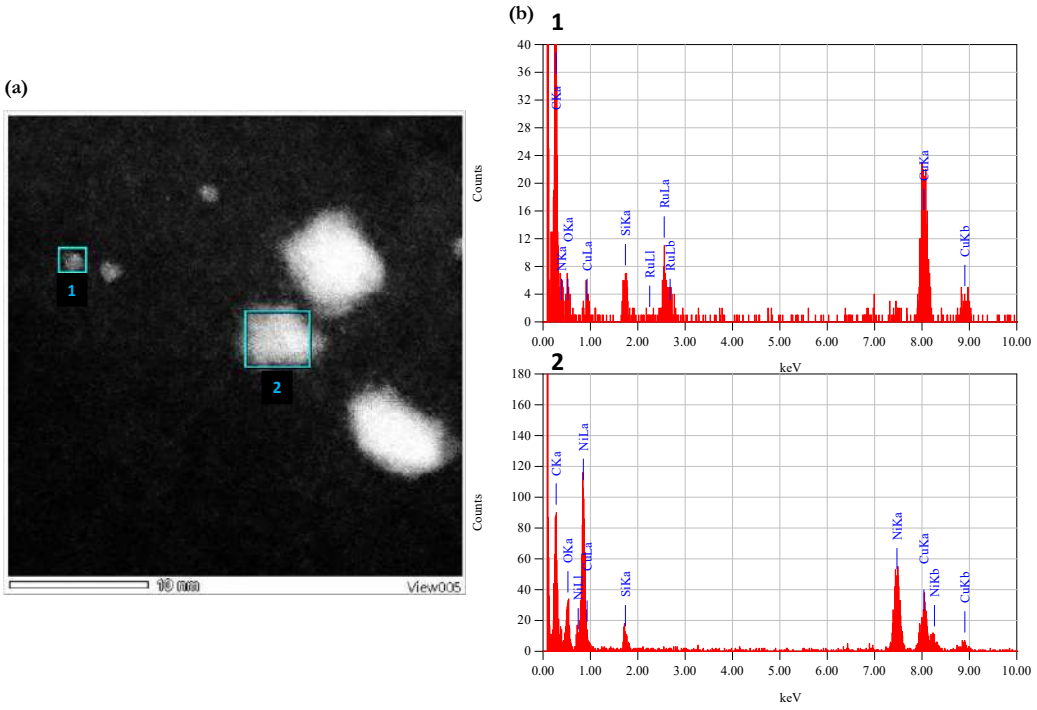

Figure 2: (a) High angle annular dark field (HAADF)-scanning transmission electron microscopy (STEM) image of Ru_1Ni_1/PVP NPs synthesised at RT together with the (b) EDX analysis of the squares 1 (top) and 2 (bottom).

In a previous work from the group, [Ni(η^4-C_8H_{12})$_2$] decomposition was achieved at 70 °C.[46] To ensure a good decomposition of the Ni precursor, thus, the synthesis reactions of the bimetallic and monometallic NPs were carried out at a higher temperature, being 85 ºC the chosen. When decomposing the [Ni(η^4-C_8H_{12})$_2$] in the presence of PVP at 85 ºC, the typical change of colour was observed within minutes, indicating the formation of Ni/PVP NPs. Transmission electron microscopy (TEM) analyses of the sample displayed the presence of NPs with a 5.6 ± 1.2 nm size and a tripodal shape (Figure 3). A series of RuNi/PVP bimetallic NPs of different compositions and the monometallic Ru/NPs were synthesised, as well, at this temperature. Table 1 summarizes the metal content of each sample, along with the size of the NPs established from the TEM images (Figures 3 to 8).

Table 1: Metal content and mean size of RuNi/PVP NPs synthesised at 85 ºC.

NP	Ru content (%)[a]	Ni content (%)[a]	NP composition (from ICP-OES)	NP Mean size (nm)[b]
Ru/PVP	24.2	-	Ru/PVP	1.0 ± 0.2
Ni/PVP	-	15.5	Ni/PVP	5.6 ± 1.2[c]
Ru_3Ni_1/PVP	17.0	3.7	$Ru_{2.7}Ni_{1.0}$/PVP	1.5 ± 0.3
Ru_1Ni_1/PVP	10.2	5.7	$Ru_{1.0}Ni_{1.0}$/PVP	1.5 ± 0.3
Ru_1Ni_3/PVP	7.9	14.6	$Ru_{1.0}Ni_{3.2}$/PVP	1.2 ± 0.2
Ru_1Ni_{20}/PVP	1.5	17.6	$Ru_{1.0}Ni_{20.0}$/PVP	1.4 ± 0.3

[a]ICP-OES analysis. [b]Mean values of NP size determined from TEM images by considering at least 200 particles. [C]Tripodal shaped NPs.

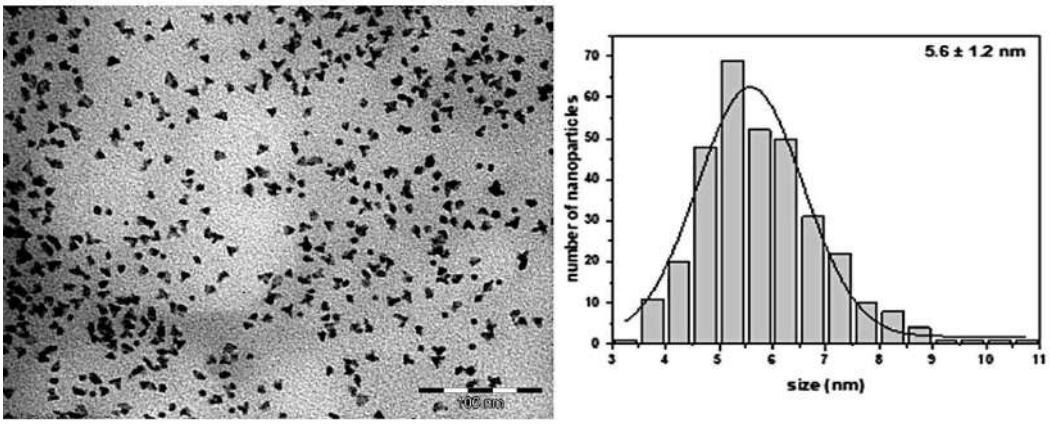

Figure 3: TEM image of the Ni/PVP NPs synthesised at 85 ºC (scale bar 100 nm) together with the respective size histogram.

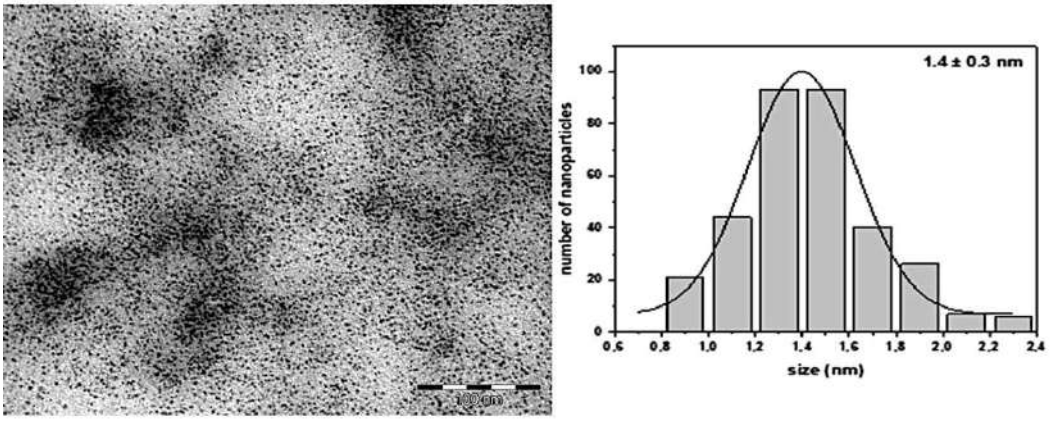

Figure 4: TEM image of the Ru_1Ni_{20}/PVP NPs synthesised at 85 ºC (scale bar 100 nm) together with the respective size histogram.

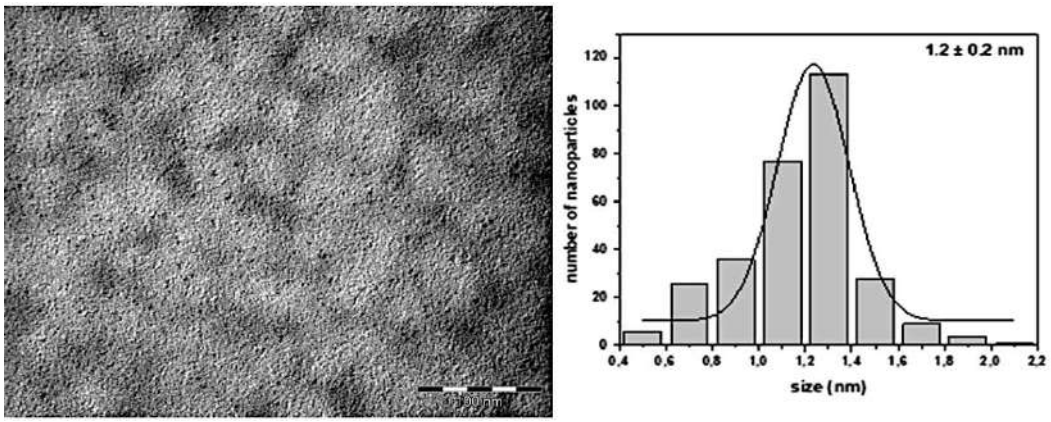

Figure 5: TEM image of the Ru_1Ni_3/PVP NPs synthesised at 85 ºC (scale bar 100 nm) together with the respective size histogram.

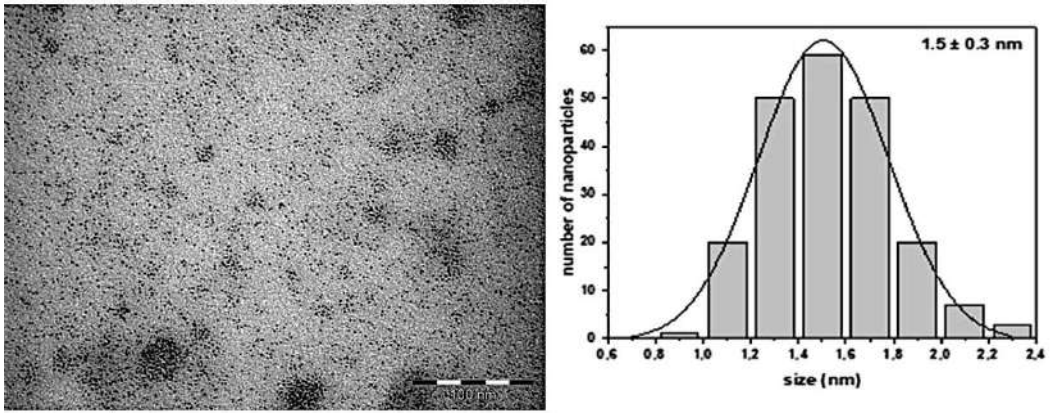

Figure 6: TEM image of the Ru_1Ni_1/PVP NPs synthesised at 85 ºC (scale bar 100 nm) together with the respective size histogram.

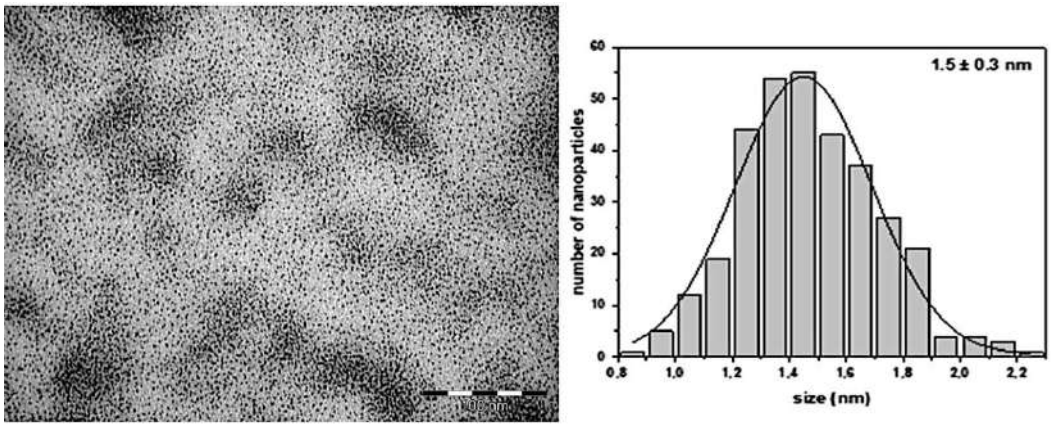

Figure 7: TEM image of the Ru_3Ni_1/PVP NPs synthesised at 85 ºC (scale bar 100 nm) together with the respective size histogram.

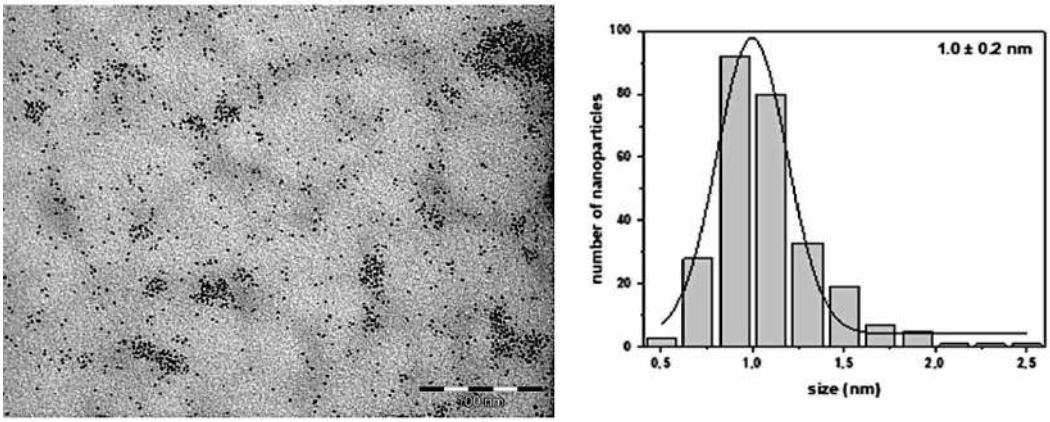

Figure 8: TEM image of the Ru/PVP NPs synthesised at 85 ºC (scale bar 100 nm) together with the respective size histogram.

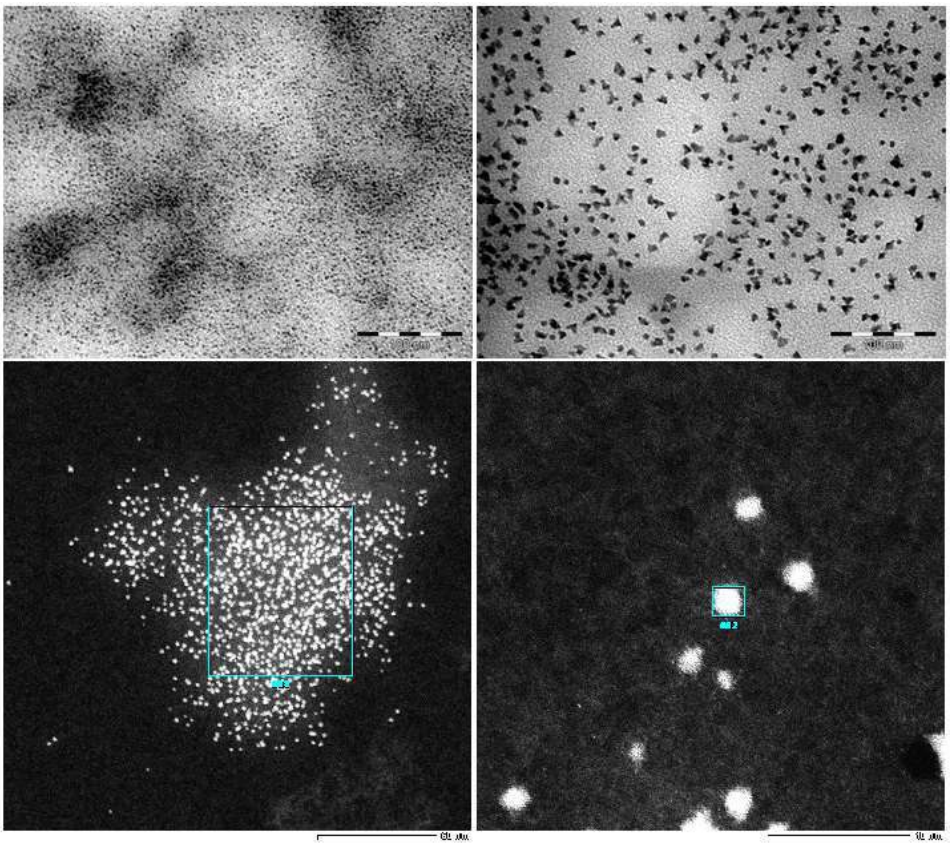

Figure 9: TEM images of Ru_1Ni_{20}/PVP NPs (top left, scale bar = 100 nm) and Ni/PVP NPs (top right, scale bar = 100 nm); HAADF-STEM images of Ru_1Ni_1/PVP NPs (bottom left, scale bar = 50 nm; bottom right scale bar = 10 nm).

In all the samples, the metallic mass percentages in weight were *ca.* 20 % and the molar ratios Ru/Ni were in agreement with the ratio of the precursors introduced for the synthesis. Concerning the sizes, small bimetallic NPs of less than 2 nm were obtained. It is worth mentioning that such a small size is observed for all Ru/Ni compositions, including the ones

displaying high Ni content, Ru_1Ni_{20}/PVP. These results are in contrast with the size of the monometallic Ni NPs (5.6 ± 1.2 nm) synthesised following the same procedure.

The differences in shape and size between the monometallic Ru NPs and the bimetallic RuNi NPs, related to the monometallic Ni ones, suggest that Ru may play the role of seed mediator and facilitate the decomposition of the Ni precursor, which could justify that at RT the Ni precursor decomposed in the presence of Ru. This hypothesis is also supported by previous observations from the literature stating that Ni^{2+} can be reduced by Ru due to a hydrogen spillover.[26,27] This is in line with the decomposition kinetics of $[Ni(\eta^4\text{-}C_8H_{12})_2]$ and $[Ru(\eta^4\text{-}C_8H_{12})(\eta^6\text{-}C_8H_{10})]$ under H_2 as we have observed that the Ru one is the fastest.

HAADF-STEM-EDX analyses on isolated NPs (Figure 10) show that Ru and Ni coexist in the NPs. The bimetallic NP lattices were analysed from HAADF-STEM images. Planes of 0.277, 0.209 and 0.199 nm were observed that can be attributed to the shorter (100), (002) and (101) planes of hexagonal close-packed (*hcp*) Ru structure. The values observed are in agreement with the incorporation of a smaller atom into the structure, thus suggesting the formation of bimetallic RuNi systems.

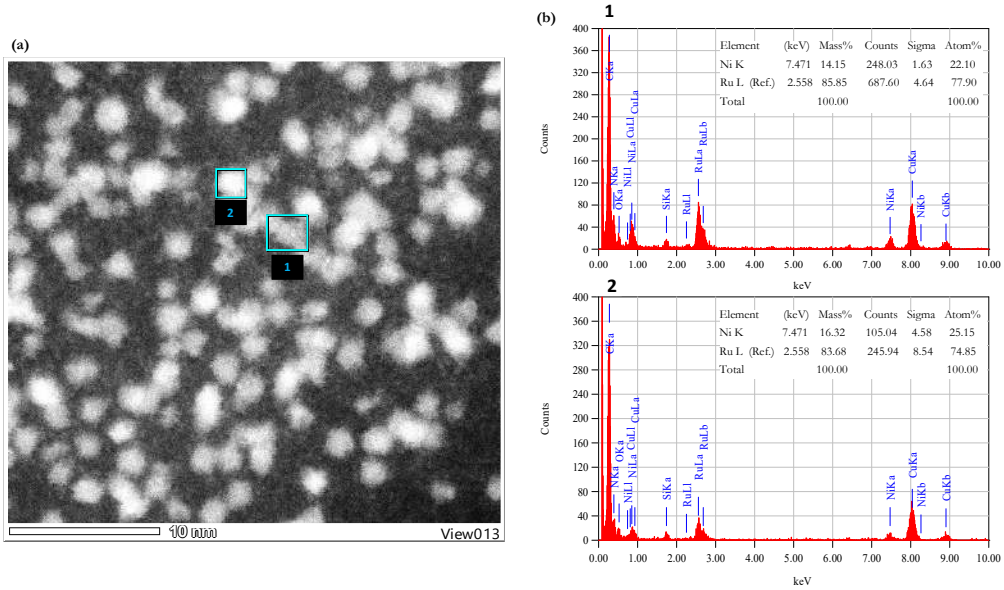

Figure 10: (a)HAADF-STEM images of Ru_1Ni_1/PVP NPs synthesised at 85 °C; (b) EDX analysis of the isolated NPs in squares 1 (top) and 2 (bottom).

Wide angle X-ray scattering (WAXS) analyses were performed on the series of PVP-stabilized monometallic and bimetallic NPs for comparison purpose (Figure 11). For the RuNi systems, the WAXS results exposed a complex structure although in agreement with the formation of bimetallic NPs. The Ni/PVP spectrum agrees with bulk Ni *fcc* structure. Correspondingly, for the Ni-rich system, the Ru_1Ni_{20}/PVP structure is well dominated by

the *fcc* of metallic Ni in spite of a loss in crystallinity. At the other side of the composition range, the situation is different. The Ru/PVP NPs synthesized at RT have the expected *hcp* structure,[47] which is distorted for the sample synthesised at 85 °C, when compared to Ru/PVP NPs synthesised at RT.[47] A concrete pattern of this distorted structure can also be detected, at 0.2–0.5 nm range, for Ru_3Ni_1/PVP and Ru_1Ni_1/PVP samples, with decreased intensity. This is in accordance with a core–shell organisation of the two metals, since for core–shell systems, the structure prevailed is dominated by the core structure.[48,49] The moderated amplitude of this pattern indicates the dilution by another component much less structured which cannot be unquestionably assigned. The case of Ru_1Ni_3/PVP NPs is more challenging as, from the radial distribution function (RDF), it is more in agreement to a Mn-β type organization often typical for very small metallic NPs.[50–54] This sample, showing an average bond length of 0.262 nm, which is in between Ni and Ru ones, 0.250 and 0.268 nm, respectively, suggests an alloy; although Mn-β is not a compact organisation which makes the exact chemical order difficult to univocally assign. Density functional theory (DFT) calculations on bimetallic RuNi NPs are ongoing in order to obtain complementary answers about the structure (Chapter 4).

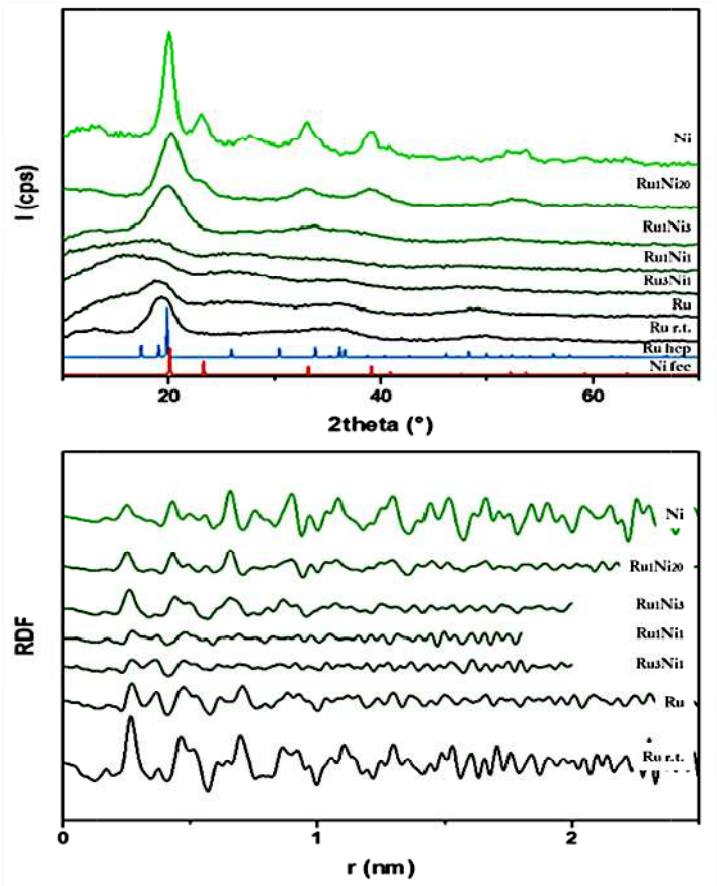

Figure 11: Diffractograms obtained by WAXS (top) from the top to the bottom of Ni/PVP, Ru_1Ni_{20}/PVP, Ru_1Ni_3/PVP, Ru_1Ni_1/PVP, Ru_3Ni_1/PVP, Ru/PVP NPs at 85 ºC and at RT and the reference of Ru *hcp* and Ni *fcc* structures; and related RDFs (bottom).

Ru/PVP, Ru_1Ni_1/PVP, Ni/PVP and PVP samples were analysed by *ex situ* XPS under ultra-high vacuum (UHV). The PVP sample was measured as a reference to compare between samples. In Figure 12 to 15, the fitting peaks for each component are displayed with the survey and high-resolution scan spectra. For the four samples, the binding energies and the fitted peaks concentration in atomic percentage are summarised in Table 2.

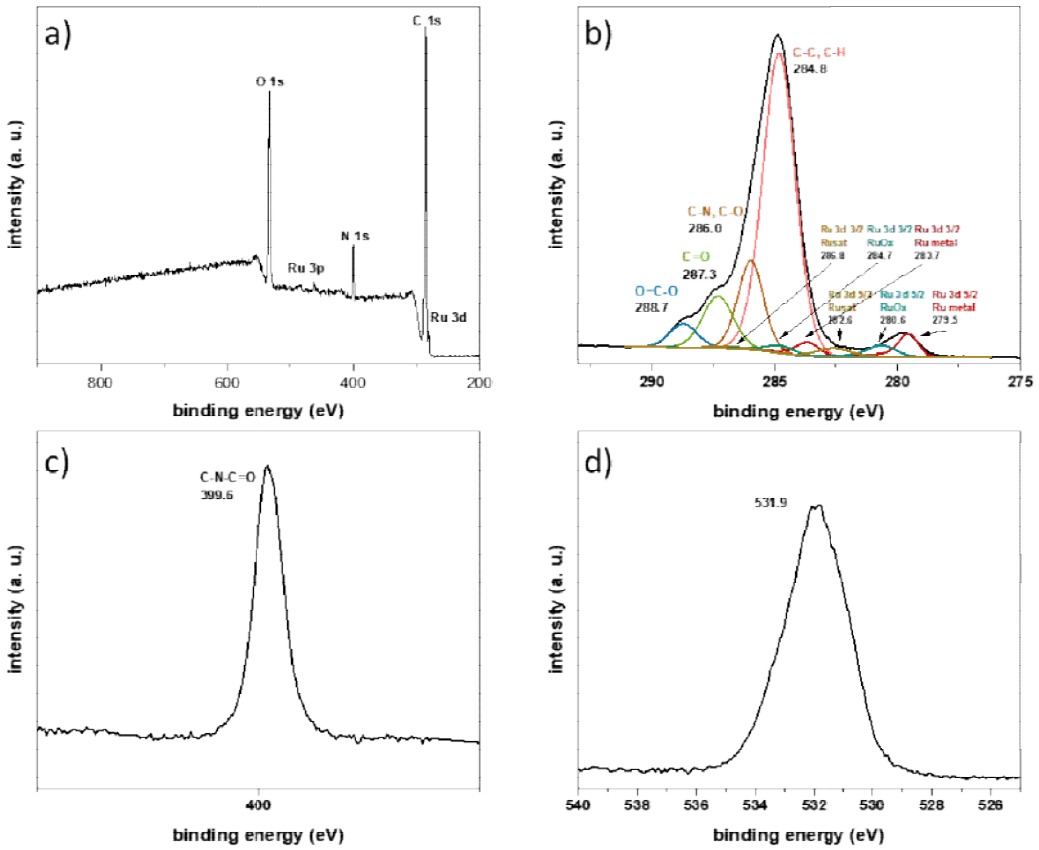

Figure 12: a) XPS survey spectrum of Ru/PVP NPs; and high-resolution scan spectra of b) C 1s and Ru 3d, c) N 1s, and d) O 1s.

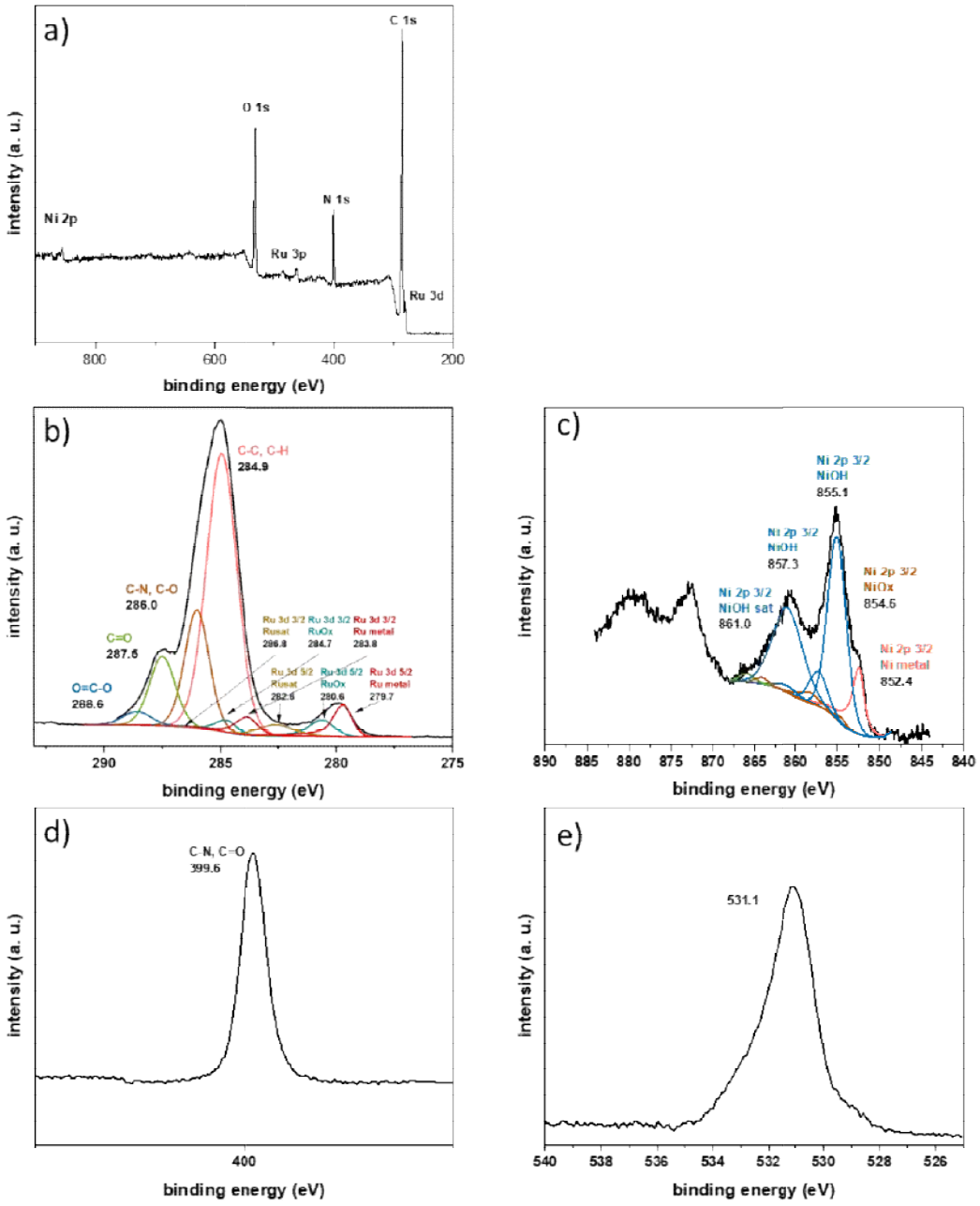

Figure 13: a) XPS survey spectrum of Ru_1Ni_1/PVP NPs; and high-resolution scan spectra of b) C 1s and Ru 3d, c) Ni 2p, d) N 1s, and e) O 1s.

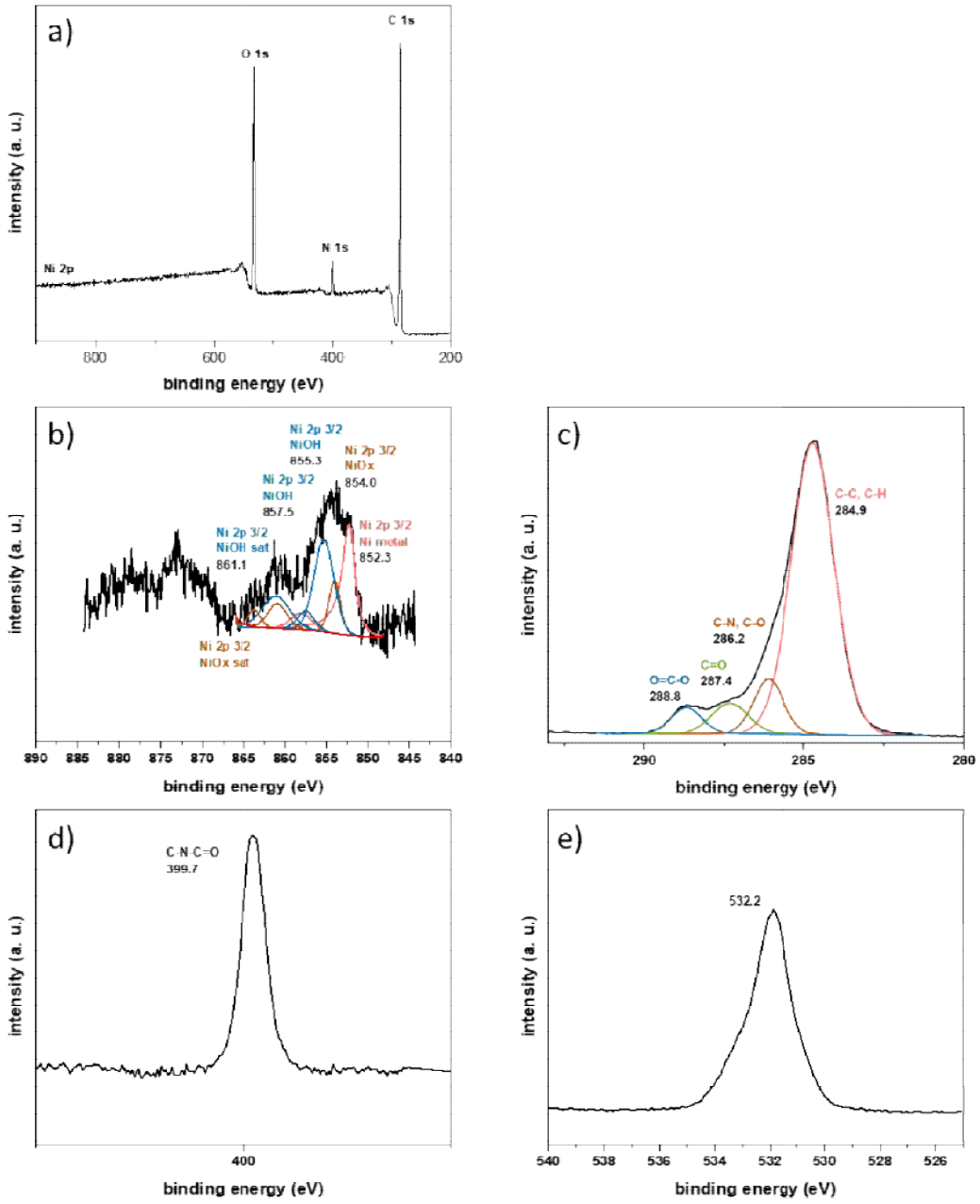

Figure 14: a) XPS survey spectrum of Ni/PVP NPs; and high-resolution scan spectra of b) Ni 2p, d) C 1s, d) N 1s, and e) O 1s.

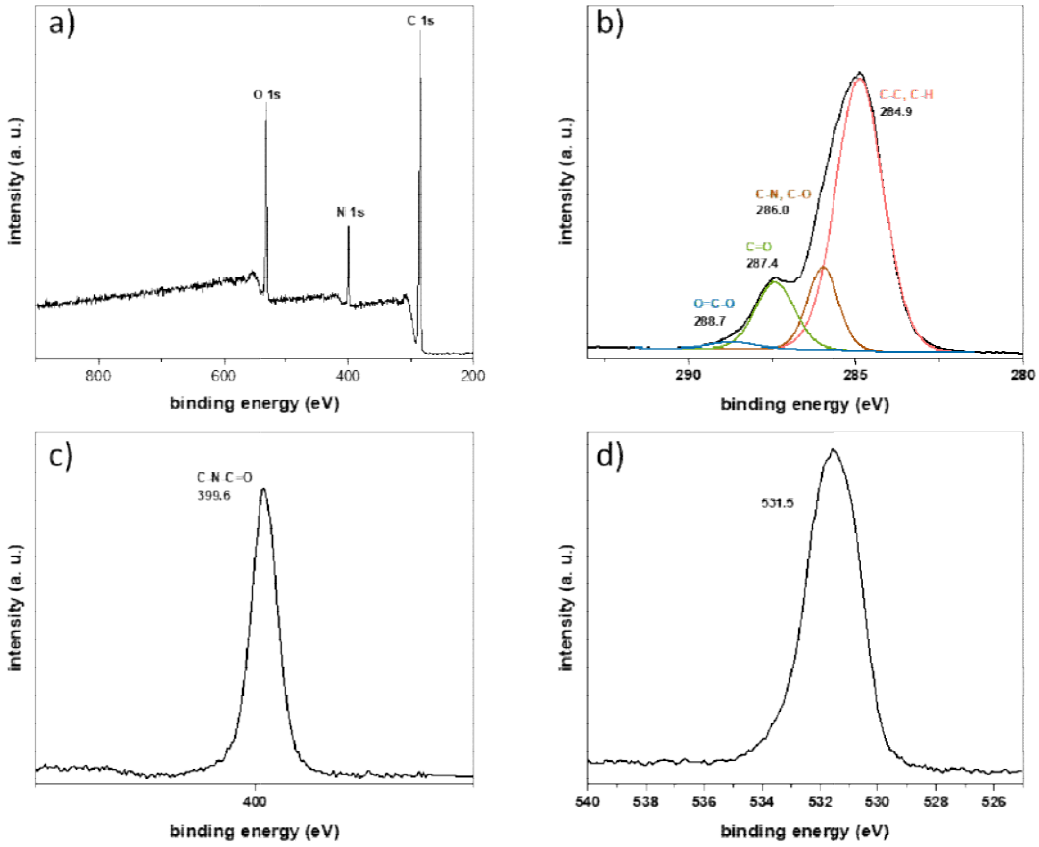

Figure 15: a) XPS survey spectrum of PVP; and high-resolution scan spectra of b) C 1s, c) N 1s, and d) O 1s.

Table 2: XPS Binding energies and atomic % of C, Ru, O and N elements found for Ru/PVP, Ru_1Ni_1/PVP, Ni/PVP, and PVP NPs.

	Ru/PVP		Ru_1Ni_1/PVP		Ni/PVP		PVP	
	Binding energy (eV)	Atomic %	Binding energy (eV)	Atomic %	Binding energy (eV)	Atomic %	Binding energy (eV)	Atomic %
$Ru3d_{5/2}$ Ru metal	279.5	0.2	279.7	0.3	-	-	-	-
$Ru3d_{5/2}$ RuOx	280.6	0.1	280.6	0.2	-	-	-	-
$Ru3d_{5/2}$ Rusat	282.6	0.1	282.6	0.2	-	-	-	-
$Ru3d_{3/2}$ Ru metal	283.7	0.1	283.8	0.2	-	-	-	-
$Ru3d_{3/2}$ RuOx	284.7	0.1	284.7	0.1	-	-	-	-
C1s C-C, C-H	284.8	50.5	284.9	46.3	284.9	54.8	284.9	51.8
C1s C-N, C-O	286.0	11.8	286.0	15.9	286.2	9.1	286.0	10.4
$Ru3d_{3/2}$ Ru sat	286.8	θ<0.1	286.8	<0.1	-	-	-	-
C1s C=O	287.3	8.2	287.5	9.8	287.4	5.0	287.4	10.4
C 1s O=C-O	288.7	3.3	288.6	2.1	288.8	4.3	288.7	1.3
N 1s C-N-C=O	399.6	7.1	399.6	9.3	399.7	4.2	399.6	9.7
O 1s	531.9	18.5	531.1	14.8	532.2	22.5	531.5	16.4
Ni $2p_{3/2}$ Ni metal	-	-	852.4	0.1	852.3	<0.1	-	-
Ni $2p_{3/2}$ NiOx/Ni(OH)	-	-	around855.1	0.8	around 855.0	<0.1	-	-

The XPS spectrum of PVP is in accordance with its composition. The XPS spectra of Ru/PVP, Ni/PVP and Ru_1Ni_1/PVP (Figures 12 to 14, respectively) are close to the one obtained for PVP (Figure 15), with supplementary peaks from the corresponding metals. The intensity of the metallic peaks is low, which makes the fitting difficult, because there is an excess of PVP in the NP compared to the metallic compounds. However, analysing both monometallic samples and bimetallic Ru_1Ni_1/PVP it can be observed that, concerning Ru, Ru $3d_{5/2}$ have minimally higher binding energies in the bimetallic sample, 279.7 eV against 279.5 eV. The Ni $2p_{3/2}$ band of Ru_1Ni_1/PVP and Ni/PVP displayed different chemical environments. The Ni $2p_{3/2}$ peak at higher binding energy, *ca.* 855 eV, agrees with an oxi(hydroxi)dation of the top surface. The other Ni $2p_{3/2}$ signals at 852.5 eV and 852.3 eV show the existence of Ni metal, in bimetallic and monometallic environments respectively.

Due to the low intensity of the Ru and Ni signals, corroborate any transfer of charge between the two metals and its direction is complex. Nevertheless, the variation on binding energies can be provisionally ascribed to Ru and Ni being in close vicinity in the bimetallic Ru_1Ni_1/PVP sample, thus corroborating further the bimetallic nature of the samples.

Attenuated total reflection infrared (ATR-FTIR) measurements were performed for all the synthesised nanomaterials inside a glovebox under argon; the spectra are displayed in Figure 16. In these spectra, the signals from the stabiliser, PVP, are observed (C-H stretching *ca.* 3000 cm^{-1}, C=O stretching ca. 1700 cm^{-1} and C-N stretching between 1500 and 1250 cm^{-1}), which confirms that the polymer is stable under the reaction conditions. These results are supported also by the ones observed in the literature which state that PVP is a stable polymer at least until 200 ºC.[55] Moreover, if metallic oxides were present on the surface of the NPs, this would be identified by the C=O stretching band, which are really sensitive to crystallographic changes or any variation on the metallic surface.[56] Carbon monoxide (CO) adsorption is known to give useful information on the NP surface state, being the CO band a vibrational probe.[57] Metallic centres with more electron density are present νCO adsorption bands of lower energy. By studying CO frequencies, the effect of a ligand on a specific metallic surface[58,59] or, in bimetallic NPs, the chemical order[39,44,45]can be determined. For this purpose, the nanomaterials in the solid state (SS) were exposed to 1 bar of CO at RT (Figure 17). A characteristic CO band was visible at 2010 cm^{-1} in samples with high Ru content. For Ni/PVP, Ru_1Ni_{20}/PVP and Ru_1Ni_3/PVP this band was not observed. For these Ni-rich samples, we hypothesised the formation of $[Ni(CO)_4]$ when exposed to CO, but as this specie is volatile, it can only be observed at low temperature.[60] The lack of CO signal for Ru_1Ni_3/PVP and Ru_1Ni_{20}/PVP samples suggests that Ru is not available for the CO adsorption. This may be explained by the presence of Ni on the NP surface which is in agreement with the core-shell structure, with Ru located in the core, as ascertained by WAXS analyses.

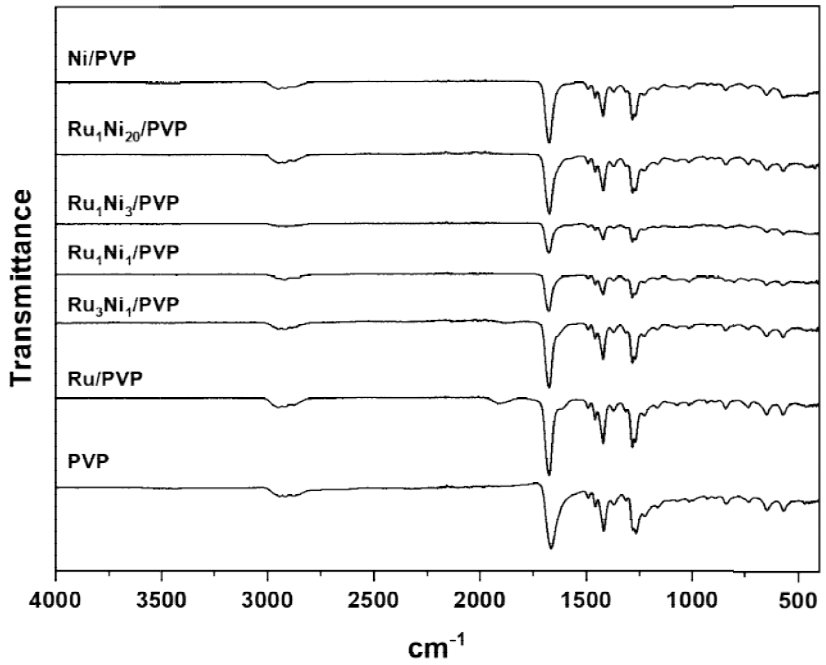

Figure 16: ATR-IR spectra of RuNi/PVP NPs in comparison with those of monometallic Ru and Ni NPs, and that of PVP.

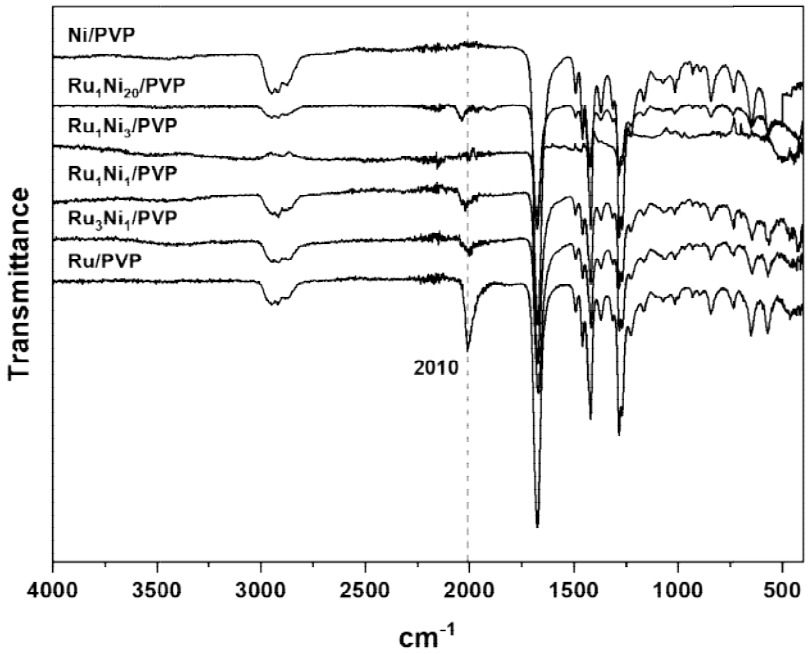

Figure 17: ATR-IR spectra of RuNi/PVP NPs in comparison with those of monometallic Ru and Ni NPs after CO exposure (1 bar, RT).

The PVP-stabilized NPs were also characterized by inductively coupled plasma - optical emission spectroscopy (ICP-OES) in order to determine the content in metals (Table 1).

From the mean sizes of the NPs determined by TEM and the metallic content from ICP-OES, an estimation of the Ni coverage of the NPs surface was made, assuming a spherical shape for all the NPs.

First, from the size of the NPs determined from TEM images, the volume of the core, the shell and the entire NP were calculated with equations 1-3, being r, the radius of the NP and the shell thickness is assumed as the half of the lattice constant, being 0.214 nm for Ru and 0.176 nm for Ni.

$$V_{total} = \frac{4}{3}\pi(r)^3 \quad (1)$$

$$V_{core} = \frac{4}{3}\pi(\text{r-shell thickness})^3 \quad (2)$$

$$V_{shell} = V_{total} - V_{core} \quad (3)$$

Secondly, the volume of a single unit cell (equation 4) was calculated by using the lattice parameters,[61,62] and knowing that in a *hcp*, 6 atoms and in a *fcc*, 4 atoms are present in the unit cell.

$$V_{unit} = (\text{atoms per unit cell})\frac{a^2\sqrt{3}}{4}c \quad (4)$$

Following, the unit cells present in the core, the shell and the entire NP were calculated by dividing the volumes from equations 1, 2 and 3 by the one from equation 4(equations 5, 7 and 9). From the obtained results, the number of atoms present in the entire NP, the core and the shell could be calculated (equations 6, 8 and 10).

$$\text{Unit cells}_{total} = \frac{V_{total}}{V_{unit}} \quad (5)$$

$$\text{Atoms}_{total} = (\text{Unit cells}_{total}) \cdot (\text{Atoms per unit cell}) \quad (6)$$

$$\text{Unit cells}_{core} = \frac{V_{core}}{V_{unit}} \quad (7)$$

$$\text{Atoms}_{core} = (\text{Unit cells}_{core}) \cdot (\text{Atoms per unit cell}) \quad (8)$$

$$\text{Unit cells}_{shell} = \frac{V_{shell}}{V_{unit}} \quad (9)$$

$$\text{Atoms}_{shell} = (\text{Unit cells}_{shell}) \cdot (\text{Atoms per unit cell}) \quad (10)$$

By dividing the results from equations 10 and 6, the estimated percentage of atoms on the surface was calculated by equation 11.

$$\%\ \text{surface atoms} = \frac{\text{Atoms}_{\text{shell}}}{\text{Atoms}_{\text{total}}} \cdot 100 \tag{11}$$

Then, from the ICP-OES results, the molar ratio of each metal in a bimetallic NP was determined by dividing the mass percentage from ICP-OES by the molar mass of the element (equation 12) and rationalising them (equation 13).

$$\text{mols of metal} = \frac{\text{Mass percentage}_{\text{metal}}}{\text{Molar mass}_{\text{metal}}} \tag{12}$$

$$\text{molar ratio}_{\text{metal}} = \frac{\text{mols}_{\text{metal}}}{\sum \text{mols}_{\text{metals}}} \tag{13}$$

Once knowing the molar ratio of the two metals in the bimetallic NP, and the total number of atoms present in the entire NP (equation 6), the number of atoms of each metal could be calculated (equation 14).

$$\text{Atoms}_{\text{metal}} = (\text{Atoms}_{\text{total}}) \cdot (\text{molar ratio}_{\text{metal}}) \tag{14}$$

As it is known from the WAXS analysis that the synthesised bimetallic NPs have a core-shell organisation, with Ru located in the core, the atoms in the core calculated with the equation 8 are all Ru. The rest of Ru atoms are considered to be on the surface. On this basis, the Ni percentage coverage can be calculated with equation 15.

$$\%\ \text{Ni surface coverage} = \frac{\text{Estimated atoms of Ni in a NP}}{\text{Estimated surface atoms}} \cdot 100 \tag{15}$$

Following the series of calculations above, the estimated Ni percentage coverage of the NPs Ru_3Ni_1/PVP ≈ 43 %, Ru_1Ni_1/PVP ≈ 77 % and for Ru_1Ni_3/PVP a completed shell of Ni is expected (Table 3). The estimation above is in agreement with the results observed in IR spectra, with the ones from catalysis discussed in Chapter 3, as well as the ones from DFT discussed in Chapter 4.

Table 3: Estimation of Ni coverage on RuNi/PVP NPs.

NP	NP composition (from ICP-OES)[a]	Mean size (nm)[b]	Estimated total atoms on the NP[c]	Estimated atoms on the core[c]	Estimated atoms on the surface[c]	Estimated atoms surface (%)[c]	Estimated number of Ru atoms in a NP[d]	Estimated number of Ni atoms in a NP[d]	Estimated surface coverage of Ni (%)[e]
Ru/PVP	Ru/PVP	1.1 ± 0.2	51	11	40	77	51	0	0
Ru_3Ni_1/PVP	$Ru_{2.7}Ni_{1.0}$/PVP	1.5 ± 0.3	130	47	83	63	94	36	≈43
Ru_1Ni_1/PVP	$Ru_{1.0}Ni_{1.0}$/PVP	1.5 ± 0.3	130	47	83	63	66	64	≈77
Ru_1Ni_3/PVP	$Ru_{1.0}Ni_{3.2}$/PVP	1.2 ± 0.2	82	29	53	65	26	62	≈116
Ru_1Ni_{20}/PVP	$Ru_{1.0}Ni_{20.0}$/PVP	1.4 ± 0.3	131	55	76	58	6	125	>2 shell

[a]ICP-OES analysis. [b]Mean values of NP size determined from TEM images by considering at least 200 particles. [C] High Ru loaded NP (Ru/PVP, Ru_3Ni_1/PVP, and Ru_1Ni_1/PVP) were calculated as follows: the number of Ru atoms in *hcp* cell (N) is 6. Ru atom radius (R_{Ru}) is 0.214 nm. The volume of Ru cell is 0.0817 nm^3. R_{NP} represents the radius of NP. The volume of all Ru atoms on the shell of NP: $V_{shell} = V_{total} - V_{core} = 4/3\pi R_{NP}^3 - 4/3\pi (R_{NP} - R_{Ru})^3$, V_{total} meaning the volume of one Ru NP, V_{core} presenting the volume of NP excluded the one outer layer of atoms. The numbers of metal atoms on the shell $N_{shell} = N*V_{shell}/0.0817$. The number of total Ru atoms $N_{total} = N*V_{total}/0.0817$. The percentage of Ru atoms on the surface of NP = $N_{shell}/ N_{total}*100$ %. High Ni loaded NP (Ru_1Ni_3/PVP and Ru_1Ni_{20}/PVP) were calculated as follows: the number of Ni atoms in *fcc* cell (N) is 4. Ni atom radius (R_{Ni}) is 0.176 nm. The volume of Ni cell is 0.0438nm^3. R_{NP} represents the radius of NP. The volume of all Ru atoms on the shell of NP: $V_{shell} = V_{total} - V_{core} = 4/3\pi R_{NP}^3 - 4/3\pi (R_{NP} - R_{Ni})^3$, V_{total} meaning the volume of one Ni NP, V_{core} presenting the volume of NP excluded the one outer layer of atoms. The numbers of Ni atoms on the shell $N_{shell} = N*V_{shell}/0.0438$. The number of total Ni atoms $N_{total} = N*V_{total}/0.0438$. The percentage of metal atoms on the surface of NP = $N_{shell}/ N_{total}*100$ %.[d]Estimated total atoms on the NP*metallic content (in mol). [e]Estimated number of Ni atoms in a NP/Estimated atoms on the surface*100.

As the syntheses of the nanomaterials are performed under H_2 pressure, adsorption of hydrides on the surface of the NPs occurs. These adsorbed hydrides have a role in the stabilisation and the growing of the NPs, and after, in catalysis, it can be determined experimentally.[38] Following a slightly modified methodology compared to that previously described in the group,[47] as detailed in Chapter 6 and summarised in Scheme 2, the number of hydrides per surface metal atom was determined on the series of RuNi/PVP NPs, and the corresponding monometallic species. The different $H/M_{surface}$ ratios of the RuNi/PVP are summarised in Table 4. It can be observed that all Ru containing NPs have a $H/M_{surface}$ ratio higher than one, and a volcano shape tendency is observed when correlating this value to the composition, which is centred at Ru_3Ni_1/PVP.

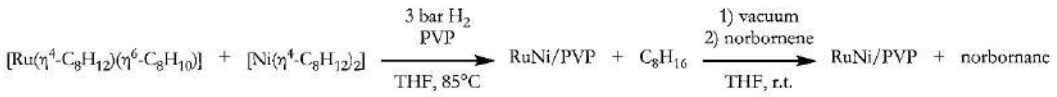

Scheme 2: Method applied for the quantification of surface hydrides on RuNi/PVP NPs.

Table 4: $H/M_{surface}$ ratios of the RuNi/PVP NPs.

NP	$H/M_{surface}$[a]
Ru/PVP	1.3 ± 0.2
Ru_3Ni_1/PVP	1.8 ± 0.1
Ru_1Ni_1/PVP	1.6 ± 0.2
Ru_1Ni_3/PVP	1.1 ± 0.4
Ni/PVP	0.9 ± 0.1

[a]Average $H/M_{surface}$ ratio obtained from 2 experiments.

Magnetic properties of the materials were measured by superconducting quantum interface device (SQUID) magnetometry. Figure 18 provides the magnetic hysteresis cycles obtained for monometallic Ni and bimetallic RuNi NPs, recorded at RT and corrected of the diamagnetic contribution of PVP. Tripodal shaped Ni/PVP NPs displayed a clear ferromagnetic behaviour with 32.4 emu·g_{Ni}^{-1} of magnetic saturation (Ms). The Ms observed is low compared to that of a bulk Ni (Ms = 54.4 emu·g_{Ni}^{-1}).[63] As it is known that the Ms of Ni NPs depends on the NP size,[64] the size of 5.6 ± 1.2 nm could explain the low value here observed. However, the hypothesis that the loss of magnetism is due to the presence of small amounts of oxidised Ni at the surface cannot be discarded. Ru_1Ni_{20}/PVP sample, containing a high Ni amount and sized 1.4 ± 0.3 nm, displays a curve typical of a paramagnetic material. Ru_3Ni_1/PVP, Ru_1Ni_1/PVP, and Ru_1Ni_3/PVP, samples with an elevated Ru content, display a clear diamagnetic behaviour. Magnetisation is thus drastically decreased even when adding a small amount of Ru to Ni in our samples. This is in agreement with previous observations,[65,66] and further confirms the incorporation of Ru on the Ni structure.

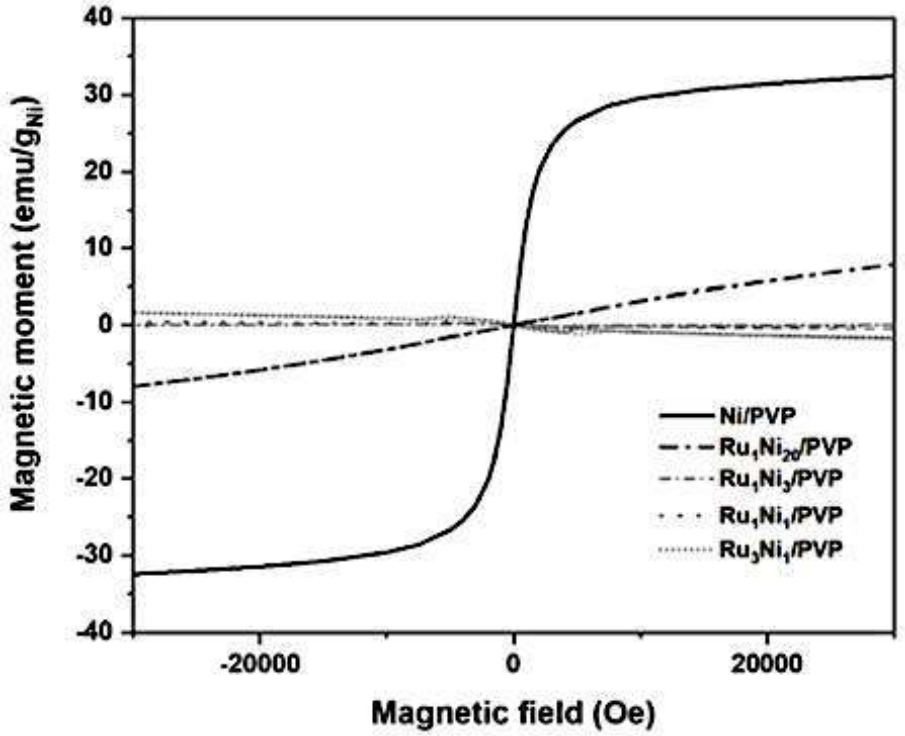

Figure 18: Magnetic hysteresis cycles of bimetallic and monometallic PVP-stabilised NPs measured at RT corrected of the diamagnetic contribution of PVP.

As conclusions of this part of Chapter 2, the importance of the reaction temperature for the successful decomposition of the Ni metallic precursor for the formation of bimetallic RuNi/PVP NPs was discussed. These synthesised bimetallic NPs were all of less than 2 nm size, even the ones with a higher Ni amount in their composition, having a core-shell structure being Ru in the core. The small shifts in XPS analyses and the drastic decrease of magnetisation when adding a small amount of Ru to Ni evidenced the presence of both Ru and Ni close in vicinity, in the same structure, certifying the success on the synthesis of the bimetallic RuNi NPs. The objective of this synthetic process was to use these synthesised NPs as catalysts for hydrogenation reactions of FF and QN, which is discussed in Chapter 3.

2.3 Synthesis of RuNi/PPh$_2$Py nanoparticles

Ru and Ni are known to be immiscible metals in the bulk.[17,18] Our first attempt to synthesise alloyed RuNi using PVP as stabiliser led to core-shell NPs, as many examples found in the literature.[67–69] With the aim to obtain alloyed RuNi NPs, the use of a directing ligand was considered for the synthetic methodology, in order to place both metals in proximity. The ligand of choice was the commercially available diphenylphosphinopyridine (PPh$_2$Py), having a short distance between the donor ligands present in the molecule and two different electron-donating atoms: P and N. This strategy has already been described for the synthesis of heterobimetallic complexes.[70–73]

Two different methodologies have been explored to synthesise RuNi NPs using PPh_2Py as directing and stabilising ligand. The first method consists in the decomposition of a pre-formed Ru or Ni complex containing the target phosphine ligand, $[Ru(\eta^4\text{-}C_8H_{12})(\kappa^2\text{-}PPh_2Py)(PPh_2Py)]$ or $[Ni(\eta^4\text{-}C_8H_{12})(PPh_2Py)_2]$, in the presence of $[Ni(\eta^4\text{-}C_8H_{12})_2]$ or $[Ru(\eta^4\text{-}C_8H_{12})(\eta^6\text{-}C_8H_{10})]$, respectively, as the source of the second metal. RuPNi/PPh_2Py and RuNiP/PPh_2Py correspond to the nomenclatures used for the bimetallic RuNi NPs synthesised from the PPh_2Py-containing Ru and Ni complexes respectively. The second method is the simultaneous decomposition of $[Ru(\eta^4\text{-}C_8H_{12})(\eta^6\text{-}C_8H_{10})]$ and $[Ni(\eta^4\text{-}C_8H_{12})_2]$ in the presence of the phosphine ligand, RuNi/PPh_2Py. For comparative purposes, monometallic Ru and Ni NPs have also been synthesised in the presence of PPh_2Py as stabiliser.

$[Ru(\eta^4\text{-}C_8H_{12})(\kappa^2\text{-}PPh_2Py)(PPh_2Py)]$ and $[Ni(\eta^4\text{-}C_8H_{12})(PPh_2Py)_2]$ complexes were first synthesised. $[Ru(\eta^4\text{-}C_8H_{12})(\kappa^2\text{-}PPh_2Py)(PPh_2Py)]$ synthetic procedure consisted in the addition of a slight excess of PPh_2Py (2.1 molar equivalents (eq.)) to a pale yellow solution of $[Ru(\eta^4\text{-}C_8H_{12})(\eta^6\text{-}C_8H_{10})]$ dissolved in dry acetone under argon (Scheme 3). After six hours of reaction at RT, the pale yellow solution turned brown. The dark brown solid obtained after evaporation of the solvent was washed three times with pentane and dried under vacuum (83 % yield). The $^{31}P\{^1H\}$ NMR spectrum of this Ru complex in THF-*d8* showed a high-field shifted singlet at δ -22.5 ppm, which is characteristic of the chelating bidentate κ^2*P*,*N* coordination mode of the Ph_2PPy ligand,[74–78] and a singlet at δ 46.8 ppm attributed to a second Ph_2PPy ligand coordinated in a monodentate mode to the Ru centre (Figure 19). The ^{1}HNMR spectrum showed characteristic peaks of the coordinated cyclooctadiene, in the range of 0.5-3.5 ppm,[59] and a set of multiplets in the range of 6.5-8.5 ppm characteristic of the aryl rings of the phosphine ligand. Crystals were grown from a saturated solution of $[Ru(\eta^4\text{-}C_8H_{12})(PPh_2Py)(\kappa^2\text{-}PPh_2Py)]$ in diethyl ether (Et_2O) but, unfortunately, they were unsuitable for X-Ray diffraction analysis.

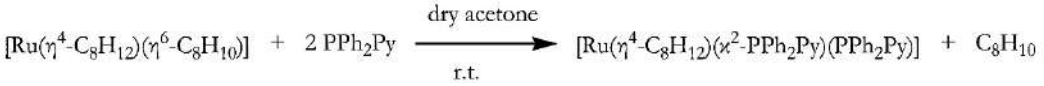

Scheme 3: Synthesis of $[Ru(\eta^4\text{-}C_8H_{12})(\kappa^2\text{-}PPh_2Py)(PPh_2Py)]$ complex.

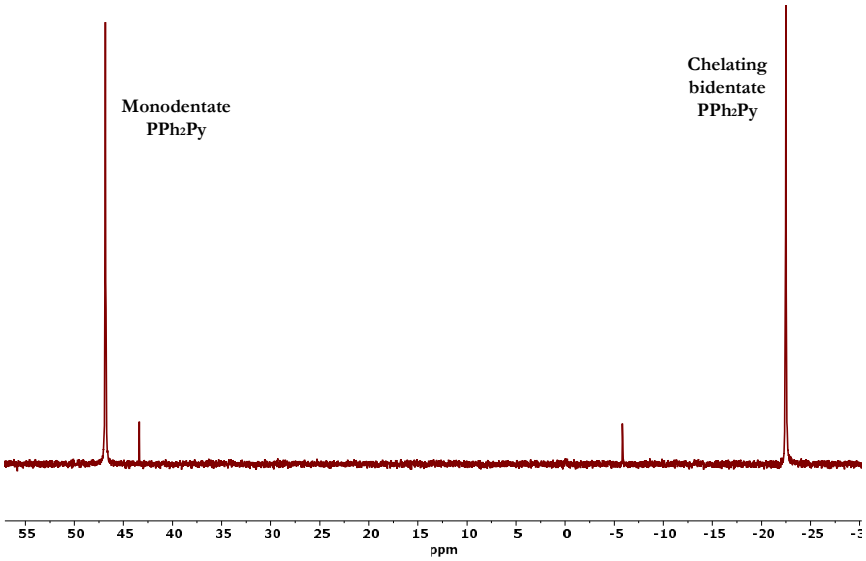

Figure 19: $^{31}P\{^{1}H\}$ NMR in THF-*d8* of [Ru(η^4-C_8H_{12})(κ^2-PPh_2Py)(PPh_2Py)].

The [Ni(η^4-C_8H_{12})(PPh_2Py)$_2$] complex was synthesised by the addition of a slight excess of PPh_2Py (2.1 molar eq.) to a pale yellow solution of [Ni(η^4-C_8H_{12})$_2$] in dry Et_2O under argon, following a slightly modified procedure described elsewhere (Scheme 4).[79] A bright orange solid precipitated after some seconds of stirring. The suspension was stirred for two additional hours, the solvent was discarded and the orange solid washed twice with Et_2O, and finally dried under reduced pressure (86 % of yield). The $^{31}P\{^{1}H\}$ NMR spectrum of the [Ni(η^4- C_8H_{12})(PPh_2Py)$_2$] in THF-*d8* displays the expected singlet peak of the coordinated phosphine in a monodentate mode at 36.7 ppm (Figure 20). Experimental details are given in Chapter 6.

$$[Ni(\eta^4\text{-}C_8H_{12})_2] + 2\ PPh_2Py \xrightarrow[r.t.]{Et_2O} [Ni(\eta^4\text{-}C_8H_{12})(PPh_2Py)_2] + C_8H_{12}$$

Scheme 4: Synthesis of [Ni(η^4-C_8H_{12})(PPh_2Py)$_2$] complex.

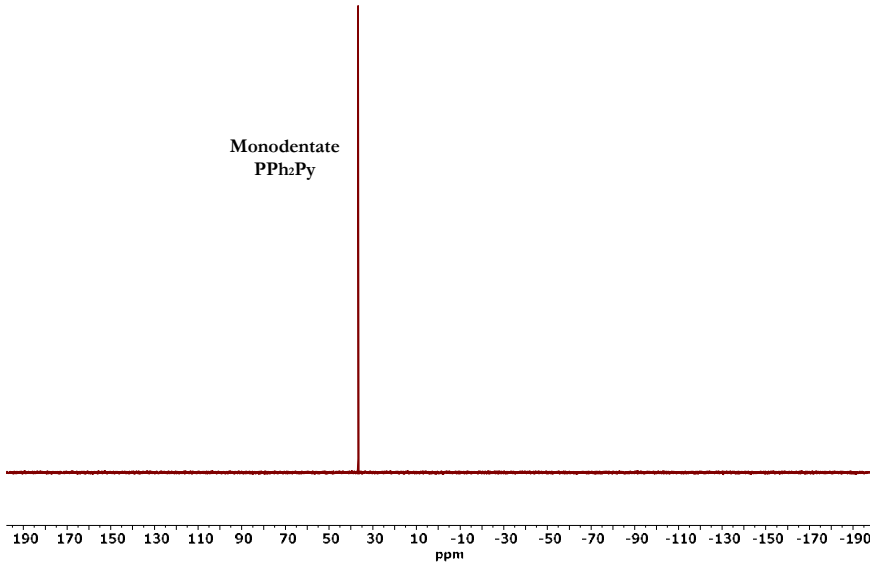

Figure 20: ^{31}P $\{^{1}H\}$ NMR in THF-*d8* of $[Ni(\eta^4\text{-}C_8H_{12})(PPh_2Py)_2]$.

Having the $[Ru(\eta^4\text{-}C_8H_{12})(\kappa^2\text{-}PPh_2Py)(PPh_2Py)]$ and $[Ni(\eta^4\text{-}C_8H_{12})(PPh_2Py)_2]$ complexes in hand, two sets of reactions were carried out in order to synthesise bimetallic RuNi NPs. First, the simultaneous decomposition of $[Ru(\eta^4\text{-}C_8H_{12})(\kappa^2\text{-}PPh_2Py)(PPh_2Py)]$ and $[Ni(\eta^4\text{-}C_8H_{12})_2]$ complexes was carried out under 3 bar of H_2 pressure in THF as solvent (Scheme 5). The reaction of synthesis of RuPNi/PPh_2Py was carried out at 85 °C and using a Ru/Ni molar ratio = 1 as detailed in Table 4. All the experimental details are given in Chapter 6.

$$[Ru(\eta^4\text{-}C_8H_{12})(\kappa^2\text{-}PPh_2Py)(PPh_2Py)] + [Ni(\eta^4\text{-}C_8H_{12})_2] \xrightarrow[THF,\ 85°C]{3\ bar\ H_2} RuPNi/PPh_2Py + C_8H_{16}$$

Scheme 5: Synthesis of RuPNi/PPh_2Py NPs from $[Ru(\eta^4\text{-}C_8H_{12})(\kappa^2\text{-}PPh_2Py)(PPh_2Py)]$ and $[Ni(\eta^4\text{-}C_8H_{12})_2]$.

Following a similar procedure, RuNiP/PPh_2Py NPs were also synthesised by the co-decomposition of $[Ru(\eta^4\text{-}C_8H_{12})(\eta^6\text{-}C_8H_{10})]$ and $[Ni(\eta^4\text{-}C_8H_{12})(PPh_2Py)_2]$ complexes under 3 bar of H_2 pressure in THF as solvent (Scheme 6). The reaction was carried out at 85 °C using a Ru/Ni molar ratio = 1 as detailed in Table 4. All the experimental details are given in Chapter 6.

$$[Ru(\eta^4\text{-}C_8H_{12})(\eta^6\text{-}C_8H_{10})] + [Ni(\eta^4\text{-}C_8H_{12})(PPh_2Py)_2] \xrightarrow[THF,\ 85°C]{3\ bars\ H_2} RuNiP/PPh_2Py + C_8H_{16}$$

Scheme 6: Synthesis of RuNiP/PPh_2Py NPs from $[Ni(\eta^4\text{-}C_8H_{12})(PPh_2Py)_2]$ and $[Ru(\eta^4\text{-}C_8H_{12})(\eta^6\text{-}C_8H_{10})]$.

Finally, RuNi/PPh_2Py NPs were synthesised by the co-decomposition of [Ru(η^4-C_8H_{12})(η^6-C_8H_{10})] and [Ni(η^4-C_8H_{12})$_2$] complexes under 3 bar of H_2 pressure in the presence of PPh_2Py ligand (0.2 molar eq.) in THF as solvent (Scheme 7). The reaction was carried out at 85 °C using a Ru/Ni molar ratio = 1 as detailed in Table 4. All the experimental details are given in Chapter 6.

$$[Ru(\eta^4\text{-}C_8H_{12})(\eta^6\text{-}C_8H_{10})] + [Ni(\eta^4\text{-}C_8H_{12})_2] + 0.2\ PPh_2Py \xrightarrow[THF,\ 85°C]{3\ bar\ H_2} RuNi/PPh_2Py + C_8H_{16}$$

Scheme 7: Synthesis of RuNi/PPh_2Py NPs by co-decomposition of [Ru(η^4-C_8H_{12})(η^6-C_8H_{10})] or [Ni(η^4- C_8H_{12})$_2$].

The monometallic Ru/PPh_2Py and Ni/PPh_2Py NPs were also synthesised using the same procedure, with the aim of comparison. [Ru(η^4-C_8H_{12})(η^6-C_8H_{10})] or [Ni(η^4- C_8H_{12})$_2$] complexes were decomposed under 3 bar of H_2 pressure in the presence of PPh_2Py ligand (0.2 molar eq.) in THF as solvent at 85 °C (Scheme 8 and 9). The colour change observed for these reactions from orange (monometallic Ni) and pale orange (monometallic Ru) to black can be observed on Figure 21. Experimental details are given in Chapter 6.

$$[Ru(\eta^4\text{-}C_8H_{12})(\eta^6\text{-}C_8H_{10})] + 0.2\ PPh_2Py \xrightarrow[THF,\ 85°C]{3\ bar\ H_2} Ru/PPh_2Py + C_8H_{16}$$

Scheme 8: Synthesis of Ru/PPh_2Py NPs from [Ru(η^4-C_8H_{12})(η^6-C_8H_{10})].

$$[Ni(\eta^4\text{-}C_8H_{12})_2] + 0.2\ PPh_2Py \xrightarrow[THF,\ 85°C]{3\ bar\ H_2} Ni/PPh_2Py + C_8H_{16}$$

Scheme 9: Synthesis of Ni/PPh_2Py NPs from [Ni(η^4- C_8H_{12})$_2$].

Figure 21: Colour change in a typical synthesis of RuNi/PPh_2Py NPs at 85 °C; left, before the hydrogenation reaction, and right, after the reaction.

Table 5 summarizes the mean size ascertained from TEM images of the synthesised materials containing PPh_2Py together with the metallic content obtained by ICP-OES analyses. All

the synthesised NPs were small (≤ 2 nm) (Figure 22 to 26), similar to the previous described RuNi/PVP NPs, which would be suitable for comparison purposes.

Table 5: Metal content and mean size of RuNi/ PPh_2Py NPs synthesised at 85 ºC.

NP	Ru content (%)[a]	Ni content (%)[a]	P content (%)[a]	NP composition (from ICP-OES)	$P/M_{surface}$ ratio	Mean size (nm)[b]
Ru/PPh_2Py	81.8	-	7.3	$Ru/PPh_2Py_{0.3}$	0.4	1.4 ± 0.2
$RuPNi/PPh_2Py$	19.8	13.4	14.8	$Ru_{1.0}Ni_{1.2}/PPh_2Py_{1.1}$	1.6	1.3 ± 0.3
Ru_1Ni_1/PPh_2Py	51.2	32.7	7.4	$Ru_{1.0}$ $Ni_{1.0}/PPh_2Py_{0.2}$	0.5	2.1 ± 0.6
$RuNiP/PPh_2Py$	19.3	13.0	10.8	$Ru_{1.0}Ni_{1.2}/PPh_2Py_{0.8}$	1.1	1.1 ± 0.2
Ni/PPh_2Py	-	65.8	7.9	$Ni/PPh_2Py_{0.2}$	0.5	2.0 ± 0.4

[a]ICP-OES analysis. [b]Mean values of NP size determined from TEM images by considering at least 200 particles.

The Ru and Ni content determined by ICP-OES are in agreement with the expected composition from the introduced materials, *i.e.* a molar Ru/Ni ratio of 1. In the case of $RuPNi/PPh_2Py$ and $RuNiP/PPh_2Py$, the total metal content was low, as more phosphine was present in the reaction media (1 eq. per metal). In contrast, with the other synthesis method, the total metal content was higher, as a ratio ligand/metal of 0.2 was used, having five times less of ligand eq. than when using the first synthesis method. The P content percentages obtained experimentally by ICP-OES are also in agreement with the expected from the materials introduced in the synthesis. The ratios $P/M_{surface}$ (Table 5) were in the range of 0.4 to 1.6.

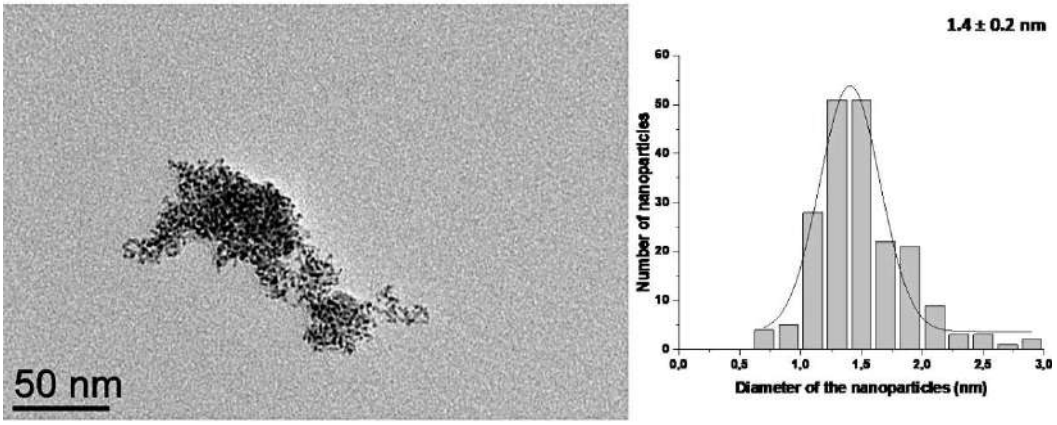

Figure 22: TEM image of Ru/PPh_2Py NPs (scale bar 50 nm) together with the respective size histogram.

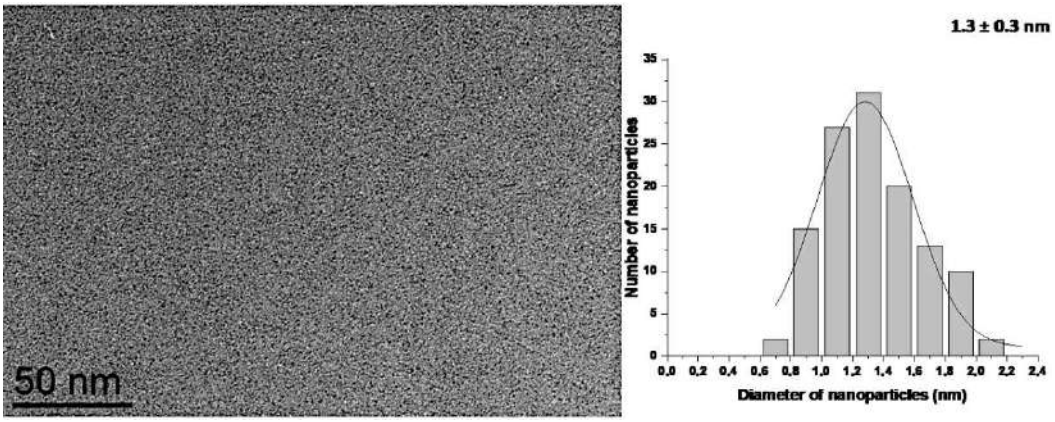

Figure 23: TEM image of RuPNi/PPh_2Py NPs (scale bar 50 nm) synthesised from [Ru(η^4-C_8H_{12})(PPh_2Py)$_2$] together with the respective size histogram.

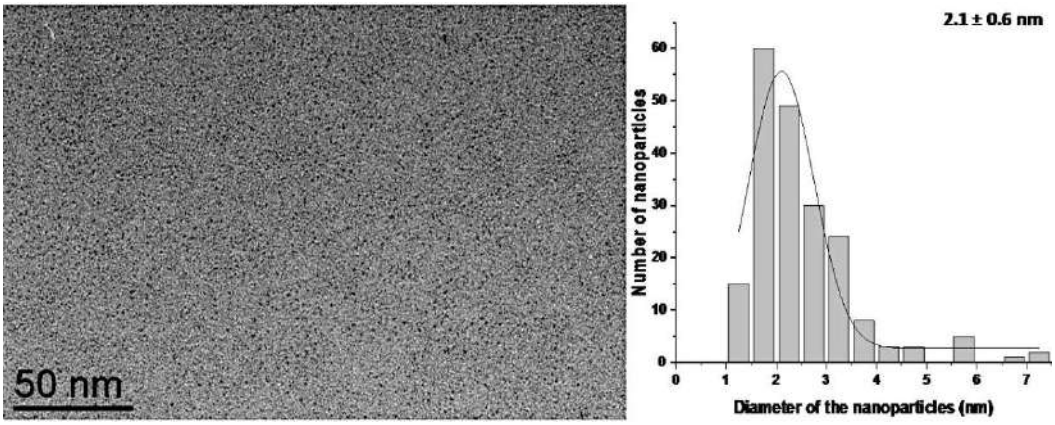

Figure 24: TEM image of RuNi/PPh_2Py NPs (scale bar 50 nm) together with the respective size histogram.

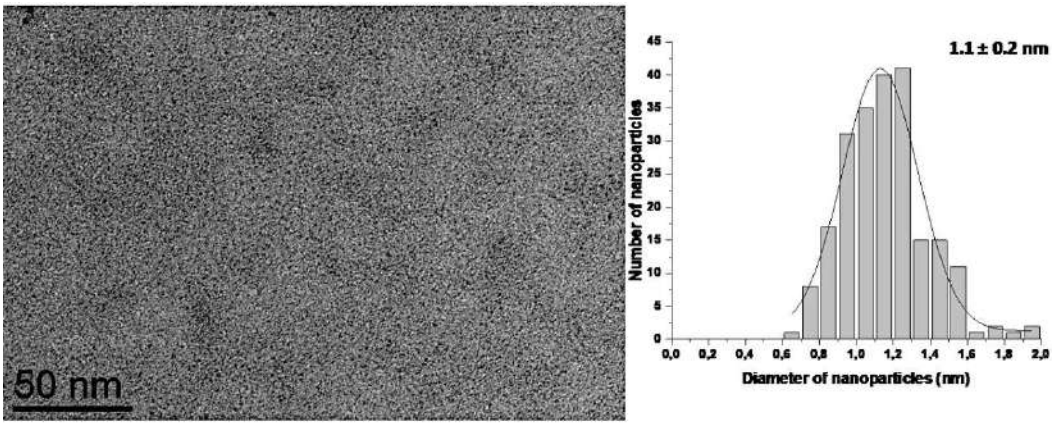

Figure 25: TEM image of RuNiP/PPh_2Py NPs (scale bar 50 nm) synthesised from [Ni(η^4-C_8H_{12})(PPh_2Py)$_2$] together with the respective size histogram.

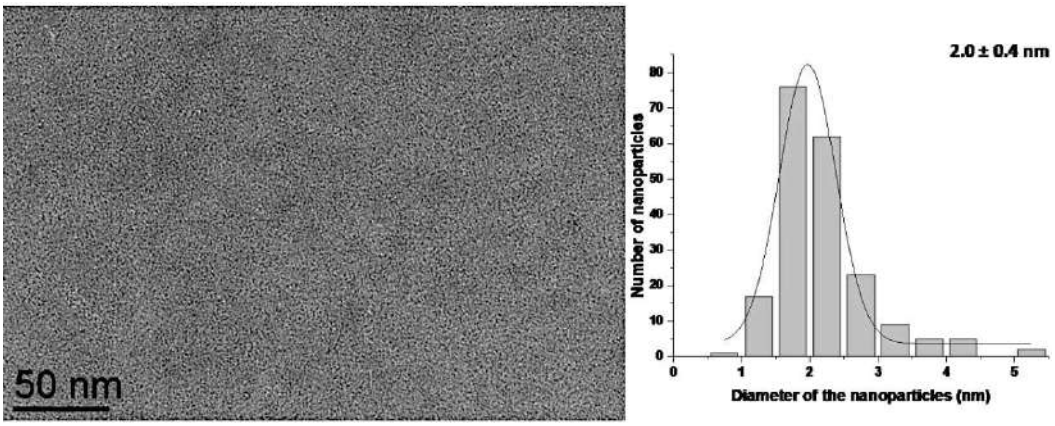

Figure 26: TEM image of Ni/PPh_2Py NPs (scale bar 200 nm) together with the respective size histogram.

WAXS analyses, performed for Ru/PPh_2Py, RuNi/PPh_2Py and Ni/PPh_2Py, (Figure 27) exposed a complex situation although in concordance with the formation of bimetallic NPs. As with PVP, the presence of two or more phases (Ru and/or Ni and PPh_2Py), complicates the extraction of structural information being the crystallinity low. However, there were some evidences like specific patterns, particularly in real space, and important changes in the metallic bond-length. The Ru/PPh_2Py sample (Figure 27 (a), top) is in agreement with bulk Ru *hcp*. Ni/PPh_2Py NPs (Figure 27 (a), bottom) fits with a Ni *fcc* structure, although it shares characteristics of a Mn-β organisation. For instance, in the RDF (Figure 27 (b)), a typical peak for *fcc* systems at 0.38 nm is not observed but the size of the NPs is closer what is expected for a *fcc* structure. This result points to a mixture between *fcc* and Mn-β organisations. In the case of RuNi/PPh_2Py, a different situation, much more complex, occurs. Regarding at different radius of the NP (Figure 27 (b)), the bimetallic RuNi/PPh_2Py nanomaterial resembles the metallic Ru. This result is in agreement to a core-shell structure, as for this kind of organisation, the RDF is always dominated by the structure of the core.[48,49] However, a loss of compact structure is also observed resembling a little to a Mn-β structure. This may correspond to an intermediate structure such as an alloy, even if the distances should be shorter. But, as the structure is distorted, WAXS analysis does not allow by itself to discard neither this possibility nor the production of a mixture of monometallic NPs. As the distances are too short to consider it like an alloy, we consider the structure of the bimetallic RuNi/PPh_2Py NPs as core-shell.

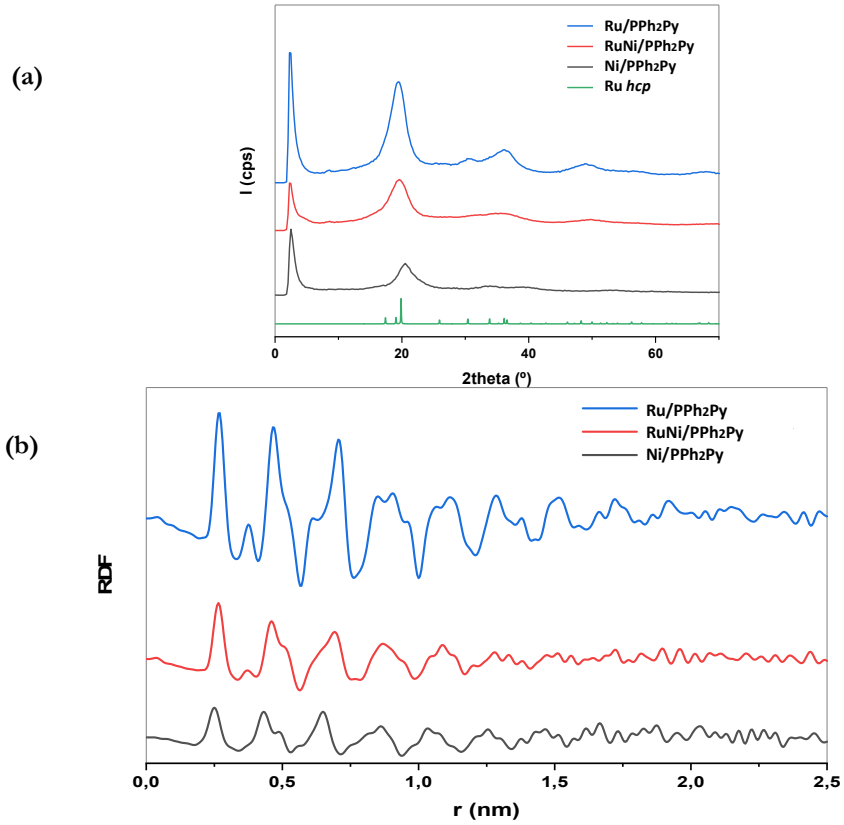

Figure 27: (a) Diffractograms of Ru/PPh_2Py, RuNi/PPh_2Py, Ni/PPh_2Py NPs and the Ru *hcp* references and (b) the related RDFs.

Following the calculation equations presented above for RuNi/PVP NPs (equations 1 to 15) and considering all bimetallic PPh_2Py NPs having a core-shell structure, the estimated Ni percentage coverage for the NPs stabilised with the phosphine ligand are as follows: RuPNi/PPh_2Py ≈ 76 %, RuNi/PPh_2Py a completed shell of Ni is expected and RuNiP/PPh_2Py ≈ 72 %. All the results for these materials are presented in Table 6.

Table 6: Estimation of Ni coverage on RuNi/PPh_2Py NPs.

NP	NP composition (from ICP-OES)[a]	Mean size (nm)[b]	Estimated total atoms on the NP[c]	Estimated atoms on the core[c]	Estimated atoms on the surface[c]	Estimated atoms surface (%)[c]	Estimated number of Ru atoms in a NP[d]	Estimated number of Ni atoms in a NP[d]	Estimated surface coverage of Ni (%)[e]
Ru/PPh_2Py	Ru/PPh_2Py	1.4 ± 0.2	105	35	70	67	105	0	0
RuPNi/PPh_2Py	$Ru_{1.0}Ni_{1.2}$/PPh_2Py	1.3 ± 0.3	84	25	59	70	39	45	≈76
RuNi/PPh_2Py	$Ru_{1.0}Ni_{1.0}$/PPh_2Py	2.1 ± 0.6	356	180	176	49	170	186	≈106
RuNiP/PPh_2Py	$Ru_{1.0}Ni_{1.2}$/PPh_2Py	1.1 ± 0.2	51	12	39	76	23	28	≈72
Ni/PPh_2Py	Ni/PPh_2Py	2.0 ± 0.4	383	214	169	44	0	383	≈227

[a]ICP-OES analysis. [b]Mean values of NP size determined from TEM images by considering at least 200 particles. [C] High Ru loaded NP (Ru/PPh_2Py, RuPNi/PPh_2Py, RuNi/PPh_2Py and RuNiP/PPh_2Py) were calculated as follows: the number of Ru atoms in *hcp* cell (N) is 6. Ru atom radius (R_{Ru}) is 0.214 nm. The volume of Ru cell is 0.0817 nm^3. R_{NP} represents the radius of NP. The volume of all Ru atoms on the shell of NP: $V_{shell} = V_{total} - V_{core} = 4/3\pi R_{NP}^3 - 4/3\pi (R_{NP} - R_{Ru})^3$, V_{total} meaning the volume of one Ru NP, V_{core} presenting the volume of NP excluded the one outer layer of atoms. The numbers of metal atoms on the shell $N_{shell} = N*V_{shell}/0.0817$. The number of total Ru atoms $N_{total} = N*V_{total}/0.0817$. The percentage of Ru atoms on the surface of NP = $N_{shell}/ N_{total}*100$ %. Ni/PPh_2Py was calculated as follows: the number of Ni atoms in *fcc* cell (N) is 4. Ni atom radius (R_{Ni}) is 0.176 nm. The volume of Ni cell is 0.0438 nm^3. R_{NP} represents the radius of NP. The volume of all Ru atoms on the shell of NP: $V_{shell} = V_{total} - V_{core} = 4/3\pi R_{NP}^3 - 4/3\pi (R_{NP} - R_{Ni})^3$, V_{total} meaning the volume of one Ni NP, V_{core} presenting the volume of NP excluded the one outer layer of atoms. The numbers of Ni atoms on the shell $N_{shell} = N*V_{shell}/0.0438$. The number of total Ni atoms $N_{total} = N*V_{total}/0.0438$. The percentage of metal atoms on the surface of NP = $N_{shell}/ N_{total}*100$ %. [d]Estimated total atoms on the NP*metallic content (in mol). [e]Estimated number of Ni atoms in a NP/Estimated atoms on the surface*100.

ATR-FTIR analyses were recorded in a glovebox for all the synthesised NPs. The spectra are depicted in Figure 28 and 29 including PPh_2Py ligand and the synthesised complexes [Ru(η^4-C_8H_{12})(κ^2-PPh_2Py)(PPh_2Py)] and [Ni(η^4-C_8H_{12})(PPh_2Py)$_2$]. [Ru(η^4-C_8H_{12})(κ^2-PPh_2Py)(PPh_2Py)] complex contains one PPh_2Py coordinated in a bidentate mode, through the P and the N atoms, which differs from the [Ni(η^4-C_8H_{12})(PPh_2Py)$_2$] complex. This difference may be observed at the P-C=N absorption band (800 cm^{-1}) appearing only in the Ru complex. Ru/PPh_2Py and Ni/PPh_2Py NPs have similar spectra, mainly showing characteristic absorption bands of the PPh_2Py ligand, such as C=C and/or C=N stretching *ca.* 1500 cm^{-1}, C-N stretching *ca.* 1000 cm^{-1} and the =C-H bending *ca.* 700 cm^{-1}. In comparison, for bimetallic systems, besides the absorption bands of the ligand, some intense new bands at 1250 and 800 cm^{-1} are observed, which have been attributed to P=O and P-C=N vibrations, evidencing some oxidation of the phosphine. Concerning the band at 800 cm^{-1}, RuNiP/PPh_2Py, with a smaller intensity, RuPNi/PPh_2Py and RuNi/PPh_2Py have the P-C=N vibration band already observed in the [Ru(η^4-C_8H_{12})(κ^2-PPh_2Py)(PPh_2Py)] complex, suggesting that some phosphine is coordinated in a bidentate mode in the bimetallic NPs.

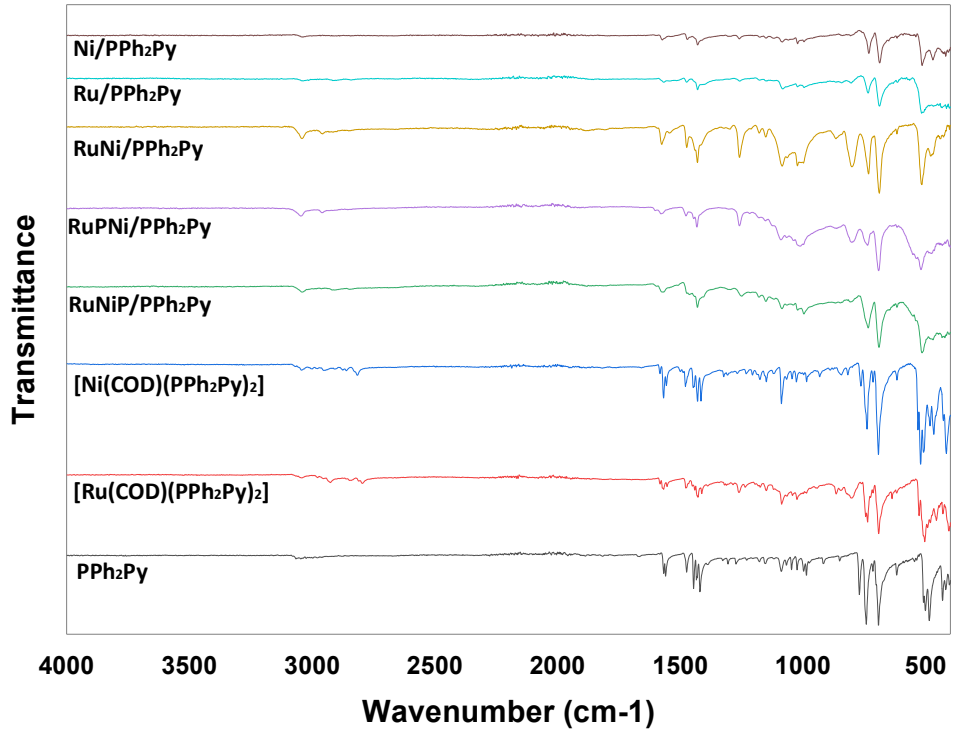

Figure 28: ATR-IR spectra of the monometallic Ru/PPh_2Py and Ni/PPh_2Py NPs, the bi-metallic RuNi/PPh_2Py NPs, the [Ru(η^4-C_8H_{12})(κ^2-PPh_2Py)(PPh_2Py)] and [Ni(η^4-C_8H_{12})(PPh_2Py)$_2$] complexes, and PPh_2Py ligand.

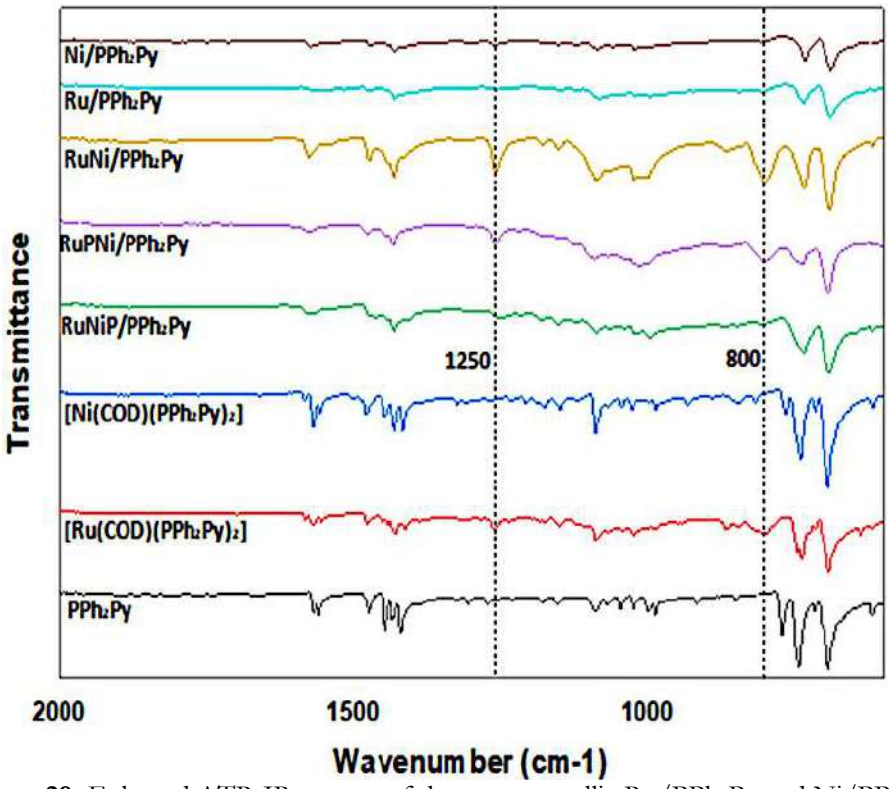

Figure 29: Enlarged ATR-IR spectra of the monometallic Ru/PPh_2Py and Ni/PPh_2Py NPs, the bimetallic RuNi/PPh_2Py NPs, the [Ru(η^4-C_8H_{12})(κ^2-PPh_2Py)(PPh_2Py)] and [Ni(η^4-C_8H_{12})(PPh_2Py)$_2$] complexes, and PPh_2Py ligand.

In order to shed some light on the coordination mode of the ligand onto the metallic surface of the NPs, ^{1}H, ^{13}C and ^{31}P SS NMR spectra were recorded (Figures 30 and 31 respectively). Large peaks were obtained on all the spectra evidencing that the T1 relaxation times were very short. This observation, together with a shift of the peaks to higher frequencies, could be attributed to the Knight shift effect. This is a paramagnetic effect that results from the presence of single electrons, in the case of paramagnetic complexes, or the presence of conduction electrons, in the case of NPs of size larger than 2 nm.[80] The presence of paramagnetic complexes adsorbed on the NP surface could explain the observation of large peaks, as Knight shift effects are usually observed in large NPs, which is not the case here.

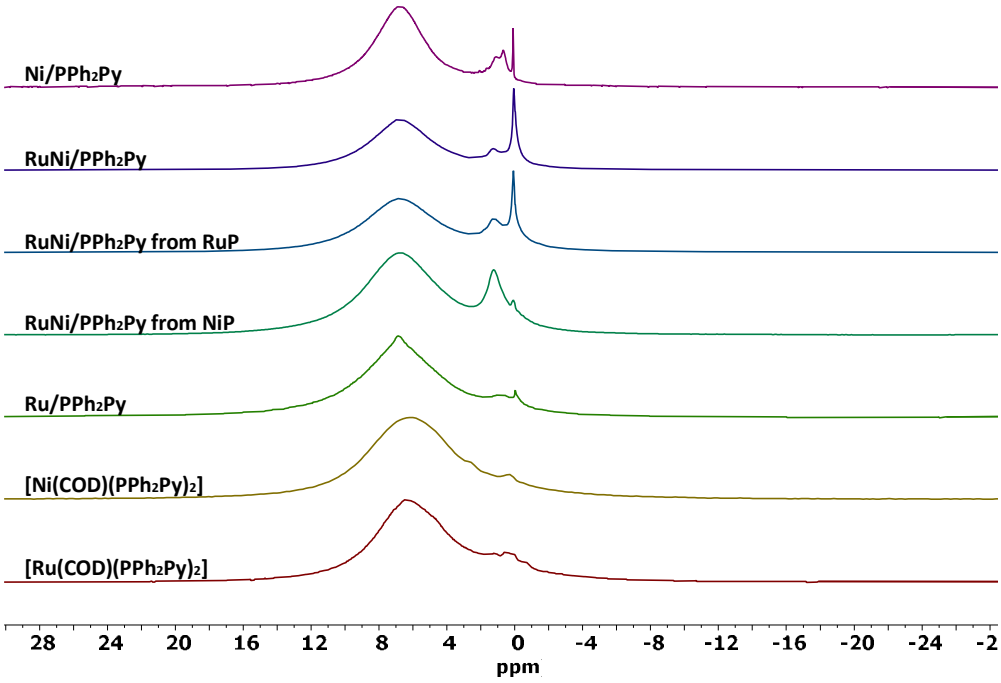

Figure 30: ^{1}H SSNMR of the monometallic and bimetallic RuNi/PPh_2Py NPs together with [Ru(η^4-C_8H_{12})(κ^2-PPh_2Py)(PPh_2Py)] and [Ni(η^4-C_8H_{12})(PPh_2Py)$_2$] complexes.

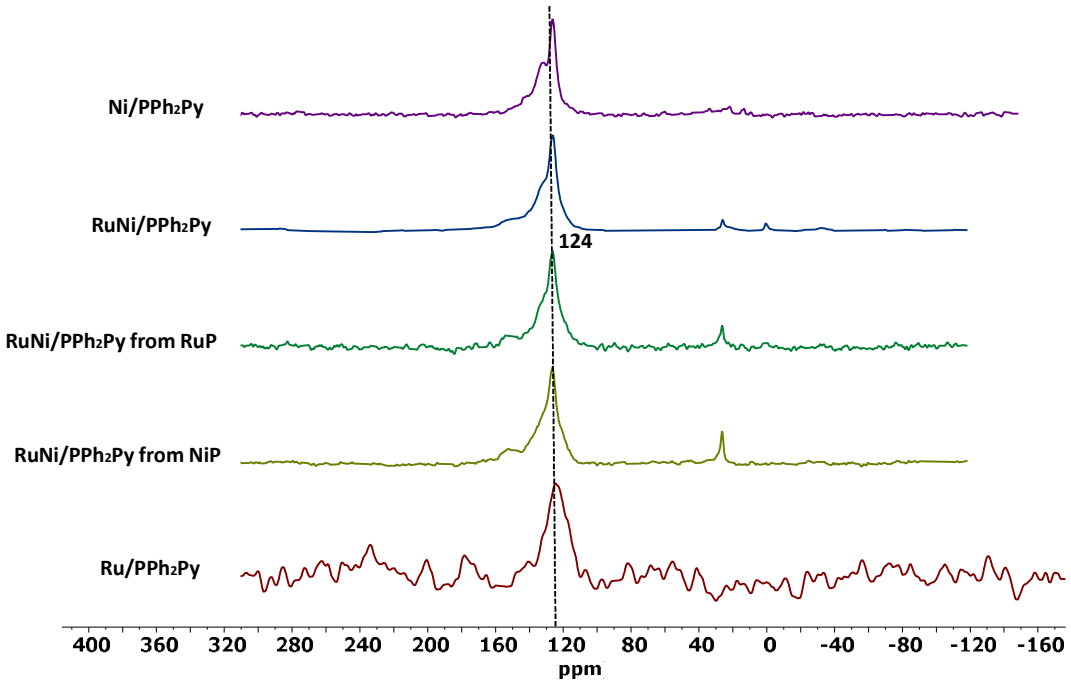

Figure 31: ^{13}C SSNMR of the monometallic and bimetallic RuNi/PPh_2Py NPs.

The peaks, observed in the ^{1}H NMR, are consistent with the signals expected from the protons of the aromatic rings of the phosphine ligand, centred at 7 ppm. The same scenario is revealed in the ^{13}C NMR of the compounds, as a broad signal centred at about 124 ppm is obtained for all materials. The ^{31}P SS NMR show as well large paramagnetic peaks at high frequencies in all materials, nevertheless, a sharper peak, can be elucidated in between 30 to 70 ppm in all the prepared NPs, which are attributed to the phosphine ligand coordinated onto the metallic surface.[81,82]

Figure 32 displays the ^{13}P SS NMR of [Ru(η^4-C_8H_{12})(κ^2-PPh_2Py)(PPh_2Py)] and [Ni(η^4-C_8H_{12})(PPh_2Py)$_2$]. Two singlets at 50.0 and -27.0 ppm were observed for [Ru(η^4-C_8H_{12})(κ^2-PPh_2Py)(PPh_2Py)], in line with the ^{31}P NMR recorded in solution. Similarly, the ^{31}P SSNMR [Ni(η^4-C_8H_{12})(PPh_2Py)$_2$] corresponds well to the one recorded in solution, displaying a singlet at 34.9 ppm. Ru/PPh_2Py and Ni/PPh_2Py showed a broad signal at 67.2 and 26.5 ppm, respectively. No peak was observed at higher fields, indicating a monodentate coordination of the phosphine ligand. Figure 33 displays the ^{31}P SS NMR of the bimetallic materials, RuPNi/PPh_2Py, RuNiP/PPh_2Py, and RuNi/PPh_2Py, together with the ones of the monometallic species, Ru/PPh_2Py and Ni/PPh_2Py. In the three bimetallic systems two peaks were observed: RuPNi/PPh_2Py displays a peak centred at 62.5 ppm, with a shoulder at 26.6 ppm; RuNiP/PPh_2Py a peak at 58.8 ppm with a shoulder at 25.9 ppm; and RuNi/PPh_2Py a peak at 69.5 ppm with a shoulder at 26.3 ppm. These peaks appear in similar chemical shifts than the ones observed for the monometallic NPs, thus indicating that the phosphine present in the bimetallic materials is both coordinated to Ru and Ni atoms.

These observations are in agreement with a bimetallic system in which both metals are present at the surface, or a mixture of monometallic NPs, being the later discarded as WAXS analyses show that the systems are bimetallic.

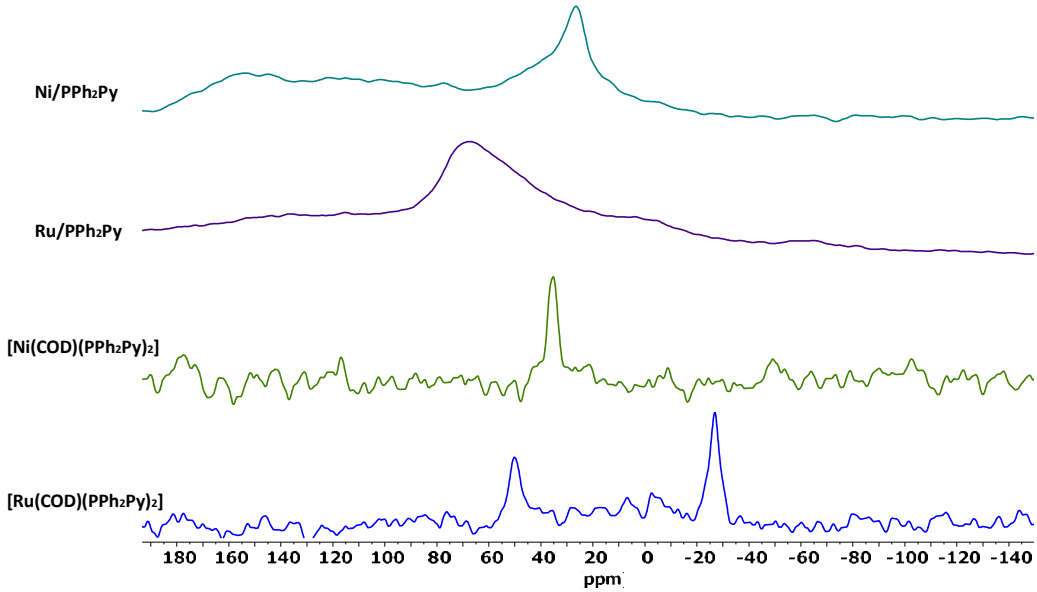

Figure 32: ^{31}P SSNMR spectra of the monometallic NPs together with those of [Ru(η^4-C_8H_{12})(κ^2-PPh_2Py)(PPh_2Py)] and [Ni(η^4-C_8H_{12})(PPh_2Py)$_2$] complexes.

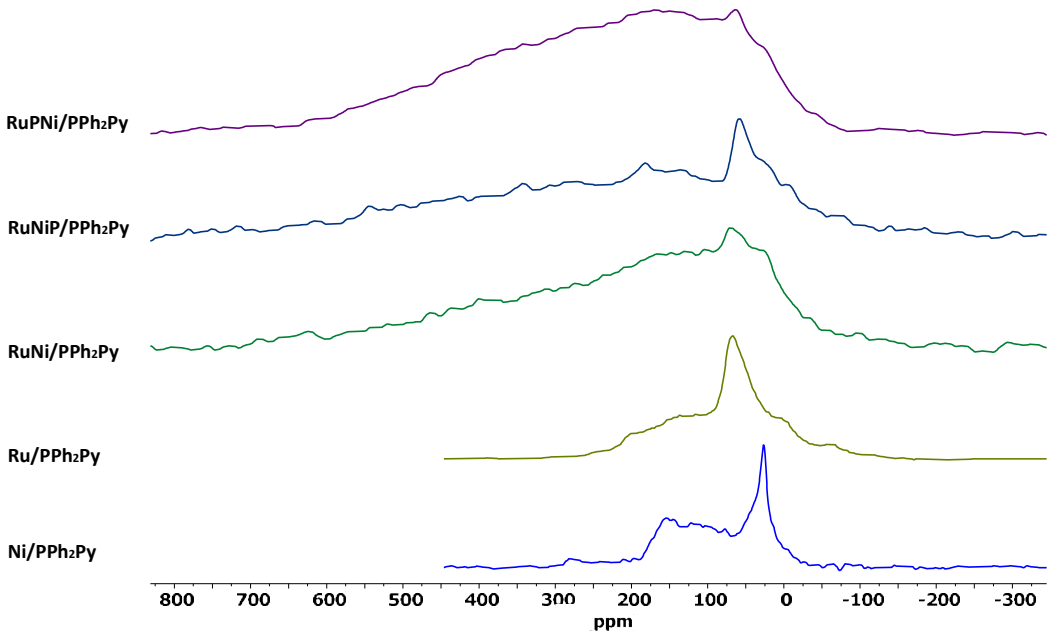

Figure 33: ^{31}P SSNMR spectra of the monometallic and bimetallic RuNi/PPh_2Py NPs.

Magnetic properties of the nanomaterials were analysed by SQUID magnetometry. Figure 34 provides the hysteresis cycles recorded for the bimetallic RuNi and monometallic Ni NPs. These curves were measured at RT and corrected of the diamagnetic contribution of PPh_2Py. Ni/PPh_2Py NP manifested a typical ferromagnetic behaviour with 32.6 emu·g_{Ni}^{-1} of

Ms, which is very similar to the one observed for Ni/PVP, 32.4 emu·g_{Ni}^{-1}. And similarly, size effect or the presence of small amounts of oxide in the surface could explain that the Ms observed is low compared to bulk Ni (Ms = 54.4 emu·g_{Ni}^{-1}).[63] The presence of PPh_2Py has a limited effect on the magnetisation of Ni NPs compared to PVP, even if a lower magnetisation should be observed due to the presence of a more donor ligand on the surface.[46] RuNi/PPh_2Py and RuNiP/PPh_2Py NPs, they present similar curves typical of paramagnetic materials, pointing to a similar structure. This is in contrast to Ru_1Ni_1/PVP which was clearly diamagnetic. RuPNi/PPh_2Py sample with 19.8 % of Ru content, displays also a clear diamagnetic behaviour. These observations show that Ni is incorporated to the Ru structure as magnetisation is rapidly decreased when adding a small amount of Ru on a Ni sample,[65,66] behaviour observed in all bimetallic systems. It can also be concluded that RuNi/PPh_2Py and RuNiP/PPh_2PyNPs are structurally close.

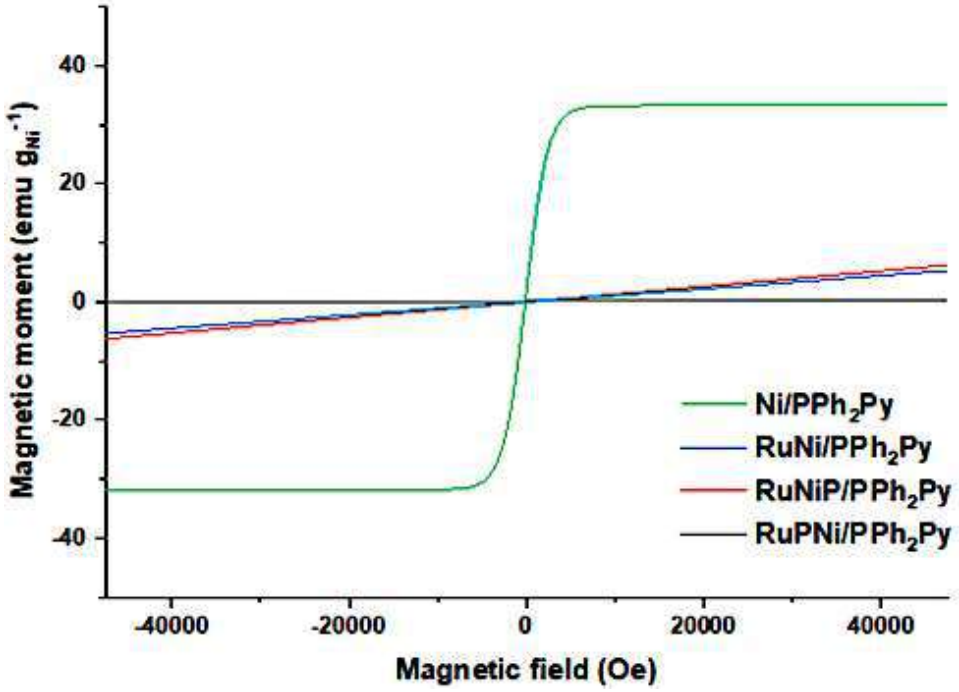

Figure 34: Magnetic hysteresis cycles of bimetallic and monometallic PPh_2Py-stabilised NPs measured at RT.

To conclude this section of Chapter 2, [Ru(η^4-C_8H_{12})(κ^2-PPh_2Py)(PPh_2Py)] and [Ni(η^4-C_8H_{12})(PPh_2Py)$_2$] complexes were successfully synthesised. Bimetallic NPs were successfully synthesised from these precursors, as well as from a mixture of [Ni(η^4-C_8H_{12})$_2$] and [Ru(η^4-C_8H_{12})(η^6-C_8H_{10})] using PPh_2Py as a stabiliser. All the synthesised monometallic and bimetallic NPs were below 2 nm of size. The bimetallic NPs have a core-shell structure being Ru in the core, even if the alloy organisation could be a possibility, as ascertained by WAXS. Future studies with more specific techniques such as EXAFS would be of interest to be able to discard or not the alloy structure. Moreover, WAXS analyses of RuPNi/PPh_2Py and

RuNiP/PPh_2Py would also be of interest to corroborate their structure. SSNMR spectra were recorded being able to observe that, in the bimetallic NPs, the phosphine is coordinated to both Ru and Ni atoms. The drastic decrease of magnetisation when adding a small amount of Ru to Ni evidenced the presence of both Ru and Ni close in vicinity, which further supports the bimetallic nature of the RuNi NPs, as suggested by WAXS measures. More analyses are needed to fully understand the structure of the RuNi/PPh_2Py.

2.4 Synthesis of RuNi/AdCOOH nanoparticles

1-Adamantanecarboxylic acid (AdCOOH) has a rigid and thermodynamically stable structure.[83–87] It has recently been described as an efficient and robust stabiliser for Ru NPs, due to the strong coordination onto the Ru surface of the ligand through its carboxylate form.[59] In order to identify if this carboxylic acid compound is a suitable stabiliser for RuNi bimetallic systems, and its effect on the structure of the NPs, RuNi/AdCOOH have been prepared.

In order to obtain the targeted RuNi/AdCOOH NPs, [Ru(η^4-C_8H_{12})(η^6-C_8H_{10})] and [Ni(η^4-C_8H_{12})$_2$] complexes were decomposed under 3 bar of H_2 pressure in the presence of AdCOOH (0.2 molar eq.) in THF (Scheme 10). The reaction was carried out at 85°C, using a Ru/Ni ratio equal to 1 as detailed in Table 6. Monometallic Ni/AdCOOH NPs were also synthesised using the same procedure with the aim of comparison. Concerning the Ru/AdCOOH NPs, the synthesis was not performed and data for comparison are taken from reference.[59] All the experimental details are given in Chapter 6.

Scheme 10: Synthesis of RuNi/AdCOOH NPs.

The reaction mixture displayed the expected characteristic colour change (from yellow to black) after a few minutes under H_2 pressure, evidencing the formation of the metallic NPs by the decomposition of the precursors and resulting to a black colloidal suspension (Figure 35). For the monometallic Ni/AdCOOH, the typical colour change indicating the decomposition of [Ni(η^4-C_8H_{12})$_2$] was observed as soon as the Fisher Porter (FP) bottle was plunged in the oil bath at 85 °C. In addition for the monometallic Ni NPs, at the end of the reaction, no homogeneous colloidal suspension was obtained but instead a colourless solution with a magnetic black material deposited onto the stirring bar were observed (Figure 36). This result seems to indicate a poor stabilisation of the NPs with the AdCOOH ligand, in contrast with the results obtained with the PVP polymer and PPh_2Py, and the RuNi/AdCOOH NPs which a black suspension was observed.

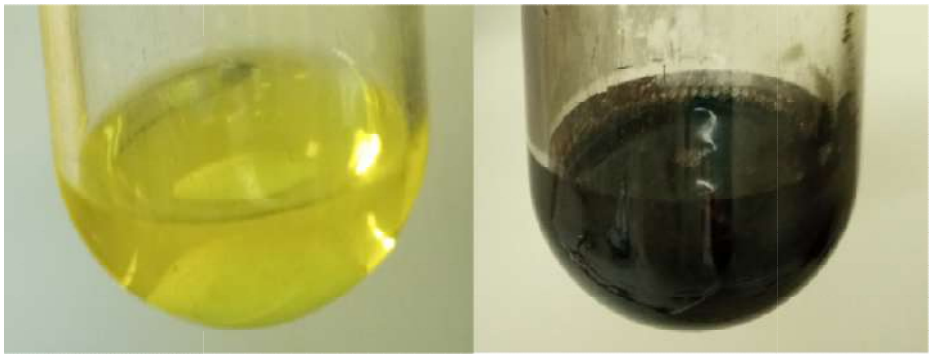

Figure 35: Colour change observed in a typical synthesis of RuNi/AdCOOH NPs at 85 ºC; left, before the hydrogenation reaction, and right, after the reaction.

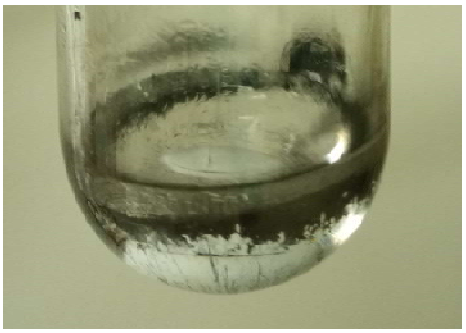

Figure 36: Reaction mixture obtained after the synthesis of Ni/AdCOOH NPs at 85 ºC.

Table 7: Metal contents and mean sizes of the monometallic Ru/AdCOOH, Ni/AdCOOH and the bimetallic RuNi/AdCOOH NPs.

NP	Ru content (%)[a]	Ni content (%)[a]	NP composition (from ICP-OES)	Mean size (nm)[b]
Ru/AdCOOH[c]	77.9	-	Ru/AdCOOH	1.5 ± 0.6 [59]
Ru_1Ni_1/AdCOOH	36,0	22,9	$Ru_{1.0}Ni_{1.1}$/AdCOOH	1.8 ± 0.3
Ni/AdCOOH	-	76,9	Ni/AdCOOH	1.5 ± 0.2

[a]ICP-OES analysis. [b]Mean values of NP size determined from TEM images by considering at least 200 particles. [C]Values extracted from reference[59].

Table 7 summarizes the mean sizes of the synthesised materials RuNi/AdCOOH and Ni/AdCOOH ascertained from TEM images together with the metallic contents obtained by ICP-OES analyses. All the synthesised NPs were small (≤ 2 nm) (Figure 37 and 38), even if, in the case of the monometallic Ni (1.5 ± 0.2 nm), the sample presented a broad dispersion. This broad dispersion would be attributed to the presence of some agglomeration (Figure 37) as, as mentioned above, the AdCOOH seems to poorly stabilise the Ni NPs compared to PVP and PPh_2Py. Furthermore, RuNi/AdCOOH (1.8 ± 0.3 nm) displays a size in line with the RuNi/PPh_2Py and RuNi/PVP samples.

The Ru and Ni content ascertained by ICP-OES were in agreement with the expected composition from the introduced materials, *i.e.* a molar Ru/Ni ratio of 1.

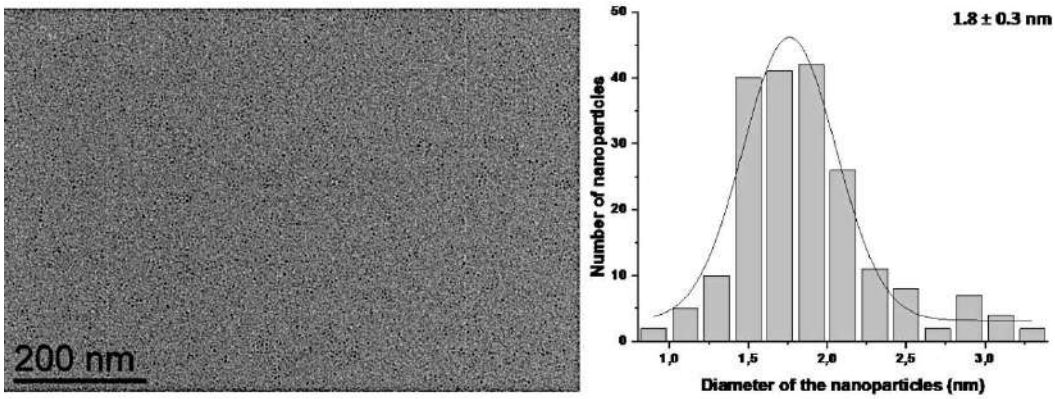

Figure 37: TEM image of RuNi/AdCOOH NPs (scale bar 200 nm) together with the respective size histogram.

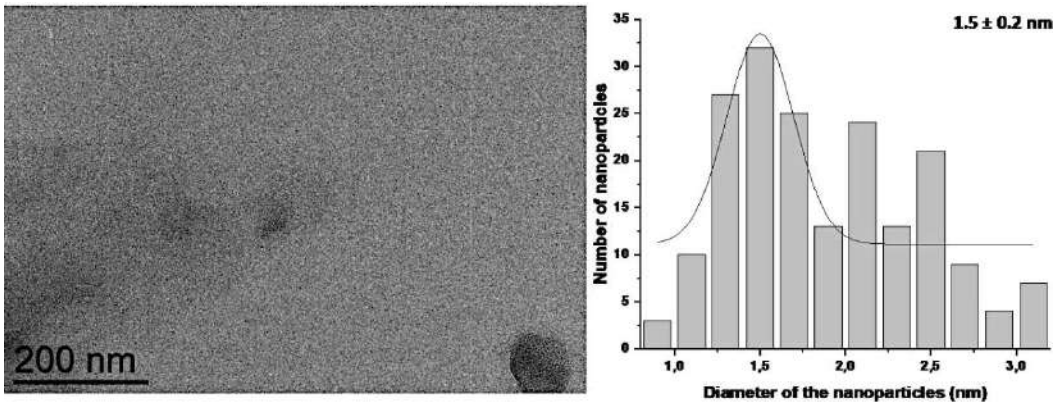

Figure 38: TEM image of Ni/AdCOOH NPs (scale bar 200 nm) together with the respective size histogram.

For a matter of time and priorities, no further characterisation analyses were performed on the AdCOOH NPs systems. Further characterisation will include IR, SSNMR, XPS, magnetic measurements, and WAXS.

2.5 Synthesis of RuCu/PVP nanoparticles

Ru, having a *hcp* structure, and Cu, having a *fcc* structure, are not miscible in the bulk state or even in the liquid phase.[19,20] Since then, a lot of efforts have been made to overcome this miscibility barrier, both experimentally and computationally, aiming a Ru-Cu alloy.[88–92] RuCu/PVP NPs has already been synthesised in the past by using several methodologies, obtaining usually large NPs.[32–34] Taking into consideration previous results and comparing it with the previous synthesised RuNi/PVP NPs, a core-shell structure is expected.

Cu/PVP NPs may be obtained from the reduction of [Cu(C_9H_{11})] in the presence of PVP in glycerol at 120 ºC.[93] It was also reported the decomposition of the [Cu(C_9H_{11})] in the presence of hexadecylamine (HDA), to form Cu/HDA NPs at 80 ºC in THF.[94] Considering these previous works, a temperature of 100 ºC was chosen for the synthesis of the series of RuCu NPs along with their corresponding monometallic counterparts.

In order to obtain the bimetallic RuCu/PVP NPs, [Ru(η^4-C_8H_{12})(η^6-C_8H_{10})] and [Cu(C_9H_{11})] complexes were decomposed under 3 bar of H_2 pressure in the presence of PVP using 30 % weight of metals with respect to the polymer, and THF as solvent (Scheme 11). The reaction was carried out at 100 °C, using several Ru/Cu ratios (Table 8). Monometallic Ru/PVP and Cu/PVP NPs were also synthesised using the same procedure with the aim of comparison. All the experimental details are given in Chapter 6.

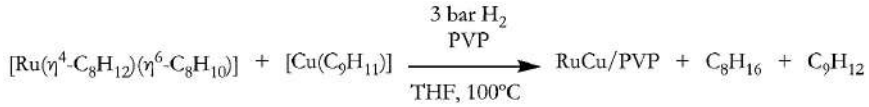

Scheme 11: Synthesis of RuCu/PVP NPs.

During the synthesis of bimetallic RuCu/PVP NPs the characteristic colour change from light brown/orange to black after a few minutes under H_2 pressure and heating at 100 ºC (Figure 39) was observed. In contrast, monometallic Cu NPs displayed a dark red colour (Figure 40).

Figure 39: Colour change observed in a typical synthesis of RuCu/PVP NPs at 100 ºC; left, before the hydrogenation reaction, and right, after the reaction.

Figure 40: Colloidal suspension obtained of the as-synthesised Cu/PVP NPs at 100 ºC.

Table 8 summarizes the metal content of each synthesised material, as well as the size of the NPs established analysing the TEM images (Figures 41 to 46).

Table 8: Metal contents and mean sizes of monometallic Ru/PVP, Cu/PVP and bimetallic RuCu/PVP NPs synthesised at 100 ºC.

NP	Ru content (%)[a]	Cu content (%)[a]	NP composition (from ICP-OES)	Mean size (nm)[b]
Ru/PVP	22.2	-	Ru/PVP	1.6 ± 0.3
Ru_2Cu_1/PVP	15.9	5.6	$Ru_{1.8}Cu_{1.0}$/PVP	1.2 ± 0.3
Ru_1Cu_1/PVP	18.6	14.1	$Ru_{1.0}Cu_{1.2}$/PVP	1.0 ± 0.2
Ru_1Cu_2/PVP	13.7	15.9	$Ru_{1.0}Cu_{1.8}$/PVP	1.0 ± 0.1
Ru_1Cu_{20}/PVP	1.7	20.2	$Ru_{1.0}Cu_{18.9}$/PVP	1.2 ± 0.2
Cu/PVP	-	19.8	Cu/PVP	4.9 ± 1.0

[a]ICP-OES analysis. [b]Mean values of NP size determined from TEM images by considering at least 200 particles.

TEM images of the monometallic Cu sample displayed the presence of NPs of 4.9 ± 1.0 nm size as well as a small population of smaller NPs (1.3 ± 1.0 nm) (Figure 41). Moreover, some of the large NPs observed seem to be hollowed as can be observed in literature for Cu_2O NPs.[95,96] Several methodologies are known for the formation of hollow NPs which, containing catalytic species in the cavity, are of great interest in catalysis.[97] These two populations may correspond to the formation of the small Cu/PVP NPs and the big hollow Cu_2O/PVP NPs. Looking at the Ru/PVP (1.6 ± 0.3 nm), it is interesting to observe that, in comparison with the Ru/PVP synthesised at 85 ºC for the RuNi/PVP series (1.0 ± 0.2 nm), at 100 ºC, the Ru/PVP NPs are larger. Other monometallic NPs, such as CuH[98] and ZnO[99] NPs, have also been described as having a dependency on the synthesis temperature for the NPs size. Concerning the bimetallic RuCu/NPs, in all cases small NPs of about 1 nm are obtained: Ru_2Cu_1/PVP, 1.2 ± 0.3 nm; Ru_1Cu_1/PVP, 1.0 ± 0.2 nm; Ru_1Cu_2/PVP, 1.0 ± 0.1 nm; and Ru_1Cu_{20}/PVP, 1.2 ± 0.2 nm. It is worth mentioning that the small size is observed for all compositions, including the ones displaying high Cu content, Ru_1Cu_{20}/PVP, which is in contrast with the size of the monometallic hollow Cu NPs (4.9 ± 1.0 nm) synthesised following the same procedure. This could point out, as in the case of RuNi/PVP NPs, to the role of Ru species as seed mediator for the synthesis of RuCu NPs. Furthermore, all these values are very small compared to the RuCu/PVP NPs observed in literature.[32–34] This size difference may come from the different methodology used as the precursors and the synthetic methods are different.

Most of the synthesised materials displayed a total metal content in weight *ca.* 20 %, with the exception of Ru_1Cu_1/PVP and Ru_1Cu_2/PVP which present a higher value. In all cases, the

molar ratios Ru/Cu were close to the ones expected theoretically from the introduced materials at the beginning of the synthesis.

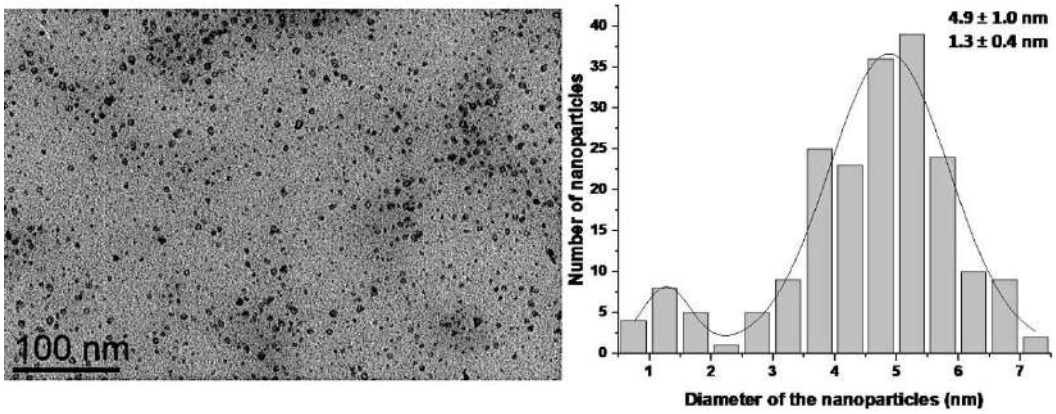

Figure 41: TEM image of Cu/PVP NPs (scale bar 100 nm) together with the respective size histogram.

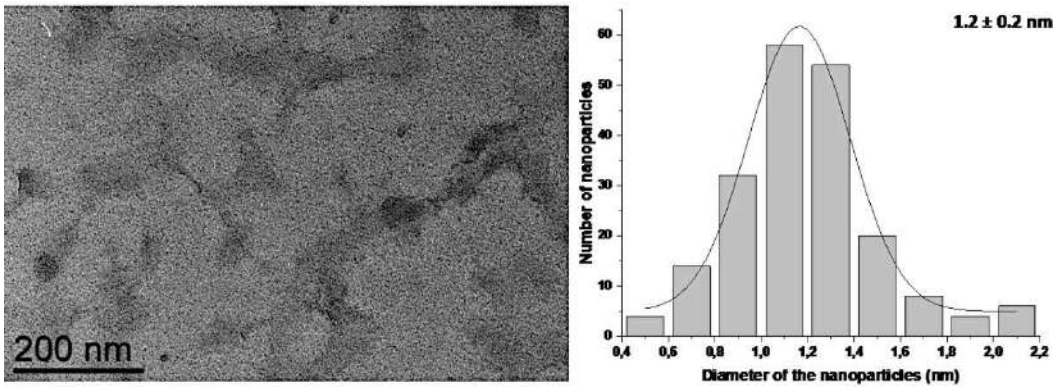

Figure 42: TEM image of Ru_1Cu_{20}/PVP NPs (scale bar 200 nm) together with the respective size histogram.

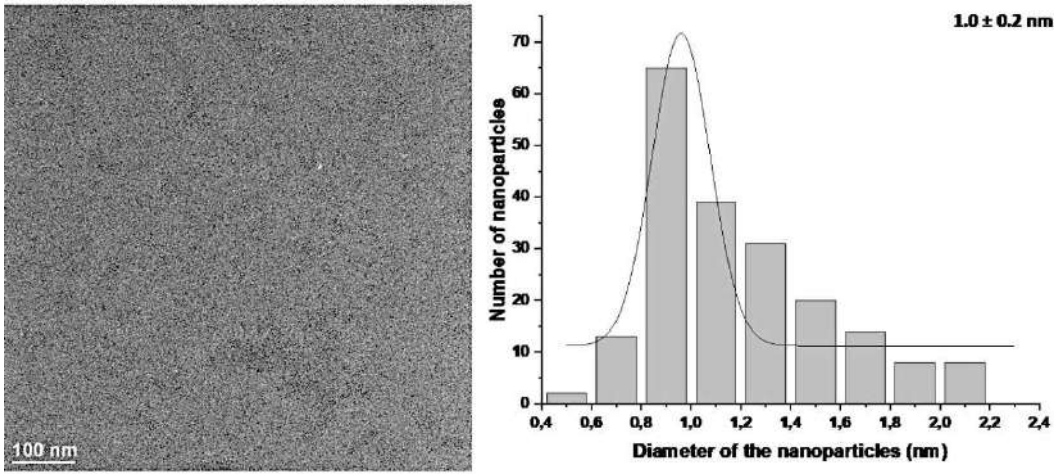

Figure 43: TEM image of Ru_1Cu_2/PVP NPs (scale bar 100 nm) together with the respective size histogram.

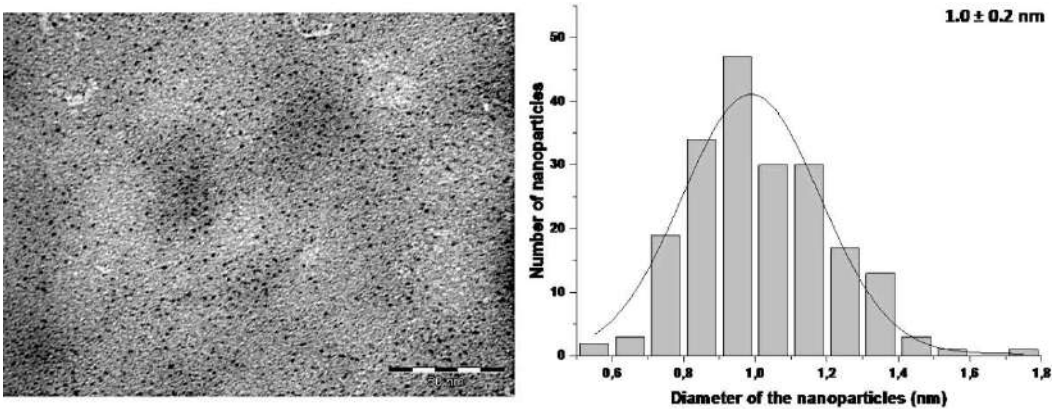

Figure 44: TEM image of Ru_1Cu_1/PVP NPs (scale bar 50 nm) together with the respective size histogram.

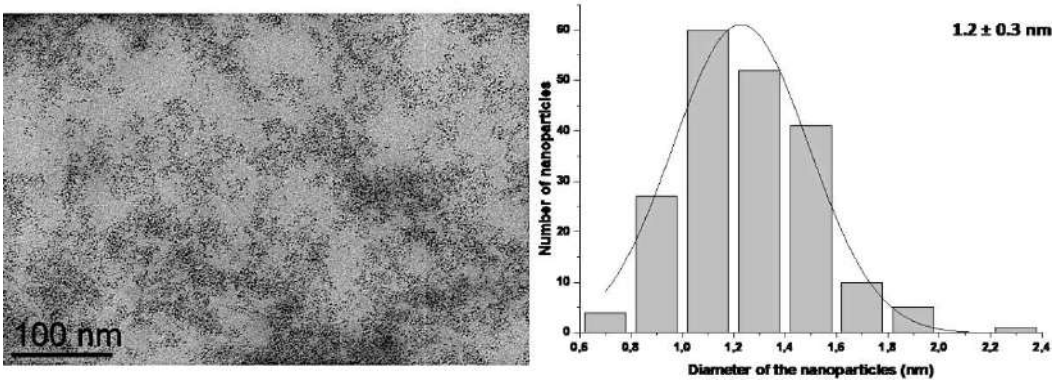

Figure 45: TEM image of Ru_2Cu_1/PVP NPs (scale bar 100 nm) together with the respective size histogram.

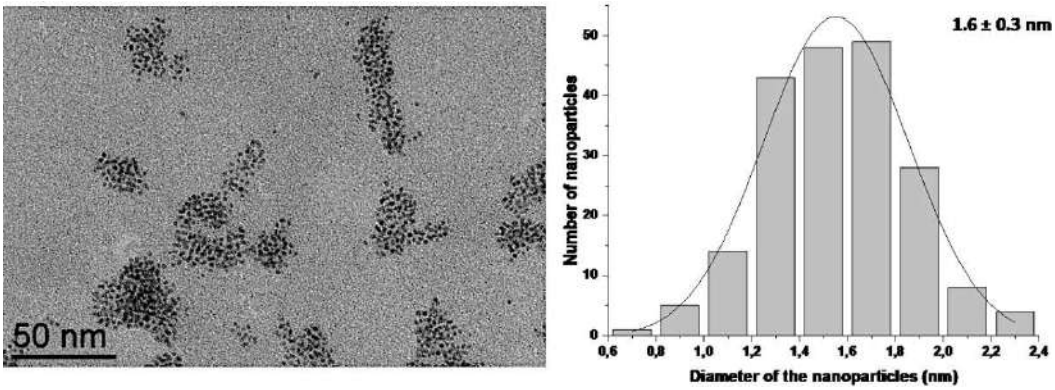

Figure 46: TEM image of Ru/PVP NPs (scale bar 50 nm) together with the respective size histogram.

HAADF-STEM-EDX analyses on isolated NPs of Ru_1Cu_1/PVP material synthesised at 100 ºC were performed (Figure 47). The results show that Ru and Cu coexist in the same NP. Nevertheless, the amounts of both metals determined by EDX analyses show that the NPs are mainly composed by Ru, which is not consistent with the composition determined by ICP-OES analyses (Figure 47 (b)).

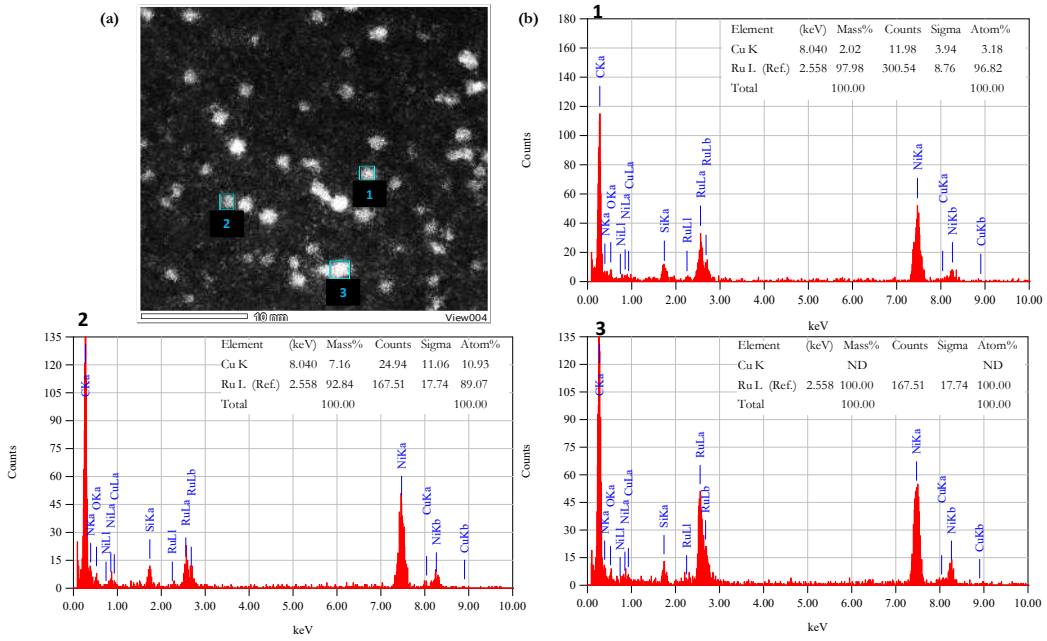

Figure 47 (a) HAADF-STEM images of Ru_1Cu_1/PVP NPs synthesised at 100 °C together with the (b) EDX analysis of the isolated NPs in squares 1 (top), 2 (bottom left) and 3 (bottom right).

In contrast, the EDX analyses of larger areas of Ru_1Cu_1/PVP material indicated a Ru/Cu ratio close to 1 (Figure 48), which is the expected value for this sample. These different results obtained depending on probing isolated NPs or an ensemble of NPs could indicate that a significant part of the copper is not incorporated into the NPs, but is present under the form of very small clusters or isolated atoms. This hypothesis was confirmed by a line scan EDX analyses (Figure 49), where Ru was detected only in the NPs (red line), while Cu was observed over all the EDX scan line (blue line), including on the Ru rich zones.

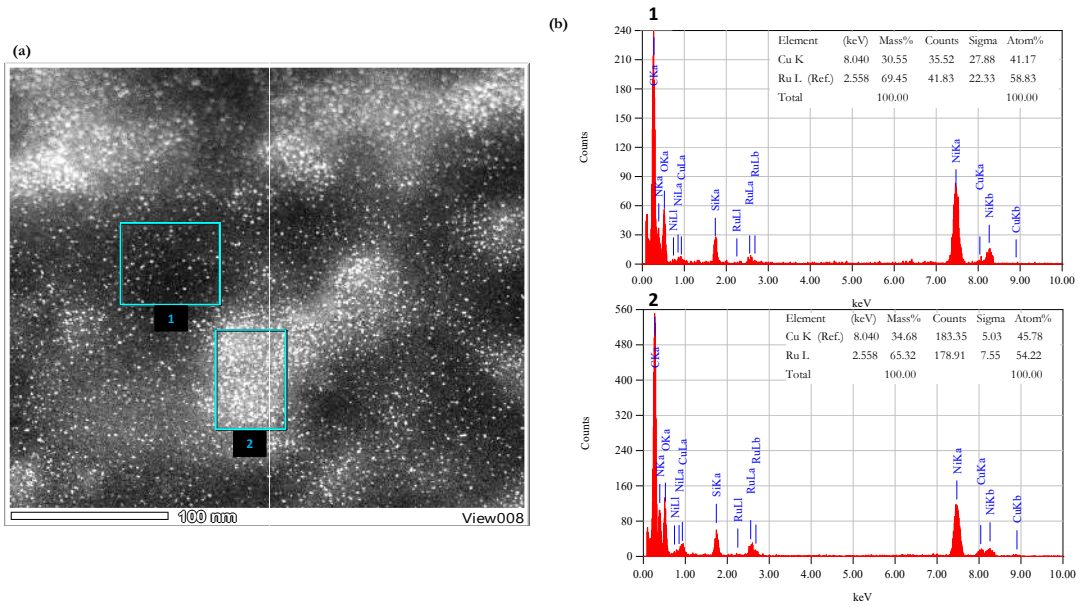

Figure 48: (a)HAADF-STEM image of Ru_1Cu_1/PVP synthesised at 100 °C together with the (b) EDX analysis of two regions 1 (top) and 2 (bottom).

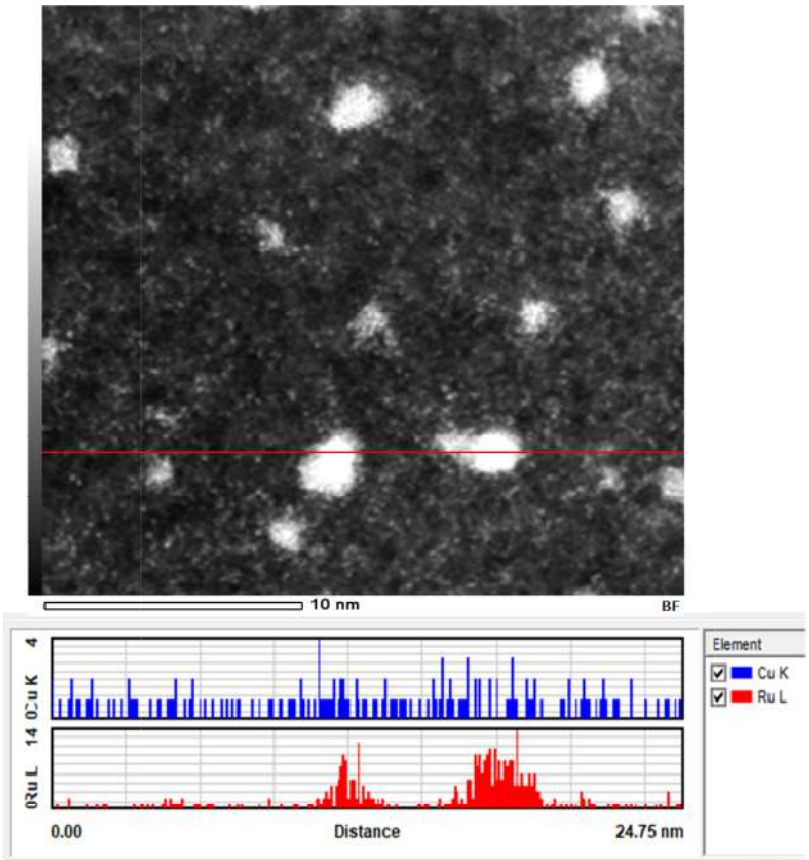

Figure 49: HAADF-STEM image of Ru_1Cu_1/PVP synthesised at 100 °C (top) together with a linear EDX analysis (bottom).

WAXS analyses are in agreement with the formation of bimetallic NPs. The data recorded for Cu/PVP (Figure 50) agree with a pure Cu_2O structure where the Cu atoms arrange in a

fcc sublattice and the O atoms in a body-centred cubic (*bcc*) sublattice. The Ru/PVP NPs synthesized at 100 °C have the expected *hcp* structure,[47] even if it is distorted as previously ascertained in Ru/PVP synthesised at 85 °C, see section 2.2. A concrete pattern of such a distorted *hcp* structure was also detected, at 0.2–0.5 nm range, for the three bimetallic NPs analysed (Ru_2Cu_1/PVP, Ru_1Cu_1/PVP and Ru_1Cu_2/PVP), with decreased amplitude. This is in accordance with a core–shell organisation of the two metals since for core–shell systems, the prevailed structure is dominated by the core.[48,49] The moderated intensity of this pattern could indicate a disordered structure, caused by the presence of more than one phase. So, in the series of RuCu bimetallic NPs, the structure observed would be a Ru core and a shell where Cu_2O is present. In all cases, Cu was not observed on the surface but Cu_2O, meaning that the samples the surfaces were oxidised. For monometallic Cu, this presence of Cu_2O would be in agreement with the observation on TEM analyses of hollow Cu_2O NPs.

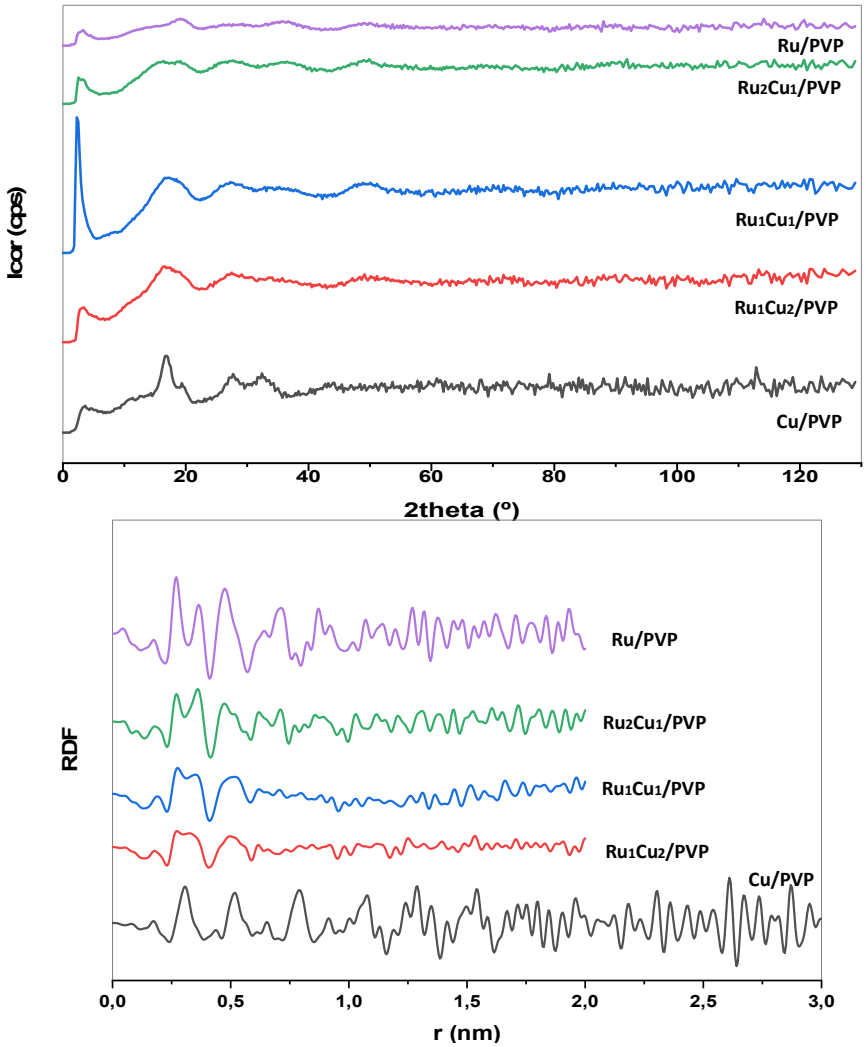

Figure 50: Diffractograms with, from the top to the bottom, the monometallic Ru NPs, the bimetallic RuCu/PVP NPs and the monometallic Cu NPs synthesised at 100 °C (top); and the related RDFs (bottom).

Following the calculations presented in section 2.2 for RuNi/PVP NPs (equations 1 to 15), the estimated Cu percentage coverage for the NPs stabilised with the PVP ligand are as follows, Ru_2Cu_1/PVP ≈ 49 %, Ru_1Cu_1/PVP ≈ 68 % and Ru_1Cu_2/PVP ≈ 77 %. All the results for these materials are presented in Table 9.

Table 9: Estimation of Cu coverage on the monometallic Ru/PVP and Cu/PVP NPs, and the bimetallic RuCu/PVP NPs.

NP	NP composition (from ICP-OES)[a]	Mean size (nm)[b]	Estimated total atoms on the NP[c]	Estimated atoms on the core[c]	Estimated atoms on the surface[c]	Estimated atoms surface (%)[c]	Estimated number of Ru atoms in a NP[d]	Estimated number of Cu atoms in a NP[d]	Estimated surface coverage of Cu (%)[c]
Ru/PVP	Ru/PVP	1.6 ± 0.3	157	62	95	61	157	0	0
Ru_2Cu_1/PVP	$Ru_{1.8}Cu_{1.0}$/PVP	1.2 ± 0.3	66	17	49	74	42	24	≈49
Ru_1Cu_1/PVP	$Ru_{1.0}Cu_{1.2}$/PVP	1.0 ± 0.2	38	7	31	82	17	21	≈68
Ru_1Cu_2/PVP	$Ru_{1.0}Cu_{1.8}$/PVP	1.0 0.1	38	7	31	82	14	24	≈77
Cu/PVP	Cu/PVP	4.9 ± 1.0	5217	4145	1072	21	0	5217	≈487

[a]ICP-OES analysis. [b]Mean values of NP size determined from TEM images by considering at least 200 particles. [c] High Ru loaded NP (Ru/PVP, Ru_2Cu_1/PVP, Ru_1Cu_1/PVP and Ru_1Cu_2/PVP) were calculated as follows: the number of Ru atoms in *hcp* cell (N) is 6. Ru atom radius (R_{Ru}) is 0.214 nm. The volume of Ru cell is 0.0817 nm^3. R_{NP} represents the radius of NP. The volume of all Ru atoms on the shell of NP: $V_{shell} = V_{total} - V_{core} = 4/3\pi R_{NP}^3 - 4/3\pi (R_{NP} - R_{Ru})^3$, V_{total} meaning the volume of one Ru NP, V_{core} presenting the volume of NP excluded the one outer layer of atoms. The numbers of metal atoms on the shell $N_{shell} = N*V_{shell}/0.0817$. The number of total Ru atoms $N_{total} = N*V_{total}/0.0817$. The percentage of Ru atoms on the surface of NP = $N_{shell}/ N_{total}*100$ %. Cu/PVP was calculated as follows: the number of Cu atoms in *fcc* cell (N) is 4. Cu atom radius (R_{Cu}) is 0.181 nm. The volume of Cu cell is 0.0472 nm^3. R_{NP} represents the radius of NP. The volume of all Ru atoms on the shell of NP: $V_{shell} = V_{total} - V_{core} = 4/3\pi R_{NP}^3 - 4/3\pi (R_{NP} - R_{Cu})^3$, V_{total} meaning the volume of one Cu NP, V_{core} presenting the volume of NP excluded the one outer layer of atoms. The numbers of Cu atoms on the shell $N_{shell} = N*V_{shell}/0.0472$. The number of total Cu atoms $N_{total} = N*V_{total}/0.0472$. The percentage of metal atoms on the surface of NP = $N_{shell}/ N_{total}*100$ %. [d]Estimated total atoms on the NP*metallic content (in mol). [e]Estimated number of Cu atoms in a NP/Estimated atoms on the surface*100.

Magnetic properties of Cu/PVP and Ru_1Cu_1/PVP NPs were measured by SQUID magnetometry. Figure 51 provides the curves recorded at RT and corrected of the diamagnetic contribution of PVP. Cu/PVP NPs manifested a typical ferromagnetic behaviour with 11.1 emu·g_{Cu}^{-1} of Ms. The Ms observed is higher compared to C coated Cu NPs (Ms = 0.2-1.5 emu·g_{Cu}^{-1}).[100] It is known that the Ms of Cu NP depends on its size,[100] which could explain the low value compared to the results on the C coated Cu NPs mentioned. It is also known that in bulk Co-Cu systems, at a 0 K temperature, the Ms decreases until 0 with the increasing Cu content, approaching Ms=0 emu·g_{Cu}^{-1} at ca. 90 % of Cu.[101] In comparison to the 5 nm Cu_2/C NPs from literature,[100] the Ms of the 5 nm Cu/PVP NPs synthesised here is 7.4 times higher. The Ru_1Cu_1/PVP sample displays a clear diamagnetic behaviour evidencing that the magnetisation is rapidly decreased when adding a small amount of Ru on the samples. This was also observed in the synthesised RuNi/PVP NPs discussed in section 2.2, RuNi/PPh_2Py NPs discussed in section 2.3 and other Ru and Ni bimetallic systems.[65,66] Cu_2O is known to have similar paramagnetism and diamagnetism contributions on its behaviour, resulting to a Ms near zero ($0.3*10^{-6}$ emu·g_{Cu}^{-1}).[102,103] Being Cu^+ and O^{2-} diamagnetic species, the paramagnetism comes either from the presence of cation vacancies or

from magnetic impurities or dopings of the sample.[104–106] In our synthesised Cu_2O NPs, no dopings were performed, becoming the hypothesis of cation vacancies the chosen for the paramagnetism observed on Cu_2O NPs.

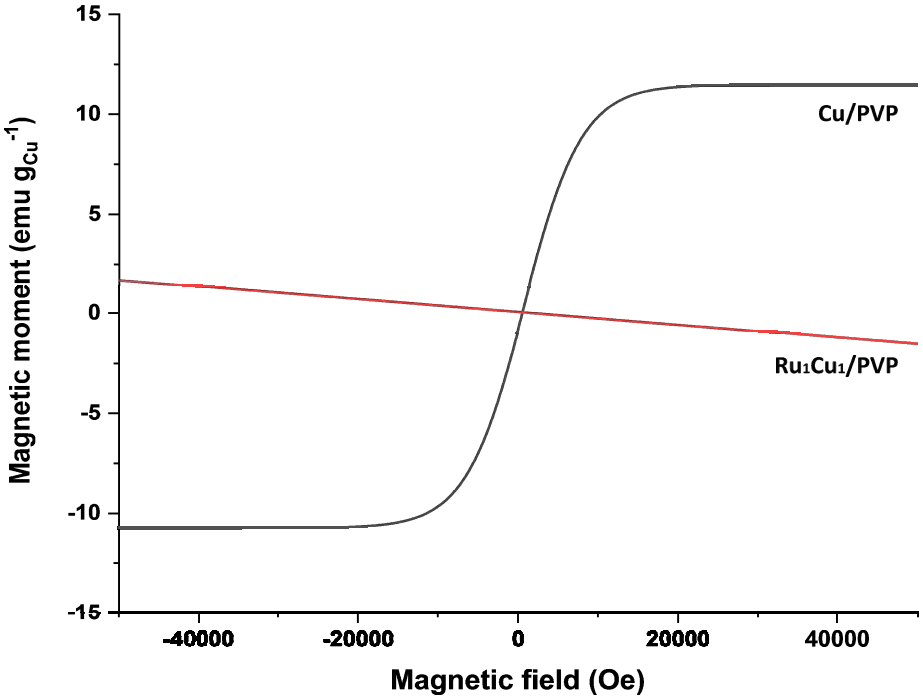

Figure 51: Magnetic hysteresis cycles of Cu/PVP and RuCu/PVP NPs measured at RT.

To conclude this section of Chapter 2, bimetallic RuCu/PVP NPs were synthesised at 100 ºC by the reduction of [Ru(η^4-C_8H_{12})(η^6-C_8H_{10})] and [Cu(C_9H_{11})]complexes. These synthesised bimetallic NPs were all between 1.0 and 1.2 nm, even the ones with a higher Cu amount in their composition. As expected, all bimetallic RuCu/PVP NPs have a core-shell structure being Ru in the core and Cu_2O on the surface but all Cu is not incorporated in the NPs remaining as clusters or isolated atoms. Monometallic Cu/PVP NPs showed two populations of NPs (1.3 nm and 4.9 nm), being the larger ones Cu_2O NPs as ascertained by WAXS analysis. Magnetisation decreased when adding a small amount of Ru to Cu evidencing the presence of both Ru and Cu close in vicinity, in the same structure, certifying the success on the synthesis of the bimetallic RuCu/PVP NPs. The objective of this synthetic process was to use these synthesised NPs as catalysts for hydrogenation reactions of FF, which is discussed in Chapter 3.

2.6 Synthesis of Cu/Amines nanoparticles

In order to study the effects of ligands on the synthesis and applications of Cu NPs, the stabiliser PVP was replaced by several amines in the synthetic procedure. Amine ligands

were chosen as they are known to be suitable stabilisers for the synthesis of Cu NPs;[94,107,108] and also to display beneficial effects in catalysis.[109,110]

[Cu(C_9H_{11})] complex was decomposed under 3 bar of H_2 pressure in the presence of HDA or dodecylamine (DDA) in THF, with the aim to obtain Cu/HDA or Cu/DDA NPs (Scheme 12). Cu/HDA NPs have been previously synthesized by decomposing the [Cu(C_9H_{11})] complex in the presence of HDA at 80 ºC, and the procedure is described elsewhere.[94] The synthesis was performed at three different temperatures 80 °C, 100 ºC or 120 ºC, in order to study the effect of temperature on the growth of the NPs. Moreover, 0.08 molar eq. of DDA were used, to reproduce the results found in literature, and in addition from 0.2 to 2 molar eq. were tested for HDA, in order to study the effect of the composition, by varying the HDA content, on the growth of the NPs. All the experimental details are given in Chapter 6. The objective was to control the growth of the NPs in order to have homogeneous large NPs with the aim to perform a doping of the surface with another metal.

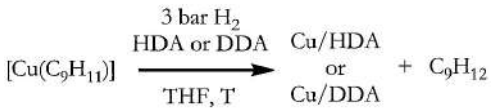

Scheme 12: Synthesis of Cu/HDA and Cu/DDA NPs.

At 80 ºC, 100 ºC and 120 ºC, the characteristic colour change from light brown/orange to dark red was observed after some minutes of heating under H_2 pressure (Figure 52).

Figure 52: Colour change in a typical synthesis of Cu/HDA NPs at 80 ºC, 100 ºC or 120 ºC; left, before the hydrogenation reaction, and right, after the reaction.

TEM images of the Cu/DDA NPs showed a mean size of 1.9 ± 0.1 nm, which is smaller than expected from the publication where large Cu/DDA NPs of 7.8 nm size were obtained, by using exactly the same reaction conditions.[94] However, the size distribution is very large and it would be of interest to repeat this synthesis to study its reproducibility. Cu/HDA samples showed the presence of NPs from 1.9 ± 0.4 nm to 10.8 ± 2.7 nm sizes

depending on the temperature and HDA content used. It can be observed that for a same HDA content, the size of the Cu/HDA NPs increases with the temperature (Cu/1 eq. HDA: at 80 ºC, 1.9 ± 0.4 nm; at 100 ºC, 3.0 ± 0.3 nm; and at 120 ºC, 5.0 ± 1.1 nm), tendency that was already observed in other type of Cu NPs.[98] Concerning the HDA content, no clear relation was observed for a fixed synthesis temperature, as the synthesised NPs of the Cu/HDA series were not really homogeneous and even aggregation is observed in some cases. Table 10 summarizes the metal content of each synthesised material, as well as the size of the NPs established analysing the TEM images (Figures 53 to 60).

Table 10: Metal content and mean size of Cu/DDA and Cu/HDA NPs.

NP	Synthesis Temperature (ºC)	Cu content (%)[a]	Mean size (nm)[b]
Cu/0.08 eq. DDA	80	70.6	1.9 ± 0.1
Cu/0.2 eq. HDA		88.9	3.7 ± 1.0
Cu/0.4 eq. HDA		97.7	4.5 ± 0.6
Cu/1 eq. HDA	100	55.2	1.9 ± 0.4
Cu/0.4 eq. HDA		77.4	8.0 ± 3.0
Cu/1 eq. HDA		57.1	3.0 ± 0.3
Cu/1 eq. HDA	120	83.1	5.0 ± 1.1
Cu/2 eq. HDA		80.8	10.8 ± 2.7

[a]ICP-OES analysis. [b]Mean values of NP size determined from TEM images by considering at least 200 particles.

In most samples, the metallic mass percentages in weight, determined by ICP-OES, were in the range 70-98 %, with the exception of Cu/1 eq. HDA NPs synthesised at 80 ºC and 100 ºC, which presented a Cu content in the range 55-57 %.

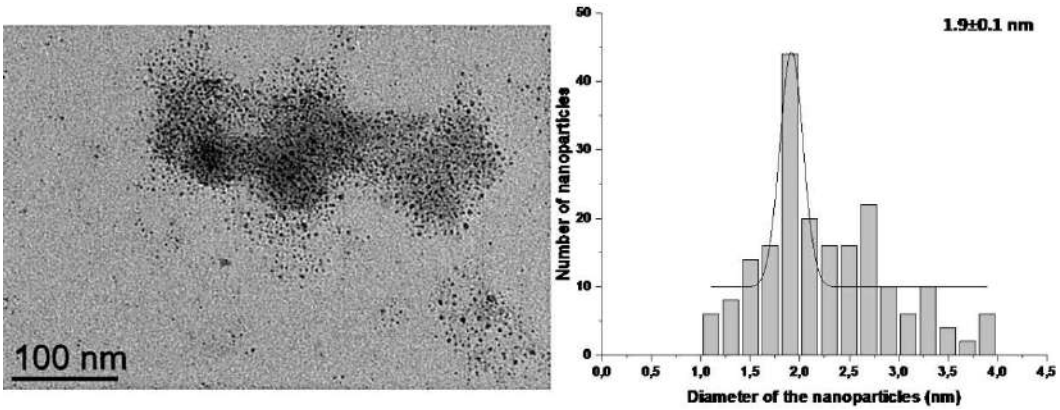

Figure 53: TEM image of Cu/0.08 eq. DDA NPs synthesised at 80 ºC (scale bar 100 nm) together with the respective size histogram.

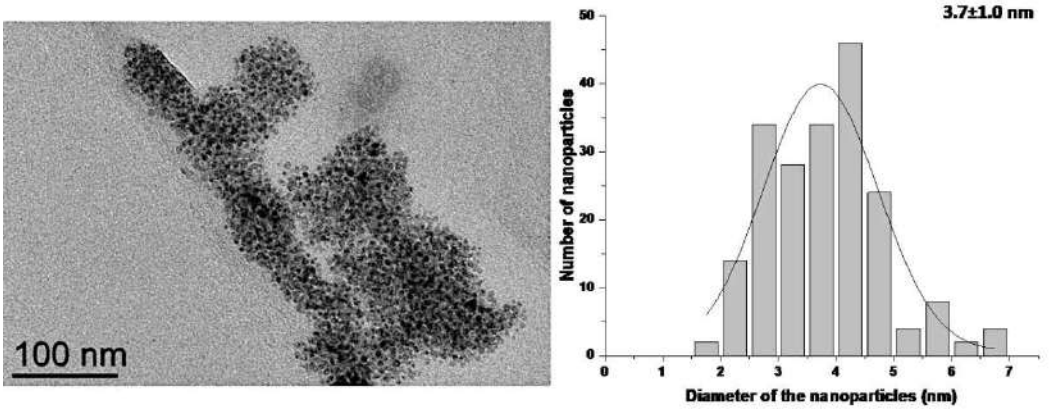

Figure 54: TEM image of Cu/0.2 eq. HDA NPs synthesised at 80 ºC (scale bar 100 nm) together with the respective size histogram.

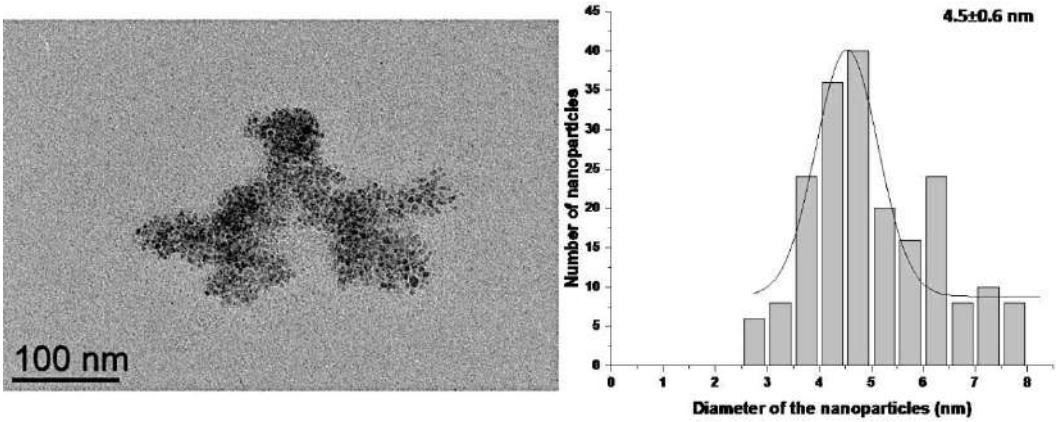

Figure 55: TEM image of Cu/0.4 eq. HDA NPs synthesised at 80 ºC (scale bar 100 nm) together with the respective size histogram.

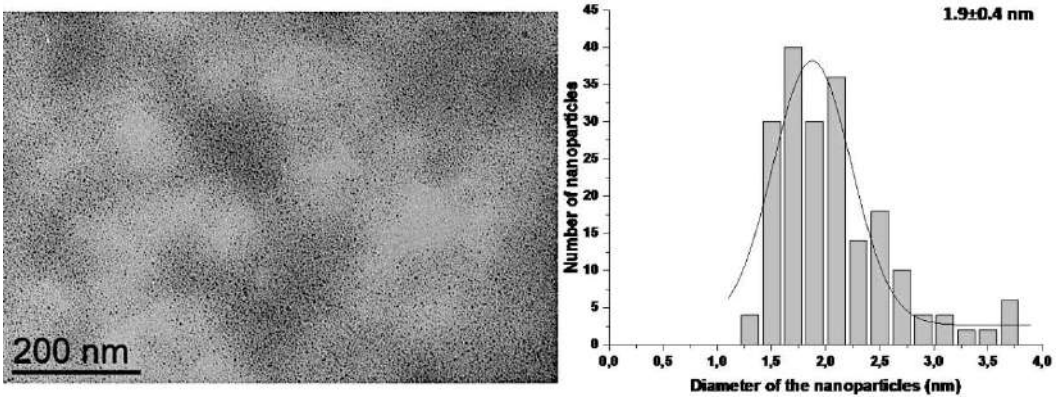

Figure 56: TEM image of Cu/1 eq. HDA NPs synthesised at 80 ºC (scale bar 200 nm) together with the respective size histogram.

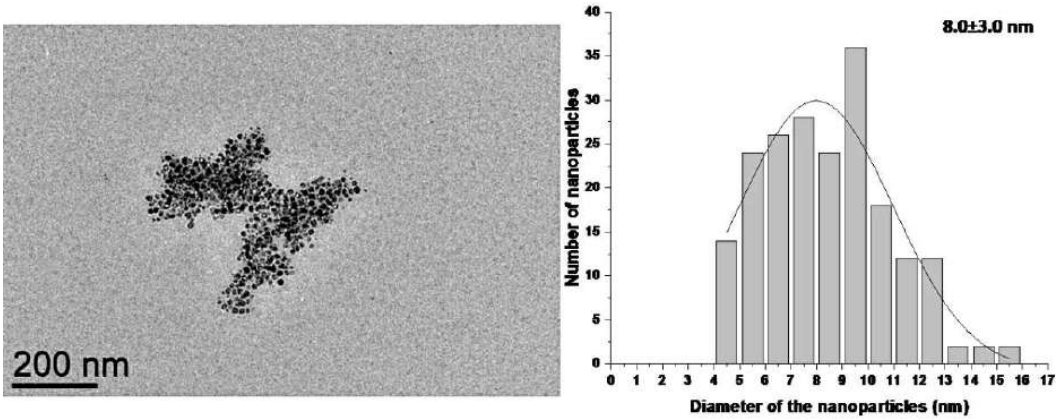

Figure 57: TEM image of Cu/0.4 eq. HDA NPs synthesised at 100 ºC (scale bar 200 nm) together with the respective size histogram.

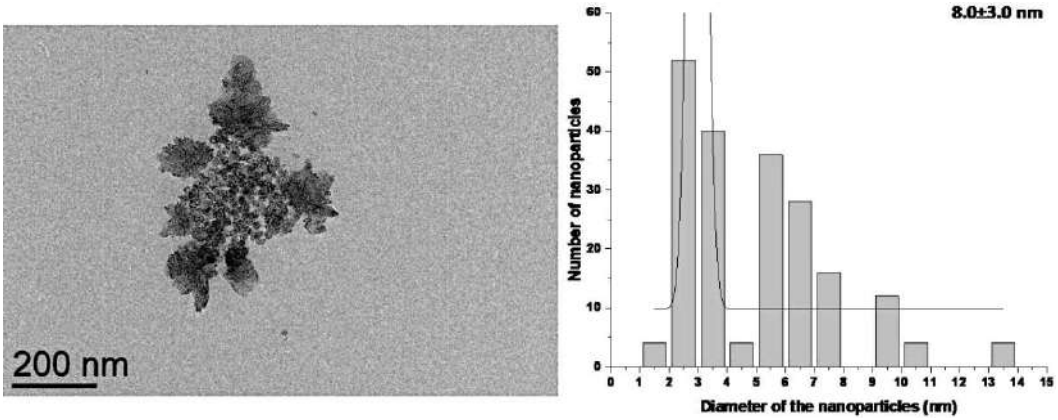

Figure 58: TEM image of Cu/1 eq. HDA NPs synthesised at 100 ºC (scale bar 200 nm) together with the respective size histogram.

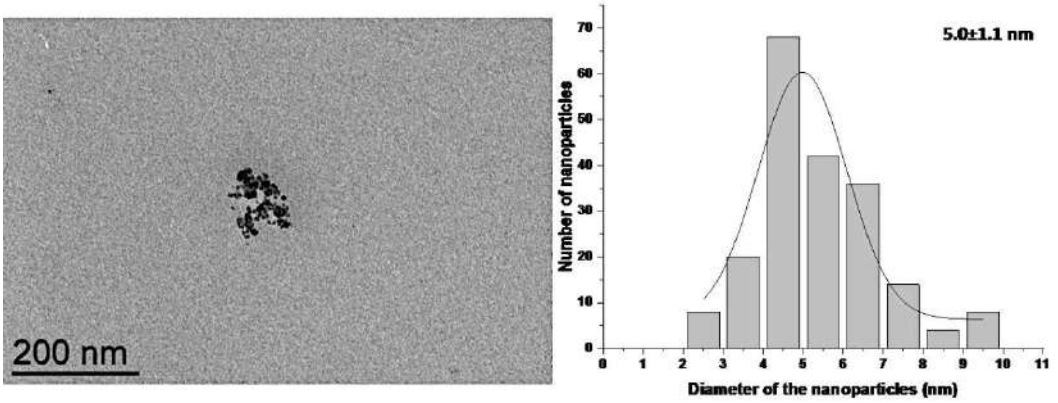

Figure 59: TEM image of Cu/1 eq. HDA NPs synthesised at 120 ºC (scale bar 200 nm) together with the respective size histogram.

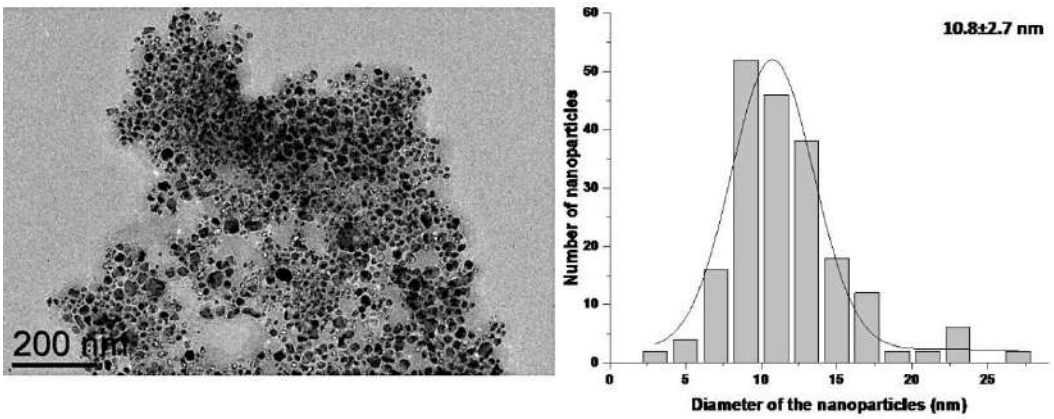

Figure 60: TEM image of Cu/2 eq. HDA NPs synthesised at 120 ºC (scale bar 200 nm) together with the respective size histogram.

To conclude this section of Chapter 2, Cu/HDA NPs were synthesised at three different temperatures (80 ºC, 100 ºC and 120 ºC) and at different HDA contents (0.1, 0.2, 0.5 and 1 molar eq.) by the reduction of [Cu(C_9H_{11})]. In general, Cu/HDA NPs were not homogeneous in size and an increase of the mean size with the temperature was observed. Further tests on the synthesis of Cu/HDA NPs should be done to improve the homogeneity and reproducibility.

2.7 Conclusions

In this Chapter 2, the synthesis and characterisation of different monometallic and bimetallic systems have been discussed.

For the RuNi/PVP NPs series, it was found the importance of the reaction temperature on the formation of bimetallic NPs for the successful decomposition of the Ni metallic precursor. All the synthesised RuNi/PVP NPs were of less than 2 nm size, even the ones with high Ni content, and had a core-shell structure with Ru in the core. Ru and Ni were evidenced to be in close vicinity in the NPs by shifts on XPS signals and the drastic decrease of magnetisation, certifying their bimetallic nature.

For the RuNi/PPh_2Py NPs series, monometallic and bimetallic NPs of 2 nm or less were obtained with a core-shell structure with Ru in the core, even if further studies using EXAFS for instance would be of interest to completely discard or not the alloy organisation. SS NMR allowed to observe the coordination of the phosphine in the bimetallic NPs. Ru and Ni are in close vicinity by the drastic decrease of magnetisation due to the presence of Ru, pointing to a bimetallic nature. Further analyses are needed to fully characterise these bimetallic NPs.

RuNi/AdCOOH NPs were of less than 2 nm of size while a broad dispersion, which may be attributed to some agglomeration, was observed. Further analyses are needed to characterise these species.

For RuCu/PVP NPs series, the bimetallic NPs synthesised at 100 ºC were between 1.0 and 1.2 nm size, even the ones with high Cu content. They possessed a core-shell structure with Ru in the core and Cu_2O present on the surface, yet, not all Cu was incorporated onto the bimetallic NPs and some remained as clusters or isolated atoms, as evidenced EDX analyses. Monometallic Cu/PVP NPs presented two populations of NPs (1.3 nm and 4.9 nm) and the larger ones appeared to be hollowed, from TEM images. WAXS analysis points the Cu NPs are oxidised. Ru and Cu were evidenced to be in close vicinity as a drastic decrease of magnetisation was observed when Ru is present in the composition.

Cu/HDA NPs were synthesised at different temperatures (80 ºC to 120 ºC) using molar eq. of 0.2, 0.4, 1 and 2 of HDA. A diversity of mean sizes was obtained for the different samples which, in general, were not homogeneous.

2.8 References

(1) Energy Production and Consumption - Our World in Data. https://ourworldindata.org/energy-production-consumption

(2) Nanda, S.; Azargohar, R.; Dalai, A. K.; Kozinski, J. A. An Assessment on the Sustainability of Lignocellulosic Biomass for Biorefining. *Renew. Sustain. Energy Rev.* **2015**, *50*, 925. https://doi.org/10.1016/j.rser.2015.05.058

(3) Putro, J. N.; Soetaredjo, F. E.; Lin, S.-Y.; Ju, Y.-H.; Ismadji, S. Pretreatment and Conversion of Lignocellulose Biomass into Valuable Chemicals. *RSC Adv.* **2016**, *6* (52), 46834. https://doi.org/10.1039/C6RA09851G

(4) Roose, P.; Eller, K.; Henkes, E.; Rossbacher, R.; Höke, H. Amines, Aliphatic. In *Ullmann's Encyclopedia of Industrial Chemistry*; Wiley-VCH Verlag GmbH & Co. KGaA, Ed.; Wiley-VCH Verlag GmbH & Co. KGaA: Weinheim, Germany, **2015**, 1. https://doi.org/10.1002/14356007.a02_001.pub2

(5) Yoshimura, M.; Komatsu, A.; Niimura, M.; Takagi, Y.; Takahashi, T.; Ueda, S.; Ichikawa, T.; Kobayashi, Y.; Okami, H.; Hattori, T.; Sawama, Y.; Monguchi, Y.; Sajiki, H. Selective Synthesis of Primary Amines from Nitriles under Hydrogenation Conditions. *Adv. Synth. Catal.* **2018**, *360* (8), 1726. https://doi.org/10.1002/adsc.201800102

(6) Bagal, D. B.; Bhanage, B. M. Recent Advances in Transition Metal-Catalyzed Hydrogenation of Nitriles. *Adv. Synth. Catal.* **2015**, *357* (5), 883. https://doi.org/10.1002/adsc.201400940

(7) Chatterjee, M.; Sato, M.; Kawanami, H.; Yokoyama, T.; Suzuki, T.; Ishizaka, T. An Efficient Hydrogenation of Dinitrile to Aminonitrile in Supercritical Carbon Dioxide. *Adv. Synth. Catal.* **2010**, *352* (14–15), 2394. https://doi.org/10.1002/adsc.201000514

(8) Rajesh, K.; Dudle, B.; Blacque, O.; Berke, H. Homogeneous Hydrogenations of Nitriles Catalyzed by Rhenium Complexes. *Adv. Synth. Catal.* **2011**, *353* (9), 1479. https://doi.org/10.1002/adsc.201000867

(9) Chin, C. S.; Lee, B. Hydrogenation of Nitriles with Iridium-Triphenylphosphine Complexes. *Catal. Lett.* **1992**, *14* (1), 135. https://doi.org/10.1007/BF00764228

(10) Sankar, M.; Dimitratos, N.; Miedziak, P. J.; Wells, P. P.; Kiely, C. J.; Hutchings, G. J. Designing Bimetallic Catalysts for a Green and Sustainable Future. *Chem. Soc. Rev.* **2012**, *41* (24), 8099. https://doi.org/10.1039/c2cs35296f
(11) Kang, X.; Li, Y.; Zhu, M.; Jin, R. Atomically Precise Alloy Nanoclusters: Syntheses, Structures, and Properties. *Chem. Soc. Rev.* **2020**, *49* (17), 6443. https://doi.org/10.1039/C9CS00633H
(12) Luneau, M.; Lim, J. S.; Patel, D. A.; Sykes, E. C. H.; Friend, C. M.; Sautet, P. Guidelines to Achieving High Selectivity for the Hydrogenation of α,β-Unsaturated Aldehydes with Bimetallic and Dilute Alloy Catalysts: A Review. *Chem. Rev.* **2020**, *120* (23), 12834. https://doi.org/10.1021/acs.chemrev.0c00582
(13) Over, H. Surface Chemistry of Ruthenium Dioxide in Heterogeneous Catalysis and Electrocatalysis: From Fundamental to Applied Research. *Chem. Rev.* **2012**, *112* (6), 3356. https://doi.org/10.1021/cr200247n
(14) Hinrichsen, O.; Rosowski, F.; Muhler, M.; Ertl, G. The Microkinetics of Ammonia Synthesis Catalyzed by Cesium-Promoted Supported Ruthenium. *Chem. Eng. Sci.* **1996**, *51* (10), 1683. https://doi.org/10.1016/0009-2509(96)00027-9
(15) Muhler, M.; Rosowski, F.; Hinrichsen, O.; Hornung, A.; Ertl, G. Ruthenium as Catalyst for Ammonia Synthesis. In *Studies in Surface Science and Catalysis*; Elsevier, **1996**, *101*, 317. https://doi.org/10.1016/S0167-2991(96)80242-4
(16) Axet, M. R.; Philippot, K. Catalysis with Colloidal Ruthenium Nanoparticles. *Chem. Rev.* **2020**, *120* (2), 1085. https://doi.org/10.1021/acs.chemrev.9b00434
(17) Zhang, R. F.; Kong, X. F.; Wang, H. T.; Zhang, S. H.; Legut, D.; Sheng, S. H.; Srinivasan, S.; Rajan, K.; Germann, T. C. An Informatics Guided Classification of Miscible and Immiscible Binary Alloy Systems. *Sci. Rep.* **2017**, *7* (1), 9577. https://doi.org/10.1038/s41598-017-09704-1
(18) Li, X. Y.; Li, Z. F.; Liu, B. X. Nonequilibrium Hcp and Fcc Phases Formed by Ion Mixing in an Immiscible Ni–Ru System. *J. Alloys Compd.* **2002**, *334* (1–2), 167. https://doi.org/10.1016/S0925-8388(01)01770-4
(19) Raevskaya, M. V.; Yanson, I. E.; Tatarkina, A. L.; Sokolova, I. G. The Effect of Nickel on Interaction in the Copper-Ruthenium System. *J. Common Met.* **1987**, *132* (2), 237. https://doi.org/10.1016/0022-5088(87)90579-0
(20) Okamoto, H. D-Ta (Deuterium-Tantalum). *J. Phase Equilibria* **1992**, *13* (4), 440. https://doi.org/10.1007/BF02674998
(21) Zhang, P.-F.; Zhang, J.-Y.; Sheng, T.; Lu, Y.-Q.; Yin, Z.-W.; Li, Y.-Y.; Peng, X.-X.; Zhou, Y.; Li, J.-T.; Wu, Y.-J.; Lin, J.-X.; Xu, B.-B.; Qu, X.-M.; Huang, L.; Sun, S.-G. Synergetic Effect of Ru and NiO in the Electrocatalytic Decomposition of Li_2CO_3 to Enhance the Performance of a Li-CO_2/O_2 Battery. *ACS Catal.* **2020**, *10* (2), 1640. https://doi.org/10.1021/acscatal.9b04138
(22) Li, M.; Wang, H.; Zhu, W.; Li, W.; Wang, C.; Lu, X. RuNi Nanoparticles Embedded in N-Doped Carbon Nanofibers as a Robust Bifunctional Catalyst for Efficient Overall Water Splitting. *Adv. Sci.* **2020**, *7* (2), 1901833. https://doi.org/10.1002/advs.201901833
(23) Zhu, L.; Sun, H.; Fu, H.; Zheng, J.; Zhang, N.; Li, Y.; Chen, B. H. Effect of Ruthenium Nickel Bimetallic Composition on the Catalytic Performance for Benzene Hydrogenation to Cyclohexane. *Appl. Catal. Gen.* **2015**, *499*, 124. https://doi.org/10.1016/j.apcata.2015.04.016
(24) Luo, Z.; Zheng, Z.; Li, L.; Cui, Y.-T.; Zhao, C. Bimetallic Ru–Ni Catalyzed Aqueous-Phase Guaiacol Hydrogenolysis at Low H_2 Pressures. *ACS Catal.* **2017**, *7* (12), 8304. https://doi.org/10.1021/acscatal.7b02317
(25) Hu, Y.; Jiang, G.; Xu, G.; Mu, X. Hydrogenolysis of Lignin Model Compounds into Aromatics with Bimetallic Ru-Ni Supported onto Nitrogen-Doped Activated Carbon Catalyst. *Mol. Catal.* **2018**, *445*, 316. https://doi.org/10.1016/j.mcat.2017.12.009
(26) Valdés-Martínez, O. U.; Suárez-Toriello, V. A.; Reyes, J. A. de los; Pawelec, B.; Fierro, J. L. G. Support Effect and Metals Interactions for $NiRu/Al_2O_3$, TiO_2 and ZrO 2 Catalysts in the Hydrodeoxygenation of Phenol. *Catal. Today* **2017**, *296*, 219. https://doi.org/10.1016/j.cattod.2017.04.007

(27) Tada, S.; Kikuchi, R.; Wada, K.; Osada, K.; Akiyama, K.; Satokawa, S.; Kawashima, Y. Long-Term Durability of Ni/TiO_2 and Ru–Ni/TiO_2 Catalysts for Selective CO Methanation. *J. Power Sources* **2014**, *264*, 59. https://doi.org/10.1016/j.jpowsour.2014.04.075

(28) Chen, G.; Desinan, S.; Rosei, R.; Rosei, F.; Ma, D. Synthesis of Ni-Ru Alloy Nanoparticles and Their High Catalytic Activity in Dehydrogenation of Ammonia Borane. *Chem. - Eur. J.* **2012**, *18* (25), 7925. https://doi.org/10.1002/chem.201200292

(29) Yang, Y.; Gao, G.; Zhang, X.; Li, F. Facile Fabrication of Composition-Tuned Ru–Ni Bimetallics in Ordered Mesoporous Carbon for Levulinic Acid Hydrogenation. *ACS Catal.* **2014**, *4* (5), 1419. https://doi.org/10.1021/cs401030u

(30) Zhang, J.; Teo, J.; Chen, X.; Asakura, H.; Tanaka, T.; Teramura, K.; Yan, N. A Series of NiM (M = Ru, Rh, and Pd) Bimetallic Catalysts for Effective Lignin Hydrogenolysis in Water. *ACS Catal.* **2014**, *4* (5), 1574. https://doi.org/10.1021/cs401199f

(31) Qadir, M. I.; Bernardi, F.; Scholten, J. D.; Baptista, D. L.; Dupont, J. Synergistic CO_2 Hydrogenation over Bimetallic Ru/Ni Nanoparticles in Ionic Liquids. *Appl. Catal. B Environ.* **2019**, *252*, 10. https://doi.org/10.1016/j.apcatb.2019.04.005

(32) Bai, S.; Yao, Q.; Xu, Y.; Cao, K.; Huang, X. Strong Synergy in a Lichen-like RuCu Nanosheet Boosts the Direct Methane Oxidation to Methanol. *Nano Energy* **2020**, *71*, 104566. https://doi.org/10.1016/j.nanoen.2020.104566

(33) Zheng, W.; Yao, J.; Zhao, Y. RuCu Cage/Alloy Nanoparticles with Controllable Electroactivity for Specific Electroanalysis Applications. *Anal. Chem.* **2021**, *93* (38), 13080. https://doi.org/10.1021/acs.analchem.1c03182

(34) Huang, B.; Kobayashi, H.; Yamamoto, T.; Matsumura, S.; Nishida, Y.; Sato, K.; Nagaoka, K.; Kawaguchi, S.; Kubota, Y.; Kitagawa, H. Solid-Solution Alloying of Immiscible Ru and Cu with Enhanced CO Oxidation Activity. *J. Am. Chem. Soc.* **2017**, *139* (13), 4643. https://doi.org/10.1021/jacs.7b01186

(35) Zhu, L.; Cao, M.; Li, L.; Sun, H.; Tang, Y.; Zhang, N.; Zheng, J.; Zhou, H.; Li, Y.; Yang, L.; Zhong, C.-J.; Chen, B. H. Synthesis of Different Ruthenium Nickel Bimetallic Nanostructures and an Investigation of the Structure-Activity Relationship for Benzene Hydrogenation to Cyclohexane. *ChemCatChem* **2014**, *6* (7), 2039. https://doi.org/10.1002/cctc.201400096

(36) Bulut, S.; Siankevich, S.; van Muyden, A. P.; Alexander, D. T. L.; Savoglidis, G.; Zhang, J.; Hatzimanikatis, V.; Yan, N.; Dyson, P. J. Efficient Cleavage of Aryl Ether C–O Linkages by Rh–Ni and Ru–Ni Nanoscale Catalysts Operating in Water. *Chem. Sci.* **2018**, *9* (25), 5530. https://doi.org/10.1039/C8SC00742J

(37) Braos-García, P.; García-Sancho, C.; Infantes-Molina, A.; Rodríguez-Castellón, E.; Jiménez-López, A. Bimetallic Ru/Ni Supported Catalysts for the Gas Phase Hydrogenation of Acetonitrile. *Appl. Catal. Gen.* **2010**, *381* (1–2), 132. https://doi.org/10.1016/j.apcata.2010.03.061

(38) Amiens, C.; Ciuculescu-Pradines, D.; Philippot, K. Controlled Metal Nanostructures: Fertile Ground for Coordination Chemists. *Coord. Chem. Rev.* **2016**, *308*, 409. https://doi.org/10.1016/j.ccr.2015.07.013

(39) Qi, X.; Axet, M. R.; Philippot, K.; Lecante, P.; Serp, P. Seed-Mediated Synthesis of Bimetallic Ruthenium–Platinum Nanoparticles Efficient in Cinnamaldehyde Selective Hydrogenation. *Dalton Trans.* **2014**, *43* (24), 9283. https://doi.org/10.1039/C3DT53539H

(40) Braga, A. H.; Costa, N. J. S.; Philippot, K.; Gonçalves, R. V.; Szanyi, J.; Rossi, L. M. Structure and Activity of Supported Bimetallic NiPd Nanoparticles: Influence of Preparation Method on CO_2 Reduction. *ChemCatChem* **2020**, *12* (11), 2967. https://doi.org/10.1002/cctc.201902329

(41) de Silva, R. M.; Palshin, V.; de Silva, K. M. N.; Henry, L. L.; Kumar, C. S. S. R. A New Role for Surfactants in the Formation of Cobalt Nanoparticles. *J. Mater. Chem.* **2008**, *18* (7), 738. https://doi.org/10.1039/b714456c

(42) Liakakos, N.; Falqui, A.; Genovese, A.; Vendier, L.; Ko, S.; Soulantica, K. The Big Impact of a Small Detail: Cobalt Nanocrystal Polymorphism as a Result of Precursor Addition Rate during Stock Solution Preparation. *J. Am. Chem. Soc.* **2012**, *134* (43), 17922. https://doi.org/10.1021/ja304487b

(43) Heuer-Jungemann, A.; Feliu, N.; Bakaimi, I.; Hamaly, M.; Alkilany, A.; Chakraborty, I.; Masood, A.; Casula, M. F.; Kostopoulou, A.; Oh, E.; Susumu, K.; Stewart, M. H.; Medintz, I. L.; Stratakis, E.; Parak, W. J.; Kanaras, A. G. The Role of Ligands in the Chemical Synthesis and Applications of Inorganic Nanoparticles. *Chem. Rev.* **2019**, *119* (8), 4819. https://doi.org/10.1021/acs.chemrev.8b00733

(44) Lara, P.; Casanove, M.-J.; Lecante, P.; Fazzini, P.-F.; Philippot, K.; Chaudret, B. Segregation at a Small Scale: Synthesis of Core–Shell Bimetallic RuPt Nanoparticles, Characterization and Solid State NMR Studies. *J. Mater. Chem.* **2012**, *22* (8), 3578. https://doi.org/10.1039/c2jm14757b

(45) Lara, P.; Ayvalı, T.; Casanove, M.-J.; Lecante, P.; Mayoral, A.; Fazzini, P.-F.; Philippot, K.; Chaudret, B. On the Influence of Diphosphine Ligands on the Chemical Order in Small RuPt Nanoparticles: Combined Structural and Surface Reactivity Studies. *Dalton Trans.* **2013**, *42* (2), 372. https://doi.org/10.1039/C2DT31646C

(46) Zaramello, L.; Albuquerque, B. L.; Domingos, J. B.; Philippot, K. Kinetic Investigation into the Chemoselective Hydrogenation of α,β-Unsaturated Carbonyl Compounds Catalyzed by Ni(0) Nanoparticles. *Dalton Trans.* **2017**, *46*, 5082. https://doi.org/10.1039/C7DT00649G

(47) García-Antón, J.; Axet, M. R.; Jansat, S.; Philippot, K.; Chaudret, B.; Pery, T.; Buntkowsky, G.; Limbach, H.-H. Reactions of Olefins with Ruthenium Hydride Nanoparticles: NMR Characterization, Hydride Titration, and Room-Temperature C-C Bond Activation. *Angew. Chem. Int. Ed.* **2008**, *47* (11), 2074. https://doi.org/10.1002/anie.200704763

(48) Bergounhou, C.; Blandy, C.; Choukroun, R.; Lecante, P.; Lorber, C.; Pellegatta, J.-L. Catalytic Evidence of the Core/Shell Structure of Bimetallic Pd/Rh Colloids. *New J. Chem.*, **2007**, *31*, 218. https://doi.org/10.1039/B614910C

(49) Kelsen, V.; Meffre, A.; Fazzini, P.-F.; Lecante, P.; Chaudret, B. How to Modulate Catalytic Properties in Nanosystems: The Case of Iron-Ruthenium Nanoparticles. *ChemCatChem* **2014**, *6* (6), 1714. https://doi.org/10.1002/cctc.201300907

(50) Dinega, D. P.; Bawendi, M. G. A Solution-Phase Chemical Approach to a New Crystal Structure of Cobalt. *Angew. Chem. Int. Ed.* **1999**, *38* (12), 1788. https://doi.org/10.1002/(SICI)1521-3773(19990614)38:12%3C1788::AID-ANIE1788%3E3.0.CO;2-2

(51) Dassenoy, F. Experimental Evidence of Structural Evolution in Ultrafine Cobalt Particles Stabilized in Different Polymers-From a Polytetrahedral Arrangement to the Hexagonal Structure. J. Chem. Phys. **2000**, 112, 8137 https://doi.org/10.1063/1.481414

(52) Margeat, O.; Respaud, M.; Amiens, C.; Lecante, P.; Chaudret, B. Ultrafine Metallic Fe Nanoparticles: Synthesis, Structure and Magnetism. *Beilstein J. Nanotechnol.* **2010**, *1*, 108. https://doi.org/10.3762/bjnano.1.13

(53) Bonnefille, E.; Novio, F.; Gutmann, T.; Poteau, R.; Lecante, P.; Jumas, J.-C.; Philippot, K.; Chaudret, B. Tin-Decorated Ruthenium Nanoparticles: A Way to Tune Selectivity in Hydrogenation Reaction. *Nanoscale* **2014**, *6* (16), 9806. https://doi.org/10.1039/C4NR00791C

(54) Choukroun, R.; de Caro, D.; Chaudret, B.; Lecante, P.; Snoeck, E. H_2-Induced Structural Evolution in Non-Crystalline Rhodium Nanoparticles. *New J. Chem.* **2001**, *25* (4), 525. https://doi.org/10.1039/b009192h

(55) Rao, V.; Latha, P.; Ashokan, P. V.; Shridhar, M. H. Thermal Degradation of Poly(N-Vinylpyrrolidone)–Poly(Vinyl Alcohol) Blends. *Polym. J.* **1999**, *31* (10), 887. https://doi.org/10.1295/polymj.31.887

(56) Yang, C.; Wöll, C. IR Spectroscopy Applied to Metal Oxide Surfaces: Adsorbate Vibrations and Beyond. *Adv. Phys. X* **2017**, *2* (2), 373. https://doi.org/10.1080/23746149.2017.1296372

(57) Novio, F.; Philippot, K.; Chaudret, B. Location and Dynamics of CO Co-ordination on Ru Nanoparticles: A Solid State NMR Study. *Catal. Lett.* **2010**, *140* (1–2), 1. https://doi.org/10.1007/s10562-010-0428-7

(58) Axet, M. R.; Conejero, S.; Gerber, I. C. Ligand Effects on the Selective Hydrogenation of Nitrobenzene to Cyclohexylamine Using Ruthenium Nanoparticles as Catalysts. *ACS Appl. Nano Mater.* **2018**, *1* (10), 5885. https://doi.org/10.1021/acsanm.8b01549
(59) Min, Y.; Nasrallah, H.; Poinsot, D.; Lecante, P.; Tison, Y.; Martinez, H.; Roblin, P.; Falqui, A.; Poteau, R.; del Rosal, I.; Gerber, I. C.; Hierso, J.-C.; Axet, M. R.; Serp, P. 3D Ruthenium Nanoparticle Covalent Assemblies from Polymantane Ligands for Confined Catalysis. *Chem. Mater.* **2020**, *32* (6), 2365. https://doi.org/10.1021/acs.chemmater.9b04737
(60) Jones, L. H. Infrared Spectrum of Solid $Ni(CO)_4$. *Spectrochim. Acta* **1963**, *19* (11), 1899. https://doi.org/10.1016/0371-1951(63)80207-6
(61) Arblaster, J. W. Crystallographic Properties of Ruthenium. *Platin. Met. Rev.* **2013**, *57* (2), 127. https://doi.org/10.1595/147106713X665030
(62) Wang, T.; Chen, L.-Q.; Liu, Z.-K. Lattice Parameters and Local Lattice Distortions in Fcc-Ni Solutions. *Metall. Mater. Trans. A* **2007**, *38* (3), 562. https://doi.org/10.1007/s11661-007-9091-z
(63) Roy, A.; Srinivas, V.; Ram, S.; Rao, T. V. C. The Effect of Silver Coating on Magnetic Properties of Oxygen-Stabilized Tetragonal Ni Nanoparticles Prepared by Chemical Reduction. *J. Phys. Condens. Matter* **2007**, *19*, 346220. https://doi.org/10.1088/0953-8984/19/34/346220
(64) He, X.; Zhong, W.; Au, C.-T.; Du, Y. Size Dependence of the Magnetic Properties of Ni Nanoparticles Prepared by Thermal Decomposition Method. **2013**, *8* (1), 446. https://doi.org/10.1186/1556-276X-8-446
(65) Jacobs, R. L. A Calculation of the Magnetisation of Alloys of Ni with Rh, Ru, Ir and Os. *J. Phys. F: Met. Phys.,* **1982**, *12*, 517. https://doi.org/10.1088/0305-4608/12/3/017
(66) Michelutti, B.; Perrier de la Bathie, R.; du Tremolet de Lacheisserie, E.; Waintal, A. Magnetization, Magnetocrystalline Anisotropy, Magnetostriction and Elastic Constants of a Ruthenium-Nickel Single Crystal. *Solid State Commun.* **1978**, *28* (10), 879. https://doi.org/10.1016/0038-1098(78)90178-3
(67) Cao, N.; Su, J.; Luo, W.; Cheng, G. Hydrolytic Dehydrogenation of Ammonia Borane and Methylamine Borane Catalyzed by Graphene Supported Ru@Ni Core–Shell Nanoparticles. *Int. J. Hydrog. Energy* **2014**, *39* (1), 426. https://doi.org/10.1016/j.ijhydene.2013.10.059
(68) Deng, S.; Pingali, K. C.; Rockstraw, D. A. Synthesis of Ru-Ni Core-Shell Nanoparticles for Potential Sensor Applications. *IEEE Sens. J.* **2008**, *8* (6), 730. https://doi.org/10.1109/JSEN.2008.923041
(69) Pingali, K. C.; Deng, S.; Rockstraw, D. A. Synthesis and Thermal Stability of Carbon-Supported Ru–Ni Core-and-Shell Nanoparticles. *Powder Technol.* **2008**, *187* (1), 19. https://doi.org/10.1016/j.powtec.2007.12.018
(70) Cho, Y.-J.; Kim, S.-Y.; Cha, H. W.; Seo, B. S.; Kim, C. H.; Son, H.-J.; Kang, S. O. Elucidation of Excited-State Properties of Bimetallic Ir(III)–Pt(II) Complexes with Conjugated Bridging Ligands. *J. Phys. Chem. C* **2018**, *122* (41), 23288. https://doi.org/10.1021/acs.jpcc.8b06665
(71) Wagner, A. T.; Zhou, R.; Quinn, K. S.; White, T. A.; Wang, J.; Brewer, K. J. Tuning the Photophysical Properties of Ru(II) Monometallic and Ru(II), Rh(III) Bimetallic Supramolecular Complexes by Selective Ligand Deuteration. *J. Phys. Chem. A* **2015**, *119* (26), 6781. https://doi.org/10.1021/acs.jpca.5b02836
(72) Kartashova, K.; Mallet-Ladeira, S.; Axet, M. R. Synthesis of a Bimetallic P–N Bridged rhodium (I)-ruthenium (II) Complex: Application in the Hydroformylation Reaction. *J. Organomet. Chem.* **2015**, *799–800*, 226. https://doi.org/10.1016/j.jorganchem.2015.09.033
(73) Calhorda, M. J.; Ceamanos, C.; Crespo, O.; Gimeno, M. C.; Laguna, A.; Larraz, C.; Vaz, P. D.; Villacampa, M. D. Heteropolynuclear Gold Complexes with Metallophilic Interactions: Modulation of the Luminescent Properties. *Inorg. Chem.* **2010**, *49* (18), 8255. https://doi.org/10.1021/ic100413x
(74) García-Álvarez, R.; García-Garrido, S. E.; Díez, J.; Crochet, P.; Cadierno, V. Arene-Ruthenium(II) and Bis(Allyl)-Ruthenium(IV) Complexes Containing

2-(Diphenylphosphanyl)Pyridine Ligands: Potential Catalysts for Nitrile Hydration Reactions? *Eur. J. Inorg. Chem.* **2012**, *2012* (26), 4218. https://doi.org/10.1002/ejic.201200592

(75) Kumar, P.; Singh, A. K.; Pandey, R.; Pandey, D. S. Bio-Catalysts and Catalysts Based on Ruthenium(II) Polypyridyl Complexes Imparting Diphenyl-(2-Pyridyl)-Phosphine as a Co-Ligand. *J. Organomet. Chem.* **2011**, *696* (22), 3454. https://doi.org/10.1016/j.jorganchem.2011.06.031

(76) Angoy, M.; Jiménez, M. V.; Modrego, F. J.; Oro, L. A.; Passarelli, V.; Pérez-Torrente, J. J. Mechanistic Investigation on the Polymerization of Phenylacetylene by 2-Diphenylphosphinopyridine Rhodium(I) Catalysts: Understanding the Role of the Co-catalyst and Alkynyl Intermediates. *Organometallics* **2018**, *37* (16), 2778. https://doi.org/10.1021/acs.organomet.8b00430

(77) Nishide, K.; Ito, S.; Yoshifuji, M. Preparation of Carbonyltungsten(0) Complexes of 2-Pyridylphosphines Showing a Stepwise Coordination Pattern by Way of Monodentate to Chelate Mode. *J. Organomet. Chem.* **2003**, *682* (1–2), 79. https://doi.org/10.1016/S0022-328X(03)00698-3

(78) Grazia Arena, C.; Rotondo, E.; Faraone, F.; Lanfranchi, M.; Tiripicchio, A. Steric Effects of the 2-(Diphenylphosphino)Pyridine Bridging Ligand in the Synthesis of Binuclear Rhodium-Palladium Complexes. Crystal Structures of $[(CN^tBu)_2Cl_2Rh(\mu\text{-}Ph_2PPy)Pd(\mu\text{-}Cl)]_2$ and $[(C_8H_{12})Rh(\mu\text{-}Cl)(\mu\text{-}Ph_2PPy)PdCl_2]$. *Organometallics* **1991**, *10* (11), 3877. https://doi.org/10.1021/om00057a018

(79) Maciejewski, H.; Sydor, A.; Marciniec, B.; Kubicki, M.; Hitchcock, P. B. Intermediates in Nickel(0)–Phosphine Complex Catalyzed Dehydrogenative Silylation of Olefins. *Inorganica Chim. Acta* **2006**, *359* (9), 2989. https://doi.org/10.1016/j.ica.2005.12.067

(80) Asensio, J. M.; Tricard, S.; Coppel, Y.; Andrés, R.; Chaudret, B.; de Jesús, E. Synthesis of Water-Soluble Palladium Nanoparticles Stabilized by Sulfonated N-Heterocyclic Carbenes. *Chem. - Eur. J.* **2017**, *23* (54), 13435. https://doi.org/10.1002/chem.201702204

(81) Gutmann, T.; Bonnefille, E.; Breitzke, H.; Debouttière, P.-J.; Philippot, K.; Poteau, R.; Buntkowsky, G.; Chaudret, B. Investigation of the Surface Chemistry of Phosphine-Stabilized Ruthenium Nanoparticles – an Advanced Solid-State NMR Study. *Phys. Chem. Chem. Phys.* **2013**, *15* (40), 17383. https://doi.org/10.1039/c3cp52927d

(82) Debouttière, P.; Coppel, Y.; Denicourt-Nowicki, A.; Roucoux, A.; Chaudret, B.; Philippot, K. PTA-Stabilized Ruthenium and Platinum Nanoparticles: Characterization and Investigation in Aqueous Biphasic Hydrogenation Catalysis. *Eur. J. Inorg. Chem.* **2012**, *2012* (8), 1229. https://doi.org/10.1002/ejic.201101159

(83) Olah, G. A.; Ramaiah, P.; Rao, C. B.; Sandford, G.; Golam, R.; Trivedi, N. J.; Olah, J. A. Electrophilic Reactions at Single Bonds. 25. Nitration of Adamantane and Diamantane with Nitronium Tetrafluoroborate. *J. Am. Chem. Soc.* **1993**, *115* (16), 7246. https://doi.org/10.1021/ja00069a024

(84) Moncea, O.; Gunawan, M. A.; Poinsot, D.; Cattey, H.; Becker, J.; Yurchenko, R. I.; Butova, E. D.; Hausmann, H.; Šekutor, M.; Fokin, A. A.; Hierso, J.-C.; Schreiner, P. R. Defying Stereotypes with Nanodiamonds: Stable Primary Diamondoid Phosphines. *J. Org. Chem.* **2016**, *81* (19), 8759. https://doi.org/10.1021/acs.joc.6b01219

(85) Nasrallah, H.; Hierso, J.-C. Porous Materials Based on 3-Dimensional Td-Directing Functionalized Adamantane Scaffolds and Applied as Recyclable Catalysts. *Chem. Mater.* **2019**, *31* (3), 619. https://doi.org/10.1021/acs.chemmater.8b04508

(86) Schwertfeger, H.; Fokin, A. A.; Schreiner, P. R. Diamonds Are a Chemist's Best Friend: Diamondoid Chemistry Beyond Adamantane. *Angew. Chem. Int. Ed.* **2008**, *47* (6), 1022. https://doi.org/10.1002/anie.200701684

(87) Gunawan, M. A.; Hierso, J.-C.; Poinsot, D.; Fokin, A. A.; Fokina, N. A.; Tkachenko, B. A.; Schreiner, P. R. Diamondoids: Functionalization and Subsequent Applications of Perfectly Defined Molecular Cage Hydrocarbons. *New J Chem* **2014**, *38* (1), 28. https://doi.org/10.1039/C3NJ00535F

(88) Huang, B.; Kobayashi, H.; Yamamoto, T.; Toriyama, T.; Matsumura, S.; Nishida, Y.; Sato, K.; Nagaoka, K.; Haneda, M.; Xie, W.; Nanba, Y.; Koyama, M.; Wang, F.; Kawa-

guchi, S.; Kubota, Y.; Kitagawa, H. A CO Adsorption Site Change Induced by Copper Substitution in a Ruthenium Catalyst for Enhanced CO Oxidation Activity. *Angew. Chem. Int. Ed.* **2019**, *58* (8), 2230. https://doi.org/10.1002/anie.201812325

(89) Fukuda, R.; Takagi, N.; Sakaki, S.; Ehara, M. Structures of Bimetallic Copper–Ruthenium Nanoparticles: Incoherent Interface and Surface Active Sites for Catalytic Nitric Oxide Dissociation. *J. Phys. Chem. C* **2017**, *121* (1), 300. https://doi.org/10.1021/acs.jpcc.6b09280

(90) Wu, Q.; Luo, M.; Han, J.; Peng, W.; Zhao, Y.; Chen, D.; Peng, M.; Liu, J.; de Groot, F. M. F.; Tan, Y. Identifying Electrocatalytic Sites of the Nanoporous Copper–Ruthenium Alloy for Hydrogen Evolution Reaction in Alkaline Electrolyte. *ACS Energy Lett.* **2020**, *5* (1), 192. https://doi.org/10.1021/acsenergylett.9b02374

(91) Huang, B.; Kobayashi, H.; Yamamoto, T.; Matsumura, S.; Nishida, Y.; Sato, K.; Nagaoka, K.; Haneda, M.; Kawaguchi, S.; Kubota, Y.; Kitagawa, H. Coreduction Methodology for Immiscible Alloys of CuRu Solid-Solution Nanoparticles with High Thermal Stability and Versatile Exhaust Purification Ability. *Chem. Sci.* **2020**, *11* (42), 11413. https://doi.org/10.1039/D0SC03373A

(92) Kim, C.; Song, J.; Choi, C.; Ha, J. P.; Lee, W.; Nam, Y. T.; Lee, D.; Kim, G.; Gereige, I.; Jung, W.; Lee, H.; Jung, Y.; Jeong, H.; Jung, H. Atomic-Scale Homogeneous Ru-Cu Alloy Nanoparticles for Highly Efficient Electrocatalytic Nitrogen Reduction. *Adv. Mater.* **2022**, *34* (40), 2205270. https://doi.org/10.1002/adma.202205270

(93) Dang-Bao, T.; Pradel, C.; Favier, I.; Gómez, M. Making Copper(0) Nanoparticles in Glycerol: A Straightforward Synthesis for a Multipurpose Catalyst. *Adv. Synth. Catal.* **2017**, *359* (16), 2832. https://doi.org/10.1002/adsc.201700535

(94) Barrière, C.; Piettre, K.; Latour, V.; Margeat, O.; Turrin, C.-O.; Chaudret, B.; Fau, P. Ligand Effects on the Air Stability of Coppernanoparticles Obtained from Organometallic Synthesis. *J. Mater. Chem.* **2012**, *22* (5), 2279. https://doi.org/10.1039/C2JM14963J

(95) Hung, L.-I.; Tsung, C.-K.; Huang, W.; Yang, P. Room-Temperature Formation of Hollow Cu_2O Nanoparticles. *Adv. Mater.* **2010**, *22* (17), 1910. https://doi.org/10.1002/adma.200903947

(96) Lee, J.-G.; Nakamura, R.; Choi, Y.-S.; Yu, J.-H.; Choi, C.-J. Formation of Hollow Copper Oxide by Oxidation of Cu Nanoparticles. *Curr. Nanosci.* **2014**, *10* (1), 101. https://doi.org/10.2174/15734137096661311082326 54

(97) Lee, J.; Kim, S. M.; Lee, I. S. Functionalization of Hollow Nanoparticles for Nanoreactor Applications. *Nano Today* **2014**, *9* (5), 631. https://doi.org/10.1016/j.nantod.2014.09.003

(98) Soroka, I. L.; Tarakina, N. V.; Korzhavyi, P. A.; Stepanenko, V.; Jonsson, M. Effect of Synthesis Temperature on the Morphology and Stability of Copper(I) Hydride Nanoparticles. *CrystEngComm* **2013**, *15* (42), 8450. https://doi.org/10.1039/c3ce41303a

(99) Hassan Basri, H.; Talib, R. A.; Sukor, R.; Othman, S. H.; Ariffin, H. Effect of Synthesis Temperature on the Size of ZnO Nanoparticles Derived from Pineapple Peel Extract and Antibacterial Activity of ZnO–Starch Nanocomposite Films. *Nanomaterials* **2020**, *10* (6), 1061. https://doi.org/10.3390/nano10061061

(100) Manukyan, A.; Gyulasaryan, H.; Kocharian, A.; Estiphanos, M.; Bernal, O.; Sharoyan, E. Ferromagnetism and Giant Paramagnetism of Copper Nanoparticles in Cu_m/C Nanocomposites. *J. Magn. Magn. Mater.* **2019**, *488*, 165336. https://doi.org/10.1016/j.jmmm.2019.165336

(101) Fan, X.; Mashimo, T.; Huang, X.; Kagayama, T.; Chiba, A.; Koyama, K.; Motokawa, M. Magnetic Properties of Co-Cu Metastable Solid Solution Alloys. *Phys. Rev. B* **2004**, *69* (9), 094432. https://doi.org/10.1103/PhysRevB.69.094432

(102) Perakis, N.; Serres, A. Étude de la semi-conductivité de l'oxyde cuivreux d'après son comportement magnétique entre 80 et 1000K. *J. Phys. Radium* **1955**, *16* (5), 387. https://doi.org/10.1051/jphysrad:01955001605038701

(103) Chen, C.; He, L.; Lai, L.; Zhang, H.; Lu, J.; Guo, L.; Li, Y. Magnetic Properties of Undoped Cu_2O Fine Powders with Magnetic Impurities and/or Cation Vacancies. *J. Phys.*

Condens. Matter **2009**, *21* (14), 145601. https://doi.org/10.1088/0953-8984/21/14/145601

(104) Kale, S. N.; Ogale, S. B.; Shinde, S. R.; Sahasrabuddhe, M.; Kulkarni, V. N.; Greene, R. L.; Venkatesan, T. Magnetism in Cobalt-Doped Cu_2O Thin Films without and with Al, V, or Zn Codopants. *Appl. Phys. Lett.* **2003**, *82* (13), 2100. https://doi.org/10.1063/1.1564864

(105) Wei, M.; Braddon, N.; Zhi, D.; Midgley, P. A.; Chen, S. K.; Blamire, M. G.; MacManus-Driscoll, J. L. Room Temperature Ferromagnetism in Bulk Mn-Doped Cu_2O. *Appl. Phys. Lett.* **2005**, *86* (7), 072514. https://doi.org/10.1063/1.1869547

(106) Liu, Y. L.; Harrington, S.; Yates, K. A.; Wei, M.; Blamire, M. G.; MacManus-Driscoll, J. L.; Liu, Y. C. Epitaxial, Ferromagnetic $Cu_{2-x}Mn_xO$ Films on (001) Si by near-Room-Temperature Electrodeposition. *Appl. Phys. Lett.* **2005**, *87* (22), 222108. https://doi.org/10.1063/1.2136349

(107) Glaria, A.; Cure, J.; Piettre, K.; Coppel, Y.; Turrin, C.-O.; Chaudret, B.; Fau, P. Deciphering Ligands' Interaction with Cu and Cu_2O Nanocrystal Surfaces by NMR Solution Tools. *Chem. - Eur. J.* **2015**, *21* (3), 1169. https://doi.org/10.1002/chem.201403835

(108) Barrière, C.; Alcaraz, G.; Margeat, O.; Fau, P.; Quoirin, J. B.; Anceau, C.; Chaudret, B. Copper Nanoparticles and Organometallic Chemical Liquid Deposition (OMCLD) for Substrate Metallization. *J. Mater. Chem.* **2008**, *18* (26), 3084. https://doi.org/10.1039/b804460k

(109) Lee, H. O.; Vallejos, A. M.; Rimsza, J. M.; Chin, C. D.-W.; Ringgold, M.; Nicholas, J. R.; Treadwell, L. J. Understanding the Effects of Polar and Non-Polar Surfactants on the Oxidation Performance of Copper Nanoparticles. *J. Mater. Sci.* **2022**, *57* (11), 6167. https://doi.org/10.1007/s10853-022-07021-1

(110) Lyu, Z.; Shang, Y.; Xia, Y. Shape-Controlled Synthesis of Copper Nanocrystals for Plasmonic, Biomedical, and Electrocatalytic Applications. *Acc. Mater. Res.* **2022**, *3* (11), 1137. https://doi.org/10.1021/accountsmr.2c00134

CHAPTER 3: Catalytic hydrogenation reactions of furfural and quinoline

Summary

3.1 Introduction

In the context of energy transition, lignocellulosic biomass has appeared as a promising renewable feedstock to replace fossil fuels for chemicals and energy production.[1,2] Concerning energy production, biofuels can be produced from bio-oil, containing plenty of oxygenated groups, via hydrogenation or reduction reactions.[3] One of these reduction methods, the hydrotreatment, can be directly integrated in the industry by using the same petroleum upgrading infrastructure. However, one of its drawbacks is the use of high pressures and temperatures, which may induce catalyst coking, a deactivation process of heterogeneous catalysts.[4]

FF is a furan aldehyde which can be obtained from lignocellulosic biomass and possesses a great interest.[5] Many commercial applications have been described, such as pesticides, industrial manufacturing, food flavouring, pharmaceuticals and personal care products, bonding agent, phenolic resins or oil refining.[6,7] Moreover, as a platform molecule it can produce a vast of molecules such as furan, furfuryl alcohol (HF), tetrahydrofurfuryl alcohol (HMTHF), tetrahydrofuran (THF), 1,2-pentanediol (1,2-PeD), 1,5-pentanediol (1,5-PeD).[5,8,9]

FF hydrogenation has been previously reported on Pt/C catalyst at 175 ºC with 80 bar of H_2, obtaining full conversion and a 50 % selectivity towards HF;[10] on Ni-Fe-B catalyst at 200 ºC with 10 bar of H_2,[11] obtaining full conversion and full selectivity towards HF, results also obtained on Ni-Sn/TiO_2 at 110 ºC with 30 bar of H_2,[12] on Cu-Ca/SiO_2 at 130 ºC with 1 bar of H_2,[13] or on Ir-ReOx/SiO_2 at 30 ºC with 8 bar of H_2.[14]

QN is an N-heterocycle that can be found in natural products or pharmaceuticals, as it has a vast of biological activities, and its main use is the production of other chemicals. Some of the applications of QN and its derivatives are in the pharmaceutical industry, because of its antimalarial, anti-inflammatory, anticancer or antimicrobial activities,[15,16] but also are useful for the conception of photovoltaic cells.[17]

QN hydrogenation has been previously reported on Ru catalysts at 100 ºC with 10 bar of H_2, obtaining 97 % of conversion with a 98 % selectivity to 1,2,3,4-tetrahydroquinoline (1-THQ),[18] or at 20 ºC with ~ 40 bar of H_2, obtaining 90 % of conversion with a 64 % selectivity to 1-THQ;[19] or on Ni catalysts at 60 ºC with 20 bar of H_2, obtaining a 21 % of conversion being also 1-THQ the product obtained;[20] or on Pd catalysts at 50 ºC with 10 bar of H_2, obtaining full conversion and selectivity towards 1-THQ.[21]

3.2 Furfural hydrogenation using RuNi/PVP NPs as catalysts

The RuNi/PVP NPs, described in Chapter 2, were used as catalysts for the selective hydrogenation of FF (Scheme 1) at 125 ºC and a continuous pressure of 20 bar of H_2. A magnetic stirring set up at 1200 rpm discards mass transfer limitations. Monometallic Ru/PVP and Ni/PVP NPs were also evaluated in the same conditions for comparison purpose. All the experimental details are given in Chapter 6.

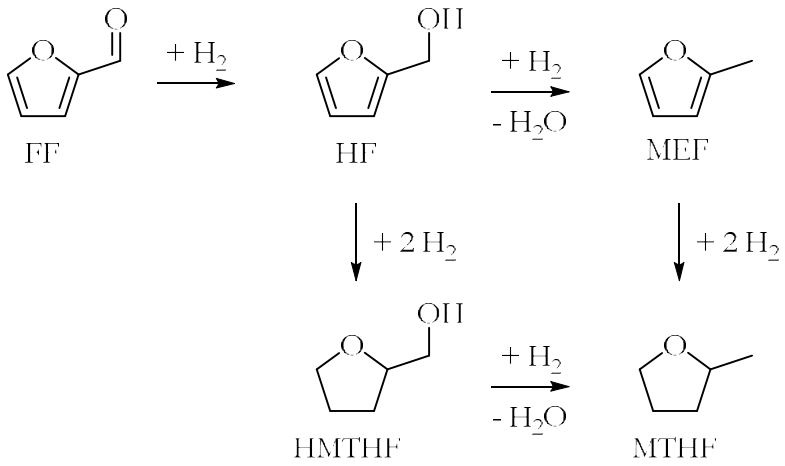

Scheme 1: Simplified reaction scheme of the selective catalytic hydrogenation of furfural into various valuable products. Furfural (FF), furfuryl alcohol (HF), tetrahydrofurfuryl alcohol (HMTHF), 2-methylfuran (MEF), and 2-methyltetrahydrofuran (MTHF).

Table 1 summarises the results of the FF hydrogenation obtained in THF for the different synthesised Ru, Ni and RuNi NPs, stabilised with polyvinylpyrrolidone (PVP). The associated time-concentration curves are represented in Figure 1.

Table 1: Selective hydrogenation of FF in THF using Ru, Ni and RuNi/PVP nanocatalysts.[a]

Entry	Catalyst	TOF (h^{-1})[b, c]	Time (h)	Conversion (%)[c]	HF (%)[c]	HMTHF (%)[c]
1	Ru/PVP	51	1	20	>99	<1
2			5	51	>99	<1
3			24	98	>99	<1
4			29	100	>99	<1
5	Ru_3Ni_1/PVP	52	1	16	98	2
6			5	33	98	2
7			24	93	98	2
8			29	98	92	8
9	Ru_1Ni_1/PVP	62	1	20	95	5
10			5	42	96	4
11			24	79	97	3
12			29	84	97	3
13	Ru_1Ni_3/PVP	51	1	18	92	8
14			5	42	93	7
15			24	85	94	6
16			29	89	94	6
17	Ru_1Ni_{20}/PVP	38	1	11	89	11
18			5	26	92	8
19			24	57	94	6
20			29	63	93	7
21	Ni/PVP	18[d]	1	9	79	21
22			5	24	84	16
23			24	44	85	15
24			29	49	72	27

[a]Reaction conditions: 2×10^{-2} mmol of metal, 4 mmol of FF, 0.5 mmol of decane (internal standard), 20 bar of H_2, 125 °C, 15 mL of THF. [b]Turnover frequency (TOFs) calculated at 1 h of reaction according to the surface amount of metal. [c]Determined by Gas Chromatography (GC) using an internal standard technique. [d]TOF calculated at 1 h of reaction according to the total metal content.

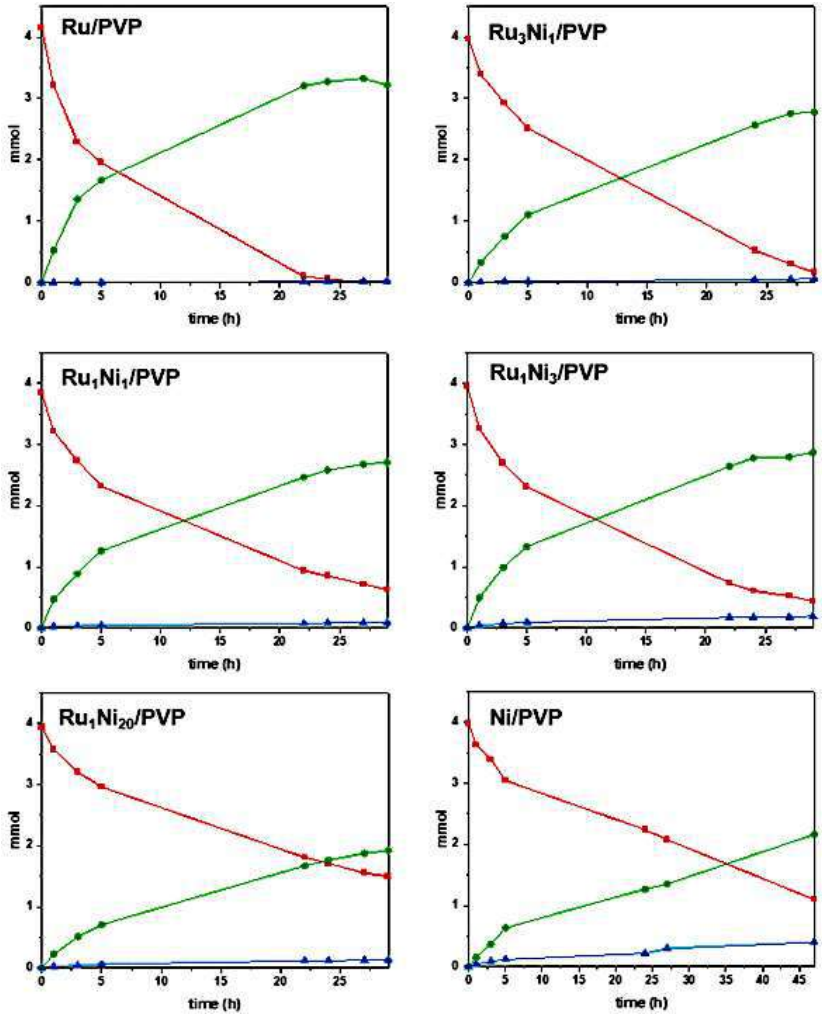

Figure 1: Time-concentration curves for the selective hydrogenation of FF in THF on all the catalysts (red square dots, FF; green circle dots, HF; blue triangle dots, HMTHF).

The results in Figure 1 evidence that the FF hydrogenation is highly selective to the hydrogenation of the aldehyde function, producing the alcohol HF as major product (72 % - 99 % of selectivity). With Ni-rich catalysts, further hydrogenation of the furfuryl ring is promoted resulting into the production of HMTHF (entries 17-24). Considering both activity and selectivity, the Ru/PVP NPs provide the best catalytic performance, reaching in less than 24 h full conversion and with a high selectivity (up to 99 %) towards HF. This result is in agreement with previously published works which showed high selectivity towards HF (up to 96 %) with Ru/PVP NPs at 30 °C.[22,23] In our case, higher reaction temperature (125 °C) was used, being interesting to point out that, even at this temperature, the hydrogenation is completely selective to the aldehyde function. An experiment using HF as the substrate was performed on Ru/PVP NPs in the same reaction conditions in order to better understand the high selectivity observed. Correspondingly, the associated time-concentration curve is depicted in Figure 2.

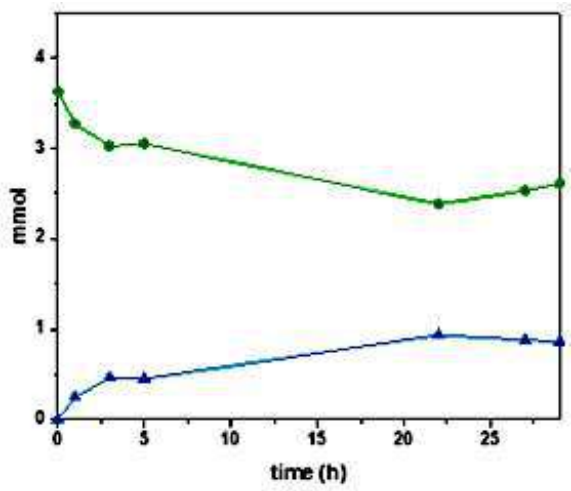

Figure 2: Time-concentration curves for the selective hydrogenation of HF in THF using Ru/PVP as catalyst (green circle dots, HF and blue triangle dots, HMTHF.

The results in Figure 2 evidence that the hydrogenation of the heteroatomic ring occurs, although it is less favoured than the reduction of the aldehyde moiety (turnover frequency (TOF) = 22 h^{-1} versus TOF = 51 h^{-1}). This can be explained by a weaker adsorption of the HF compared to the FF on the surface of the Ru/PVP NPs. This hypothesis is confirmed by density functional theory (DFT) calculations, detailed in Chapter 4, which revealed that the coordination of the C=O bond (η^1(O) or η^2(C=O)) on a hydrogenated Ru NP is favoured compared with the coordination of the heteroaromatic ring (-12.0 kcal·mol^{-1} *vs.* -7.1 kcal·mol^{-1}). This coordination facility of the aldehyde group agrees with the preference of hydrogenation of this function.

Significant solvent effects were observed for this catalytic system. The use of 1-propanol (1-PrOH) instead of THF revealed significant effects, showing high solvent dependency on the observed catalytic performances. Table 2 summarises the results of FF hydrogenation when using 1-PrOH as a solvent under the same catalytic conditions as those detailed above for THF. The associated time-concentration curves are presented in Figure 3.

Table 2: Selective hydrogenation of FF in 1-PrOH using Ru, Ni and RuNi/PVP nanocatalysts.[a]

Entry	Catalyst	TOF (h^{-1})[b, c]	Time (h)	Conversion (%)[c]	HF (%)[c]	HMTHF (%)[c]	Acetal (%)[c, d]
1	Ru/PVP	104 (77)	1	39	50	1	49
2			5	90	67	1	32
3			24	>99	51	18	28[e]
4			29	>99	41	26	28[e]
5	Ru_3Ni_1/PVP	110 (95)	1	34	83	2	15
6			5	71	81	2	17
7			24	>99	82	2	15
8			29	>99	78	2	19
9	Ru_1Ni_1/PVP	149 (137)	1	47	92	3	5
10			5	81	90	3	8
11			24	>99	89	3	8
12			29	>99	90	3	7
13	Ru_1Ni_3/PVP	110 (92)	1	40	95	4	1
14			5	71	94	4	2
15			24	96	93	4	3
16			29	97	93	4	3
17	Ru_1Ni_{20}/PVP	103 (103)	1	30	93	7	-
18			5	57	94	6	-
19			24	87	94	6	-
20			29	90	94	6	-
21	Ni/PVP	31[f]	1	15	99	1	-
22			5	43	88	6	6
23			24	88	83	5	12
24			29	93	83	5	12

[a]Reaction conditions: 2×10^{-2} mmol of metal, 4 mmol of FF, 0.5 mmol of decane (internal standard), 20 bar of H_2, 125 °C, 15 mL of 1-propanol. [b]TOFs calculated at 1 h of reaction according to the surface amount of metal; in brackets: TOFs of hydrogenation reaction. [c]Determined by GC using an internal standard technique. [d]Determined by Gas Chromatography-Mass Spectroscopy (GC-MS).[e]1,2 pentanediol also detected. [f]TOF calculated at 1 h of reaction according to the total amount of metal.

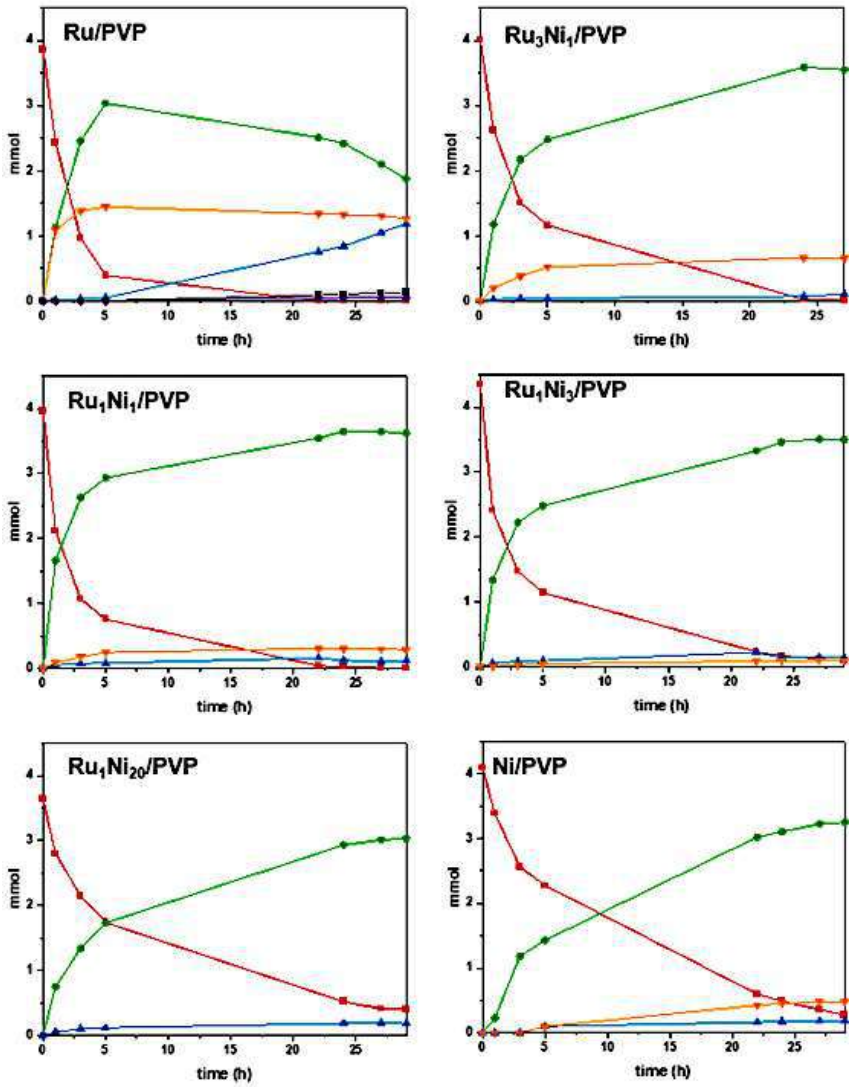

Figure 3: Time-concentration curves for the selective hydrogenation of FF in 1-PrOH on all the catalysts (red square dots, FF; green circle dots, HF; blue triangle dots, HMTHF; orange inversed triangle dots, acetal).

The TOF values are in all cases higher in 1-PrOH than in THF (Table 1 *vs.* Table 2), but this higher performance cannot be attributed to a better solubility of H_2 in 1-PrOH compared to THF.[24–26] Furthermore, it can be pointed out the formation of acetal on Ru-rich NPs, where Ru is present at the surface (Table 2, entries 1-8). DFT calculations, discussed in Chapter 4, support these results evidencing that the presence of propanolate species adsorbed on the surface of the hydrogenated Ru NP can induce higher activities.

The TOF displayed by Ru_1Ni_{20}/PVP in 1-PrOH is three times greater than in THF (Table 1, entry 17 *vs.* Table 2, entry 17) while the TOF values of all the other Ni-containing catalyst are increased *ca.* by twice. Concerning the monometallic Ru/PVP NPs, a beneficial effect of the 1-PrOH was also observed, being also in this case the TOF values higher by a factor of 2 when compared to THF (Tables 1, entry 1 *vs.* Table 2, entry 1). This catalyst was able to

catalyse the formation of acetal, which drops the selectivity into HF. This reaction is in competition with the FF hydrogenation and, interestingly, it is related to the Ru loading (Ru/PVP, Ru_3Ni_1/PVP, and Ru_1Ni_1/PVP). Indeed, on catalysts with only Ni at the surface Ru_1Ni_3/PVP and Ru_1Ni_{20}/PVP NPs, the acetalisation reaction is not observed. Comparing the obtained results, a good correlation between the amount of acetal formed during the reaction and the Ru present on the surface of the NPs is found; 1.5 mmol of acetal were produced on monometallic Ru/PVP *vs.* 0.5 and 0.3 mmol on Ru_3Ni_1/PVP, and Ru_1Ni_1/PVP respectively. These values correlate better with the Ru content on the NP surface than with the total Ru amount in the catalysts. Moreover, apart from the Ru content on the surface, these results may also be assigned to electronic effects, compared to literature. Being Ru/PVP an electron-deficient nanocatalyst,[27] acetalisation reactions[28,29] can occur. When increasing the Ni content in the NPs, the Ru electron density[30] is increased which has the effect of eliminating or lowering the acetal formation.

Apart from the acetal byproduct formation, the use of 1-PrOH is detrimental for the selectivity into HF as it promotes the hydrogenation of the heteroaromatic ring, which was impeded when using THF. In Chapter 4, the difference of coordination ability of the aromatic ring in THF and 1-PrOH is discussed, being the latter the most favoured, which is in line with the experimental results. The hydrogenation of HF on Ru/PVP in 1-PrOH was separately studied, using the same reaction conditions as described above. Figure 4 displays the corresponding time-concentration curves.

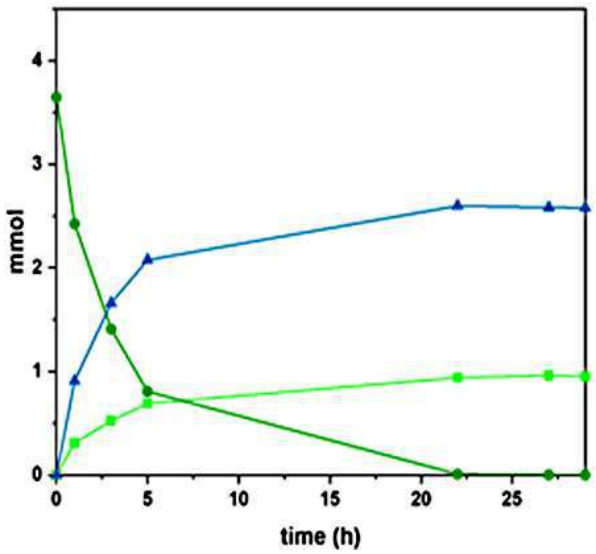

Figure 4: Time-concentration curves for the selective hydrogenation of HF in 1-PrOH using Ru/PVP as catalyst (green circle dots, HF; blue triangle dots, HMTHF; bright green square dots, 1,2-PeD).

In this experiment, the heteroaromatic ring was efficiently reduced with a TOF value of 79 h^{-1}, similar to the TOF value for the hydrogenation of the aldehyde moiety (TOF = 77 h^{-1}),

evidencing a similar affinity for the Ru metallic surface in both cases. Comparing this TOF value to the one obtained in THF (Figure 2, TOF = 22 h^{-1}), it can be concluded that 1-PrOH facilitates the ring hydrogenation. Also, the C-O bond cleavage of the aromatic ring occurs, leading to the production of 1,2-PeD in a selectivity of 27 %, similar to some results already described for Ru-Mn,[31] Ru/MnO_x[32] and Ru/Al_2O_3[33]. [33] Ru/PVP modified with a long alkyl chain amine was able to produce 1,2-PeD directly from FF as well, in relatively high yields (36 %).[34]

Figure 5 compares the TOF values and selectivities towards HF in both solvents (THF and 1-PrOH) for all catalysts tested. A volcano shape tendency is displayed for the activity, centred on Ru_1Ni_1/PVP, which points to a synergetic effect between both metals. Monometallic Ni/PVP was a slow catalyst compared to all the other ones, which could be explained by the size and shape of the NPs (5.6 ± 1.2 nm trigonal NPs). Moreover, concerning the selectivity to HF, the Ni/PVP was the catalyst with the lowest performance among all the tested ones, as HMTHF was produced since the beginning of the reaction.

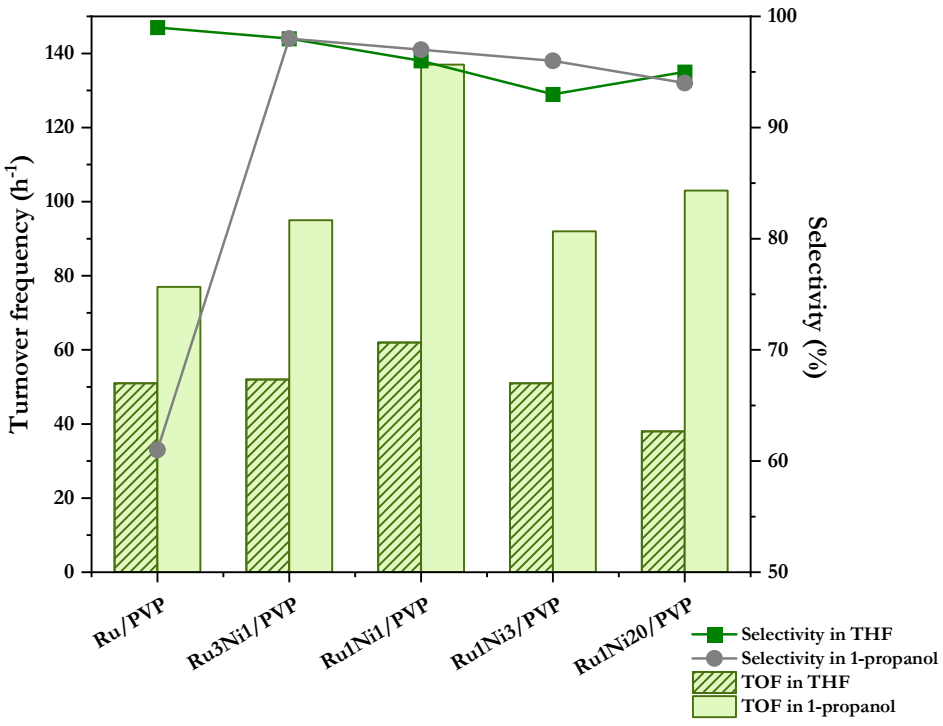

Figure 5: Turnover frequency (bars) and selectivity towards HF(dots) as function of the catalysts in the selective hydrogenation of FF in THF (dashed bars, square dots) and 1-PrOH (green bars, circle dots).

Comparing the Ni/PVP and the Ru_1Ni_{20}/PVP, it is important to highlight that the reaction is size-sensitive. The bimetallic Ru_1Ni_{20}/PVP NPs, which have a high Ni content (17.6 % in mass) and a mean size of 1.4 ± 0.3 nm, display 94 % of selectivity towards HF at *ca.* 57 % of conversion. The monometallic Ni/PVP, with a higher size and different shape, reached

only 72 % of selectivity to HF at *ca.* 49 % of conversion (Table 1). These results pointing out selectivity size dependence in THF may be of interest to obtain other interesting products such as MEF from FF or DMF from 2,5-hydroxymethylfurfural (HMF). The results obtained indicate that NPs of less than 2 nm are, in THF, less suitable for the hydrogenation of the aromatic ring, although in 1-PrOH (Table 2), almost the same selectivity to HMTHF was obtained for all the Ni-containing catalysts. Regarding the catalytic reactions, size effects of NPs have already been reported in the past.[35,36] In the case of FF hydrogenation, size effects have also been previously described,[37] specially for the hydrogenation of aldehyde function of FF on Pt NPs[38] and Cu nanowires,[39] without reaching the hydrogenation of the aromatic ring. Furthermore, FF hydrogenation towards HMTHF is structure-sensitive as was observed on a series of Ni/SiO_2 catalysts with sizes from 2.6 to 12.8 nm. In larger Ni NPs, such as Ni/PVP, lower TOF values were obtained, meaning that in small NPs, the reduction of the aromatic ring was favoured.[40] Even if it could seem that the results in this publication are opposed to our results, it is worth to mention that the large NPs described in this work have a 12 nm size and the small NPs are between 2.6 nm to 5.0 nm, which corresponds more to the mean size of our Ni/PVP NPs.

Ru_1Ni_1/PVP NPs represented the perfect equilibrium between activity and selectivity, showing the highest TOF value with almost no ring hydrogenation and acetal formation. It is also important to highlight the catalytic performance of the Ru_1Ni_{20}/PVP NPs, regarding the high content of Ni present in the NP and the decrease of size compared to monometallic Ni/PVP NPs.

The spent nanocatalysts were analysed by transition electron microscopy (TEM) and the resulting catalytic solutions were filtered through an alumina path, evaporated until dryness and analysed by ICP. ICP results showed no leaching for the series of catalytic reactions performed in THF. Concerning the analyses of the catalysis in 1-PrOH, Ru and Ni were detected under the detection limit, except in the case of the Ru_1Ni_{20}/PVP NPs, for which ICP results evidenced a 15 % of catalyst leaching. This behaviour is attributed to the good solubility of PVP in 1-PrOH, which disfavours the catalyst separation. For the same reason, the catalyst recycling tests performed were not successful, being the separation of the catalysts complicated in both solvents. Hot filtration experiments, consisting on filtering the catalysts from the reaction media after 1 h of reaction and reengaging the filtrate in catalysis under the same reaction conditions, showed that no additional products were obtained, evidencing the heterogeneous nature of the used Ru_1Ni_1/PVP catalyst (Figure 6).

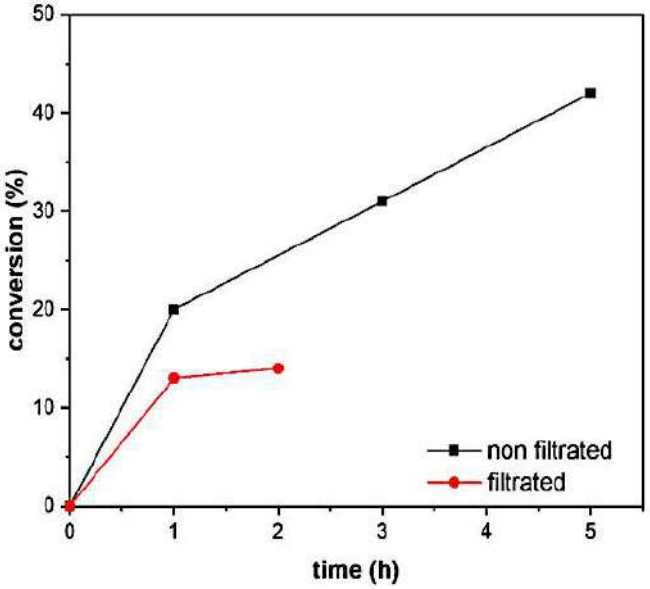

Figure 6: Time-conversion curves for the hot filtration experiment of the selective hydrogenation of FF in THF on Ru_1Ni_1/PVP catalyst in a non-filtered reaction (grey square dots) and in a filtered reaction (red circle dots).

TEM analyses after catalysis do not display any significant changes in whether size or shape, with the exception of the Ru_1Ni_{20}/PVP NPs when using 1-PrOH (Table3 and Figures 7 to 18). In 1-PrOH, this catalyst showed a broadening size distribution, which may be correlated to the high leaching observed for this catalyst, increasing the NP size probably due to Ostwald ripening. The size and the shape of the monometallic Ni/PVP NPs also evolved during the reaction although it is a more robust catalyst as no leaching was detected in this case. The size evolution observed for Ni/PVP and Ru_1Ni_{20}/PVP catalysts evidences that, in the other systems, the Ru stabilises the Ni atoms on the surface of the NPs, being an advantage for avoiding leaching in catalytic hydrogenations in liquid-phase.[41]

Table 3: Mean size of metal NPs before and after catalysis.

NP	Mean size before catalysis (nm)[a]	Mean size after catalysis in THF (nm)[a]	Mean size after catalysis in 1-PrOH (nm)[a]
Ru/PVP	1.1 ± 0.2	1.6 ± 0.3	1.5 ± 0.3
Ni/PVP	5.5 ± 1.2[b]	4.4 ± 0.5[c]	4.7 ± 1.6[c]
Ru_3Ni_1/PVP	1.5 ± 0.3	1.4 ± 0.4	1.6 ± 0.5
Ru_1Ni_1/PVP	1.5 ± 0.3	1.5 ± 0.4	1.4 ± 0.4
Ru_1Ni_3/PVP	1.2 ± 0.2	1.3 ± 0.3	1.5 ± 0.6
Ru_1Ni_{20}/PVP	1.4 ± 0.3	1.6 ± 0.3	2.2 ± 0.8

[a]Mean values of NP size determined from TEM images by considering at least 200 particles. [b]Tripodal shaped NPs. [c]Irregularly shaped NPs.

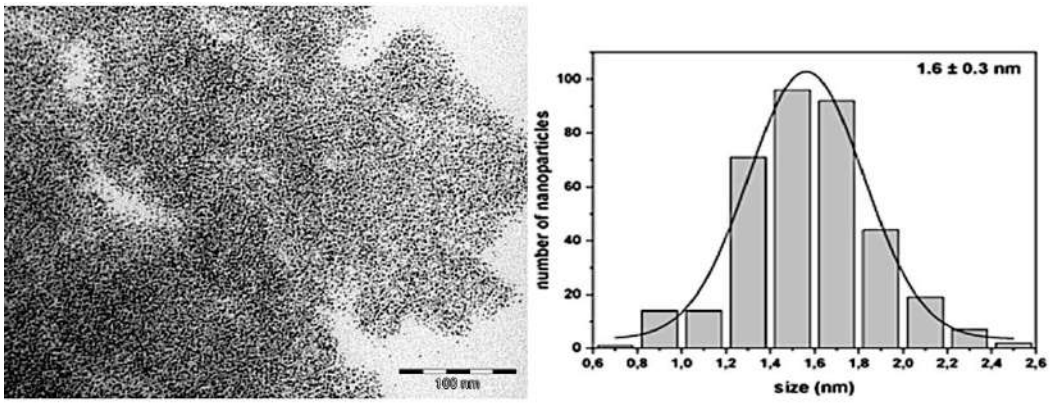

Figure 7: TEM image of Ru/PVP after catalysis in THF (scale bar 100 nm) together with the respective size histogram.

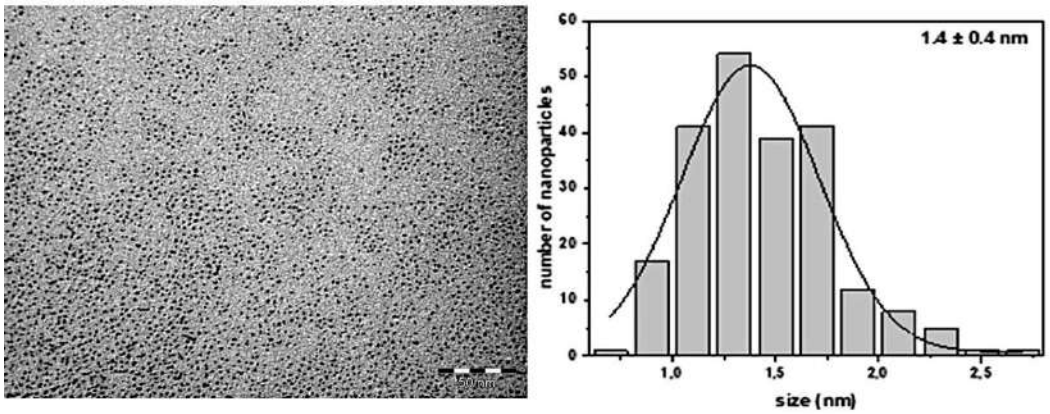

Figure 8: TEM image of Ru_3Ni_1/PVP after catalysis in THF (scale bar 50 nm) together with the respective size histogram.

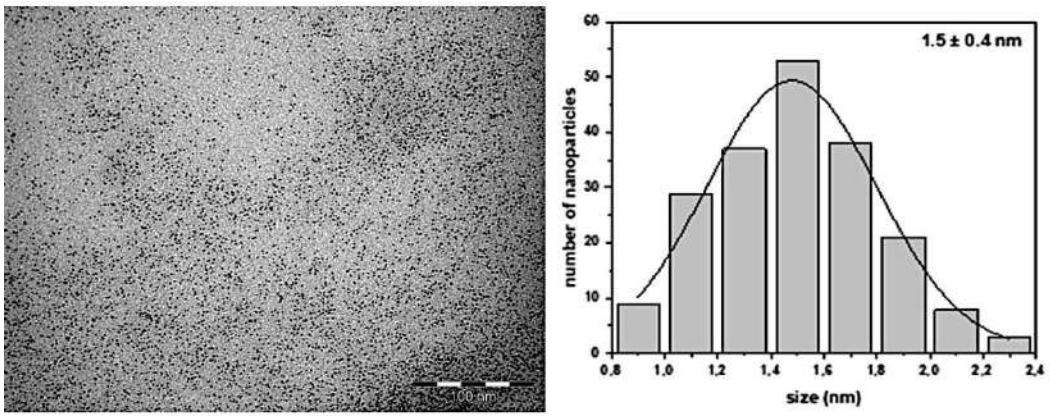

Figure 9: TEM image of Ru_1Ni_1/PVP after catalysis in THF (scale bar 100 nm) together with the respective size histogram.

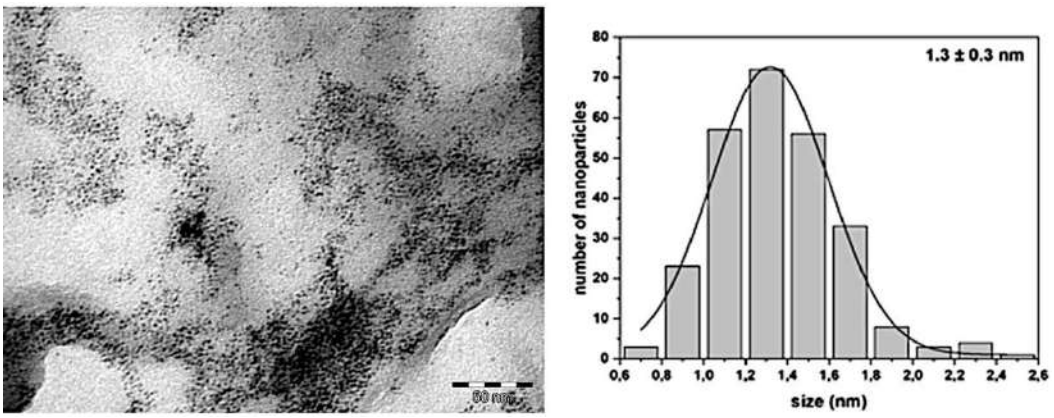

Figure 10: TEM image of Ru_1Ni_3/PVP after catalysis in THF (scale bar 50 nm) together with the respective size histogram.

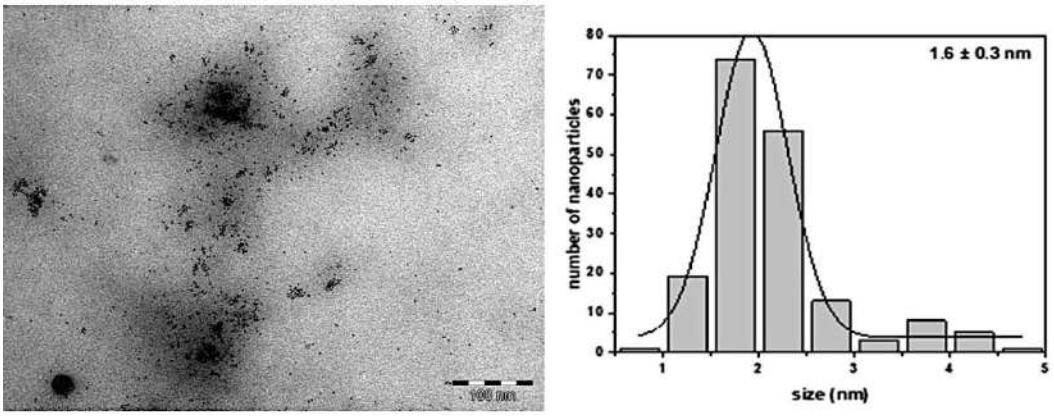

Figure 11: TEM image of Ru_1Ni_{20}/PVP after catalysis in THF (scale bar 100 nm) together with the respective size histogram.

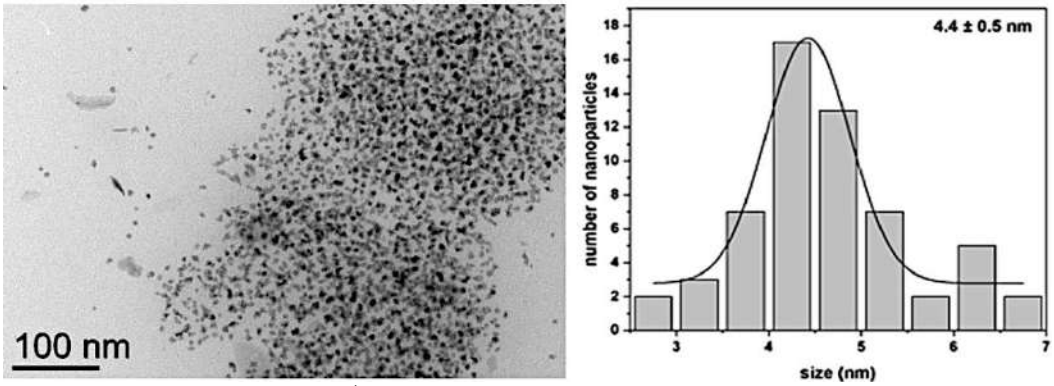

Figure 12: TEM image of Ni/PVP after catalysis in THF (scale bar 100 nm) together with the respective size histogram.

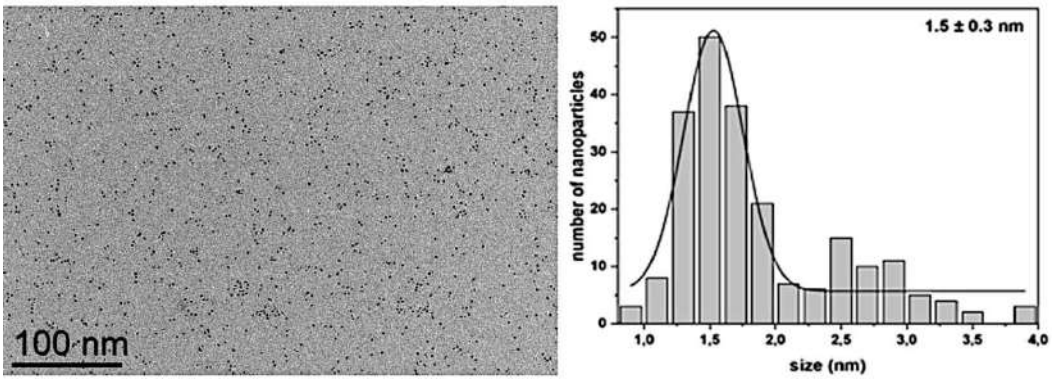

Figure 13: TEM image of Ru/PVP after catalysis in 1-PrOH (scale bar 100 nm) together with the respective size histogram.

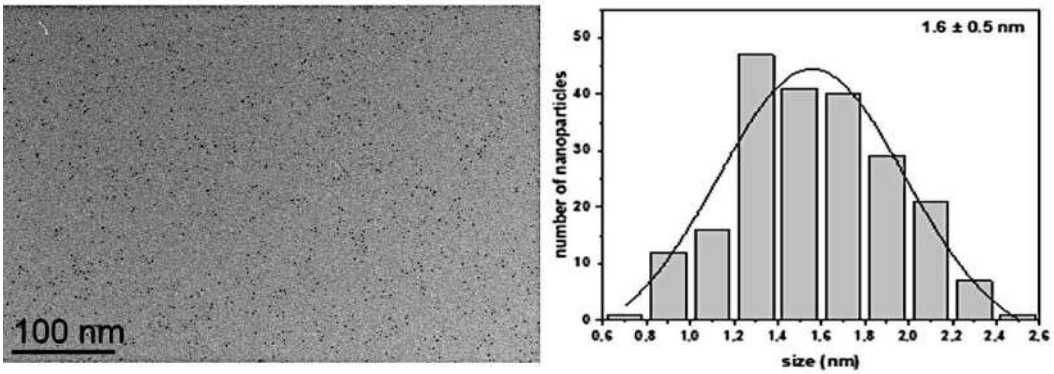

Figure 14: TEM image of Ru_3Ni_1/PVP after catalysis in 1-PrOH (scale bar 100 nm) together with the respective size histogram.

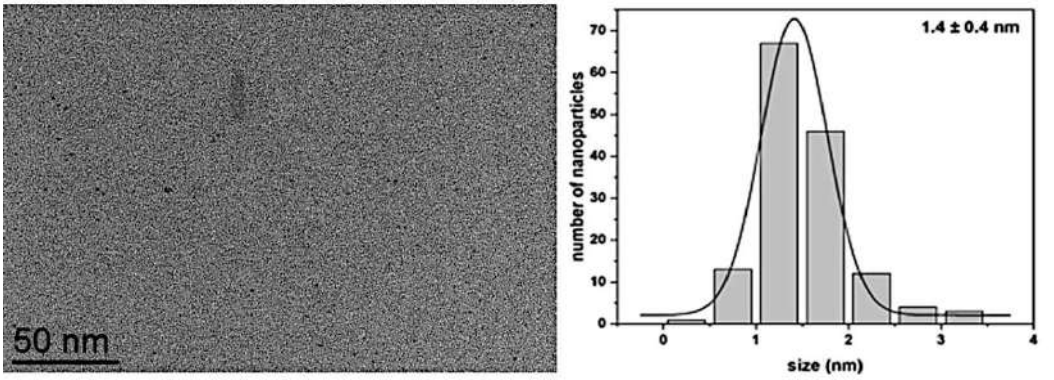

Figure 15: TEM image of Ru_1Ni_1/PVP after catalysis in 1-PrOH (scale bar 50 nm) together with the respective size histogram.

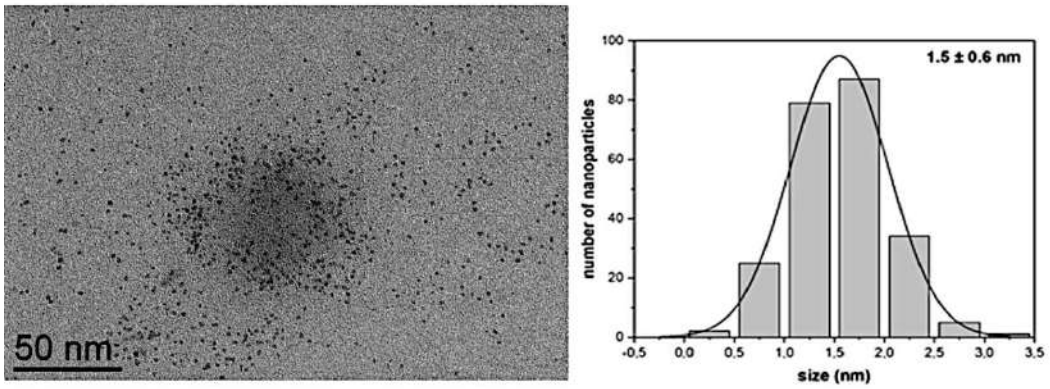

Figure 16: TEM image of Ru_1Ni_3/PVP after catalysis in 1-PrOH (scale bar 50 nm) together with the respective size histogram.

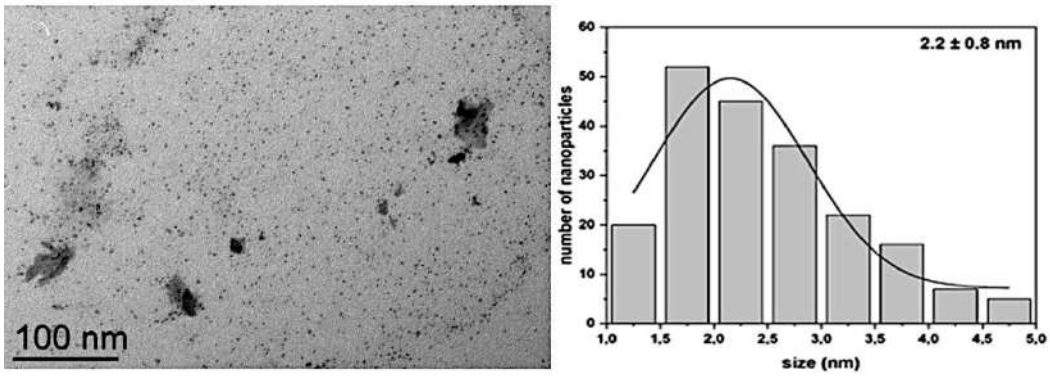

Figure 17: TEM image of Ru_1Ni_{20}/PVP after catalysis in 1-PrOH (scale bar 100 nm) together with the respective size histogram.

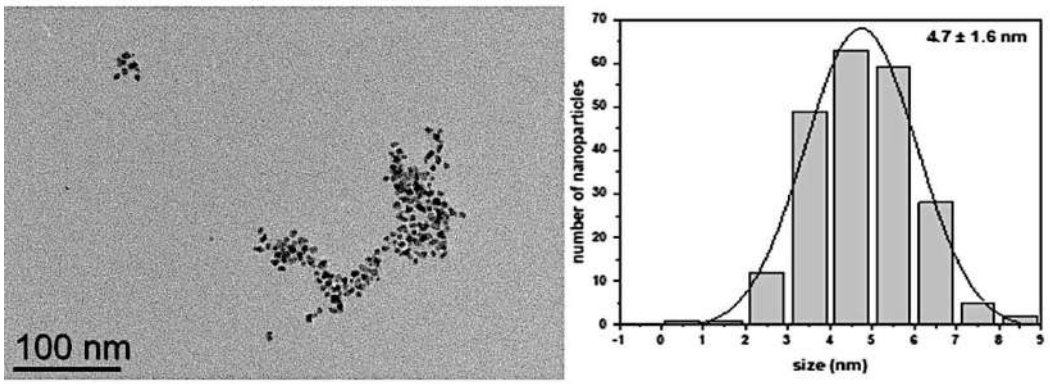

Figure 18: TEM image of Ni/PVP after catalysis in 1-PrOH (scale bar 100 nm) together with the respective size histogram.

To sum up this section of Chapter 3, synergetic effects between Ru and Ni were observed in both THF and 1-PrOH, following a volcano shape tendency centred at the Ru_1Ni_1/PVP catalyst for the TOF values obtained. Moreover, solvents effects were observed and high selectivity towards HF was observed in all cases. Further hydrogenation of the ring and the opening of the ring, leading to HMTHF and 1,2-PeD respectively, were reached on Ru/PVP NPs in 1-PrOH. In general, no leaching was observed during the catalytic reactions, with the only exception of Ru_1Ni_{20}/PVP NPs in 1-PrOH, associated to the Ostwald

ripening effect for an increase of its mean size. As future perspectives, it would be interesting to test the same reaction by substituting 1-PrOH by H_2O, to further study the formation of 1,2-PeD, and to test other RuNi catalyst being Ni in the core or by using other stabilisers.

3.3 Furfural hydrogenation using RuCu/PVP NPs as catalysts

The RuCu/PVP NPs, described in Chapter 2, were evaluated as catalysts in the selective hydrogenation of FF (Scheme 1) in the same reaction conditions as for the RuNi systems but using 1-PrOH as solvent (T=125 ºC; H_2 pressure of 20 bar). A magnetic stirring set up at 1200 rpm discards mass transfer limitations. All the experimental details are given in Chapter 6.

Table 4 summarises the results of the FF hydrogenation obtained in 1-PrOH for the different synthesised Ru, Cu and RuCu NPs, stabilised with PVP. The associated time-concentration curves are represented in Figure 19 and the different TOF values and selectivities towards HF on the Ru and/or Cu NPs are presented in Figure 20.

Table 4: Selective hydrogenation of FF in 1-PrOH using Ru, Cu and RuCu/PVP nanocatalysts.[a]

Entry	Catalyst	TOF (h^{-1})[b, c]	Time (h)	Conversion (%)[c]	HF (%)[c]	Acetal (%)[c, d]
1	Ru/PVP	129 (124)	1	40	96	4
2			5	90	97	3
3			24	100	97	3
4			29	100	97	3
5	Ru_2Cu_1/PVP	32	1	12	99	1
6			5	42	97	3
7			24	96	89	11
8			29	99	90	10
9	Ru_1Cu_1/PVP	42	1	18	100	0
10			5	41	97	3
11			24	94	86	14
12			29	97	86	14
13	Ru_1Cu_2/PVP	41	1	17	100	0
14			5	46	99	1
15			24	95	96	4
16			29	98	96	4
17	Cu/PVP	136	1	11	100	0
18			5	33	99	1
19			24	75	93	7
20			29	83	92	8

[a]Reaction conditions: 2×10^{-2} mmol of metal, 4 mmol of FF, 0.5 mmol of decane (internal standard), 20 bar of H_2, 125 °C, 15 mL of 1-PrOH. [b]TOFs calculated at 1 h of reaction according to the surface amount of metal; in brackets: TOFs of hydrogenation reaction. [c]Determined by GC using an internal standard technique. [d]Determined by GC-MS. [e]1,2 pentanediol also detected. [f]TOF calculated at 1 h of reaction according to the total amount of metal.

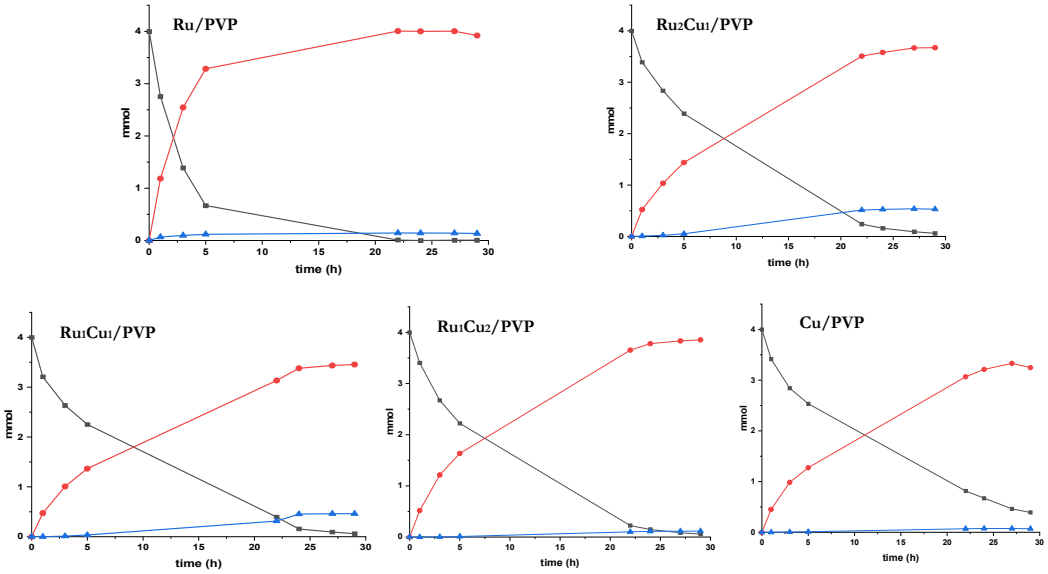

Figure 19: Time-concentration curves for the selective hydrogenation of FF in 1-PrOH using Ru, Cu and RuCu/PVP catalysts (black square dots, FF; red circle dots, HF; blue triangle dots, acetal).

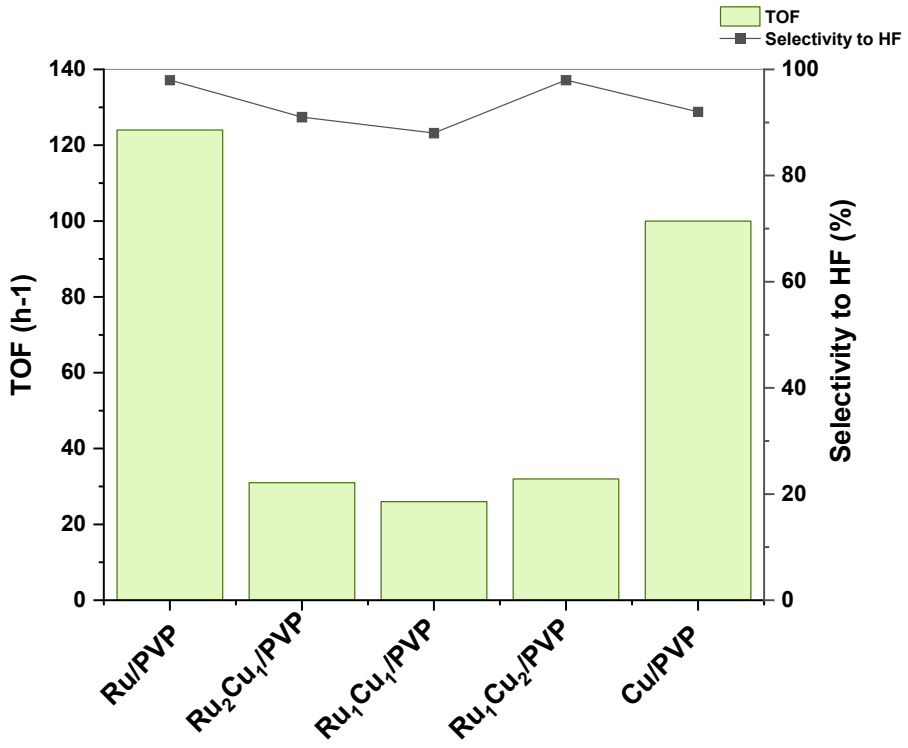

Figure 20: Turnover frequency (bars) and selectivity towards HF(dots) as function of catalysts in the selective hydrogenation of FF in 1-PrOH.

The TOF values obtained with the monometallic Ru and Cu NPs were higher than those obtained with the bimetallic RuCu/PVP. Moreover, the Cu/PVP NPs are the only tested catalyst which does not reach full conversion after 24 h. Furthermore, the acetal formation

was observed on all the different NP surfaces, decreasing the selectivity of the FF hydrogenation towards HF, but in a much lower content than the observed with RuNi/PVP NPs. The highest selectivities towards acetal were obtained on Ru_1Cu_1/PVP and Ru_2Cu_1/PVP (14 % and 10 % after 29 h of reaction, respectively), observing a difference in the acetal formation depending on the catalyst composition, a higher Cu content leading to less acetal. As pointed out previously, the acetal formation is favoured by acidic conditions,[42–44] such as electron-deficient Ru nanocatalysts,[27] such as our Ru/PVP catalytic system.[45]

Knowing that Cu_2O is present in the catalysts (see Chapter 2) and that copper oxide is known to be basic and can replace bases in some reactions;[46] its presence could be the cause of the reduction of acetal formation for the bimetallic catalysts. The basicity of Cu_2O, which is present in our NPs, may explain the decrease of acetal formation in the RuCu/PVP systems compared to the RuNi/PVP ones.

Interestingly, the selectivity of the Ru/PVP NPs synthesised at 100 ºC in the RuCu/PVP series, as their catalytic activity changes from that of the Ru/PVP NPs synthesised at 85 ºC in the RuNi/PVP series (Figure 21), as the former does not produce acetal, in contrast to the later.

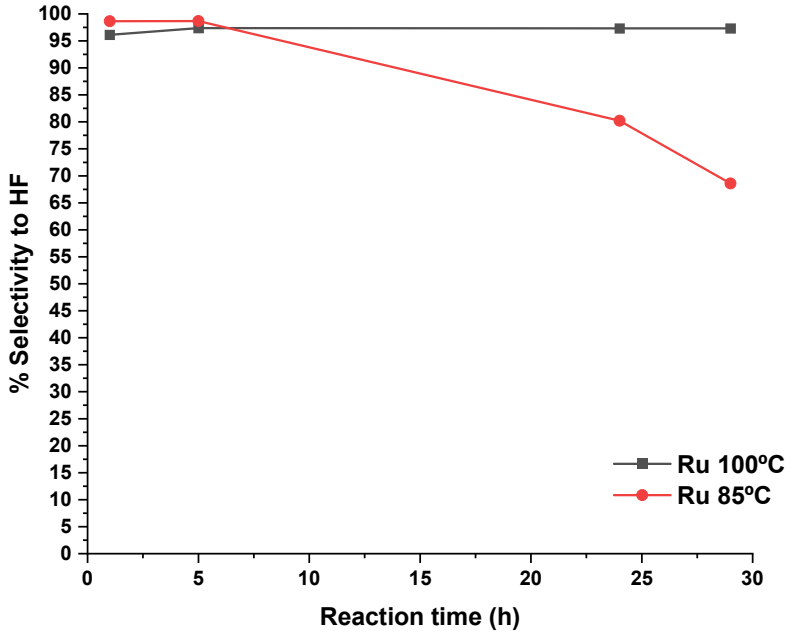

Figure 21: Selectivity towards HF (dots) over time as function of the temperature of the synthesis of the Ru/PVP NPs for the selective hydrogenation of FF in 1-PrOH.

As can be observed, Figure 21 displays a loss of selectivity with the Ru/PVP synthesised at 85 ºC, when leaving the catalytic reaction overnight, resulting from the formation of acetal. The divergence of catalytic performance, depending on the Ru NPs synthesis temperature,

may derive from differences on the metallic structure of the NPs. Further analyses are needed to elucidate the origin of the different selectivities.

TEM analyses after catalysis do not display any significant changes in whether size or shape, except for the Cu/PVP NPs. After catalysis in 1-PrOH, this catalyst showed a broadening size distribution (Table 5 and Figures 22 to 26), in a range between 4 and 14 nm. The size of the monometallic Cu/PVP evolved during the reaction and the shape distribution after catalysis is diverse, showing a non homogeneous population of NPs (Figure 26).

Table 5: Mean size of Ru and Cu with PVP NPs before and after catalysis

NP	Mean size before catalysis (nm)[a]	Mean size after catalysis in 1-PrOH (nm)[a]
Ru/PVP	1.6 ± 0.3	1.4 ± 0.2
Ru2Cu1/PVP	1.2 ± 0.3	1.3 ± 0.1
Ru1Cu1/PVP	1.0 ± 0.2	1.2 ± 0.1
Ru1Cu2/PVP	1.0 ± 0.1	1.0 ± 0.2
Cu/PVP	4.9 ± 1.0	9.0 ± 5.0

[a]Mean values of NP size determined from TEM images by considering at least 200 particles.

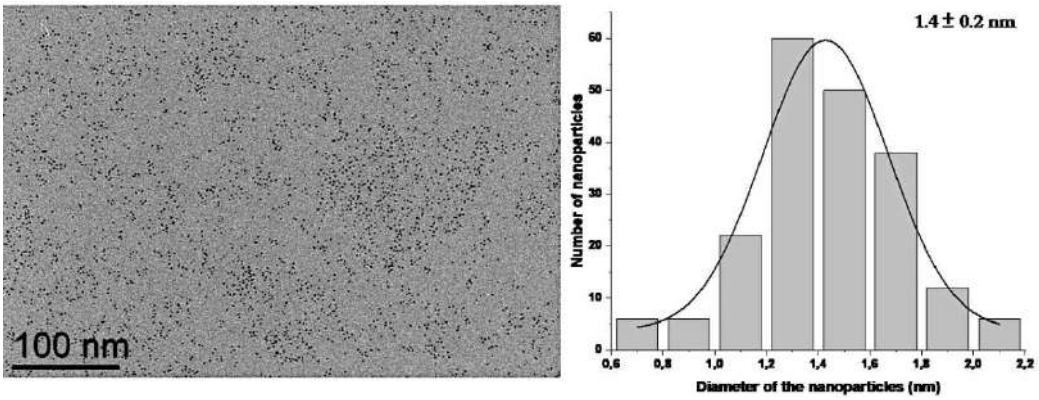

Figure 22: TEM image of Ru/PVP after catalysis in 1-PrOH (scale bar 100 nm) together with the respective size histogram.

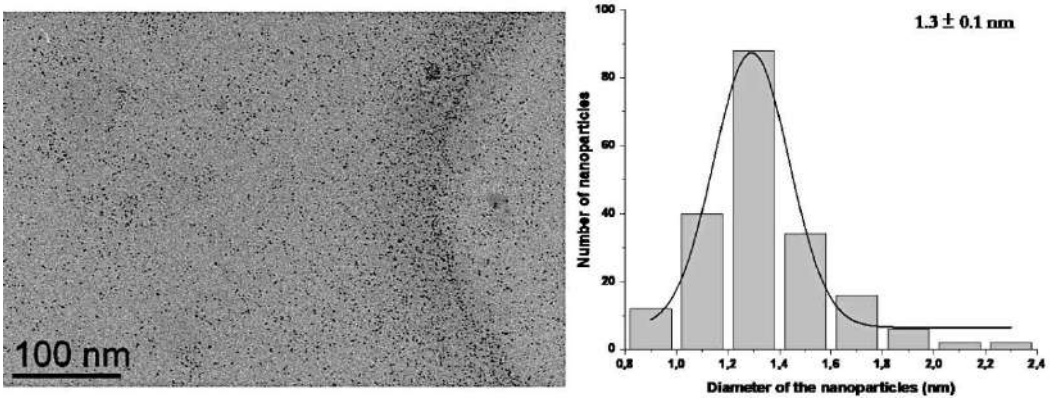

Figure 23: TEM image of Ru_2Cu_1/PVP after catalysis in 1-PrOH (scale bar 100 nm) together with the respective size histogram.

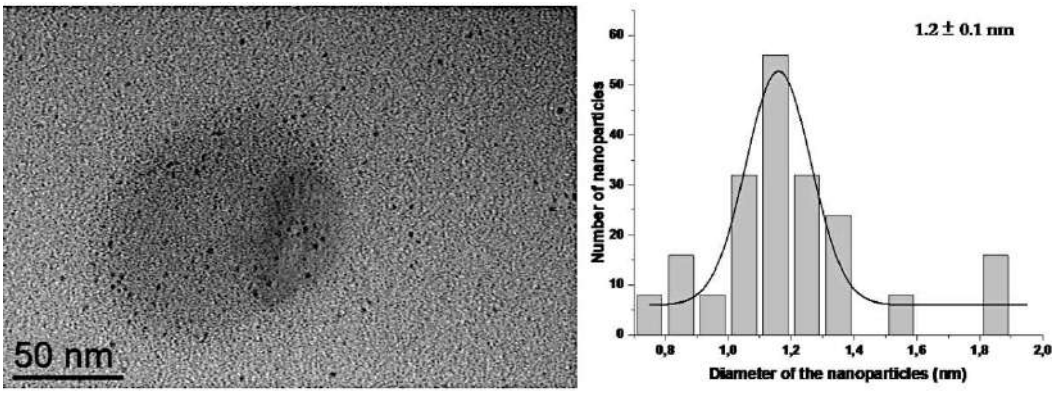

Figure 24: TEM image of Ru_1Cu_1/PVP after catalysis in 1-PrOH (scale bar 50 nm) together with the respective size histogram.

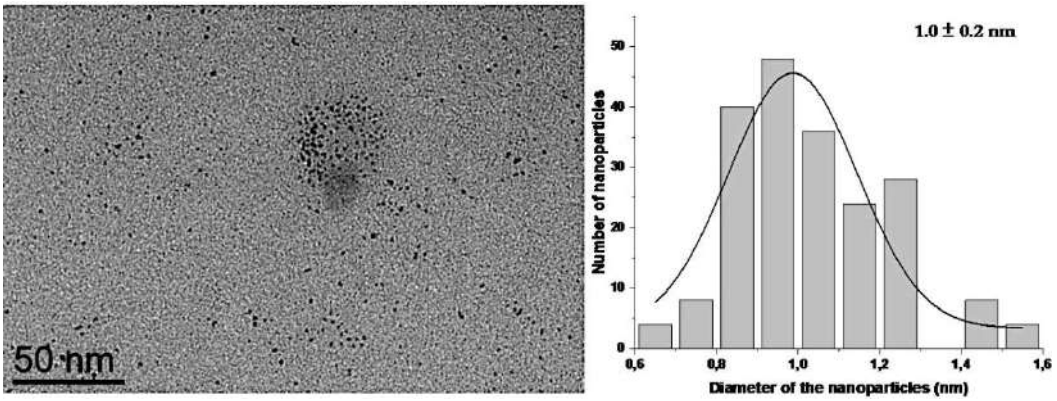

Figure 25: TEM image of Ru_1Cu_2/PVP after catalysis in 1-PrOH (scale bar 50 nm) together with the respective size histogram.

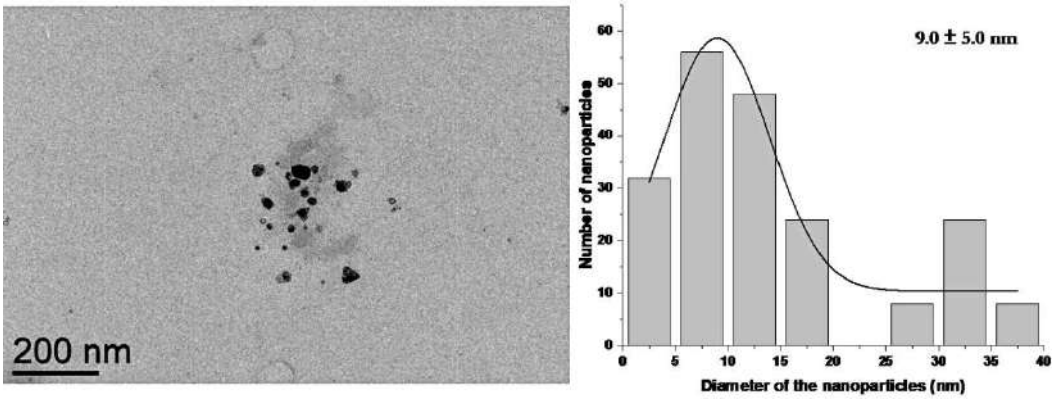

Figure 26: TEM image of Cu/PVP after catalysis in 1-PrOH (scale bar 200 nm) together with the respective size histogram.

To sum up this section of Chapter 3, a high selectivity towards HF was obtained for all the series of Ru and/or Cu/PVP NPs, being the monometallic catalysts the ones with higher TOF values. Acetal formation was also observed, even if in less amount than for RuNi/PVP catalysts from section 3.2, which could be explained by the presence of the basic Cu_2O in the RuCu/PVP NPs. Concerning the stability, the mean size of all the NPs except for the Cu/PVP remained unchanged after the catalytic reaction. As future perspec-

tives, it would be interesting to test in catalysis the synthesised Cu/HDA NPs described in section 2.6 of Chapter 2 and also to try RuCu NPs, being Cu in the core.

3.4 Quinoline hydrogenation using RuNi NPs as catalysts

Ru_1Ni_1/PVP NPs, described in Chapter 2, were also used as catalysts in the selective hydrogenation of QN (Scheme 2) in 1-PrOH at different temperatures and keeping a continuous pressure of 35 bar of H_2. A magnetic stirring set up at 1200 rpm discards mass transfer limitations. All the experimental details are given in Chapter 6.

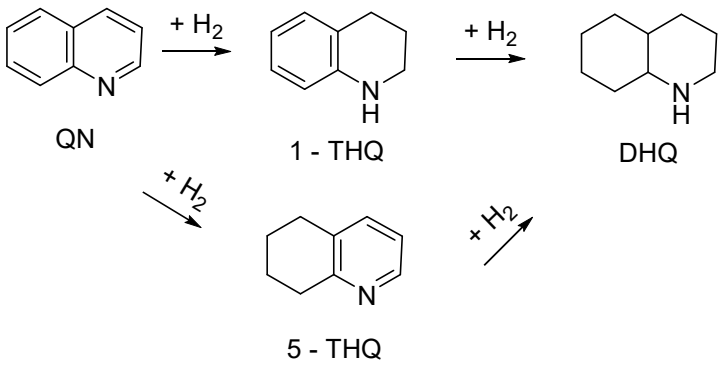

Scheme 2: Simplified reaction scheme of the selective catalytic hydrogenation of Quinoline into various valuable products. Quinoline (QN), 1,2,3,4-Tetrahydroquinoline (1-THQ), 5,6,7,8-Tetrahydroquinoline (5-THQ), and Decahydroquinoline (DHQ).

The synthesis of 1-THQ from the partial hydrogenation of QN, or substituted homologues, has been described to be catalysed by different metals[47,48] such as Pt,[49] Pd,[50] Co,[51] Ni,[52,53] Ru,[54,55] Rh,[56,57] Ir,[58,59] Os[60] and Mo.[61]

Table 6 summarises the results of QN hydrogenation in 1-PrOH obtained for the bimetallic Ru_1Ni_1/PVP NPs. The associated time-concentration curves are represented in Figure 27. The reaction conditions have been chosen after an unpublished work in our group dealing with Ru catalysts, and the literature survey. Different temperatures were tested. Figure 28 depicts the TOF values and the selectivity *vs.* the reaction temperature. The results obtained at these different temperatures were used to calculate the activation energy (Ea), by the Arrhenius equation (Equation 1) and its linear rearrangement (Equation 2), which is equal to 23 kJ·mol^{-1}.

Table 6: Selective hydrogenation of QN in 1-PrOH using Ru_1Ni_1/PVP catalyst at different temperatures.[a]

Entry	T (°C)	TOF (h^{-1})[b, c]	Time (h)	Conversion (%)[c]	1-THQ (%)[c]	5-THQ (%)[c]	DHQ (%)[c]	N.D. (%)[c, d]	DHPQ (%)[c, e]	1-THPQ (%)[c, e]
1	20	2	1	1	100	0	0	0	0	0
2			5	4	94	6	0	0	0	0
3			24	7	95	5	0	0	0	0
4			29	11	94	5	1	0	0	0
5	50	13	1	4	76	5	0	0	0	19
6			5	9	80	6	2	5	0	7
7			24	25	81	5	4	9	0	2
8			29	29	80	5	4	9	0	2
9			48	39	81	5	4	9	0	1
10	75	15	1	4	73	5	0	7	0	15
11			5	14	77	5	0	7	0	15
12			24	44	84	3	3	9	0	1
13			29	51	85	3	3	8	0	1
14	100	24	1	1	85	6	0	0	0	9
15			5	15	90	5	2	2	0	2
16			24	63	93	3	2	1	0	0
17			29	75	93	3	2	1	0	0
18			48	93	94	3	2	1	1	0
19	125	62	1	10	82	16	0	2	0	0
20			5	56	86	11	0	3	0	0
21			24	98	84	7	1	2	6	1
22			29	100	83	6	0	2	8	1
23			47	97	76	6	0	0	14	3
24	150	117	1	23	85	10	0	4	0	0
25			5	99	91	5	0	2	1	1
26			24	100	84	4	0	2	6	4
27			29	100	80	4	0	2	8	7
Entry	T (°C)	TOF (h^{-1})[b, c]	Time (h)	Conversion (%)[c]	1-THQ (%)[c]	5-THQ (%)[c]	DHQ (%)[c]	N.D. (%)[c, d]	DHPQ (%)[c, e]	1-THPQ (%)[c, e]
28			48	100	74	3	0	6	9	8

[a]Reaction conditions: 2×10^{-2} mmol of metal, 4 mmol of QN, 0.5 mmol of dodecane (internal standard), 35 bar of H_2, 15 mL of 1-PrOH. [b]TOFs calculated at 1 h of reaction according to the surface amount of metal. [c]Determined by GC using an internal standard technique. [d]Non-determined product. [e]Determined by GCMS.

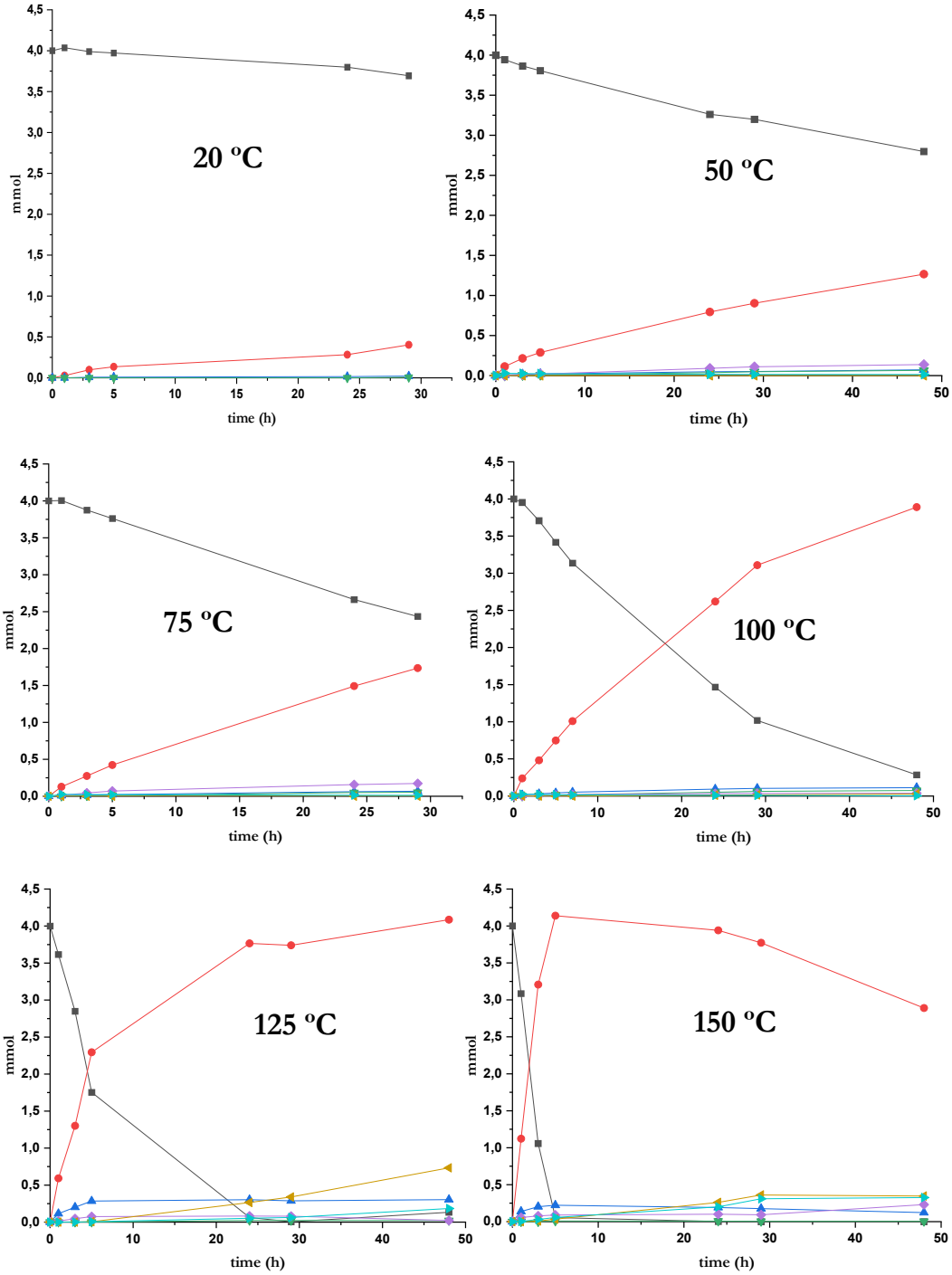

Figure 27: Time-concentration curves for the selective hydrogenation of QN in 1-PrOH on Ru_1Ni_1/PVP catalyst at different temperatures (black square dots, QN; red circle dots, 1-THQ; blue triangle dots, 5-THQ; green inversed triangle dots, DHQ; violet twisted square dots, non-determined (N.D.); brown twisted triangle dots, decahydro-1-propyl-quinoline (DHPQ); light blue twisted triangle dots, 1,2,3,4-tetrahydro-n-propyl-quinoline (1-THPQ)).

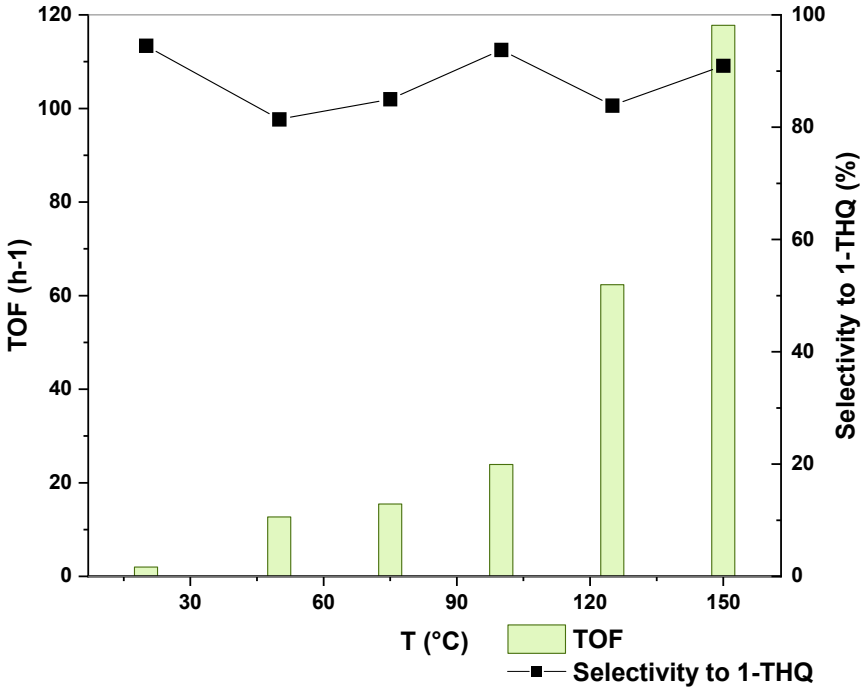

Figure 28: Turnover frequency (bars) and selectivity towards 1-THQ (dots) as function of the reaction temperature in the selective hydrogenation of QN in 1-PrOH on the Ru_1Ni_1/PVP catalyst.

$$k = Ae^{-\frac{E_a}{RT}} \quad (1)$$

$$\ln k = \ln A - \frac{E_a}{R}\frac{1}{T} \quad (2)$$

At all tested temperatures, the selectivity towards the semi hydrogenated product, 1-THQ, was high (73 to 99 %) and with very low formation of the fully hydrogenated product, DHQ. It is worth mentioning that the condensation products of 1-THQ and DHQ with the solvent were also detected (Schemes 3 and 4),

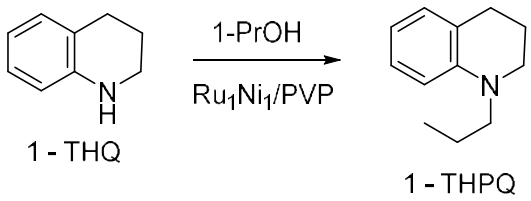

Scheme 3: Simplified reaction scheme of the condensation reaction between 1-THQ and 1-PrOH on Ru_1Ni_1/PVP catalyst, forming 1-THPQ.

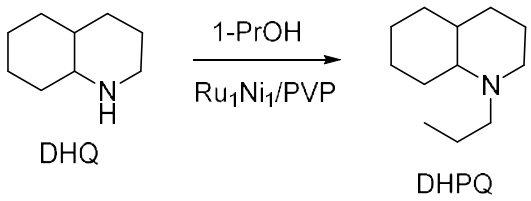

Scheme 4: Simplified reaction scheme of the condensation reaction between DHQ and 1-PrOH on Ru_1Ni_1/PVP catalyst, forming DHPQ.

Condensation reactions between alcohols and amines have already been known and reported in the literature. Several metals have been studied for this type of reactions such as Rh,[62] Co,[63,64] Ir,[65–67] Pd,[68–70] Cu,[71] Au,[72] Fe,[73,74] Mn,[75,76] Ni,[77] but, Ru-based catalysts are the most common.[78–81]

Together with the monometallic Ru and Ni systems, the catalytic performance has been further studied in the same reaction at 150 ºC. Table 7 summarises the results of QN hydrogenation in 1-PrOH at 150 ºC on Ni/PVP, Ru_1Ni_1/PVP and Ru/PVP. The associated time-concentration curves are presented in Figure 29. Figure 30 depicts TOFs and selectivity towards catalyst composition.

Table 7: Selective hydrogenation of QN in 1-PrOH at 150 ºC.[a]

Entry	Catalyst	TOF (h^{-1})[b, c]	Time (h)	Conversion (%)[c]	1-THQ (%)[c]	5-THQ (%)[c]	DHQ (%)[c]	N.D. (%)[c, d]	DHPQ (%)[c, e]	1-THPQ (%)[c, e]
1	Ni/PVP	37	1	10	34	0	0	66	0	0
2			5	29	59	1	0	40	0	0
3			24	83	87	0	0	12	0	1
4			29	94	88	0	0	11	0	1
5			48	100	73	0	0	25	0	2
6	Ru_1Ni_1/PVP	117	1	23	85	10	0	4	0	0
7			5	99	91	5	0	2	1	1
8			24	100	84	4	0	2	6	4
9			29	100	80	4	0	2	8	7
10			48	100	74	3	0	6	9	8
11	Ru/PVP	322	1	89	89	7	2	0	1	0
12			5	100	86	6	2	0	5	0
13			24	100	78	6	0	0	14	2
14			29	100	77	6	0	0	15	2
15			48	99	75	6	0	0	16	3

[a]Reaction conditions: 2×10^{-2} mmol of metal, 4 mmol of QN, 0.5 mmol of dodecane (internal standard), 35 bar of H_2, 150 ºC, 15 mL of 1-PrOH. [b]TOFs calculated at 1 h of reaction according to the surface amount of metal. [c]Determined by GC using an internal standard technique. [d]Non-determined product. [c]Determined by GCMS.

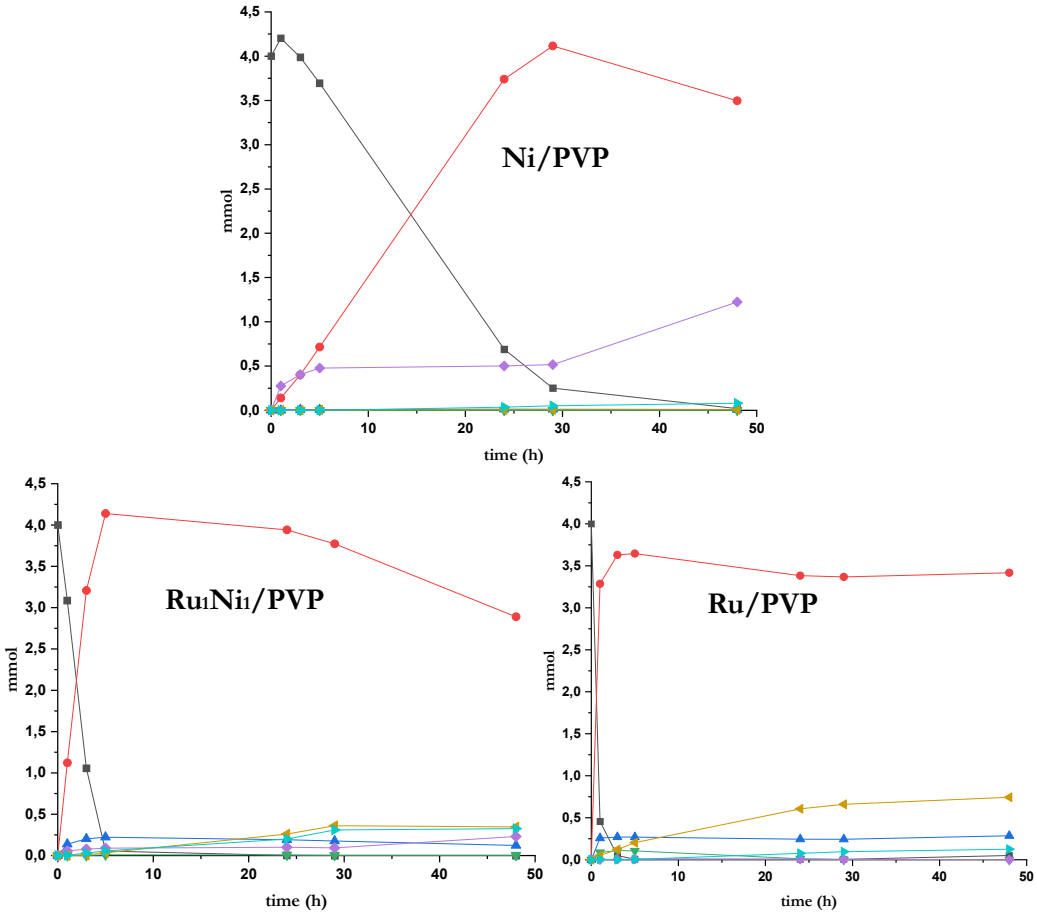

Figure 29: Time-concentration curves for the selective hydrogenation of QN in 1-PrOH at 150 ºC (black square dots, QN; red circle dots, 1-THQ; blue triangle dots, 5-THQ; green inversed triangle dots, DHQ; violet twisted square dots, N.D.; brown twisted triangle dots, DHPQ; light blue twisted triangle dots, 1-THPQ).

All three catalysts selectively produced 1-THQ, but some differences were observed. Ru/PVP displayed the highest activity, as expected taking into consideration previous reported works.[18,82,83] Ni/PVP displayed TOFs comparable to previously described Ni catalysts.[20,84] Ru_1Ni_1/PVP TOF is estimated to be intermediary between those of Ru/PVP and Ni/PVP. This result appears to be in opposition of a synergistic effect between both metals in this reaction. Regarding selectivity, the three catalysts were highly selective to the formation of 1-THQ; nevertheless, concerning the by-products, subtle differences were observed. Ru/PVP is active in the *N*-alkylation of 1-THQ and DHQ with 1-PrOH, producing the corresponding *N*-alkylated products around 20 % at long reaction times. On the other side, Ni/PVP, did not produce these two *N*-alkylated products, but an unidentified product at a selectivity of 25 %, which needs to be characterised to provide further explanations. Lastly, Ru_1Ni_1/PVP was slightly better in terms of selectivity than its corresponding Ru catalyst, reaching a selectivity of 91 % towards 1-THQ at full conversion.

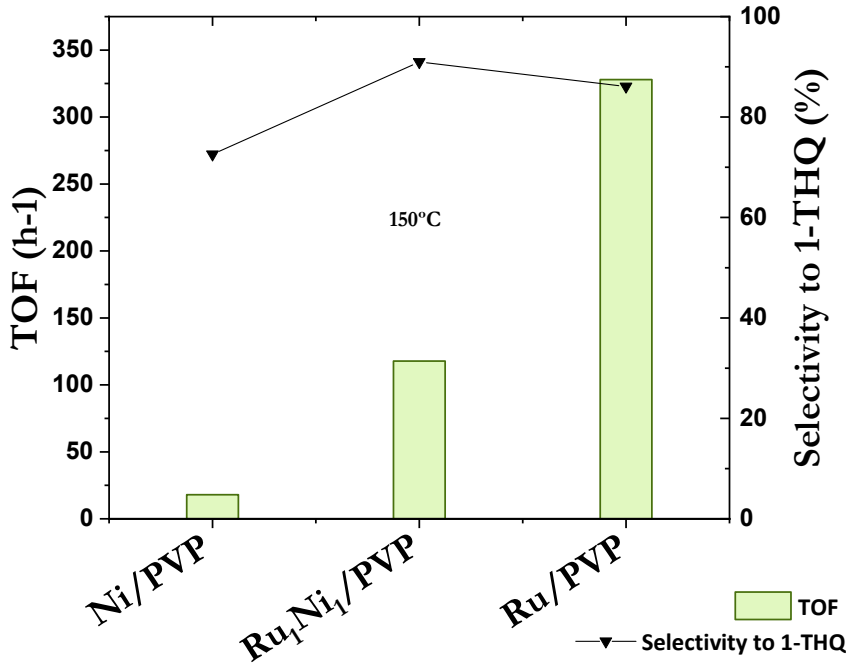

Figure 30: Turnover frequency (bars) and selectivity towards 1-THQ (dots) as function of the catalyst used in the selective hydrogenation of QN in 1-PrOH performed at 150 ºC.

Then, the catalytic performances of the monometallic Ru/PVP and Ru/ PPh_2Py and the bimetallic RuNi/PVP and RuNi/PPh_2Py nanocatalysts were compared for QN hydrogenation at 20 ºC and 125 ºC respectively. The reaction was performed using the same reaction conditions described above, except for the temperature which was room temperature (RT) for the monometallic Ru and 125 ºC for the bimetallics. Results are summarized in Table 8; time-concentration curves are depicted in Figure 31.

Table 8: Selective hydrogenation of QN in 1-PrOH with monometallic Ru catalysts at 20 ºC and with bimetallic RuNi catalysts at 125 ºC.[a]

Entry	Catalyst	T (ºC)	TOF (h^{-1})[b, c]	Time (h)	Conversion (%)[c]	1-THQ (%)[c]	5-THQ (%)[c]	DHQ (%)[c]	N.D. (%)[c, d]	DHPQ (%)[c, e]	1-THPQ (%)[c, e]
1	Ru/PVP	20	31	1	6	95	5	0	0	0	0
2				5	31	94	5	1	0	0	0
3				24	93	92	5	2	0	0	0
4				29	99	92	5	3	0	0	0
5	Ru /PPh_2Py	20	17	1	4	81	0	0	0	0	19
6				5	11	94	0	0	2	0	4
7				24	35	97	0	0	2	0	0
8				29	38	97	1	0	2	0	0
9	RuNi/PVP	125	62	1	10	82	16	0	2	0	0
10				5	56	86	11	0	3	0	0
11				24	98	84	7	1	2	6	1
12				29	100	83	6	0	2	8	1
13	RuNi/PPh_2Py	125	64	1	3	76	2	0	19	0	3
14				5	33	82	2	0	16	0	1
Entry	Catalyst	T (ºC)	TOF (h^{-1})[b, c]	Time (h)	Conversion (%)[c]	1-THQ (%)[c]	5-THQ (%)[c]	DHQ (%)[c]	N.D. (%)[c, d]	DHPQ (%)[c, e]	1-THPQ (%)[c, e]
15				24	95	90	1	0	8	0	0
16				29	99	90	1	0	7	0	0

[a]Reaction conditions: 2×10^{-2} mmol of metal, 4 mmol of QN, 0.5 mmol of dodecane (internal standard), 35 bar of H_2, 20 ºC, 15 mL of 1-PrOH. [b]TOFs calculated at 1 h of reaction according to the surface amount of metal. [c]Determined by GC using an internal standard technique. [d]Non-determined product. [e]Determined by GCMS.

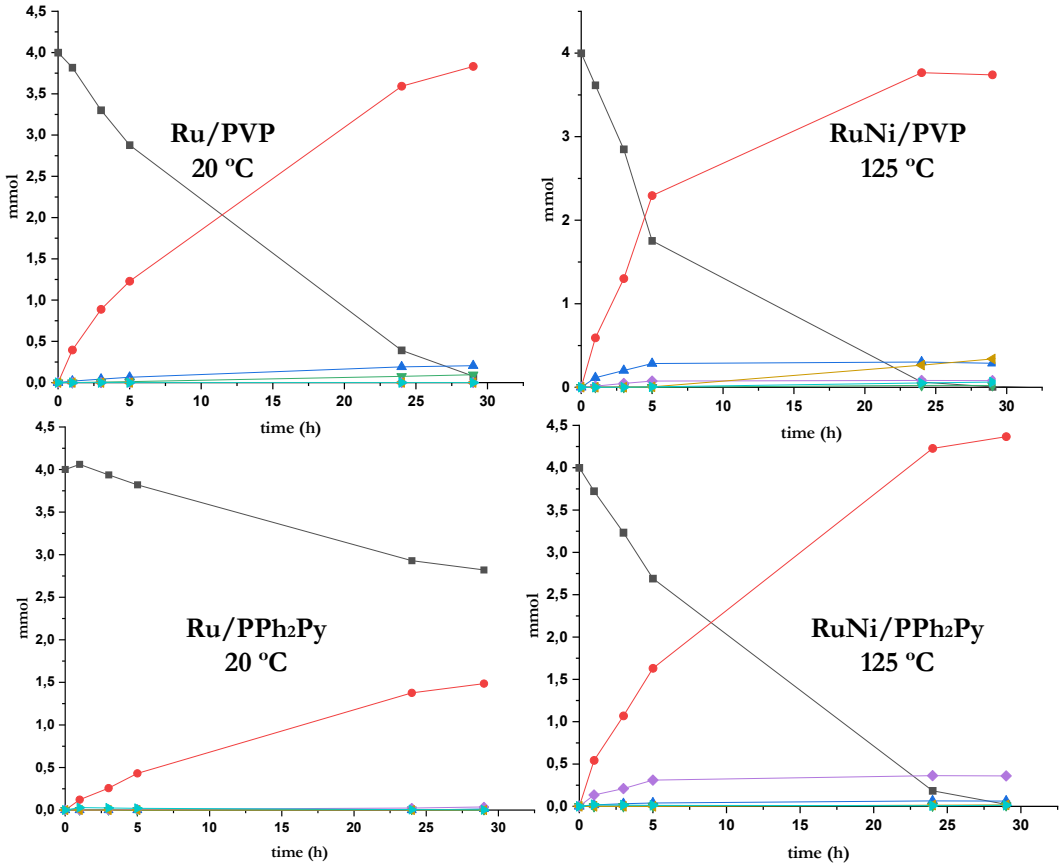

Figure 31: Time-concentration curves for the selective hydrogenation of QN in 1-PrOH with monometallic Ru catalysts (left) at 20 ºC and with bimetallic RuNi catalysts (right) at 125 ºC (black square dots, QN; red circle dots, 1-THQ; blue triangle dots, 5-THQ; green inversed triangle dots, DHQ; violet twisted square dots, N.D.; brown twisted triangle dots, DHPQ; light blue twisted triangle dots, 1-THPQ).

The Ru/PVP system was active at RT, displaying a TOF = 31 h^{-1}, a full conversion was attained at 24 h of reaction, and a selectivity of 92 % towards 1-THQ. The presence of a phosphine onto the surface of the Ru/PPh_2Py NPs, hampered the reaction, and a lower activity was observed with a TOF = 17 h^{-1}. This result is in line with previous results obtained for the selective hydrogenation of FF using a Ru-based catalyst, modified with the diphenylphosphinopyridine (PPh_2Py) ligand.[34]

The RuNi/PVP bimetallic system at 125 ºC showed a high activity (TOF = 62 h^{-1}), displaying a full conversion at 24 h of reaction. The same results were obtained with RuNi/PPh_2Py displaying the same TOF value (64 h^{-1}) as the PVP-stabilised catalyst. Concerning the selectivity, 84 % and 90 % towards 1-THQ were obtained for RuNi/PVP and Ru/PPh_2Py respectively. In the PVP-stabilised, 1-THPQ and DHPQ were obtained as minor products from the condensation of the amine products with the solvent (1-PrOH), while in the phosphine stabilised catalyst, a non-determined product was obtained. For this reason, to

better conclude on the ligand effect for QN hydrogenation, further reactions should be carried out.

To sum up this section of Chapter 3, a high selectivity towards 1-THQ was obtained for both monometallic and bimetallic PVP and phosphine stabilised catalysts. Some minor products were detected, two of them produced from the condensation of 1-THQ and DHQ with 1-PrOH leading to N-alkylation reactions. A dependence on the reaction temperature for the activity of the catalysts was also observed. As future perspectives, it would be interesting to determine a third minor detected product, to better understand the system reactivity, and further studies for the comparison between the PVP and the phosphine catalysts are also of great interest.

3.5 Conclusions

In this chapter, bimetallic nanomaterials, RuNi and RuCu, were tested as catalysts in the selective hydrogenations of FF and QN, in comparison with their monometallic counterparts. Interesting results have been obtained; some of them being rationalized by DFT calculations (see Chapter 4).

RuNi/PVP displayed synergetic effects between both metals in the hydrogenation of FF, which were maximised at a composition Ru/Ni = 1. Solvent effects were also observed in this reaction being supported by DFT calculations, as detailed further in Chapter 4. Theoretical results point to differences of adsorption energies of the reactants due to the presence of propanolate species onto the NP surface when using 1-PrOH as solvent, which is beneficial for the catalytic performance.

Cu/PVP NPs showed promising catalytic performances for the hydrogenation of FF, giving activities similar to those observed on pure Ru/PVP nanocatalyst. Unfortunately, RuCu/PVP NPs displayed lower catalytic performances than their monometallic counterparts; nevertheless the properties of these catalysts could be of interest for other catalytic transformations.

Ru_1Ni_1/PVP nanocatalysts were less performants in QN hydrogenation, compared to FF hydrogenation, even if high selectivity towards 1-THQ was obtained. N-alkylation reactions were also observed by the condensation of 1-THPQ and DHQ products with 1-PrOH as minor products.

As future perspectives, FF hydrogenation on RuNi/PVP NPs in H_2O instead of 1-PrOH would be interesting to study the 1,2-PeD production. Moreover, for FF hydrogenation tests with other catalysts such as Cu/HDA NPs or with bimetallic NPs with Cu or Ni in the

core will also be of interest. Finally, for QN hydrogenation, for a better comparison between the PVP-stabilised and the PPh_2Py-stabilised catalysts, further studies should be performed.

3.6 References

(1) Nanda, S.; Azargohar, R.; Dalai, A. K.; Kozinski, J. A. An Assessment on the Sustainability of Lignocellulosic Biomass for Biorefining. *Renew. Sustain. Energy Rev.* **2015**, *50*, 925. https://doi.org/10.1016/j.rser.2015.05.058

(2) Putro, J. N.; Soetaredjo, F. E.; Lin, S.-Y.; Ju, Y.-H.; Ismadji, S. Pretreatment and Conversion of Lignocellulose Biomass into Valuable Chemicals. *RSC Adv.* **2016**, *6* (52), 46834. https://doi.org/10.1039/C6RA09851G

(3) Lam, C. H.; Deng, W.; Lang, L.; Jin, X.; Hu, X.; Wang, Y. Minireview on Bio-Oil Upgrading via Electrocatalytic Hydrogenation: Connecting Biofuel Production with Renewable Power. *Energy Fuels* **2020**, *34* (7), 7915. https://doi.org/10.1021/acs.energyfuels.0c01380

(4) Han, Y.; Gholizadeh, M.; Tran, C.-C.; Kaliaguine, S.; Li, C.-Z.; Olarte, M.; Garcia-Perez, M. Hydrotreatment of Pyrolysis Bio-Oil: A Review. *Fuel Process. Technol.* **2019**, *195*, 106140. https://doi.org/10.1016/j.fuproc.2019.106140

(5) Yan, K.; Wu, G.; Lafleur, T.; Jarvis, C. Production, Properties and Catalytic Hydrogenation of Furfural to Fuel Additives and Value-Added Chemicals. *Renew. Sustain. Energy Rev.* **2014**, *38*, 663. https://doi.org/10.1016/j.rser.2014.07.003

(6) Reed, N. R.; Kwok, E. S. C. Furfural. In *Encyclopedia of Toxicology*; Elsevier, **2014**, 685. https://doi.org/10.1016/B978-0-12-386454-3.00147-0

(7) Pulicharla, R.; Lonappan, L.; Brar, S. K.; Verma, M. Production of Renewable C5 Platform Chemicals and Potential Applications. In *Platform Chemical Biorefinery*; Elsevier, **2016**, 201. https://doi.org/10.1016/B978-0-12-802980-0.00011-0

(8) Xu, W.; Wang, H.; Liu, X.; Ren, J.; Wang, Y.; Lu, G. Direct Catalytic Conversion of Furfural to 1,5-Pentanediol by Hydrogenolysis of the Furan Ring under Mild Conditions over Pt/Co_2AlO_4 Catalyst. *Chem. Commun.* **2011**, *47* (13), 3924. https://doi.org/10.1039/c0cc05775d

(9) Alphy, M. P.; Balakumaran, P. A.; Sindhu, R.; Pandey, A.; Binod, P. Chapter 6 - Integrated Bio-Based Processes for the Production of Industrially Important Chemicals. In *Biomass, Biofuels, Biochemicals*; Varjani, S., Pandey, A., Bhaskar, T., Mohan, S. V., Tsang, D. C. W., Eds.; Elsevier, **2022**, 163. https://doi.org/10.1016/B978-0-323-89855-3.00024-8

(10) Hronec, M.; Fulajtarová, K. Selective Transformation of Furfural to Cyclopentanone. *Catal. Commun.* **2012**, *24*, 100. https://doi.org/10.1016/j.catcom.2012.03.020

(11) Li, H.; Luo, H.; Zhuang, L.; Dai, W.; Qiao, M. Liquid Phase Hydrogenation of Furfural to Furfuryl Alcohol over the Fe-Promoted Ni-B Amorphous Alloy Catalysts. *J. Mol. Catal. Chem.* **2003**, *203* (1–2), 267. https://doi.org/10.1016/S1381-1169(03)00368-6

(12) Rodiansono; Khairi, S.; Hara, T.; Ichikuni, N.; Shimazu, S. Highly Efficient and Selective Hydrogenation of Unsaturated Carbonyl Compounds Using Ni–Sn Alloy Catalysts. *Catal. Sci. Technol.* **2012**, *2* (10), 2139. https://doi.org/10.1039/c2cy20216f

(13) Wu, J.; Shen, Y.; Liu, C.; Wang, H.; Geng, C.; Zhang, Z. Vapor Phase Hydrogenation of Furfural to Furfuryl Alcohol over Environmentally Friendly $Cu–Ca/SiO_2$ Catalyst. *Catal. Commun.* **2005**, *6* (9), 633. https://doi.org/10.1016/j.catcom.2005.06.009

(14) Tamura, M.; Tokonami, K.; Nakagawa, Y.; Tomishige, K. Rapid Synthesis of Unsaturated Alcohols under Mild Conditions by Highly Selective Hydrogenation. *Chem. Commun.* **2013**, *49* (63), 7034. https://doi.org/10.1039/c3cc41526k

(15) Collin, G.; Höke, H. Quinoline and Isoquinoline. In *Ullmann's Encyclopedia of Industrial Chemistry*; Wiley-VCH Verlag GmbH & Co. KGaA, Ed.; Wiley-VCH Verlag GmbH & Co. KGaA: Weinheim, Germany, **2000**, a22_465. https://doi.org/10.1002/14356007.a22_465

(16) Aly, A. A.; Ramadan, M.; Abuo-Rahma, G. E.-D. A.; Elshaier, Y. A. M. M.; Elbastawesy, M. A. I.; Brown, A. B.; Bräse, S. Quinolones as Prospective Drugs: Their Syntheses and Biological Applications. In *Advances in Heterocyclic Chemistry*; Elsevier, **2021**, *135*, 147. https://doi.org/10.1016/bs.aihch.2020.08.001

(17) Lewinska, G.; Sanetra, J.; Marszalek, K. W. Application of Quinoline Derivatives in Third-Generation Photovoltaics. *J. Mater. Sci. Mater. Electron.* **2021**, *32* (14), 18451. https://doi.org/10.1007/s10854-021-06225-6

(18) Tang, M.; Deng, J.; Li, M.; Li, X.; Li, H.; Chen, Z.; Wang, Y. 3D-Interconnected Hierarchical Porous N-Doped Carbon Supported Ruthenium nanoparticles as an Efficient Catalyst for Toluene and Quinoline Hydrogenation. *Green Chem.* **2016**, *18* (22), 6082. https://doi.org/10.1039/C6GC01858K

(19) Lu, S.-M.; Han, X.-W.; Zhou, Y.-G. An Efficient Catalytic System for the Hydrogenation of Quinolines. *J. Organomet. Chem.* **2007**, *692* (14), 3065. https://doi.org/10.1016/j.jorganchem.2007.03.032

(20) Zou, Z.; Chen, C.; Hu, Z.; Shen, Y.; Fu, Z.; Li, W.; Zhang, Y.; Zhang, H.; Zhao, H.; Wang, G. Core Shell Hetero-Structured SiO_2@Ni/SiO_2 Catalyst for Efficient Aqueous-Phase Hydrogenation of Bio-Derived Unsaturated Compounds. *Fuel* **2022**, *318*, 123694. https://doi.org/10.1016/j.fuel.2022.123694

(21) Guo, M.; Li, C.; Yang, Q. Accelerated Catalytic Activity of Pd NPs Supported on Amine-Rich Silica Hollow Nanospheres for Quinoline Hydrogenation. *Catal. Sci. Technol.* **2017**, *7* (11), 2221. https://doi.org/10.1039/C7CY00394C

(22) Herbois, R.; Noël, S.; Léger, B.; Bai, L.; Roucoux, A.; Monflier, E.; Ponchel, A. Cyclodextrins as Growth Controlling Agents for Enhancing the Catalytic Activity of PVP-Stabilized Ru(0) NPs. *Chem. Commun.* **2012**, *48* (28), 3451. https://doi.org/10.1039/c2cc17355g

(23) Herbois, R.; Noël, S.; Léger, B.; Tilloy, S.; Menuel, S.; Addad, A.; Martel, B.; Ponchel, A.; Monflier, E. Ruthenium-Containing β-Cyclodextrin Polymer Globules for the Catalytic Hydrogenation of Biomass-Derived Furanic Compounds. *Green Chem.* **2015**, *17* (4), 2444. https://doi.org/10.1039/C5GC00005J

(24) Young, C. L. *Hydrogen and Deuterium*, 1st ed.; Young, C. L., Ed.; Solubility data series; Pergamon Press: Oxford ; New York, **1981**. https://srdata.nist.gov/solubility/IUPAC/SDS-5-6/SDS-5-6.pdf

(25) Trinh, T.-K.-H.; de Hemptinne, J.-C.; Lugo, R.; Ferrando, N.; Passarello, J.-P. Hydrogen Solubility in Hydrocarbon and Oxygenated Organic Compounds. *J. Chem. Eng. Data* **2016**, *61* (1), 19. https://doi.org/10.1021/acs.jced.5b00119

(26) Brunner, E. Solubility of Hydrogen in 10 Organic Solvents at 298.15, 323.15, and 373.15 K. *J. Chem. Eng. Data* **1985**, *30* (3), 269. https://doi.org/10.1021/je00041a010

(27) Axet, M. R.; Conejero, S.; Gerber, I. C. Ligand Effects on the Selective Hydrogenation of Nitrobenzene to Cyclohexylamine Using Ruthenium NPs as Catalysts. **2018**, *1* (10), 5885. https://doi.org/10.1021/acsanm.8b01549

(28) Leng, F.; Gerber, I. C.; Axet, M. R.; Serp, P. Selectivity Shifts in Hydrogenation of Cinnamaldehyde on Electron-Deficient Ruthenium NPs. *Comptes Rendus Chim.* **2018**, *21* (3–4), 346. https://doi.org/10.1016/j.crci.2017.04.001

(29) Wu, D.; Hernández, W. Y.; Zhang, S.; Vovk, E. I.; Zhou, X.; Yang, Y.; Khodakov, A. Y.; Ordomsky, V. V. In Situ Generation of Brønsted Acidity in the Pd-I Bifunctional Catalysts for Selective Reductive Etherification of Carbonyl Compounds under Mild Conditions. *ACS Catal.* **2019**, *9* (4), 2940. https://doi.org/10.1021/acscatal.8b04925

(30) Li, M.; Wang, H.; Zhu, W.; Li, W.; Wang, C.; Lu, X. RuNi NPs Embedded in N-Doped Carbon Nanofibers as a Robust Bifunctional Catalyst for Efficient Overall Water Splitting. *Adv. Sci.* **2020**, *7* (2), 1901833. https://doi.org/10.1002/advs.201901833

(31) Wang, X.; Weng, Y.; Zhao, X.; Xue, X.; Meng, S.; Wang, Z.; Zhang, W.; Duan, P.; Sun, Q.; Zhang, Y. Selective Hydrogenolysis and Hydrogenation of Furfuryl Alcohol in the Aqueous Phase Using Ru–Mn-Based Catalysts. *Ind. Eng. Chem. Res.* **2020**, *59* (39), 17210. https://doi.org/10.1021/acs.iecr.0c01023

(32) Zhang, B.; Zhu, Y.; Ding, G.; Zheng, H.; Li, Y. Selective Conversion of Furfuryl Alcohol to 1,2-Pentanediol over a Ru/MnO_x Catalyst in Aqueous Phase. *Green Chem.* **2012**, *14* (12), 3402. https://doi.org/10.1039/c2gc36270h

(33) Götz, D.; Lucas, M.; Claus, P. C–O Bond Hydrogenolysis vs. C=C Group Hydrogenation of Furfuryl Alcohol: Towards Sustainable Synthesis of 1,2-Pentanediol. *React. Chem. Eng.* **2016**, *1* (2), 161. https://doi.org/10.1039/C5RE00026B
(34) Bruna, L.; Cardona-Farreny, M.; Colliere, V.; Philippot, K.; Axet, M. R. In Situ Ruthenium Catalyst Modification for the Conversion of Furfural to 1,2-Pentanediol. *Nanomaterials* **2022**, *12* (3), 328. https://doi.org/10.3390/nano12030328
(35) Somorjai, G. A.; Park, J. Y. Colloid Science of Metal NP Catalysts in 2D and 3D Structures. Challenges of Nucleation, Growth, Composition, Particle Shape, Size Control and Their Influence on Activity and Selectivity. *Top. Catal.* **2008**, *49* (3–4), 126. https://doi.org/10.1007/s11244-008-9077-0
(36) Pushkarev, V. V.; An, K.; Alayoglu, S.; Beaumont, S. K.; Somorjai, G. A. Hydrogenation of Benzene and Toluene over Size Controlled Pt/SBA-15 Catalysts: Elucidation of the Pt Particle Size Effect on Reaction Kinetics. *J. Catal.* **2012**, *292*, 64. https://doi.org/10.1016/j.jcat.2012.04.022
(37) Yu, Z.; Lu, X.; Wang, X.; Xiong, J.; Li, X.; Zhang, R.; Ji, N. Metal-Catalyzed Hydrogenation of Biomass-Derived Furfural: Particle Size Effects and Regulation Strategies. *ChemSusChem* **2020**, *13* (19), 5185. https://doi.org/10.1002/cssc.202001467
(38) Pushkarev, V. V.; Musselwhite, N.; An, K.; Alayoglu, S.; Somorjai, G. A. High Structure Sensitivity of Vapor-Phase Furfural Decarbonylation/Hydrogenation Reaction Network as a Function of Size and Shape of Pt NPs. *Nano Lett.* **2012**, *12* (10), 5196. https://doi.org/10.1021/nl3023127
(39) Sun, C.; Zeng, P.; He, M.; He, X.; Xie, X. Morphological Effect of Non-Supported Copper Nanocrystals on Furfural Hydrogenation. *Catal. Commun.* **2016**, *86*, 5. https://doi.org/10.1016/j.catcom.2016.07.024
(40) Nakagawa, Y.; Nakazawa, H.; Watanabe, H.; Tomishige, K. Total Hydrogenation of Furfural over a Silica-Supported Nickel Catalyst Prepared by the Reduction of a Nickel Nitrate Precursor. *ChemCatChem* **2012**, *4* (11), 1791. https://doi.org/10.1002/cctc.201200218
(41) Nakagawa, Y.; Tomishige, K. Total Hydrogenation of Furan Derivatives over Silica-Supported Ni–Pd Alloy Catalyst. *Catal. Commun.* **2010**, *12* (3), 154. https://doi.org/10.1016/j.catcom.2010.09.003
(42) da Silva, M. J.; Teixeira, M. G. Assessment on the Double Role of the Transition Metal Salts on the Acetalization of Furfural: Lewis and Brønsted Acid Catalysts. *Mol. Catal.* **2018**, *461*, 40. https://doi.org/10.1016/j.mcat.2018.10.002
(43) Teixeira, M. G.; Natalino, R.; da Silva, M. J. A Kinetic Study of Heteropolyacid-Catalyzed Furfural Acetalization with Methanol at Room Temperature via Ultraviolet Spectroscopy. *Catal. Today* **2020**, *344*, 143. https://doi.org/10.1016/j.cattod.2018.11.071
(44) Pizzi, R.; van Putten, R.-J.; Brust, H.; Perathoner, S.; Centi, G.; van der Waal, J. High-Throughput Screening of Heterogeneous Catalysts for the Conversion of Furfural to Bio-Based Fuel Components. *Catalysts* **2015**, *5* (4), 2244. https://doi.org/10.3390/catal5042244
(45) Cardona-Farreny, M.; Lecante, P.; Esvan, J.; Dinoi, C.; del Rosal, I.; Poteau, R.; Philippot, K.; Axet, M. R. Bimetallic RuNi NPs as Catalysts for Upgrading Biomass: Metal Dilution and Solvent Effects on Selectivity Shifts. *Green Chem.* **2021**, *23* (21), 8480. https://doi.org/10.1039/D1GC02154K
(46) Chun, J.; Lee, H. S.; Jung, I. G.; Lee, S. W.; Kim, H. J.; Son, S. U. Cu_2O: A Versatile Reagent for Base-Free Direct Synthesis of NHC-Copper Complexes and Decoration of 3D-MOF with Coordinatively Unsaturated NHC-Copper Species. *Organometallics* **2010**, *29* (7), 1518. https://doi.org/10.1021/om900768w
(47) Katritzky, A. R.; Rachwal, S.; Rachwal, B. Recent Progress in the Synthesis of 1,2,3,4,-Tetrahydroquinolines. *Tetrahedron* **1996**, *52* (48), 15031. https://doi.org/10.1016/S0040-4020(96)00911-8
(48) Sridharan, V.; Suryavanshi, P. A.; Menéndez, J. C. Advances in the Chemistry of Tetrahydroquinolines. *Chem. Rev.* **2011**, *111* (11), 7157. https://doi.org/10.1021/cr100307m
(49) Moon, M. W.; Hsi, R. S. P. Synthesis of (R)-5-(Di[2,3-$^3H_2$]Propylamino)5,6-Dihydro-4H-Imidazo[4,5,1-Ij]Quinolin-2(^{1}H) - One ([^{3}H]U-86170) and (R)-5-([2,3-

$^{3}H_2$]Propylamino)-5,6-Dihydro-4H-Imidazo[4,5,1-Ij]Quinolin-2(^{1}H)-One ([^{3}H]U-91356). *J. Label. Compd. Radiopharm.* **1992**, *31* (11), 933. https://doi.org/10.1002/jlcr.2580311112

(50) Wee, A. G. H.; Liu, B.; Zhang, L. Dirhodium Tetraacetate Catalyzed Carbon-Hydrogen Insertion Reaction in N-Substituted a-Carbomethoxy-a-Diazoacetanilidesand Structural Analogues. Substituent and Conformational Effects' *J. Org. Chem.* **1992**, 57, 16, 4404. https://doi.org/10.1021/jo00042a018

(51) Alvanipour, A.; Kispert, L. D. Cobalt Stearate-Aluminum Alkyl Catalyzed Hydrogenation of Substituted Quinolines, Isoquinoline and Naphthalene. *J. Mol. Catal.* **1988**, *48* (2–3), 277. https://doi.org/10.1016/0304-5102(88)85011-9

(52) Zhuravleva, Yu. A.; Zimichev, A. V.; Zemtsova, M. N.; Klimochkin, Yu. N. Synthesis of Substituted 1,2,3,4-Tetrahydroquinoline-4-Carboxylic Acids. *Russ. J. Org. Chem.* **2009**, *45* (4), 609. https://doi.org/10.1134/S1070428009040228

(53) Czaplik, W. M.; Neudörfl, J.-M.; von Wangelin, A. J. On the Quantitative Recycling of Raney–Nickel Catalysts on a Lab-Scale. *Green Chem.* **2007**, *9* (11), 1163. https://doi.org/10.1039/b708057c

(54) Sun, B.; Carnevale, D.; Süss-Fink, G. Selective N-Cycle Hydrogenation of Quinolines with Sodium Borohydride in Aqueous Media Catalyzed by Hectorite-Supported Ruthenium NPs. *J. Organomet. Chem.* **2016**, *821*, 197. https://doi.org/10.1016/j.jorganchem.2016.07.010

(55) Sánchez-Delgado, R. A.; Machalaba, N.; Ng-a-qui, N. Hydrogenation of Quinoline by Ruthenium NPs Immobilized on Poly(4-Vinylpyridine). *Catal. Commun.* **2007**, *8* (12), 2115. https://doi.org/10.1016/j.catcom.2007.04.006

(56) Campanati, M.; Vaccari, A.; Piccolo, O. Mild Hydrogenation of Quinoline 1. Role of Reaction Parameters. **2002**, *179* (1-2), 287. https://doi.org/10.1016/S1381-1169(01)00401-0

(57) Frediani, P.; Rosi, L.; Cetarini, L.; Frediani, M. Quinoline Transfer Hydrogenation by a Rhodium Bipyridine Catalyst. *Inorganica Chim. Acta* **2006**, *359* (9), 2650. https://doi.org/10.1016/j.ica.2005.10.044

(58) Fujita, I.-C.; Yamaguchi, R. Cp*Ir Complex-Catalyzed Hydrogen Transfer Reactions Directed toward Environmentally Benign Organic Synthesis. *N. Y.* **2005**, *4*, 560. https://doi.org/10.1055/s-2005-862381

(59) Rosales, M.; Vallejo, R.; Bastidas, L. J.; González, B.; González, A. Hydrogenation of Heteroaromatic Nitrogen Compounds Catalyzed by Rhodium and Iridium Systems Containing Diphosphine Ligands. *React. Kinet. Catal. Lett.* **2007**, *92* (1), 99. https://doi.org/10.1007/s11144-007-5150-0

(60) Rosales, M.; González, A.; Navarro, J.; Soscún, H.; Zárraga, J. Synthesis and Catalytic Properties of the Complex [OsH(CO) $(NCMe)_2(PPh_3)_2BF_4$. *Inorganica Chim. Acta* **1997**, *257* (1), 131. https://doi.org/10.1016/S0020-1693(96)05434-5

(61) Zhu, G.; Pang, K.; Parkin, G. New Modes for Coordination of Aromatic Heterocyclic Nitrogen Compounds to Molybdenum: Catalytic Hydrogenation of Quinoline, Isoquinoline, and Quinoxaline by $Mo(PMe_3)_4H_4$. *J. Am. Chem. Soc.* **2008**, *130* (5), 1564. https://doi.org/10.1021/ja078102d

(62) Grigg, R.; Mitchell, T. R. B.; Sutthivaiyakit, S.; Tongpenyai, N. Transition Metal-Catalysed N-Alkylation of Amines by Alcohols. *J. Chem. Soc. Chem. Commun.* **1981**, *12*, 611. https://doi.org/10.1039/c39810000611

(63) Rösler, S.; Ertl, M.; Irrgang, T.; Kempe, R. Cobalt-Catalyzed Alkylation of Aromatic Amines by Alcohols. *Angew. Chem. Int. Ed.* **2015**, *54* (50), 15046. https://doi.org/10.1002/anie.201507955

(64) Zhang, G.; Yin, Z.; Zheng, S. Cobalt-Catalyzed N-Alkylation of Amines with Alcohols. *Org. Lett.* **2016**, *18* (2), 300. https://doi.org/10.1021/acs.orglett.5b03461

(65) Cumpstey, I.; Agrawal, S.; Borbas, K. E.; Martín-Matute, B. Iridium-Catalysed Condensation of Alcohols and Amines as a Method for Aminosugar Synthesis. *Chem. Commun.* **2011**, *47* (27), 7827. https://doi.org/10.1039/c1cc12800k

(66) Ruch, S.; Irrgang, T.; Kempe, R. New Iridium Catalysts for the Selective Alkylation of Amines by Alcohols under Mild Conditions and for the Synthesis of Quinolines by Ac-

ceptor-Less Dehydrogenative Condensation. *Chem. - Eur. J.* **2014**, *20* (41), 13279. https://doi.org/10.1002/chem.201402952

(67) Fujita, K.; Li, Z.; Ozeki, N.; Yamaguchi, R. N-Alkylation of Amines with Alcohols Catalyzed by a Cp*Ir Complex. *Tetrahedron Lett.* **2003**, *44* (13), 2687. https://doi.org/10.1016/S0040-4039(03)00371-X

(68) Corma, A.; Ródenas, T.; Sabater, M. A Bifunctional Pd/MgO Solid Catalyst for the One-Pot Selective N-Monoalkylation of Amines with Alcohols. *Chem. - Eur. J.* **2010**, *16* (1), 254. https://doi.org/10.1002/chem.200901501

(69) Shiraishi, Y.; Fujiwara, K.; Sugano, Y.; Ichikawa, S.; Hirai, T. N-Monoalkylation of Amines with Alcohols by Tandem Photocatalytic and Catalytic Reactions on TiO_2 Loaded with Pd NPs. *ACS Catal.* **2013**, *3* (3), 312. https://doi.org/10.1021/cs300756f

(70) Mamidala, R.; Mukundam, V.; Dhanunjayarao, K.; Venkatasubbaiah, K. Cyclometalated Palladium Pre-Catalyst for N-Alkylation of Amines Using Alcohols and Regioselective Alkylation of Sulfanilamide Using Aryl Alcohols. *Tetrahedron* **2017**, *73* (16), 2225–2233. https://doi.org/10.1016/j.tet.2017.03.001.

(71) Martínez-Asencio, A.; Ramón, D. J.; Yus, M. N-Alkylation of Poor Nucleophilic Amines and Derivatives with Alcohols by a Hydrogen Autotransfer Process Catalyzed by Copper(II) Acetate: Scope and Mechanistic Considerations. *Tetrahedron* **2011**, *67* (17), 3140. https://doi.org/10.1016/j.tet.2011.02.075

(72) Yang, H.; Mao, R.; Luo, C.; Lu, C.; Cheng, G. An Efficient Homogeneous Gold(I) Catalyst for N-Alkylation of Amines with Alcohols by Hydrogen Autotransfer. *Tetrahedron* **2014**, *70* (46), 8829. https://doi.org/10.1016/j.tet.2014.10.007

(73) Nayal, O. S.; Thakur, M. S.; Kumar, M.; Kumar, N.; Maurya, S. K. Ligand-Free Iron(II)-Catalyzed N-Alkylation of Hindered Secondary Arylamines with Non-Activated Secondary and Primary Alcohols *via* a Carbocationic Pathway. *Adv. Synth. Catal.* **2018**, *360* (4), 730. https://doi.org/10.1002/adsc.201701183

(74) Yan, T.; Feringa, B. L.; Barta, K. Iron Catalysed Direct Alkylation of Amines with Alcohols. *Nat. Commun.* **2014**, *5* (1), 5602. https://doi.org/10.1038/ncomms6602

(75) Fertig, R.; Irrgang, T.; Freitag, F.; Zander, J.; Kempe, R. Manganese-Catalyzed and Base-Switchable Synthesis of Amines or Imines via Borrowing Hydrogen or Dehydrogenative Condensation. *ACS Catal.* **2018**, *8* (9), 8525. https://doi.org/10.1021/acscatal.8b02530

(76) Elangovan, S.; Neumann, J.; Sortais, J.-B.; Junge, K.; Darcel, C.; Beller, M. Efficient and Selective N-Alkylation of Amines with Alcohols Catalysed by Manganese Pincer Complexes. *Nat. Commun.* **2016**, *7* (1), 12641. https://doi.org/10.1038/ncomms12641

(77) Shimizu, K.; Imaiida, N.; Kon, K.; Hakim Siddiki, S. M. A.; Satsuma, A. Heterogeneous Ni Catalysts for N-Alkylation of Amines with Alcohols. *ACS Catal.* **2013**, *3* (5), 998. https://doi.org/10.1021/cs4001267

(78) Pingen, D.; Lutz, M.; Vogt, D. Mechanistic Study on the Ruthenium-Catalyzed Direct Amination of Alcohols. *Organometallics* **2014**, *33* (7), 1623. https://doi.org/10.1021/om4011998

(79) Hamid, M. H. S. A.; Williams, J. M. J. Ruthenium Catalysed N-Alkylation of Amines with Alcohols. *Chem. Commun.* **2007**, *7*, 725. https://doi.org/10.1039/b616859k

(80) Hamid, M. H. S. A.; Williams, J. M. J. Ruthenium-Catalysed Synthesis of Tertiary Amines from Alcohols. *Tetrahedron Lett.* **2007**, *48* (47), 8263. https://doi.org/10.1016/j.tetlet.2007.09.134

(81) Murahashi, S.-I.; Kondo, K.; Hakata, T. Ruthenium Catalyzed Synthesis of Secondary or Tertiary Amines from Amines and Alcohols. *Tetrahedron Lett.* **1982**, *23* (2), 229. https://doi.org/10.1016/S0040-4039(00)86792-1

(82) Sánchez-Delgado, R. A.; Machalaba, N.; Ng-a-qui, N. Hydrogenation of Quinoline by Ruthenium NPs Immobilized on Poly(4-Vinylpyridine). *Catal. Commun.* **2007**, *8* (12), 2115. https://doi.org/10.1016/j.catcom.2007.04.006

(83) Tian, Z.; Jiang, H.; Huang, M.; Wang, G. Facile Synthesis of Size-Controlled Nitrogen-Doped Mesoporous Carbon Nanosphere Supported Ultrafine Ru NPs for Selective Hydrogenation of Quinolines. *Chem. – Eur. J.* **2020**, *26* (71), 17000. https://doi.org/10.1002/chem.202003492

(84) Zhu, Y.; Gu, J.; Huang, Z.; Ding, H.; Xia, H.; Qiu, S.; Xie, K. Facile Fabrication of Ni NPs Embedded within Highly N-Doped Carbon Nanofibers as an Outstanding Catalyst for Quinoline Hydrogenation. *J. Alloys Compd.* **2022**, *925*, 166703. https://doi.org/10.1016/j.jallcom.2022.166703

CHAPTER 4: DFT calculations of Ru and Ni models for furfural hydrogenation

Summary

4.1 Introduction

In Chapters 1 and 2, the need to find high performing catalysts for the implementation in the industry of lignocellulosic biomass, as an alternative to fossil fuels, was discussed. Density functional theory (DFT) studies have risen as a useful tool for the simulation and design of high performing materials for numerous applications like, for example, –C-H olefination.[1] Some of the applications of DFT studies are: calculation of electronic structures of materials with correlated electrons,[2–4] electrodynamics of materials with correlated electrons,[5,6] analysis of structural, magnetic and spectroscopic properties of metal complexes,[7] investigation of large molecules such as proteins,[8] analysis of the hydration, molecular docking and effect of biomolecules in DNA,[9] study of the damage human serum by IR irradiation,[10] or spectral analysis of a sinusoid.[11]

DFT studies have appeared to be a powerful tool to probe the properties of inorganic compounds by reaching high accuracy with low computational cost.[12] DFT methods are built on the Hohenberg-Kohn theorem,[13–15] which presents that, if the system electron density is known, all electronic properties of the compound can be calculated. Many chemical properties can be accurately calculated by the available functionals (a function of a function), even without knowing the precise form of all functional components. The majority of current density functionals were initially developed by changing little parameters of different molecules reference sets. DFT has become an effective alternative to classical Hartree-Fock and post-Hartree-Fock methods to investigate metal complexes. However, because of the scalability of the methods, the application of DFT on larger systems is limited by the availability of computational resources, even if the application on small molecular complexes of *ab initio* computational methods with high-level correlated wavefunctions has been already reported.[16,17] The advantages of DFT for metal-containing systems are mainly the good scalability of the system with the size, being thus able to calculate large molecular complexes, and the suitability of the computed orbitals for their analysis and the interpretation of the bonding between atoms and the system properties. Nevertheless, some important limitations of DFT to treat some systems have been observed.[18] Non exhaustive examples are: proton transfer and hydrogen bonding reactions[19] or metal complexes where low coordination numbers are favoured by DFT.[20]

DFT has also demonstrated to be useful in bioinorganic chemistry, by modelling structures, properties and processes in relation to photosynthesis, becoming a useful tool to validate experimental conclusions or to elucidate between different possibilities.[21] DFT allows to calculate several properties which may contribute to understand spectroscopic, electronic or geometric properties in a complementary way with experimental studies.[22] Some examples

of this symbiosis between DFT and experimental data have been reported for calculations of: geometries,[23–25] energy and reaction mechanisms,[26–28] vibrational frequencies,[29,30] and spectroscopic properties.[31,32]

DFT studies have also been reported to be a powerful approach to probe the properties of nanomaterials, such as magnetic, optical or catalytic, being in agreement with the experimental results.[33] Several studies trying to improve the already mentioned calculations on metallic centres[20] have been reported.[34] DFT studies coupled to algorithms have been reported for the optimisation of nanoparticles (NPs) or clusters on the basis of calculating the total energies and forces.[35] Some studies show the dependency of the structure on the composition and sizes of the NPs or clusters of Au,[36] Rh,[37] Ru,[38] Pd,[39] Ni,[40] and Pt.[41]

Vienna *ab initio* simulation package (VASP) has been used for DFT calculations on a large number of metallic systems. VASP allows to calculate the total energy and the electronic structure of metallic systems by using a plane-wave basis set.[42–45] The Perdew, Burke and Ernzerhof (PBE) proposition of the generalised gradient approach was used for the approximation of the exchange correlation potential.[46] Projector augmented wave (PAW) method is an electronic structure method, which acts on the core wave functions and the full valence, with high accuracy for the molecular dynamics simulations. This PAW method is of high precision, with errors on the bond lengths of less than 0.5 %, even in difficult situations such as large differences of electronegativity and strong magnetic moments.[47,48]

This chapter reports on DFT calculations using VASP with PAW method and PBE approximation are run on hydrogenated $Ru_{55}H_{70}$, $Ni_{38}H_{35}$ NPs and $Ru_{13}Ni_{25}$ models. DFT studies have been performed in collaboration with the group of R. Poteau at LPCNO,[49] which has a great expertise in this type of studies. These calculations have been done to better understand the catalytic study on furfural (FF) hydrogenation previously described in Chapter 3.

Ru_{55} NP model has already been characterised and described as a hexagonal close-packed (*hcp*) structure spheroid.[50] Some DFT studies on hydrogenated Ru NPs models ($Ru_{55}H_{70}$, $Ru_{55}H_{32}$, $Ru_{55}H_{15}$) have been previously reported in the group, exploring the adsorption effect of imidazolium-amidinates[51] and ethanoic acid[52] on their surface. The $Ru_{55}H_{70}$ is a good model under hydrogenation conditions for the Ru/polyvinylpyrrolidone (PVP) NPs,[50] with a H metallic surface coverage theoretically calculated[50] similar to that experimentally determined[53] (see Chapter 2).

Ni_{38} NP model has already been characterised and described as a highly symmetric face-centred cubic (*fcc*) structure,[54] being the Ni cluster that better represents the *fcc* structure,

from the ones containing between 13 to 55 atoms.[55] The Ni_{38} NP atoms are distributed by 6 atoms in the nuclei and 32 at the surface, as has been previously reported.[56] The $Ni_{38}H_{35}$ is a good model under hydrogenation saturated conditions for the Ni/PVP NPs described in Chapter 2, knowing that 36 hydrogen atoms can be adsorbed on the Ni_{38} surface by a dissociative chemisorption.[55]

Several types of bimetallic RuNi systems have been theoretically described: as a mixture of monometallic Ru and Ni NPs,[57] as small $Ru_{13}Ni_{13}$ clusters,[58] as adsorbed Ni atoms on a Ru nanosheet,[59,60] as a Ru surface covered by a Ni surface[61,62] or as a mixture of Ru and Ni atoms simulating an alloy.[63,64] The most similar systems to our $Ru_{13}Ni_{25}$ are the $Ru_{13}Ni_{13}$ clusters, where the Ru atoms are mainly located in the core.

DFT calculations screening on the adsorption and hydrogenation of platform molecules, such as FF or 2,5-hydroxymethylfurfural (HMF), on metallic NPs are scarce.[65] In the case of Ru[66–68] and Ni,[69] only theoretical studies on flat surfaces have been studied. It has been reported that the presence of co-adsorbed solvents,[70] ligands[71] and hydrides[70,72] on metallic surfaces has an important effect on the adsorption energies of substrates. From our knowledge, this work is the first theoretical study of the catalytic reactivity of FF and derivates on a hydrogenated Ru and Ni NPs surface.

4.2 DFT calculations on Ru_{55} models

Ru_{55} model is a spheroid with a *hcp* structure which its geometrical characteristics, and surface hydrides coverage has already been published.[50] In addition, several hydrogenation Ru NPs models ($Ru_{55}H_{70}$, $Ru_{55}H_{32}$, $Ru_{55}H_{15}$) have been studied for the adsorption of imidazolium-amidinates [51] and ethanoic acid[52] on their surface.

The $Ru_{55}H_{70}$ model describes well the Ru/PVP NPs under hydrogenation conditions used in our catalytic studies.[50] First, considering the size, the $Ru_{55}H_{70}$ model displays a size of *ca.* 1 nm, which is very similar to that of the Ru/PVP NPs described in previous chapters (1.0 ± 0.2 nm). Second, regarding the hydride surface coverage, this model displays a ratio H/(Ru on the surface) of 1.7, which corresponds to the coverage under hydrogenation conditions theoretically calculated,[50] that is close to the previously reported experimental value[53] and confirmed in this work (see Chapter 2).

In Chapter 3, the results obtained on the hydrogenation of FF,[66–68] catalysed by the monometallic Ru/PVP and Ni/PVP NPs as well as the bimetallic RuNi/PVP NPs, were described in two solvents: tetrahydrofuran (THF) and 1-PrOH. Given the differences observed in this reaction depending on the solvent used, several scenarios were computed in

order to decipher the underlying reasons. First, the adsorption energies of THF and 1-PrOH molecules adsorbed on a $Ru_{55}H_{70}$ NP were compared. Then hydrogenation of FF was studied considering the two solvents used in catalysis.

4.2.1 Determination of adsorption energies of THF and 1-PrOH on Ru_{55} models

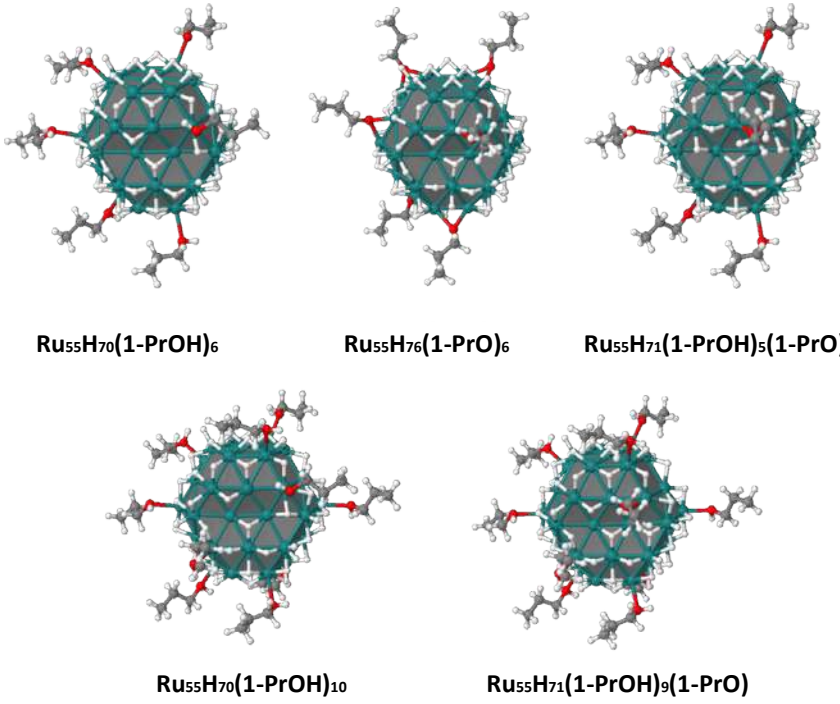

Figure 1: Dissociative or non-dissociative adsorption of 1-Propanol (1-PrOH) on the $Ru_{55}H_{70}$ model.

1-PrOH can adsorb on the Ru hydrogenated surface by the oxygen atom either upon the dissociation of the H of the alcohol moiety, forming the corresponding alkoxide, or without dissociate onto the surface. Figure 1 displays the optimised structures obtained by the adsorption of 1-PrOH (six or ten molecules), or the propanolate (six molecules), on a $Ru_{55}H_{70}$ model. It also depicts the adsorption of a propanolate in a hydrogenated Ru NP with five or nine molecules of propanol adsorbed. The adsorption of six 1-PrOH is exothermic (ΔE = -8.9 kcal·mol^{-1}), while the dissociative adsorption of all six 1-PrOH species (Scheme 2) is unfavourable (ΔE = -1.1 kcal·mol^{-1}). An intermediate scenario was also computed: the dissociative adsorption of only one of the six 1-PrOH molecules. If the dissociation happens at the moment of the adsorption (Scheme 3, ΔE = -9.0 kcal·mol^{-1}) it is favourable; if the dissociation takes place after adsorption, thus the dissociation of one of the six 1-PrOH molecules already adsorbed (Scheme 4), the ΔE is -0.2 kcal·mol^{-1}. Looking at all these energy

values, an equilibrium between propanol and propanolate species exists on the surface of the Ru NP (PrOH* ↔ (PrO* + H*)).

Other calculations were performed for ten molecules of 1-PrOH, Scheme 5 to 7. The adsorption of ten 1-PrOH molecules on the surface is exothermic (ΔE = -8.0 kcal·mol^{-1}, Scheme 5) as for six molecules (Scheme 1). The dissociative adsorption of only one of the 1-PrOH molecules at the moment of the adsorption, ΔE = -9.0 kcal·mol^{-1} (Scheme 6) or once the ten 1-PrOH molecules are adsorbed, ΔE = -9.6 kcal·mol^{-1} (Scheme 7), are both favourable towards the formation of the propanolate structure. Comparing the energies from Schemes 4 and 7, where the only difference between the structures is the addition of four 1-PrOH molecules, shows a great difference on the adsorption energy. The stabilisation observed when adding four 1-PrOH molecules (Scheme 7) could mean that they help to stabilise the structure containing one adsorbed propanolate molecule.

$$Ru_{55}H_{70} + 6\ 1PrOH \rightarrow Ru_{55}H_{70}(1PrOH)_6 \qquad \Delta E = -8.9\ kcal\cdot mol^{-1}$$

Scheme 1: Adsorption of six 1-PrOH molecules.

$$Ru_{55}H_{70} + 6\ 1PrOH \rightarrow Ru_{55}H_{76}(1PrO)_6 \qquad \Delta E = -1.1\ kcal\cdot mol^{-1}$$

Scheme 2: Dissociative adsorption of six 1-PrOH molecules.

$$Ru_{55}H_{70} + 6\ 1PrOH \rightarrow Ru_{55}H_{71}(1PrOH)_5(1PrO) \qquad \Delta E = -9.0\ kcal\cdot mol^{-1}$$

Scheme 3: Dissociative adsorption of one of the six 1-PrOH molecules.

$$Ru_{55}H_{70}(1PrOH)_6 \rightarrow Ru_{55}H_{71}(1PrOH)_5(1PrO) \qquad \Delta E = -0.2\ kcal\cdot mol^{-1}$$

Scheme 4: Dissociation of one of the six adsorbed 1-PrOH molecules.

$$Ru_{55}H_{70} + 10\ 1PrOH \rightarrow Ru_{55}H_{70}(1PrOH)_{10} \qquad \Delta E = -8.0\ kcal\cdot mol^{-1}$$

Scheme 5: Adsorption of ten 1-PrOH molecules.

$$Ru_{55}H_{70} + 10\ 1PrOH \rightarrow Ru_{55}H_{71}(1PrOH)_9(1PrO) \qquad \Delta E = -9.0\ kcal\cdot mol^{-1}$$

Scheme 6: Dissociative adsorption of one of the ten 1-PrOH molecules.

$$Ru_{55}H_{70}(1PrOH)_{10} \rightarrow Ru_{55}H_{71}(1PrOH)_9(1PrO) \qquad \Delta E = -9.6\ kcal\cdot mol^{-1}$$

Scheme 7: Dissociation of one of the ten adsorbed 1-PrOH molecules.

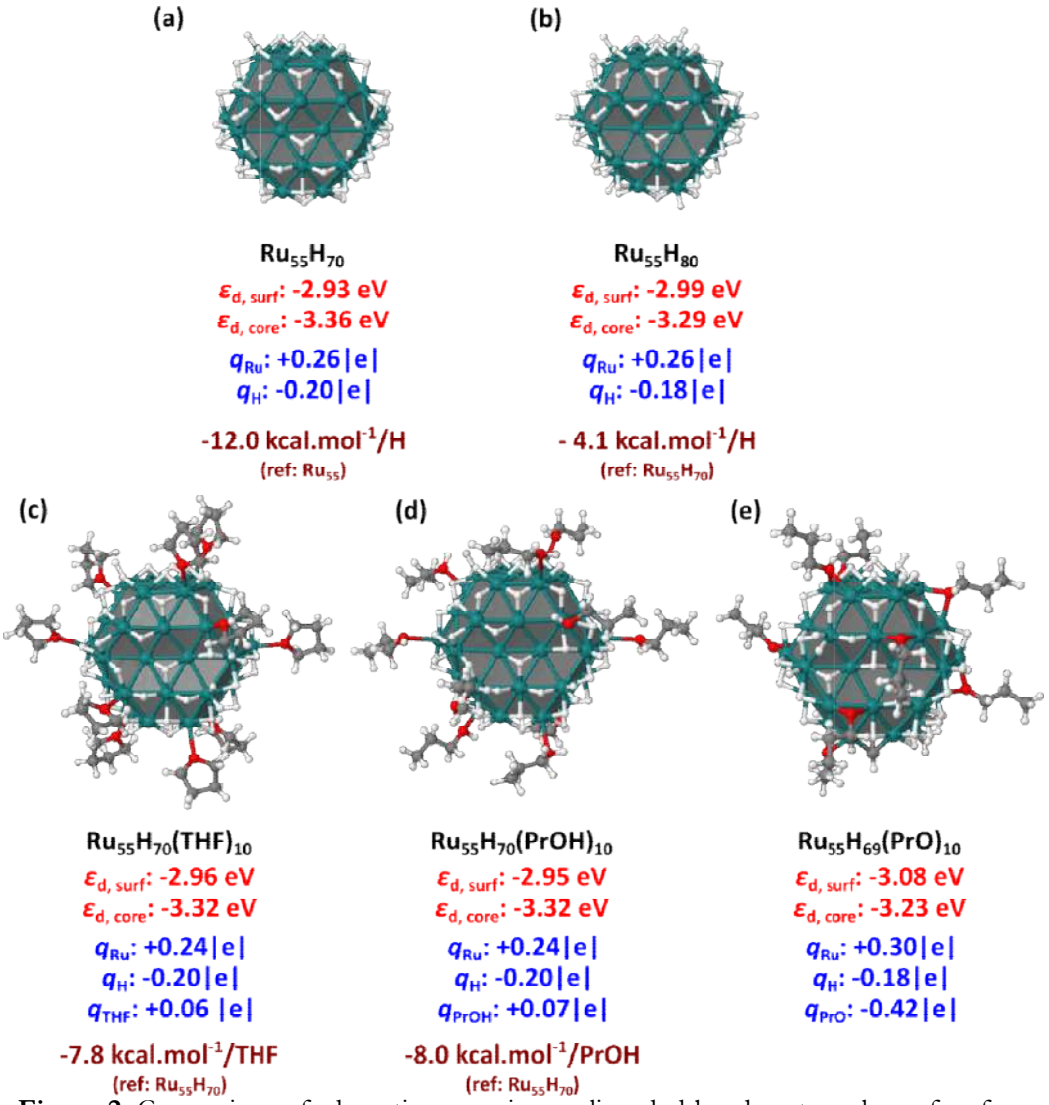

Figure 2: Comparison of adsorption energies per ligand, d-band center values of surface ($\varepsilon_{d,surf}$) and core ($\varepsilon_{d,core}$) Ru atoms, and average charges of hydrides (q_H) and metal atoms (q_{Ru}). $Ru_{55}H_{69}(PrO)_{10}$ was only considered to hypothetically assess the influence of ten propanolate ligands on the surface.

Next, the stability of the hydrogenated Ru species upon adsorption of THF or 1-PrOH was compared. Figure 2 depicts these structures together with the adsorption energies per ligand, d-band centre values of surface ($\varepsilon_{d,surf}$) and core ($\varepsilon_{d,core}$) Ru atoms, and average charges of hydrides (q_H) and metal atoms (q_{Ru}). The average adsorption energy of ten molecules of 1-PrOH is almost the same as for ten THF molecules, around -8 kcal·mol^{-1}.

The adsorption of ten additional hydrides to the surface of a $Ru_{55}H_{70}$ (ΔE = -4.1 kcal·mol^{-1}), is less favourable than the coordination of ten molecules of THF or 1-PrOH. Thus, both solvents can coordinate on the surface of Ru NPs with almost the same facility, meaning that the different FF conversion observed, in the two studied solvents, is related to a different mechanistic pathway and not to a different accessibility of the NP surface. It is also

noticeable that the dissociative adsorption of the ten 1-PrOH molecules as propanolates is not favourable, even if the dissociation of some of them is favourable, behaving as transient species in the reaction mechanisms. Electron charges and d-band centre values are also displayed, from where it can be concluded that the adsorbed solvent molecules have a slightly effect on d-band centres of the surface Ru atoms.[73] This is in accordance with the weak σ-donor character typical of this type of species which, differing from hydrides or other strongly bound ligands, are not supposed to influence in a significant way the catalytic activity of the surface atoms.

4.2.2 Possible reaction intermediates in furfural hydrogenation

Some reaction intermediates possibly involved in the hydrogenation mechanisms were investigated for the two solvents used in catalysis. In comparison to bare surfaces, adsorbed hydrides on the surface can modulate the reactivity of the NPs.[74] However, these hydrides have a high mobility, making the identification of stationary points along the reaction pathway much more complicated. Consequently, a complete relevant mechanistic study of the FF hydrogenation on small Ru NPs is challenging to achieve and was not the purpose of our work.[75] O-H activation has recently been reported of being a favoured reaction on the surface of Ru NPs for carboxylic acids.[52,76,77] Furthermore, C-H activation and formation have also been reported as being favourable on the surface of Ru NPs, in the case of H/D exchange at the alpha carbon of several substituted amines.[78,79] As the study of the mechanistic pathway is complicated, in our DFT calculations, the barrier heights were assumed to be low or moderate to focus mainly on the adsorption energies of the different reactions, intermediates and products of the reaction. Two different models for the two reaction media (THF or 1-PrOH) were studied to elucidate the hydrogenation mechanism for each solvent used. The THF model consisted of a $Ru_{55}H_{70}$ cluster while its 1-PrOH counterpart has two 1-PrOH molecules adsorbed on the surface of the hydrogenated Ru NP close to the studied active site (highlighted in yellow in Figure 3). This active site is placed in both cases at the interface between the facets (001) and (101) in the Ru NPs.[80]

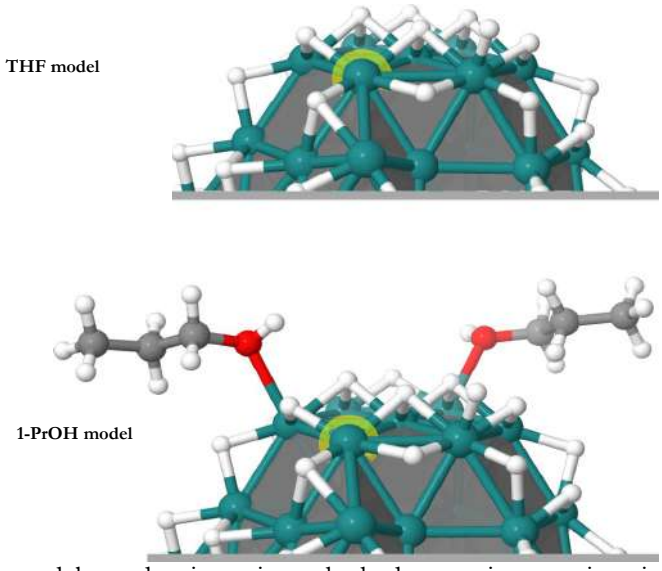

Figure 3: $Ru_{55}H_{70}$ models used to investigate the hydrogenation reactions in THF (top) and in 1-PrOH (bottom). The considered active site is highlighted with a yellow halo. The lower part of the models is not shown for the sake of clarity.

Figure 4 provides the atomic charges, from where it can be pointed out that for the hydrogenation catalysed by the Ru NPs, the hydrogen species on the surface are hydrides, while the reactions from Schemes 8 and 9 take place in acidic conditions. On the other hand, the hydrogen atoms dissociated from the 1-PrOH molecules are positively charged. Before entering into the mechanistic pathways, some energetic data, at the chosen DFT level, have to be given for the different hydrogenation reactions (Scheme 8-11).

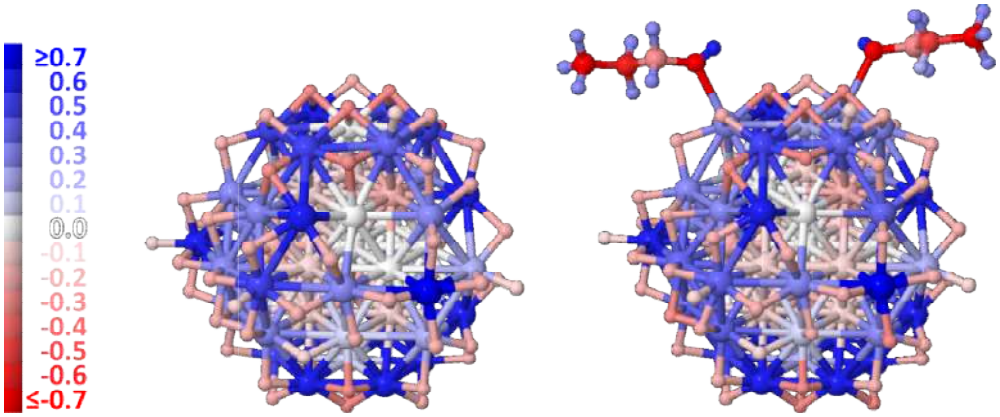

Figure 4: Atomic charges of the two model systems plotted as colour maps. Surface ruthenium atoms, in blue, are oxidized by all hydrides (average charges: $q_{Hydride}$ = -0.20 in both models, $q_{H(OH)}$ = +0.54).

FF + H_2 → HF ΔE = -18.0 kcal·mol^{-1}

Scheme 8: Hydrogenation of FF to furfuryl alcohol (HF).

$$HF + 2\ H_2 \rightarrow HMTHF \qquad \Delta E = -44.3\ kcal \cdot mol^{-1}$$

Scheme 9: Hydrogenation of HF to HMTHF.

$$HMTHF + H_2 \rightarrow 1,2\text{-PeD} \qquad \Delta E = -26.7\ kcal \cdot mol^{-1}$$

Scheme 10: Hydrogenation of HMTHF to 1,2-pentanediol (1,2-PeD).

$$FF + 2\ 1PrOH \rightarrow acetal + H_2O \qquad \Delta E = -6.5\ kcal \cdot mol^{-1}$$

Scheme 11: Acetalisation of FF with 1-PrOH.

The reactions from Schemes 8 to 10 are all exothermic, -18.0 kcal·mol^{-1}, -44.3 kcal·mol^{-1} and -26.7 kcal·mol^{-1}, respectively, and the reaction from Scheme 11, which occurs in presence of alcoholic solvents, is less exothermic (-6.5 kcal·mol^{-1}). Hydrogenation reactions are not easy processes kinetically even if from a thermodynamically point of view they are exothermic. For this reason, the use of hydrogenated Ru NPs is of great interest for catalysis as they have various and versatile active sites, as well as they present the dissociative chemisorption of hydrogen (H_2) on the surface with no energy barrier. The hydrides on the metallic surface have a high mobility and can coordinate the surface either in top, face-capping or edge-bridging as it has been previously reported from nuclear magnetic resonance (NMR) experiments[81] and DFT calculations.[82] The energies associated to the last four mentioned reactions should be exactly the same for their homologous on the active sites (*) on the Ru NPs (Schemes 12 to 15).

$$FF + H_2 + 2^* \rightarrow HF + 2^*$$

Scheme 12: Hydrogenation of FF to HF on 2 Ru active sites.

$$HF + 2\ H_2 + 3^* \rightarrow HMTHF + 3^*$$

Scheme 13: Hydrogenation of HF to HMTHF on 3 Ru active sites.

$$HMTHF + H_2 + 2^* \rightarrow 1,2\text{-PeD} + 2^*$$

Scheme 14: Hydrogenation of HMTHF to 1,2-PeD on 2 Ru active sites.

$$FF + 2\ 1PrOH + 3^* \rightarrow acetal + H_2O + 3^*$$

Scheme 15: Acetalisation of FF with 1-PrOH on 3 Ru active sites.

In these four schemes, 2* and 3* represent the number of different active sites on the Ru NP involved in the reaction, being an active site either a single Ru atom on the surface, a bimetallic edge or a coordination site with a higher μn index.

4.2.3 Determination of hydrogenation energy profiles in THF

Figures 5 and 6 describe a possible mechanism for FF hydrogenation in THF, where both FF and THF can be adsorbed on the $Ru_{55}H_{70}$ active site by a σ-donating coordination of the oxygen atom. The adsorption of FF is the most favourable compared to that of THF (-12 kcal·mol^{-1} against -10.6 kcal·mol^{-1}).

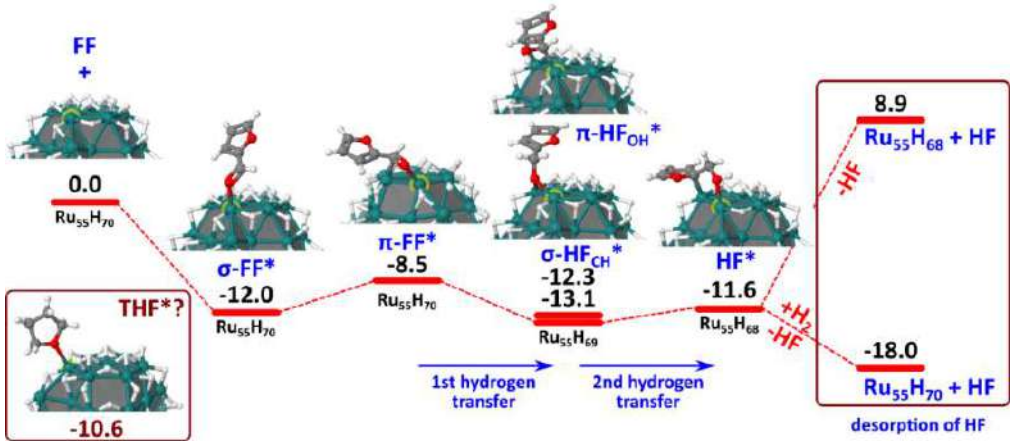

Figure 5: Energy profile for the FF hydrogenation on a $Ru_{55}H_{70}$ NP in THF. Energies are given in kcal·mol^{-1}.

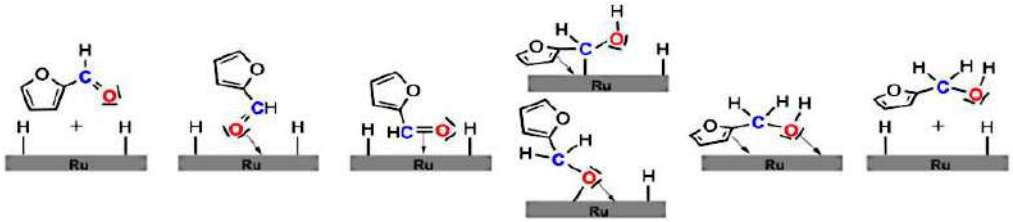

Figure 6: Simplified energy profile for the FF hydrogenation on a $Ru_{55}H_{70}$ NP in THF.

Once the FF molecule is adsorbed, the first transfer of hydride from the NP surface to the adsorbed FF* molecule may be favoured by the π coordination of the carbonyl function. Two intermediates are possible σ-HF_{CH}*$Ru_{55}H_{69}$ and π-HF_{OH}*$Ru_{55}H_{69}$. The first contains a bridging bidentate oxygen atom and its energy is equal to -13.1 kcal·mol^{-1}. The second involves a surface hydride transfer to the oxygen of the carbonyl function and a coordination of the carbon from the carbonyl to the surface, being slightly less stable (-12.3 kcal·mol^{-1}). Next, a second hydride transfer may occur from the surface to the oxygen of the alcoholate intermediate or to the carbon of the furfuryl resulting to the adsorbed HF* on a $Ru_{55}H_{68}$ NP. This intermediate is coordinated to the surface by both the oxygen from the alcohol function and a π interaction with the heterocycle with an energy value of -11.6 kcal·mol^{-1}. At mild temperature, the desorption of the HF* molecule is not favoured, being the desorption energy from the $Ru_{55}H_{68}$ NP of 8.9 kcal·mol^{-1}. Nevertheless, if H_2 pressure is present,

the $Ru_{55}H_{70}$ NP is regenerated favouring, from a thermodynamically point of view, the release of the adsorbed HF* molecule (-18.0 kcal·mol^{-1}).

Further hydrogenation of HF (Scheme 13 in Section 4.2.2) in THF, which seemed to be experimentally not favoured, has been also investigated. The hydrogenation of the furanyl cycle to form HMTHF requires its π coordination on the surface of the Ru NP. However, this coordination is challenging given the high quantity of hydrides present on the NP surface. The adsorption was studied at different sites of the NP and the adsorption energies appeared to be too weak in all cases because of the high H-coverage (Figure 7).

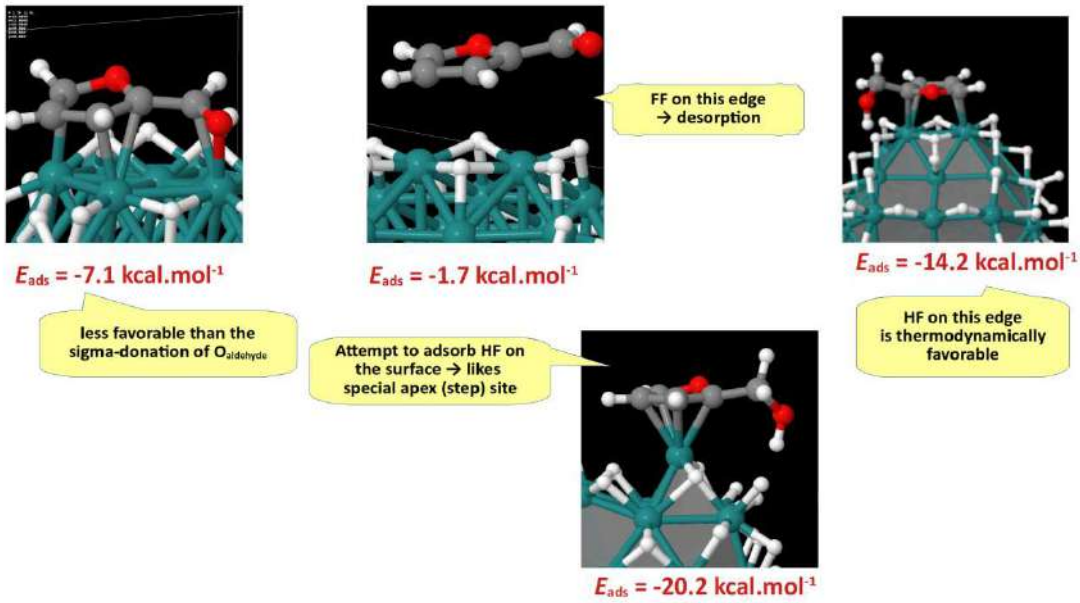

Figure 7: Possible π adsorption of 2-(hydroxymethyl)furan (HF), or FF, preliminary to the hydrogenation step of the furanyl cycle. Energies are given in kcal·mol^{-1}.

The most favoured structure is that where the coordination of the π system is on the apex atom of the $Ru_{55}H_{70}$ NP. As can be seen in Figure 8, the adsorption of the HF furanyl cycle on the two Ru active sites is favoured (-26.9 kcal·mol^{-1}), and even more than the HF desorption.

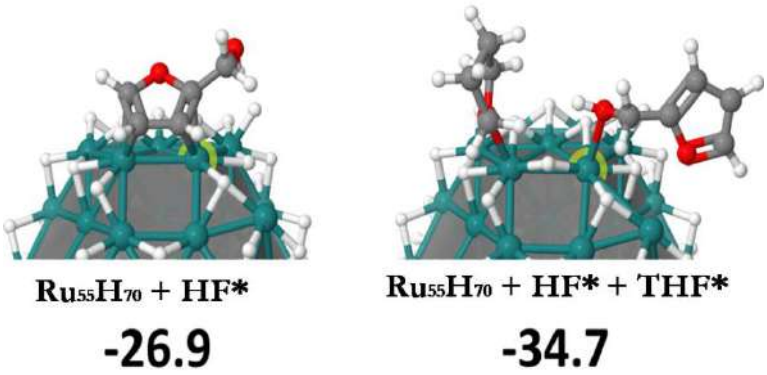

Figure 8: Possible species involved in the HF furanyl cycle hydrogenation, following the reaction of Scheme 13. Energies are given in kcal·mol^{-1}.

However, it is also observed (Figure 8) that the μ–η^2:η^2 coordination requires two metal sites which are not available when there is co-adsorption of one THF and one HF molecules. In this latter case, the reaction is clearly exothermic with an energy value of -34.7 kcal·mol^{-1}, suggesting that the coordination of THF is hampering the π coordination of HF and its further hydrogenation to HMTHF.

4.2.4 Determination of hydrogenation energy profiles in 1-PrOH

In THF, the only possible source of hydrogen atoms needed for the hydrogenation of FF is the Ru NP surface hydrides. However, in the case of 1-PrOH, the hydrogen of the alcohol function may also be a source of hydrogen atoms. This hypothesis has thus been investigated.

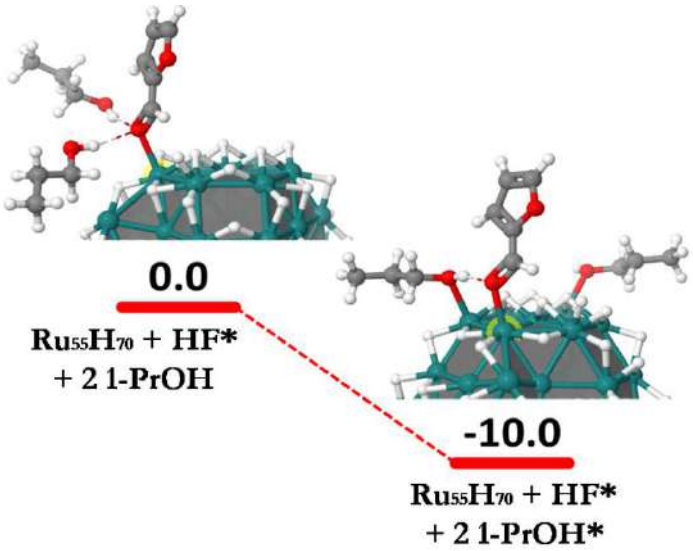

Figure 9: Possible adsorption modes of two 1-PrOH molecules on a $Ru_{55}H_{70}$ NP. Energies are given in kcal·mol^{-1}.

Figure 9 shows that two 1-PrOH molecules can interact with the FF substrate in two different ways: either by outer-sphere H-bond interactions with the adsorbed FF*, or by adsorbing also on the surface of the $Ru_{55}H_{70}$ NP, through the OH functions. After optimisation, it is observed that the adsorption of the two 1-PrOH molecules is 10 kcal·mol^{-1} more stable than the outer-sphere way, where H-bond interactions with the adsorbed FF* occur. The favourable adsorption indicates that, if 1-PrOH is involved in the hydrogenation mechanism, this involvement is after the adsorption of the 1-PrOH molecule on the surface of the NP.

Given this result, the two hydrogen atoms leading to the hydrogenation of the aldehyde group of FF can be: a) from the hydrides adsorbed on the Ru NP, following the mechanism of THF; b) from the alcohol functions of the 1-PrOH molecules after adsorption on the surface of the NP and c) from both the hydrides on the surface of the $Ru_{55}H_{70}$ NP and the OH groups.

The $Ru_{55}H_{70}$ NP with two adsorbed 1-PrOH molecules was chosen as model for the hydrogenation of FF in 1-PrOH (Figures 10 and 11).

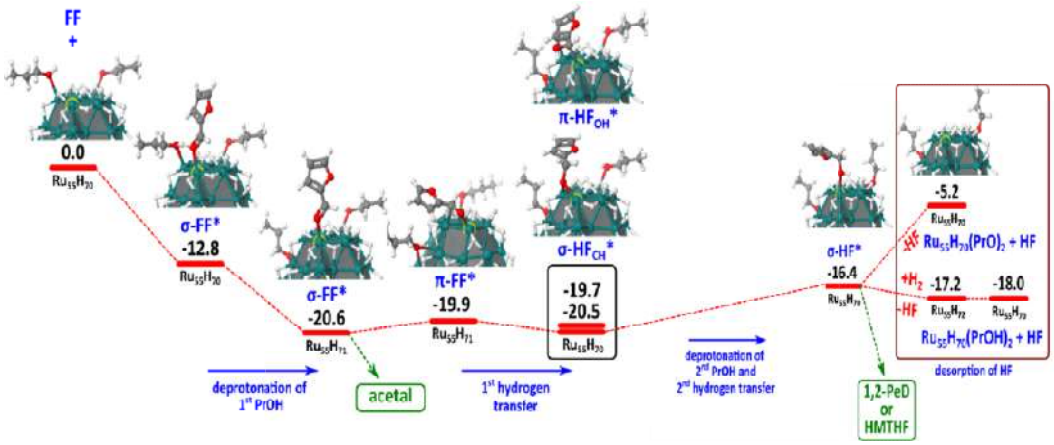

Figure 10: A possible energy profile for the FF hydrogenation on a $Ru_{55}H_{70}$ NP in 1-PrOH. Possible starting points toward the formation of acetal, HMTHF or 1,2-PeD are also shown. Energies are given in kcal·mol^{-1}.

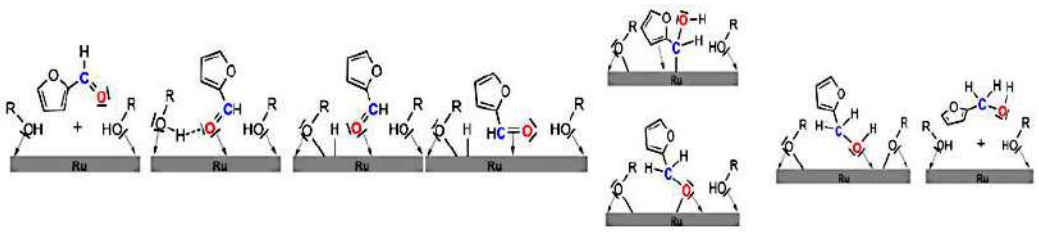

Figure 11: Simplified possible energy profile for the FF hydrogenation on a $Ru_{55}H_{70}$ NP in 1-PrOH. Possible starting points toward the formation of acetal, HMTHF or 1,2-PeD are also shown.

The first step consists on the adsorption of FF on the surface (σ-FF*$Ru_{55}H_{70}$) with an energy value of -12.8 kcal·mol^{-1}, followed by the dissociation of the O-H bond of one of the adsorbed 1-PrOH molecules on the surface of the NP (σ-FF*$Ru_{55}H_{71}$) with an energy value of -20.6 kcal·mol^{-1}. Next, the first hydride from the Ru surface is transferred to the carbonyl function of the adsorbed FF* molecule. As in the THF case, there are two hypotheses for the hydrogen transfer: to the carbonyl carbon, giving as product the alkoxide molecule coordinated through the oxygen as a bidentate ligand (σ-HF_{CH}*$Ru_{55}H_{70}$: -20.5 kcal·mol^{-1}) or to the carbonyl oxygen, providing a less stable intermediate coordinated to the surface by the carbonyl carbon (π-HF_{OH}*$Ru_{55}H_{70}$: -19.7 kcal·mol^{-1}). Then, the second hydrogen transfer involves either a hydride from the Ru NP surface transferred to the carbon of the carbonyl group or the hydrogen atom of the other adsorbed 1-PrOH, here transferred to the oxygen of the alkoxide. In both cases, the resulting product is the adsorbed HF* molecule on the NP surface coordinated through the oxygen of the OH function (σ-HF*$Ru_{55}H_{70}$: -16.4 kcal·mol^{-1}). Under H_2 pressure, the two 1-propanolate molecules are regenerated, returning to the initial state of the NP after desorption of the adsorbed HF* molecule (-18.0 kcal·mol^{-1}).

As the formation of furfuryl acetal was observed in catalysis (Chapter 3), this was also investigated which allowed to have a complete scheme of the FF hydrogenation reaction in 1-PrOH. By assuming that the energy barriers are low or moderate, several possible intermediates were studied to elucidate the acetal formation (Figures 12 and 13).

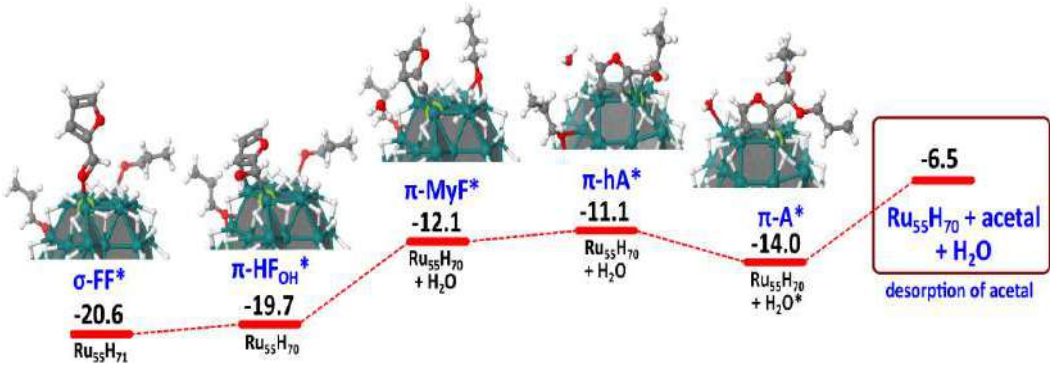

Figure 12: Energy clues on a possible reaction pathway for the formation of acetal in 1-PrOH, starting from the σ-FF* intermediate reported in Figure 10. Energies are given in kcal·mol^{-1}.

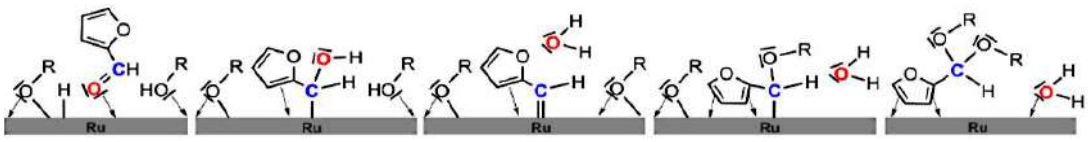

Figure 13: Simplified energy clues on a possible reaction pathway for the formation of acetal in 1-PrOH, starting from the σ-FF* intermediate reported in Figure 10.

The first part of the mechanism for acetal formation is exactly the same as for FF hydrogenation, starting by the adsorption of the FF to the $Ru_{55}H_{70}$ NP with two adsorbed 1-PrOH molecules (σ-FF*$Ru_{55}H_{70}$: -12.8 kcal·mol^{-1}, Figure. 10), followed by the dissociation of the O-H bond of one of the 1-PrOH molecules adsorbed on the NP (σ-FF*$Ru_{55}H_{71}$: -20.6 kcal·mol^{-1}). The first hydride transfer from the Ru NP surface to the oxygen of the carbonyl group of the adsorbed FF* may occur, being the FF molecule coordinated to the surface by the carbon atom of the carbonyl function (π-HF_{OH}*$Ru_{55}H_{70}$: -19.7 kcal·mol^{-1}). The transfer of a second hydrogen may then occur either from the surface of the NP or the second 1-PrOH molecule. This second hydrogenation may protonate the hydroxo group, thus releasing a water molecule. At the same time, the furfuryl molecule results to a relatively stable intermediate (π-MyF*$Ru_{55}H_{70}$: -12.1 kcal·mol^{-1}), containing a carbon atom with a sp2 hybridisation which is strongly bonded to the $Ru_{55}H_{70}$ surface. Figure 14 shows a comparison of some selected geometry parameters and charges of π-MyF*$Ru_{55}H_{70}$ and π-HF_{OH}*$Ru_{55}H_{70}$.

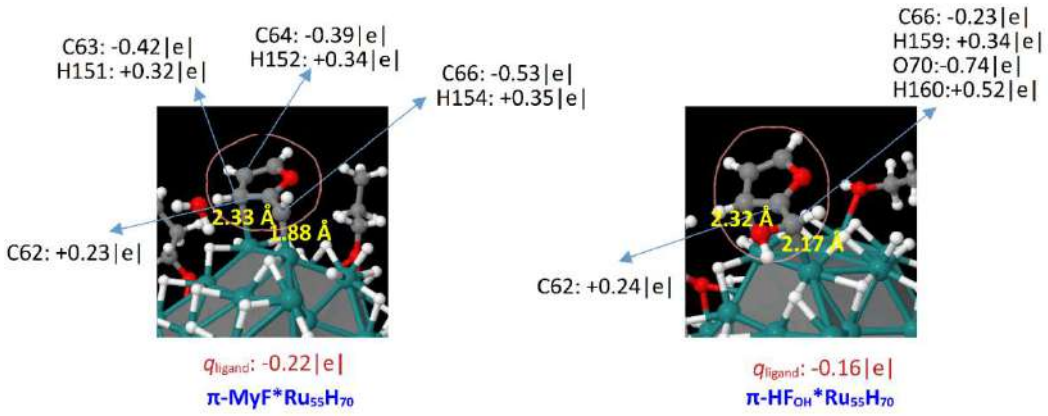

Figure 14: Comparison between π-MyF*$Ru_{55}H_{70}$ and π-HF_{OH}*$Ru_{55}H_{70}$of selected geometry parameters and charges. π-MyF*$Ru_{55}H_{70}$ is a dimetallacycle intermediate found on the acetal formation pathway. A vibrational analysis confirmed that it is a minimum on the potential energy surface. See also Figure 11, main text. The short Ru-$C_{methyne}(sp^2)$ bond length in this intermediate and the negative charge on the methyne fragment both suggest a kind of Ru=C double bond.

After, π-MyF*$Ru_{55}H_{70}$ can be attacked by one of the propanolate molecules, adsorbed on the surface of the NP, forming the monoether (hemiacetal) and then, by the second propanolate molecule, the diether (acetal) specie with -11.1 and -14.0 kcal·mol^{-1} respectively,. The stepwise formation of acetal and hemiacetal were also investigated although they were discarded as the formation of the adsorbed hemiacetal after the coupling with one 1-PrOH was not favoured (4.6 kcal·mol^{-1}).

Further hydrogenation of the aromatic ring followed by the ring-opening to obtain 1,2-PeD[83] has also been studied since the formation of this product has also been observed in catalysis. As before, being kinetic studies more complex and time consuming, only thermodynamics have been considered. Three points has to be stated: a) hydrogenated Ru NPs are good catalysts for hydrogenation reactions,[84] b) the furanyl hydrogenation implies a previous π coordination on the metallic surface and c) ring-opening reactions are easier from HMTHF than from HF. Taking into consideration these three statements, the results of these studies are reported in Figure 15.

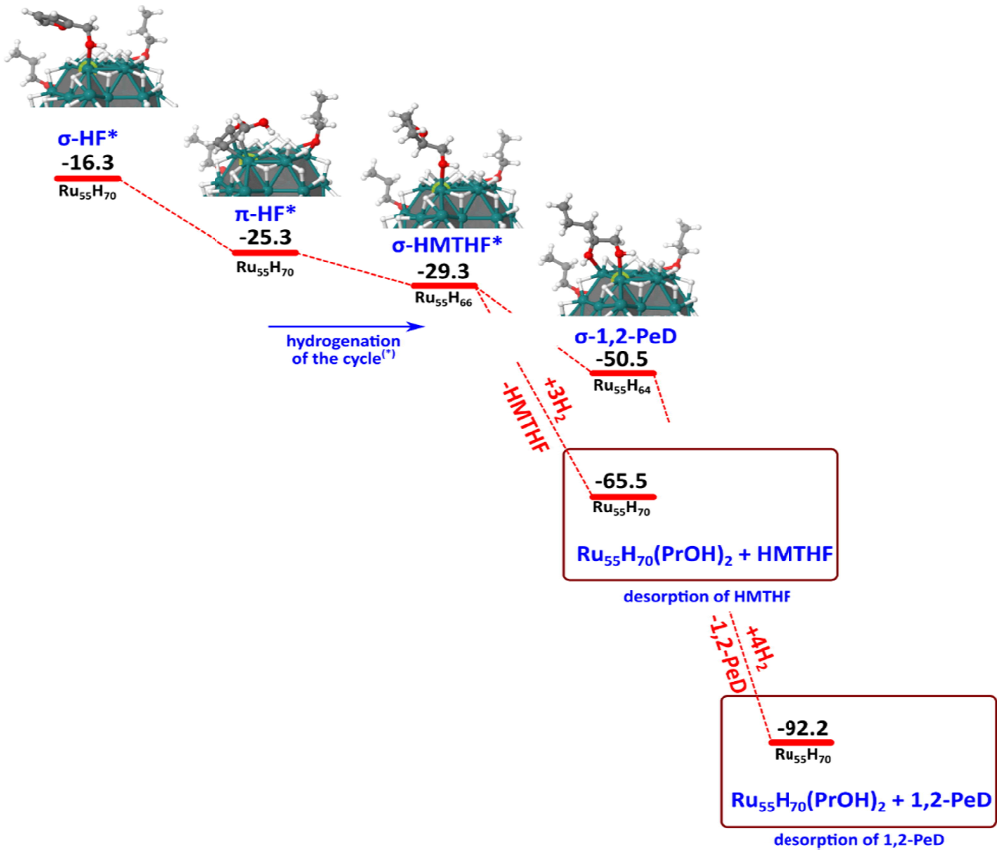

Figure 15: Possible reaction pathways for the formation of HMTHF (Scheme 13) and 1,2-PeD, in 1-PrOH. They both originate from the σ-HF* intermediate reported in Figure 10. (*): the four activated hydrides ongoing from π-HF* to σ-HMTHF* were randomly removed from the surface. Energies are given in kcal·mol^{-1}.

The π coordination of the HF molecules represents an extra stabilisation of 9 kcal·mol^{-1} in comparison to the σ-HF* conformation. Then, the breaking of a Ru-H bond is counterbalanced by the cycle hydrogenation. In this process, three H_2 molecules were used, taking into account the regeneration of the two 1-PrOH molecules adsorbed on the surface, exothermically releasing at the end a HMTHF molecule (Scheme 13, -65.5 kcal·mol^{-1}). Continuing

with the supposition that the ring-opening energy barrier is low, σ-HMTHF* may also provide 1,2-PeD, whose desorption is highly exothermic (-92.2 kcal·mol^{-1}). This exothermic value could make us think that it is a strong thermodynamic driving force although kinetics could make uneasy this reaction. π-HF* intermediate is stronger than the σ-HF* intermediate, which are competing for the same active sites, differentiating from other intermediates or even the solvent molecules.

To conclude this section of Chapter 4, two models representing the hydrogenated nanocatalysts with the two solvents used (THF and 1-PrOH) in catalysis (Chapter 3) were computed, being the Ru surface hydrides negatively charged, and the protons from 1-PrOH, positively charged. FF hydrogenation on the THF $Ru_{55}H_{70}$ NPs model reveals a competition between THF and FF for the adsorption on the NP surface. HF desorption is favoured by the continuous flow of H_2, and the ring hydrogenation hampered by the presence of THF. FF hydrogenation on the 1-PrOH $Ru_{55}H_{70}$ NPs model indicates that 1-PrOH plays an active role on the hydrogenation. DFT calculations allowed explaining the ring hydrogenation and ring opening experimentally observed (Chapter 3). 1,2-PeD formation is thermodynamically favoured and may act as driving force. FF can also react with 1-PrOH, being the acetal formation in competition with the FF hydrogenation, producing H_2O and acetal *via* the hemiacetal.

4.3 DFT calculations on Ni_{38} models

The Ni_{38} model chosen for this study is a NP of highly symmetric *fcc* structure whose geometrical characteristics have been previously published.[54] This Ni_{38} is interesting as it is the Ni cluster from the range 13 to 55 atoms whose structure represents the most likely the *fcc*.[55] The 38 atoms are distributed in three atomic layers with different facets, in an organisation with 6 atoms composing the core and 32 the surface of t he Ni cluster.[56]

The $Ni_{38}H_{35}$ model describes well the Ni/PVP system used in catalysis. First, because, as mentioned above, this model represents the *fcc* structure the best. Second, the hydride coverage of the Ni hydrogenated model $Ni_{38}H_{35}$ was optimized according to the hydrides surface coverage determined experimentally as described in Chapter 2. It is known that, under conditions of hydrogen saturation, the Ni_{38} model can bind 36 hydrogen atoms on its surface by the dissociative chemisorption of dihydrogen, being the $Ni_{38}H_{35}$ model in the good saturation range.[55]

Some binding rules previously reported for the adsorption of deuterium on Ni, have been considered suitable for hydrogen: (a) a H atom does not bind onto a top site; (b) the bind-

ing energies for bridge, three-fold and four-fold sites are equal; (c) binding of two bridge sites near an unoccupied three-fold or four-fold sites does not occur as well as the binding of a H to a bridge site surrounded by occupied three-fold or four-fold sites; (d) two adjacent three-fold sites cannot bind a H at the shared edge, which differentiates from the case of two four-fold sites; (e) two adjacent bridge sites at the same line of atoms cannot bind a H atom; and (f) each surface atom can bind a maximum of three H atoms.[85]

As for Ru, being the complete mechanism difficult to elucidate, in our calculations the focus has been placed on the determination of the adsorption energies of the different possible species (reactants, intermediates and products) of the reaction, supposing the energy barrier heights low or moderate.

4.3.1 Study of adsorption of FF onto $Ni_{38}H_{35}$ model

As for Ru/PVP, with the Ni/PVP nanocatalyst some differences were observed regarding the reaction media used. Consequently, two models to represent the use of THF and 1-PrOH in catalysis (Chapter 3) were also built and investigated. In the hydrogenation mechanism studies, some possible intermediates involved were considered for each solvent. As for the Ru/PVP case,[7] the hydrides present on the surface may also influence the catalytic activity of the Ni surface atoms of the Ni/PVP NPs. In THF, the model consisted of a $Ni_{38}H_{35}$ cluster while the counterpart in 1-PrOH has two 1-PrOH molecules adsorbed on the surface of the hydrogenated Ni NP close to the studied active site (Figure 16).

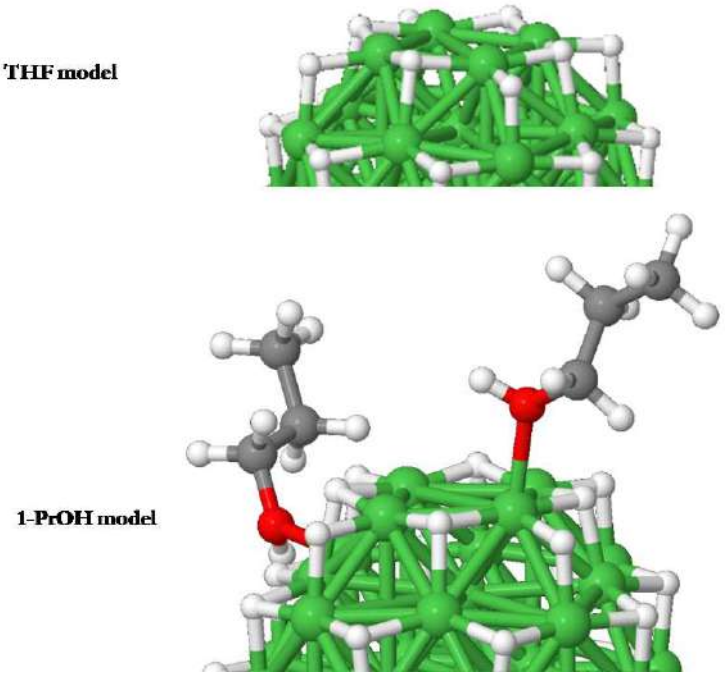

Figure 16: $Ni_{38}H_{35}$ models used to investigate the hydrogenation reactions in THF (top) and in 1-PrOH (bottom). The lower part of the models is not shown for the sake of clarity.

As observed in Figure 4 for Ru NPs, the atomic charges pointed out that the hydrogen species on the surface are hydrides. In the case of Ni NPs, the situation is the same being the hydrides placed at a certain distance, following the binding rules, because of the repulsion interactions.[55,86]

The reaction from Scheme 8 previously studied on the $Ru_{55}H_{70}$ model, has been also investigated on $Ni_{38}H_{35}$ system. As a reminding, this reaction is exothermic (-18.0 kcal·mol^{-1}). The negative adsorption energy should remain the same on the Ni NP active sites.

Figure 17 shows that the adsorption of the FF molecule is in competition with that of THF and 1-PrOH, being the FF the most stable in the two cases (-9.6 kcal·mol^{-1} *vs.* -8.6 kcal·mol^{-1} and -7.8 kcal·mol^{-1}, respectively).

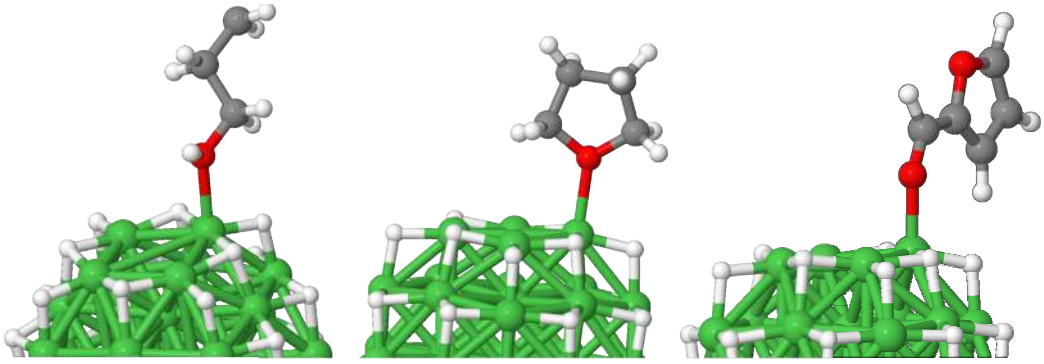

Figure 17: Adsorption energies on a $Ni_{38}H_{35}$ NP in kcal mol^{-1} of 1-PrOH, THF and FF (from left to right).

4.3.2 Determination of hydrogenation energy profiles in THF

Figure 18 and 19 show a possible mechanism for the FF hydrogenation in THF on the $Ni_{38}H_{35}$ NP model.

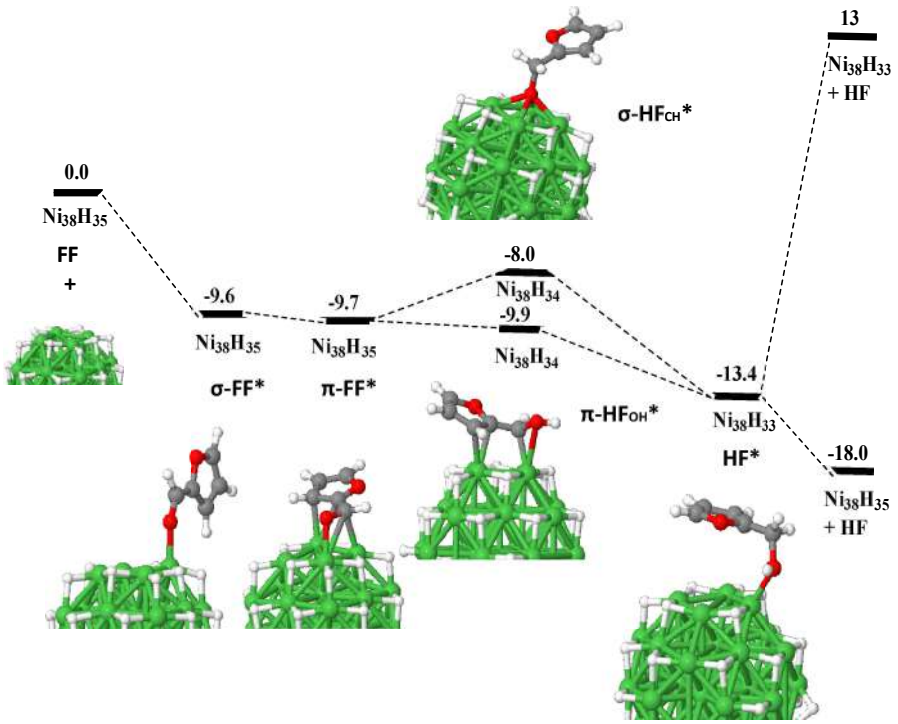

Figure 18: Energy profile for the FF hydrogenation on a $Ni_{38}H_{35}$ NP in THF. Energies are given in kcal·mol^{-1}.

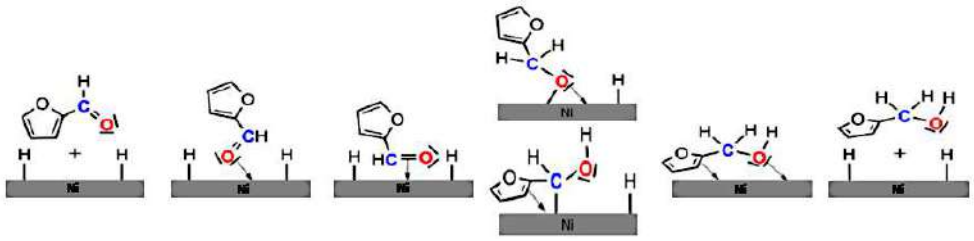

Figure 19: Simplified energy profile for the FF hydrogenation on a $Ni_{38}H_{35}$ NP in THF.

Once the FF molecule is adsorbed, a first hydride transfer from the Ni NP surface to the adsorbed FF* may be favoured by a π coordination of the carbonyl group. Two intermediates are possible σ-HF_{CH}*$Ni_{38}H_{34}$ and π-HF_{OH}*$Ni_{38}H_{34}$. The first contains an oxygen atom at a four-fold site and its energy is equal to -8.0 kcal·mol^{-1}. The second one involves a hydrogen transfer from the Ni NP surface to the oxygen of the carbonyl and the coordination of the carbon of the carbonyl to the metal surface, being the most stable (-9.9 kcal·mol^{-1}). This latter configuration may be more stable because of the interaction of a second Ni atom with the π system of the adsorbed FF* furanyl cycle. This π coordination may also explain the hydrogenation of the furan cycle observed experimentally (section 3.2 of Chapter 3). However, further calculations are needed to be able to conclude on this hypothesis. Next, the transfer of a second hydride may occur from the Ni NP surface to the oxygen of the alkoxide intermediate or to the carbon of the furfuryl cycle resulting to the adsorbed HF* on a $Ni_{38}H_{33}$ NP. This intermediate is coordinated to the surface by the oxygen from the

alcohol function with an energy value of -13.4 kcal·mol^{-1}. At mild temperature, the HF* molecule desorption is not favoured from the $Ni_{38}H_{33}$ NP, showing an energy of 13.0 kcal·mol^{-1}. However, under H_2 pressure, the $Ni_{38}H_{35}$ NP is regenerated thermodynamically favouring the release of the adsorbed HF* molecule (-18.0 kcal·mol^{-1}).

Comparing to the hydrogenation in THF on $Ru_{55}H_{70}$ NPs, the adsorption of the FF on the surface is less favoured on the $Ni_{38}H_{35}$ NP. This result may explain the higher activity on Ru observed in catalysis compared to Ni catalyst (see Chapter 3). Moreover, the reaction intermediates σ-HF_{CH}*$Ni_{38}H_{34}$ and π-HF_{OH}*$Ni_{38}H_{34}$ are more separated in energy than their Ru homologues σ-HF_{CH}*$Ru_{55}H_{69}$ and π-HF_{OH}*$Ru_{55}H_{69}$.

4.3.3 Determination of hydrogenation energy profiles in 1-PrOH

In the case of using 1-PrOH as reaction media on the $Ru_{55}H_{70}$ NP model, it was observed that the hydrogen of the alcohol group plays an important role in the hydrogenation mechanism. For this reason, even if data from Figure 18 evidences that the adsorption of the FF molecule is more favourable than the adsorption of the 1-PrOH molecule, two 1-PrOH molecules were adsorbed on this $Ni_{38}H_{35}$ model for the hydrogenation of FF in 1-PrOH (Figures 20 and 21).

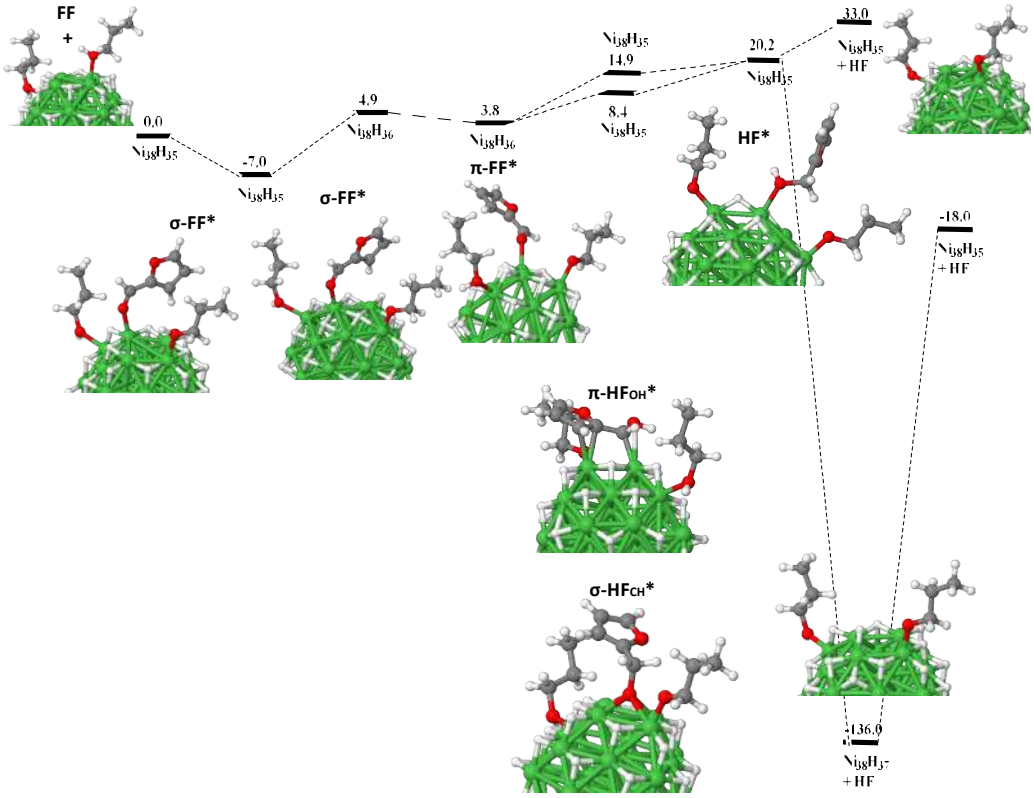

Figure 20: A possible energy profile for the FF hydrogenation on a $Ni_{38}H_{35}$ NP in 1-PrOH. Energies are given in kcal·mol^{-1}.

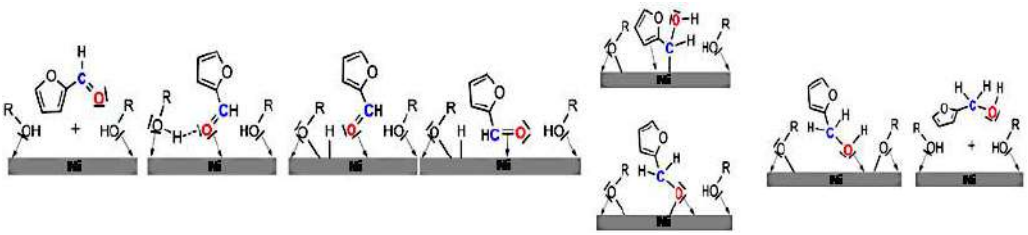

Figure 21: Simplified possible energy profile for the FF hydrogenation on a $Ni_{38}H_{35}$ NP in 1-PrOH.

The first step consists on the adsorption of FF on the Ni NP surface (σ-FF*$Ni_{38}H_{35}$) with an energy value of -7.0 kcal·mol^{-1}, followed by the dissociation of the O-H bond of one of the adsorbed 1-PrOH molecules on the metal surface (σ-FF*$Ni_{38}H_{36}$) with an energy value of 4.9 kcal·mol^{-1}. Next, the first hydride from the Ni surface is transferred to the carbonyl function of the adsorbed FF* molecule. As in the THF case, two configurations are possible: the hydride transfer to the carbonyl carbon, giving as product the alcoholate molecule coordinated through the oxygen as a bidentated ligand (σ-HF_{CH}*$Ni_{38}H_{35}$: 8.4 kcal·mol^{-1}) and the hydride transfer to the carbonyl oxygen, providing a less stable intermediate coordinated to the surface by the carbonyl carbon (π-HF_{OH}*$Ni_{38}H_{35}$: 14.9 kcal·mol^{-1}). The second hydrogen transfer involves either a hydride of the surface transferred to the carbon of the carbonyl group or the proton of the other 1-PrOH adsorbed transferred to the oxygen of the alcoholate. In both cases, the resulting product is the adsorbed HF* molecule on the surface of the NP coordinated through the oxygen of the OH function (σ-HF*$Ni_{38}H_{35}$: 20.2 kcal·mol^{-1}). Under H_2 pressure, the two 1-propanolate molecules are regenerated, returning to the initial state of the NP after desorption of the adsorbed HF* molecule (-18.0 kcal·mol^{-1}). Finally, the desorption without H regeneration is not favoured (33.0 kcal·mol^{-1}) while the adsorption of two H atoms on the Ni surface to regenerate the two 1-PrOH molecules ($Ni_{38}H_{37}$: -136.0 kcal·mol^{-1}), is highly exothermic.

Regarding all the energy values of the mechanism in Figure 20, it can be observed that almost all are positive, which is unexpected comparing to the previous cases of Ru and Ni already discussed in this chapter. However, these results may support the data obtained experimentally in catalysis: FF hydrogenation on Ni/PVP NPs in 1-PrOH is less performant from the series in 1-PrOH. The value -136.0 of kcal·mol^{-1} may explain that, even if two H are adsorbed at the end on the surface, the 1-PrOH molecules adsorbed are not going to be regenerated.

To conclude this section of Chapter 4, two models representing hydrogenated nanocatalysts with the two solvents used (THF and 1-PrOH) in catalysis (Chapter 3) were computed. FF hydrogenation on the THF $Ni_{38}H_{35}$ NPs model shows that HF desorption is favoured by the continuous flow of H_2. The ring hydrogenation in THF, observed experimentally with

Ni/PVP NPs (section 3.2 of Chapter 3) may be explained by the π coordination at the intermediate π-HF_{OH}*$Ni_{38}H_{34}$. FF hydrogenation on the 1-PrOH $Ni_{38}H_{35}$ NP model shows a great amount of positive adsorption energy values. These values are found strange in comparison to all the other computed reactions but, they may explain why experimentally the Ni/PVP catalyst is the less active of the series in 1-PrOH. Unfortunately, because of a lack of time, no further calculations were run to finally corroborate the FF hydrogenation mechanism on a $Ni_{38}H_{35}$ NP in 1-PrOH. As future perspectives, it will also be interesting to study for both models the further hydrogenation and the acetal formation reactions in order to have a full comparison of the NP catalytic properties.

4.4 DFT calculations on $Ru_{13}Ni_{25}$ models

Previously published computational studies on RuNi catalysts show bimetallic RuNi systems composed by monometallic Ru and Ni NPs,[57] small clusters $Ru_{13}Ni_{13}$,[58] a Ru nanosheet with adsorbed Ni atoms,[59,60] or a Ni surface covered by Ru surface below[61,62] or a mixture of the Ru and Ni surfaces simulating an alloy.[63,64]

Given the bimetallic NPs proved to be the most active in FF hydrogenation catalysis (Chapter 3), building a model for RuNi NPs is crucial. For this purpose, the $H/M_{surface}$ ratios of all the RuNi/PVP catalysts were determined experimentally (Chapter 2).

Different $Ru_{13}Ni_{25}$ models were built starting from the Ni_{38} model and replacing several Ni atoms of the NP by Ru atoms. This strategy was based on the wide angle X-ray scattering (WAXS) data from where a core-shell structure was experimentally determined, being the Ru in the core. The model used for Ni contains 38 atoms organised into 6 central atoms and 32 surface atoms. By following the Ni coverage estimations reported in Chapter 2, Ru_1Ni_1/PVP NPs have a Ni coverage of 77 % of the surface, which represents here 25 Ni atoms from the 32 atoms present on the surface. Three $Ru_{13}Ni_{25}$ models were thus built containing a pure Ru core (Figure 22, $Ru_{13}Ni_{25}$-A to C). With the aim of comparison, two more $Ru_{13}Ni_{25}$ models were studied simulating alloy structures (Figure 22, $Ru_{13}Ni_{25}$-D and E).

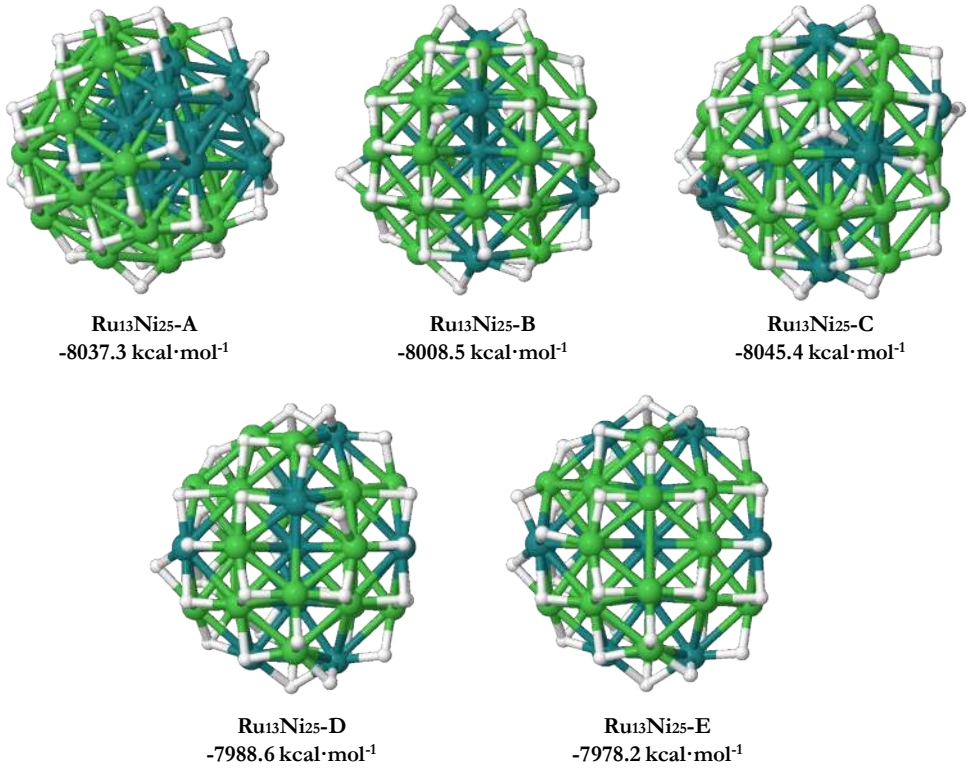

Figure 22: $Ru_{13}Ni_{25}$ models with a Ru core (A to C) and with an alloy structure (D and E) with their associated energies in kcal·mol^{-1}.

$Ru_{13}Ni_{25}$ models with a Ru core (A to C) are the most stable ones, supporting the experimental results obtained for the bimetallic RuNi NPs. Adsorptions of different species should be optimised in order to study the possible hydrogenation mechanism.

To conclude this section of Chapter 4, five hydrogenated $Ru_{13}Ni_{25}$ models were optimised, three of them ($Ru_{13}Ni_{25}$-A to C) maintaining the Ru core determined by WAXS analysis and two ($Ru_{13}Ni_{25}$-D and E) representing alloyed structures. As future perspectives, the plan is to continue with the adsorption of the different species studied in the monometallic Ru and Ni cases, in order to compare the catalytic properties of the bimetallic RuNi NPs to the Ru and Ni counterparts.

4.5 Conclusions

In this Chapter 4, different models of monometallic and bimetallic Ru and Ni hydrogenated NPs have been built and discussed for the hydrogenation reaction of FF and, in the case of 1-PrOH, the formation of acetal.

For the Ru NPs, in order to represent the two solvents (THF and 1-PrOH) used in catalysis (Chapter 3), two different models were built. The charges of the H atoms were observed to be negative on the Ru surface and positive at the 1-PrOH molecules. On the THF $Ru_{55}H_{70}$

NPs model, a competition between FF and THF for the adsorption on the actives sites of the NP surface was observed. The importance of a continuous flow of H_2 was observed as favourable for the desorption of HF and the presence of THF was seen to hamper the furfuryl cycle hydrogenation. On the 1-PrOH $Ru_{55}H_{70}$ NPs model, 1-PrOH was seen to play an active role on the FF hydrogenation and the importance of the continuous flow of H_2 was also observed. The ring hydrogenation and ring opening reactions observed experimentally (Chapter 3) were successfully explained by DFT calculations. The ring opening to form 1,2-PeD was observed to be favoured from a thermodynamic point of view, as well as potentially being the driving force of the reaction. Acetal formation is observed to be possible through the formation of hemiacetal and H_2O and to be in competition with FF hydrogenation.

Two different models of Ni NPs were built, in order to represent the two solvents (THF and 1-PrOH) used in catalysis (Chapter 3). On the THF $Ni_{38}H_{35}$ NPs model, the importance of a continuous flow of H_2 was observed as favourable for the desorption of HF. The π coordination of the intermediate $\pi\text{-}HF_{OH}{*}Ni_{38}H_{34}$ may explain the ring hydrogenation in THF, as observed experimentally with Ni/PVP NPs (section 3.2 of Chapter 3). On the 1-PrOH $Ni_{38}H_{35}$ NPs model, almost all the adsorption energy values were seen to be positive. By comparing to all the other studied reactions, these values are found unusual as in the other cases they were all negative. However, being the adsorption energies positive mean that they are not thermodynamically favoured, which may explain why experimentally, in the 1-PrOH series, the Ni/PVP is the less active catalyst. Unfortunately, the FF hydrogenation mechanism on a $Ni_{38}H_{35}$ NP in 1-PrOH was not corroborated as a matter of time. Finally, further hydrogenation and acetal formation studies on both solvent models will be of great interest to be able to compare on the catalytic properties of the monometallic and bimetallic series.

For the RuNi NPs, three models ($Ru_{13}Ni_{25}$-A to C) of hydrogenated $Ru_{13}Ni_{25}$ were built, considering a Ru core and two more models ($Ru_{13}Ni_{25}$-D and E), simulating alloys, were optimised for comparison purposes, being the core-shell structures the most stables. The future plan is to continue with the adsorption of the different species as studied in the other cases. In order to conclude on the catalytic properties of the monometallic and bimetallic series, running DFT calculation for the adsorption of the different molecules, as studied for the monometallic NPs, is among the perspective of this computational work.

4.6 References

(1) Ali, W.; Prakash, G.; Maiti, D. Recent Development in Transition Metal-Catalysed C–H Olefination. *Chem. Sci.* **2021**, *12* (8), 2735. https://doi.org/10.1039/D0SC05555G

(2) Kotliar, G.; Vollhardt, D. Strongly Correlated Materials: Insights From Dynamical Mean-Field Theory. *Physics Today*, **2004**, *57* (3), 53. https://doi.org/10.1063/1.1712502

(3) Kotliar, G.; Savrasov, S. Y.; Haule, K.; Oudovenko, V. S.; Parcollet, O.; Marianetti, C. A. Electronic Structure Calculations with Dynamical Mean-Field Theory. *Rev. Mod. Phys.* **2006**, *78* (3), 865. https://doi.org/10.1103/RevModPhys.78.865

(4) Held, K. Electronic Structure Calculations Using Dynamical Mean Field Theory. *Adv. Phys.* **2007**, *56* (6), 829. https://doi.org/10.1080/00018730701619647

(5) Basov, D. N.; Averitt, R. D.; van der Marel, D.; Dressel, M.; Haule, K. Electrodynamics of Correlated Electron Materials. *Rev. Mod. Phys.* **2011**, *83* (2), 471. https://doi.org/10.1103/RevModPhys.83.471

(6) Georges, A.; Kotliar, G.; Krauth, W.; Rozenberg, M. J. Dynamical Mean-Field Theory of Strongly Correlated Fermion Systems and the Limit of Infinite Dimensions. *Rev. Mod. Phys.* **1996**, *68* (1), 13. https://doi.org/10.1103/RevModPhys.68.13

(7) Platas-Iglesias, C.; Roca-Sabio, A.; Regueiro-Figueroa, M.; Esteban-Gomez, D.; de Blas, A.; Rodriguez-Blas, T. Applications of Density Functional Theory (DFT) to Investigate the Structural, Spectroscopic and Magnetic Properties of Lanthanide(III) Complexes. *Curr. Inorg. Chem.* **2011**, *1* (1), 91. https://doi.org/10.2174/1877944111101010091

(8) Hirao, H.; Thellamurege, N.; Zhang, X. Applications of Density Functional Theory to Iron-Containing Molecules of Bioinorganic Interest. *Front. Chem.* **2014**, *2*. https://doi.org/10.3389/fchem.2014.00014

(9) Alcolea Palafox, M.; Franklin Benial, A. M.; K. Rastogi, V. Biomolecules of 2-Thiouracil, 4-Thiouracil and 2,4-Dithiouracil: A DFT Study of the Hydration, Molecular Docking and Effect in DNA:RNA Microhelixes. *Int. J. Mol. Sci.* **2019**, *20* (14), 3477. https://doi.org/10.3390/ijms20143477

(10) Onami, Y.; Koya, R.; Kawasaki, T.; Aizawa, H.; Nakagame, R.; Miyagawa, Y.; Haraguchi, T.; Akitsu, T.; Tsukiyama, K.; Palafox, M. A. Investigation by DFT Methods of the Damage of Human Serum Albumin Including Amino Acid Derivative Schiff Base Zn(II) Complexes by IR-FEL Irradiation. *Int. J. Mol. Sci.* **2019**, *20* (11), 2846. https://doi.org/10.3390/ijms20112846

(11) Smith, J. O. Mathematics of the Discrete Fourier Transform (DFT), Stanford University, **2002**. https://library.uoh.edu.iq/admin/ebooks/70319-mathematics-of-the-discrete-fourier-transform.pdf

(12) Koch, W.; Holthausen, M. C. *A Chemist's Guide to Density Functional Theory*, 1st ed.; Wiley, **2001**. https://doi.org/10.1002/3527600043

(13) Hohenberg, P.; Kohn, W. Inhomogeneous Electron Gas. *Phys. Rev.* **1964**, *136* (3B), B864. https://doi.org/10.1103/PhysRev.136.B864

(14) Dreizler, R. M.; Gross, E. K. U. *Density Functional Theory*; An Approach to the Quantum Many-Body Problem, Springer Berlin Heidelberg: Berlin, Heidelberg, **1990**. https://doi.org/10.1007/978-3-642-86105-5

(15) Görling, A. Density-Functional Theory beyond the Hohenberg-Kohn Theorem. *Phys. Rev. A* **1999**, *59* (5), 3359. https://doi.org/10.1103/PhysRevA.59.3359

(16) Takeda, K.; Tsuchiya, T.; Nakano, H.; Taketsugu, T.; Hirao, K. Stability of Multiply Charged Anions of Lanthanide Hexafluorides LnF_6^{2-} and LnF_6^{3-} (Ln=Ce to Lu). *J. Mol. Struct.* **2001**, *537*, 107. https://doi.org/10.1016/S0166-1280(00)00667-9

(17) Cao, X.; Dolg, M. Pseudopotential Study of Lanthanum and Lutetium Dimers. *Theor. Chem. Acc. Theory Comput. Model. Theor. Chim. Acta* **2002**, *108* (3), 143. https://doi.org/10.1007/s00214-002-0372-8

(18) Fritsche, L.; Koller, J.; Reinert, Th. Borderline Cases in Density Functional Theory. *Int. J. Quantum Chem.* **2004**, *100* (4), 681. https://doi.org/10.1002/qua.20113

(19) Sadhukhan, S.; Muñoz, D.; Adamo, C.; Scuseria, G. E. Predicting Proton Transfer Barriers with Density Functional Methods. *Chem. Phys. Lett.* **1999**, *306* (1–2), 83. https://doi.org/10.1016/S0009-2614(99)00442-X
(20) Rotzinger, F. P. Treatment of Substitution and Rearrangement Mechanisms of Transition Metal Complexes with Quantum Chemical Methods. *Chem. Rev.* **2005**, *105* (6), 2003. https://doi.org/10.1021/cr030715v
(21) Wu, X.; Kang, F.; Duan, W.; Li, J. Density Functional Theory Calculations: A Powerful Tool to Simulate and Design High-Performance Energy Storage and Conversion Materials. *Prog. Nat. Sci. Mater. Int.* **2019**, *29* (3), 247. https://doi.org/10.1016/j.pnsc.2019.04.003
(22) Orio, M.; Pantazis, D. A.; Neese, F. Density Functional Theory. *Photosynth. Res.* **2009**, *102* (2–3), 443. https://doi.org/10.1007/s11120-009-9404-8
(23) Neese, F. A Critical Evaluation of DFT, Including Time-Dependent DFT, Applied to Bioinorganic Chemistry. *JBIC J. Biol. Inorg. Chem.* **2006**, *11* (6), 702. https://doi.org/10.1007/s00775-006-0138-1
(24) Bühl, M.; Reimann, C.; Pantazis, D. A.; Bredow, T.; Neese, F. Geometries of Third-Row Transition-Metal Complexes from Density-Functional Theory. *J. Chem. Theory Comput.* **2008**, *4* (9), 1449. https://doi.org/10.1021/ct800172j
(25) Rao, P. V. R.; Srishailam, K.; Reddy, B. V.; Rao, G. R. Theoretical (DFT) and Experimental (FT-IR & FT Raman) Approach to Investigate the Molecular Geometry and Vibrational Properties of 2,5- and 2,6-Dihydroxytoluenes. *J. Mol. Struct.* **2021**, *1240*, 130617. https://doi.org/10.1016/j.molstruc.2021.130617
(26) Siegbahn, P. E. M. The Performance of Hybrid DFT for Mechanisms Involving Transition Metal Complexes in Enzymes. *JBIC J. Biol. Inorg. Chem.* **2006**, *11* (6), 695. https://doi.org/10.1007/s00775-006-0137-2.
(27) Sproviero, E. M.; Shinopoulos, K.; Gascón, J. A.; McEvoy, J. P.; Brudvig, G. W.; Batista, V. S. QM/MM Computational Studies of Substrate Water Binding to the Oxygen-Evolving Centre of Photosystem II. *Philos. Trans. R. Soc. B Biol. Sci.* **2008**, *363* (1494), 1149. https://doi.org/10.1098/rstb.2007.2210
(28) Bhandari, S.; Rangarajan, S.; Maravelias, C. T.; Dumesic, J. A.; Mavrikakis, M. Reaction Mechanism of Vapor-Phase Formic Acid Decomposition over Platinum Catalysts: DFT, Reaction Kinetics Experiments, and Microkinetic Modeling. *ACS Catal.* **2020**, *10* (7), 4112. https://doi.org/10.1021/acscatal.9b05424
(29) Sproviero, E. M.; McEvoy, J. P.; Gascón, J. A.; Brudvig, G. W.; Batista, V. S. Computational Insights into the O_2-Evolving Complex of Photosystem II. *Photosynth. Res.* **2008**, *97* (1), 91. https://doi.org/10.1007/s11120-008-9307-0
(30) Eftimie, E.-L. A.; Roman, R.; Nicolov, M.; Ledeti, I.; Szabadai, Z.; Avram, N. M. DFT Calculation of Vibrational Frequencies for Betulinic Acid Methanol Monosolvate; Heidelberg, Germany, **2017**, 030012. https://doi.org/10.1063/1.4972377
(31) Radula-Janik, K.; Kupka, T.; Ejsmont, K.; Daszkiewicz, Z.; Sauer, S. P. A. DFT and Experimental Studies on Structure and Spectroscopic Parameters of 3,6-Diiodo-9-Ethyl-9H-Carbazole. *Struct. Chem.* **2016**, *27* (1), 199. https://doi.org/10.1007/s11224-015-0711-8
(32) Sima Abdollahi, Mrs.; Nemati-Kande, E.; Poursattar Marjani, A. Experimental and DFT Studies on the FT-IR, NMR and UV/Vis Spectra of a Xanthene Derivative: The Case of 9-benzoyl-3,4,5,6,7,9-hexahydro-1*h*-xanthene-1,8(2*h*)-dione. *ChemistrySelect* **2020**, *5* (13), 3971. https://doi.org/10.1002/slct.201904165
(33) Makkar, P.; Ghosh, N. N. A Review on the Use of DFT for the Prediction of the Properties of Nanomaterials. *RSC Adv.* **2021**, *11* (45), 27897. https://doi.org/10.1039/D1RA04876G.
(34) Verga, L. G.; Skylaris, C.-K. DFT Modeling of Metallic Nanoparticles. In *Frontiers of Nanoscience*; Elsevier, **2018**, *12*, 239. https://doi.org/10.1016/B978-0-08-102232-0.00008-7
(35) Heiles, S.; Johnston, R. L. Global Optimization of Clusters Using Electronic Structure Methods. *Int. J. Quantum Chem.* **2013**, *113* (18), 2091. https://doi.org/10.1002/qua.24462

(36) Häberlen, O. D.; Chung, S.-C.; Stener, M.; Rösch, N. From Clusters to Bulk: A Relativistic Density Functional Investigation on a Series of Gold Clusters Au_n, n=6,…,147. *J. Chem. Phys.* **1997**, *106* (12), 5189. https://doi.org/10.1063/1.473518
(37) Wang, L.; Ge, Q. Studies of Rhodium Nanoparticles Using the First Principles Density Functional Theory Calculations. *Chem. Phys. Lett.* **2002**, *366* (3–4), 368. https://doi.org/10.1016/S0009-2614(02)01577-4
(38) Nanba, Y.; Ishimoto, T.; Koyama, M. Structural Stability of Ruthenium Nanoparticles: A Density Functional Theory Study. *J. Phys. Chem. C* **2017**, *121* (49), 27445. https://doi.org/10.1021/acs.jpcc.7b08672
(39) Viñes, F.; Illas, F.; Neyman, K. M. Density Functional Calculations of Pd Nanoparticles Using a Plane-Wave Method. *J. Phys. Chem. A* **2008**, *112* (38), 8911. https://doi.org/10.1021/jp8014854
(40) Smerieri, M.; Pal, J.; Savio, L.; Vattuone, L.; Ferrando, R.; Tosoni, S.; Giordano, L.; Pacchioni, G.; Rocca, M. Spontaneous Oxidation of Ni Nanoclusters on MgO Monolayers Induced by Segregation of Interfacial Oxygen. *J. Phys. Chem. Lett.* **2015**, *6* (15), 3104. https://doi.org/10.1021/acs.jpclett.5b01362
(41) Xiao, L.; Wang, L. Structures of Platinum Clusters: Planar or Spherical? *J. Phys. Chem. A* **2004**, *108* (41), 8605. https://doi.org/10.1021/jp0485035
(42) Kresse, G.; Furthmüller, J. Efficient Iterative Schemes for *Ab Initio* Total-Energy Calculations Using a Plane-Wave Basis Set. *Phys. Rev. B* **1996**, *54* (16), 11169. https://doi.org/10.1103/PhysRevB.54.11169
(43) Kresse, G.; Furthmüller, J. Efficiency of Ab-Initio Total Energy Calculations for Metals and Semiconductors Using a Plane-Wave Basis Set. *Comput. Mater. Sci.* **1996**, *6* (1), 15. https://doi.org/10.1016/0927-0256(96)00008-0
(44) Hafner, J. *Ab-Initio* Simulations of Materials Using VASP: Density-Functional Theory and Beyond. *J. Comput. Chem.* **2008**, *29* (13), 2044. https://doi.org/10.1002/jcc.21057
(45) Kresse, G.; Hafner, J. *Ab Initio* Molecular Dynamics for Liquid Metals. *Phys. Rev. B* **1993**, *47* (1), 558. https://doi.org/10.1103/PhysRevB.47.558
(46) Perdew, J. P.; Burke, K.; Ernzerhof, M. Generalized Gradient Approximation Made Simple. *Phys. Rev. Lett.* **1996**, *77* (18), 3865. https://doi.org/10.1103/PhysRevLett.77.3865
(47) Blöchl, P. E. Projector Augmented-Wave Method. *Phys. Rev. B* **1994**, *50* (24), 17953. https://doi.org/10.1103/PhysRevB.50.17953
(48) Kresse, G.; Joubert, D. From Ultrasoft Pseudopotentials to the Projector Augmented-Wave Method. *Phys. Rev. B* **1999**, *59* (3), 1758. https://doi.org/10.1103/PhysRevB.59.1758
(49) Research Groups - Physical and Chemical Modelization. Laboratoire de Physique et Chimie des Nano-Objets. https://lpcno.insa-toulouse.fr/research-groups/physical-and-chemical-modelization/
(50) Cusinato, L.; Martínez-Prieto, L. M.; Chaudret, B.; del Rosal, I.; Poteau, R. Theoretical Characterization of the Surface Composition of Ruthenium Nanoparticles in Equilibrium with Syngas. *Nanoscale* **2016**, *8* (21), 10974. https://doi.org/10.1039/C6NR01191H
(51) Martínez-Prieto, L. M.; Cano, I.; Márquez, A.; Baquero, E. A.; Tricard, S.; Cusinato, L.; del Rosal, I.; Poteau, R.; Coppel, Y.; Philippot, K.; Chaudret, B.; Cámpora, J.; van Leeuwen, P. W. N. M. Zwitterionic Amidinates as Effective Ligands for Platinum Nanoparticle Hydrogenation Catalysts. *Chem. Sci.* **2017**, *8* (4), 2931. https://doi.org/10.1039/C6SC05551F
(52) González-Gómez, R.; Cusinato, L.; Bijani, C.; Coppel, Y.; Lecante, P.; Amiens, C.; del Rosal, I.; Philippot, K.; Poteau, R. Carboxylic Acid-Capped Ruthenium Nanoparticles: Experimental and Theoretical Case Study with Ethanoic Acid. *Nanoscale* **2019**, *11* (19), 9392. https://doi.org/10.1039/C9NR00391F
(53) García-Antón, J.; Axet, M. R.; Jansat, S.; Philippot, K.; Chaudret, B.; Pery, T.; Buntkowsky, G.; Limbach, H.-H. Reactions of Olefins with Ruthenium Hydride Nanoparticles: NMR Characterization, Hydride Titration, and Room-Temperature C-C Bond Ac-

tivation. *Angew. Chem. Int. Ed.* **2008**, *47* (11), 2074. https://doi.org/10.1002/anie.200704763
(54) Knickelbein, M. B. Electric Dipole Polarizabilities of $Ni_{12–58}$. *J. Chem. Phys.* **2001**, *115* (13), 5957. https://doi.org/10.1063/1.1398578
(55) Parks, E. K.; Nieman, G. C.; Kerns, K. P.; Riley, S. J. Reactions of Ni_{38} with N_2, H_2, and CO: Cluster Structure and Adsorbate Binding Sites. *J. Chem. Phys.* **1997**, *107* (6), 1861. https://doi.org/10.1063/1.474536
(56) Zhang, Q.-M.; Wells, J. C.; Gong, X. G.; Zhang, Z. Adsorption of a Carbon Atom on the Ni_{38} Magic Cluster and Three Low-Index Nickel Surfaces: A Comparative First-Principles Study. *Phys. Rev. B* **2004**, *69* (20), 205413. https://doi.org/10.1103/PhysRevB.69.205413
(57) Luo, Z.; Zheng, Z.; Li, L.; Cui, Y.-T.; Zhao, C. Bimetallic Ru–Ni Catalyzed Aqueous-Phase Guaiacol Hydrogenolysis at Low H_2 Pressures. *ACS Catal.* **2017**, *7* (12), 8304. https://doi.org/10.1021/acscatal.7b02317
(58) Masuda, S.; Mori, K.; Sano, T.; Miyawaki, K.; Chiang, W.-H.; Yamashita, H. Simple Route for the Synthesis of Highly Active Bimetallic Nanoparticle Catalysts with Immiscible Ru and Ni Combination by Utilizing a TiO_2 Support. *ChemCatChem* **2018**, *10* (16), 3526. https://doi.org/10.1002/cctc.201800329
(59) Mao, J.; He, C.-T.; Pei, J.; Liu, Y.; Li, J.; Chen, W.; He, D.; Wang, D.; Li, Y. Isolated Ni Atoms Dispersed on Ru Nanosheets: High-Performance Electrocatalysts toward Hydrogen Oxidation Reaction. *Nano Lett.* **2020**, *20* (5), 3442. https://doi.org/10.1021/acs.nanolett.0c00364
(60) Wang, Y.; Furukawa, S.; Song, S.; He, Q.; Asakura, H.; Yan, N. Catalytic Production of Alanine from Waste Glycerol. *Angew. Chem. Int. Ed.* **2020**, *59* (6), 2289. https://doi.org/10.1002/anie.201912580
(61) Li, R.; Qiu, J.; Chen, H.; Shu, R.; Chen, Y.; Liu, Y.; Liu, P.-F. Hydrodeoxygenation of Phenolic Compounds and Raw Lignin-Oil over Bimetallic RuNi Catalyst: An Experimental and Modeling Study Focusing on Adsorption Properties. *Fuel* **2020**, *281*, 118758. https://doi.org/10.1016/j.fuel.2020.118758
(62) Han, X.; Si, T.; Liu, Q.; Zhu, F.; Li, R.; Chen, X.; Liu, J.; Sun, H.; Zhao, J.; Ling, H.; Zhang, Q.; Wang, H. 2D Bimetallic RuNi Alloy Co-Catalysts Remarkably Enhanced the Photocatalytic H_2 Evolution Performance of g-C_3N_4 Nanosheets. *Chem. Eng. J.* **2021**, *426*, 130824. https://doi.org/10.1016/j.cej.2021.130824
(63) Bai, X.; Pang, Q.-Q.; Du, X.; Yi, S.-S.; Zhang, S.; Qian, J.; Yue, X.-Z.; Liu, Z.-Y. Integrating RuNi Alloy in S-Doped Defective Carbon for Efficient Hydrogen Evolution in Both Acidic and Alkaline Media. *Chem. Eng. J.* **2021**, *417*, 129319. https://doi.org/10.1016/j.cej.2021.129319
(64) Huang, C.-P.; Tsai, M.-C.; Wang, X.-M.; Cheng, H.-S.; Mao, Y.-H.; Pan, C.-J.; Lin, J.-N.; Tsai, L.-D.; Chan, T.-S.; Su, W.-N.; Hwang, B.-J. Engineering Heterometallic Bonding in Bimetallic Electrocatalysts: Towards Optimized Hydrogen Oxidation and Evolution Reactions. *Catal. Sci. Technol.* **2020**, *10* (3), 893. https://doi.org/10.1039/C9CY02181G
(65) Chen, S.; Wojcieszak, R.; Dumeignil, F.; Marceau, E.; Royer, S. How Catalysts and Experimental Conditions Determine the Selective Hydroconversion of Furfural and 5-Hydroxymethylfurfural. *Chem. Rev.* **2018**, *118* (22), 11023. https://doi.org/10.1021/acs.chemrev.8b00134
(66) Banerjee, A.; Mushrif, S. H. Reaction Pathways for the Deoxygenation of Biomass-Pyrolysis-Derived Bio-Oil on Ru: A DFT Study Using Furfural as a Model Compound. *ChemCatChem* **2017**, *9* (14), 2828. https://doi.org/10.1002/cctc.201700036
(67) Sampath, A.; Chang, S. A.; Flaherty, D. W. Catalytic Hydrogen Transfer and Decarbonylation of Aromatic Aldehydes on Ru and Ru Phosphide Model Catalysts. *J. Phys. Chem. C* **2018**, *122* (41), 23600. https://doi.org/10.1021/acs.jpcc.8b07920
(68) Dong, H.; Zheng, Y.; Hu, P. A DFT Study of Direct Furfural Conversion to 2-Methylfuran on the Ru/Co_3O_4 Surface. *Phys. Chem. Chem. Phys.* **2019**, *21* (3), 1597. https://doi.org/10.1039/C8CP06545D

(69) Ren, G.; Wang, G.; Mei, H.; Xu, Y.; Huang, L. A Theoretical Insight into Furfural Conversion Catalyzed on the Ni(111) Surface. *Phys. Chem. Chem. Phys.* **2019**, *21* (42), 23685. https://doi.org/10.1039/C9CP03245B.

(70) Shangguan, J.; Hensley, A. J. R.; Gradiski, M. V.; Pfriem, N.; McEwen, J.-S.; Morris, R. H.; Chin, Y.-H. C. The Role of Protons and Hydrides in the Catalytic Hydrogenolysis of Guaiacol at the Ruthenium Nanoparticle–Water Interface. *ACS Catal.* **2020**, *10* (20), 12310. https://doi.org/10.1021/acscatal.0c01963

(71) Luo, Z.; Min, Y.; Nechiyil, D.; Bacsa, W.; Tison, Y.; Martinez, H.; Lecante, P.; Gerber, I. C.; Serp, P.; Axet, M. R. Chemoselective Reduction of Quinoline over Rh–C $_{60}$ Nanocatalysts. *Catal. Sci. Technol.* **2019**, *9* (24), 6884. https://doi.org/10.1039/C9CY02025J

(72) Leng, F.; Gerber, I. C.; Lecante, P.; Moldovan, S.; Girleanu, M.; Axet, M. R.; Serp, P. Controlled and Chemoselective Hydrogenation of Nitrobenzene over Ru@C_{60} Catalysts. *ACS Catal.* **2016**, *6* (9), 6018. https://doi.org/10.1021/acscatal.6b01429

(73) Hammer, B.; Nørskov, J. K. Electronic Factors Determining the Reactivity of Metal Surfaces. *Surf. Sci.* **1995**, *343* (3), 211. https://doi.org/10.1016/0039-6028(96)80007-0

(74) del Rosal, I.; Poteau, R. Chapter 15: Sabatier principle and surface properties of small ruthenium nanoparticles and clusters: case studies, in Nanoparticles in catalysis, ed. K. P. a. A. Roucoux, **2021**, 331. https://doi.org/10.1002/9783527821761.ch15

(75) Moraru, I.-T.; Martínez-Prieto, L. M.; Coppel, Y.; Chaudret, B.; Cusinato, L.; del Rosal, I.; Poteau, R. A Combined Theoretical/Experimental Study Highlighting the Formation of Carbides on Ru Nanoparticles during CO Hydrogenation. *Nanoscale* **2021**, *13* (14), 6902. https://doi.org/10.1039/D0NR08735A

(76) Min, Y.; Nasrallah, H.; Poinsot, D.; Lecante, P.; Tison, Y.; Martinez, H.; Roblin, P.; Falqui, A.; Poteau, R.; del Rosal, I.; Gerber, I. C.; Hierso, J.-C.; Axet, M. R.; Serp, P. 3D Ruthenium Nanoparticle Covalent Assemblies from Polymantane Ligands for Confined Catalysis. *Chem. Mater.* **2020**, *32* (6), 2365. https://doi.org/10.1021/acs.chemmater.9b04737

(77) Leng, F.; Gerber, I. C.; Lecante, P.; Bentaleb, A.; Muñoz, A.; Illescas, B. M.; Martín, N.; Melinte, G.; Ersen, O.; Martinez, H.; Axet, M. R.; Serp, P. Hexakis [60]Fullerene Adduct-Mediated Covalent Assembly of Ruthenium Nanoparticles and Their Catalytic Properties. *Chem. - Eur. J.* **2017**, *23* (54), 13379. https://doi.org/10.1002/chem.201701043

(78) Taglang, C.; Martínez-Prieto, L. M.; del Rosal, I.; Maron, L.; Poteau, R.; Philippot, K.; Chaudret, B.; Perato, S.; Sam Lone, A.; Puente, C.; Dugave, C.; Rousseau, B.; Pieters, G. Enantiospecific C-H Activation Using Ruthenium Nanocatalysts. *Angew. Chem. Int. Ed.* **2015**, *54* (36), 10474. https://doi.org/10.1002/anie.201504554

(79) Pfeifer, V.; Certiat, M.; Bouzouita, D.; Palazzolo, A.; Garcia-Argote, S.; Marcon, E.; Buisson, D.; Lesot, P.; Maron, L.; Chaudret, B.; Tricard, S.; Rosal, I.; Poteau, R.; Feuillastre, S.; Pieters, G. Hydrogen Isotope Exchange Catalyzed by Ru Nanocatalysts: Labelling of Complex Molecules Containing *N* -Heterocycles and Reaction Mechanism Insights. *Chem. – Eur. J.* **2020**, *26* (22), 4988. https://doi.org/10.1002/chem.201905651

(80) Fu, W.; Chen, W.; Qian, G.; Chen, D.; Yuan, W.; Zhou, X.; Duan, X. Kinetics-Assisted Discrimination of Active Sites in Ru Catalyzed Hydrolytic Dehydrogenation of Ammonia Borane. *React. Chem. Eng.* **2019**, *4* (2), 316. https://doi.org/10.1039/C8RE00223A

(81) Pery, T.; Pelzer, K.; Buntkowsky, G.; Philippot, K.; Limbach, H.-H.; Chaudret, B. Direct NMR Evidence for the Presence of Mobile Surface Hydrides on Ruthenium Nanoparticles. *ChemPhysChem* **2005**, *6* (4), 605. https://doi.org/10.1002/cphc.200400621

(82) Truflandier, L. A.; Del Rosal, I.; Chaudret, B.; Poteau, R.; Gerber, I. C. Where Does Hydrogen Adsorb on Ru Nanoparticles? A Powerful Joint ^{2}H MAS-NMR/DFT Approach. *ChemPhysChem* **2009**, *10* (17), 2939. https://doi.org/10.1002/cphc.200900597

(83) Zhang, B.; Zhu, Y.; Ding, G.; Zheng, H.; Li, Y. Selective Conversion of Furfuryl Alcohol to 1,2-Pentanediol over a Ru/MnO_x Catalyst in Aqueous Phase. *Green Chem.* **2012**, *14* (12), 3402. https://doi.org/10.1039/c2gc36270h

(84) Axet, M. R.; Philippot, K. Catalysis with Colloidal Ruthenium Nanoparticles. *Chem. Rev.* **2020**, *120* (2), 1085. https://doi.org/10.1021/acs.chemrev.9b00434
(85) Parks, E. K.; Nieman, G. C.; Riley, S. J. Binding of Deuterium to Icosahedral Nickel and Cobalt Clusters. *Surf. Sci.* **1996**, *355* (1–3), 127. https://doi.org/10.1016/0039-6028(95)01364-4
(86) Yang, H.; Whitten, J. L. Dissociative Adsorption of H_2 on Ni(111). *J. Chem. Phys.* **1993**, *98* (6), 5039. https://doi.org/10.1063/1.464958

CHAPTER 5: Deuteration of organic molecules on Ru/PVP nanoparticles

Summary

5.1 Introduction

The use of deuterium has attracted increasing interest in several domains of applications, such as standards for mass spectroscopy,[1] study of reaction mechanisms,[2–4] tuning of the properties of materials,[5,6] determination of protein conformations or the development of drugs.[7] The majority of deuterated compounds are used in the pharmaceutical industry for the research of new drugs, as they permit to study the metabolic pathways of drugs.[8–10] By the H-D isotope effect,[11–14] biological activities of non-labelled drugs could be improved in pharmaceutical chemistry.[15–17] The incorporation of deuterium in a specific site of a given molecule is a pertinent way to tune the properties of drugs, such as absorption, distribution, metabolism or drug excretion.[18,19] Deuterated drugs containing several deuterium atoms are more resistant to degradation, which can be explained because cleaving a C-D bond requires more energy than cleaving a C-H bond.[20] In 2017 the Food and Drug Administration (FDA) of the U.S. accepted deuterated drugs.[21,22] Develop methodologies for large-scale deuterium labelling at industrial level is thus of high interest.

Among the diverse methods studied for the synthesis of deuterated,[9,23–25] one of the most attractive is the Hydrogen Isotope Exchange (HIE), where the incorporation of deuterium at certain positions is modulated by a catalyst. HIE is particularly interesting for the functionalisation of bioactive molecules.[26–32]

The use of inexpensive deuterated water (D_2O) under hydrogen (H_2) pressure is an easily scalable deuteration methodology, as demonstrated by the synthesis of deuterium-containing products on the kilogram scale, and it allows the isotope labelling of several substrates. Pd/C and Pt/C are known to catalyse multi H/D exchange.[33] Ru- and Ir-based catalysts under D_2 pressure are also active for this reaction.[25] A heterogeneous Fe-based catalyst proved to be highly efficient for the selective deuteration of (hetero)arenes.[34] Also, earth abundant metal based catalysts, such as Mn[19] or Ni,[35] have been described as active for deuterations reactions. Finally, Ru nanocatalysts have been reported for the deuteration of several organic molecules under D_2 pressure.[36,37] Given this context, we have decided to explore the catalytic properties of the nanocatalysts prepared for hydrogenation reactions as described in previous chapters in the deuteration of target compounds of interest. This work has been performed during a three months internship in M. Beller's group, at Leibniz Institute for Catalysis (LIKAT), in Rostock,[38] with a financial support from NanoX Toulouse.[39] The subgroup of Catalysis for life sciences from M. Beller's group, is specialised in deuteration reactions and has reported several examples of deuteration reactions on heteroarenes.[19,34,40–42]

5.2 4-Methoxyaniline deuteration using Ru/PVP NPs as catalysts

Anilines are building blocks of some of the most sold medications.[43] For their deuteration several synthetic methods have been reported, including the use of heterogeneous[19,34,44–46] and homogeneous[47–50] catalysts, or deuterated bases or acids.[51–54]

Usually, the reaction conditions for deuteration reactions vary from 40 ºC to 400 ºC, in the presence (up to 20 bar), or not, of H_2. As starting conditions, D_2O as solvent and deuterium source, a temperature of 80 ºC and a pressure of 10 bar of H_2 or no H_2 pressure were chosen in the absence of any acids or co-solvent. All reactions were performed in 1.5 mL of D_2O with a metal molar ratio of 0.02 % with respect to the substrate, using as catalyst the Ru/PVP NPs synthesised at 85 ºC as described in section 2.2 of Chapter 2 (Scheme 1). The evolution of the reaction was followed by solution ^{1}H NMR. All the experimental details are given in Chapter 6.

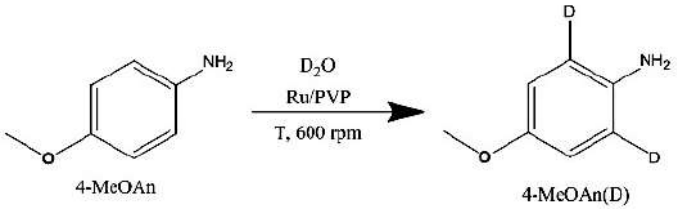

Scheme 1: Catalytic deuteration of 4-Methoxyaniline (4-MeOAn) into 4-MeOAn(D).

After 16 h of reaction at 80 ºC with 10 bar of H_2 in D_2O (1.5 mL), the reaction mixture of 4-MeOAn (0.25 mmol) was washed three times with chloroform ($CHCl_3$), the organic phase dried with Na_2SO_4 and evaporated to dryness. Figure 1 depicts the ^{1}H NMR spectra of the dried reaction organic phase in deuterated chloroform ($CDCl_3$), of the aqueous phase, and of the pure substrate in $CDCl_3$. The NMR spectrum of the dried reaction organic phase does not show any signal in the aromatic region, but a new set of peaks in the aliphatic area. These results point to the hydrogenation of the aromatic ring catalysed by the Ru NPs, that are well-known to provide this type of transformation.[55]

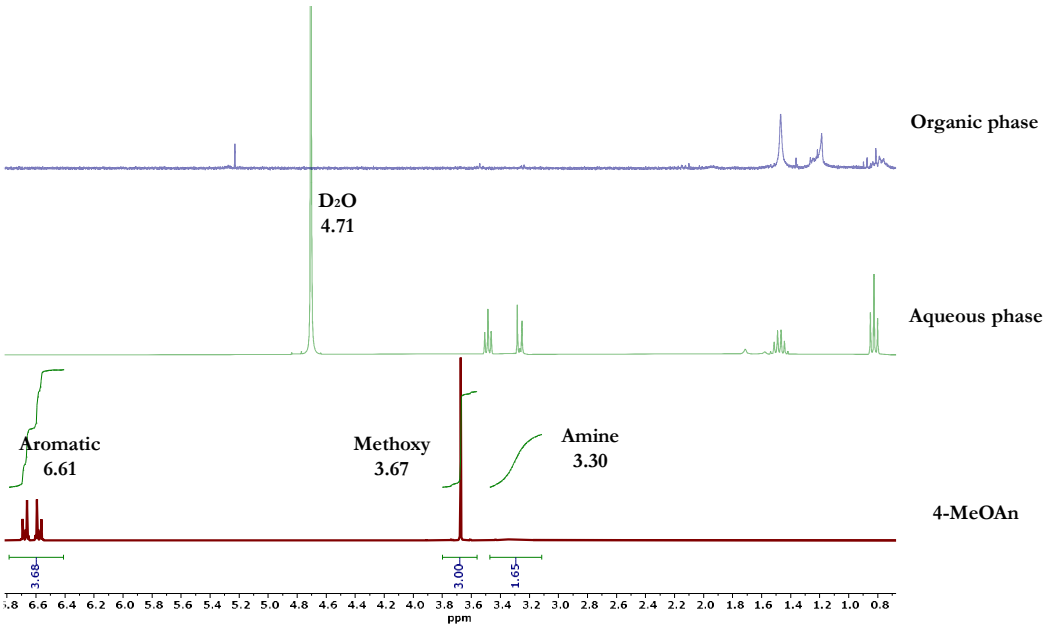

Figure 1: ^{1}H NMR spectra of the substrate 4-MeOAn in $CDCl_3$ (bottom), of the dried reaction organic phase in $CDCl_3$ (top) and of the reaction aqueous phase in D_2O (middle), after the reaction of 0.25 mmol of 4-MeOAn at 80 °C with 10 bar of H_2 on Ru/PVP NPs in 1.5 mL of D_2O.

In order to avoid the hydrogenation of the aromatic ring, the reaction was performed using the same reaction conditions but in the absence of H_2. The ^{1}H NMR spectrum of the crude D_2O phase did not show any deuteration of the aromatic ring, as the ratio of the integrals of the methoxy group with respect to the aromatic signals did not change. A new set of peaks appeared which were attributed to PVP after gas chromatography-mass spectroscopy (GC-MS) analyses of the reaction medium. PVP is known to be well soluble in water.

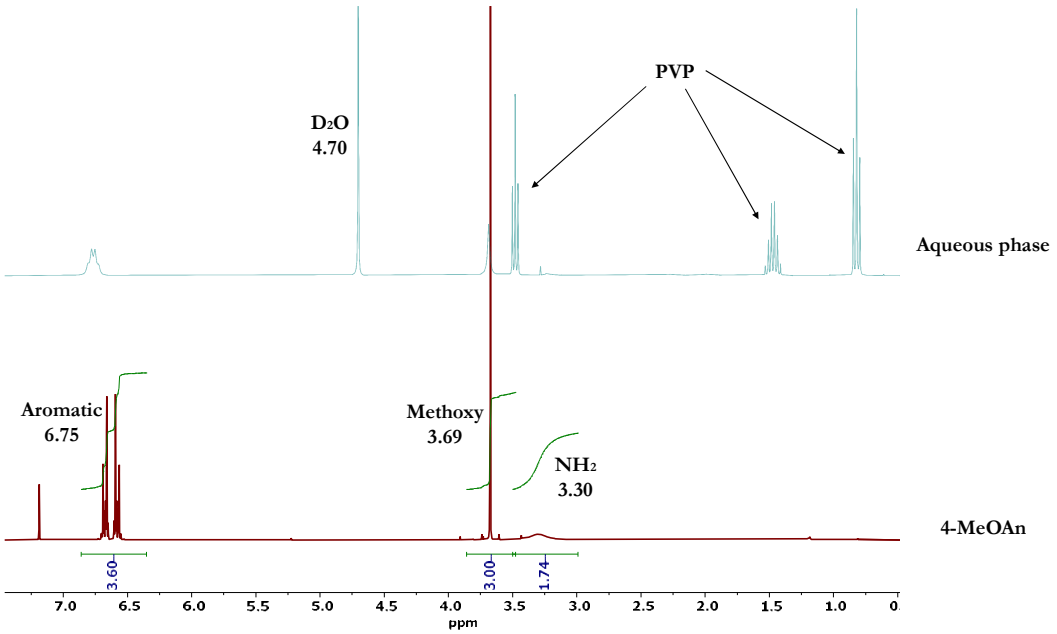

Figure 2: ^{1}H NMR spectra of the substrate 4-MeOAn in $CDCl_3$ (bottom) and of the D_2O reaction mixture (top), after the reaction of 0.25 mmol of 4-MeOAn at 80 °C on Ru/PVP NPs in 1.5 mL of D_2O.

Unfortunately, no deuteration of this aniline was observed in any of the reaction conditions tested, and no more catalytic tests were performed.

5.3 4-(Trifluoromethyl)benzaldehyde deuteration using Ru/PVP NPs as catalyst

Aromatic aldehydes are interesting building blocks in pharmaceutical industry,[56] due to their inherent and easy reactivity to create C-C and C-X bonds. Thus, their selective deuteration is appealing to produce compounds of interest for the application in this domain. Diverse methodologies have been explored, such as, the photoredox catalysed deoxygenative deuteration of carboxylic acids;[57] the aldehyde deuteration *via* the HIE,[40,58,59]or *via* the hydrogen atom transfer (HAT),[56,60] the reaction of amides with the Schwartz's reagent,[61] the reduction of esters by $LiAlD_4$ with an oxidation final step,[62] or the Pd/Rh catalysed reductive carbonylation of aryl halides.[63] However, the development of new reaction pathways to access deuterated aldehydes at a lower cost is required.

The study of the 4-(Trifluoromethyl)benzaldehyde (TFMBAL) deuteration (Scheme 2) was performed using similar reaction conditions as for 4-MeOAn: 80 °C, D_2O as solvent and deuterium source, eventually 10 bar of H_2, and Ru/PVP NPs synthesised at 85 °C (see section 2.2 Chapter 2, and Chapter 6 for the experimental details) with a metal molar ratio of 0.02 % with respect to the substrate.

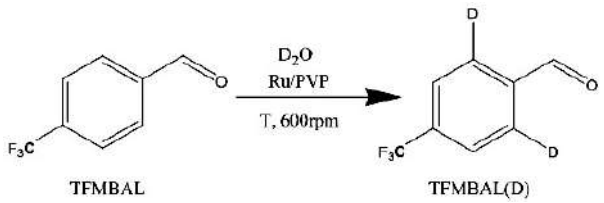

Scheme 2: Catalytic deuteration of TFMBAL into TFMBAL(D).

The ^1H NMR spectrum of the substrate TFMBAL in $CDCl_3$ is displayed in Figure 3 (bottom), together with that of the organic phase extracted, from the reaction mixture at 80 ºC under 10 bar of H_2, after workup. Likewise, the previous substrate, 4-MeOAn, the spectrum of the organic phase of the reaction points to the hydrogenation of the aromatic ring, as well as of the aldehyde, as the peaks corresponding to these two moieties are no longer observed, and a new set of peaks appear in the aliphatic region of the ^1H NMR spectrum.

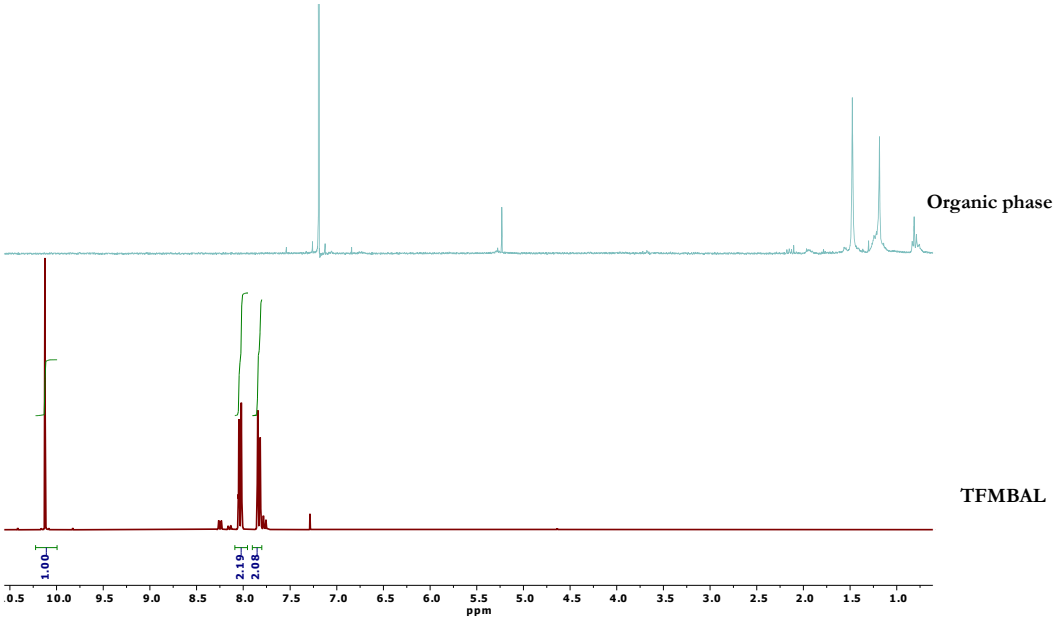

Figure 3: ^1H NMR spectra in $CDCl_3$ of the substrate TFMBAL (bottom) and of the organic phase extracted from the reaction mixture (top), after the reaction of 0.25 mmol of TFMBAL at 80 ºC with 10 bar of H_2 on Ru/PVP NPs in 1.5 mL of D_2O.

Then, the reaction was performed without H_2 in order to avoid the hydrogenation reaction. The ^1H spectrum of the products in the organic phase extracted from the reaction medium is displayed in Figure 4, in comparison to that of the TFMBAL substrate. This spectrum reveals that the peaks in the aromatic region are slightly shifted while the proton corresponding to the aldehyde moiety at 10.04 ppm is almost vanished. These results indicate a possible deuteration at this position. GC-MS analysis of the reaction medium shows two main peaks, one with a mass-to-charge (m/z) of 174 attributed to the substrate TFMBAL, with a contribution of m/z 175, which could correspond to the deuterated product. There is also a sec-

ond peak with a m/z of 155 that could be attributed to the TFMBAL molecule after the loss of a F atom (Figure 5).

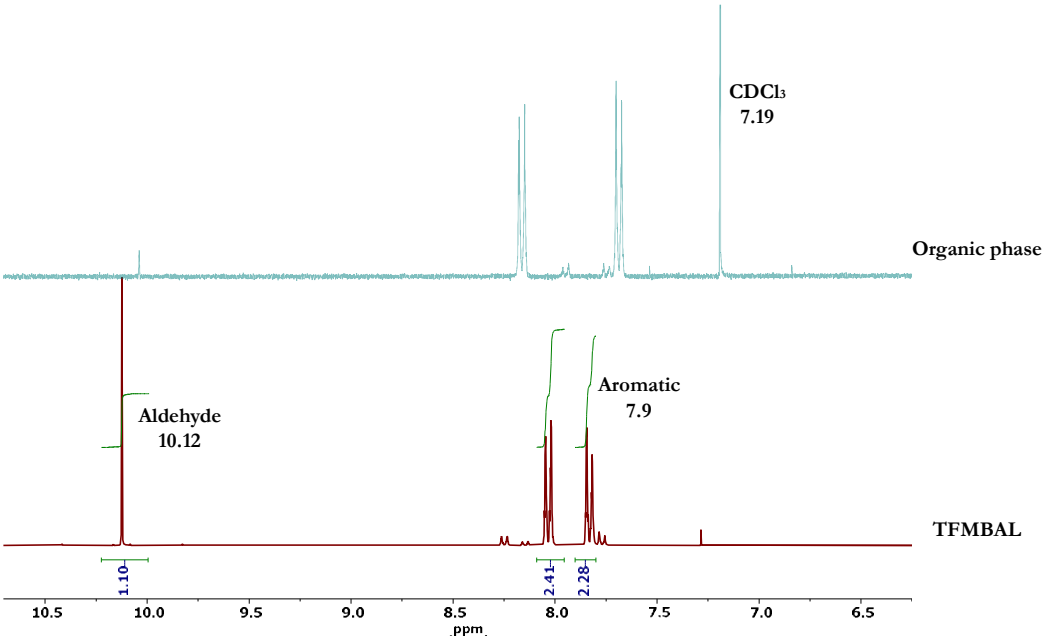

Figure 4: ^{1}H NMR spectra in $CDCl_3$ of the substrate TFMBAL (bottom) and the organic phase extracted from the reaction mixture (top), after the reaction of 0.25 mmol of TFMBAL at 80 °C on Ru/PVP NPs in 1.5 mL of D_2O.

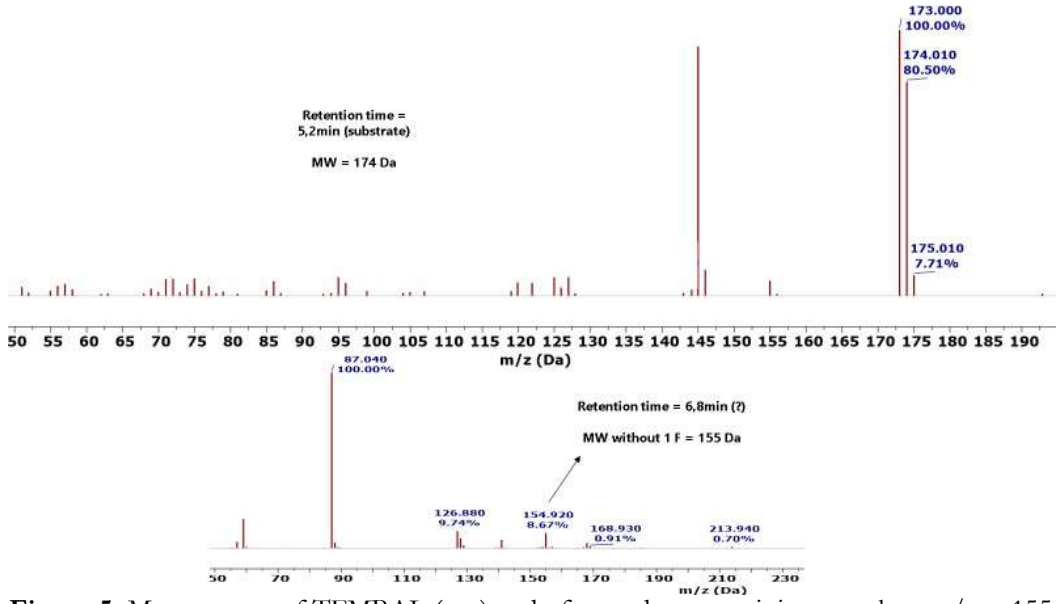

Figure 5: Mass spectra of TFMBAL (top) and of a product containing a peak at m/z = 155 Da corresponding to a loss of a F atom (bottom) and their respective retention times in GC-MS.

In order to verify the hypothesis of a selective defluorination, an analogue substrate, 4 -(Trifluoromethyl)acetophenone (TFMAPO), was submitted to the same reaction conditions

(Scheme 3). The ^{1}H NMR of the organic phase of the reaction medium, in $CDCl_3$, revealed that a partial deuteration of the methyl moiety occurred (Figure 6). Nevertheless, the GC-MS analysis of the reaction medium did not reveal a defluorination of the $-CF_3$ group (Figure 7), discarding thus defluorination on the TFMBAL substrate.

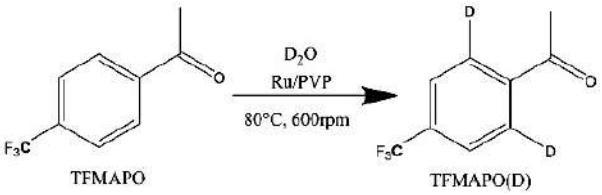

Scheme 3: Catalytic deuteration of TFMAPO into TFMAPO(D).

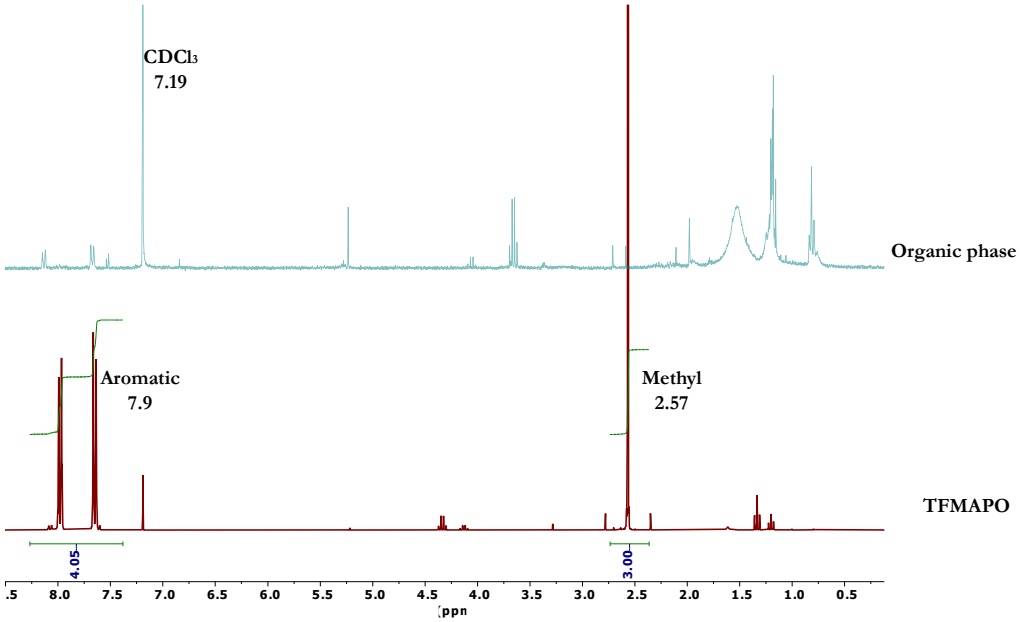

Figure 6: ^{1}H NMR spectra in $CDCl_3$ of the substrate TFMAPO (bottom) and of the organic phase extracted from the reaction mixture (top), after the reaction of 0.25 mmol of TFMAPO at 80 ºC on Ru/PVP NPs in 1.5 mL of D_2O.

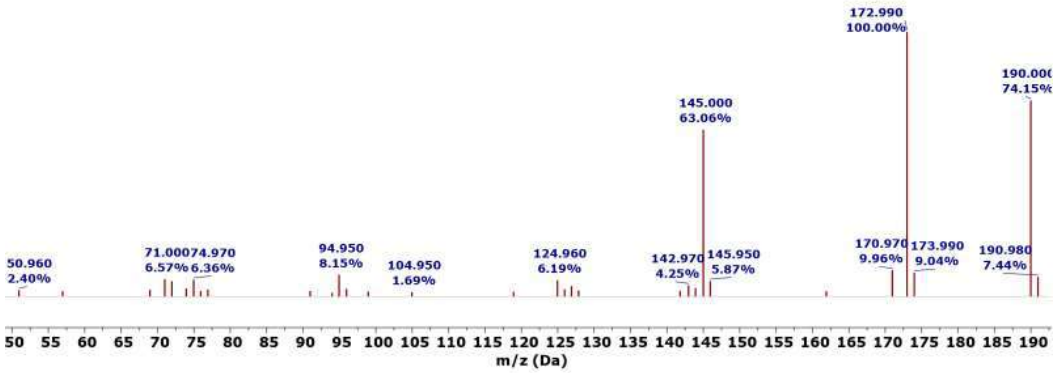

Figure 7: Mass spectrum from the reaction of TFMAPO showing no peak corresponding to the loss of one, two or three F atoms.

5.4 Methyl 2,3-O-Isopropylidene-β-D-ribofuranoside deuteration using Ru/PVP NPs as catalysts

Sugars labelled with deuterium are interesting organic molecules for *in vivo* kinetics studies[64–67] as well as for the structural studies of macromolecules such as nucleic acids and glycoproteins.[68–75] Deuterium labelled sugars are also of interest as they act as building blocks[76,77] for the synthesis of deuterated chiral bioactive compounds. Several synthetic methods have been reported to access these molecules; ketone reduction by $LiAlD_4$ and $NaBD_4$,[78–80] enzymatic synthesis,[81,82] epimerisation of sugars containing a carbonyl group at the adjacent position[83] and multistep synthesis from small deuterium labelled compounds.[84] All these processes have a high cost and poor atom economy, thus using D_2O as an alternative deuterium source it is appealing.[4,18,85–94]

Methyl 2,3-O-Isopropylidene-β-D-ribofuranoside (MOIBRIBOF) deuteration (Scheme 4) was investigated in D_2O at a temperature of 80 ºC and eventually under 10 bars of H_2 using Ru/PVP NPs as catalyst. All the experimental details are given in Chapter 6.

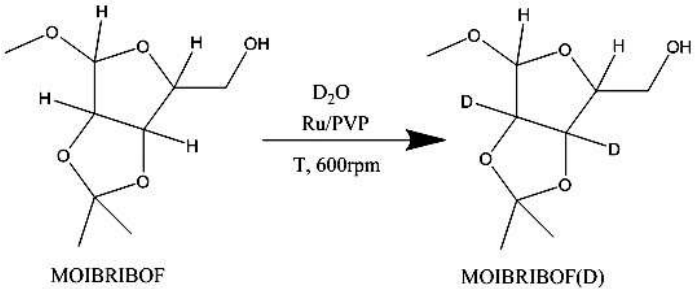

Scheme 4: Catalytic deuteration of MOIBRIBOF into MOIBRIBOF(D).

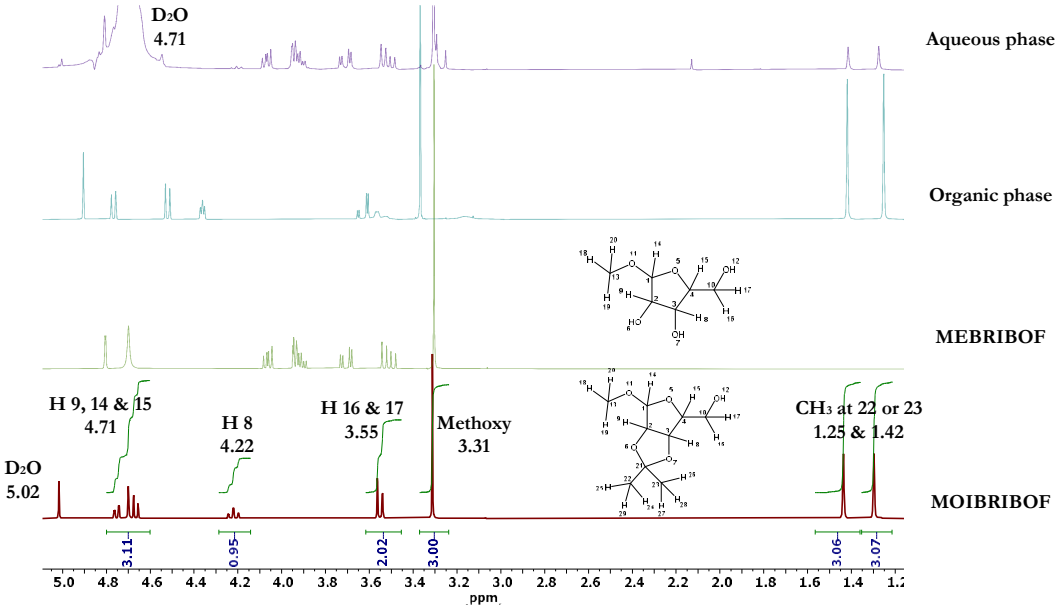

Figure 8: ^{1}H NMR sepctra of the protected sugar MOIBRIBOF in D_2O (bottom), of the unprotected sugar Methyl β-D-Ribofuranoside (MEBRIBOF) in D_2O (1st middle), of the organic phase extracted from the reaction medium in $CDCl_3$ (2nd middle) and of the aqueous phase of the reaction medium in D_2O (top), after the reaction of 0.25 mmol of MOIBRIBOF at 80 ºC with 10 bars of H_2 on Ru/PVP NPs in 1.5 mL of D_2O.

Under H_2 pressure, a partial deprotection of the isopropylidene moiety of MOIBRIBOF occurred, leading to the formation of the corresponding unprotected sugar, MEBRIBOF, found in the aqueous phase, while the remaining substrate was observed in the organic phase (Figure 8). This deprotection is known to occur under acidic conditions.[95–97] This result may be due to the acidic character of the Ru/PVP NPs, which were shown to produce an acetal from furfural, as previously discussed in Chapter 3.

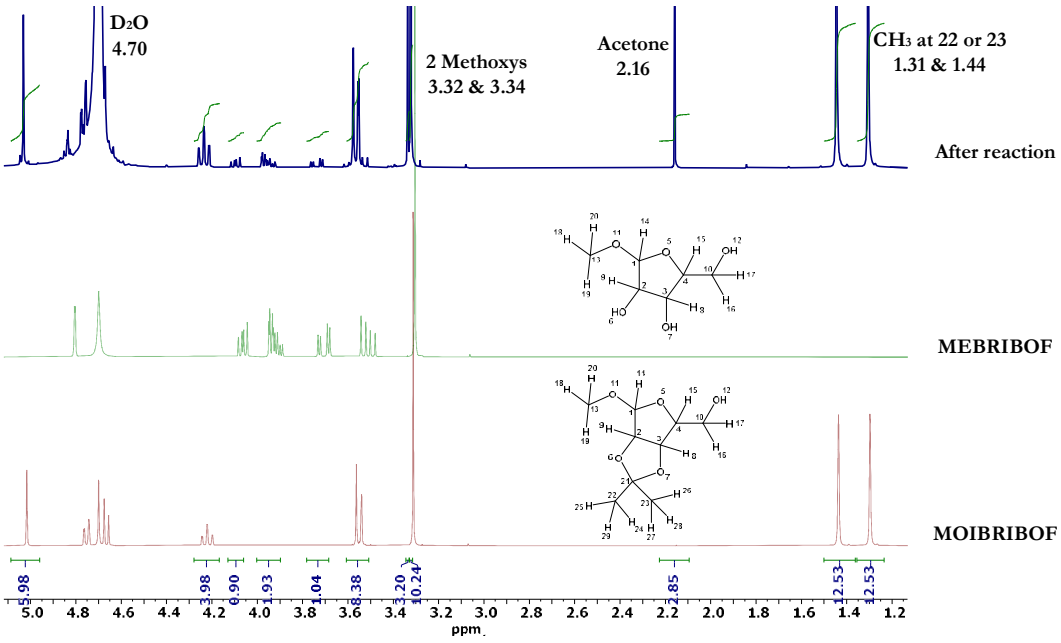

Figure 9: ^{1}H NMR spectra in D_2O of the protected sugar MOIBRIBOF (bottom), of the unprotected sugar MEBRIBOF (middle) and of the reaction medium (top), after the reaction of 0.25 mmol of MOIBRIBOF at 50 ºC on Ru/PVP NPs, in 1.5 mL of D_2O.

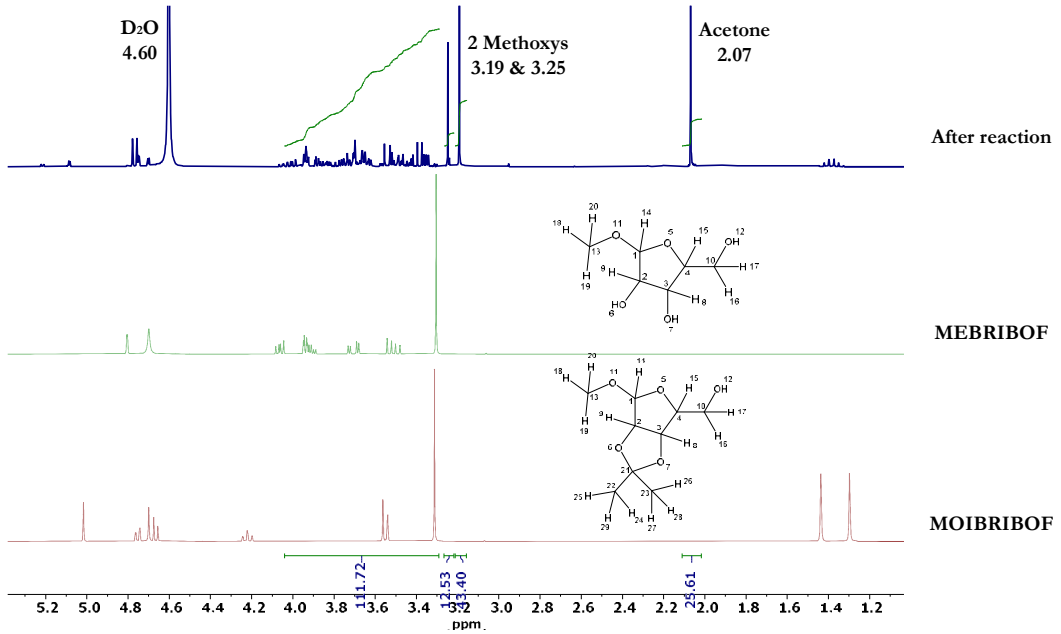

Figure 10: ^{1}H NMR spectra in D_2O of the protected sugar MOIBRIBOF (bottom), of the unprotected sugar MEBRIBOF (middle) and of the reaction medium (top), after the reaction of 0.25 mmols of MOIBRIBOF at 80 ºC on Ru/PVP NPs, in 1.5 mL of D_2O.

Next, the deuteration of MOIBRIBOF was performed without H_2 pressure, at different temperatures. At RT, no reaction occurred, while increasing the temperature to 50 °C, the partial deprotection of the sugar happened. ^{1}H NMR spectrum of the reaction mixture (Figure 9; top), shows two different methoxy peaks at 3.32 and 3.34 ppm that can be attributed

to MOIBRIBOF and MEBRIBOF respectively. A peak is also visible at 2.16 ppm, which can be attributed to the presence of acetone, resulting from the deprotection of MOIBRIBOF. At 80 °C, a full deprotection of MOIBRIBOF was observed, as shown by the ^{1}H NMR spectrum (Figure 10). In addition, several multiplets are visible in the range of 3.2 to 4.1 ppm, which can be attributed to epimerization products of the unprotected sugar MEBRIBOF. Such epimerisation reactions, are known to occur in aqueous acidic media.[98–100] Here, they could be explained as the synthesised Ru/PVP NPs have previously been determined as acidic when catalysing the acetal formation of furfural (see Chapter 3).

Then, the deuteration of the unprotected sugar, MEBRIBOF, was attempted in D_2O, following the same reaction conditions as described above (Scheme 5). In the presence of H_2 at 80 °C, no reaction occurred. The ^{1}H NMR spectrum of the reaction medium (Figure 11) clearly showed the peaks of the MEBRIBOF substrate. In the absence of H_2, epimerisation of the sugar occurred, as it can be discerned by the presence of several multiplets in the range of 3.2 to 4.2 ppm in the ^{1}H NMR spectrum (Figure 11).

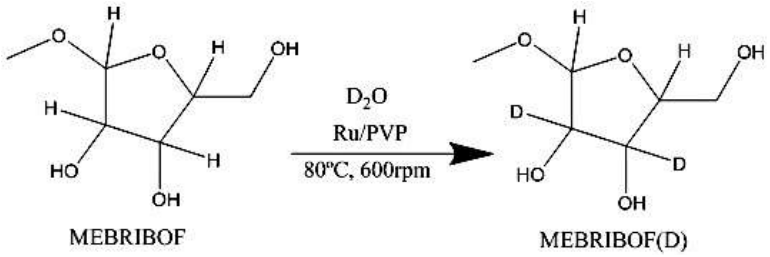

Scheme 5: Catalytic deuteration of MEBRIBOF into MEBRIBOF(D).

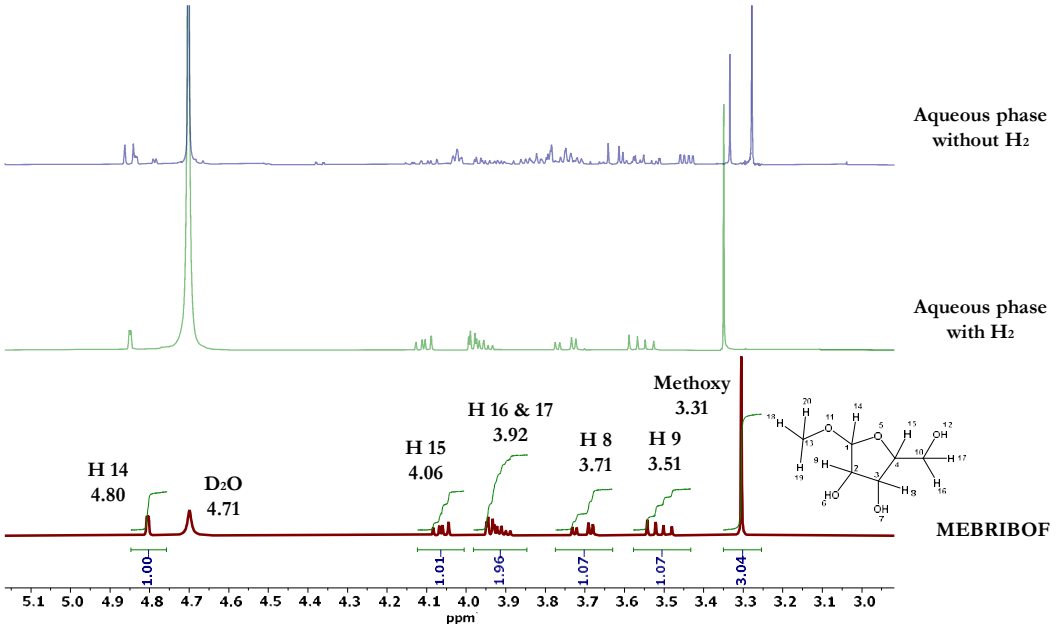

Figure 11: ^{1}H NMR spectra of the unprotected sugar MEBRIBOF in D_2O (bottom) and of the aqueous reaction medium with (middle) and without (top) H_2, after the reaction of 0.25 mmol of MEBRIBOF at 80 °C with (bottom) and without (top) 10 bar of H_2 on Ru/PVP NPs, in 1.5 mL of D_2O.

As conclusion, the deuteration of MOIBRIBOF and MEBRIBOF was not observed on the Ru/PVP NPs in the investigated reaction conditions. In the case of the protected sugar, MOIBRIBOF, reactions performed under 10 bar of H_2, led to the partial or total deprotection of the substrate. In the absence of H_2, epimerisation of the unprotected sugar, MEBRIBOF, was observed. Deuteration reactions of the unprotected sugar, MEBRIBOF, as substrate confirmed that epimerisation occurs in the absence of H_2. Additional experiments are needed to determine if the Ru/PVP nanocatalyst is responsible of this reactivity, which is typically performed in acidic conditions.

5.5 Adenosine deuteration using Ru/PVP NPs as catalysts

Deuterated nucleosides such as adenosine (ADNS) are another class of interesting organic molecules; they act as building blocks of nucleic acids and they allow to perform structural studies of biological macromolecules.[68–75,101] Deuterated ADNSs, are often obtained *via* multi-steps tedious syntheses.[102] Some other methodologies from the literature include the fission and reclosure of rings,[103] exchange of H atom catalysed by Pt with D_2,[104] performed also in water,[105,106] or by isotopic hydrogenolysis.[107]

The deuteration of ADNS (Scheme 6) was also investigated on Ru/PVP NPs and using similar reaction conditions as those applied for the previous substrates (see details in Chapter 6).

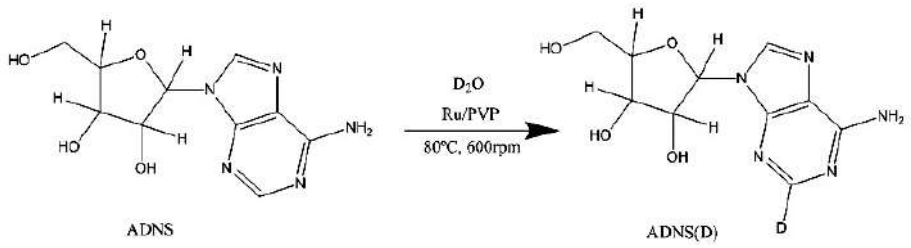

Scheme 6: Catalytic deuteration of ADNS into ADNS(D).

The ^{1}H NMR spectrum recorded after 16 h of reaction at 80 °C without H_2 (Figure 12) is very clean. It shows that a total deuteration of the proton in the C16 position occurred, a reaction that has already been reported through a multi-step mechanism finishing with the condensation of 3-β-D-ribofuranosyl-4-amino-5-(imidazol-2-yl)imidazole with deuterated ethyl orthoformate ($CD(OEt)_3$) at 100 °C in dimethylacetamide (DMA) during 4 h, followed by the unmasking of the etheno moiety with chloroacetaldehyde in H_2O.[102]

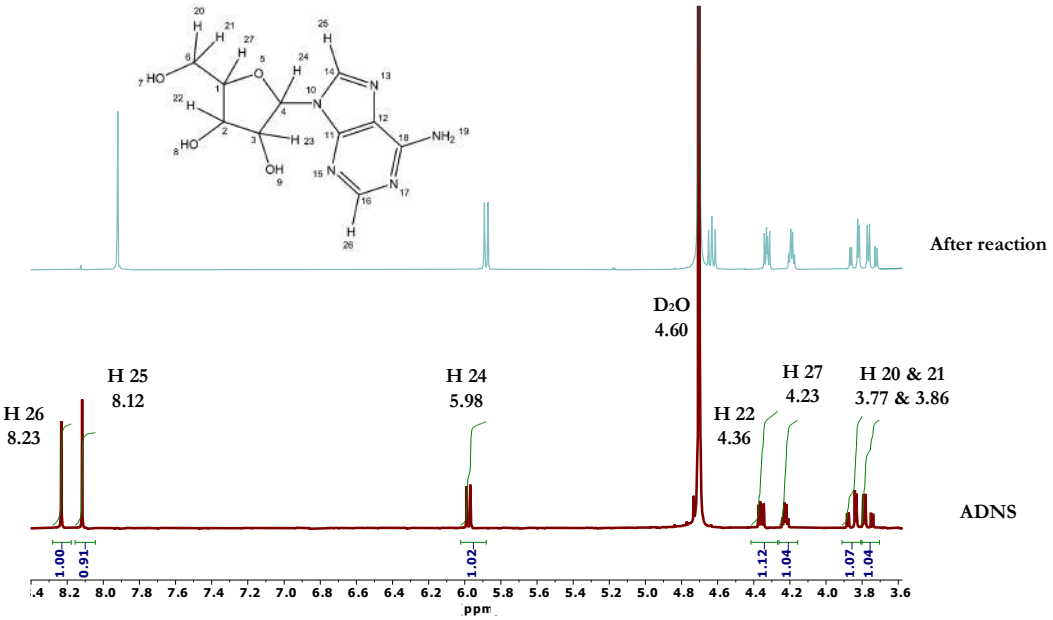

Figure 12: ^{1}H NMR spectra in D_2O of the substrate ADNS (bottom) and of the resulting reaction mixture (top), after the reaction of 0.25 mmol of ADNS at 80 °C on Ru/PVP NPs, in 1.5 mL of D_2O.

This result evidencing a full selective deuteration of ADNS at the position 16, without any epimerisation of the sugar backbone, is very interesting. It could be due to the presence of the nitrogen moiety of the adenosine. This encouraging result opens the door to further investigations.

5.6 Conclusions

Catalytic deuterations of several organic molecules on Ru/PVP NPs have been performed.

For the 4-MeOAn, at any reaction conditions, no deuterium labelling was observed. When pressurising the reactor with 10 bar of H_2 at 80 ºC, only hydrogenated products were obtained and, without pressurising with H_2, at 80 ºC, PVP leaching was observed.

Similarly TFMBAL was hydrogenated under 10 bar of H_2 at 80 ºC. In the absence of H_2, TFMBAL was deuterated on the formyl H.

Sugar derivatives were epimerized in the absence of H_2, and the protected sugar MOIBRIBOF, was deprotected while applying H_2 pressure. Finally, ADNS was selectively deuterium labelled at C16 position, without any epimerisation of the sugar backbone.

The exploratory work performed at LIKAT is very encouraging in some of the molecules tested and open the doors for future research in deuteration reactions.

5.7 References

(1) Atzrodt, J.; Derdau, V. Pd- and Pt-Catalyzed H/D Exchange Methods and Their Application for Internal MS Standard Preparation from a Sanofi-Aventis Perspective. *J. Label. Compd. Radiopharm.* **2010**, *53* (11–12), 674. https://doi.org/10.1002/jlcr.1818

(2) Simmons, E. M.; Hartwig, J. F. On the Interpretation of Deuterium Kinetic Isotope Effects in C-H Bond Functionalizations by Transition-Metal Complexes. *Angew. Chem. Int. Ed.* **2012**, *51* (13), 3066. https://doi.org/10.1002/anie.201107334

(3) Simmons, E. M.; Hartwig, J. F. Zur Interpretation des kinetischen Isotopeneffekts bei der Funktionalisierung von C-H-Bindungen durch Übergangsmetallkomplexe. *Angew. Chem.* **2012**, *124* (13), 3120. https://doi.org/10.1002/ange.201107334

(4) Sawama, Y.; Monguchi, Y.; Sajiki, H. Efficient H–D Exchange Reactions Using Heterogeneous Platinum-Group Metal on Carbon–H_2–D_2O System. *Synlett*, **2012**, *23*, 959. https://doi.org/10.1055/s-0031-1289696

(5) Shao, M.; Keum, J.; Chen, J.; He, Y.; Chen, W.; Browning, J. F.; Jakowski, J.; Sumpter, B. G.; Ivanov, I. N.; Ma, Y.-Z.; Rouleau, C. M.; Smith, S. C.; Geohegan, D. B.; Hong, K.; Xiao, K. The Isotopic Effects of Deuteration on Optoelectronic Properties of Conducting Polymers. *Nat. Commun.* **2014**, *5* (1), 3180. https://doi.org/10.1038/ncomms4180

(6) Grimm, J. B.; Xie, L.; Casler, J. C.; Patel, R.; Tkachuk, A. N.; Falco, N.; Choi, H.; Lippincott-Schwartz, J.; Brown, T. A.; Glick, B. S.; Liu, Z.; Lavis, L. D. A General Method to Improve Fluorophores Using Deuterated Auxochromes. *JACS Au* **2021**, *1* (5), 690. https://doi.org/10.1021/jacsau.1c00006

(7) Konermann, L.; Pan, J.; Liu, Y.-H. Hydrogen Exchange Mass Spectrometry for Studying Protein Structure and Dynamics. *Chem. Soc. Rev.* **2011**, *40* (3), 1224. https://doi.org/10.1039/C0CS00113A

(8) Gant, T. G. Using Deuterium in Drug Discovery: Leaving the Label in the Drug. *J. Med. Chem.* **2014**, *57* (9), 3595. https://doi.org/10.1021/jm4007998

(9) Atzrodt, J.; Derdau, V.; Kerr, W. J.; Reid, M. C−H Functionalisation for Hydrogen Isotope Exchange. *Angew. Chem. Int. Ed.* **2018**, *57* (12), 3022. https://doi.org/10.1002/anie.201708903
(10) Pirali, T.; Serafini, M.; Cargnin, S.; Genazzani, A. A. Applications of Deuterium in Medicinal Chemistry. *J. Med. Chem.* **2019**, *62* (11), 5276. https://doi.org/10.1021/acs.jmedchem.8b01808
(11) Wiberg, K. B. The Deuterium Isotope Effect. *Chem. Rev.* **1955**, *55* (4), 713. https://doi.org/10.1021/cr50004a004
(12) Fenoll, L. G.; Peñalver, M. J.; Rodríguez-López, J. N.; García-Ruiz, P. A.; García-Cánovas, F.; Tudela, J. Deuterium Isotope Effect on the Oxidation of Monophenols and O-Diphenols by Tyrosinase. *Biochem. J.* **2004**, *380* (3), 643. https://doi.org/10.1042/bj20040136
(13) Perrin, C. L.; Dong, Y. Secondary Deuterium Isotope Effects on the Acidity of Carboxylic Acids and Phenols. *J. Am. Chem. Soc.* **2007**, *129* (14), 4490. https://doi.org/10.1021/ja069103t
(14) Takeda, M.; Jee, J.; Ono, A. M.; Terauchi, T.; Kainosho, M. Hydrogen Exchange Rate of Tyrosine Hydroxyl Groups in Proteins As Studied by the Deuterium Isotope Effect on C_ζ Chemical Shifts. *J. Am. Chem. Soc.* **2009**, *131* (51), 18556. https://doi.org/10.1021/ja907911y
(15) Foster, A. B. Deuterium Isotope Effects in Studies of Drug Metabolism. *Trends Pharmacol. Sci.* **1984**, *5*, 524. https://doi.org/10.1016/0165-6147(84)90534-0
(16)Kushner, D. J.; Baker, A.; Dunstall, T. G. Pharmacological uses and perspectives of heavy water and deuterated compounds. *Can. J. Physiol. Pharmacol.* 1999, *77* (2), 79. https://doi.org/10.1139/y99-005
(17) Sanderson, K. Big Interest in Heavy Drugs. *Nature* **2009**, 458269a. https://doi.org/10.1038/458269a
(18) Sawama, Y.; Yabe, Y.; Iwata, H.; Fujiwara, Y.; Monguchi, Y.; Sajiki, H. Stereo- and Regioselective Direct Multi-Deuterium-Labeling Methods for Sugars. *Chem. Eur. J.* **2012**, *18* (51), 16436. https://doi.org/10.1002/chem.201202852
(19) Bourriquen, F.; Rockstroh, N.; Bartling, S.; Junge, K.; Beller, M. Manganese-Catalysed Deuterium Labelling of Anilines and Electron-Rich (Hetero)Arenes. *Angew. Chem. Int. Ed.* **2022**, *61* (27). https://doi.org/10.1002/anie.202202423
(20) Maitra, U.; Chandrasekhar, J. Use of Isotopes for Studying Reaction Mechanisms. *Resonance* **1997**, *2*, 18. https://doi.org/10.1007/BF02834997
(21) Mullard, A. FDA Approves First Deuterated Drug. *Nat. Rev. Drug Discov.* **2017**, *16* (5), 305. https://doi.org/10.1038/nrd.2017.89
(22) Schmidt, C. First Deuterated Drug Approved. *Nat. Biotechnol.* **2017**, *35* (6), 493. https://doi.org/10.1038/nbt0617-493
(23) Atzrodt, J.; Derdau, V.; Fey, T.; Zimmermann, J. The Renaissance of H/D Exchange. *Angew. Chem. Int. Ed.* **2007**, *46* (41), 7744. https://doi.org/10.1002/anie.200700039
(24) Herbert, J. M. Deuterium Exchange Promoted by Iridium Complexes Formed in Situ. *J. Label. Compd. Radiopharm.* **2010**, *53* (11–12), 658. https://doi.org/10.1002/jlcr.1790
(25) Kopf, S.; Bourriquen, F.; Li, W.; Neumann, H.; Junge, K.; Beller, M. Recent Developments for the Deuterium and Tritium Labeling of Organic Molecules. *Chem. Rev.* **2022**, *122* (6), 6634. https://doi.org/10.1021/acs.chemrev.1c00795
(26) Tlahuext-Aca, A.; Hartwig, J. F. Site-Selective Silver-Catalyzed C–H Bond Deuteration of Five-Membered Aromatic Heterocycles and Pharmaceuticals. *ACS Catal.* **2021**, *11* (3), 1119. https://doi.org/10.1021/acscatal.0c04917
(27) Müller, V.; Weck, R.; Derdau, V.; Ackermann, L. Ruthenium(II)-Catalyzed Hydrogen Isotope Exchange of Pharmaceutical Drugs by C−H Deuteration and C−H Tritiation. *ChemCatChem* **2020**, *12* (1), 100. https://doi.org/10.1002/cctc.201902051
(28) Pfeifer, V.; Zeltner, T.; Fackler, C.; Kraemer, A.; Thoma, J.; Zeller, A.; Kiesling, R. Palladium Nanoparticles for the Deuteration and Tritiation of Benzylic Positions on Complex Molecules. *Angew. Chem. Int. Ed.* **2021**, *60* (51), 26671. https://doi.org/10.1002/anie.202109043

(29) Zarate, C.; Yang, H.; Bezdek, M. J.; Hesk, D.; Chirik, P. J. Ni(I)–X Complexes Bearing a Bulky α-Diimine Ligand: Synthesis, Structure, and Superior Catalytic Performance in the Hydrogen Isotope Exchange in Pharmaceuticals. *J. Am. Chem. Soc.* **2019**, *141* (12), 5034. https://doi.org/10.1021/jacs.9b00939

(30) Uttry, A.; Mal, S.; van Gemmeren, M. Late-Stage β-C(Sp^3)–H Deuteration of Carboxylic Acids. *J. Am. Chem. Soc.* **2021**, *143* (29), 10895. https://doi.org/10.1021/jacs.1c06474

(31) Palazzolo, A.; Feuillastre, S.; Pfeifer, V.; Garcia-Argote, S.; Bouzouita, D.; Tricard, S.; Chollet, C.; Marcon, E.; Buisson, D.; Cholet, S.; Fenaille, F.; Lippens, G.; Chaudret, B.; Pieters, G. Efficient Access to Deuterated and Tritiated Nucleobase Pharmaceuticals and Oligonucleotides Using Hydrogen-Isotope Exchange. *Angew. Chem. Int. Ed.* **2019**, *58* (15), 4891. https://doi.org/10.1002/anie.201813946

(32) Kang, Q.-K.; Shi, H. Catalytic Hydrogen Isotope Exchange Reactions in Late-Stage Functionalization. *Synlett* **2022**, *33* (04), 329. https://doi.org/10.1055/a-1354-0367

(33) Maegawa, T.; Fujiwara, Y.; Inagaki, Y.; Esaki, H.; Monguchi, Y.; Sajiki, H. Mild and Efficient H/D Exchange of Alkanes Based on C-H Activation Catalyzed by Rhodium on Charcoal. *Angew. Chem. Int. Ed.* **2008**, *47* (29), 5394. https://doi.org/10.1002/anie.200800941

(34) Li, W.; Rabeah, J.; Bourriquen, F.; Yang, D.; Kreyenschulte, C.; Rockstroh, N.; Lund, H.; Bartling, S.; Surkus, A.-E.; Junge, K.; Brückner, A.; Lei, A.; Beller, M. Scalable and Selective Deuteration of (Hetero)Arenes. *Nat. Chem.* **2022**, *14* (3), 334. https://doi.org/10.1038/s41557-021-00846-4

(35) Gao, J.; Ma, R.; Feng, L.; Liu, Y.; Jackstell, R.; Jagadeesh, R. V.; Beller, M. Ambient Hydrogenation and Deuteration of Alkenes Using a Nanostructured Ni-Core–Shell Catalyst. *Angew. Chem. Int. Ed.* **2021**, *60* (34), 18591. https://doi.org/10.1002/anie.202105492

(36) Palazzolo, A.; Naret, T.; Daniel-Bertrand, M.; Buisson, D.; Tricard, S.; Lesot, P.; Coppel, Y.; Chaudret, B.; Feuillastre, S.; Pieters, G. Tuning the Reactivity of a Heterogeneous Catalyst Using N-Heterocyclic Carbene Ligands for C−H Activation Reactions. *Angew. Chem. Int. Ed.* **2020**, *59* (47), 20879. https://doi.org/10.1002/anie.202009258

(37) Pfeifer, V.; Certiat, M.; Bouzouita, D.; Palazzolo, A.; Garcia-Argote, S.; Marcon, E.; Buisson, D.; Lesot, P.; Maron, L.; Chaudret, B.; Tricard, S.; Rosal, I.; Poteau, R.; Feuillastre, S.; Pieters, G. Hydrogen Isotope Exchange Catalyzed by Ru Nanocatalysts: Labelling of Complex Molecules Containing *N* -Heterocycles and Reaction Mechanism Insights. *Chem. Eur. J.* **2020**, *26* (22), 4988. https://doi.org/10.1002/chem.201905651

(38) Catalysis. Leibniz-Institut Für Katalyse. Forschung Über Katalysatoren Applied Homogeneous Catalysis. https://www.catalysis.de/en/research/applied-homogeneous-catalysis

(39) Home - NanoX. https://nanox-toulouse.fr/

(40) Kopf, S.; Neumann, H.; Beller, M. Manganese-Catalyzed Selective C–H Activation and Deuteration by Means of a Catalytic Transient Directing Group Strategy. *Chem. Commun.* **2021**, *57* (9), 1137. https://doi.org/10.1039/D0CC07675A

(41) Kopf, S.; Liu, J.; Franke, R.; Jiao, H.; Neumann, H.; Beller, M. Base-Mediated Remote Deuteration of *N* -Heteroarenes – Broad Scope and Mechanism. *Eur. J. Org. Chem.* **2022**, *2022* (19), e202200204. https://doi.org/10.1002/ejoc.202200204

(42) Papa, V.; Cao, Y.; Spannenberg, A.; Junge, K.; Beller, M. Development of a Practical Non-Noble Metal Catalyst for Hydrogenation of N-Heteroarenes. *Nat. Catal.* **2020**, *3* (2), 135. https://doi.org/10.1038/s41929-019-0404-6

(43) Gruhn, R. Evidence Grows for Early Peopling of the Americas began more than 20,000 years ago. *Nature* **2020**, *584*, 47. https://doi.org/10.1038/d41586-020-02137-3

(44) Macdonald, C. G.; Shannon, J. S. Selective Nickel-Catalysed Hydrogen Exchange of Phenol, Aniline and Pyridine Derivatives. *Tetrahedron Lett.* **1964**, *45-46*, 3351. https://doi.org/10.1016/0040-4039(64)83098-7

(45) Sajiki, H.; Ito, N.; Esaki, H.; Maesawa, T.; Maegawa, T.; Hirota, K. Aromatic Ring Favorable and Efficient H–D Exchange Reaction Catalyzed by Pt/C. *Tetrahedron Lett.* **2005**, *46* (41), 6995. https://doi.org/10.1016/j.tetlet.2005.08.067

(46) Valero, M.; Bouzouita, D.; Palazzolo, A.; Atzrodt, J.; Dugave, C.; Tricard, S.; Feuillastre, S.; Pieters, G.; Chaudret, B.; Derdau, V. NHC-Stabilized Iridium Nanoparticles as Catalysts in Hydrogen Isotope Exchange Reactions of Anilines. *Angew. Chem. Int. Ed.* **2020**, *59* (9), 3517. https://doi.org/10.1002/anie.201914369

(47) Li, W.; Wang, M.-M.; Hu, Y.; Werner, T. $B(C_6F_5)_3$-Catalyzed Regioselective Deuteration of Electron-Rich Aromatic and Heteroaromatic Compounds. *Org. Lett.* **2017**, *19* (21), 5768. https://doi.org/10.1021/acs.orglett.7b02701

(48) Liu, W.; Cao, L.; Zhang, Z.; Zhang, G.; Huang, S.; Huang, L.; Zhao, P.; Yan, X. Mesoionic Carbene–Iridium Complex Catalyzed *Ortho* -Selective Hydrogen Isotope Exchange of Anilines with High Functional Group Tolerance. *Org. Lett.* **2020**, *22* (6), 2210. https://doi.org/10.1021/acs.orglett.0c00402

(49) Dong, B.; Cong, X.; Hao, N. Silver-Catalyzed Regioselective Deuteration of (Hetero)Arenes and α-Deuteration of 2-Alkyl Azaarenes. *RSC Adv.* **2020**, *10* (43), 25475. https://doi.org/10.1039/D0RA02358B

(50) Farizyan, M.; Mondal, A.; Mal, S.; Deufel, F.; van Gemmeren, M. Palladium-Catalyzed Nondirected Late-Stage C–H Deuteration of Arenes. *J. Am. Chem. Soc.* **2021**, *143* (40), 16370. https://doi.org/10.1021/jacs.1c08233

(51) Junk, T.; Catallo, W. J.; Civils, L. D. Synthesis of Polydeuterated Benzothiazoles via Supercritical Deuteration of Anilines. *J. Label. Compd. Radiopharm.* **1997**, *39* (8), 625. https://doi.org/10.1002/(SICI)1099-1344(199708)39:8<625::AID-JLCR15>3.0.CO;2-X

(52) Martins, A.; Lautens, M. A Simple, Cost-Effective Method for the Regioselective Deuteration of Anilines. *Org. Lett.* **2008**, *10* (19), 4351. https://doi.org/10.1021/ol801763j

(53) Giles, R.; Lee, A.; Jung, E.; Kang, A.; Jung, K. W. Hydrogen–Deuterium Exchange of Aromatic Amines and Amides Using Deuterated Trifluoroacetic Acid. *Tetrahedron Lett.* **2015**, *56* (5), 747. https://doi.org/10.1016/j.tetlet.2014.12.102

(54) Fischer, O.; Hubert, A.; Heinrich, M. R. Shifted Selectivity in Protonation Enables the Mild Deuteration of Arenes Through Catalytic Amounts of Bronsted Acids in Deuterated Methanol. *J. Org. Chem.* **2020**, *85* (18), 11856. https://doi.org/10.1021/acs.joc.0c01604

(55) Leng, F.; Gerber, I. C.; Lecante, P.; Moldovan, S.; Girleanu, M.; Axet, M. R.; Serp, P. Controlled and Chemoselective Hydrogenation of Nitrobenzene over $Ru@C_{60}$ Catalysts. *ACS Catal.* **2016**, *6* (9), 6018. https://doi.org/10.1021/acscatal.6b01429

(56) Dong, J.; Wang, X.; Wang, Z.; Song, H.; Liu, Y.; Wang, Q. Formyl-Selective Deuteration of Aldehydes with D_2O *via* Synergistic Organic and Photoredox Catalysis. *Chem. Sci.* **2020**, *11* (4), 1026. https://doi.org/10.1039/C9SC05132E

(57) Zhang, M.; Yuan, X.-A.; Zhu, C.; Xie, J. Deoxygenative Deuteration of Carboxylic Acids with D_2O. *Angew. Chem. Int. Ed.* **2019**, *58* (1), 312. https://doi.org/10.1002/anie.201811522

(58) Kerr, W. J.; Reid, M.; Tuttle, T. Iridium-Catalyzed Formyl-Selective Deuteration of Aldehydes. *Angew. Chem. Int. Ed.* **2017**, *56* (27), 7808. https://doi.org/10.1002/anie.201702997

(59) Isbrandt, E.; Vandavasi, J.; Zhang, W.; Jamshidi, M.; Newman, S. Catalytic Deuteration of Aldehydes with D_2O. *Synlett* **2017**, *28* (20), 2851. https://doi.org/10.1055/s-0036-1588540

(60) Le, C.; Liang, Y.; Evans, R. W.; Li, X.; MacMillan, D. W. C. Selective Sp^3 C–H Alkylation via Polarity-Match-Based Cross-Coupling. *Nature* **2017**, *547* (7661), 79. https://doi.org/10.1038/nature22813

(61) Spletstoser, J. T.; White, J. M.; Tunoori, A. R.; Georg, G. I. Mild and Selective Hydrozirconation of Amides to Aldehydes Using $Cp_2Zr(H)Cl$: Scope and Mechanistic Insight. *J. Am. Chem. Soc.* **2007**, *129* (11), 3408. https://doi.org/10.1021/ja066362+

(62) Olsen, E. P. K.; Singh, T.; Harris, P.; Andersson, P. G.; Madsen, R. Experimental and Theoretical Mechanistic Investigation of the Iridium-Catalyzed Dehydrogenative Decarbonylation of Primary Alcohols. *J. Am. Chem. Soc.* **2015**, *137* (2), 834. https://doi.org/10.1021/ja5106943

(63) Ibrahim, M. Y. S.; Denmark, S. E. Palladium/Rhodium Cooperative Catalysis for the Production of Aryl Aldehydes and Their Deuterated Analogues Using the Water–Gas Shift Reaction. *Angew. Chem.* **2018**, *130* (32), 10519. https://doi.org/10.1002/ange.201806148

(64) Kozarich, J. W.; Worth, L.; Frank, B. L.; Christner, D. F.; Vanderwall, D. E.; Stubbe, J. Sequence-Specific Isotope Effects on the Cleavage of DNA by Bleomycin. *Science* **1989**, *245* (4924), 1396. https://doi.org/10.1126/science.2476851

(65) Adhikary, A.; Khanduri, D.; Kumar, A.; Sevilla, M. D. Photoexcitation of Adenine Cation Radical [$A^{\bullet+}$] in the near UV−vis Region Produces Sugar Radicals in Adenosine and in Its Nucleotides. *J. Phys. Chem. B* **2008**, *112* (49), 15844. https://doi.org/10.1021/jp808139e

(66) Bier, D. M.; Sherman, W. R.; Holmes, W. F. In-Vivo Measurement of Glucose and Alanine Metabolism with Stable Isotopic Tracers. **1977**, *26* (11), 1005. https://doi.org/10.2337/diab.26.11.1005

(67) Indurugalla, D.; Bennet, A. J. A Kinetic Isotope Effect Study on the Hydrolysis Reactions of Methyl Xylopyranosides and Methyl 5-Thioxylopyranosides: Oxygen versus Sulfur Stabilization of Carbenium Ions. *J. Am. Chem. Soc.* **2001**, *123* (44), 10889. https://doi.org/10.1021/ja011232g

(68) Toyama, A.; Takino, Y.; Takeuchi, H.; Harada, I. Ultraviolet Resonance Raman Spectra of Ribosyl C(1')-Deuterated Purine Nucleosides: Evidence of Vibrational Coupling between Purine and Ribose Rings. *J. Am. Chem. Soc.* **1993**, *115* (24), 11092. https://doi.org/10.1021/ja00077a005

(69) Földesi, A.; Nilson, F. P. R.; Glemarec, C.; Gioeli, C.; Chattopadhyaya, J. NMR Spectroscopic Properties (^{1}H at 500 MHz) of Deuterated∗ Ribonucleotide-Dimers ApU∗, GpC∗, Partially Deuterated 2'-Deoxyribonucleotide-Dimers d(TpA∗, d(ApT∗, d(GpC∗ and Their Comparison with Natural Counterparts (^{1}H-NMR Window). *J. Biochem. Biophys. Methods* **1993**, *26* (1), 1. https://doi.org/10.1016/0165-022X(93)90018-J

(70) Tolbert, T. J.; Williamson, J. R. Preparation of Specifically Deuterated RNA for NMR Studies Using a Combination of Chemical and Enzymatic Synthesis. *J. Am. Chem. Soc.* **1996**, *118* (34), 7929. https://doi.org/10.1021/ja961274i

(71) Földesi, A.; Trifonova, A.; Dinya, Z.; Chattopadhyaya, J. Total Synthesis of 2',3',4',5',5"-$^2H_5$-Ribonucleosides: The Key Building Blocks for NMR Structure Elucidation of Large RNA. *J. Org. Chem.* **2001**, *66* (20), 6560. https://doi.org/10.1021/jo010097n

(72) Kundu, M. K.; Trifonova, A.; Dinya, Z.; Földesi, A.; Chattopadhyaya, J. Synthetic Studies to Improve the Deuterium Labelling in Nucleosides for Facilitating Structural Studies of Large RNAs by High-Field NMR Spectroscopy. *Nucleosides Nucleotides Nucleic Acids* **2001**, *20* (4–7), 1333. https://doi.org/10.1081/NCN-100002549

(73) MacDonald, D.; Lu, P. Determination of DNA Structure in Solution: Enzymatic Deuteration of the Ribose 2' Carbon. *J. Am. Chem. Soc.* **2002**, *124* (33), 9722. https://doi.org/10.1021/ja026678r

(74) Kundu, M. K.; Földesi, A.; Chattopadhyaya, J. Studies on the Stereoselective Synthesis of Deuterated D-Ribose Derivatives. *Helv. Chim. Acta* **2003**, *86* (3), 633. https://doi.org/10.1002/hlca.200390062

(75) Vallurupalli, P.; Scott, L.; Hennig, M.; Williamson, J. R.; Kay, L. E. New RNA Labeling Methods Offer Dramatic Sensitivity Enhancements in ^{2}H NMR Relaxation Spectra. *J. Am. Chem. Soc.* **2006**, *128* (29), 9346. https://doi.org/10.1021/ja0632512

(76) Miljkovic, M. Carbohydrates. Synthesis, Mechanisms, and Stereoelectronic Effects. *Springer* **2009**. https://link.springer.com/book/10.1007/978-0-387-92265-2

(77) Levy, D. E.; Fügedi, P. The Organic Chemistry of Sugars. Levy, D. E.; Fügedi, P. Eds., *Taylor&Francis Group* **2005**. https://doi.org/10.1201/9781420027952

(78) De Voss, J. J.; Hangeland, J. J.; Townsend, C. A. General Approach to the Synthesis of Specifically Deuterium-Labeled Nucleosides. *J. Org. Chem.* **1994**, *59* (10), 2715. https://doi.org/10.1021/jo00089a013

(79) Chen, B.; Jamieson, E. R.; Tullius, T. D. A General Synthesis of Specifically Deuterated Nucleotides for Studies of DNA and RNA. *Bioorg. Med. Chem. Lett.* **2002**, *12* (21), 3093. https://doi.org/10.1016/S0960-894X(02)00650-9

(80) Babu, B. S.; Balasubramanian, K. K. Stereoselective Synthesis of a Ketohexofuranose from an Aldohexopyranose by a [6+1−1] Strategy. *Carbohydr. Res.* **2005**, *340* (4), 753. https://doi.org/10.1016/j.carres.2005.01.008
(81) Palmer, J. L.; Abeles, R. H. The Mechanism of Action of S-Adenosylhomocysteinase. *J. Biol. Chem.* **1979**, *254* (4), 1217. https://doi.org/10.1016/S0021-9258(17)34190-X
(82) Wu, J. C.; Kozarich, J. W.; Stubbe, J. The Mechanism of Free Base Formation from DNA by Bleomycin. A Proposal Based on Site Specific Tritium Release from Poly(DA.DU). *J. Biol. Chem.* **1983**, *258* (8), 4694. https://doi.org/10.1016/S0021-9258(18)32476-1
(83) Persky, R.; Albeck, A. Synthesis of Selectively Labeled D-Fructose and D-Fructose Phosphate Analogues Locked in the Cyclic Furanose Form. *J. Org. Chem.* **2000**, *65* (18), 5632. https://doi.org/10.1021/jo0003908
(84) Hudlicky, T.; Pitzer, K. K.; Stabile, M. R.; Thorpe, A. J.; Whited, G. M. Biocatalytic Syntheses of Protected D-Mannose-d_5, D-Mannose-d_7, D-Mannitol-2,3,4,5,6-d_5, and D-Mannitol-1,1,2,3,4,5,6,6-d_8. *J. Org. Chem.* **1996**, *61* (12), 4151. https://doi.org/10.1021/jo951666s
(85) Koch, H. J.; Stuart, R. S. The Synthesis of Per-c-deuterated d-Glucose*. *Carbohydr. Res.* **1978**, *64*, 127. https://doi.org/10.1016/S0008-6215(00)83694-0
(86) Angyal, S. J.; Stevens, J. D.; Odier, L. Selective Deuteration over Raney Nickel in Deuterium Oxide: Methyl Glycosides. *Carbohydr. Res.* **1986**, *157*, 83. https://doi.org/10.1016/0008-6215(86)85061-3
(87) Cioffi, E. A.; Prestegard, J. H. Deuterium Labelling of a Glycosphingolipid Using an Ultrasonicated Nickel Catalyst. *Tetrahedron Lett.* **1986**, *27* (4), 415. https://doi.org/10.1016/S0040-4039(00)85493-3
(88) Angyal, S. J.; Stevens, J. D.; Odier, L. Selective Deuteration over Raney Nickel in Deuterium Oxide: 1,6-Anhydrohexoses. *Carbohydr. Res.* **1987**, *169*, 151. https://doi.org/10.1016/0008-6215(87)80247-1
(89) Cioffi, E. A.; Willis, W. S.; Suib, S. L. Ultrasonically Induced Enhancement of Isotope-Exchange Catalysts: Surface Analysis of Raney Nickel Alloys. *Langmuir* **1988**, *4* (3), 697. https://doi.org/10.1021/la00081a034
(90) Cioffi, E. A.; Willis, W. S.; Suib, S. L. Morphological and Surface Studies of Ultrasonically Treated Raney Nickel Hydrogen-Deuterium Exchange Catalysts. *Langmuir* **1990**, *6* (2), 404. https://doi.org/10.1021/la00092a020
(91) Cioffi, E. A. Solvent-Induced Control of Ultrasonic Deuterium Labelling. *Tetrahedron Lett.* **1996**, *37* (35), 6231. https://doi.org/10.1016/0040-4039(96)01345-7
(92) Kurita, T.; Aoki, F.; Mizumoto, T.; Maejima, T.; Esaki, H.; Maegawa, T.; Monguchi, Y.; Sajiki, H. Facile and Convenient Method of Deuterium Gas Generation Using a Pd/C-Catalyzed H_2–D_2 Exchange Reaction and Its Application to Synthesis of Deuterium-Labeled Compounds. *Chem. Eur. J.* **2008**, *14* (11), 3371. https://doi.org/10.1002/chem.200701245
(93) Maegawa, T.; Fujiwara, Y.; Inagaki, Y.; Monguchi, Y.; Sajiki, H. A Convenient and Effective Method for the Regioselective Deuteration of Alcohols. *Adv. Synth. Catal.* **2008**, *350* (14–15), 2215. https://doi.org/10.1002/adsc.200800407
(94) Fujiwara, Y.; Iwata, H.; Sawama, Y.; Monguchi, Y.; Sajiki, H. Method for Regio-, Chemo- and Stereoselective Deuterium Labeling of Sugars Based on Ruthenium-Catalyzed C–H Bond Activation. *Chem. Commun.* **2010**, *46* (27), 4977. https://doi.org/10.1039/c0cc01197e
(95) Ali, I. A. I.; Ali, O. M.; Abdel-Rahman, A. A.-H. Amino Acid Derivatives, IV [1]: Synthesis and Antiviral Evaluation of New α-Amino Acid Esters Bearing Methyl β-d-Ribofuranoside Side Chain. *Monatshefte Für Chem. - Chem. Mon.* **2007**, *138* (9), 909. https://doi.org/10.1007/s00706-007-0643-0
(96) Župančić, N.; Ban, Ž.; Matić, J.; Saftić, D.; Glavaš-Obrovac, L.; Žinić, B. Synthesis and Biological Activity of Reversed Pyrimidine Nucleosides. *Croat. Chem. Acta* **2015**, *88* (1), 43. https://doi.org/10.5562/cca2531
(97) André-Joyaux, E.; Santana, A. G.; González, C. C. Synthesis of Chiral Polyhydroxylated Benzimidazoles by a Tandem Radical Fragmentation/Cyclization Reaction: A Straight

Avenue to Fused Aromatic-Carbohydrate Hybrids. *J. Org. Chem.* **2019**, *84* (2), 506. https://doi.org/10.1021/acs.joc.8b01988

(98) Iñigo, S.; Porro, M. T.; Montserrat, J. M.; Iglesias, L. E.; Iribarren, A. M. Deprotection of Peracetylated Methyl D-Ribosides through Enzymatic Alcoholysis: Different Recognition of the Anomers. *J. Mol. Catal. B Enzym.* **2005**, *35* (1–3), 70. https://doi.org/10.1016/j.molcatb.2005.05.010

(99) Clark, E. L.; Hayes, M. L.; Barker, R. Paramolybdate Anion-Exchange Resin, an Improved Catalyst for the C_{-1}-C_{-2} Rearrangement and 2-Epimerization of Aldoses. *Carbohydr. Res.* **1986**, *153* (2), 263. https://doi.org/10.1016/s0008-6215(00)90268-4

(100) Jones, J. K. N.; Nicholson, W. H. The Epimerisation of Sugars. *J. Chem. Soc.*, **1955**, *0* 3050. https://doi.org/10.1039/JR9550003050

(101) Rubio, B. Chapter 11: Biochemistry *CHEM 100: Chemistry and Society*. Honolulu Community College. 379. https://chem.libretexts.org/Courses/Honolulu_Community_College/CHEM_100%3A_Chemistry_and_Society

(102) Sako, M.; Hayashi, T.; Hirota, K.; Maki, Y. A Newly Devised Method for the Oxidative Unmasking of 1,N^6-Etheno-adenosines: Facile Conversion of Adenosine into 2-Deuterateed Adenosine. *Chem. Pharm. Bull.*, **1992**, *40* (6), 1656. https://doi.org/10.1248/cpb.40.1656

(103) Fujii, T.; Saito, T.; Kizu, K.; Hayashibara, H.; Kumazawa, Y.; Nakajima, S.; Fujisawa, T. Purines. XLVIII.[1)] Syntheses and Proton Nuclear Magnetic Resonance Study of 2-Deuterioadenines Substituted or Unsubstituted at the 9-Position and of Their N-Oxygenated Derivatives. *Chem. Pharm. Bull.*, **1991**, *39* (2), 301. https://doi.org/10.1248/cpb.39.301

(104) Kawazoe, Y. CHEMICAL ALTERATION OF NUCLEIC ACIDS AND THEIR COMPONENTS. X1.l) HYDROGEN-DEUTERIUM EXCHANGE OF NUCLEOSIDES AND NUCLEOTIDES CATALYZED BY PLATINUM. **1975**, No. 19, 4.

(105) Maeda, M.; Saneyoshi, M.; Kawazoe, Y. Studies on Hydrogen Exchange. XII. Reaction Mechanism for Hydrogen Exchange of C-8 Hydrogen of Purine Ribosides. *Chem. Pharm. Bull.* **1971**, *19* (8), 1641. https://doi.org/10.1248/cpb.19.1641

(106) Maki, Y.; Suzuki, M.; Kameyama, K.; Sako, M. Accelerative Effect of N^6-Acyl Groups on the C(8)-Hydrogen Exchange of 9-Substituted Adenines. *J. Chem. Soc. Chem. Commun.* **1981**, *14*, 658. https://doi.org/10.1039/c39810000658

(107) Sugiyama, T.; Iwasawa, H.; Hashizume, T. Synthesis of Deuterated N^6-(*o*-Hydroxybenzyl)Adenosine-d_3. *Agric. Biol. Chem.* **1980**, *44* (5), 1057. https://doi.org/10.1080/00021369.1980.10864069

CHAPTER 6:
Experimental details

Summary

6.1 General methods

The studied metallic system being air sensitive,[1–4] all the operations were carried out under inert atmosphere to avoid the passivation and/or oxidation of the metallic surface. MBraun gloveboxes and standard Schlenk techniques were used being argon chosen as the non-reactive gas.

Tetrahydrofuran (THF) and pentane were purified by an MBraun SPS-800 solvent purification system or by standard methods at the Laboratoire de Chimie de Coordination (LCC) in Toulouse. At Leibniz Institute for Catalysis (LIKAT) in Rostock, THF was purified by distillation over Na/benzophenone and pentane by distillation using lithium aluminium hydride

($LiAlH_4$). The metallic precursors [Ru(η^4-C_8H_{12})(η^6-C_8H_{10})], [Ni(η^4- C_8H_{12})$_2$] and Cu(C_9H_{11}) were purchased at Nanomeps Toulouse, Strem Chemicals and Merck respectively. Polyvinylpyrrolidone (PVP), dodecane, decane, 1-propanol (1-PrOH), furfural (FF), alumina, hexadecylamine (HDA), 1-adamantanecarboxylic acid (AdCOOH) and THF were purchased at Merck, while furfuryl alcohol (HF) and tetrahydrofurfuryl alcohol (HMTHF) at Alfa Aesar, diphenylphosphinopyridine (PPh_2Py) at TCI and dodecylamine (DDA) at Fluka. Carbon monoxide (CO) and hydrogen (H_2) were obtained from Air Liquid. At LIKAT in Rostock, THF was purchased at Acros organics, $CHCl_3$ at VWR, ethylacetate at Walter CMP and pentane at Fischer. Deuterated chloroform ($CDCl_3$) and deuterated water (D_2O) were purchased at Deuteron. 4-(trifluoromethyl)benzaldehyde (TFMBAL) and methyl 2,3-O-isopropylidene-β-D-ribofuranoside (MOIBRIBOF) were purchased at Fluorochem. 4-(trifluoromethyl)acetophenone (TFMAPO) was purchased at abcr and methyl β-D-ribofuranoside (MEBRIBOF) at Alfa Aesar. 4-methoxyaniline (4-MeOAn), adenosine (ADNS), 1-PrOH and Na_2SO_4 were purchased at Merck. H_2, helium He, Ar and N_2 were supplied by Air Liquide. All these products were used as arrived.

The metal content was determined by inductively coupled plasma - optical emission spectroscopy (ICP-OES) on mineralised samples using nitric and hydrochloric acids. At the LCC in Toulouse by a Thermo Fisher Scientific ICAP 6300 Duo instrument. A charge injection device (CID) array detector was used. The solutions were introduced into the ICP through an introduction system containing a quartz nebulizer, a cyclonic spray chamber and a quartz torch. At LIKAT in Rostock, the metal content was determined in a Varian 715-ES instrument. A charge coupled device (CCD) detector was used for this simultaneous echelle spectrometer. The solutions were introduced into the ICP through a sample delivery system consisting in a crossflow nebulizer and a quartz torch.

Elemental analyses were performed at the LCC in Toulouse by a Perkin Elmer 2400 series II by the Dumas method consisting on burning the sample into simple gases such as CO_2, H_2O and N_2.The combustion was executed at 1800 ºC with the presence of oxygen. He was used as the vector gas using a katharometer as thermal conductivity detector.

Liquid nuclear magnetic resonance (NMR) analyses were executed at the LCC in Toulouse with a Bruker Avance 300 or 400 instruments; at LIKAT, in Rostock, using a Bruker Avance 300 or a Fourier 300 instrument.

Solid NMR measurements were performed for some of the synthesised catalysts on a Bruker Avance III HD 400 with a magnetic field of 9.4 T at the LCC in Toulouse. The samples were placed into ZrO_2 rotors of 3.2 mm or 2.5 mm. Their rotating speed near the magic angle was set at 12 kHz and the experiments were done at RT.

Attenuated total reflection infrared (ATR-IR) spectra were registered in the range of 4000-400 cm^{-1} at the LCC in Toulouse on a PerkinElmer GX2000 spectrometer placed in a glovebox under an argon atmosphere.

Transmission electron microscopy (TEM) and high resolution transmission electron microscopy (HRTEM) were carried out at the "Centre de microcaractérisation Raimond Castaing" in Toulouse on a JEOL JEM 1400 electron microscope operating at 120 kV with a point resolution of 2.0 Å or on a JEOL JEM 1011 CXT operating at 100 kV with a point resolution of 4.5 Å. High resolution images were acquired on a JEOL JEM 2100F coupled with a Field Emission Gun (FEG) operating at 200 kV with a point resolution of 2.3 Å or on a JEOL JEM ARM200F Cold FEG operating at 200 kV with a point resolution of >1.9 Å. A Cu-grid (mesh 400) or a Ni-grid (mesh 400), with a collodion film and a carbon film deposited, was used for the deposition of the samples. At LIKAT in Rostock, scanning transmission electron microscopy (STEM) measurements were performed at 200kV with an aberration-corrected JEM-ARM200F (JEOL, Corrector: CEOS) with a point resolution of 1.4Å. Energy dispersive X-ray (EDX) analysis was done with a JED-2300 (JEOL) energy-dispersive-X-ray spectrometer having a silicon drift detector (dry SD60GV).High angle annular dark field (HAADF) and annular bright field (ABF) detectors were used for general imaging. A holey carbon supported Cu-grid (mesh 300, Micro to Nano) was used for the deposition of the samples. Subsequently, the grid was transferred to the microscope. The mean size of the nanoparticles (NPs) was determined by measuring manually at least 200 particles from the TEM images with the ImageJ software.

Magnetism analysis were performed at the LCC in Toulouse, obtaining the hysteresis curves by a MPMS 5 Quantum design magnetometer (cryo-magnet 5 T; cryostat 2 K – 400 K) with a superconducting quantum interface device (SQUID).

Thermogravimetric analysis (TGA) measurements were carried out at the LCC in Toulouse through a Mettler TGA/DSC 3+ by using an alumina sample container. N_2 was used as a carrier gas with a 50 mL·min^{-1} flow. The temperature was increased 10 ºC·min^{-1} until 1000 ºC, temperature hold for 5 min.

Wide angle X-ray scattering (WAXS) analyses were performed at the Centre d'Élaboration de Matériaux et d'Etudes Structurales (CEMES) in Toulouse. The diffractometer for pair distribution function (PDF) analyses is equipped with a monochromatized molybdenum radiation (0.07169 nm), solid-state detection and a low background setup. In order to avoid the oxidation of the samples, Lindemann glass capillaries of 1 mm of diameter were sealed after being filled with the sample in a glovebox. The PDF analyses were obtained for 457 data points lasting 150 s per each on an extended angular range of 129 degrees in 2 theta. Fourier transform and classic corrections related to polarization and absorption in cylindrical geometries were employed before reduction.

X-ray photoelectron spectroscopy (XPS) measurements were performed at the Centre Inter-universitaire de Recherche et d'Ingénierie des Matériaux (CIRIMAT) in Toulouse in a Thermo Scientific K-Alpha instrument under ultra high vacuum (UHV) by a X-ray source of monochromatised Al Kα (EAl Kα = 1486.6 eV). The spot size for the X-ray was of 400 μm fixing the pass energy at 30 eV with a step for core levels of 0.1 eV and for surveys of 160 eV. The Au 4f7/2 (83.9 ± 0.1 eV) and the Cu 2p3/2 (932.8 ± 0.1 eV) photoelectron lines were employed for the calibration of the spectrometer energy. The XPS spectra were register in direct mode N (Ec) by removing the background signal following the Shirley method and by neutralising the charge effects on the top surface by applying the flood gun.

Gas chromatography (GC) analyses were carried out on a Shimadzu GC-2014 furnished with a SUPELCOWAX 10 capillary column (30 m x 0.25 mm x 0.25 μm) at LCC in Toulouse. The analysis method for the FF and quinoline (QN) hydrogenations consisted on a 1.25 mL·min^{-1} flow of He as carrier gas, 250 ºC for the injector temperature, 250 ºC for the flame ionisation detector (FID), with the following oven program: 50 ºC hold during 3.0 min followed by a ramp of 20 ºC·min^{-1} until 240 ºC holding this temperature during 10.0 min displaying a total run time of 22.5 min. The retention times of the different products for the FF hydrogenation are the following: dodecane, 6.8 min; FF, 9.2 min; HMTHF, 9.4 min; acetal, 10.0 min; HF, 10.4 min; 2-propoxymethyl furan, 10.6 min; and 1,2-pentanediol

(1,2-PeD), 11.1 min. The retention times of the different products for the quinoline hydrogenation are the following: unidentified product, 3.9 min; dodecane, 6.8 min; decahydroquinoline (DHQ), 9.4 min; decahydro-1-propylquinoline (DHPQ), 9.7 min; 5,6,7,8-tetrahydroquinoline (5-THQ), 11.3 min; quinoline, 12.5 min; N-propyl 1,2,3,4-tetrahydroquinoline (1-THPQ), 12.8 min; and 1,2,3,4-tetrahydroquinoline (1-THQ), 13.2 min.

Gas chromatography – mass spectroscopy (GC-MS) analyses were executed in a Shimadzu QP2010 Ultra GC-MS with electron impact as ionisation method supplied with a ZEBRON ZB-5 ms capillary column (30 m x 0.25 mm x 0.25µm) at LCC in Toulouse. The analysis method for the FF and quinoline hydrogenation consisted on a 1 mL·min^{-1} flow of He as carrier gas, 250 ºC for the injector temperature, 250 ºC for the FID, with the following oven program: 40 ºC hold during 0.5 min followed by a ramp of 20 ºC·min^{-1} until 250 ºC holding this temperature during 10.0 min displaying a total run time of 21.0 min. The retention times of the different products for the FF hydrogenation are the following: FF, 3.6 min; HF, 3.8 min; HMTHF, 4.0 min; 1,2-PeD, 4.3 min; 2-propoxymethyl furan, 4.7 min; dodecane, 6.3 min; and acetal, 6.7min. The retention times of the different products for the quinoline hydrogenation are the following: DHQ, 6.1 min; dodecane, 6.2 min; 5-THQ, 6.4 min; quinoline, 6.6 min; 1-THQ, 7.3 min; DHPQ, 7.4 min; and 1-THPQ, 8.4 min. The analysis method for the norbornene hydrogenation, used for the quantification of hydrides on the surface of the NPs, consisted on a 1 mL·min^{-1} flow of He as carrier gas, 250 ºC for the injector temperature, 250 ºC for the FID, with the following oven program: 35 ºC hold during 1.0 min followed by a ramp of 15 ºC·min^{-1} until 250 ºC, temperature hold for 5.0 min displaying a total run time of 20.3 min. The retention times of the different products are the following: DHQ, 6.1 min; dodecane, 6.2 min; 5-THQ, 6.4 min; quinoline, 6.6 min; 1-THQ, 7.3 min; DHPQ, 7.4 min; and 1-THPQ, 8.4 min.

GC-MS analyses were performed at LIKAT in Rostock using an Agilent 5977B GC/MSD with electron impact as ionisation method supplied with a HP-5 ms ultra inert column (30 m x 0.25 mm x 0.25µm). The analysis method for the 4-MeOAn deuteration consisted on a 1.2 mL·min^{-1} flow of He as carrier gas, 200 ºC for the injector temperature, 310 ºC for the FID, with the following oven program: starting at 50 ºC, followed by a ramp of 10 ºC·min^{-1} until 260 ºC, followed by a ramp of 50 ºC·min^{-1} until 300 ºC and holding during 2.0 min displaying a total run time of 23.8 min. The retention time of 4-MeOAn is 8.5 min. The analysis method for the TFMBAL and MOIBRIBOF deuteration consisted on a 1.2 mL·min^{-1} flow of He as carrier gas, 200 ºC for the injector temperature, 310 ºC for the FID, with the following oven program: starting at 50 ºC, followed by a ramp of 8 ºC·min^{-1} until

260 ºC and holding during 5.0 min displaying a total run time of 31.0 min. The retention time of TFMBAL is 5.2 min and of MOIBRIBOF is 11.3 min.

Catalysed deuterations at LIKAT in Rostock were centrifuged in a Thermo electron corporation Heraeus Pico 17 centrifuge, in order to separate the catalysts from the solution. The sample was introduced in a 1.5 mL Eppendorf and was centrifuged at 13000 rpm during 10 minutes. It was followed by the addition of 1.5mL of ethyl acetate to wash by centrifuging at 13000 rpm during 2 minutes. A Christ Alpha 3-4 LSC basic freeze dryer was also used to concentrate some diluted samples.

6.2 Computational details

6.2.1 DFT calculations of metal nanoclusters

The software employed for the theoretical calculations is the Vienna Ab initio Simulation Package (VASP)[5,6] using spin polarized density functional theory (DFT). The generalised gradient approach from Perdew, Burke and Ernzerhof (PBE)[7] was applied to approximate the exchange-correlation potential. The projector augmented wave (PAW)[8,9] data sets utilised for the full-potential reconstruction treat the states (n-1)p, (n-1)d and ns (i.e. 14 valence electrons) for Ru. 500 eV were fixed as the kinetic energy cut-off, 0.02 eV of width for the Gaussian smearing (σ), being the energies extrapolated for σ = 0.00 eV. 0.02 eV $Å^{-1}$ was set as threshold for the residual forces on any direction for the geometry optimisation. Finally, for all the Γ-centred calculations[10], a supercell of 20 x 23 x 20 $Å^3$ was established to ensure, between periodic images of the nanoclusters, a vacuum space of circa 10 Å).

6.2.2 Ru_{55} model

The Ru_{55} model is a *hcp* spheroid which its geometrical characteristics, surface hydrides coverage are published elsewhere.[11] Adsorption of phenylpyridine[12] and ethanoic acid[13] have also been studied on the surface of hydrogenated Ru NPs ($Ru_{55}H_{70}$, $Ru_{55}H_{32}$, $Ru_{55}H_{15}$).

6.2.3 Ni_{38} model

The Ni_{38} model is a face-centred cubic (*fcc*) spheroid. The hydride coverage of the Ni hydrogenated model $Ni_{38}H_{35}$ was optimized according to the hydrides surface coverage determined experimentally, following the procedure described below.

6.2.4 $Ru_{13}Ni_{25}$ model

The $Ru_{13}Ni_{25}$ model was built starting from the Ni_{38} model by replacing several Ni atoms on the core of the NP by Ru atoms, according to the WAXS analyses which determined the core-shell structure obtained experimentally. The number of Ru and Ni atoms was decided taking into consideration the experimental results.

6.2.5 Adsorption energies

$$E_{ads}(H) = \frac{1}{n}\left[E(nH^*) - E(NP) - \frac{n}{2}E(H_2)\right]$$

$$E_{ads}(\mathbf{L}) = \frac{1}{n}[E(n\mathbf{L}^*) - E(NP) - \mathbf{n}E(\mathbf{L})]$$

To clarify, this adsorption energy is dissociative in the case of hydrides.

6.2.6 Charge calculations

The density of states projected onto an atomic Slater basis set (pDOS) were integrated up to the Fermi energy to perform from the VASP wavefunction a Mulliken population analysis (MPA). The Lobster software, by using the basis set pbeVASPfit, allowed the projection of the PAW wavefunction.[14]The charge spilling, a factor evaluating the projection quality, was regularly lower than 1%. An assessment comparing these MPA charges to other schemes of electronic density decomposition (CM5, Natural Population Analysis, AIM-Bader) is available.[15]

6.2.7 d-band centre values (Ɛd)

The d-band centre values were computed using the pDOS acquired with the LOBSTER software.[16]This model is supported by the principle that the binding energy of an adsorbate on a metal surface depends mainly on the electronic structure of the surface.[17] The strength of the bonding on the surface increases with the closeness of the $\varepsilon_d$to the Fermi energy (E_F). Weak adsorption energies are therefore related to a large difference (E_F–ε_d).

6.3 Synthesis of metal nanoparticles

6.3.1 RuNi/PVP

In a classic reaction, the metallic precursors [Ru(η^4-C_8H_{12})(η^6-C_8H_{10})] and/or [Ni(η^4-C_8H_{12})$_2$] and PVP were added in a Fisher Porter (FP) bottle in a glovebox, where they were

dissolved in THF. At the fume hood, the FP bottle with the yellow solution was pressurized with 3 bars of H_2 and heated to 85 ºC in an oil bath. The solution became black after some minutes evidencing the decomposition of the metallic complexes. The synthesis remained under vigorous stirring at 85 ºC overnight. The day after, the excess of H_2 was removed from the FP bottle followed by the concentration of the colloidal suspension under vacuum. To ensure a good precipitation of the NP, pentane was added. The black solid, after filtrating through a cannula under argon, was washed twice with pentane, following the same procedure. The washed NPs were then dried under reduced pressure overnight. For each metallic composition of the studied NPs, the reactant quantities are noted herein.

Ru/PVP. 140.4 mg (0.445 mmol) of [Ru(η^4-C_8H_{12})(η^6-C_8H_{10})], 150 mg of PVP, and 40 mL of THF. Yield: 102.7 mg. ICP anal.: 24.2 % Ru.

Ru_3Ni_1/PVP. 105.3 mg (0.334 mmol) of [Ru(η^4-C_8H_{12})(η^6- C_8H_{10})], 30.6 mg (0.111 mmol) of [Ni(η^4-C_8H_{12})$_2$], 150 mg of PVP, and 40mL of THF. Yield: 131.2mg. ICP anal.: 17.0 % Ru; 3.7 % Ni.

Ru_1Ni_1/PVP. 45.0 mg (0.143 mmol) of [Ru(η^4-C_8H_{12})(η^6-C_8H_{10})], 39.2 mg (0.143 mmol) of [Ni(η^4-C_8H_{12})$_2$], 100 mg of PVP, and 40 mL of THF. Yield: 72.3 mg. ICP anal.: 10.2 % Ru; 5.7 % Ni.

Ru_1Ni_3/PVP. 35.1 mg (0.111 mmol) of [Ru(η^4-C_8H_{12})(η^6-C_8H_{10})], 91.8 mg (0.334 mmol) of [Ni(η^4-C_8H_{12})$_2$], 150 mg of PVP, and 40 mL of THF. Yield: 147.8 mg. ICP anal.: 7.9 % Ru; 14.6 % Ni.

Ru_1Ni_{20}/PVP. 7.0 mg (0.022 mmol) of [Ru(η^4-C_8H_{12})(η^6-C_8H_{10})], 116.3 mg (0.423 mmol) of [Ni(η^4-C_8H_{12})$_2$], 150 mg of PVP, and 40 mL of THF. Yield: 92.9 mg. ICP anal.: 1.5 % Ru; 17.6 % Ni.

Ni/PVP. 117.6 mg (0.425 mmol) of [Ni(η^4-C_8H_{12})$_2$], 150 mg of PVP, and 40 mL of THF. Yield: 114.1 mg. ICP anal.: 17.9 % Ni.

6.3.2 RuNi/PPh_2Py

In a classic reaction, the metallic precursors [Ru(η^4-C_8H_{12})(η^6-C_8H_{10})] and/or [Ni(η^4-C_8H_{12})$_2$] complexes and PPh_2Py were added in a FP bottle in a glovebox, where they were dissolved in THF. At the fume hood, the FP bottle with the orange solution was pressurized with 3 bars of H_2 and heated to 85 ºC in an oil bath. The solution became black after some minutes evidencing the decomposition of the metallic complexes. The synthesis re-

mained under vigorous stirring at 85 ºC overnight. The day after, the excess of H_2 was removed from the FP bottle followed by the concentration of the colloidal suspension under vacuum. To ensure a good precipitation of the NP, pentane was added. The black solid, after filtrating through a cannula under argon, was washed twice with pentane, following the same procedure. The washed NPs were then dried under reduced pressure overnight.

When using $[Ru(\eta^4\text{-}C_8H_{12})(PPh_2Py)_2]$ or $[Ni(\eta^4\text{-}C_8H_{12})(PPh_2Py)_2]$ complexes as precursors for the synthesis of Ru_1Ni_1/PPh_2Py, they were decomposed, with $[Ru(\eta^4\text{-}C_8H_{12})(\eta^6\text{-}C_8H_{10})]$ and $[Ni(\eta^4\text{-}C_8H_{12})_2]$ respectively, under 3 bars of H_2 an heated at 85 ºC in an oil bath. In these cases, no additional PPh_2Py was added. The colour of the solution changed in both cases from dark red to black when pressurising. The day after, the excess of H_2 was removed from the FP bottle followed by the concentration of the colloidal suspension under vacuum. To ensure a good precipitation of the NP, pentane was added. The black solid, after filtrating through a cannula under argon, was washed twice with pentane, following the same procedure. The washed NPs were then dried under reduced pressure overnight.

For each metallic composition of the studied NPs, the reactant quantities are noted herein:

Ru/PPh_2Py. 149.8 mg (0.475 mmol) of $[Ru(\eta^4\text{-}C_8H_{12})(\eta^6\text{-}C_8H_{10})]$, 25.0 mg of PPh_2Py, and 40 mL of THF. Yield: 42.0 mg. ICP anal.: 81.8 % Ru; 7.3 % P. P/Ru (surface) = 0.05

RuPNi/PPh_2Py. 100.0 mg (0.136 mmol) of $[Ru(\eta^4\text{-}C_8H_{12})(PPh_2Py)_2]$, 37.4 mg (0.136 mmol) of $[Ni(\eta^4\text{-}C_8H_{12})_2]$ and 40 mL of THF. Yield: 33.7 mg. ICP anal.: 19.8 % Ru; 13.4 % Ni; 14.8% P. P/M (surface) =0 .1

RuNi/PPh_2Py. 74.9 mg (0.237 mmol) of $[Ru(\eta^4\text{-}C_8H_{12})(\eta^6\text{-}C_8H_{10})]$, 65.3 mg (0.237 mmol) of $[Ni(\eta^4\text{-}C_8H_{12})_2]$, 25.0 mg of PPh_2Py, and 40 mL of THF. Yield: 30.9 mg. ICP anal.: 51.2 % Ru; 32.7 % Ni; 7.4 % P. P/Ni (surface) = 0.08

RuNiP/PPh_2Py. 45.5 mg (0.144 mmol) of $[Ru(\eta^4\text{-}C_8H_{12})(\eta^6\text{-}C_8H_{10})]$, 100.3 mg (0.145 mmol) of $[Ni(\eta^4\text{-}C_8H_{12})(PPh_2Py)_2]$ and 40 mL of THF. Yield: 34.3 mg . ICP anal.: 19.3 % Ru; 13.0 % Ni; 10.8 % P. P/M (surface) = 0.06

Ni/PPh_2Py. 130.6 mg (0.475 mmol) of $[Ni(\eta^4\text{-}C_8H_{12})_2]$, 25.0 mg of PPh_2Py, and 40 mL of THF. Yield: 16.6 mg. ICP anal.: 65.8 % Ni; 7.9 % P. P/Ni (surface) = 0.08

6.3.3 RuNi/AdCOOH

In a classic reaction, the metallic precursors $[Ru(\eta^4\text{-}C_8H_{12})(\eta^6\text{-}C_8H_{10})]$ and/or $[Ni(\eta^4\text{-}C_8H_{12})_2]$ and AdCOOH were added in a FP bottle in a glovebox, where they were dissolved

in THF. At the fume hood, the FP bottle with the yellow solution was pressurized with 3 bars of H_2 and heated to 85 ºC in an oil bath. The solution became black after some minutes evidencing the decomposition of the metallic complexes going through an orange colour. In the case of the Ni/AdCOOH NPs, no colour change was observed before heating while, with the Ru-containing NPs, the solution became black when pressurizing with H_2. The synthesis remained under vigorous stirring at 85 ºC overnight. The day after, the excess of H_2 was removed from the FP bottle followed by the concentration of the mixture under vacuum. To ensure a good precipitation of the NP, pentane was added. The black solid, after filtrating through a cannula under argon, was washed twice with pentane, following the same procedure. The washed NPs were then dried under reduced pressure overnight. For each metallic composition of the studied NPs, the reactant quantities are noted herein.

Ru_1Ni_1/AdCOOH. 65.62 mg (0.208 mmol) of [Ru(η^4-C_8H_{12})(η^6-C_8H_{10})], 57.14 mg (0.208 mmol) of [Ni(η^4-C_8H_{12})$_2$], 14.98 mg of AdCOOH, and 40 mL of THF. Yield: 7.3 mg. ICP anal.: 36.0 % Ru; 22.9 % Ni.

Ni/AdCOOH. 114.56 mg (0.417 mmol) of [Ni(η^4-C_8H_{12})$_2$], 14.98 mg of AdCOOH, and 40 mL of THF. Yield: 1.9 mg. ICP anal.: 76,9 % Ni.

6.3.4 RuCu/PVP

In a classic reaction, the metallic precursors [Ru(η^4-C_8H_{12})(η^6-C_8H_{10})] and/or [Cu(C_9H_{11})] and PVP were added in a FP bottle in a glovebox, where they were dissolved in THF. At the fume hood, the FP bottle with the yellow (for bimetallic and monometallic Ru reactions) or brown/dark orange solution (monometallic Cu reactions) was pressurized with 3 bars of H_2 and heated to 100 ºC in an oil bath. The solution became black (for monometallic Cu, dark Bordeaux red) after some minutes evidencing the decomposition of the metallic complexes. The synthesis remained under vigorous stirring at 100 ºC overnight. The day after, the excess of H_2 was removed from the FP bottle followed by the concentration of the colloidal suspension under vacuum. To ensure a good precipitation of the NP, pentane was added. The black solid, after filtrating through a cannula under argon, was washed twice with pentane, following the same procedure. The washed NPs were then dried under reduced pressure overnight. For each metallic composition of the studied NPs, the reactant quantities are noted herein.

Ru/PVP. 140.6 mg (0.446 mmol) of [Ru(η^4-C_8H_{12})(η^6-C_8H_{10})], 150 mg of PVP, and 40 mL of THF. Yield: 162.5 mg. ICP anal.: 22.2 % Ru.

Ru_2Cu_1/PVP. 105.3 mg (0.334 mmol) of [Ru(η^4-C_8H_{12})(η^6- C_8H_{10})], 32.3 mg (0.177 mmol) of [Cu(C_9H_{11})], 150 mg of PVP, and 40 mL of THF. Yield: 163.5 mg. ICP anal.: 15.9 % Ru; 5.6 % Cu.

Ru_1Cu_1/PVP. 111.7 mg (0.354 mmol) of [Ru(η^4-C_8H_{12})(η^6-C_8H_{10})], 64.7 mg (0.354 mmol) of [Cu(C_9H_{11})], 150 mg of PVP, and 40 mL of THF. Yield: 155.6 mg. ICP anal.: 18.6 % Ru; 14.1 % Cu.

Ru_1Cu_2/PVP. 70.2 mg (0.222 mmol) of [Ru(η^4-C_8H_{12})(η^6-C_8H_{10})], 64.7 mg (0.354 mmol) of [Cu(C_9H_{11})], 150 mg of PVP, and 40 mL of THF. Yield: 149.8 mg. ICP anal.: 13.7 % Ru; 15.9 % Cu.

Ru_1Cu_{20}/PVP. 11.2 mg (0.036 mmol) of [Ru(η^4-C_8H_{12})(η^6-C_8H_{10})], 122.9 mg (0.673 mmol) of [Cu(C_9H_{11})], 150 mg of PVP, and 40 mL of THF. Yield: 161.3 mg. ICP anal.: 1.7 % Ru; 20.2 % Cu.

Cu/PVP. 129.4 mg (0.708 mmol) of [Cu(C_9H_{11})], 150 mg of PVP, and 40 mL of THF. Yield: 136.8 mg. ICP anal.: 19.8 % Cu.

6.3.5 Cu/amines

In a classic reaction, the metallic precursor [Cu(C_9H_{11})] and an amine (DDA or HDA) were added in a FP bottle in a glovebox, where they were dissolved in THF. At the fume hood, the FP bottle with the dark orange/brown solution was pressurized with 3 bars of H_2 and heated to 80, 100 or 120 ºC in an oil bath. The synthesis remained under vigorous stirring and heating overnight. The day after, the excess of H_2 was removed from the FP bottle followed by the concentration of the colloidal suspension under vacuum. To ensure a good precipitation of the NP, pentane was added. The black solid, after filtrating through a cannula under argon, was washed twice with pentane, following the same procedure. The washed NPs were then dried under reduced pressure overnight. For each metallic composition of the studied NPs, the reactant quantities are noted herein.

Ru_1Cu_1/1 equivalents (eq.) HDA@100 ºC. 111.7 mg (0.354 mmol) of [Ru(η^4-C_8H_{12})(η^6-C_8H_{10})], 64.8 mg (0.354 mmol) of [Cu(C_9H_{11})], 85.7 mg of HDA, and 40 mL of THF. Yield: 63.2 mg. ICP anal.: 6.2 % Ru; 4.0 % Cu.

Cu/2 eq. HDA 120 ºC. 131.6 mg (0.720 mmol) of [Cu(C_9H_{11})], 173.8 mg of HDA, and 20 mL of THF. Yield: 23.7 mg. ICP anal.: 80.8 % Cu.

Cu/1 eq. HDA 120 ºC. 131.6 mg (0.720 mmol) of [Cu(C_9H_{11})], 86.9 mg of HDA, and 20 mL of THF. Yield: 28.9 mg. ICP anal.: 83.1 % Cu.

Cu/1 eq. HDA 100 ºC. 131.6 mg (0.720 mmol) of [Cu(C_9H_{11})], 86.9 mg of HDA, and 20 mL of THF. Yield: 39.2 mg. ICP anal.: 57.1 % Cu.

Cu/1 eq. HDA 80 ºC. 32.9 mg (0.180 mmol) of [Cu(C_9H_{11})], 21.7 mg of HDA, and 5 mL of THF. Yield: 28.0 mg. ICP anal.: 17.1 % Cu.

Cu/0.4 eq. HDA 100 ºC. 131.6 mg (0.720 mmol) of [Cu(C_9H_{11})], 34.8 mg of HDA, and 20 mL of THF. Yield: 4.4 mg. ICP anal.: 77.4 % Cu.

Cu/0.4 eq. HDA 80 ºC. 32.9 mg (0.180 mmol) of [Cu(C_9H_{11})], 8.7 mg of HDA, and 5 mL of THF. Yield: 4.4 mg. ICP anal.: 97.7 % Cu.

Cu/0.2 eq. HDA 80 ºC. 32.9 mg (0.180 mmol) of [Cu(C_9H_{11})], 4.4 mg of HDA, and 5 mL of THF. Yield: 7.4 mg. ICP anal.: 88.9 % Cu.

Cu/0.08 eq. DDA 80 ºC. 32.9 mg (0.180 mmol) of [Cu(C_9H_{11})], 1.7 mg of DDA, and 5 mL of THF. Yield: 5.7 mg. ICP anal.: 70.6 % Cu.

6.4 Synthesis of metals complexes

6.4.1 [Ru(η^4-C_8H_{12})(PPh_2Py)$_2$]

[Ru(η^4-C_8H_{12})(η^6-C_8H_{10})] complex was added in a Schlenk flask (SF) in a glovebox, where they were dissolved in dry acetone. PPh_2Py was added in the flask turning the pale yellow solution to orange. After 6 h stirring at RT in the glovebox, the solution became brown. At the fume hood, the acetone was evaporated obtaining a dark residue. This solid was washed three times with dry pentane to eliminate the cyclooctatriene and the excess of ligand. The resulting black solid was dried overnight under reduced pressure.

[Ru(η^4-C_8H_{12})(PPh_2Py)$_2$]. 100.1 mg (0.317 mmol) of [Ru(η^4-C_8H_{12})(η^6-C_8H_{10})], 208.1 mg of PPh_2Py, and 10 mL of dry acetone. Yield: 129.0 mg. ICP anal.: 11.7 % Ru; 9.3 % P.

6.4.2 [Ni(η^4-C_8H_{12})(PPh_2Py)$_2$]

[Ni(η^4-C_8H_{12})$_2$] complex was added in a SF in a glovebox, where they were dissolved in diethyl ether (Et_2O). PPh_2Py was added in the flask turning the pale yellow solution to orange together with the appearance of an orange precipitate. After, it was stirred 2 h at RT in

the glovebox, and then, the solvent was removed by decantation. The bright orange solid obtained was washed twice with Et_2O to eliminate the cyclooctatriene and the excess of ligand. The resulting black solid was dried overnight under reduced pressure.

$[Ni(\eta^4\text{-}C_8H_{12})(PPh_2Py)_2]$. 100.0 mg (0.364 mmol) of $[Ni(\eta^4\text{-}C_8H_{12})_2]$, 197.1 mg of PPh_2Py, and 5 mL of Et_2O. Yield: 157.4 mg. ICP anal.: 10.8 % Ni; 10.5 % P.

6.5 Surface reactivity with CO

To study the surface reactivity, CO was adsorbed on the surface of the NP in the solid state (SS). The reactivity test consisted on inserting a pure solid sample of NP in a FP that was then pressurised with 1.5 bar of CO during 24 h. The day after, the CO was removed from the FP under reduced pressure during 20 minutes. Then, the ATR-IR spectra were recorded in a glovebox.

6.6 Quantification of hydrides on RuNi/PVP metal nanoparticles

The quantification of hydrides per surface metal atoms was performed by slightly modifying a previous methodology previously described.[19]

The metallic precursors $[Ru(\eta^4\text{-}C_8H_{12})(\eta^6\text{-}C_8H_{10})]$ and/or $[Ni(\eta^4\text{-}\ C_8H_{12})_2]$ and PVP were added in a FP in a glovebox, where they were dissolved in THF. At the fume hood, the FP with the yellow solution was pressurized with 3 bars of H_2 and heated to 85 ºC in an oil bath. The solution became black after some minutes evidencing the decomposition of the metallic complexes. The synthesis remained under vigorous stirring at 85 ºC overnight. The day after, the excess of H_2 was removed from the FP followed by the evaporation of the THF from the colloidal suspension until drying. In a glovebox, 52.7 mg (0.56 mmol) of norbornene and 11.9 mg (0.07 mmol) of dodecane as internal standard were added in the FP bottle, together with THF (10 mL). The solution was stirred and samples were collected at 0 h, 24 h and 48 h, under Ar, filtrated through an alumina column and analysed by GC-MS.

Knowing that two hydrides are needed for the conversion of norbornene to norbornane, the number of mmol of hydrides was calculated in correlation to the mmol of norbornane established through GC analyses. The number of mmol of metal present on the surface was calculated from the amount of NPs weighted taking into account the ICP results and their

size. For each metallic composition of the studied NPs, the reactant quantities are noted herein. The ratio $H/M_{surface}$ was calculated for the following NPs:

Ru/PVP. 35.1 mg (0.111 mmol) of [Ru(η^4-C_8H_{12})(η^6-C_8H_{10})], 37.5 mg of PVP, and 10 mL of THF. $H/M_{surface} = 1.3 \pm 0.2$

Ru_3Ni_1/PVP. 26.5 mg (0.084 mmol) of [Ru(η^4-C_8H_{12})(η^6- C_8H_{10})], 7.7 mg (0.028 mmol) of [Ni(η^4-C_8H_{12})$_2$], 37.5 mg of PVP, and 10 mL of THF. $H/M_{surface} = 1.8 \pm 0.1$

Ru_1Ni_1/PVP. 17.6 mg (0.056 mmol) of [Ru(η^4-C_8H_{12})(η^6-C_8H_{10})], 15.3 mg (0.056 mmol) of [Ni(η^4-C_8H_{12})$_2$], 37.5 mg of PVP, and 10 mL of THF. $H/M_{surface} = 1.6 \pm 0.2$

Ru_1Ni_3/PVP. 8.8 mg (0.028 mmol) of [Ru(η^4-C_8H_{12})(η^6-C_8H_{10})], 23.1 mg (0.084 mmol) of [Ni(η^4-C_8H_{12})$_2$], 37.5 mg of PVP, and 10 mL of THF. $H/M_{surface} = 1.1 \pm 0.4$

Ni/PVP. 30.5 mg (0.111 mmol) of [Ni(η^4-C_8H_{12})$_2$], 37.5 mg of PVP, and 10 mL of THF. $H/M_{surface} = 0.9 \pm 0.1$

6.7 Catalytic hydrogenation reactions

The catalytic hydrogenations were performed at LCC in Toulouse in a stainless steel high-pressure batch TOP Industries reactor of 200 mL. In a classic reaction, a mixture of 4 mmol of substrate, 0.5 mmol of internal standard and the 0.02 mmol of metal present in the catalyst in 15 mL of the wished solvent were filled in the autoclave in a glovebox. At the fume hood, the inert atmosphere inside the reactor was eliminated by purging with H_2 three times. Then, the autoclave was heated, loaded with the desired H_2 pressure, and stirred at 1200 rpm. During the catalytic reaction, samples were collected at different times and analysed by GC, using the internal standard method. A quantitative analysis was performed by preparing several calibration solutions from the available commercial products.

6.7.1 Furfural

In a classic catalytic FF hydrogenation, a mixture of 384.3 mg (4 mmol) of FF, 71.1 mg (0.5 mmol) of decane (with THF as solvent) or 85.2 mg (0.5 mmol) of dodecane (with 1-PrOH as solvent) and the 0.02 mmol of metal present in the RuNi/PVP or RuCu/PVP series of catalysts, in 15 mL of THF or 1-PrOH were filled in the autoclave in a glovebox.

In the case of RuNi/PVP NPs for the FF hydrogenation in THF, hot filtration was also executed by stopping the reaction after one hour reaction. The reactor was then introduced in a glovebox where the catalyst was filtrated through an alumina path. Afterwards, the

autoclave was filled again with the solution, this time, free of catalyst. The reactor was pressurised with 20 bars of H_2 and heated at 125 ºC. After one hour stirring at 1200 rpm, the reaction was stopped and analysed by GC.

6.7.2 Quinoline

In a classic catalytic quinoline hydrogenation, a mixture of 516.6 mg (4 mmol) of quinoline, 85.2 mg (0.5 mmol) of dodecane and the 0.02 mmol of metal present in the catalysts, in 15 mL of 1-PrOH were filled in the autoclave in a glovebox.

6.8 Catalytic deuteration reactions

The catalytic deuterations were performed at LIKAT in Rostock. The deuterations were carried out in glass vials. When using H_2 pressure the septum of the vials was perforated, and the vials were placed in a stainless steel high-pressure batch Parr Instrument reactor of 300 mL. In a classic reaction, a mixture of 0.250 mmol of substrate and the 0.02 mmol of metal present in the Ru/PVP were filled in the glass vials in a glovebox. At the fume hood, 1.5 mL of D_2O were added under Ar flow. Then, the vial was heated on a hotplate and stirred at 600 rpm overnight. When using H_2 pressure, the stainless steel was purged with H_2 three times. Then, the autoclave was loaded with 10 bar of H_2, heated at the desired temperature and stirred at 600 rpm.

After the catalytic reaction, an NMR analysis was performed for each sample. The reaction was filtrated or centrifuged to eliminate the catalyst. Next, chloroform ($CHCl_3$) or ethyl acetate (1.5 mL) were added to the aqueous mixture. The organic phase was extracted and dried with Na_2SO_4. Both phases were dried overnight and the resulting solid was analysed by NMR.

6.8.1 4-Methoxyaniline

In a classic catalytic 4-MeOAn deuteration reaction, a mixture of 30.8 mg (0.250 mmol) of 4-MeOAn and the 0.02 mmol of metal present in the Ru/PVP were added in the glass vial. At the fume hood, 1.5 mL of D_2O were added under Ar flow. Then, the vial was heated on a hotplate or in the autoclave with a needle through a septum and stirred at 600 rpm overnight.

6.8.2 4-(Trifluoromethyl)benzaldehyde

In a classic catalytic 4-TFMBAL deuteration, a mixture of 43.5 mg (0.250 mmol) of 4-TFMBAL and the 0.02 mmol of metal present in the Ru/PVP were added in the glass vial. At the fume hood, 1.5 mL of D_2O were added under Ar flow. Then, the vial was heated on a hotplate or in the autoclave with a needle through a septum and stirred at 600 rpm overnight.

6.8.3 Methyl 2,3-O-isopropylidene-β-D-ribofuranoside

In a classic catalytic MOIBRIBOF deuteration, a mixture of 51.1 mg (0.250 mmol) of MOIBRIBOF and the 0.02 mmol of metal present in the Ru/PVP were added in the glass vial. At the fume hood, 1.5 mL of D_2O were added under Ar flow. Then, the vial was heated on a hotplate or in the autoclave with a needle through a septum and stirred at 600 rpm overnight.

6.8.4 Methyl β-D-ribofuranoside

In a classic catalytic MEBRIBOF deuteration, a mixture of 41.0 mg (0.250 mmol) of MEBRIBOF and the 0.02 mmol of metal present in the Ru/PVP were added in the glass vial. At the fume hood, 1.5 mL of D_2O were added under Ar flow. Then, the vial was heated on a hotplate or in the autoclave with a needle through a septum and stirred at 600 rpm overnight.

6.8.5 Adenosine

In a classic catalytic ADNS deuteration, a mixture of 66.8 mg (0.250 mmol) of ADNS and the 0.02 mmol of metal present in the Ru/PVP were added in the glass vial. At the fume hood, 1.5 mL of D_2O were added under Ar flow. Then, the vial was heated on a hotplate or in the autoclave with a needle through a septum and stirred at 600 rpm overnight.

6.9 References

(1) Costa, N. J. S.; Jardim, R. F.; Masunaga, S. H.; Zanchet, D.; Landers, R.; Rossi, L. M. Direct Access to Oxidation-Resistant Nickel Catalysts through an Organometallic Precursor. *ACS Catal.* **2012**, *2* (6), 925. https://doi.org/10.1021/cs200609e

(2) Hou, Y.; Kondoh, H.; Ohta, T.; Gao, S. Size-Controlled Synthesis of Nickel Nanoparticles. *Appl. Surf. Sci.* **2005**, *241* (1–2), 218. https://doi.org/10.1016/j.apsusc.2004.09.045

(3) Chen, D.-H.; Wu, S.-H. Synthesis of Nickel Nanoparticles in Water-in-Oil Microemulsions. *Chem. Mater.* **2000**, *12* (5), 1354. https://doi.org/10.1021/cm991167y

(4) Chen, D.-H.; Hsieh, C.-H. Synthesis of Nickel Nanoparticles in Aqueous Cationic Surfactant Solutions. *J. Mater. Chem.* **2002**, *12* (8), 2412. https://doi.org/10.1039/b200603k
(5) Kresse, G.; Furthmüller, J. Efficient Iterative Schemes for *Ab Initio* Total-Energy Calculations Using a Plane-Wave Basis Set. *Phys. Rev. B* **1996**, *54* (16), 11169. https://doi.org/10.1103/PhysRevB.54.11169
(6) Kresse, G.; Furthmüller, J. Efficiency of Ab-Initio Total Energy Calculations for Metals and Semiconductors Using a Plane-Wave Basis Set. *Comput. Mater. Sci.* **1996**, *6* (1), 15. https://doi.org/10.1016/0927-0256(96)00008-0
(7) Perdew, J. P.; Burke, K.; Ernzerhof, M. Generalized Gradient Approximation Made Simple. *Phys. Rev. Lett.* **1996**, *77* (18), 3865. https://doi.org/10.1103/PhysRevLett.77.3865
(8) Blöchl, P. E. Projector Augmented-Wave Method. *Phys. Rev. B* **1994**, *50* (24), 17953. https://doi.org/10.1103/PhysRevB.50.17953
(9) Kresse, G.; Joubert, D. From Ultrasoft Pseudopotentials to the Projector Augmented-Wave Method. *Phys. Rev. B* **1999**, *59* (3), 1758. https://doi.org/10.1103/PhysRevB.59.1758
(10) Monkhorst, H. J.; Pack, J. D. Special Points for Brillouin-Zone Integrations. *Phys. Rev. B* **1976**, *13* (12), 5188. https://doi.org/10.1103/PhysRevB.13.5188
(11) Cusinato, L.; Martínez-Prieto, L. M.; Chaudret, B.; del Rosal, I.; Poteau, R. Theoretical Characterization of the Surface Composition of Ruthenium Nanoparticles in Equilibrium with Syngas. *Nanoscale* **2016**, *8* (21), 10974. https://doi.org/10.1039/C6NR01191H
(12) Martínez-Prieto, L. M.; Cano, I.; Márquez, A.; Baquero, E. A.; Tricard, S.; Cusinato, L.; del Rosal, I.; Poteau, R.; Coppel, Y.; Philippot, K.; Chaudret, B.; Cámpora, J.; van Leeuwen, P. W. N. M. Zwitterionic Amidinates as Effective Ligands for Platinum Nanoparticle Hydrogenation Catalysts. *Chem. Sci.* **2017**, *8* (4), 2931. https://doi.org/10.1039/C6SC05551F
(13) González-Gómez, R.; Cusinato, L.; Bijani, C.; Coppel, Y.; Lecante, P.; Amiens, C.; del Rosal, I.; Philippot, K.; Poteau, R. Carboxylic Acid-Capped Ruthenium Nanoparticles: Experimental and Theoretical Case Study with Ethanoic Acid. *Nanoscale* **2019**, *11* (19), 9392. https://doi.org/10.1039/C9NR00391F
(14) Maintz, S.; Deringer, V. L.; Tchougréeff, A. L.; Dronskowski, R. LOBSTER: A Tool to Extract Chemical Bonding from Plane-Wave Based DFT: Tool to Extract Chemical Bonding. *J. Comput. Chem.* **2016**, *37* (11), 1030. https://doi.org/10.1002/jcc.24300
(15) Gerber, I. C.; Poteau, R. Critical Assessment of Charge Transfer Estimates in Non-Covalent Graphene Doping. *Theor Chem Acc* **2018**, *137* (11), 156. https://doi.org/10.1007/s00214-018-2365-2
(16) Cusinato, L.; del Rosal, I.; Poteau, R. Shape, Electronic Structure and Steric Effects of Organometallic Nanocatalysts: Relevant Tools to Improve the Synergy between Theory and Experiment. *Dalton Trans.* **2017**, *46* (2), 378. https://doi.org/10.1039/C6DT04207D
(17) Hammer, B.; Nørskov, J. K. Electronic Factors Determining the Reactivity of Metal Surfaces. *Surf. Sci.* **1995**, *343* (3), 211. https://doi.org/10.1016/0039-6028(96)80007-0
(18) Amiens, C.; Ciuculescu-Pradines, D.; Philippot, K. Controlled Metal Nanostructures: Fertile Ground for Coordination Chemists. *Coordination Chemistry Reviews* **2016**, *308*, 409. https://doi.org/10.1016/j.ccr.2015.07.013
(19) García-Antón, J.; Axet, M. R.; Jansat, S.; Philippot, K.; Chaudret, B.; Pery, T.; Buntkowsky, G.; Limbach, H.-H. Reactions of Olefins with Ruthenium Hydride Nanoparticles: NMR Characterization, Hydride Titration, and Room-Temperature C-C Bond Activation. *Angew. Chem. Int. Ed.* **2008**, *47* (11), 2074. https://doi.org/10.1002/anie.200704763

General conclusions and future perspectives

In this thesis, we have designed a series of bimetallic nanoparticles (NPs) by nanoalloying Ru with two earth-abundant metals: Ni and Cu. Several ligands have been used as stabilisers, such as polyvinvylpyrrolidone (PVP), diphenylphosphinopyridine (PPh_2Py), 1-adamantanecarboxylic acid (AdCOOH) and hexadecylamine (HDA). The main objective was to apply these new materials in catalysis to obtain value-added chemicals thinking on the energy transition.

RuNi/PVP NPs were successfully synthesised, observing the importance of the reaction temperature for a successful decomposition of the Ni metallic precursor during the NPs synthesis. All these synthesised materials were sized between 1 and 2 nm, including the NPs containing a higher amount of Ni. Moreover, a core-shell structure with Ru in the core was determined, through WAXS analyses, for the bimetallic catalysts. XPS measurements and the reduction of the magnetisation compared to the monometallic Ni, confirmed further that Ru and Ni are in close vicinity in the bimetallic NPs.

The RuNi/PVP NPs were then tested as catalysts for the hydrogenation of furfural (FF). Synergetic effects were observed between both metals, being the maximum of this synergy at the metallic ratio Ru/Ni = 1. Solvent effects were seen when comparing the catalytic results in tetrahydrofuran (THF) and 1-propanol (1-PrOH). With the latter solvent, it was observed the possibility of further hydrogenation of the furfuryl ring and C-O bond cleavage leading to tetrahydrofurfuryl alcohol (HMTHF) and 1,2-pentanediol (1,2-PeD) respectively.

These solvent effects were further studied by running density functional theory (DFT) calculations. Two models of NPs were built for each metal (Ru and Ni) to represent both THF and 1-PrOH solvents. When comparing the results, it was observed that 1-PrOH plays an important role in the hydrogenation of FF on Ru NPs, as propanolate species were adsorbed on the NPs surface showing beneficial catalytic effects.

RuCu/PVP NPs were successfully synthesised resulting to small NPs between 1 and 1.2 nm size, including the ones with high Cu content. WAXS analyses indicated a core-shell structure for the bimetallic NPs being Ru in the core and a surface rich on Cu_2O. EDX analyses pointed out that not all the Cu was adsorbed on the bimetallic NPs but some remained as clusters or isolated atoms. The bimetallic nature of the RuCu/PVP NPs was confirmed by the decrease of magnetisation compared to monometallic Cu.

The RuCu/PVPs were tested as catalysts for the hydrogenation of FF. Monometallic Cu/PVP NPs displayed interesting results in catalysis, reaching similar activities to monometallic Ru/PVP NPs.

However, bimetallic RuCu/PVP showed lower turnover frequency (TOF) values than the monometallic counterparts.

RuNi/PPh_2Py NPs were successfully synthesised resulting to small NPs of 2 nm or less. WAXS analyses indicated a core-shell structure with Ru in the core, even if it would be interesting to confirm the results using extended X-ray absorption fine structure (EXAFS) analysis. The coordination of the phosphine ligand in bimetallic NPs was observed by solid state nuclear magnetic resonance (SS NMR). The bimetallic nature of the NPs was confirmed by the magnetisation decrease observed for the RuNi/PPh_2Py sample, compared to monometallic Ni.

The RuNi/PVP NPs and RuNi/PPh_2Py NPs were also tested as catalysts for the hydrogenation of quinoline (QN). In comparison to FF hydrogenation, the Ru_1Ni_1/PVP performance was lower in QN hydrogenation, even if a high selectivity towards 1,2,3,4-tetrahydroquinoline (1-THQ) was obtained. N-alkylation reactions were obtained from the condensation of the amine products, 1-THQ and decahydroquinoline (DHQ), with 1-PrOH. RuNi/PPh_2Py NPs preliminary results showed promising performances on the QN hydrogenation compared to the monometallic Ru/PPh_2Py catalyst.

During the 3-months internship at LIKAT in Rostock (Germany), Ru/PVP NPs were used as catalysts for deuteration reactions of several organic molecules. 4-methoxyaniline (4-MeOAn) resulted to hydrogenated products, when performing the reaction under H_2 pressure, and PVP leaching, without pressurising. 4-trifluoromethylbenzaldehyde (TFMBAL) resulted to hydrogenated products, when using H_2 pressure, and the deuteration of formyl H, without pressurising. Methyl 2,3-O-Isopropylidene-β-D-ribofuranoside (MOIBRIBOF), a protected sugar, was deprotected under H_2 pressure and epimerised without pressurising. Adenosine (ADNS) resulted to a selective deuterium labelling without observing any epimerisation of the sugar backbone.

The results obtained and described in this doctoral thesis are inspiring for the perspectives of future research:

a) RuNi/AdCOOH of less than 2 nm size has already been synthesised but need further characterisation. After, it would be interesting to test them as catalyst for some hydrogenation reactions. In the same way, Cu/HDA NPs with different compositions have also been synthesised. After obtaining some homogeneity, it may be interesting to synthesise bimetallic core-shell RuCu NPs with Cu in the core and try their performance in catalysis.
b) After observing the production of 1,2-PeD during the FF hydrogenation performed on RuNi/PVP NPs in 1-PrOH, it would be of interest to replace the solvent (1-PrOH) by H_2O, aiming to increase 1,2-PeD formation.

c) Concerning QN hydrogenation, further catalytic reactions are needed to better compare the performance of RuNi/PVP NPs and RuNi/PPh_2Py NPs.

d) Looking at DFT studies, further calculations would be needed to corroborate the mechanism of FF hydrogenation on $Ni_{38}H_{35}$ NP in 1-PrOH. Moreover, different bimetallic $Ru_{13}Ni_{25}$ models have already been built and it would be of interest to continue the study with the adsorption of the different species. Like this, a complete study of the system would be obtained and the high performance of Ru_1Ni_1/PVP would be also supported by DFT.

Résumé de thèse : Conception rationnelle de catalyseurs à base de nanoparticules bimétalliques : application à la valorisation de la biomasse.

1. Introduction

Le changement climatique est une préoccupation grandissante, en raison des conséquences sur la planète Terre, notamment la vie végétale et animale, et donc sur la vie des populations et sur leur santé. Le rapport Lancet Countdown de 2020 mentionne 43 indicateurs du changement climatique.[1] L'Organisation météorologique mondiale, une agence spécialisée des Nations unies, a quant à elle publié en 2018 six indicateurs majeurs pour évaluer l'état du climat : la température, les gaz à effet de serre et l'ozone, les océans, la cryosphère, les facteurs de variabilité interannuelle et les événements extrêmes.[2] Les participants à la 21e Conférence des Parties (COP21) en 20115 ont convenu de limiter l'augmentation de la température moyenne mondiale à 1,5 °C par rapport aux niveaux préindustriels.[3,4] L'une des recommandations de la COP21, est de maintenir une recherche continue dans le domaine de l'énergie afin de disposer de sources d'énergie renouvelables en remplacement des énergies fossiles. Comme on peut l'observer sur la figure 1, les combustibles fossiles représentaient, en 2021, 77 % de la consommation mondiale d'énergie.[5] Leur substitution par des sources d'énergie renouvelables est donc parmi les enjeux majeurs de notre société pour aller vers une transition énergétique. Ceci requiert le développement de technologies durables.

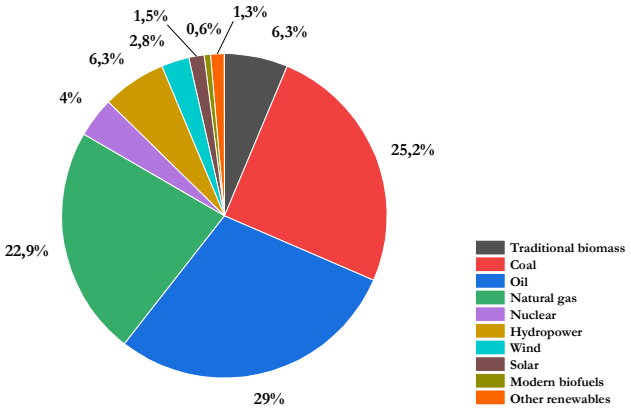

Figure 1: Consommation mondiale d'énergie primaire par source en 2021.

Différents types de sources d'énergies renouvelables, telles que l'énergie solaire ou éolienne, ont déjà été développés et commercialisés.[6] En ce qui concerne la filière chimique, le remplacement des ressources fossiles est principalement axé sur l'utilisation de la biomasse.[7] La biomasse lignocellulosique constitue une matière première renouvelable prometteuse pour remplacer les ressources fossiles dans la production d'énergie et de produits chimiques de valeur ajoutée.[8,9]

A partir des trois composants de la biomasse lignocellulosique, la cellulose, l'hémicelluloses et la lignine, il est possible d'obtenir plusieurs molécules plateformes telles que le furfural (FF) et le 2,5-hydroxymethdylfurfural (HMF), qui peuvent à leur tour être transformées en d'autres produits chimiques, par exemple par des réactions d'hydrogénation, d'oxydation, d'acétalisation ou de décarbonylation.[10–12] Les molécules provenant de la biomasse traitée par des étapes de craquage et d'hydrotraitement sont similaires à celles des combustibles fossiles, ce qui permet d'utiliser les mêmes équipements de production.[13] Les nanoalliages utilisés comme catalyseurs dans les raffineries de pétrole, la fabrication pétrochimique, la chimie fine, les réactions d'évolution de l'hydrogène ou de réduction de l'oxygène, sont donc censés être également efficaces pour la conversion des molécules issues de la biomasse.[14,15] Toutes ces transformations doivent pouvoir être réalisées de manière efficace pour qu'elles soient intégrées dans l'industrie de la transition énergétique; la mise au point de catalyseurs performants en termes d'activité et de sélectivité est donc une étape indispensable.[16]

Les nano-alliages, qui contiennent deux métaux ou plus, sont des matériaux intéressants pour de nombreuses applications.[17,18] En catalyse, les nano-alliages peuvent conduire à une activité supérieure à celle de leurs homologues monométalliques en raison d'un effet de synergie entre les métaux associés. L'activité catalytique dépend des propriétés des nanoparticules, telles que la composition, la structure, la taille ou la forme. La différence de propriétés électroniques entre les métaux qui les composent est un autre paramètre qui peut influencer sur la performance catalytique en termes d'activité et de sélectivité.[19] Les catalyseurs bimétalliques sont utilisés dans une grande variété d'applications en lien avec la valorisation de la biomasse lignocellulosique pour l'accès à divers produits chimiques de valeur ajoutée. Ces produits sont obtenus via différentes réactions telles que le reformage, l'oxydation, l'hydrogénolyse, l'hydrodésoxygénation ou les hydrogénations.[20]

Par exemple, l'hydrogénolyse du glycérol a conduit au 1,2-propanediol sur un catalyseur bimétallique RuCu (à 230 °C et 80 bar de H_2), tandis qu'il a été converti en 1,3-propanediol sur un catalyseur bimétallique PtCu (à 210 °C et 1 bar de H_2).[21,22] Parmi les réactions d'hydrodésoxygénation, la vanilline a été convertie en méthylcyclohexanol sur un catalyseur bimétallique CoNi (à 200 °C et 10 bar de H_2). Plusieurs molécules oxygénées de la biomasse, comme le HMF, ont été transformées à leur tour en obtenant les meilleures activités et sélectivités avec les catalyseurs bimétalliques, $Co_5Zn_1O_x$, qu'avec leurs homologues monométalliques.[23,24] En catalyse d'hydrogénation, on peut citer la conversion de l'acide lévulinique en γ-valérolactone sur un catalyseur bimétallique RuSn (à 180 °C et 35 bar de H_2), et celle de plusieurs aldéhydes oxygénés de la biomasse, tels que le FF, en leurs alcools correspondants sur un catalyseur bimétallique PtNi (à 100 °C et 10 bar de H_2), avec de meilleures performances qu'en utilisant les homologues monométalliques.[25,26]

Des effets synergiques entre les métaux ont également été observés avec des catalyseurs bimétalliques RuNi pour les réactions d'hydrogénation de la quinoléine (QN) et du FF. L'hydrogénation de la QN a été

testée sur des catalyseurs bimétalliques $NiRu/Al_2O_3$ (à des températures de 300 ºC à 400 ºC avec des pressions d'H_2 de 200 bar et 250 bar), montrant une augmentation de l'activité avec la température, et la possibilité d'une réaction d'hydrodéshydrogénation à 400 ºC résultant en la formation de 2-hexène.[27] L'hydrogénation de la QN sur RuNi/C (à 100 ºC avec 50 bar de H_2) a mis en évidence des effets synergiques entre les métaux, avec une activité plus élevée par rapport aux homologues monométalliques et en faveur de la formation majoritaire du 1,2,3,4-Tetrahydroquinoléine (1-THQ).[28] L'hydrogénation du FF sur des catalyseurs bimétalliques $Ru\text{-}Ni/Al_2O_3$ (à 100 ºC avec 54 bar de H_2), a aussi mis en lumière des effets synergiques entre les métaux, avec une activité comparativement à celle des homologues monométalliques, et surtout une sélectivité quasi complète pour l'alcool furfurylique (HF).[29]

Une étude bibliographique a montré que les connaissances disponibles concernant les hydrogénations de la QN et du FF sur des catalyseurs bimétalliques RuNi sont rares; le travail rapporté dans cette thèse a permis d'obtenir de nouveaux résultats, conduisant ainsi à de nouvelles connaissances dans un domaine en évolution, la valorisation de la biomasse. Des NPs de RuCu ont aussi été synthétisées et évaluées en catalyse.

2. Synthèse et caractérisation des nanoparticules métalliques RuNi et RuCu

En lien avec la transition énergétique, l'implémentation de technologies pour l'utilisation de la biomasse lignocellulosique à l'échelle industrielle nécessite la mise au point de catalyseurs performants et bon marché. Les métaux nobles tels que Pt,[30] Ru,[31] Rh,[32] Re[33] et Ir[34] sont connus pour conduire à des catalyseurs actifs dans des conditions douces, mais leur faible abondance implique qu'ils sont chers. Pour réduire le coût des catalyseurs, une solution est d'utiliser des métaux abondants, mais ils ont comme inconvénient de nécessiter des conditions de réaction drastiques, telles que 200-400 bars de H_2.[35] En conséquence allier les métaux nobles et les métaux abondants dans des catalyseurs bimétalliques apparait comme une alternative à explorer plus avant. Les catalyseurs bimétalliques et trimétalliques, voire plus, ont déjà montré leur intérêt en catalyse, en raison de performances améliorées par rapport à celles de leurs homologues monométalliques grâce à des effets synergiques.[19]

Notre étude s'est focalisée sur le développement de catalyseurs nanométriques pour l'hydrogénation de molécules plateforme provenant de la biomasse lignocellulosique. Dans ce but, nous avons choisi le Ru, l'un des métaux nobles les moins chers, bien connu pour son activité dans diverses réactions de réduction.[36] Comme métaux abondants, nous avons choisi le Ni et le Cu, même s'ils sont tous deux connus pour être des métaux non miscibles avec le Ru à l'état massif.[37] La présence de Ni ou de Cu sur un catalyseur de Ru induit des propriétés électroniques différentes qui peuvent conduire à des effets synergiques entre les métaux, comme confirmé par des analyses XPS.[38] Une modification de la structure[39] ou du ratio entre les deux métaux[38] peut permettre d'optimiser l'activité catalytique et la sélectivité.

Pour l'élaboration des catalyseurs, nous avons considéré la décomposition de complexes organométalliques sous pression d'hydrogène (H_2) qui est une méthode efficace et adaptable pour la synthèse de nanoparticules (NPs) de caractéristiques contrôlées,[40] telles que la taille, la forme, la composition et l'ordre chimique. De plus cette méthodologie de synthèse a déjà fait ses preuves pour la synthèse de NPs bimétalliques avec des propriétés intéressantes en catalyse.[41,42] La nature des précurseurs métalliques et leur cinétique de décomposition peuvent influencer les différentes caractéristiques des NPs. En plus d'agir comme stabilisants des nanoparticules en empêchant leur croissance et coalescence les ligands peuvent également influer sur les propriétés électroniques, en particulier lorsque la taille des NPs est inférieure à 5 nm,[43] ce qui peut être bénéfique pour la catalyse.

La première partie de ce travail de thèse a consisté à développer des catalyseurs bimétalliques à base de Ru et Ni stabilisés par la polyvinylpyrrolidone (PVP) et des ligands. Ainsi, des NPs bimétalliques RuNi/PVP ont été synthétisées par décomposition des complexes $[Ru(\eta^4\text{-}C_8H_{12})(\eta^6\text{-}C_8H_{10})]$ et $[Ni(\eta^4\text{-}C_8H_{12})_2]$ sous une pression de 3 bar de H_2, en présence de PVP (teneur en métaux = 10 % wt./PVP) et en utilisant le tétrahydrofurane (THF) comme solvant (Schéma 1). Des NPs monométalliques de Ru et Ni ont aussi été préparées dans les mêmes conditions pour comparaison.

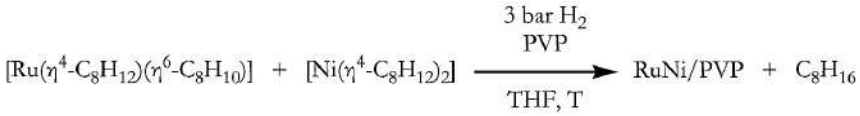

Schéma 1: Synthèse des NPs de RuNi/PVP.

Les caractéristiques des NPs ont été déterminées par une combinaison de différentes techniques, à savoir : la spectroscopie d'émission optique au plasma à couplage inductif (ICP-OES) pour déterminer la teneur en métal des NPs ou des solutions catalytiques,[44] la microscopie électronique à transmission (TEM) pour déterminer la taille et la forme des NPs,[45] et la microscopie électronique à transmission en mode balayage couplée à un détecteur champ sombre annulaire à grand angle (HAADF-STEM) pour mieux déterminer les NPs dont on est intéressés grâce au contraste en relation au nombre atomique,[46] la spectroscopie de rayons X à dispersion d'énergie (EDX) couplée à la microscopie électronique pour déterminer qualitativement les éléments constituant les NPs,[47] l'infrarouge (IR)[48] et la spectroscopie de résonance magnétique nucléaire (NMR)[49] pour étudier la chimie de surface telle que l'interaction métal-ligand, la spectroscopie photoélectronique à rayons X (XPS) pour déterminer l'état d'oxydation des métaux et analyser le transfert de charge entre les métaux dans le cas de NPs bimétalliques,[50] la technique de magnétométrie sur un équipement d'interférence quantique supraconducteur (SQUID) pour mesurer la magnétisation des échantillons[51] et la diffusion des rayons X aux grands angles (WAXS) pour déterminer la structure cristalline à l'échelle atomique.[52]

Des essais à température ambiante (TA) on conduit à une population non homogène constituée d'un mélange de grandes NPs de Ni et de petites NPs de Ru (Figure 2). Ce résultat peut s'expliquer par la décomposition plus lente du précurseur de nickel alors que celle du complexe de ruthénium est rapide à cette température. Les synthèses suivantes ont donc été réalisées à 85 °C en utilisant des ratios [Ru]/[Ni] variable afin de disposer d'une série de NPs de compositions en métaux différentes.

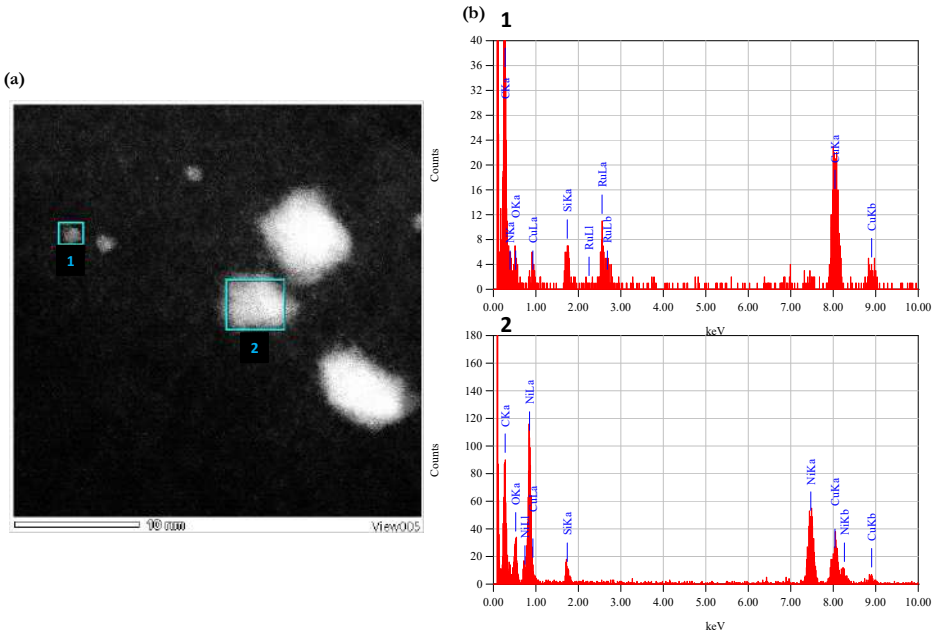

Figure 2: (a) Image HAADF-STEM de NPs synthétisées à TA (Ru/Ni :1/1 ; PVP) ; (b) analyse EDX des nano-objets numérotés 1 et 2.

Toutes les NPs bimétalliques RuNi/PVP synthétisées à 85 ºC ont présenté une taille inférieure à 2 nm, y compris celles synthétisées avec une teneur en Ni élevée (Figure 3) et celle avec une activité plus élevée en catalyse (Figure 4). Une structure de type cœur-coquille avec le Ru au cœur et le Ni en surface, a pu être établie par analyses TEM et WAXS.

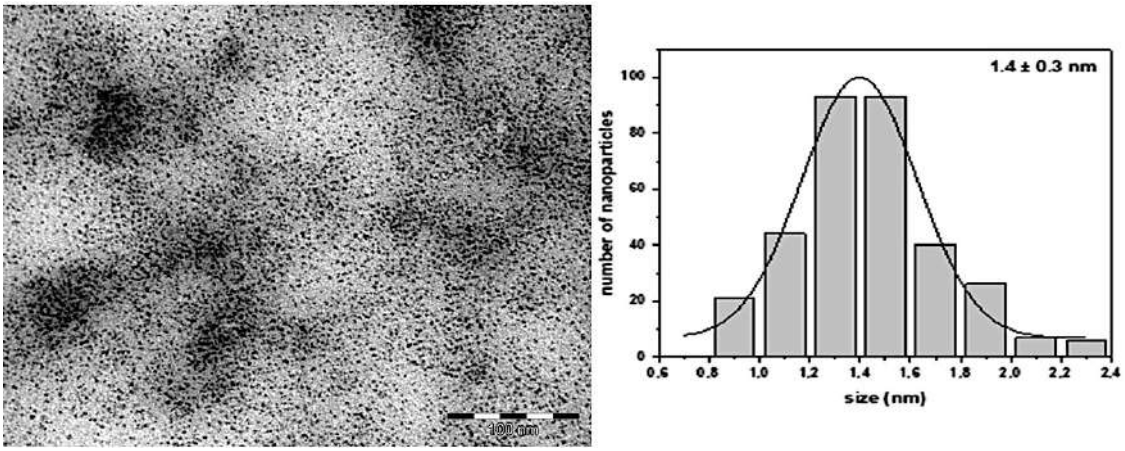

Figure 3: Image TEM des NPs de Ru_1Ni_{20}/PVP synthétisées à 85 ºC (barre d'échelle 100 nm) et l'histogramme de taille respectif.

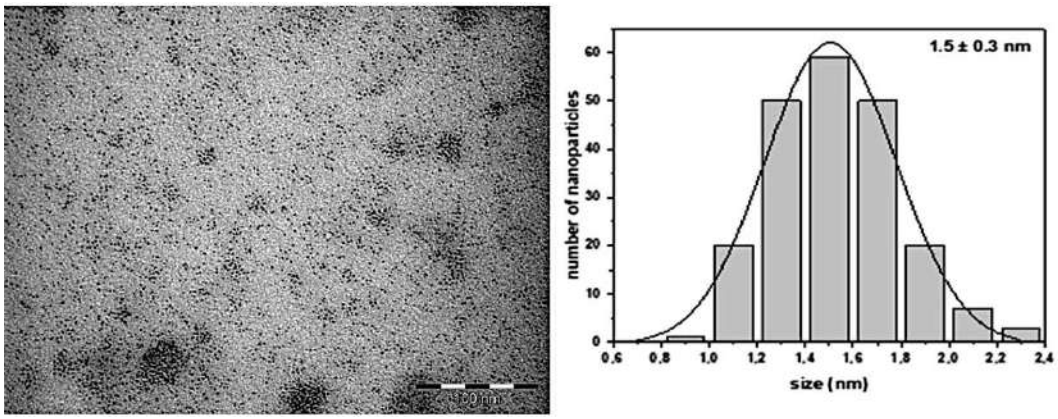

Figure 4: Image TEM des NPs de Ru_1Ni_1/PVP synthétisées à 85 ºC (barre d'échelle 100 nm) et l'histogramme de taille respectif.

En XPS, un décalage des énergies de liaison du Ru et du Ni a été observé. Par ailleurs une diminution drastique de l'aimantation à saturation a été obtenue par SQUID (Figure 5). Ces résultats sont indicateurs de la proximité du Ru et du Ni dans les NPs et ont permis de conclure quant à leur nature bimétallique.

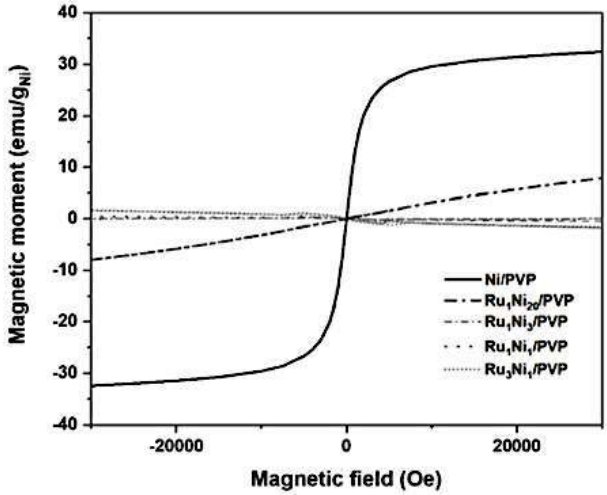

Figure 5: Cycles d'hystérésis magnétiques des NPs bimétalliques et monométalliques stabilisées par la PVP mesurés à RT et corrigés de la contribution diamagnétique de la PVP.

La synthèse de NPs bimétalliques RuNi ([Ru]/[Ni]=1) en utilisant la diphenylphosphinopyridine (PPh_2Py) comme ligand a également été réalisée. La première stratégie de synthèse à consister à partir des complexes $[Ru(\eta^4\text{-}C_8H_{12})(\varkappa^2\text{-}PPh_2Py)(PPh_2Py)]$ et $[Ni(\eta^4\text{-}C_8H_{12})(PPh_2Py)_2]$ qui ont été synthétisés selon les Schémas 2 et 3. L'objectif était de tirer parti de la présence des ligands dans la sphère de coordination des métaux pour orienter la croissance des NPs.

$$[Ru(\eta^4\text{-}C_8H_{12})(\eta^6\text{-}C_8H_{10})] + 2\,PPh_2Py \xrightarrow[\text{r.t.}]{\text{dry acetone}} [Ru(\eta^4\text{-}C_8H_{12})(\varkappa^2\text{-}PPh_2Py)(PPh_2Py)] + C_8H_{10}$$

Schéma 2: Synthèse du complexe $[Ru(\eta^4\text{-}C_8H_{12})(\varkappa^2\text{-}PPh_2Py)(PPh_2Py)]$.

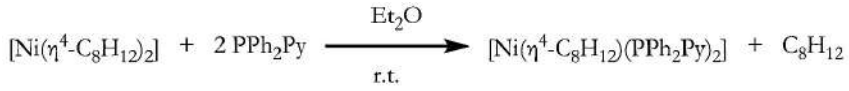

Schéma 3: Synthèse du complexe $[Ni(\eta^4\text{-}C_8H_{12})(PPh_2Py)_2]$.

La décomposition de ces complexes n'ayant pas conduit à des NPs contrôlées comme espéré, la méthode précédemment appliquée pour la synthèse des NPs RuNi/PVP a donc été utilisée. Les mêmes conditions ont été utilisées en remplaçant la PVP par le ligand PPh_2Py ajouté dans un rapport Molaire [M]/[L] de 0.2 (Schéma 4). Des NPs monométalliques de Ru et Ni ont également été préparées de cette façon, pour comparaison.

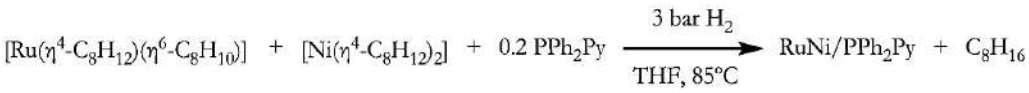

Schéma 4: Synthèse de NPs $RuNi/PPh_2Py$ par co-décomposition de $[Ru(\eta^4\text{-}C_8H_{12})(\eta^6\text{-}C_8H_{10})]$ ou $[Ni(\eta^4\text{-}C_8H_{12})_2]$.

Des NPs monométalliques et bimétalliques de taille ≤ à 2 nm (Figure 6) ont été obtenues dont la structure semble être de type cœur-coquille avec le Ru au cœur et le Ni en surface. Cependant une étude structurale plus approfondie en utilisant l'EXAFS (structure fine d'absorption des rayons X étendue) est nécessaire pour confirmer la structure cœur-coquille.

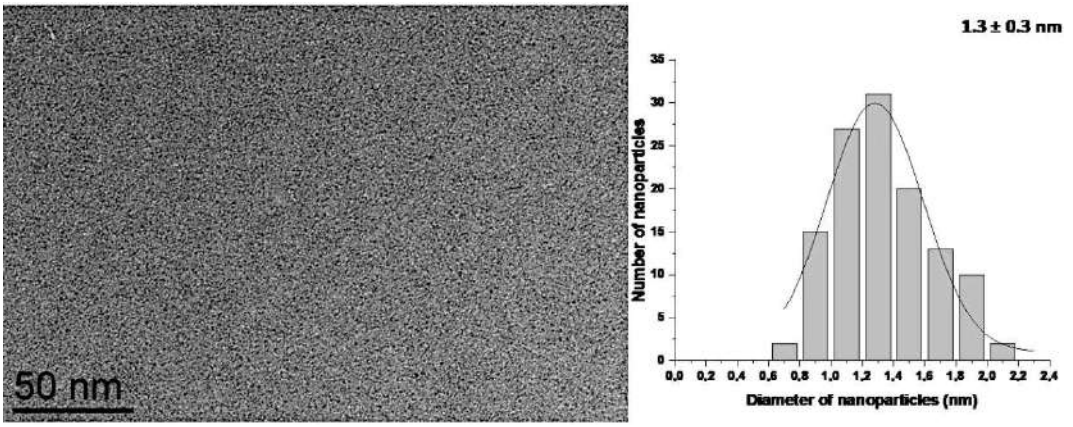

Figure 6: Image TEM de NPs de $RuPNi/PPh_2Py$ (barre d'échelle 50 nm) synthétisées à partir de $[Ru(\eta^4\text{-}C_8H_{12})(PPh_2Py)_2]$ et l'histogramme de taille correspondant.

Une étude par RMN du solide a mis en évidence la coordination de la phosphine selon un mode bidenté à la surface des NPs RuNi. Les mesures magnétiques ont montré une diminution drastique de l'aimantation avec la présence de Ru indiquant la proximité du Ru et du Ni (Figure 7), certifiant ainsi la nature bimétallique des NPs RuNi.

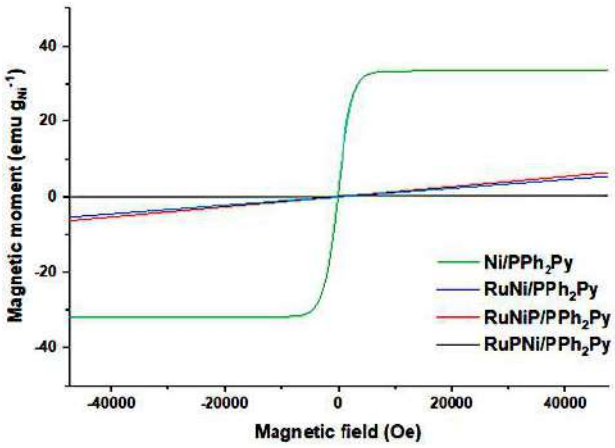

Figure 7: Cycles d'hystérésis magnétiques des NPs bimétalliques RuNi et monométalliques de Ni stabilisées par PPh_2Py, mesurés à température ambiante.

Nous avons ensuite considéré le 1-Adamantanecarboxylic acid (AdCOOH) comme ligand stabilisant. Des conditions de synthèse identiques à celles utilisées pour la PVP ont été appliquées (Schéma 5) avec un ratio rapport molaire [M]/[L] de 5. Pour les NPs monométalliques de Ni, une faible stabilisation a été observée par rapport aux stabilisants PVP et PPh_2Py ; les NPs étaient agrégées sur le barreau aimanté introduit pour l'agitation du milieu réactionnel, ce qui caractérise en général la formation de grosses NPs ou une agglomération. La taille moyenne des NPs de RuNi/AdCOOH synthétisées (Schéma 5) s'est avérée inférieure à 2 nm (Figure 8). L'analyse TEM des NPs monométalliques Ni/AdCOOH a mis en évidence une large dispersion en taille qui peut être attribuée à la présence de NPs plus grosses et/ou de l'agglomération.

$$[Ru(\eta^4\text{-}C_8H_{12})(\eta^6\text{-}C_8H_{10})] + [Ni(\eta^4\text{-}C_8H_{12})_2] + AdCOOH \xrightarrow[THF,\ 85°C]{3\ bar\ H_2} RuNi/AdCOOH + C_8H_{16}$$

Schéma 5: Synthèse des NPs de RuNi/AdCOOH.

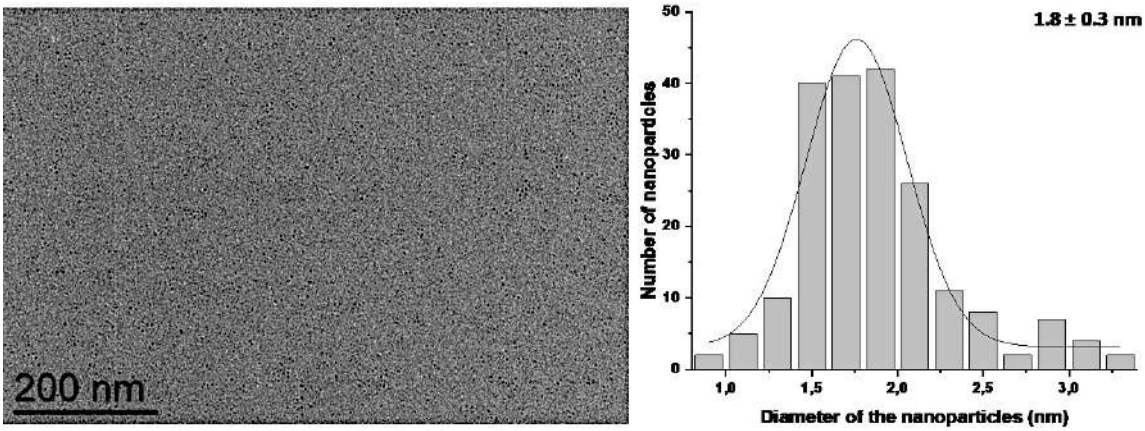

Figure 8: Image TEM de NPs de RuNi/AdCOOH (barre d'échelle 200 nm) et l'histogramme de taille respectif.

Nous nous sommes ensuite intéressés à la synthèse d'une série de NPs bimétalliques RuCu/PVP de composition en Ru et Ni variables et stabilisées par la PVP dans des conditions similaires mais à 100 ºC (Schéma 6). Les NPs ainsi obtenues ont montré une taille comprise entre 1.0 et 1.2 nm, y compris celles préparées à une teneur élevée en Cu. Des NPs monométalliques de cuivre ont aussi été préparées dans un objectif de comparaison.

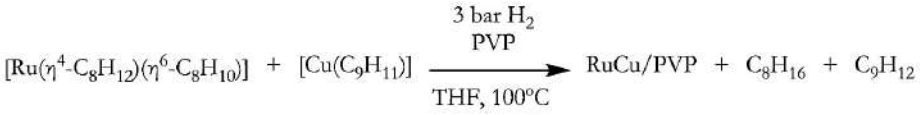

Schéma 6: Synthèse des NPs de RuCu/PVP

L'analyse structurale (TEM-EDX) a mis en évidence une structure cœur-coquille avec du Ru au cœur et du Cu_2O à la surface mais tout le Cu introduit pour la synthèse n'a pas été incorporé, restant sous forme de clusters ou d'atomes isolés (Figure 9).

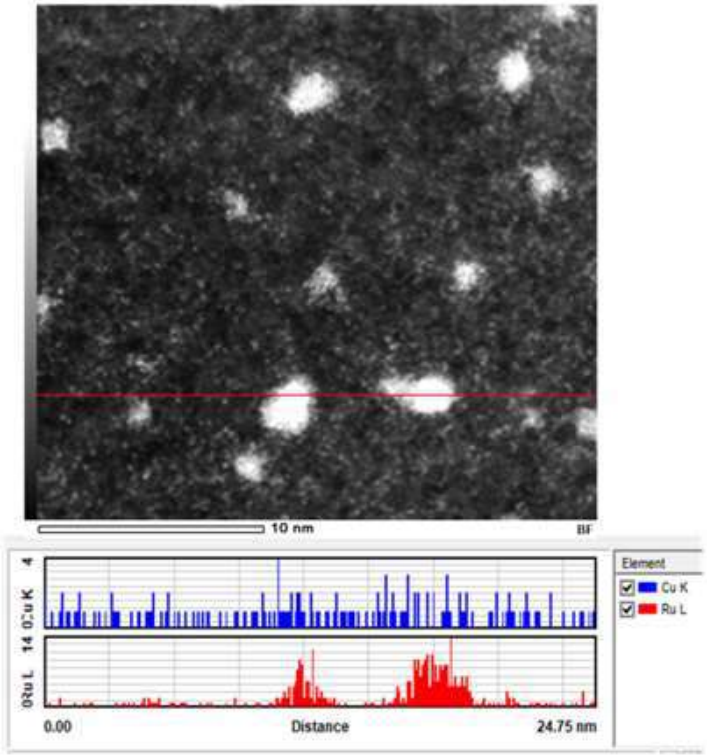

Figure 9: Image HAADF-STEM de Ru_1Cu_1/PVP synthétisé à 100 °C (en haut) ainsi qu'une analyse EDX linéaire (en bas).

Quant aux NPs Cu/PVP, l'analyse TEM a montré la présence de deux populations de NPs (1,3 nm et 4,9 nm) les plus grosses semblant être des NPs creuses (Figure 10). L'analyse WAXS a indiqué des NPs de Cu_2O/PVP.

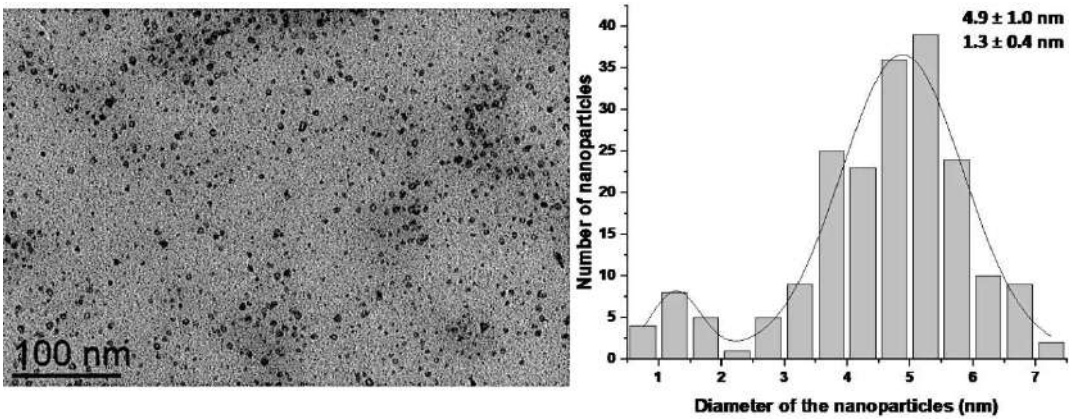

Figure 10: Image TEM de NPs de Cu/PVP (barre d'échelle 100 nm) et l'histogramme de taille respectif.

Pour les bimétalliques RuCu, la proximité du Ru et du Cu a aussi été mise en évidence par la diminution drastique de l'aimantation en présence de Ru (Figure 11), confirmant leur nature bimétallique.

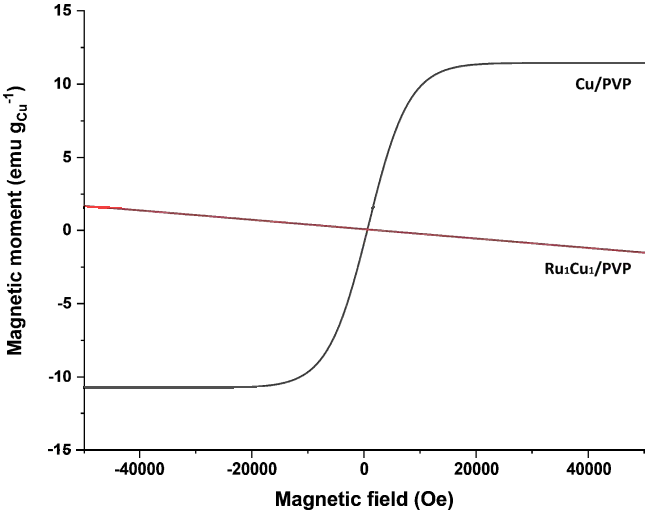

Figure 11: Cycles d'hystérésis magnétique des NPs de Cu/PVP et RuCu/PVP mesurés à RT.

Un dernier ligand a été testé, l'hexadécylamine (HDA). Tout d'abord des NPs de Cu/HDA (HDA) ont été synthétisées à 80 °C, 100 °C et 120 °C et en utilisant des éq. molaires de HDA de 0.2, 0.4, 1.0 et 2.0 (Schéma 7).

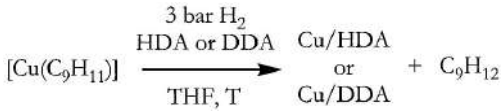

Schéma 7: Synthèse des NPs de Cu/HDA et Cu/DDA.

Des échantillons non homogènes avec une augmentation des tailles avec la température ont été observés. Le meilleur compromis entre taille et homogénéité s'est trouvé avec la synthèse de NPs bimétalliques de Cu/HDA à 100 °C et 0.4 équivalents (eq.) molaire de HDA (Figure 12), a conduit à une population de NPs plus homogène suggérant leur nature bimétallique.

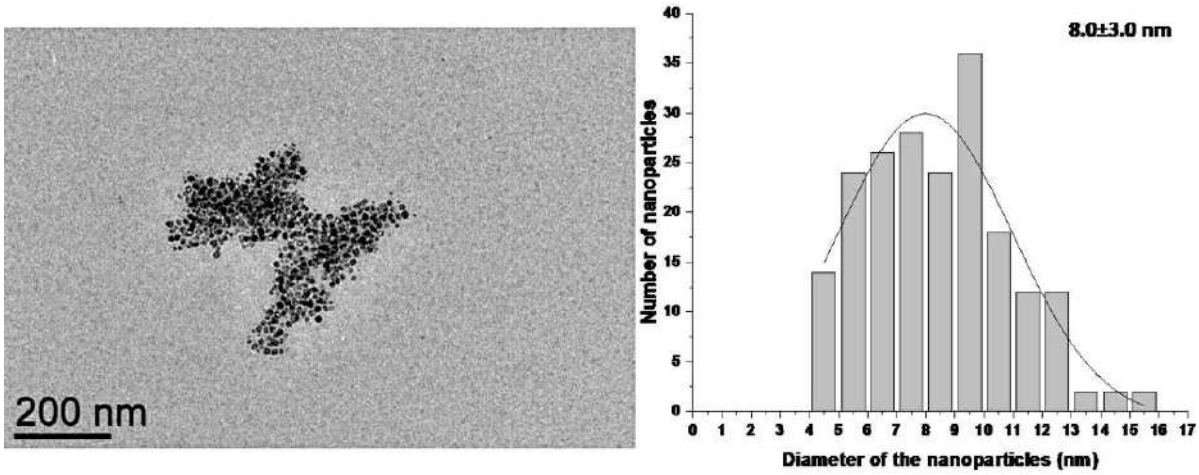

Figure 12: Image TEM de NPs de Cu/0.4 eq. HDA synthétisées à 100 °C (barre d'échelle 200 nm) et l'histogramme de taille respectif.

3. Catalyse d'hydrogénation du furfural et de la quinoléine

Le furfural (FF) est un aldéhyde furanique qui peut être obtenu à partir de la biomasse lignocellulosique et qui présente un grand intérêt dans l'industrie chimique pour la synthèse de carburants ou comme intermédiaire de synthèse.[53] La quinoléine(QN) est un N-hétérocycle que l'on peut trouver dans des produits naturels, qui possède une vaste gamme d'activités biologiques.[54] La QN est également utile pour la conception de cellules photovoltaïques organiques.[55] Les nanoparticules de RuNi et RuCu décrites ci-dessus, ont été évaluées comme catalyseurs pour les réactions d'hydrogénation du FF et de la QN, en comparaison avec leurs homologues monométalliques, dans des conditions douces comparativement à celles de la littérature.

Les tests catalytiques réalisés à 125 °C sous 20 bar de H_2 avec la série de NPs RuNi/PVP ont mis en évidence des effets synergiques entre les deux métaux dans la réaction d'hydrogénation du FF (Schéma 8) conduisant sélectivement à l'alcool furfurylique (HF). Ces effets ont été maximisés avec la composition Ru/Ni = 1 (Figure 13). Un effet important du solvant (THF ou 1-propanol, 1-PrOH) a également été observé dans cette réaction, le 1-PrOH conduisant à une meilleure réactivité. Des calculs de Density Functional Theory (DFT) ont été menés afin de corroborer les observations expérimentales par une analyse de l'adsorption du substrat et du solvant et du mécanisme réactionnel potentiel (voir section suivante). Les calculs d'énergies d'adsorption des réactifs ont mis en évidence des différences notables en fonction du solvant. Le 1-PrOH induit la présence d'espèces de propanolate à la surface métallique, ce qui a un effet bénéfique sur la performance catalytique. L'hydrogénation du cycle furanique et son ouverture, conduisant respectivement à l'alcool tétrahydrofurfurylique (HMTHF) et au 1,2-Pentanediol (1,2-PeD), ont été observées sur les NPs de Ru/PVP dans le 1-PrOH. Fait intéressant, aucune lixiviation n'a été observée sur les solutions obtenues par filtration à chaud après la catalyse, ce qui indique une bonne stabilité des NPs dans les conditions de catalyse appliquées.

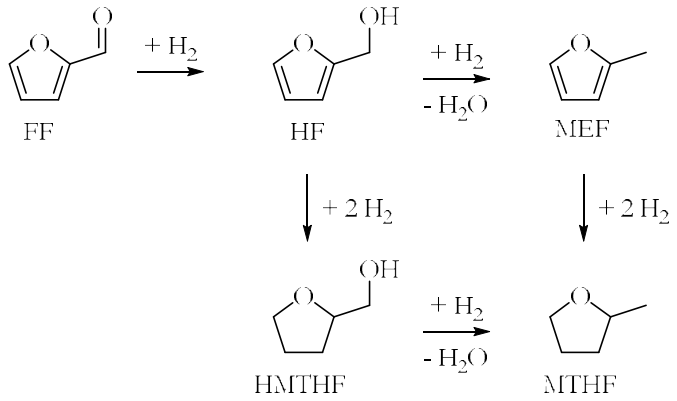

Schéma 8: Schéma réactionnel simplifié de l'hydrogénation catalytique du FF en divers produits de valeur ajoutée. Furfural (FF), alcool furfurylique (HF), alcool tétrahydrofurfurylique (HMTHF), 2-méthylfurane (MEF) et 2-méthyltétrahydrofurane (MTHF).

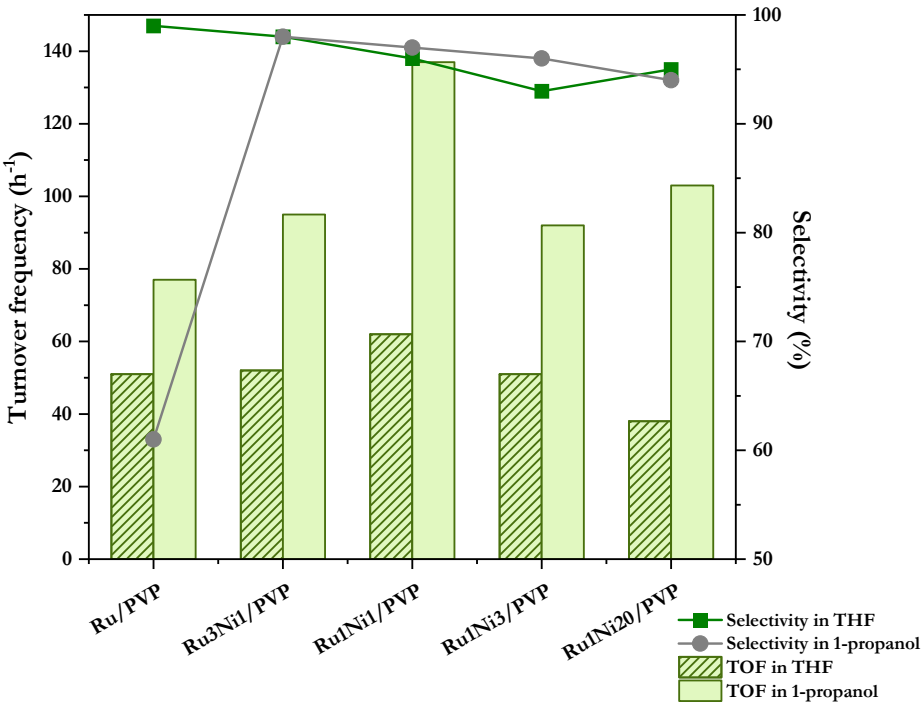

Figure 13: Fréquence de rotation (barres) et sélectivité (points) vis-à-vis de HF en fonction des catalyseurs dans l'hydrogénation de FF dans le THF (barres pointillées, points carrés) et le 1-PrOH (barres vertes, points circulaires).

Les NPs de Cu/PVP ont aussi montré des performances catalytiques prometteuses pour l'hydrogénation de FF, donnant des activités similaires à celles observées sur le nanocatalyseur Ru/PVP pur. Malheureusement, les NPs de RuCu/PVP ont montré des performances catalytiques inférieures à celles de leurs homologues monométalliques (Figure 14); néanmoins, les propriétés de ces catalyseurs pourraient être intéressantes pour d'autres transformations catalytiques.

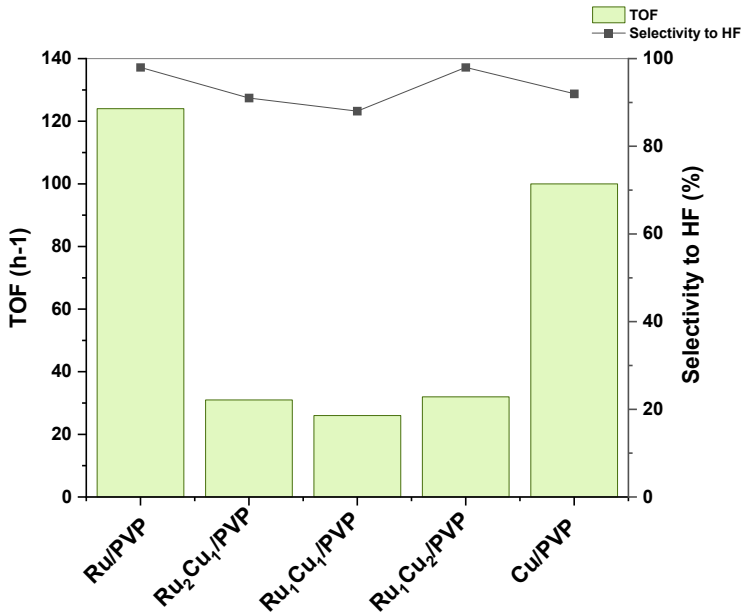

Figure 14: Fréquence de rotation (barres) et sélectivité (points) envers HF en fonction des catalyseurs dans l'hydrogénation sélective de FF dans 1-PrOH.

Concernant l'hydrogénation de la QN (Schéma 9), les nanocatalyseurs Ru_1Ni_1/PVP se sont avérés moins performants que pour l'hydrogénation du FF, mais une haute sélectivité vers 1-THQ a été obtenue. Des réactions de N-alkylation ont également été observées résultant de la condensation des produits 1,2,3,4-Tetrahydro-n-propyl-quinoléine(1-THPQ) et decahydro-1-propyl-quinoléine(DHPQ) avec le 1-PrOH (Schémas 10 et 11). Enfin, des résultats préliminaires obtenus sur les NPs de RuNi/PPh_2Py pour la même réaction montrent qu'il s'agit d'un catalyseur actif et plus performant qu'un système monométallique de Ru/PPh_2Py. Ce résultat peut être attribué à un effet de synergie entre les deux métaux.

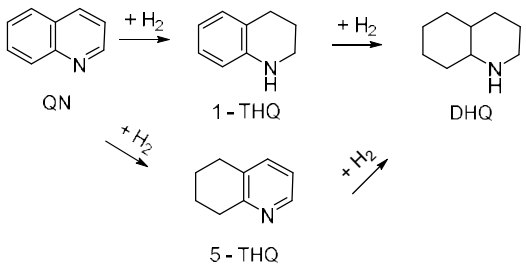

Schéma 9: Schéma réactionnel simplifié de l'hydrogénation catalytique de la QN en divers produits de valeur. Quinoléine (QN), 1,2,3,4-Tétrahydroquinoléine (1-THQ), 5,6,7,8-Tétrahydroquinoléine (5-THQ), et Décahydroquinoléine (DHQ).

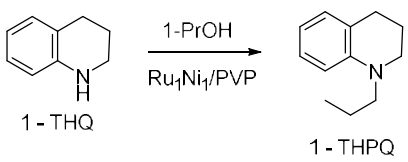

Schéma 10: Schéma réactionnel simplifié de la réaction de condensation entre 1-THQ et 1-PrOH sur le catalyseur Ru_1Ni_1/PVP, formant 1-THPQ.

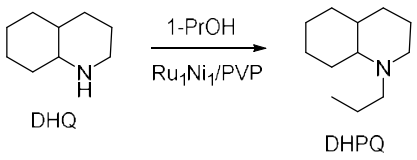

Schéma 11: Schéma réactionnel simplifié de la réaction de condensation entre DHQ et 1-PrOH sur le catalyseur Ru_1Ni_1/PVP, formant du DHPQ.

En regard des données de la bibliographie, de parles conditions douces appliquées les résultats obtenus en hydrogénation catalytique du FF sont très intéressants. De plus ils valident l'approche de synthèse suivie pour le développement de catalyseurs bimétalliques RuNi performants pour cette réaction. La catalyse d'hydrogénation de la QN ouvre également des pistes intéressantes.

4. Calculs DFT des modèles Ru et Ni pour l'hydrogénation du furfural

Les calculs par DFT (Density Functional Theory) constituent une approche pertinente pour la simulation et la conception de matériaux très performants pour un grand nombre d'applications,[56] en particulier pour l'étude des propriétés de composés inorganiques compliqués, et ont au fil des travaux atteint une grande précision pour un faible coût de calcul.[57] Les calculs DFT sont basés sur le théorème de Hohenberg-Kohn,[58] qui indique que, si la densité électronique du système est connue, toutes les propriétés électroniques du composé objet de l'étude peuvent être calculées. La DFT est ainsi devenue une alternative efficace aux méthodes classiques Hartree-Fock et post-Hartree-Fock pour l'étude des complexes métalliques. L'application de la DFT sur des systèmes de plus grande dimension reste limitée par la disponibilité des ressources informatiques, en raison de l'extensibilité de ces méthodes, même si l'application sur de petits complexes a déjà été rapportée.[59] Les principaux avantages de la DFT pour les systèmes contenant des métaux sont : la bonne extensibilité du système avec la taille, l'adéquation des orbitales calculées pour leur analyse et l'interprétation de la liaison entre les atomes et les propriétés du système.[60]

La DFT permet de calculer plusieurs propriétés qui peuvent être utiles pour comprendre les géométries,[61] l'énergie et les mécanismes de réactions,[62] les fréquences vibrationnelles,[63] et les propriétés spectroscopiques,[64] observées expérimentalement. Des études DFT ont permis d'étudier différentes propriétés telles que magnétiques, catalytiques ou optiques pour des nanomatériaux, en accord avec les résultats expérimentaux.[65]

Le progiciel de simulation Vienna *ab initio* simulation package (VASP) est un outil intéressant en DFT car il permet de calculer l'énergie totale et la structure électronique des systèmes métalliques *via* un ensemble

de base à ondes planes.[66] La proposition Perdew, Burke et Ernzerhof (PBE) de l'approche du gradient généralisé est utilisée pour l'approximation du potentiel de corrélation d'échange.[67] La méthode des ondes augmentées par projecteur (PAW) est d'une grande précision, avec des erreurs sur les longueurs de liaison inférieures à 0,5 %, y compris pour des systèmes difficiles telles que ceux présentant de grandes différences d'électronégativité et de forts moments magnétiques.[68]

Une collaboration entre notre équipe et celle du Pr R. Poteau au LPCNO-Toulouse, a permis de réaliser des calculs DFT et d'en comparer les résultats avec les données expérimentales de catalyse d'hydrogénation du furfural. Les calculs DFT réalisés dans ce travail de thèse ont été menés à partir de modèles de NPs de Ru et Ni déjà publiés, constitués de 55 et 38 atomes, respectivement.

Le modèle Ru_{55} est sphéroïde et de structure hexagonale compacte (*hcp*).[69] Des études sur des versions hydrogénés de modèle ($Ru_{55}H_{70}$, $Ru_{55}H_{32}$, $Ru_{55}H_{15}$) ont permis d'étudier l'adsorption de ligands tels que l'imidazolium-amidinates[70] et l'acide éthanoïque[71] sur la surface de NPs de Ru. Le $Ru_{55}H_{70}$ est un modèle de choix pour simuler le comportement des NPs Ru/PVP en condition d'hydrogénation,[69] car le taux de couverture de la surface métallique par des atomes d'hydrogènes (H) calculé théoriquement[69] est similaire à celui trouvé expérimentalement.[72]

Le modèle de NP de Ni_{38} a déjà été caractérisé et décrit comme une structure cubique à faces centrées (*fcc*) hautement symétrique,[73] étant le cluster Ni qui représente le mieux la structure *fcc* parmi ceux contenant entre 13 et 55 atomes. Le $Ni_{38}H_{35}$ est un bon modèle dans des conditions d'hydrogénation saturée pour les NPs de Ni/PVP, sachant que 36 atomes d'hydrogène peuvent être adsorbés sur la surface du Ni_{38} par une chimisorption dissociative.[74]

En ce qui concerne les systèmes RuNi bimétallique nous avons utilisé le modèle $Ru_{13}Ni_{25}$, où les atomes de Ru sont principalement dans le cœur. Ce modèle est assez proche des clusters $Ru_{13}Ni_{13}$ déjà rapportés.[75]

Les calculs DFT sur l'adsorption et l'hydrogénation de molécules plateformes, telles que le FF ou le HMF, sur des NPs métalliques sont rares.[76] A notre connaissance, ce travail est la première étude théorique de la réactivité catalytique du FF et de ses dérivés sur une surface hydrogénée de NPs de Ru et de Ni.

Afin de représenter les deux solvants (THF et 1-PrOH) utilisés en catalyse, deux modèles différents de NPs de Ru ont été construits (Figure 15). Les charges des atomes d'hydrogène (H) se sont avérées négatives sur la surface du Ru dans le cas du THF mais positives pour les H proches des molécules de 1-PrOH adsorbées sur la surface métallique.

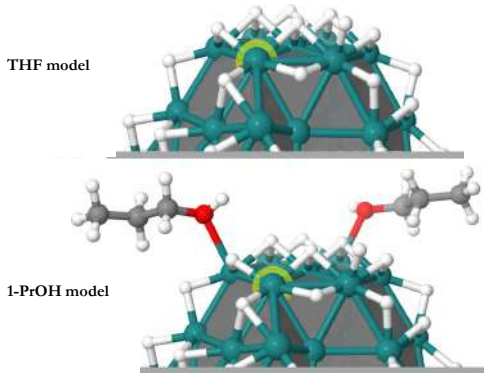

Figure 15 Modèles de $Ru_{55}H_{70}$ utilisés pour étudier les réactions d'hydrogénation dans le THF (en haut) et dans le 1-PrOH (en bas). Le site actif considéré est mis en évidence par un halo jaune. La partie inférieure des modèles n'est pas représentée pour des raisons de clarté.

Une compétition entre FF et THF pour l'adsorption sur les sites actifs de la surface de la NP a été observée pour le modèle $Ru_{55}H_{70}$/THF. Un flux continu de H_2 a été observé comme étant favorable à la désorption de HF et la présence de THF comme entravant l'hydrogénation du cycle furanique (Figure 16).

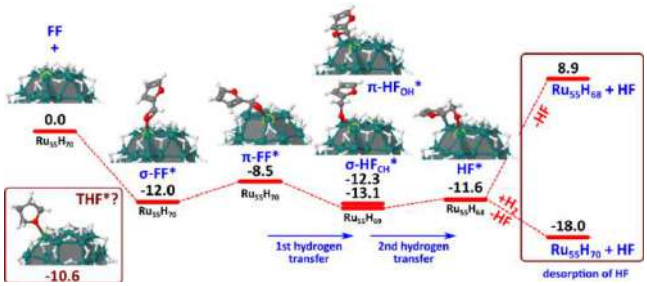

Figure 16: Profil énergétique pour l'hydrogénation du FF sur une nanoparticule de $Ru_{55}H_{70}$ dans le THF. Les énergies sont données en kcal·mol^{-1}.

Sur le modèle $Ru_{55}H_{70}$/1-PrOH, le 1-PrOH s'est avéré intervenir dans l'hydrogénation du FF et un flux continu de H_2 favorable à l'hydrogénation. Les réactions d'hydrogénation et d'ouverture de cycle pour former respectivement HMTHF et 1,2-PeD, ainsi que la formation d'acétal ont pu être expliquées par des calculs DFT (Figure 17).

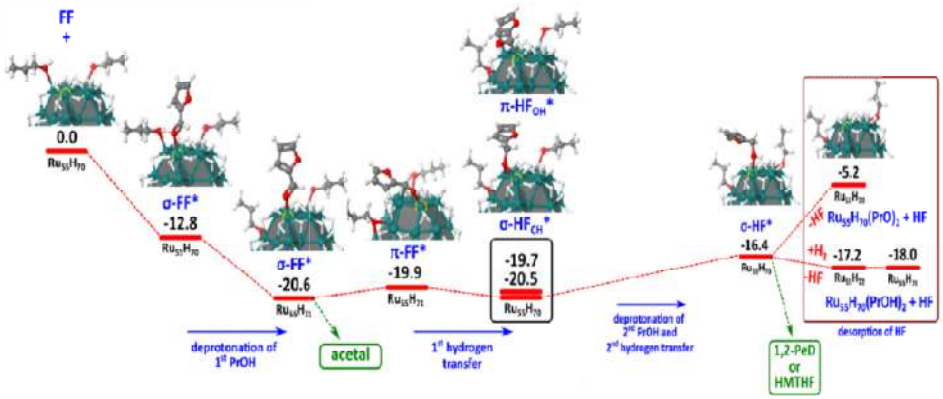

Figure 17: Profil énergétique potentiel pour l'hydrogénation du FF sur une NP de $Ru_{55}H_{70}$ dans le 1-PrOH. Les possibles points de départ vers la formation d'acétal, de HMTHF ou de 1,2-PeD sont également indiqués. Les énergies sont données en kcal·mol^{-1}.

Deux modèles différents de NPs de Ni ont été également construits, afin de représenter les deux solvants (THF et 1-PrOH) utilisés en catalyse (Figure 18).

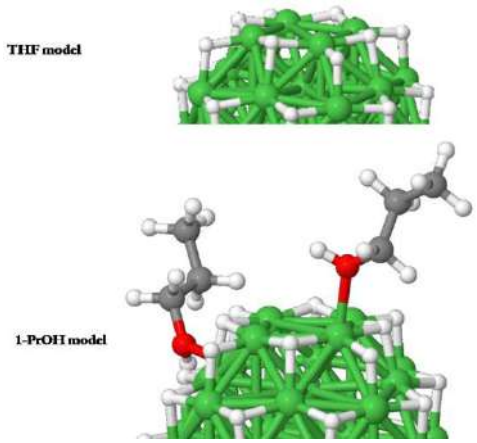

Figure 18: Modèles de $Ni_{38}H_{35}$ utilisés pour étudier l'hydrogénation du FF dans le THF (en haut) et dans le 1-PrOH (en bas). La partie inférieure des modèles n'est pas représentée pour plus de clarté.

Sur le modèle $Ni_{38}H_{35}$/THF, un flux continu de H_2 s'est avéré favorable à la désorption de HF (Figure 19). La coordination π de l'intermédiaire π-$HF_{OH*}Ni_{38}H_{34}$ peut expliquer l'hydrogénation du cycle furanique observé expérimentalement avec les NPs Ni/PVP lors de l'utilisation du THF. De façon surprenante, toutes les valeurs d'énergie d'adsorption calculées sur le modèle $Ni_{38}H_{35}$/1-PrOH sont positives (Figure 20) alors que dans les autres cas elles étaient toutes négatives. Le fait que les énergies d'adsorption soient positives signifie qu'elles ne sont pas thermodynamiquement favorisées. Ceci peut expliquer les résultats expérimentaux à savoir que dans la série 1-PrOH, le Ni/PVP est le catalyseur le moins actif. Le mécanisme d'hydrogénation du FF sur une NP $Ni_{38}H_{35}$/1-PrOH n'a pas pu être élucidé complètement, faute de temps (Figure 20).

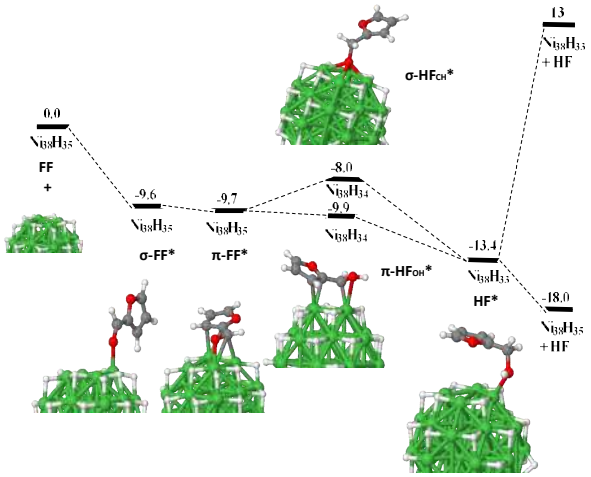

Figure 19: Profil énergétique pour l'hydrogénation du FF sur une NP de $Ni_{38}H_{35}$ dans le THF. Les énergies sont données en kcal·mol^{-1}.

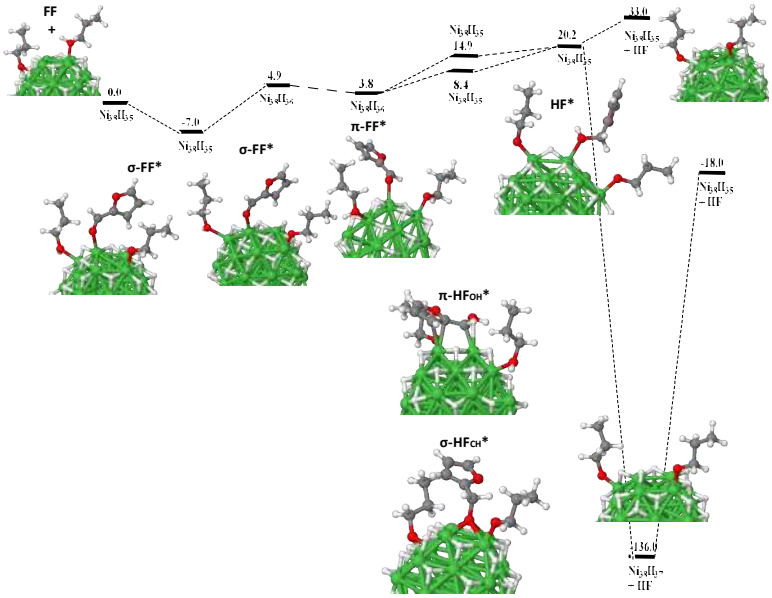

Figure 20: Profil énergétique potentiel pour l'hydrogénation du FF sur une NP de $Ni_{38}H_{35}$ dans le 1-PrOH. Les énergies sont données en kcal·mol^{-1}.

Pour simuler les NPs bimétalliques RuNi, trois modèles de $Ru_{13}Ni_{25}$ hydrogéné ($Ru_{13}Ni_{25}$-A à C) avec un cœur de Ru tel que déterminé par WAXS, et deux modèles ($Ru_{13}Ni_{25}$-D et E), simulant des alliages, ont été construits (Figure 21). L'objectif a été de sonder l'adsorption des mêmes espèces que celles précédemment étudiées sur les NPs monométalliques de Ru et Ni.

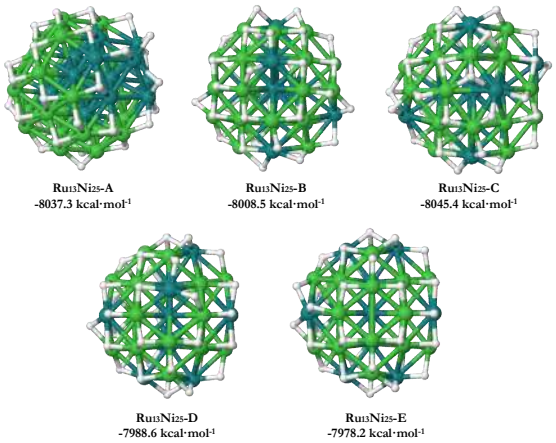

Figure 21: Modèles de $Ru_{13}Ni_{25}$ avec un cœur de Ru (A à C) et avec une structure d'alliage (D et E) avec leurs énergies associées en kcal·mol^{-1}.

5. Réactions de deutération de molécules organiques sur des nanoparticules de Ru/PVP

Le deutérium, un isotope stable et sûr de l'hydrogène, présente un fort intérêt dans différents domaines scientifiques. Son utilisation est développée dans l'industrie pharmaceutique pour la recherche de nouveaux médicaments car il permet d'en suivre le métabolisme.[77] Pour information ce n'est qu'en 2017 que la Food and Drug Administration (FDA) des États-Unis a accepté les médicaments deutérés.[78]

Parmi les nombreuses méthodes pour la synthèse de molécules deutérées, l'une des plus attrayantes est l'échange isotopique d'hydrogène (HIE), où l'incorporation de deutérium à des positions clés peut être modulée par le choix adéquat du catalyseur. Les molécules organiques étant riches en liaisons C-H, la deutération sélective de sites spécifiques est une voie pertinente pour le développement de pharmacophores et de produits naturels.[79]

Les anilines[80] et les aldéhydes aromatiques[81] étant constitutifs de nombreux médicaments, ce donc des molécules clés dans l'industrie pharmaceutique. Les sucres marqués au deutérium permettent l'étude structurelle de macromolécules telles que les acides nucléiques et les glycoprotéines.[82] Ils sont également constitutifs[83] de composés bioactifs chiraux deutérés. Les nucléosides deutérés tels que les adénosines sont constitutifs des acides nucléiques, et donc des molécules d'intérêt pour les études structurelles des macromolécules biologiques.[83] Tous ces procédés présentent un coût élevé et une faible économie d'atomes, bien que le D_2O soit apparu comme une source alternative de deutérium.[84]

Les Ru PVP NPs ont été testées dans la deutération sélective de molécules modèles dans l'eau. Cette étude a été réalisée en collaboration avec le groupe du Pr M. Beller au LIKAT de Rostock, Allemagne.

Pour la deutération de la 4-Methoxyaniline (4-MeOAn) (Schéma 12), aucun marquage au deutérium n'a pu être observé malgré la variation des conditions de réaction. Sous 10 bar de H_2 à 80 °C, seuls des

produits hydrogénés ont été obtenus. Curieusement, sans H_2 que ce soit à RT ou à 80 °C, une lixiviation de la PVP a été observée.

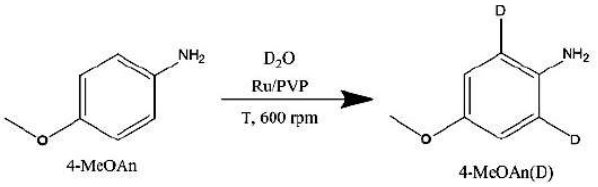

Schéma 12: Schéma réactionnel simplifié de la deutération catalytique de 4-MeOAn en 4-MeOAn(D).

Pour la deutération de 4-(Trifluoromethyl)benzaldehyde (TFMBAL) (Schéma 13), l'hydrogénation du TFMBAL sous 10 bar de H_2 à 80 °C a été observée. Par contre, en l'absence de H_2, les deux hydrogènes du cycle du TFMBAL en position ortho de la fonction aldéhyde ont pu être deutérés.

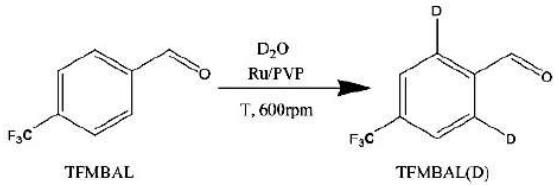

Schéma 13: Schéma réactionnel simplifié de la deutération catalytique de TFMBAL en TFMBAL(D).

Pour la deutération d'un furanose protégé, le Methyl 2,3-O-Isopropylidene-β-D-ribofuranoside (MOIBRIBOF) (Schéma 14), aucune deutériation n'a été observée mais une épimérisation en l'absence de H_2 et une déprotection sous pression de H_2.

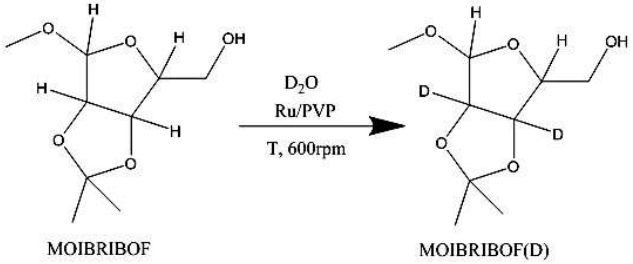

Schéma 14: Schéma réactionnel simplifié de la deutération catalytique du MOIBRIBOF en MOIBRIBOF(D).

Enfin, l'adénosine (ADNS) a pu être sélectivement marquée au deutérium, sans aucune épimérisation du squelette du sucre (Schéma 15).

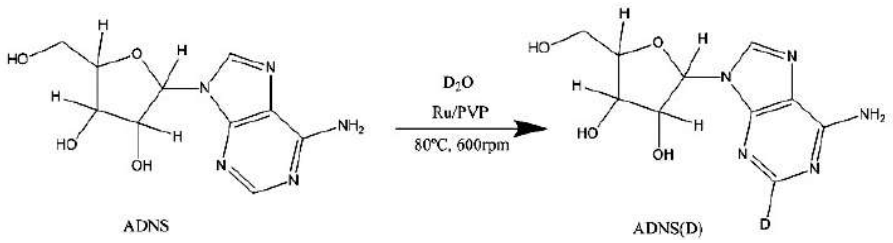

Schéma 15: Schéma réactionnel simplifié de la deutération catalytique de l'ADNS en ADNS(D).

Avec une optimisation des conditions réactionnelles et/ou des tests sur d'autres molécules les résultats de cette étude préliminaire pourraient ouvrir des pistes de recherche intéressantes.

6. Références

(1) Watts, N.; Amann, M.; Arnell, N.; Ayeb-Karlsson, S.; Beagley, J.; Belesova, K.; Boykoff, M.; Byass, P.; Cai, W.; Campbell-Lendrum, D.; Capstick, S.; Chambers, J.; Coleman, S.; Dalin, C.; Daly, M.; Dasandi, N.; Dasgupta, S.; Davies, M.; Di Napoli, C.; Dominguez-Salas, P.; Drummond, P.; Dubrow, R.; Ebi, K. L.; Eckelman, M.; Ekins, P.; Escobar, L. E.; Georgeson, L.; Golder, S.; Grace, D.; Graham, H.; Haggar, P.; Hamilton, I.; Hartinger, S.; Hess, J.; Hsu, S.-C.; Hughes, N.; Jankin Mikhaylov, S.; Jimenez, M. P.; Kelman, I.; Kennard, H.; Kiesewetter, G.; Kinney, P. L.; Kjellstrom, T.; Kniveton, D.; Lampard, P.; Lemke, B.; Liu, Y.; Liu, Z.; Lott, M.; Lowe, R.; Martinez-Urtaza, J.; Maslin, M.; McAllister, L.; McGushin, A.; McMichael, C.; Milner, J.; Moradi-Lakeh, M.; Morrissey, K.; Munzert, S.; Murray, K. A.; Neville, T.; Nilsson, M.; Sewe, M. O.; Oreszczyn, T.; Otto, M.; Owfi, F.; Pearman, O.; Pencheon, D.; Quinn, R.; Rabbaniha, M.; Robinson, E.; Rocklöv, J.; Romanello, M.; Semenza, J. C.; Sherman, J.; Shi, L.; Springmann, M.; Tabatabaei, M.; Taylor, J.; Triñanes, J.; Shumake-Guillemot, J.; Vu, B.; Wilkinson, P.; Winning, M.; Gong, P.; Montgomery, H.; Costello, A. The 2020 Report of The Lancet Countdown on Health and Climate Change: Responding to Converging Crises. *The Lancet* **2021**, *397* (10269), 129. https://doi.org/10.1016/S0140-6736(20)32290-X

(2) Taalas, P.; Guterres, A. *WMO Statement on the State of the Global Climate in 2018*; World Meteorological Organization (WMO): Genf, **2019**. https://library.wmo.int/doc_num.php?explnum_id=10211

(3) Alfieri, L.; Bisselink, B.; Dottori, F.; Naumann, G.; de Roo, A.; Salamon, P.; Wyser, K.; Feyen, L. Global Projections of River Flood Risk in a Warmer World. *Earths Future* **2017**, *5* (2), 171. https://doi.org/10.1002/2016EF000485

(4) Watts, N.; Amann, M.; Arnell, N.; Ayeb-Karlsson, S.; Belesova, K.; Berry, H.; Bouley, T.; Boykoff, M.; Byass, P.; Cai, W.; Campbell-Lendrum, D.; Chambers, J.; Daly, M.; Dasandi, N.; Davies, M.; Depoux, A.; Dominguez-Salas, P.; Drummond, P.; Ebi, K. L.; Ekins, P.; Montoya, L. F.; Fischer, H.; Georgeson, L.; Grace, D.; Graham, H.; Hamilton, I.; Hartinger, S.; Hess, J.; Kelman, I.; Kiesewetter, G.; Kjellstrom, T.; Kniveton, D.; Lemke, B.; Liang, L.; Lott, M.; Lowe, R.; Sewe, M. O.; Martinez-Urtaza, J.; Maslin, M.; McAllister, L.; Mikhaylov, S. J.; Milner, J.; Moradi-Lakeh, M.; Morrissey, K.; Murray, K.; Nilsson, M.; Neville, T.; Oreszczyn, T.; Owfi, F.; Pearman, O.; Pencheon, D.; Pye, S.; Rabbaniha, M.; Robinson, E.; Rocklöv, J.; Saxer, O.; Schütte, S.; Semenza, J. C.; Shumake-Guillemot, J.; Steinbach, R.; Tabatabaei, M.; Tomei, J.; Trinanes, J.; Wheeler, N.; Wilkinson, P.; Gong, P.; Montgomery, H.; Costello, A. The 2018 Report of the Lancet Countdown on Health and Climate Change: Shaping the Health of Nations for Centuries to Come. *The Lancet* **2018**, *392* (10163), 2479. https://doi.org/10.1016/S0140-6736(18)32594-7

(5) Energy Production and Consumption - Our World in Data. https://ourworldindata.org/energy-production-consumption

(6) Owusu, P. A.; Asumadu-Sarkodie, S. A Review of Renewable Energy Sources, Sustainability Issues and Climate Change Mitigation. *Cogent Eng.* **2016**, *3* (1), 1167990. https://doi.org/10.1080/23311916.2016.1167990

(7) Gallezot, P. Process Options for Converting Renewable Feedstocks to Bioproducts. *Green Chem.* **2007**, *9* (4), 295. https://doi.org/10.1039/b615413a
(8) Nanda, S.; Azargohar, R.; Dalai, A. K.; Kozinski, J. A. An Assessment on the Sustainability of Lignocellulosic Biomass for Biorefining. *Renew. Sustain. Energy Rev.* **2015**, *50*, 925. https://doi.org/10.1016/j.rser.2015.05.058
(9) Putro, J. N.; Soetaredjo, F. E.; Lin, S.-Y.; Ju, Y.-H.; Ismadji, S. Pretreatment and Conversion of Lignocellulose Biomass into Valuable Chemicals. *RSC Adv.* **2016**, *6* (52), 46834. https://doi.org/10.1039/C6RA09851G
(10) Cai, C. M.; Zhang, T.; Kumar, R.; Wyman, C. E. Integrated Furfural Production as a Renewable Fuel and Chemical Platform from Lignocellulosic Biomass: Furfural Production from Lignocellulosic Biomass. *J. Chem. Technol. Biotechnol.* **2014**, *89* (1), 2. https://doi.org/10.1002/jctb.4168
(11) D. Mthembu, L.; Gupta, R.; Deenadayalu, N. Conversion of Cellulose into Value-Added Products. In *Cellulose Science and Derivatives*; Sand, A., Banga, S., Eds.; IntechOpen, **2021**. https://doi.org/10.5772/intechopen.100022
(12) Yue, X.; Queneau, Y. 5-Hydroxymethylfurfural and Furfural Chemistry Toward Biobased Surfactants. *ChemSusChem* **2022**, *15* (13), e202102660. https://doi.org/10.1002/cssc.202102660
(13) Huber, G. W.; Corma, A. Synergies between Bio- and Oil Refineries for the Production of Fuels from Biomass. *Angew. Chem. Int. Ed.* **2007**, *46* (38), 7184. https://doi.org/10.1002/anie.200604504
(14) Gilroy, K. D.; Ruditskiy, A.; Peng, H.-C.; Qin, D.; Xia, Y. Bimetallic Nanocrystals: Syntheses, Properties, and Applications. *Chem. Rev.* **2016**, *116* (18), 10414. https://doi.org/10.1021/acs.chemrev.6b00211
(15) Wei, Q.; Wang, L.; Chen, X.; Wu, C.; Liang, J.; Wei, X.; Deng, K. MoNi Nano-Alloy Loaded on Carbon Nanotubes with High Activity and Stability for the Catalytic Hydrogenation of Petro Resin. *React. Kinet. Mech. Catal.* **2022**, *135* (5), 2503. https://doi.org/10.1007/s11144-022-02250-6
(16) Palkovits, R.; Delidovich, I. Efficient Utilization of Renewable Feedstocks: The Role of Catalysis and Process Design. *Philos. Trans. R. Soc. Math. Phys. Eng. Sci.* **2018**, *376* (2110), 20170064. https://doi.org/10.1098/rsta.2017.0064
(17) Ferrando, R.; Jellinek, J.; Johnston, R. L. Nanoalloys: From Theory to Applications of Alloy Clusters and Nanoparticles. *Chem. Rev.* **2008**, *108* (3), 845. https://doi.org/10.1021/cr040090g
(18) Jiang, H.; Liu, X.; Zhu, M.-N.; Xu, J.; An, L.; Sui, P.-F.; Luo, J.-L.; Cheng, G. J. Nanoalloy Libraries from Laser-Induced Thermionic Emission Reduction. *Sci. Adv.* **2022**, *8* (16), eabm6541. https://doi.org/10.1126/sciadv.abm6541
(19) Kang, X.; Li, Y.; Zhu, M.; Jin, R. Atomically Precise Alloy Nanoclusters: Syntheses, Structures, and Properties. *Chem. Soc. Rev.* **2020**, *49* (17), 6443. https://doi.org/10.1039/C9CS00633H
(20) Alonso, D. M.; Wettstein, S. G.; Dumesic, J. A. Bimetallic Catalysts for Upgrading of Biomass to Fuels and Chemicals. *Chem. Soc. Rev.* **2012**, *41* (24), 8075. https://doi.org/10.1039/c2cs35188a
(21) Jiang, T.; Zhou, Y.; Liang, S.; Liu, H.; Han, B. Hydrogenolysis of Glycerol Catalyzed by Ru-Cu Bimetallic Catalysts Supported on Clay with the Aid of Ionic Liquids. *Green Chem.* **2009**, *11* (7), 1000. https://doi.org/10.1039/b901425j
(22) Priya, S. S.; Bhanuchander, P.; Kumar, V. P.; Bhargava, S. K.; Chary, K. V. R. Activity and Selectivity of Platinum–Copper Bimetallic Catalysts Supported on Mordenite for Glycerol Hydrogenolysis to 1,3-Propanediol. *Ind. Eng. Chem. Res.* **2016**, *55* (16), 4461. https://doi.org/10.1021/acs.iecr.6b00161
(23) Liu, M.; Zhang, J.; Zheng, L.; Fan, G.; Yang, L.; Li, F. Significant Promotion of Surface Oxygen Vacancies on Bimetallic CoNi Nanocatalysts for Hydrodeoxygenation of Biomass-Derived Vanillin to Produce Methylcyclohexanol. *ACS Sustain. Chem. Eng.* **2020**, *8* (15), 6075. https://doi.org/10.1021/acssuschemeng.0c01015
(24) He, Z.-H.; Jiang, C.-S.; Wang, Z.-Y.; Wang, K.; Sun, Y.-C.; Yao, M.-Q.; Li, Z.-H.; Liu, Z.-T. Catalytic Hydrodeoxygenation of Biomass-Derived Oxygenates to Bio-Fuels over Co-Based Bimetallic Catalysts. *Sustain. Energy Fuels* **2020**, *4* (9), 4558. https://doi.org/10.1039/d0se00332h
(25) Wettstein, S. G.; Bond, J. Q.; Alonso, D. M.; Pham, H. N.; Datye, A. K.; Dumesic, J. A. RuSn Bimetallic Catalysts for Selective Hydrogenation of Levulinic Acid to γ-Valerolactone. *Appl. Catal. B Environ.* **2012**, *117–118*, 321. https://doi.org/10.1016/j.apcatb.2012.01.033
(26) Wu, J.; Liu, C.; Zhu, Y.; Song, X.; Wen, C.; Zhang, X.; Wang, C.; Ma, L. Understanding the Geometric and Electronic Factors of PtNi Bimetallic Surfaces for Efficient and Selective Catalytic Hydrogenation of Biomass-Derived Oxygenates. *J. Energy Chem.* **2021**, *60*, 16. https://doi.org/10.1016/j.jechem.2020.12.011

(27) Xie, D.; Liu, X.; Lv, H.; Guo, Y. Products, Pathways, and Kinetics for Catalytic Hydrodenitrogenation of Quinoline in Hydrothermal Condition. *J. Supercrit. Fluids* **2022**, *182*, 105509. https://doi.org/10.1016/j.supflu.2021.105509
(28) Zhang, H.; Pei, A.; Liao, J.; Ruan, L.; Yang, K.; Wang, J.; Zhu, L.; Chen, B. H. PtRuNi/C Novel Nanostructures of Platinum-Ruthenium Island-on-Ni/$Ni(OH)_2$ Nanoparticles for the Selective Hydrogenation of Quinoline. *J. Alloys Compd.* **2020**, *834*, 155203. https://doi.org/10.1016/j.jallcom.2020.155203
(29) Lee, J.; Kim, Y. T.; Huber, G. W. Aqueous-Phase Hydrogenation and Hydrodeoxygenation of Biomass-Derived Oxygenates with Bimetallic Catalysts. *Green Chem.* **2014**, *16* (2), 708. https://doi.org/10.1039/c3gc41071d
(30) Yoshimura, M.; Komatsu, A.; Niimura, M.; Takagi, Y.; Takahashi, T.; Ueda, S.; Ichikawa, T.; Kobayashi, Y.; Okami, H.; Hattori, T.; Sawama, Y.; Monguchi, Y.; Sajiki, H. Selective Synthesis of Primary Amines from Nitriles under Hydrogenation Conditions. *Adv. Synth. Catal.* **2018**, *360* (8), 1726. https://doi.org/10.1002/adsc.201800102
(31) Bagal, D. B.; Bhanage, B. M. Recent Advances in Transition Metal-Catalyzed Hydrogenation of Nitriles. *Adv. Synth. Catal.* **2015**, *357* (5), 883. https://doi.org/10.1002/adsc.201400940
(32) Chatterjee, M.; Sato, M.; Kawanami, H.; Yokoyama, T.; Suzuki, T.; Ishizaka, T. An Efficient Hydrogenation of Dinitrile to Aminonitrile in Supercritical Carbon Dioxide. *Adv. Synth. Catal.* **2010**, *352* (14–15), 2394. https://doi.org/10.1002/adsc.201000514
(33) Rajesh, K.; Dudle, B.; Blacque, O.; Berke, H. Homogeneous Hydrogenations of Nitriles Catalyzed by Rhenium Complexes. *Adv. Synth. Catal.* **2011**, *353* (9), 1479. https://doi.org/10.1002/adsc.201000867
(34) Chin, C. S.; Lee, B. Hydrogenation of Nitriles with Iridium-Triphenylphosphine Complexes. *Catal. Lett.* **1992**, *14* (1), 135. https://doi.org/10.1007/BF00764228
(35) Roose, P.; Eller, K.; Henkes, E.; Rossbacher, R.; Höke, H. Amines, Aliphatic. In *Ullmann's Encyclopedia of Industrial Chemistry*; Wiley-VCH Verlag GmbH & Co. KGaA, Ed.; Wiley-VCH Verlag GmbH & Co. KGaA: Weinheim, Germany, **2015**; 1. https://doi.org/10.1002/14356007.a02_001.pub2
(36) Axet, M. R.; Philippot, K. Catalysis with Colloidal Ruthenium Nanoparticles. *Chem. Rev.* **2020**, *120* (2), 1085. https://doi.org/10.1021/acs.chemrev.9b00434
(37) Zhang, R. F.; Kong, X. F.; Wang, H. T.; Zhang, S. H.; Legut, D.; Sheng, S. H.; Srinivasan, S.; Rajan, K.; Germann, T. C. An Informatics Guided Classification of Miscible and Immiscible Binary Alloy Systems. *Sci. Rep.* **2017**, *7* (1), 9577. https://doi.org/10.1038/s41598-017-09704-1
(38) Bai, S.; Yao, Q.; Xu, Y.; Cao, K.; Huang, X. Strong Synergy in a Lichen-like RuCu Nanosheet Boosts the Direct Methane Oxidation to Methanol. *Nano Energy* **2020**, *71*, 104566. https://doi.org/10.1016/j.nanoen.2020.104566
(39) Zhu, L.; Cao, M.; Li, L.; Sun, H.; Tang, Y.; Zhang, N.; Zheng, J.; Zhou, H.; Li, Y.; Yang, L.; Zhong, C.-J.; Chen, B. H. Synthesis of Different Ruthenium Nickel Bimetallic Nanostructures and an Investigation of the Structure-Activity Relationship for Benzene Hydrogenation to Cyclohexane. *ChemCatChem* **2014**, *6* (7), 2039. https://doi.org/10.1002/cctc.201400096
(40) Amiens, C.; Ciuculescu-Pradines, D.; Philippot, K. Controlled Metal Nanostructures: Fertile Ground for Coordination Chemists. *Coord. Chem. Rev.* **2016**, *308*, 409. https://doi.org/10.1016/j.ccr.2015.07.013
(41) Qi, X.; Axet, M. R.; Philippot, K.; Lecante, P.; Serp, P. Seed-Mediated Synthesis of Bimetallic Ruthenium–Platinum Nanoparticles Efficient in Cinnamaldehyde Selective Hydrogenation. *Dalton Trans.* **2014**, *43* (24), 9283. https://doi.org/10.1039/C3DT53539H
(42) Braga, A. H.; Costa, N. J. S.; Philippot, K.; Gonçalves, R. V.; Szanyi, J.; Rossi, L. M. Structure and Activity of Supported Bimetallic NiPd Nanoparticles: Influence of Preparation Method on CO_2 Reduction. *ChemCatChem* **2020**, *12* (11), 2967. https://doi.org/10.1002/cctc.201902329
(43) Dufour, F.; Fresch, B.; Durupthy, O.; Chaneac, C.; Remacle, F. Ligand and Solvation Effects on the Structural and Electronic Properties of Small Gold Clusters. *J. Phys. Chem. C* **2014**, *118* (8), 4362. https://doi.org/10.1021/jp409019z
(44) Godoy, N. V.; Galazzi, R. M.; Chacón-Madrid, K.; Arruda, M. A. Z.; Mazali, I. O. Evaluating the Total Gold Concentration in Metallic Nanoparticles with a High Content of Organic Matter through Microwave-Assisted Decomposition Platform and Plasma-Based Spectrometric Techniques (ICP-MS and ICP OES). *Talanta* **2021**, *224*, 121808. https://doi.org/10.1016/j.talanta.2020.121808

(45) Lacroix, L.-M.; Lachaize, S.; Falqui, A.; Respaud, M.; Chaudret, B. Iron Nanoparticle Growth in Organic Superstructures. *J. Am. Chem. Soc.* **2009**, *131* (2), 549. https://doi.org/10.1021/ja805719c
(46) Utsunomiya, S.; Ewing, R. C. Application of High-Angle Annular Dark Field Scanning Transmission Electron Microscopy, Scanning Transmission Electron Microscopy-Energy Dispersive X-Ray Spectrometry, and Energy-Filtered Transmission Electron Microscopy to the Characterization of Nanoparticles in the Environment. *Environ. Sci. Technol.* **2003**, *37* (4), 786. https://doi.org/10.1021/es026053t
(47) Hodoroaba, V.-D.; Motzkus, C.; Macé, T.; Vaslin-Reimann, S. Performance of High-Resolution SEM/EDX Systems Equipped with Transmission Mode (TSEM) for Imaging and Measurement of Size and Size Distribution of Spherical Nanoparticles. *Microsc. Microanal.* **2014**, *20* (2), 602. https://doi.org/10.1017/S1431927614000014
(48) Lagunas, A.; Jimeno, C.; Font, D.; Solà, L.; Pericàs, M. A. Mechanistic Studies on the Conversion of Dicobalt Octacarbonyl into Colloidal Cobalt Nanoparticles. *Langmuir* **2006**, *22* (8), 3823. https://doi.org/10.1021/la053016h
(49) Marbella, L. E.; Millstone, J. E. NMR Techniques for Noble Metal Nanoparticles. *Chem. Mater.* **2015**, *27* (8), 2721. https://doi.org/10.1021/cm504809c
(50) Prieto, P.; Nistor, V.; Nouneh, K.; Oyama, M.; Abd-Lefdil, M.; Díaz, R. XPS Study of Silver, Nickel and Bimetallic Silver–Nickel Nanoparticles Prepared by Seed-Mediated Growth. *Appl. Surf. Sci.* **2012**, *258* (22), 8807. https://doi.org/10.1016/j.apsusc.2012.05.095
(51) Billas, I. M. L.; Châtelain, A.; de Heer, W. A. Magnetism of Fe, Co and Ni Clusters in Molecular Beams. *J. Magn. Magn. Mater.* **1997**, *168* (1–2), 64. https://doi.org/10.1016/S0304-8853(96)00694-4
(52) Asset, T.; Gommes, C. J.; Drnec, J.; Bordet, P.; Chattot, R.; Martens, I.; Nelayah, J.; Job, N.; Maillard, F.; Dubau, L. Disentangling the Degradation Pathways of Highly Defective PtNi/C Nanostructures - An Operando Wide and Small Angle X-Ray Scattering Study. *ACS Catal.* **2019**, *9* (1), 160. https://doi.org/10.1021/acscatal.8b02665
(53) Yan, K.; Wu, G.; Lafleur, T.; Jarvis, C. Production, Properties and Catalytic Hydrogenation of Furfural to Fuel Additives and Value-Added Chemicals. *Renew. Sustain. Energy Rev.* **2014**, *38*, 663. https://doi.org/10.1016/j.rser.2014.07.003
(54) Aly, A. A.; Ramadan, M.; Abuo-Rahma, G. E.-D. A.; Elshaier, Y. A. M. M.; Elbastawesy, M. A. I.; Brown, A. B.; Bräse, S. Quinolones as Prospective Drugs: Their Syntheses and Biological Applications. In *Advances in Heterocyclic Chemistry*; Elsevier, **2021**, *135*, 147. https://doi.org/10.1016/bs.aihch.2020.08.001
(55) Lewinska, G.; Sanetra, J.; Marszalek, K. W. Application of Quinoline Derivatives in Third-Generation Photovoltaics. *J. Mater. Sci. Mater. Electron.* **2021**, *32* (14), 18451. https://doi.org/10.1007/s10854-021-06225-6
(56) Ali, W.; Prakash, G.; Maiti, D. Recent Development in Transition Metal-Catalysed C–H Olefination. *Chem. Sci.* **2021**, *12* (8), 2735. https://doi.org/10.1039/D0SC05555G
(57) Koch, W.; Holthausen, M. C. *A Chemist's Guide to Density Functional Theory*, 1st ed.; Wiley, **2001**. https://doi.org/10.1002/3527600043
(58) Görling, A. Density-Functional Theory beyond the Hohenberg-Kohn Theorem. *Phys. Rev. A* **1999**, *59* (5), 3359. https://doi.org/10.1103/PhysRevA.59.3359
(59) Cao, X.; Dolg, M. Pseudopotential Study of Lanthanum and Lutetium Dimers. *Theor. Chem. Acc. Theory Comput. Model. Theor. Chim. Acta* **2002**, *108* (3), 143. https://doi.org/10.1007/s00214-002-0372-8
(60) Fritsche, L.; Koller, J.; Reinert, Th. Borderline Cases in Density Functional Theory. *Int. J. Quantum Chem.* **2004**, *100* (4), 681. https://doi.org/10.1002/qua.20113
(61) Rao, P. V. R.; Srishailam, K.; Reddy, B. V.; Rao, G. R. Theoretical (DFT) and Experimental (FT-IR & FT Raman) Approach to Investigate the Molecular Geometry and Vibrational Properties of 2,5- and 2,6-Dihydroxytoluenes. *J. Mol. Struct.* **2021**, *1240*, 130617. https://doi.org/10.1016/j.molstruc.2021.130617
(62) Bhandari, S.; Rangarajan, S.; Maravelias, C. T.; Dumesic, J. A.; Mavrikakis, M. Reaction Mechanism of Vapor-Phase Formic Acid Decomposition over Platinum Catalysts: DFT, Reaction Kinetics Experiments, and Microkinetic Modeling. *ACS Catal.* **2020**, *10* (7), 4112. https://doi.org/10.1021/acscatal.9b05424

(63) Eftimie, E.-L. A.; Roman, R.; Nicolov, M.; Ledeti, I.; Szabadai, Z.; Avram, N. M. DFT Calculation of Vibrational Frequencies for Betulinic Acid Methanol Monosolvate; Heidelberg, Germany, **2017**, *1796*, 030012. https://doi.org/10.1063/1.4972377
(64) Radula-Janik, K.; Kupka, T.; Ejsmont, K.; Daszkiewicz, Z.; Sauer, S. P. A. DFT and Experimental Studies on Structure and Spectroscopic Parameters of 3,6-Diiodo-9-Ethyl-9H-Carbazole. *Struct. Chem.* **2016**, *27* (1), 199. https://doi.org/10.1007/s11224-015-0711-8
(65) Makkar, P.; Ghosh, N. N. A Review on the Use of DFT for the Prediction of the Properties of Nanomaterials. *RSC Adv.* **2021**, *11* (45), 27897. https://doi.org/10.1039/D1RA04876G
(66) Hafner, J. *Ab-Initio* Simulations of Materials Using VASP: Density-Functional Theory and Beyond. *J. Comput. Chem.* **2008**, *29* (13), 2044. https://doi.org/10.1002/jcc.21057
(67) Perdew, J. P.; Burke, K.; Ernzerhof, M. Generalized Gradient Approximation Made Simple. *Phys. Rev. Lett.* **1996**, *77* (18), 3865. https://doi.org/10.1103/PhysRevLett.77.3865
(68) Kresse, G.; Joubert, D. From Ultrasoft Pseudopotentials to the Projector Augmented-Wave Method. *Phys. Rev. B* **1999**, *59* (3), 1758. https://doi.org/10.1103/PhysRevB.59.1758
(69) Cusinato, L.; Martínez-Prieto, L. M.; Chaudret, B.; del Rosal, I.; Poteau, R. Theoretical Characterization of the Surface Composition of Ruthenium Nanoparticles in Equilibrium with Syngas. *Nanoscale* **2016**, *8* (21), 10974. https://doi.org/10.1039/C6NR01191H
(70) Martínez-Prieto, L. M.; Cano, I.; Márquez, A.; Baquero, E. A.; Tricard, S.; Cusinato, L.; del Rosal, I.; Poteau, R.; Coppel, Y.; Philippot, K.; Chaudret, B.; Cámpora, J.; van Leeuwen, P. W. N. M. Zwitterionic Amidinates as Effective Ligands for Platinum Nanoparticle Hydrogenation Catalysts. *Chem. Sci.* **2017**, *8* (4), 2931. https://doi.org/10.1039/C6SC05551F
(71) González-Gómez, R.; Cusinato, L.; Bijani, C.; Coppel, Y.; Lecante, P.; Amiens, C.; del Rosal, I.; Philippot, K.; Poteau, R. Carboxylic Acid-Capped Ruthenium Nanoparticles: Experimental and Theoretical Case Study with Ethanoic Acid. *Nanoscale* **2019**, *11* (19), 9392. https://doi.org/10.1039/C9NR00391F
(72) García-Antón, J.; Axet, M. R.; Jansat, S.; Philippot, K.; Chaudret, B.; Pery, T.; Buntkowsky, G.; Limbach, H.-H. Reactions of Olefins with Ruthenium Hydride Nanoparticles: NMR Characterization, Hydride Titration, and Room-Temperature C-C Bond Activation. *Angew. Chem. Int. Ed.* **2008**, *47* (11), 2074. https://doi.org/10.1002/anie.200704763
(73) Knickelbein, M. B. Electric Dipole Polarizabilities of Ni_{12-58}. *J. Chem. Phys.* **2001**, *115* (13), 5957. https://doi.org/10.1063/1.1398578
(74) Parks, E. K.; Nieman, G. C.; Kerns, K. P.; Riley, S. J. Reactions of Ni_{38} with N_2, H_2, and CO: Cluster Structure and Adsorbate Binding Sites. *J. Chem. Phys.* **1997**, *107* (6), 1861. https://doi.org/10.1063/1.474536
(75) Masuda, S.; Mori, K.; Sano, T.; Miyawaki, K.; Chiang, W.-H.; Yamashita, H. Simple Route for the Synthesis of Highly Active Bimetallic Nanoparticle Catalysts with Immiscible Ru and Ni Combination by Utilizing a TiO_2 Support. *ChemCatChem* **2018**, *10* (16), 3526. https://doi.org/10.1002/cctc.201800329
(76) Chen, S.; Wojcieszak, R.; Dumeignil, F.; Marceau, E.; Royer, S. How Catalysts and Experimental Conditions Determine the Selective Hydroconversion of Furfural and 5-Hydroxymethylfurfural. *Chem. Rev.* **2018**, *118* (22), 11023. https://doi.org/10.1021/acs.chemrev.8b00134
(77) Pirali, T.; Serafini, M.; Cargnin, S.; Genazzani, A. A. Applications of Deuterium in Medicinal Chemistry. *J. Med. Chem.* **2019**, *62* (11), 5276. https://doi.org/10.1021/acs.jmedchem.8b01808
(78) Mullard, A. FDA Approves First Deuterated Drug. *Nat. Rev. Drug Discov.* **2017**, *16* (5), 305. https://doi.org/10.1038/nrd.2017.89
(79) Prakash, G.; Paul, N.; Oliver, G. A.; Werz, D. B.; Maiti, D. C–H Deuteration of Organic Compounds and Potential Drug Candidates. *Chem. Soc. Rev.* **2022**, *51* (8), 3123. https://doi.org/10.1039/D0CS01496F
(80) Gruhn, R. Evidence Grows for Early Peopling of the Americas began more than 20,000 years ago. *Nature*. **2020**, *584* (7819), 47. https://doi.org/10.1038/d41586-020-02137-3
(81) Dong, J.; Wang, X.; Wang, Z.; Song, H.; Liu, Y.; Wang, Q. Formyl-Selective Deuteration of Aldehydes with D_2O *via* Synergistic Organic and Photoredox Catalysis. *Chem. Sci.* **2020**, *11* (4), 1026. https://doi.org/10.1039/C9SC05132E
(82) MacDonald, D.; Lu, P. Determination of DNA Structure in Solution: Enzymatic Deuteration of the Ribose 2' Carbon. *J. Am. Chem. Soc.* **2002**, *124* (33), 9722. https://doi.org/10.1021/ja026678r

(83) Földesi, A.; Trifonova, A.; Dinya, Z.; Chattopadhyaya, J. Total Synthesis of 2',3',4',5',5''-$^{2}H_5$-Ribonucleosides: The Key Building Blocks for NMR Structure Elucidation of Large RNA. *J. Org. Chem.* **2001**, *66* (20), 6560. https://doi.org/10.1021/jo010097n
(84) Sawama, Y.; Monguchi, Y.; Sajiki, H. AEcfcofuinctient H–D Exchange Reactions Using Heterogeneous Platinum-Group Metal on Carbon–H_2–D_2O System. *N. Y.* **2012**, *23* (7), 959. https://doi.org/10.1055/s-0031-1289696